

NASA/CP-1999-209692/VOL1/PT1



1998 NASA High-Speed Research Program Aerodynamic Performance Workshop

Volume I—Configuration Aerodynamics

Edited by
S. Naomi McMillin
Langley Research Center, Hampton, Virginia



December 1999

The NASA STI Program Office . . . in Profile

Since its founding, NASA has been dedicated to the advancement of aeronautics and space science. The NASA Scientific and Technical Information (STI) Program Office plays a key part in helping NASA maintain this important role.

The NASA STI Program Office is operated by Langley Research Center, the lead center for NASA's scientific and technical information. The NASA STI Program Office provides access to the NASA STI Database, the largest collection of aeronautical and space science STI in the world. The Program Office is also NASA's institutional mechanism for disseminating the results of its research and development activities. These results are published by NASA in the NASA STI Report Series, which includes the following report types:

- **TECHNICAL PUBLICATION.** Reports of completed research or a major significant phase of research that present the results of NASA programs and include extensive data or theoretical analysis. Includes compilations of significant scientific and technical data and information deemed to be of continuing reference value. NASA counterpart of peer-reviewed formal professional papers, but having less stringent limitations on manuscript length and extent of graphic presentations.
- **TECHNICAL MEMORANDUM.** Scientific and technical findings that are preliminary or of specialized interest, e.g., quick release reports, working papers, and bibliographies that contain minimal annotation. Does not contain extensive analysis.
- **CONTRACTOR REPORT.** Scientific and technical findings by NASA-sponsored contractors and grantees.

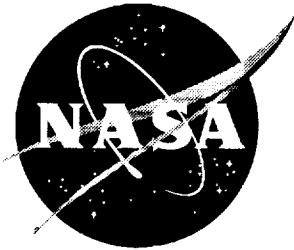
- **CONFERENCE PUBLICATION.** Collected papers from scientific and technical conferences, symposia, seminars, or other meetings sponsored or co-sponsored by NASA.
- **SPECIAL PUBLICATION.** Scientific, technical, or historical information from NASA programs, projects, and missions, often concerned with subjects having substantial public interest.
- **TECHNICAL TRANSLATION.** English-language translations of foreign scientific and technical material pertinent to NASA's mission.

Specialized services that complement the STI Program Office's diverse offerings include creating custom thesauri, building customized databases, organizing and publishing research results . . . even providing videos.

For more information about the NASA STI Program Office, see the following:

- Access the NASA STI Program Home Page at <http://www.sti.nasa.gov>
- Email your question via the Internet to help@sti.nasa.gov
- Fax your question to the NASA STI Help Desk at (301) 621-0134
- Telephone the NASA STI Help Desk at (301) 621-0390
- Write to:
NASA STI Help Desk
NASA Center for AeroSpace Information
7121 Standard Drive
Hanover, MD 21076-1320

NASA/CP-1999-209692/VOL1/PT1



1998 NASA High-Speed Research Program Aerodynamic Performance Workshop

Volume I—Configuration Aerodynamics

Edited by
S. Naomi McMillin
Langley Research Center, Hampton, Virginia

Proceedings of a workshop sponsored by the
National Aeronautics and Space Administration,
Washington, D.C., and held in
Los Angeles, California
February 9–13, 1998

National Aeronautics and
Space Administration

Langley Research Center
Hampton, Virginia 23681-2199

December 1999

Available from:

NASA Center for AeroSpace Information (CASI)
7121 Standard Drive
Hanover, MD 21076-1320
(301) 621-0390

National Technical Information Service (NTIS)
5285 Port Royal Road
Springfield, VA 22161-2171
(703) 605-6000

PREFACE

The High-Speed Research Program sponsored the NASA High-Speed Research Program Aerodynamic Performance Review on February 9-13, 1998 in Los Angeles, California. The review was designed to bring together NASA and industry High-Speed Civil Transport (HSCT) Aerodynamic Performance technology development participants in areas of: Configuration Aerodynamics (transonic and supersonic cruise drag prediction and minimization), High-Lift, and Flight Controls. The review objectives were to: (1) report the progress and status of HSCT aerodynamic performance technology development; (2) disseminate this technology within the appropriate technical communities; and (3) promote synergy among the scientist and engineers working HSCT aerodynamics. In particular, single- and multi-point optimized HSCT configurations, HSCT high-lift system performance predictions, and HSCT Motion Simulator results were presented along with executive summaries for all the Aerodynamic Performance technology areas. The HSR AP Technical Review was held simultaneously with the annual review of the following airframe technology areas: Materials and Structures, Environmental Impact, Flight Deck, and Technology Integration. Thus, a fourth objective of the Review was to promote synergy between the Aerodynamic Performance technology area and the other technology areas within the airframe element of the HSR Program.

The workshop was organized in three sections as follows:

- Section I Independent Sessions
- Section II Plenary Session
- Section III Executive Summaries

The work performed in the Configuration Aerodynamics element of the High-Speed Research Program during 1997 was presented in the following sessions:

- Analysis Methods and CFD Validation
- Viscous Drag Predictions and Testing Methods
- Aerodynamic Design Optimization Capability
- Nacelle/Diverter Design and Airplane Integration
- Configuration Assessments and Fundamental Studies
- Technology Integration (TI) Studies related to Configuration Aerodynamics
(CA / TI Joint Session)

The work performed in the High Lift (HL) element of the High-Speed Research Program during 1997 was presented in the following sessions:

- Concept Development
- Test Programs and Techniques
- Analytical Methods

The proceedings for the Aerodynamic Performance Annual Review are published in two volumes:

Volume I, Parts 1 and 2 Configuration Aerodynamics

Volume II High Lift

AP Review Chairperson: Naomi McMillin
NASA Langley Research Center

CONTENTS

Preface.....	iii
--------------	-----

Volume 1, Part 1 -- Configuration Aerodynamics

Configuration Aerodynamics ITD Summary	1
--	---

Propulsion Airframe Integration Working Group Summary	31
---	----

Analysis Methods and CFD Validation

Overview of Analysis Methods and CFD Validation	41
<i>Shreekant Agrawal, The Boeing Company</i>	

Cycle 2 Nonlinear Design Optimization Analytical Cross Checks	45
<i>Dan Bencze, NASA Ames Research Center</i>	

AIRPLANE Mesh Development with Grid Density Studies.....	75
<i>Susan Cliff and Scott Lawrence, NASA Ames Research Center, Timothy Baker, Princeton University, Scott Thomas and Mark Rimlinger, Sterling Software Inc.</i>	

High Reynolds Number Predictions for the Baseline Arrow Wing at Mach 2.48	147
<i>Melissa Rivers and Richard Wahls, NASA Langley Research Center</i>	

Applications of Parallel Processing in Configuration Analyses	171
<i>Pichuraman Sundaram and James Hager, The Boeing Company, and Robert Biedron, NASA Langley Research Center</i>	

TCA Full Configuration Performance and S&C Characteristics	205
<i>Grant Martin, Raul Mendoza, Paul Kubiato, and Shreekant Agrawal, The Boeing Company</i>	

Unstructured Grid Euler Method Assessment for Aerodynamic Performance Prediction of the Complete TCA Configuration at Supersonic Cruise Speed	287
<i>Farhad Ghaffari, NASA Langley Research Center</i>	

Unstructured Navier-Stokes Analysis of Full TCA Configuration	309
<i>Neal Frink and Shahyar Pirzadeh, NASA Langley Research Center</i>	

Viscous Drag Predictions and Testing Methods

Overview of Viscous Drag Predictions and Testing Methods	329
<i>Robert Kulfan, The Boeing Company</i>	

Skin Friction Drag Predictions: Summary of CFD Cross Checks, Wing/Body.....	333
<i>Scott Lawrence and Goetz Klopfer, NASA Ames Research Center</i>	

TCA and Symmetric Model Viscous Drag Predictions.....	355
<i>Max Kandula, Dynacs Engineering Co. Inc.</i>	

Feasibility Study of a TCA Symmetric Model for Accurate Skin-Friction Measurements	427
<i>Raul Mendoza and Pichuraman Sundaram, The Boeing Company</i>	

Historic Background on Flat Plate Turbulent Flow Skin Friction and Boundary Layer Growth.....	477
Robert Kulfan, <i>The Boeing Company</i>	
CA Testing Workshops: Process, Issues, Results.....	515
Robert Kennelly, <i>NASA Ames Research Center</i>	
High Reynolds Number Assessment of Boundary Layer Transition Trip Drag at Mach 2.48 on an HSCT Configuration	539
Richard Wahls and Melissa Rivers, <i>NASA Langley Research Center</i> , and Todd Magee and Michael Novean, <i>The Boeing Company</i>	
Experimental Bias and Precision Errors: Requirements, Analysis & Recommendations	571
Michael Novean and Todd Magee, <i>The Boeing Company</i>	
Aerodynamic Design Optimization Capability	
Overview of Aerodynamic Design Optimization Capability.....	621
Dan Bencze, <i>NASA Ames Research Center</i>	
BCAG Design Optimization Activities	625
Roy S. Conner, <i>The Boeing Company</i>	
SYN107-MB Aerodynamic Shape Optimization Method: Recent Improvements and Current Status	693
James Reuther, <i>RIACS</i> , Mark Rimlinger and David Saunders, <i>Sterling Software Inc.</i> , and Raymond Hicks, <i>MCAT</i>	
The AEROSHOP (AERodynamic Shape OPTimization) Toolkit.....	777
Eric Unger, Robert Narducci, James Hager, Peter Hartwich, Raul Mendoza, and Geojoe Kuruvila, <i>The Boeing Company</i>	
TCA6 Configuration Optimization.....	837
Raymond Hicks, <i>MCAT</i> , Mark Rimlinger, <i>Sterling Software Inc.</i> , and James Reuther, <i>RIACS</i>	

Volume 1, Part 2 -- Configuration Aerodynamics

Aerodynamic Design Optimization Capability - continued

Aerodynamic Gradients Using Three Methods.....	931
Geojoe Kuruvila, James Hager, and Pichuraman Sundaram, <i>The Boeing Company</i>	
CFD-Based Flap Optimization for the TCA in Transonic Flight Conditions	979
Robert Narducci, Eric Unger, David Yeh, Michael Novean, Pichuraman Sundaram, Todd Magee, Geojoe Kuruvila, Grant Martin, Alan Arslan, and Shreekant Agrawal, <i>The Boeing Company</i>	
Viscous Design of TCA Configurations	1043
Steven Krist, Steven Bauer, and Richard Campbell, <i>NASA Langley Research Center</i>	
Progress Towards a Multipoint Optimization Procedure.....	1071
Robert Narducci and Shreekant Agrawal, <i>The Boeing Company</i>	

Nacelle/Diverter Design and Airplane Integration

Overview of Nacelle/Diverter Design and Airplane Integration	1139
Francis Capone, <i>NASA Langley Research Center</i>	
Rigid Power Effects: Inlet Bleed, Spillage, and Bypass	1143
Mike Malone, Bryan Westra, Arsenio Dimanlig, Bill Bard, and Charlie Peavey, <i>Northrop Grumman</i>	
Propulsion Induced Effects (PIE) Test Program.....	1187
Gelsomina Cappuccio and Mark Won, <i>NASA Ames Research Center</i>	
Transonic Installed Nacelle Analyses.....	1241
Steve Chaney and Gordon Blom, <i>The Boeing Company</i>	
Nacelle Diverter Design and Nozzle Boattail Drag Studies	1365
Pichuraman Sundaram, Chih Shieh, Alan Arslan, Hoyt Wallace, and Shreekant Agrawal, <i>The Boeing Company</i>	

Configuration Assessments and Fundamental Studies

Overview of Configuration Assessments and Fundamental Studies.....	1457
Doug Wilson, <i>The Boeing Company</i>	
Model 2b Test Results.....	1461
Aga Goodsell, <i>NASA Ames Research Center</i>	
Nonlinear Cruise-pt. Validation (NCV) Model Wind Tunnel Test Summary and Posttest Analysis.....	1505
Kevin Mejia, <i>The Boeing Company</i>	
Aftbody Closure Model Design - Lessons Learned.....	1545
Francis Capone, <i>NASA Langley Research Center</i>	
HSR Model Deformation Measurements from Subsonic to Supersonic Speeds	1569
Al Burner, Gary Erickson, Wes Goodman, and G. Flemming, <i>NASA Langley Research Center</i>	
The Effect of Aeroelasticity on the Aerodynamic Performance of the TCA.....	1589
Geojoe Kuruvila, Peter Hartwich, and Myles Baker, <i>The Boeing Company</i>	
Initial TCA Stability and Control Assessment.....	1649
David Blake, Paul Glessner, Paul Kubiatico, Brian Nishida, and Douglas Wilson, <i>The Boeing Company</i>	
Initial Predictions of Canard Integration	1671
Todd Magee, James Hager, and David Yeh, <i>The Boeing Company</i> , and Tim Haynes, <i>Dynacs Engineering Co. Inc.</i>	

Technology Integration (TI) Studies related to Configuration Aerodynamics (CA / TI Joint Session)

Overview of Technology Integration Activities Related to Configuration Aerodynamics.....	1757
Chester Nelson, <i>The Boeing Company</i>	

Cross-Discipline Evaluation of Optimized Designs and Features	1777
Chris Vegter and Greg Stanislaw, <i>The Boeing Company</i>	
TRANAIR Applications for Technology Integration Propulsion Trades.....	1797
Paul Dees, <i>The Boeing Company</i>	
CFD Data Generation Process for Nonlinear Loads	1817
Alan Arslan, Todd Magee, Eric Unger, Peter Hartwich, Shreekant Agrawal, Joseph Giesing, and Bala Bharadvaj, <i>The Boeing Company</i> , and Neal Chaderjian and Scott Murman, <i>NASA Ames Research Center</i>	

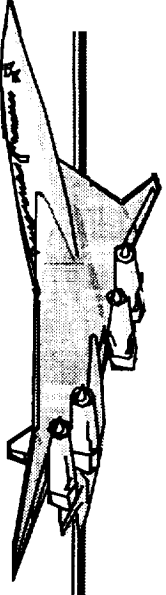
Volume 2 -- High Lift

High Lift ITD Summary	1873
Concept Development	
TCA High Lift Preliminary Assessment	1897
Paul Meredith, Gregory Wyatt, Mike Elzey, John Tran, David Yeh, and Ryan Polito, <i>The Boeing Company</i>	
TCA Planform and Leading-Edge Study at High-Lift Conditions	1933
David Yeh and Roger Clark, <i>The Boeing Company</i>	
Prediction of High-Lift Characteristics of the Preliminary Technology Concept (PTC)	2005
Keith Ebner, <i>The Boeing Company</i>	
Correlation of CFD Calculations and Wind Tunnel Measurements for the M2.4-7A Arrow Wing Configuration	2055
C. J. Woan, <i>The Boeing Company</i>	
Test Programs and Techniques	
4% Arrow Wing Model Test in NASA Ames 12 Ft. Pressure Tunnel	2107
Robin Edwards, Ryan Polito, and Roger Clark, <i>The Boeing Company</i>	
Power Effects on the High-Lift S & C Characteristics of the TCA Model Tested in the LaRC 14x22 Wind Tunnel	2161
Paul Glessner, <i>The Boeing Company</i>	
Assessment of Boundary-Layer Transition Detection and Fixing Techniques	2187
Marvine Hamner and Roger Clark, <i>The Boeing Company</i>	
Experimental Study of Static and Dynamic Ground Effects for Low Aspect Ratio Wings	2233
Lewis Owens, <i>NASA Langley Research Center</i> , Arthur Powell, <i>The Boeing Company</i> , and Robert Curry, <i>NASA Ames Research Center</i>	
Analytical Methods	
Potential Flow Analysis of Dynamic Ground Effect.....	2299
Winfried Feifel, <i>The Boeing Company</i>	

Dynamic Ground Effects Simulation Using OVERFLOW-D	2387
Bill Dwyer, <i>Northrop Grumman</i>	
Recent Results in the Study of Static Ground Effect Using an Inviscid Unstructured Grid Code	2471
Steve Yaros, <i>NASA Langley Research Center</i>	
Potential Flow Analysis of the Mark-XVI Flow Survey Probe	2509
Eric Roth, <i>The Boeing Company</i>	
Aerodynamic Design of Inboard Sealed Slats for the TCA-3 Wind Tunnel Test.....	2545
Robert Griffiths, <i>The Boeing Company</i>	
Navier-Stokes Results for HSCT High-Lift Configurations	2585
Anthony Saladino, <i>Dynacs Engineering Co. Inc.</i> , and Allen Chen, <i>The Boeing Company</i>	
Code Calibration Applied to the TCA High-Lift Model in the 14x22 Wind Tunnel (Simulation With and Without Model Post-Mount).....	2691
Wendy Lessard, <i>NASA Langley Research Center</i>	
Aerodynamic Analysis of TCA Wing/Body/Nacelle High-Lift Configurations	2735
Xuetong Fan and Paul Hickey, <i>ASE Technologies, Inc.</i>	
Canard Integration for CFD Analysis of HSCT High Lift Configurations	2765
David Yeh, <i>The Boeing Company</i>	
Comparison of CFL3D Results using Alternative Grid Interfacing Schemes	2831
Xuetong Fan and Paul Hickey, <i>ASE Technologies, Inc.</i>	

HSR

High Speed Research



HSR Airframe Technical Review

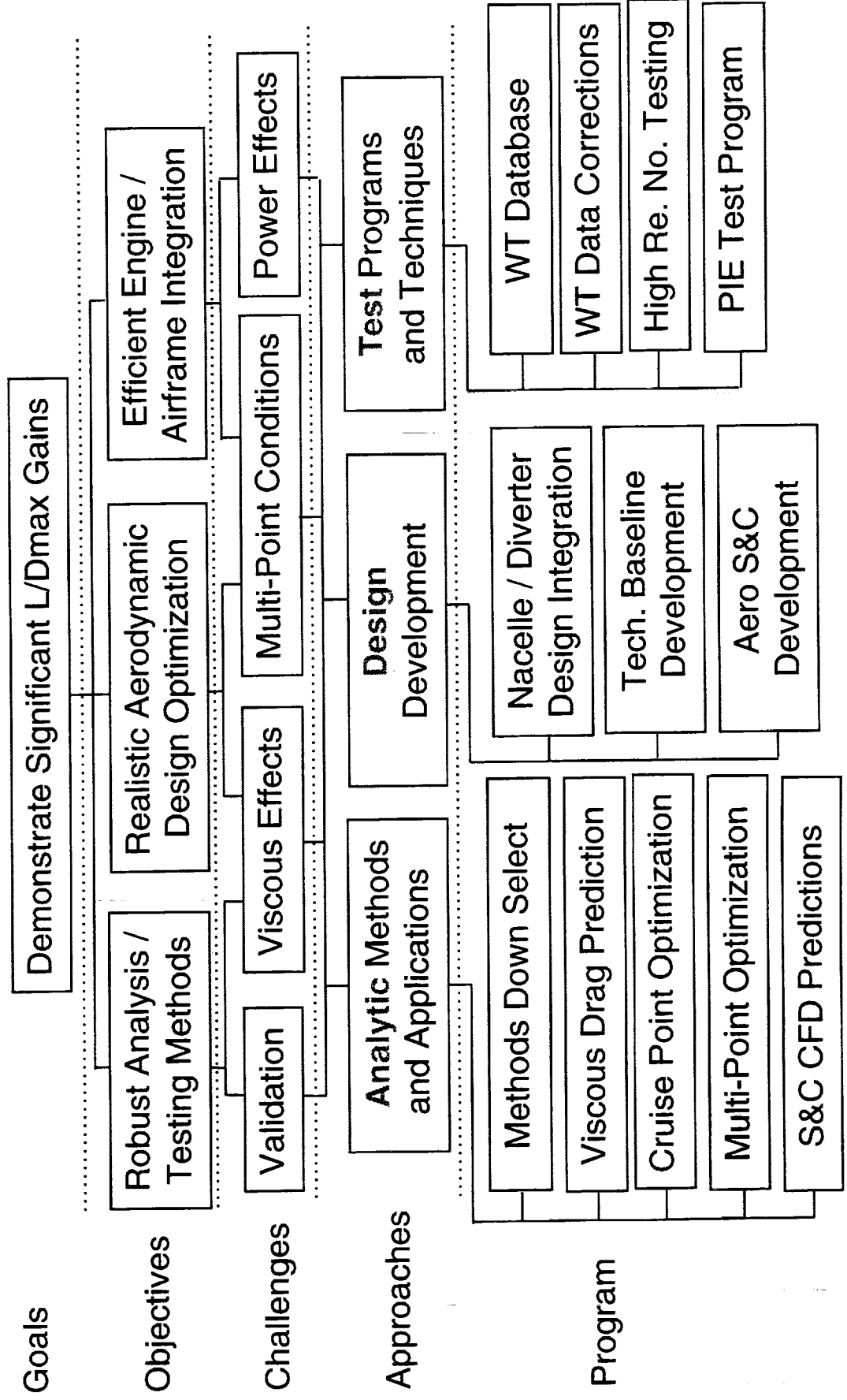
Configuration Aerodynamics ITD Team

Douglas L. Wilson
The Boeing Co.

February 9 - 13, 1998
Los Angeles, CA

Configuration Aerodynamics Technology Development

Program Selects Best Analysis / Design Optimization Methods



Configuration Aerodynamics ITD Team Membership

- Doug Wilson - Team Leader Boeing - Seattle
- Francis Capone NASA - Langley
- Dan Bencze NASA - Ames
- Shreekant Agrawal Boeing - Long Beach
- Bob Kulfan Boeing - Seattle

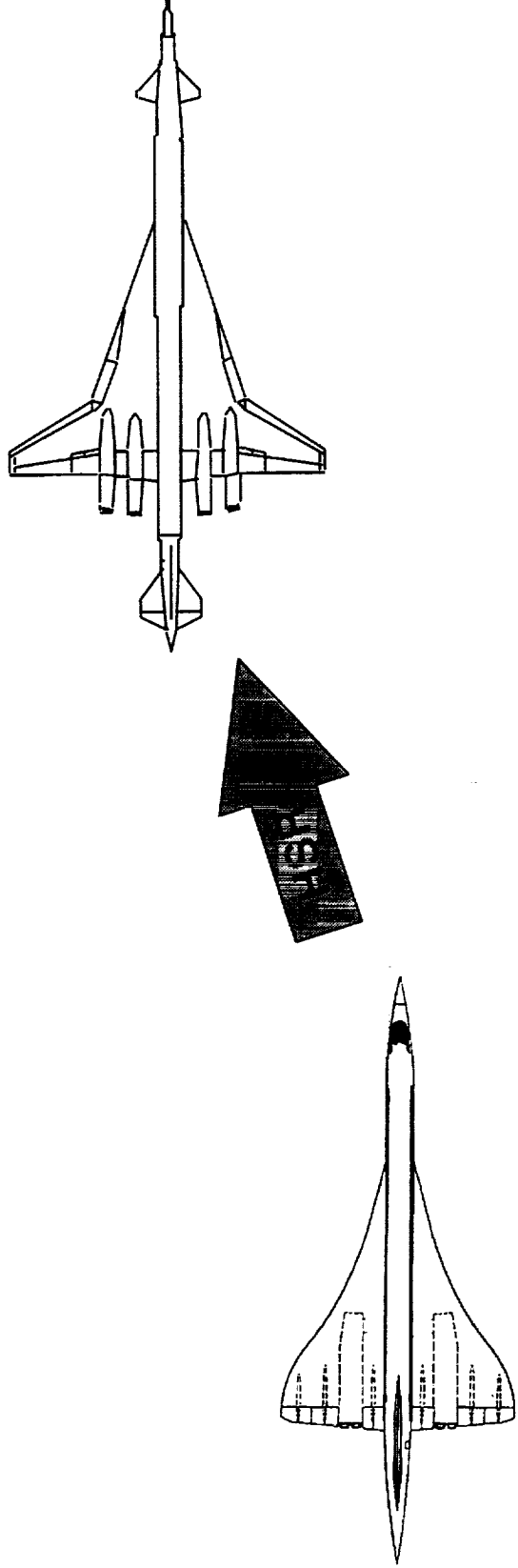
- Chet Nelson - TI Rep Boeing - Seattle

Goals

Significant Improvement in L/D Relative to Concorde Technology

- 25% Improvement in supersonic cruise L/D
- 80% Improvement in subsonic cruise L/D

(relative to Concorde technology)



Program Objectives

Develop and Demonstrate Robust Methods and Projections

Objectives:

- **Robust, validated aerodynamic analysis methods**
- **Robust aerodynamic design optimization methods for realistic configurations**
- **Efficient engine/airframe integration methods**
- **Realistic aerodynamic performance projections**

Technical Challenges

HSR is Pushing the Limits in Aerodynamics and Optimization

- **Variation in prediction of viscous effects**
- **CFD validation only possible at low Reynolds Number (esp. Supersonic)**
- **Large, highly constrained design optimization problems require new methods, extensive computational resources**
- **Multi-point design approaches are untested**
- **Power effects are costly to simulate or test**

Approach

Design, Analysis, and Testing Methods Advance Together

Design Optimization:

- starts from baseline configuration
- depends on validated analysis tools

Analysis Methods:

- address specific issues--
viscous drag
aft-body flow
full configuration/S&C predictions
nacelle/airframe integration

Wind-Tunnel Testing:

- validates analysis methods
- builds understanding
- develops test techniques
- establishes correction methods

**Meet
Goals
&
Objectives**

Major Accomplishments, FY '97

Progress--and a Few Surprises

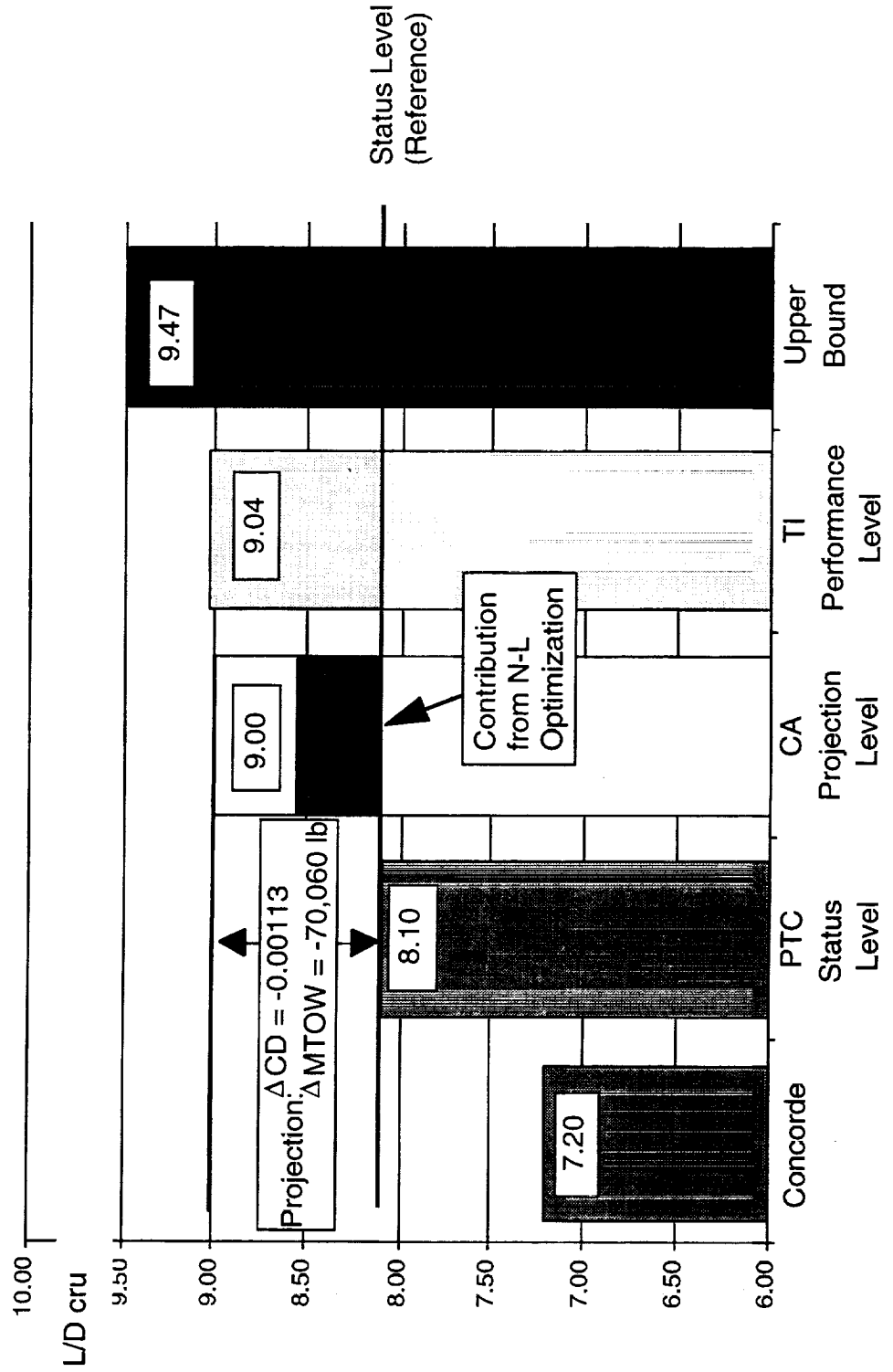
- **MS 3-3 Non-Linear Cruise Point Design Optimization
Cycle 2 design
analytical CFD methods cross-checks
experimental validation**
- **MS 3-4 Multi-Point Design Formulation**
- **MS 4-6 Definition of TCA Nonlinear OML**
- **MS 4-10 Nozzle Design and Boattail Drag Assessment**
- **MS 4-2 Rigid Full-Configuration CFD Analysis**
- **MS 4-12,13 TCA Baseline Performance and S&C Assessment**
- **Transonic Flap Optimization**
- **High Re Supersonic Testing**
- **Nacelle/Airframe Integration & Inlet Flow Field Measurement**
- **Test Planning: PIE, Aft-body Closure**

Non-Linear Cruise Point Design Optimization

Non-Linear Optimization Accounts for ~1/2 of Projection

L/D Projections for: PTC Configuration

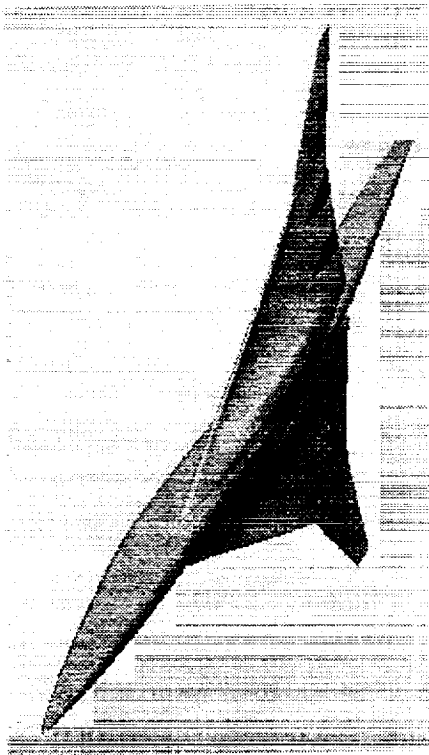
Mach = 2.4 CL = 0.092



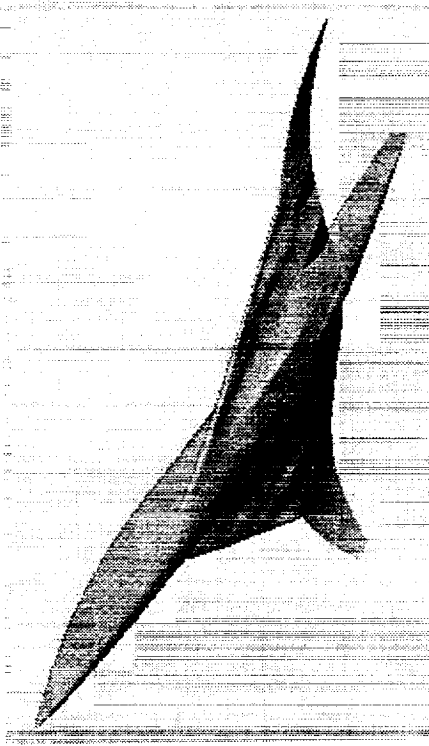
Non-Linear Cruise Point Design Optimization

Designs Differed, But All Improved Performance

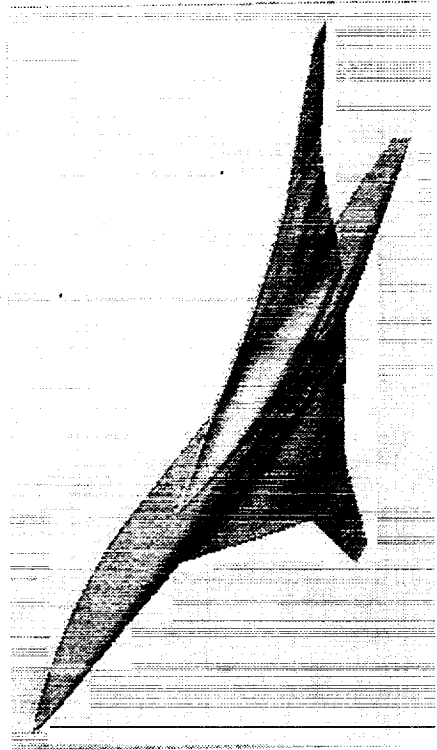
TCA Baseline



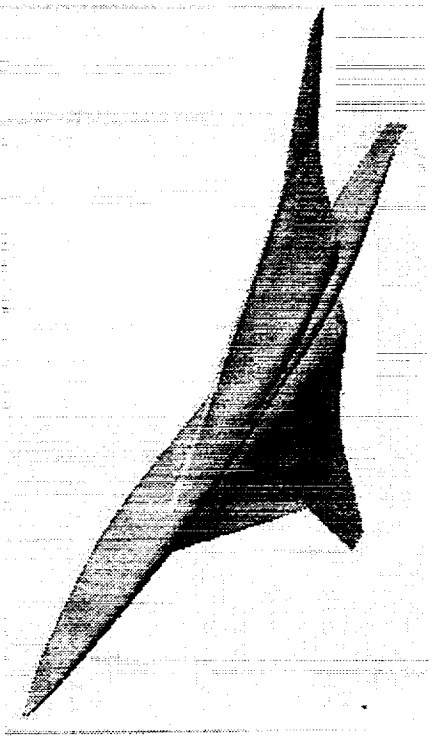
BCA Design



Ames Design

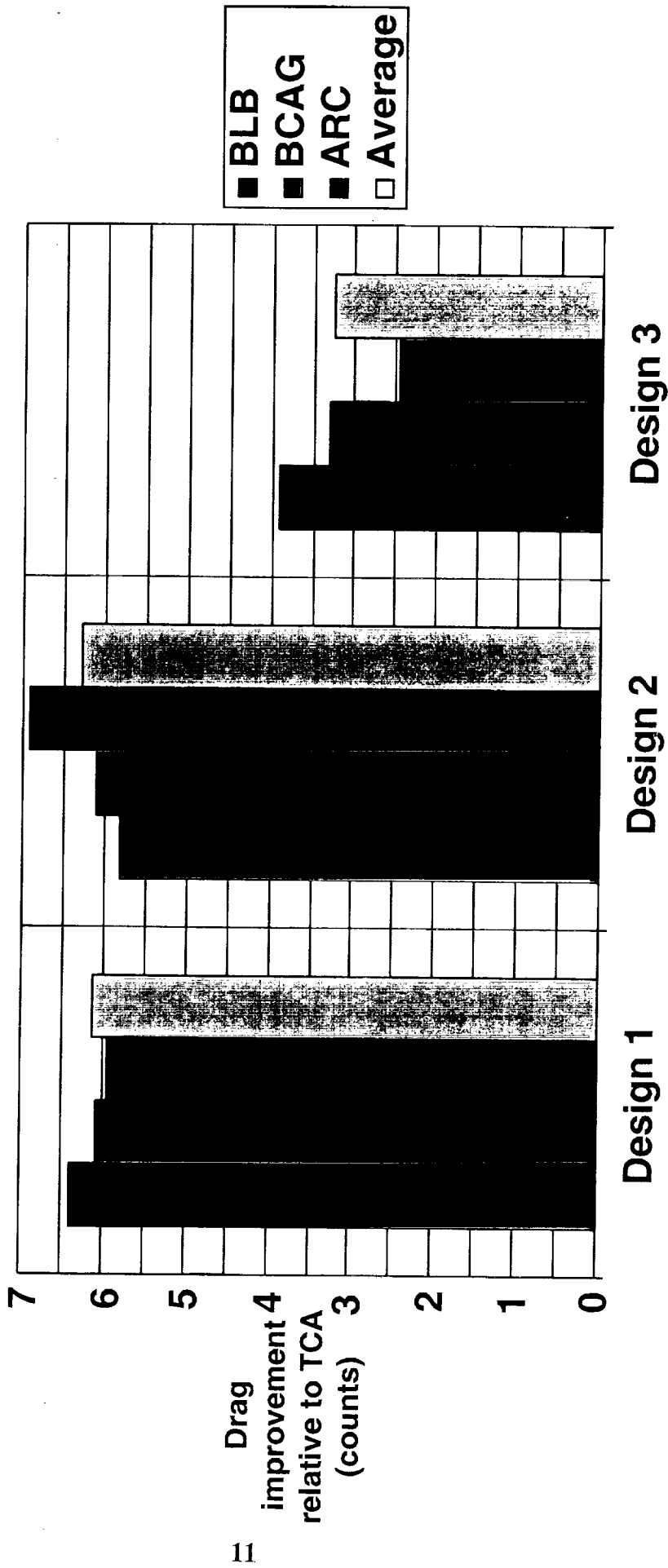


BLB Design



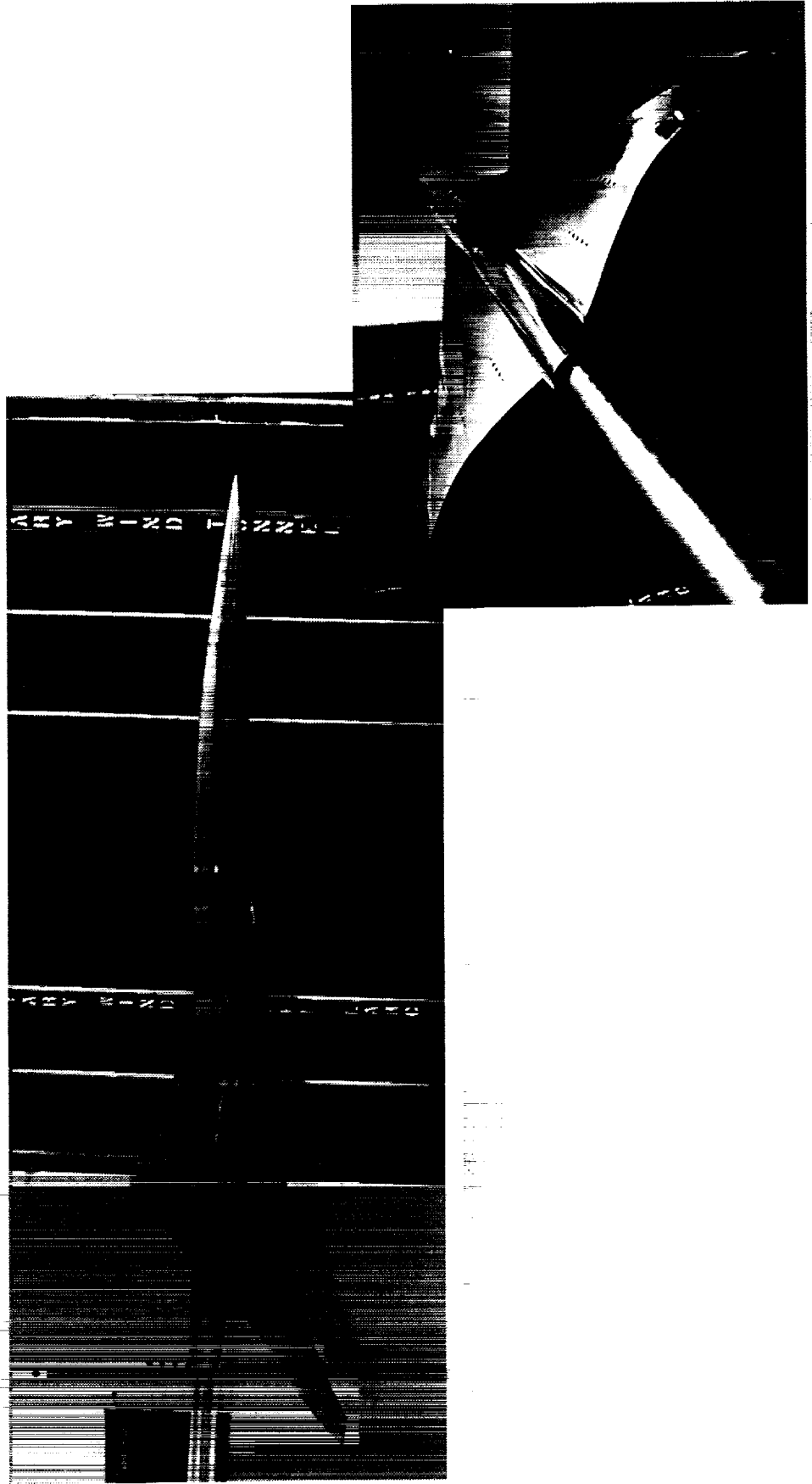
Non-Linear Cruise Point Design Optimization

Various N-S CFD Codes Agreed on Performance Improvements



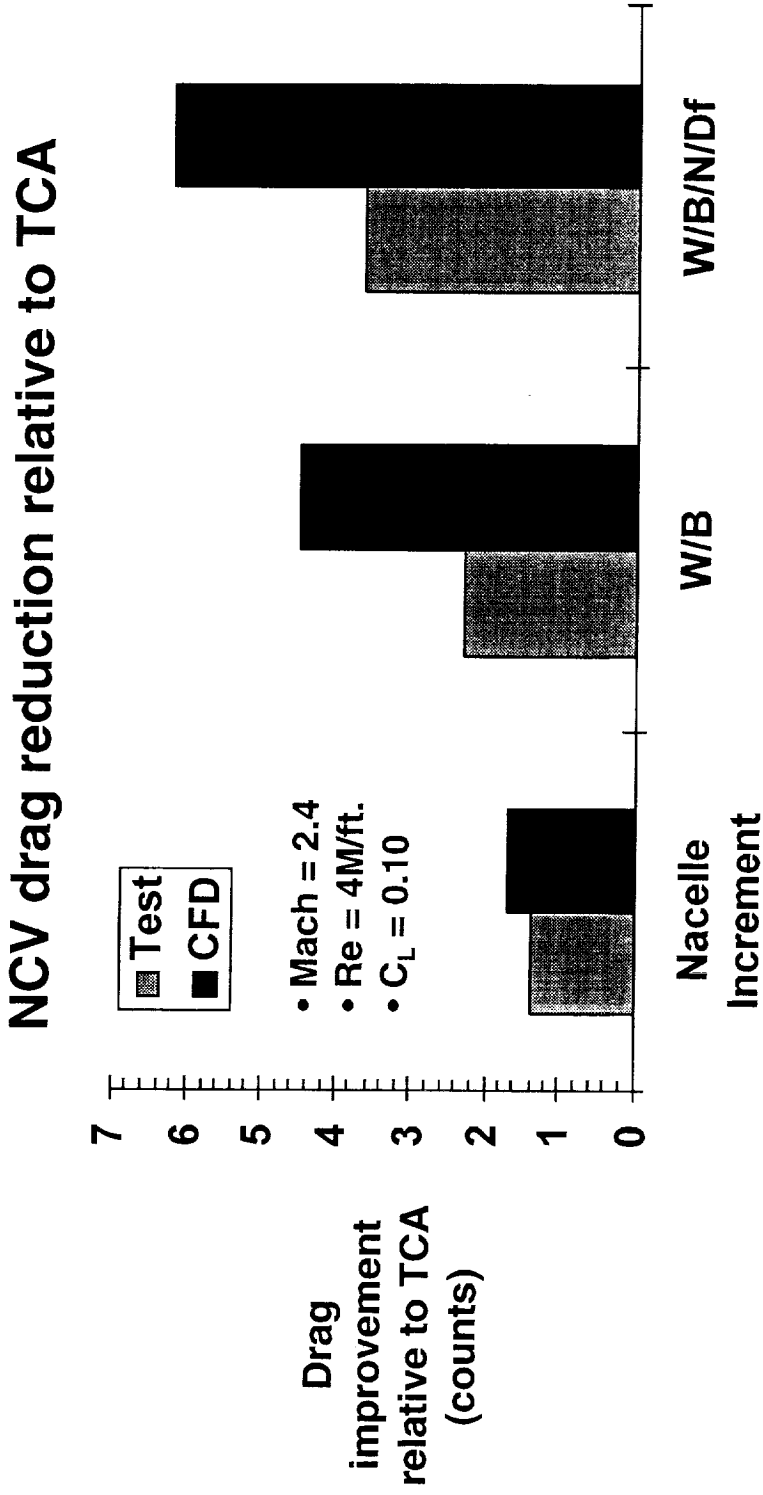
Non-Linear Cruise Point Design Optimization

One Optimized Design Was Selected for Experimental Validation.



Non-Linear Cruise Point Design Optimization

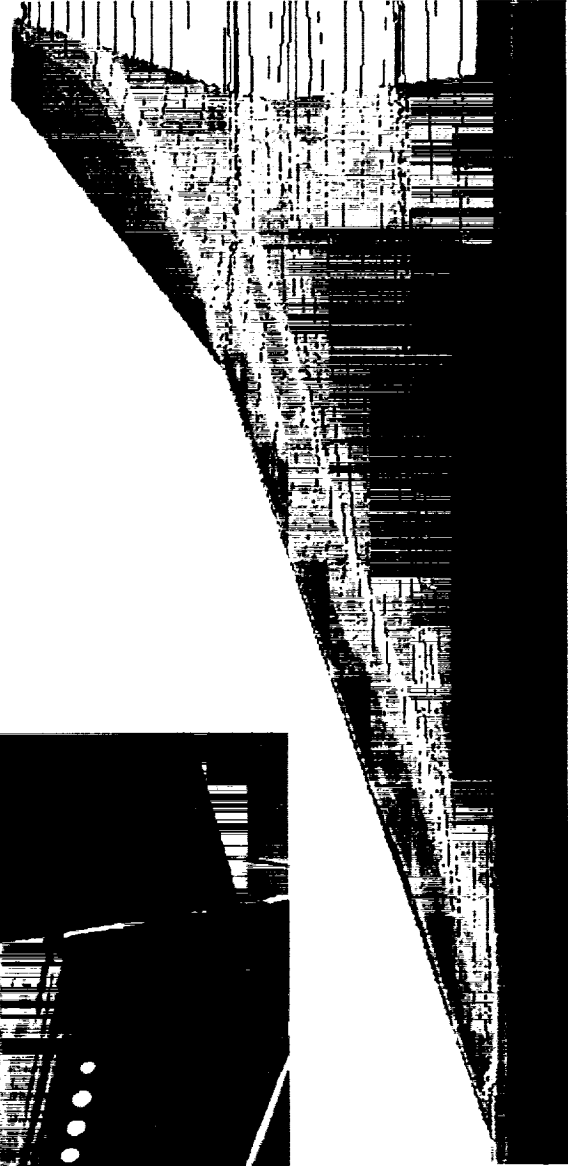
Wind-Tunnel Test Did Not Show Predicted Performance Gain



- Test conducted in LaRC UPWT (low Reynolds Number)
- Follow-on test at higher Re scheduled in BSWT 2/98

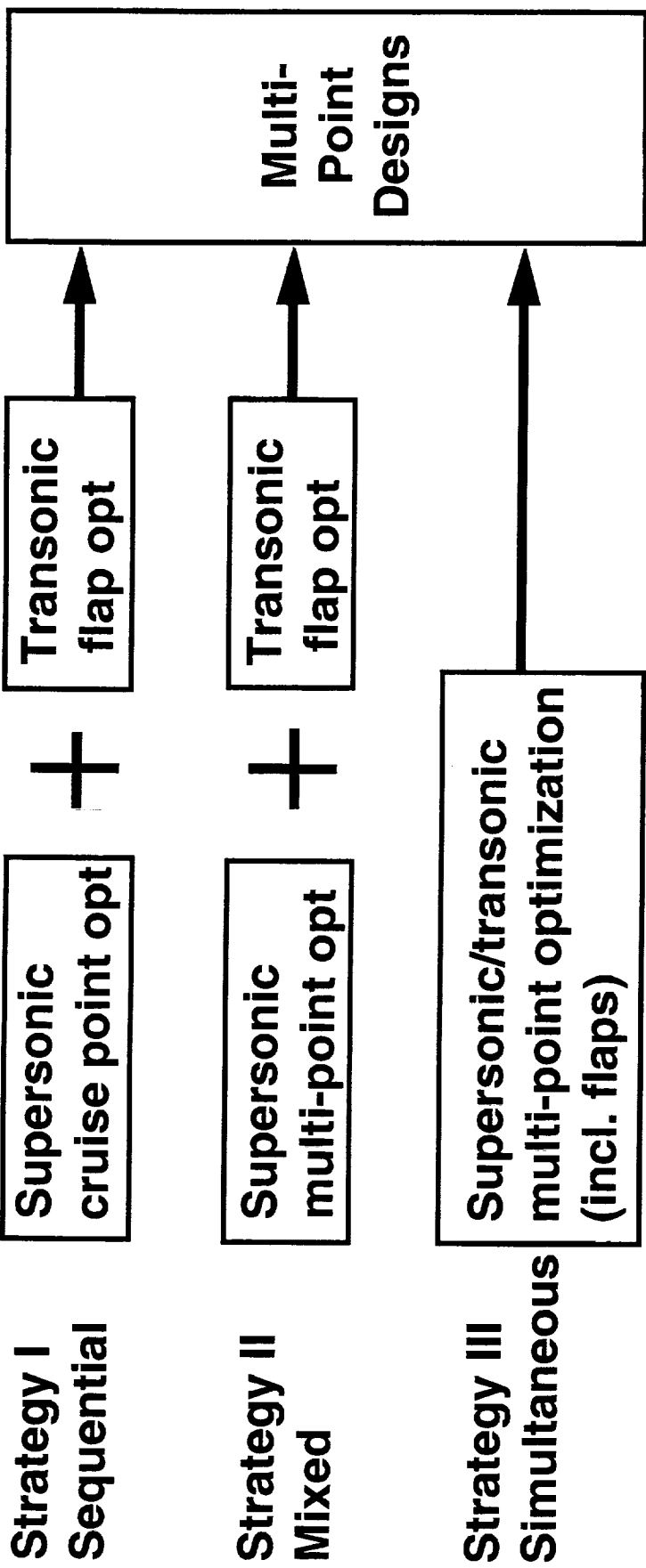
Non-Linear Cruise Point Design Optimization

CFD Predictions Did Not Agree With Observed Surface Flow



Multi-Point Design Formulation

Milestone 3-4 Discussions Guided FY98+ Plans (PCD Update)



Issues:

- Aeroelastics
- Trim, thrust
- 3-Surface configurations
- Viscous flow

TCA Baseline Performance, S&C

Wind Tunnel Tests Confirmed Status Performance Levels

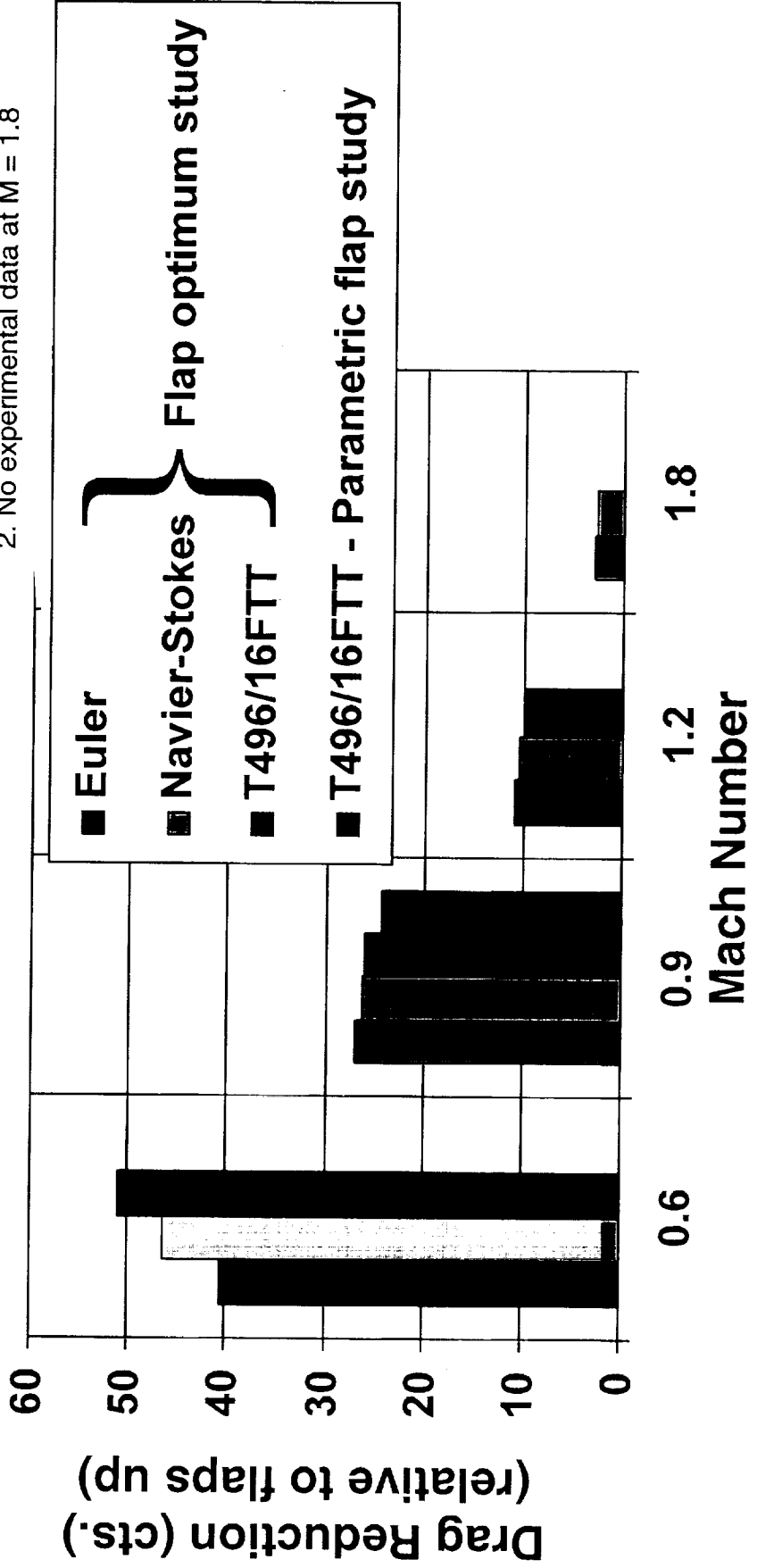
- **3 TCA models tested:**
 - 1.675% solid wing**
 - 1.675% flapped-wing**
 - 1.5% controls model with tail**
- **Foundation for performance and S&C assessments**
- **Baseline for design optimization work**
- **Status levels used in TI buildups confirmed**
- **Longitudinal stability a concern**

Transonic Flap Optimization

Predicted Performance Increments Validated in Wind Tunnel

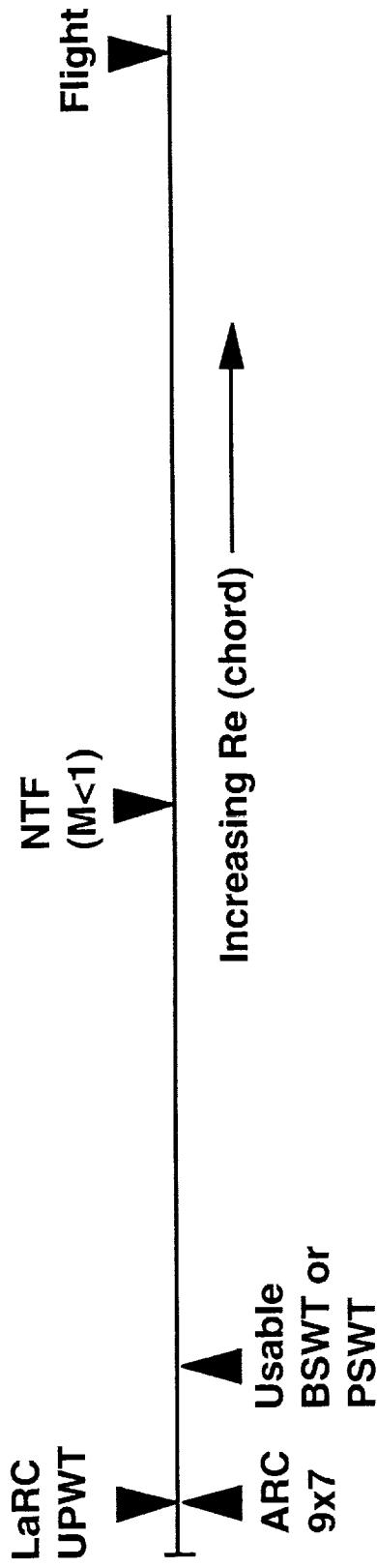
- Automated optimization applied for first time to flap deflections
- Inviscid optimization method appeared to give proper flap deflection

Note: 1. Only outboard leading and trailing edge flaps deflected for experimental parametric study
 2. No experimental data at $M = 1.8$



High Reynolds Number Supersonic Testing

High-Re Industry Blowdown Facilities Promising, but Enough Re?



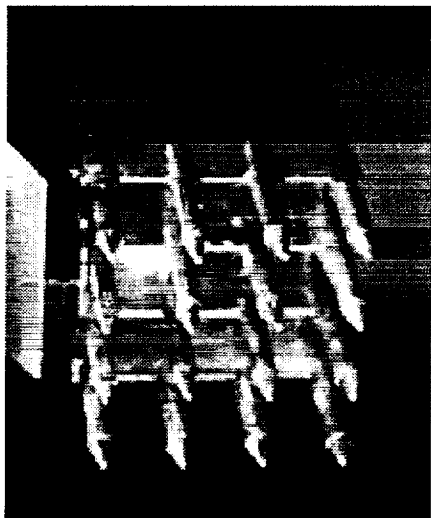
- 2 tests conducted in Boeing PSWT (St. Louis)
- Upcoming NCV test in Boeing BSWT (Seattle)
- Limitations on usable Re due to model/sting loads
- Natural transition achievable with baseline design--
optimized designs may require higher Reynolds Number

Nacelle/AF Integration & Inlet Flow Field

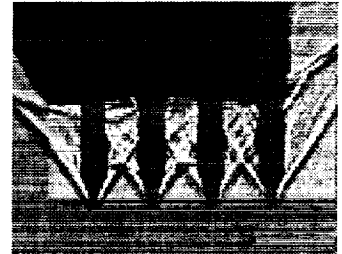
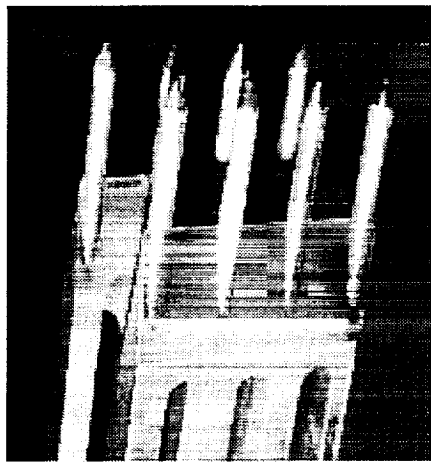
Flow Probes Developed to Measure Inlet Flow Conditions

5-Hole Flow Field Rake Configurations

Original Configuration



Revised Configuration



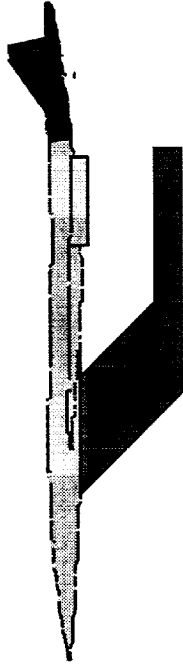
M=2.15

Test Planning Activities

Up-Front Work Is Crucial for Successful Test Programs

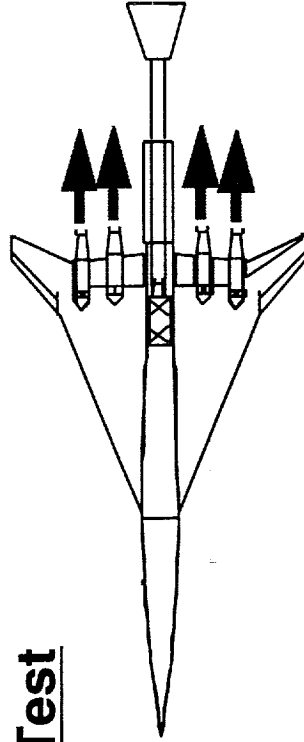
Aft-Body Closure Test

- Closure, Trim Drag
- Control Effectiveness
- CFD Validation
- Start ~ 4/98



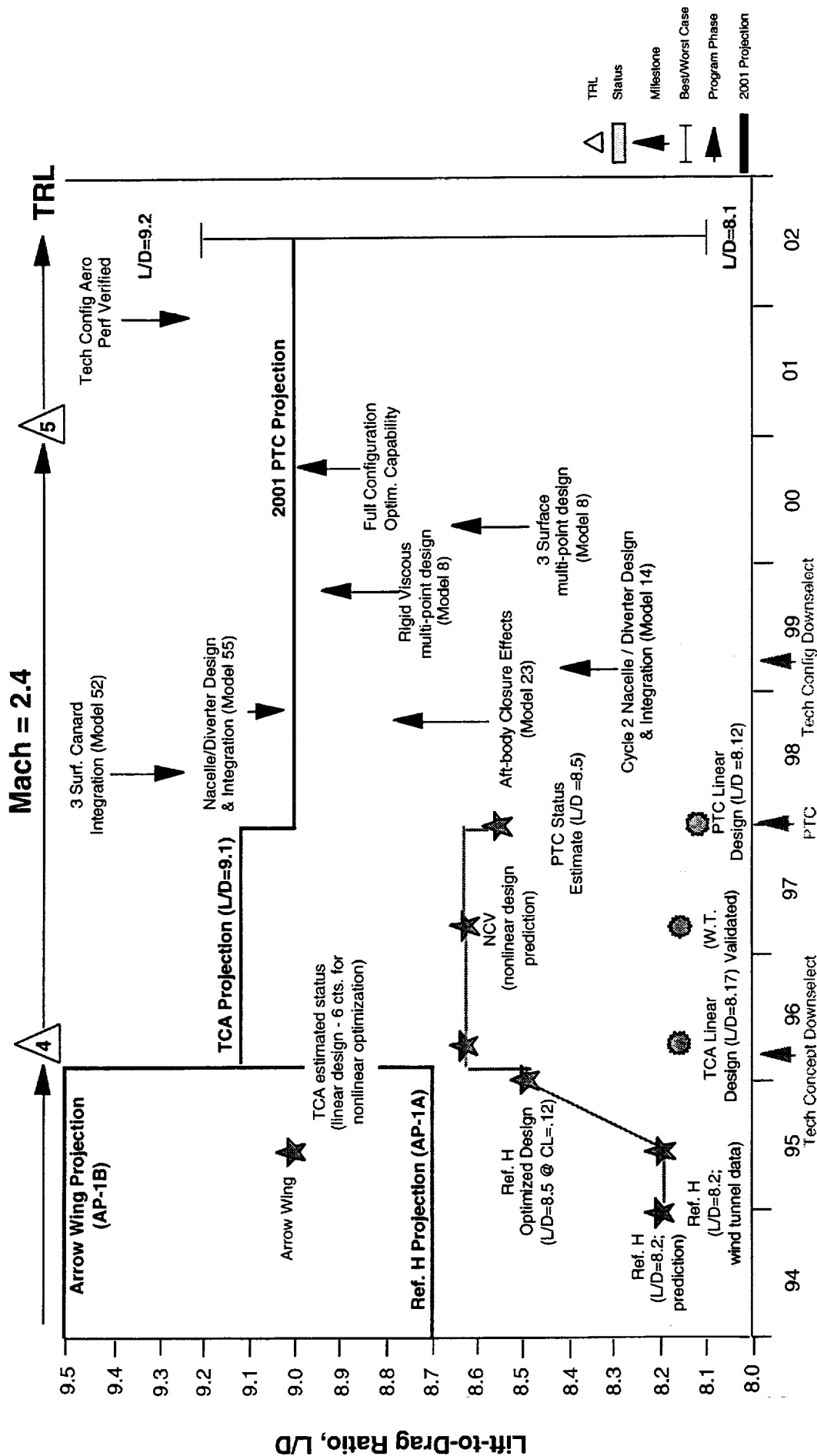
Propulsion-Induced Effects (PIE) Test

- Spillage, Bypass, Jet Effects
- CFD Validation
- Start ~ 1/00



AP-1 Metric

Supersonic L/D Metric

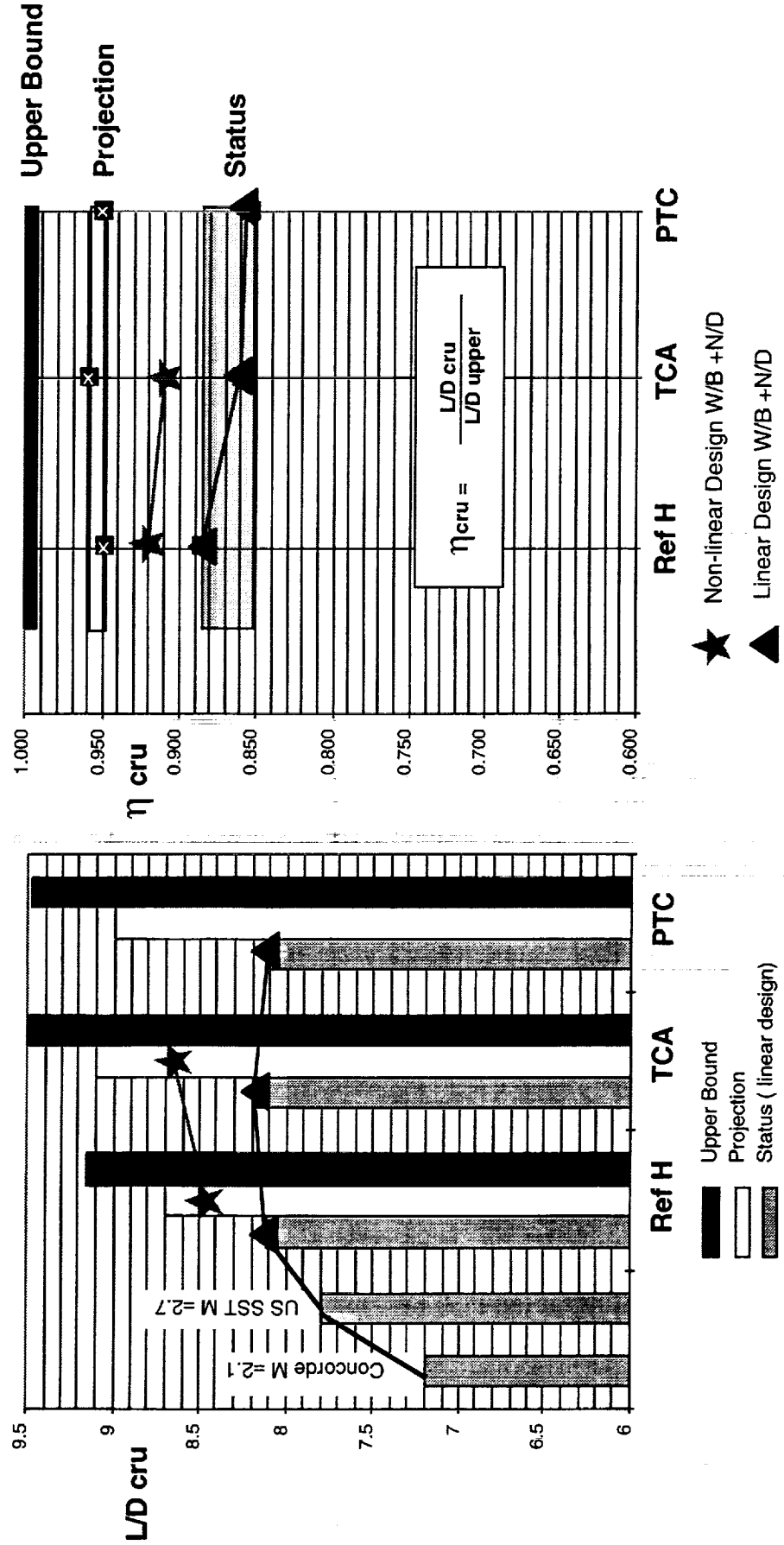


Configuration Aerodynamics - Supersonic Metric

Supersonic Cruise L/D Projection Based on ~ 95% of Upper Bound

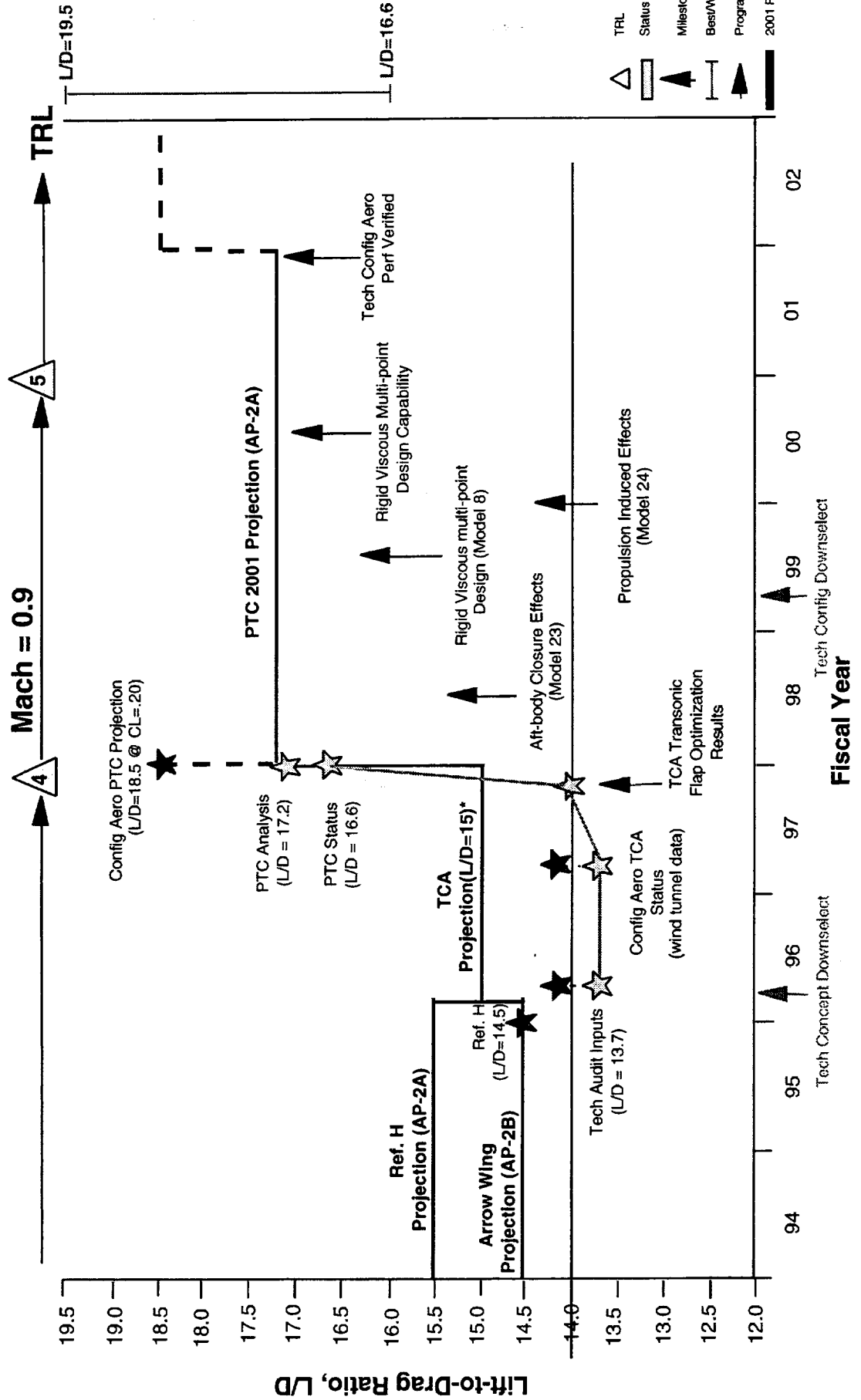
Aerodynamic Design Efficiency Comparisons

HSCT: Mach = 2.4



AP-2 Metric

Sub/Transonic L/D Metric

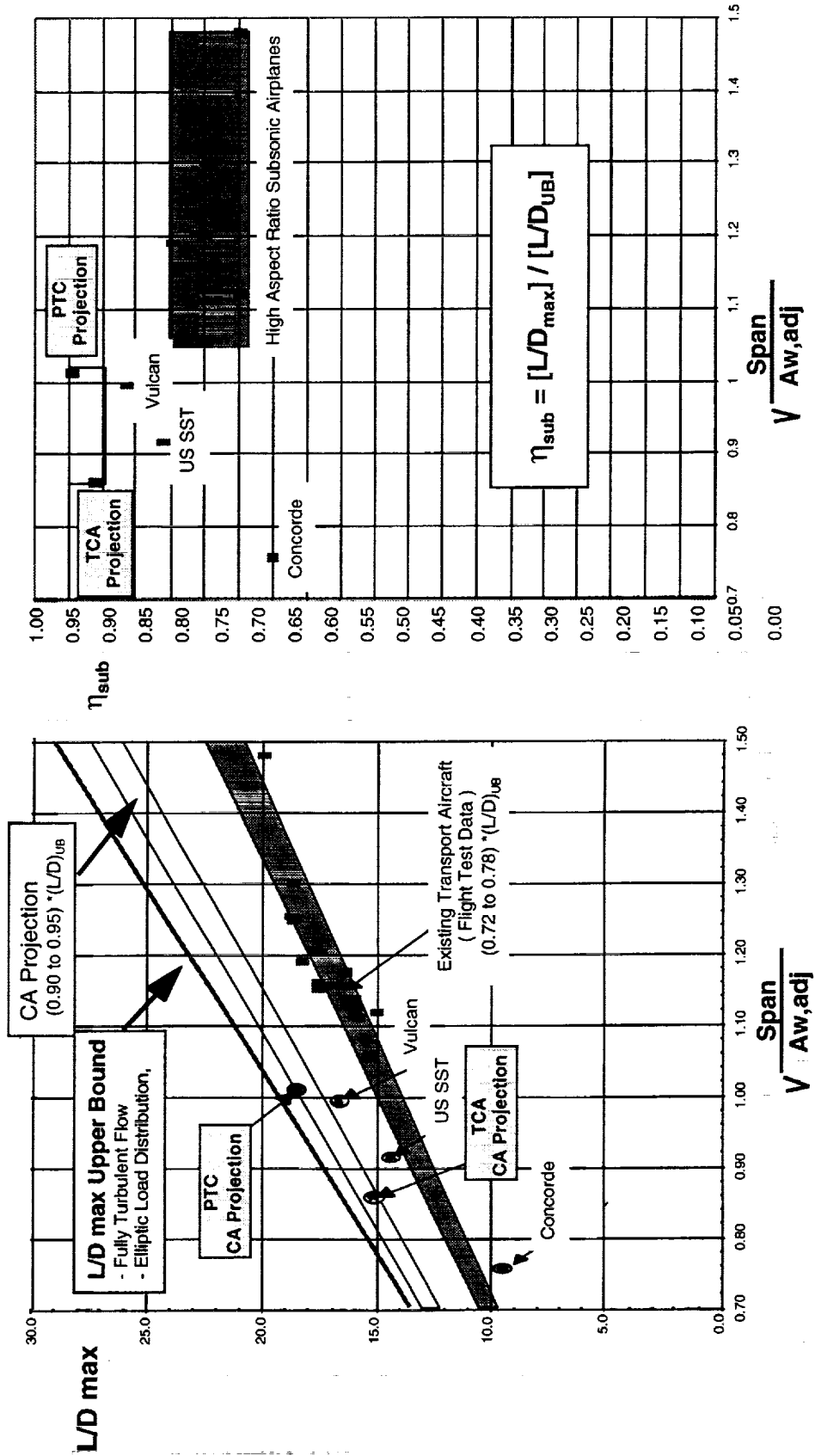


Configuration Aerodynamics - Subsonic Metrics

Subsonic Cruise L/D Projection Is Consistent With Trends

Subsonic Transport Aircraft L/D max Potential

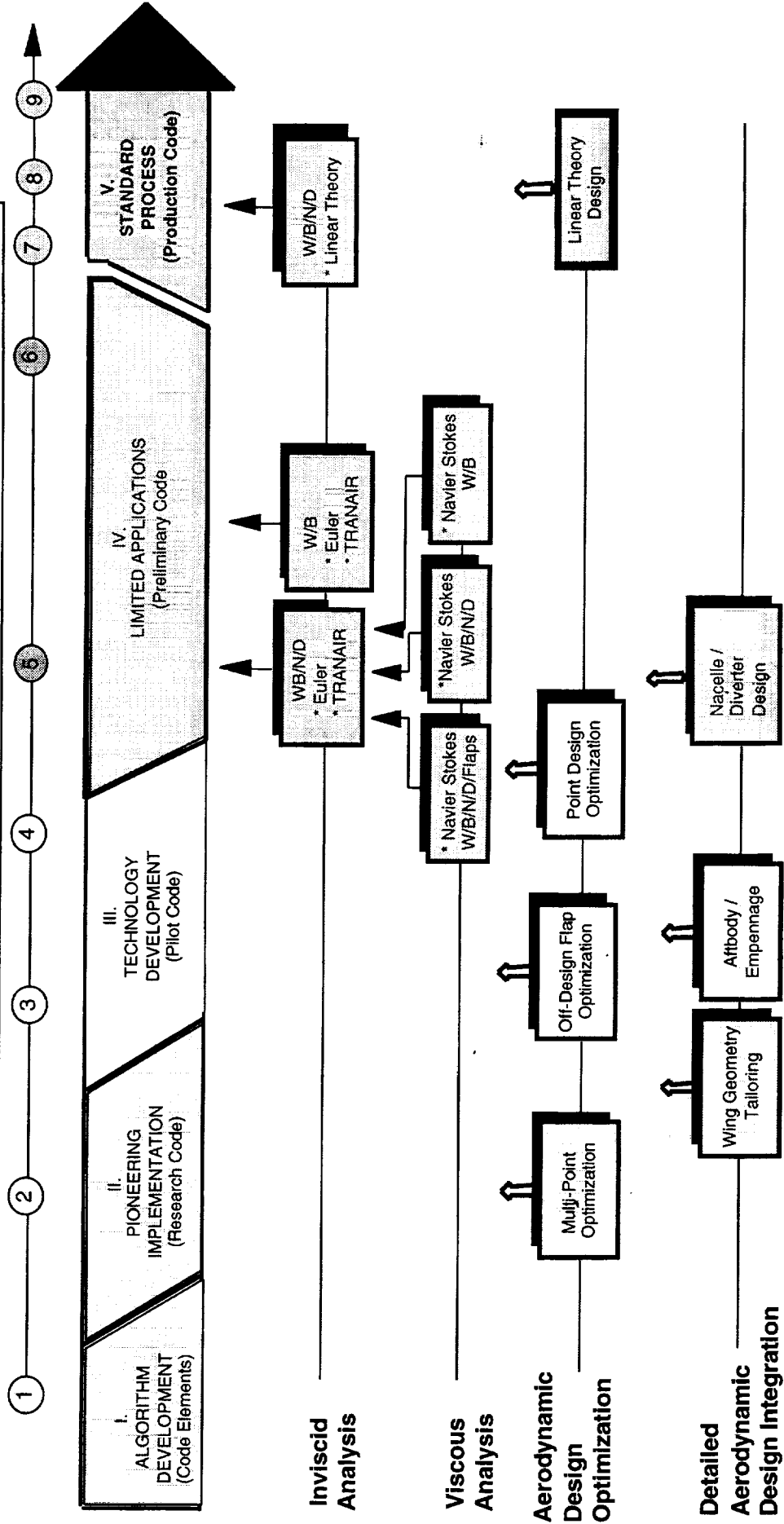
HSCT: Mach = 0.9



Configuration Aerodynamics--Metrics

TRL 6 on Methods Means We Believe the Answer, but Not Robust

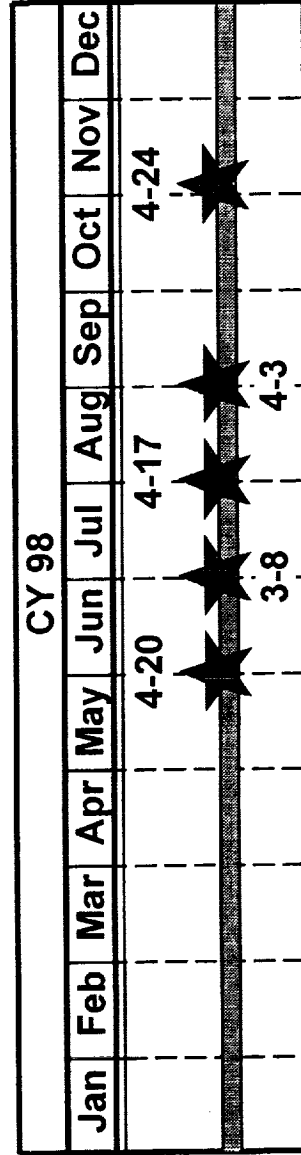
1998 HSCT CFD DEVELOPMENT STATUS



CY98 Milestones

'98 Activities Support '98 and Future Milestones

- MS 4-17** Transonic Analysis Methods (supports MS 3-3)
- MS 4-24** Testing Methods for Performance Predictions
- MS 4-20** Rigid Flap Optimization
- MS 4-3** Initial Propulsion Induced Effects
- MS 3-8** TCA Assessment



CY98 Technical Approach

Strong Focus on Viscous Drag, 3-Surface, Aftbody, PIE Configurations

- **Analysis & Test Methods:**
 - Viscous drag--symmetric model test
 - Trip drag test and correction methods
 - Aft-body flow analysis and test
 - Full configuration/S&C predictions
 - Analysis of TU-144 data
 - 3-surface analysis methods and validation test
- **Design Activities:**
 - Multi-point design
 - Viscous flap optimization
 - 3-surface cruise point design
- **Nacelle/Diverter Design & Integration Activities:**
 - Nacelle inlet flow field measurements
 - 2-D Inlet and optimized nacelle design and test
 - PIE test analysis and hardware fabrication

CY98 Technical Approach

Much Wind Tunnel Testing Still Remains

	1997			1998												1999						
	O	N	D	J	F	M	A	M	J	J	A	S	O	N	D	J	F	M	A	M	J	
Analysis and Test Methods																						
- Viscous Drag - Symmetric model															NTF N					PST ▼		▲ UPWT
- Trip Drag Test and Corrections																	UPWT ▲					
- NCV at High Re																						
- Aftbody Closure																						
Nacelle Diverter Design and Airplane Integration Activities																						
- Inlet Flow Field Measurements																						
- 2D Inlet and Optimized Nacelle																						
- PIE Nacelle Calibration Tests																						
Configuration Assessments and Fundamental Studies																						
- Canard Integration Test																						
- Rounded Leading Edge Test																						
	O	N	D	J	F	M	A	M	J	J	A	S	O	N	D	J	F	M	A	M	J	

Conclusions & Issues

Overguideline Funding Required to Complete Program Through PCD3

High-value/urgent issues demanded attention:

- Viscous drag & trip drag issues
- 3-Surface configuration analysis and design
- Unexpected results of NCV validation test

Additional activities added to address above issues:

- Symmetric model test and analysis
- 3-surface analysis and validation test
- High Re, diagnostic tests of NCV

Planned activities in PIE, multi-point optimization delayed:

- PIE test starts ~1/00
- MP Full-Config Design Milestone 7/00

Program Review with TMT planned 4/98

This page is intentionally left blank.

Propulsion Airframe Integration Advisory Group Report

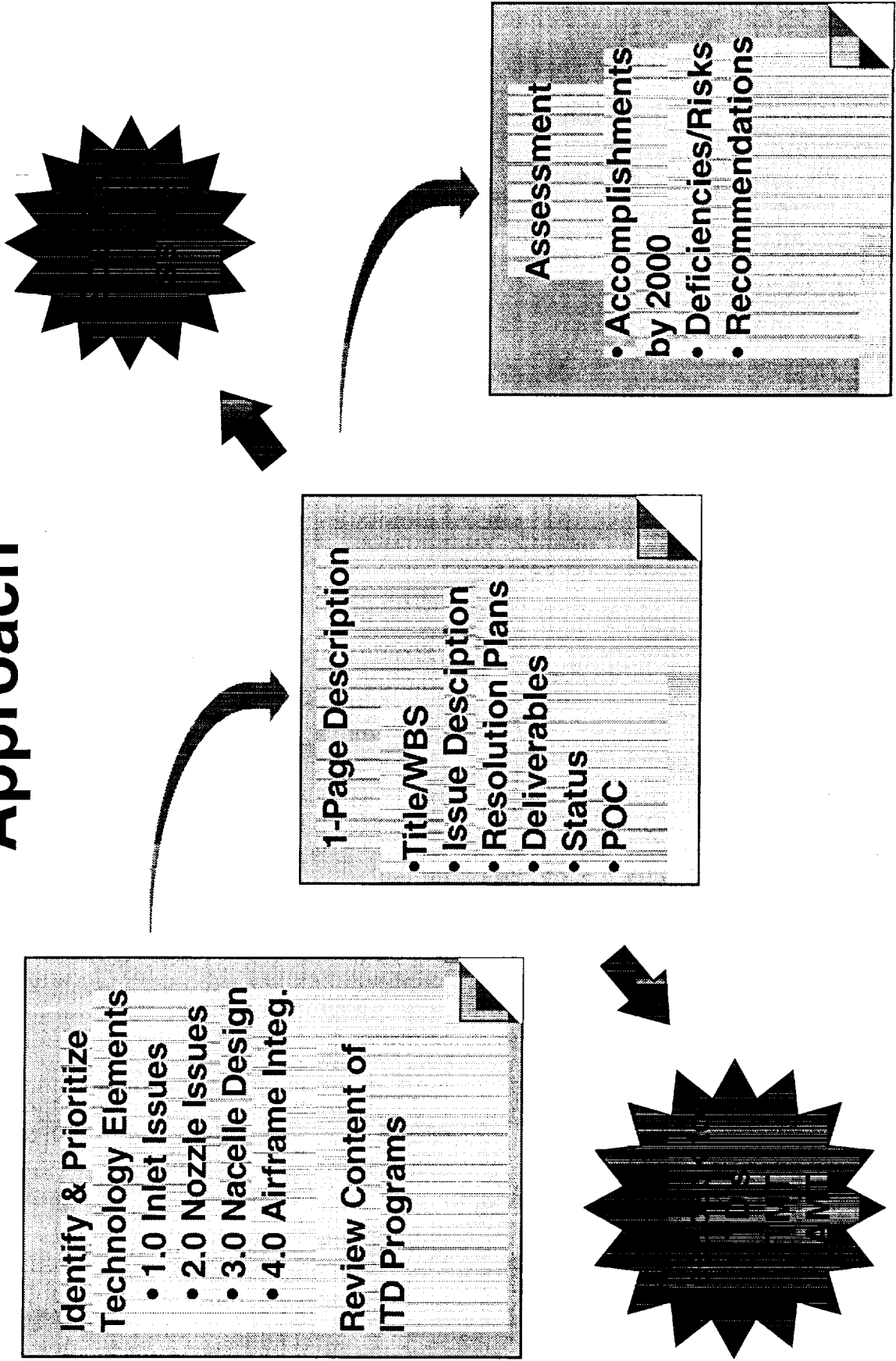


Dan Bencze
February 9-13, 1998
Los Angeles, CA

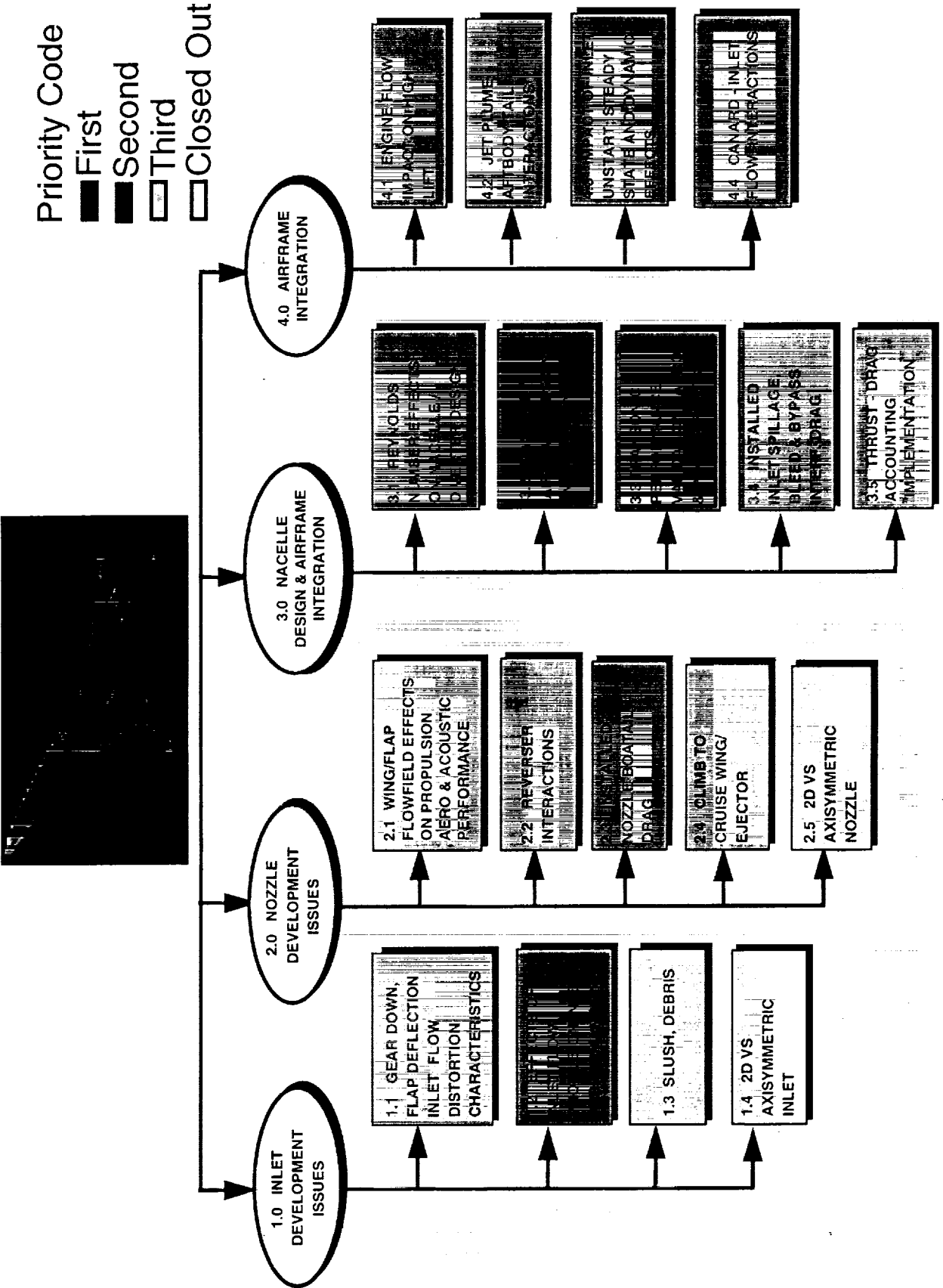
Advisory Group Members

Member	Organization
• Shreekant Agrawal	BLB
• Tony Antani	BLB
• Dan Bencze	ARC
• Fran Capone	LARC
• Mina Cappuccio	ARC
• Roger Clark	BLB
• Joe Koncsek	BCAG
• Bob Kulfan	BCAG
• Steve McMahon	BCAG
• Phil Viars	GE
• Hoyt Wallace	BST
• Bob Welge	BLB

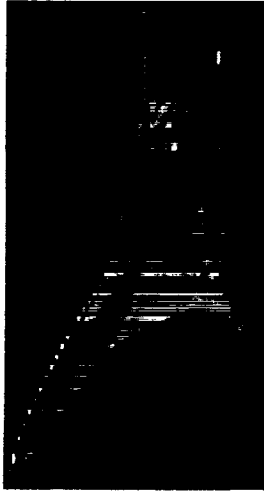
PAI Advisory Group Approach



PAI Technology Development Elements

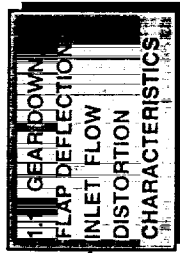
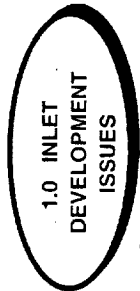


PAI Technology Development Elements



Priority Code

- First
- Second
- Third
- Closed Out

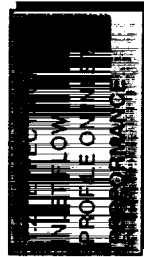


• Lack of Quantitative Distortion Data

Deficiencies/Risks

Recommendations

• If Qualitative Data is Unfavorable Pursue Follow-on Test

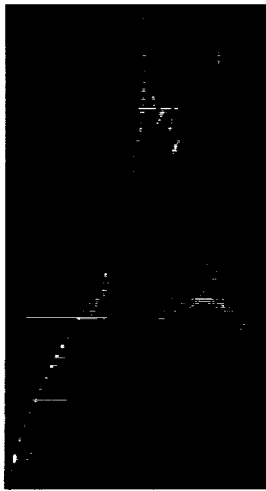


• Effects of Aeroelastics & Atmospheric Disturbances Unknown

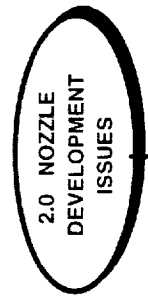
• Pursue CFD Analyses of Both



PAI Technology Development Elements



- Priority Code
- First
 - Second
 - Third
 - Closed Out



- 2.1 WING/FLAP FLOWFIELD EFFECTS ON PROPULSION AERO & ACOUSTIC PERFORMANCE
- 2.2 REVERSER INTERACTIONS
- NOZZLE SCATTERING DRAG
- 2.4 CLIMB TO CRUISE WING / EJECTOR INTERACTIONS
- 2.5 2D VS AXISYMMETRIC NOZZLE

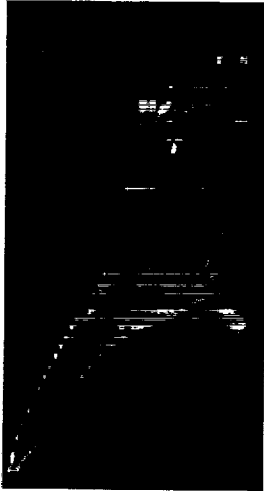
Deficiencies/Risks

- Data on Inboard Nacelle Only
- No Data for $M > 0.4$
- No Integrated Test Planned
- CFD/WT Data Not in Agreement
- CFD is Limited by CPU & MP
- Rn Effects: Turb. Model & WT
- HEAT 1 Data Limited to $M=0.3$
- HEAT 1A Data => Cold Flow
- No Aero-Acoustic Data Base for Axi Nozzles

Recommendations

- Continue Isolated Nozzle Tests at Higher Mach Numbers
- Work Re-injection Problem after Config is Defined
- Fully Fund the PIE Test
- Expand CFD Effort
- Develop Correlations / Extrapolations Based on Existing Data

PAI Technology Development Elements



Priority Code

- First
- Second
- Third
- Closed Out



3.1 REYNOLDS NUMBER EFFECTS ON NACELLE / DIVERTER DESIGN

3.2 NACELLE / AIRFRAME DESIGN INTEGRATION

3.3 TRANSONIC PERFORMANCE VALIDATION - AERO & PROPEFFECTS

NACELLE BLEED BYPASS INTERF. DRAG

ACCOUNTING IMPLEMENTATION

Deficiencies/Risks

- Supersonic Rn's < 10M
- Very Limited Transonic High Rn Data
- Uncertainties in Nacelle Internal & Base Drag
- 3% Model => Low Rn, Reduced Model Fidelity, Limited Instrumentation
- CFD is Complex & Costly
- Single Entry of PIE Model

Recommendations

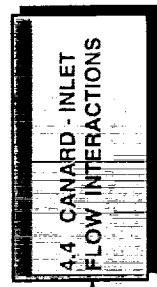
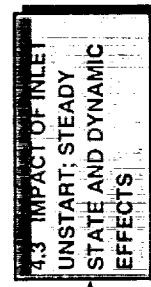
- High Rn Supersonic (BSWT/PSWT) and Transonic (NTF) WT Tests
- CFD Studies
- Need to calibrate nacelles for internal drag and acquire detailed base pressure measurements
- Fully Fund PIE Test Program
- Stronger CFD Effort
- Consider 2 Entries of PIE Model
- Incorporate into PIE Test

PAI Technology Development Elements



Priority Code

- First
- Second
- Third
- Closed Out



Deficiencies/Risks

- Facility Funding
- Limited CFD Analyses
- Limited Design Guidelines
- No Plans to Analyze CPC PAI/ Unstart Data from Aero Perspective

Recommendations

- Resolve Facility Funding Issues
- Fully Fund PIE
- Analyze CPC Data

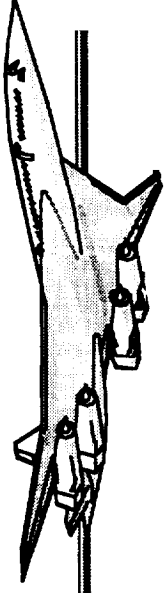
HSR PAI PROGRAM

Activity	ITD Team	Technology Elements Supported
Non-Linear Design Opt	CA	1.2, 1.4, 3.2
High Rn Tests	CA	3.1, 3.2
3-Surface Test	CA	4.4
Inlet Flow Field Measurem'ts	CA	1.2, 3.2, 4.3, 4.4
PIE Test	CANNOZ	2.3, 3.2, 3.3, 3.4, 3.5, 4.2
After-Body Test	CA	4.2
HEAT 1A Test	HL	4.1
5% TCA Test	HL	1.1, 4.2
PAI/Inlet Unstart Test	INLET	4.3
Inlet/Flowfield Simulator Test	INLET	1.2

This page is intentionally left blank.

HSR

High Speed Research



**Configuration Aerodynamics ITD Team
Year End Technical Review**

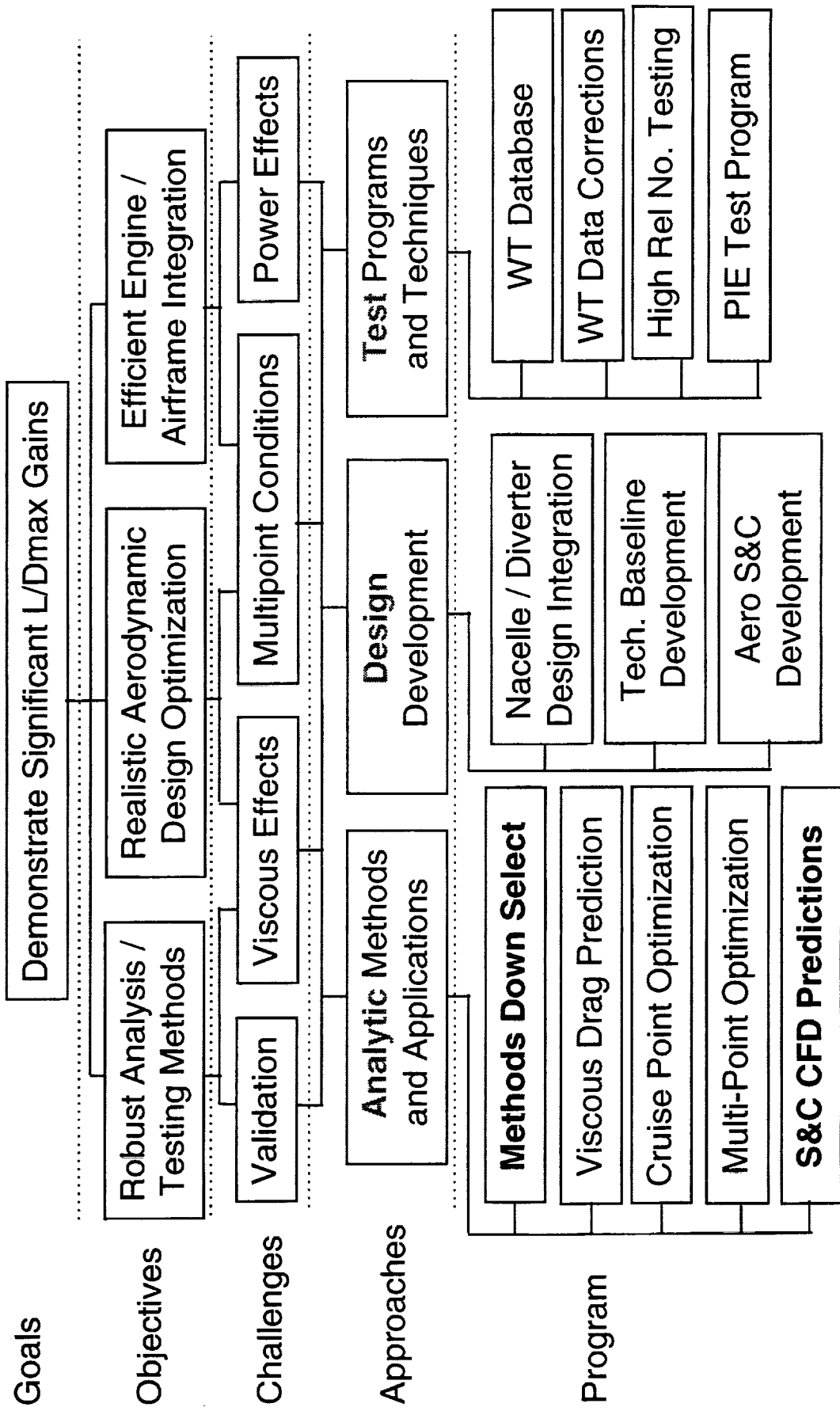
February 9 - 11, 1998

Session 1: Analysis Methods and CFD Validation

Session Chairman: Shreekant Agrawal

Configuration Aerodynamics Technology Development

Session 1: Analysis Methods and CFD Validation



Configuration Aerodynamics Technology Development

Session 1: Analysis Methods and CFD Validation

Objectives:

- Select CFD methods for prediction of high-speed aerodynamic performance and S&C characteristics
- Support in design method development, configuration assessment, and fundamental studies

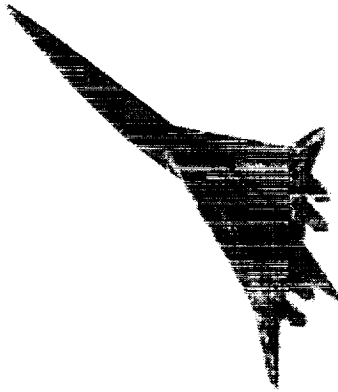
Issues:

- Accurate, efficient, and robust CFD analysis methods
- Ability to predict aerodynamics of deformed elastic airplane in flight

Configuration Aerodynamics 1997 Year-End Review

Session 1: Analysis Methods and CFD Validation

8:05 - 8:15	Overview of WBS 4.3.1.1 - Part 1	Shreekant Agrawal, BLB
8:15 - 8:35	Analytical Cross Checks on Cycle 2 Designs	Dan Bencze, ARC
8:35 - 8:55	AIRPLANE Validation Efforts	Susan Cliff, ARC
8:55 - 9:15	High Reynolds Number Predictions for the Baseline Arrow Wing at Mach 2.48	Melissa Rivers, LaRC
9:15 - 9:35	Applications of Parallel Computing in Configuration Analyses	P. Sundaram, BLB
9:35 - 9:45	BREAK	
9:45 - 10:20	TCA Full Configuration Performance and S&C Characteristics	Grant Martin, BLB
10:20 - 10:45	Unstructured Grid Euler Method Assessment for Predicting the Aerodynamic Performance of the Complete TCA Configuration at Supersonic Cruise Speed	Farhad Ghaffari, LaRC
10:45 - 11:05	Unstructured Grid Navier Stokes Analysis of Full TCA Configuration	Neal Frink, LaRC
11:05 - 12:00	Panel Discussion	Presenters



HSR Airframe Technical Review



Configuration Aerodynamics

**Cycle 2 Nonlinear
Design Optimization
Analytical Cross Checks**

Dan Bencze

NASA Ames Research Center

February 9-12, 1998

Los Angeles , CA

Chart 1. Configuration Aero Technology Development

This activity is an integral to both the Cruise Point Design/Optimization and the Methods Downselect activities.

Configuration Aerodynamics Technology Development

Program Selects Best Analysis / Design Optimization Methods

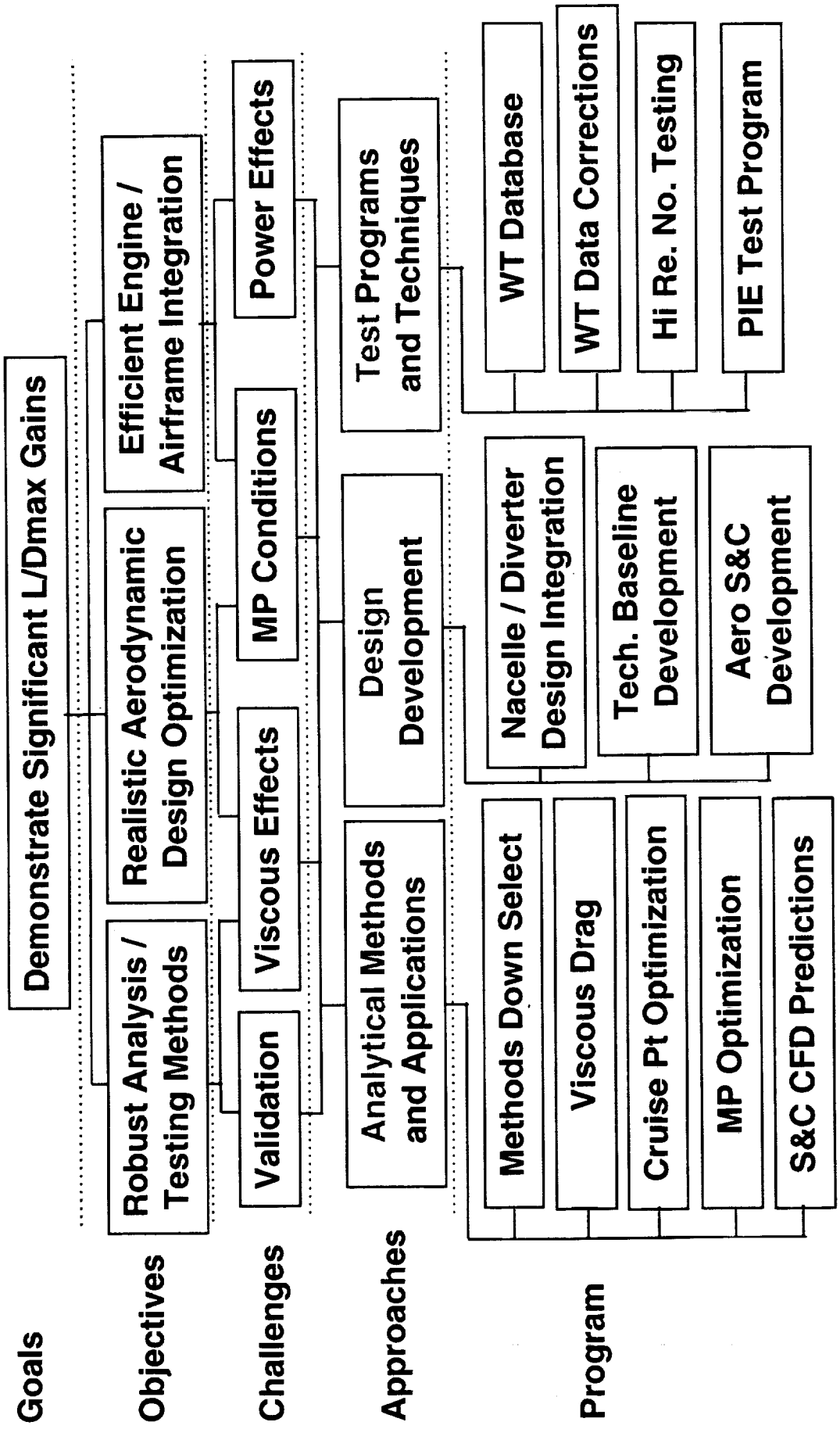


Chart 2 - Objectives

Throughout the Cycle 2 design activity, each participating organization used their preferred analysis tools to evaluate their respective configurations. To better understand both the relative performance differences among the configurations and variability introduced by the various analysis codes, the Configuration Aero team initiated an analytical cross-check activity, in which each organization analyzed each of the configuration using their respective analysis codes. The objectives of the analytical cross-check effort are listed in chart 2.

Objectives

- **Understand the variability in the predicted performance levels of the nonlinear designs arising from the use of different inviscid (full potential/Euler) and viscous (Navier-Stokes) analysis methods**
- **Provide the information required to allow the performance levels of all three designs to be validated using the data from the NCV model test.**

Chart 3 - Analysis Codes

The analysis tools that were employed in the analytical cross-checks as used by each participating organization are listed in Chart 3. A total of six different codes were used.

Analysis Codes

Boeing Commercial Airplane Group BCAG	Boeing Long Beach BLB	Ames Research Center ARC
• TRANAIR	• CFL3D, Euler	• AIRPLANE
• OVERFLOW, S-A	• CFL3D, N-S, B-L	• SYN87-MB, Euler
		• UPS*, Euler
		• UPS*, N-S, B-L
		• OVERFLOW, S-A

*** W/B only**

Chart 4 - Code Descriptions

The pertinent characteristics of each code is given in the table shown in Chart 4.

The TCA baseline and each of the three nonlinear designs were analyzed using each of the analysis codes. Both the W/B and W/B/N/D configurations were analyzed, except in the case of the UPS code, which does not have the capability to handling nacelles. In the cases where an inviscid code was employed, the performing organization incorporated an estimate of the skin-friction drag, based on a flat plate analysis, into their estimate of the total drag of the configuration.

Since the nonlinear design activity was conducted at a Mach number of 2.4 and a nominal lift coefficient of 0.1, the computations were focused at these conditions. Lift, drag (pressure and viscous), and pitching moment were computed at Mach 2.4 for a range of angles-of-attack in the neighborhood of $C_L=0.1$.

Although every effort was made to insure as much consistency as possible among the results, a couple of small discrepancies were identified. The BLB geometry was not closed and had a 474.4 sq in base area that was not included in the force accounting. It is estimated that the base drag for this area is on the order of 0.4 to 0.7 counts. For ARC NS computations for the BCAG and BLB were done with the upper nacelle fairing in place. It is estimated that decreases the pressure drag for these configurations by 0.2 counts. Neither of these adjustments were incorporated into the results presented in the following charts.

Code Descriptions

Code	Equation Set	Grid Topology	Turbulence Model or Flat Plate Correlation
TRANAIR	Full Potential	Cartesian Mesh	Sommer & Short
OVERFLOW	Navier-Stokes	Structured Overset	Spalart-Allmaras
CFL3D/E	Euler	Structured Patched	Van Driets II
CFL3D/NS	Navier-Stokes	Structured Patched	Baldwin-Lomax
AIRPLANE	Euler	Unstructured Tetrahedral	Nicolai
SYN87-MB	Euler	Structured Point-Matched	Nicolai
UPS/E	Parabolized Euler	Structured O - Mesh	Nicolai
UPS/NS	Parabolized Navier-Stokes	Structured O - Mesh	Baldwin-Lomax

Chart 5 - Summary of Drag Improvements at the end of Cycle 2 Design Effort

Chart 5 illustrates the predicted results for each of the configurations as generated by the organization doing the design at the end of the Cycle 2 Design Effort in January 1997. The BCAG results are based on TRANAIR and OVERFLOW/ Spalart-Allmaras, the ARC results on SYN87 and OVERFLOW/ Spalart-Allmaras, and the BLB results on CFL3D, Euler and Navier-Stokes/Baldwin-Lomax.

Summary of Drag Improvements TCA Cycle 2 W/B/N/D Solutions at $M=2.4$, $CL=0.1$, $Rn=6.3M$ (NS)

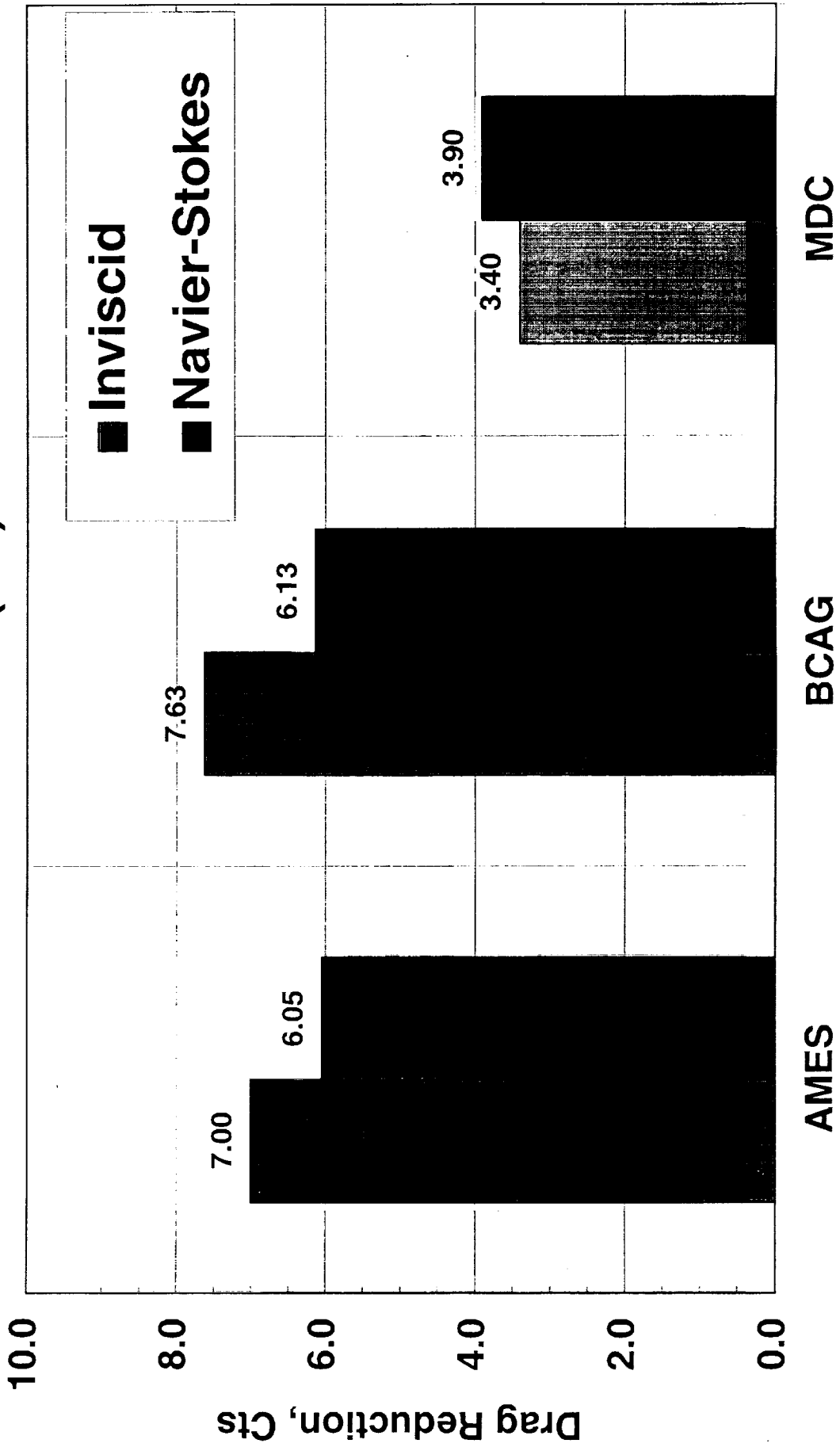


Chart 6 - Wing/Body Pressure Drag Increments

The wing/body (W/B) pressure increments for each of the nonlinear designs relative to the TCA baseline configuration are shown in Chart 6. The results are presented in terms of drag improvement at $C_L = 0.1$.

All of the codes predicted that the BCAG design exhibited the best W/B performance increment, on the order of 4 drag counts, versus 3 for the ARC design and 2.0 for the BLB design. The overall variability among the codes is on the order of ± 1.0 cts, with a greater variability among the inviscid codes than the viscous codes. The pressure drag for the viscous codes are in particularly good agreement, with a variation of less than ± 0.5 cts. Furthermore, there are some inconsistencies among the codes. For example TRANAIR, predicted a noticeably greater improvement for the ARC and BCAG configurations than the other inviscid codes, but predicted one of the lower levels of improvement for the BLB configurations. A second example, is the AIRPLANE code which predicts fairly consistent results for the ARC and BCAG configurations, but predicts the lowest performance gain for the BLB configuration.

W/B Pressure Drag Increments Relative to the TCA Baseline

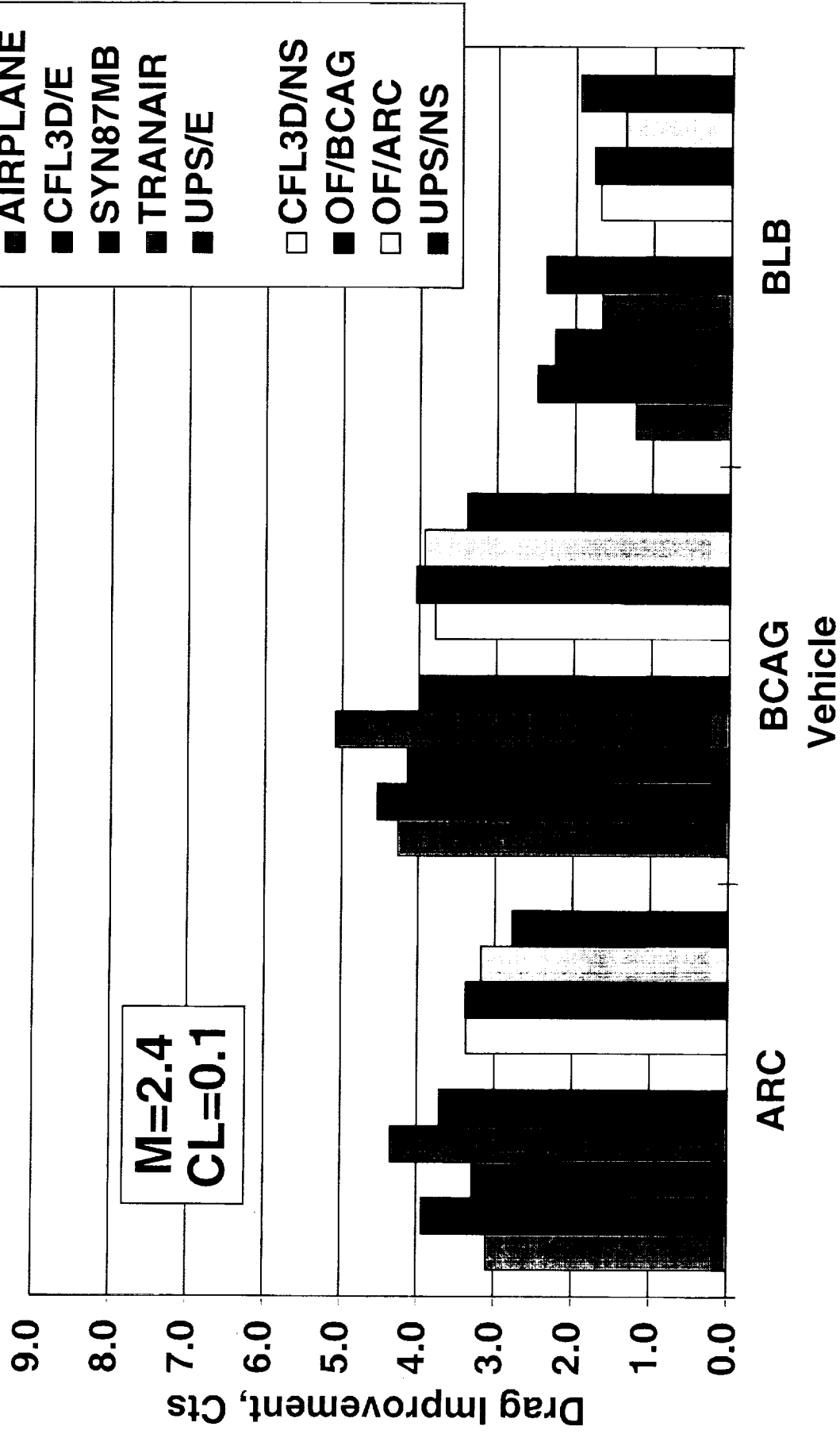


Chart 7 - Wing/Body Total Drag Increments

The results for the total wing/body drag increments are very similar to the pressure drag results, with the exception of the ARC/OVERFLOW results for the BCAG configuration. In this case, the ARC/OVERFLOW prediction is more than one drag count greater than the other viscous results. Since the ARC/OVERFLOW pressure drag increment is consistent with the other codes, this difference must be attributable the differences in viscous drag prediction.

W/B Total Drag Increments Relative to the TCA Baseline

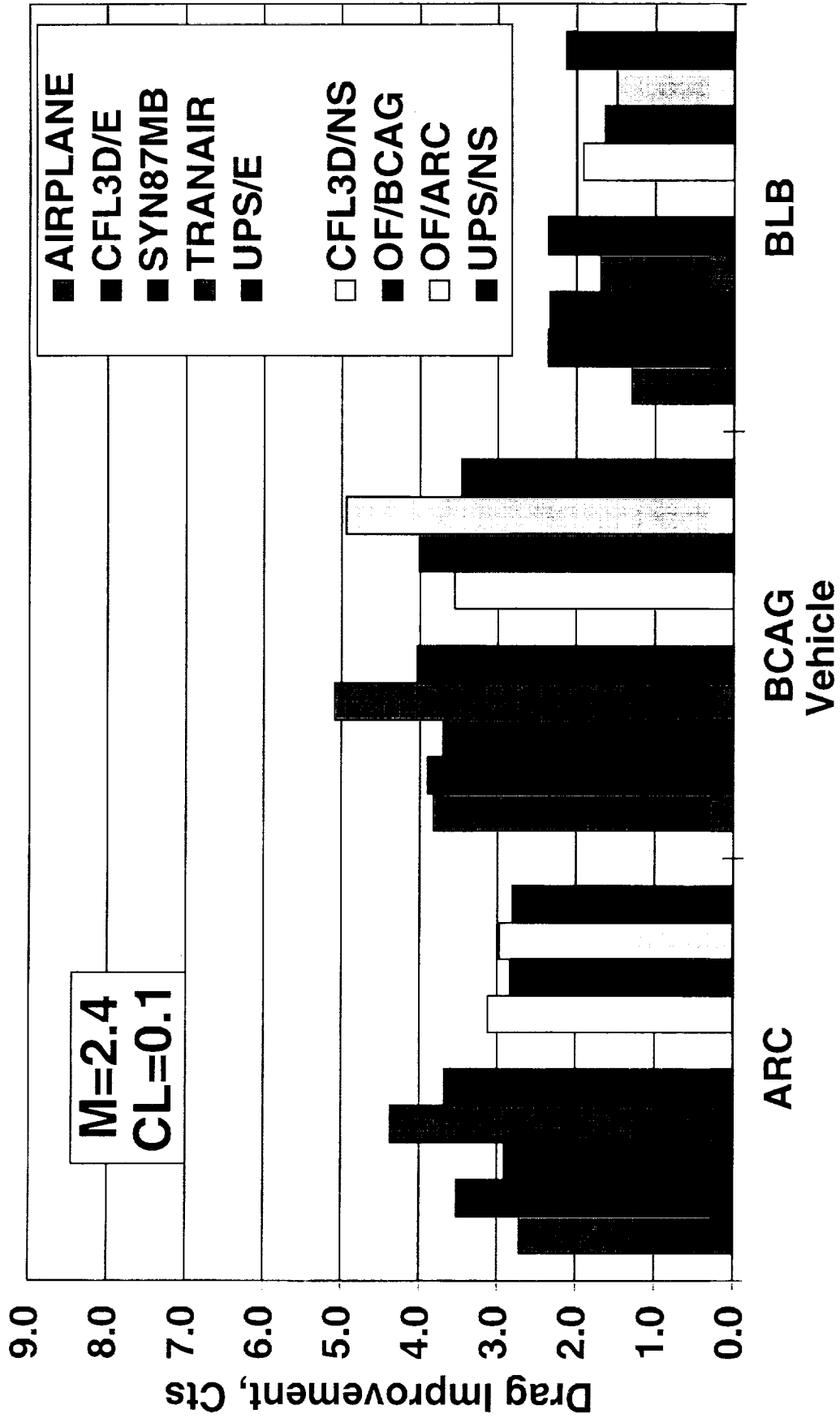


Chart 8 - Wing/Body/Nacelle Pressure Drag Increments:

The wing/body/nacelle/diverter (W/B/N/D) pressure drag increments for each of the nonlinear designs relative the TCA baseline configuration are shown in Chart 8. The results are presented in terms of drag improvement at $C_L = 0.1$. No UPS results are shown because the code does not have the capability to include the nacelles into the computation.

The results for the wing/body/nacelle/diverter configuration are generally similar to the wing/body results, with the variability on the order of ± 0.75 cts. Again, the TRANAIR and AIRPLANE results appear to be less consistent than the remaining results. From a pressure drag perspective, W/B/N/D performance of the ARC design appears to be slightly higher than the BCAG design.

W/B/N/D Pressure Drag Increments Relative to the TCA Baseline

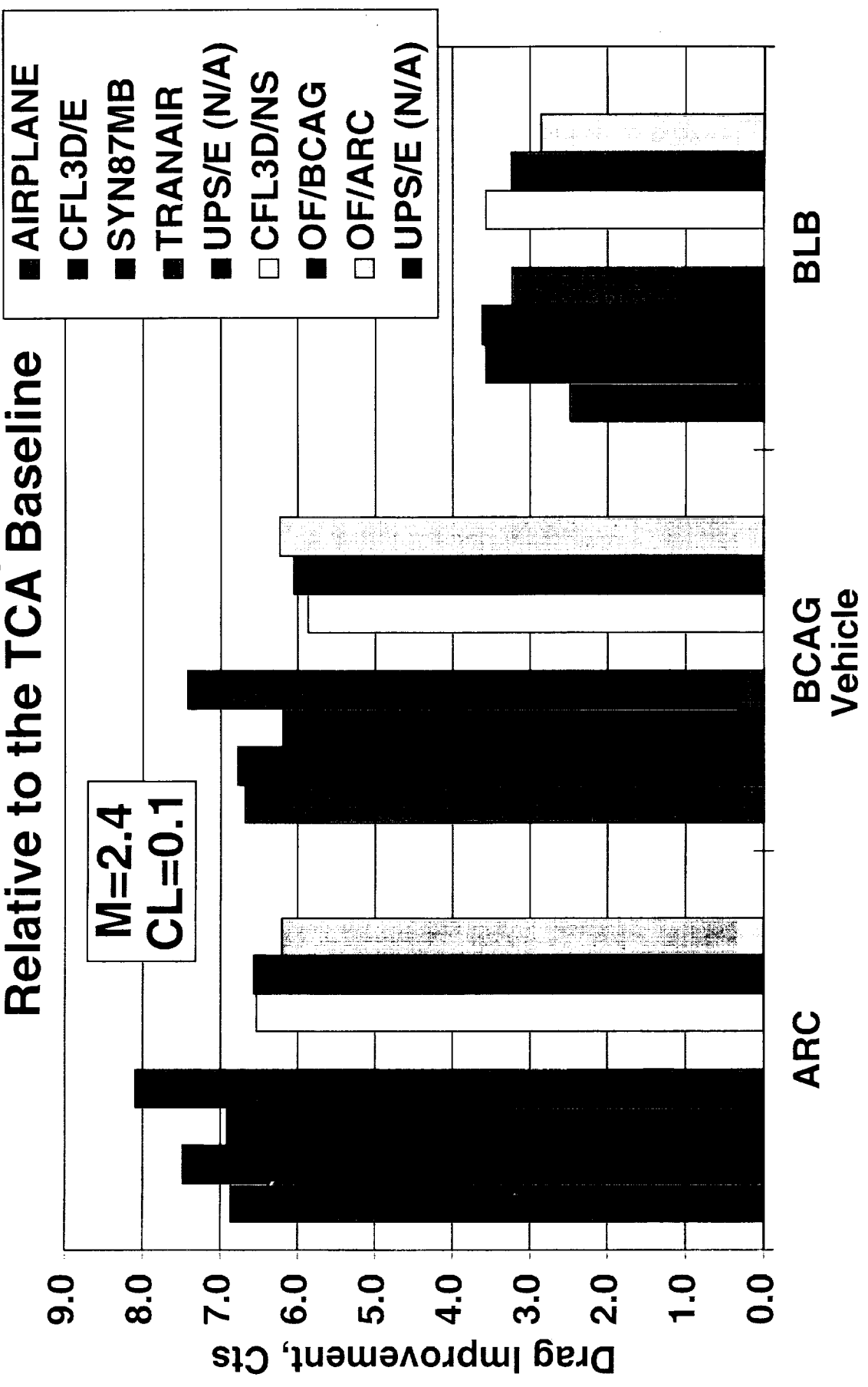


Chart 9 - Wing/Body/Nacelle Total Drag Increments:

The total drag increments are very similar to the pressure drag increments and show the same inconsistencies as the wing/body results.

W/B/N/D Total Drag Increments Relative to the TCA Baseline

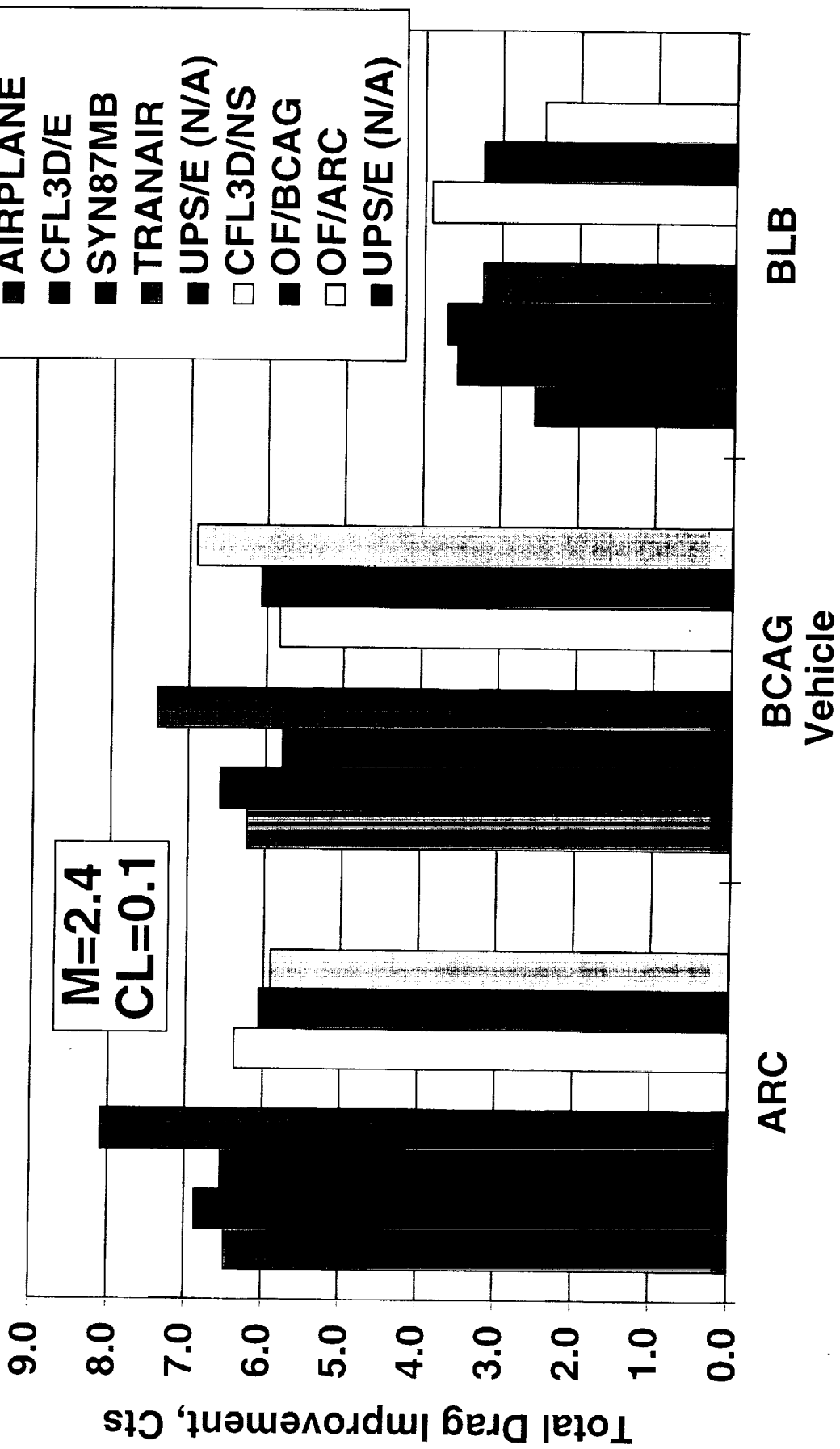


Chart 10 - Nacelle Pressure Drag Increments

The predicted nacelle pressure drag increments (W/B/N/D-W/B) for the various designs are presented in Chart 10. In general, the inviscid methods consistently predict a larger penalty than the viscous codes. The differences being on the order of 1.0 to 1.5 counts. Again the inviscid and viscous results tend to track one another.

Since the nacelles were the same for all four configurations, it is obvious that the nonlinear designs reflect better job of integrating the nacelles into the configuration than the linear based TCA.

Nacelle Pressure Drag Increment W/B/N/D-W/B

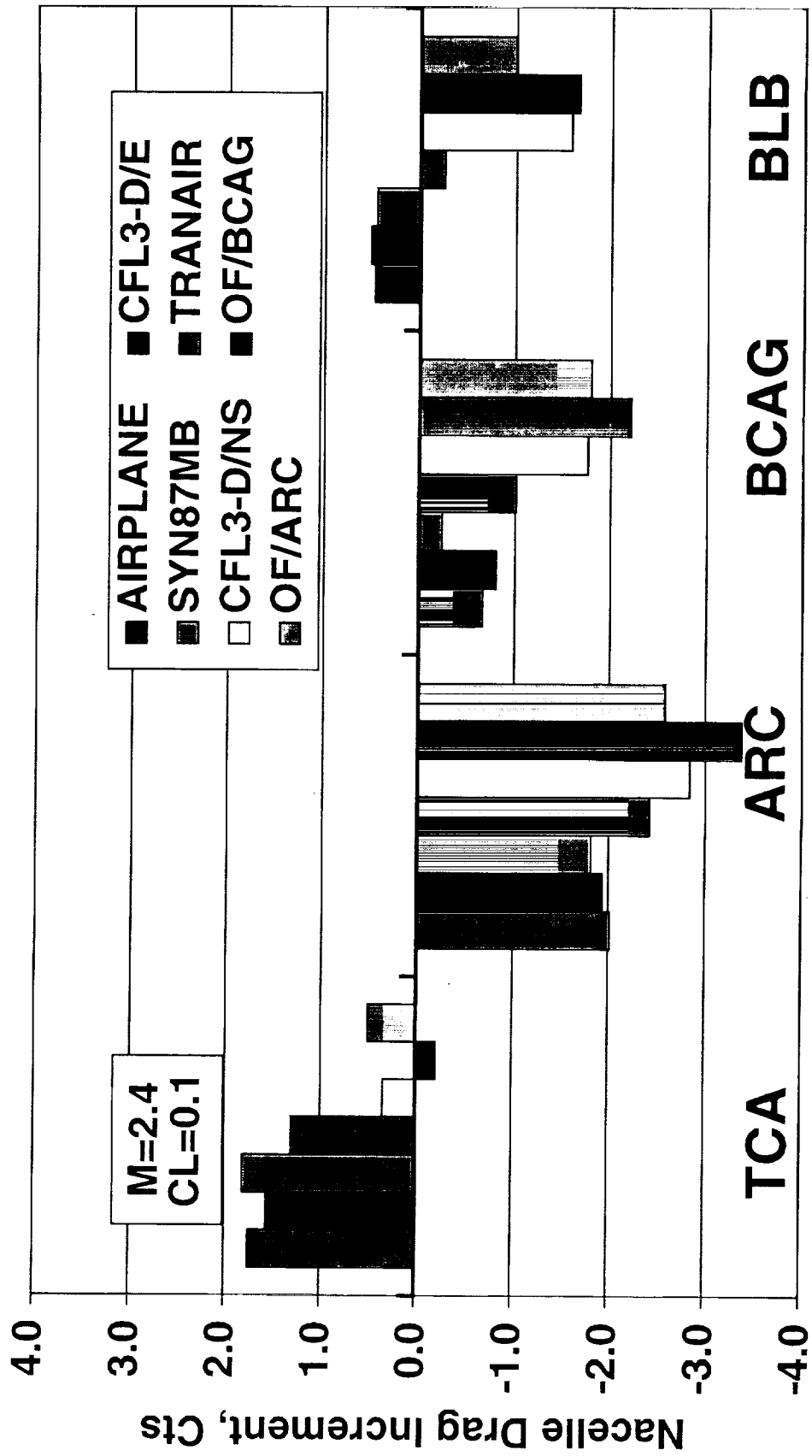


Chart 11 - Nacelle Total Drag Increments

The total nacelle drag increment including viscous effects for each configuration is presented in Chart 8. (Note the scale difference between this and previous chart). With the viscous effects included in the analysis, the differences between the inviscid and viscous results are less evident. The most notable change is in the CFL3D/NS results. For all the configurations, the CFL3D/NS results predict a greater drag penalty than the other NS codes by almost 2 drag counts.

Nacelle Total Drag Increment W/B/N/D-W/B

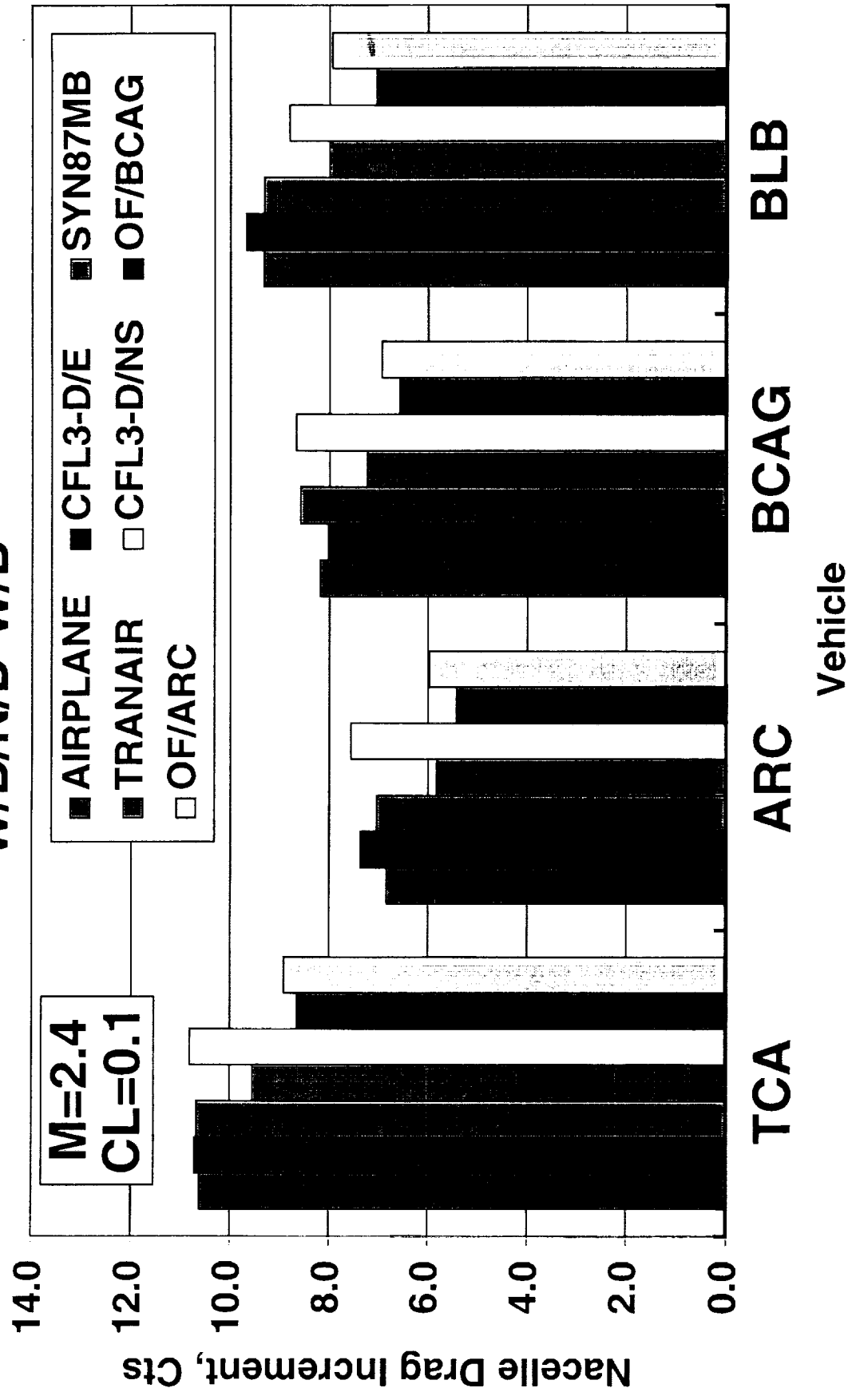


Chart 12 - Nacelle Total Drag Increments Relative to the TCA Increment

To examine the benefit derived from the nonlinear optimization on the nacelle increment, the nacelle increment for each configuration relative to that obtained on the TCA baseline is shown in Chart 12. The increment shown for the three configuration and for each code is: $(W/B/N/D-W/B)_{\text{CONFIG}} - (W/B/N/D-W/B)_{\text{TCA}}$. These results clearly demonstrate the performance improvements derived from the nonlinear design efforts. The ARC design was able to achieve a 3.0 to 3.5 drag count improvement relative to the TCA baseline; the BCAG design a 2.0 to 2.5 count improvement and the BLB design a 1.0 to 2.0 count improvement.

Nacelle Total Drag Increment Relative to the TCA

W/B/N/D-W/BIConfig - W/B/N/D-W/BITCA

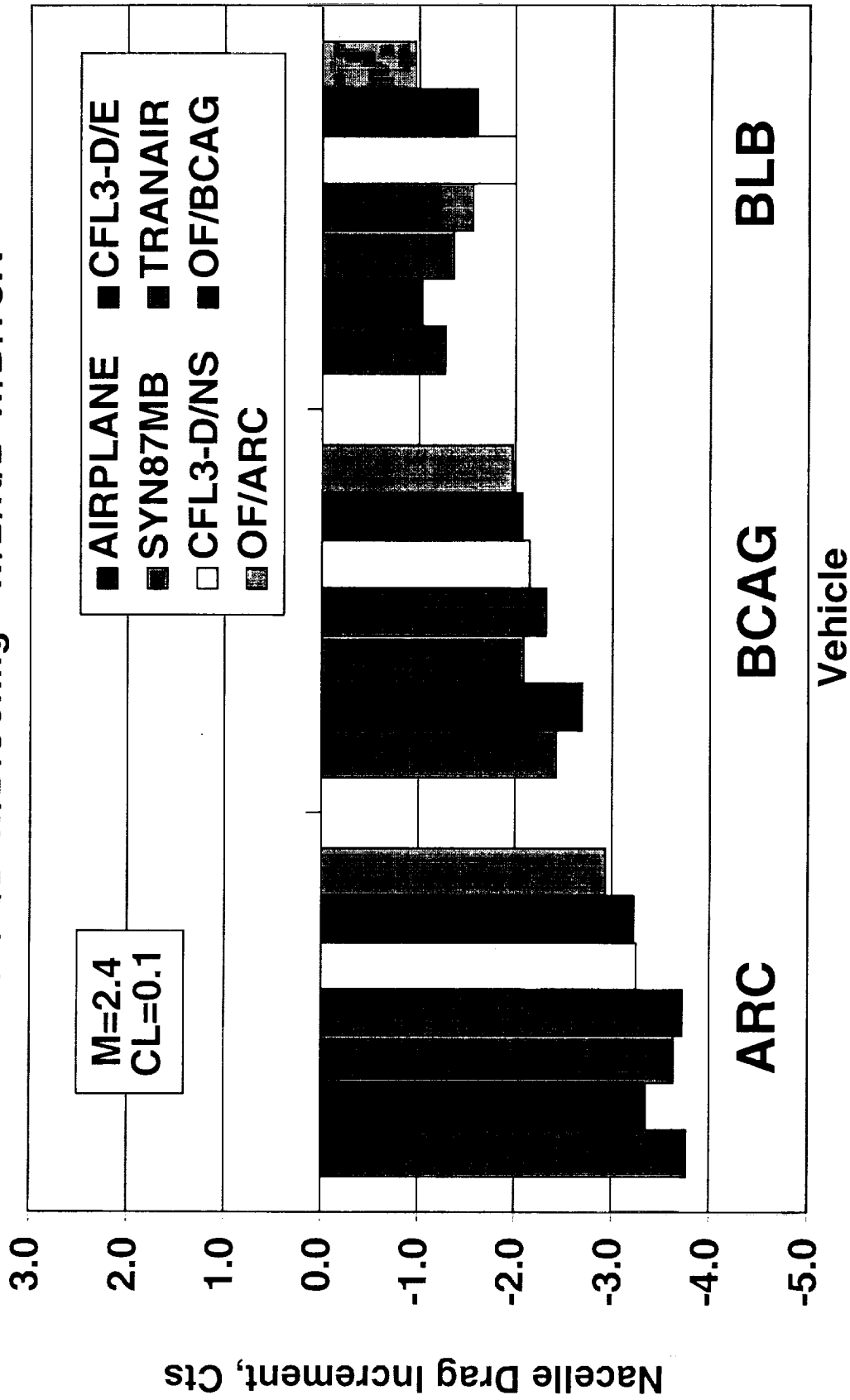


Chart 13 - CL vs. Alpha Comparisons

Since this was a design effort focused on improving the TCA baseline, the performance increments generated as part of the analytical cross checks process were of primary interest. However, from a methods point of view, comparisons of the absolute levels of the performance parameters predicted by the various codes are also of interest.

The lift curves for the four configurations are presented in Chart 10. The local lift curve slopes in the neighborhood of $C_L = 0.1$ are nearly identical for all the configurations and the various codes. However, there are a substantial shifts in alpha for zero lift (assuming totally linear $C_L - \alpha$ curves) among the configurations that are captured fairly accurately by all of the codes. (Note the shift in the alpha scale among the four plots.) In addition, the viscous codes tend to predict an alpha at zero lift that is approximately a 0.1° higher than that for the inviscid codes. This shift in alpha for zero lift reflects the effective decambering of the configurations caused by the viscous displacement effects.

Cycle 2 Analytical Cross Checks CLvs Alpha, M=2.4

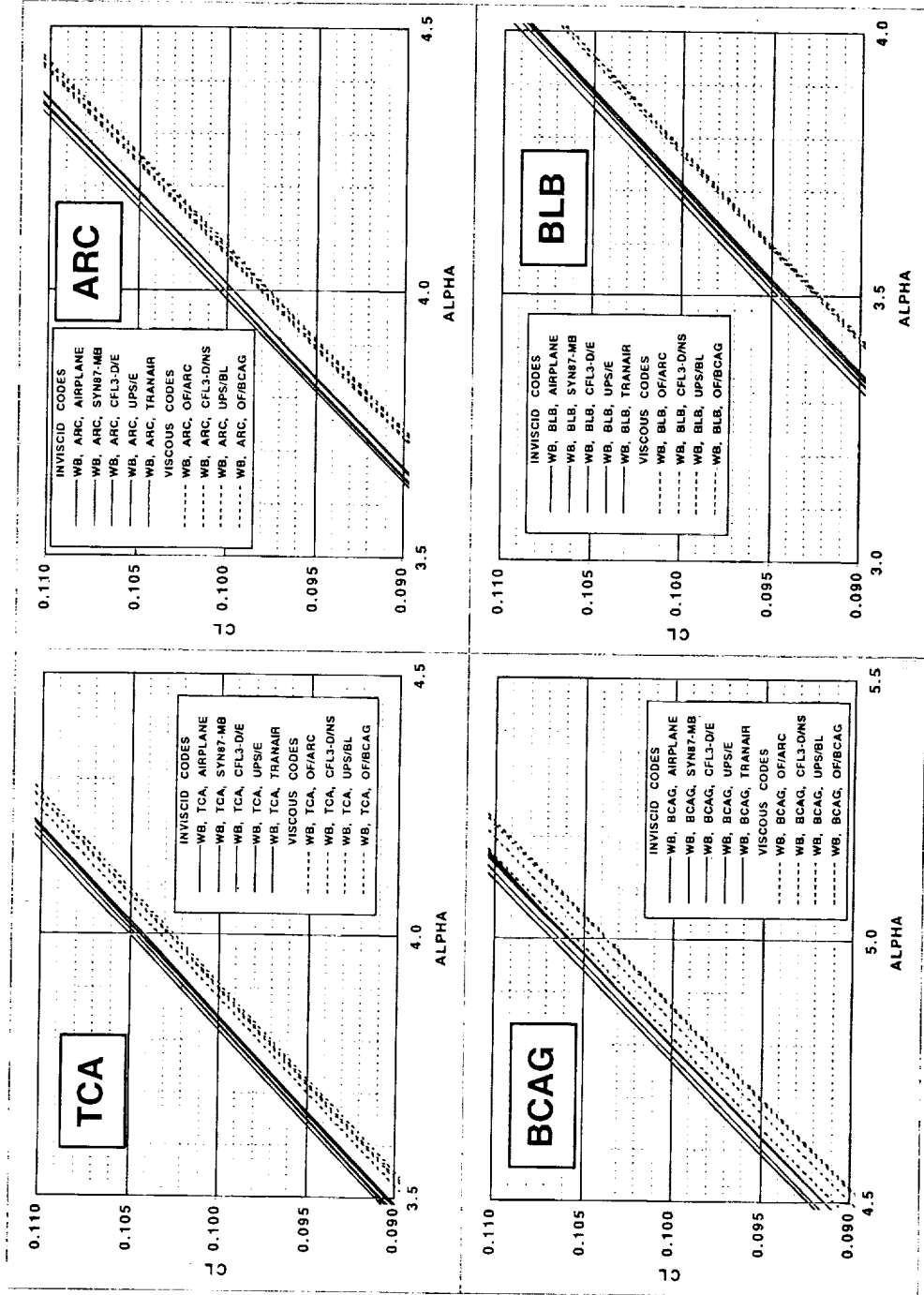


Chart 14- Drag Characteristics at $C_L = 0.1$

Since a comprehensive set wind tunnel data is not available, the predicted performance levels can only be compared to each other in terms of the scatter among the various predictions. Using the individual mean value of the computations for each combination of design (TCA, ARC, BCAG, BLB) and configuration (WB & WBND) as a reference for that combination, the variations in predicted pressure and total drags are presented in Chart 11. It is important to realize that variations presented in Chart 11 do not represent the uncertainty in the predicted performance increments derived from the design/optimization process documented in this milestone. The variations in anticipated performance increments presented in Charts 6 and 7 are much smaller. This is especially true in the case of the Navier-Stokes results which were used to evaluate the various designs. In this case the variations in predicted performance increments were on the order ± 0.25 cts. for the pressure drag results and ± 0.5 cts for the total drag results.

For the WB pressure drag, generally all the codes are with ± 2.0 drag counts for all of the designs. In this case, the inviscid and viscous codes tend to group together, with the exception of the AIRPLANE results. The viscous codes tend to predict a higher level of pressure drag than the inviscid codes. The shift in the AIRPLANE results is felt to be associated with the coarseness of the unstructured mesh in the flow field close to the vehicle, while the shift in the viscous results reflects the displacement effects of the viscous flow on the overall pressure drag. All of the codes tend to retain their position relative to the individual means across the various designs.

For the WB total drag, the variability is ± 2.5 cts. vs. the ± 2.0 cts. for the pressure drag results. In addition, there notable shifts in the relative order of the results. The CFL3D/E results shift from being about 1.5 cts below the mean to 1.5 cts. above the mean, reflecting a larger flat plate estimate of the viscous drag. Although the pressure drag predicted by the three viscous codes, OF/ARC, CFL3D/NS, and OF/BCAG, is in very good agreement, within ± 0.5 cts., the variations in total drag are on the order of ± 2.5 cts. Obviously these differences are tied up in the different turbulence models and gridding techniques used in the three codes.

The maximum variation in pressure drag for the WBND configuration is also on the order of ± 2.0 counts, however there tends to be more overlap of the inviscid and viscous results. Again there is very good agreement, ± 0.5 cts., among the viscous codes. The variation in the total drag prediction for the WBND configuration, grows to ± 3.0 cts., with a similar dispersion of the viscous results.

This page is intentionally left blank.

AIRPLANE Mesh Development with Grid Density Studies

Susan E. Cliff, NASA Ames Research Center

Timothy J. Baker, Princeton University

Scott D. Thomas, Sterling Software Inc

Scott L. Lawrence, NASA Ames Research Center

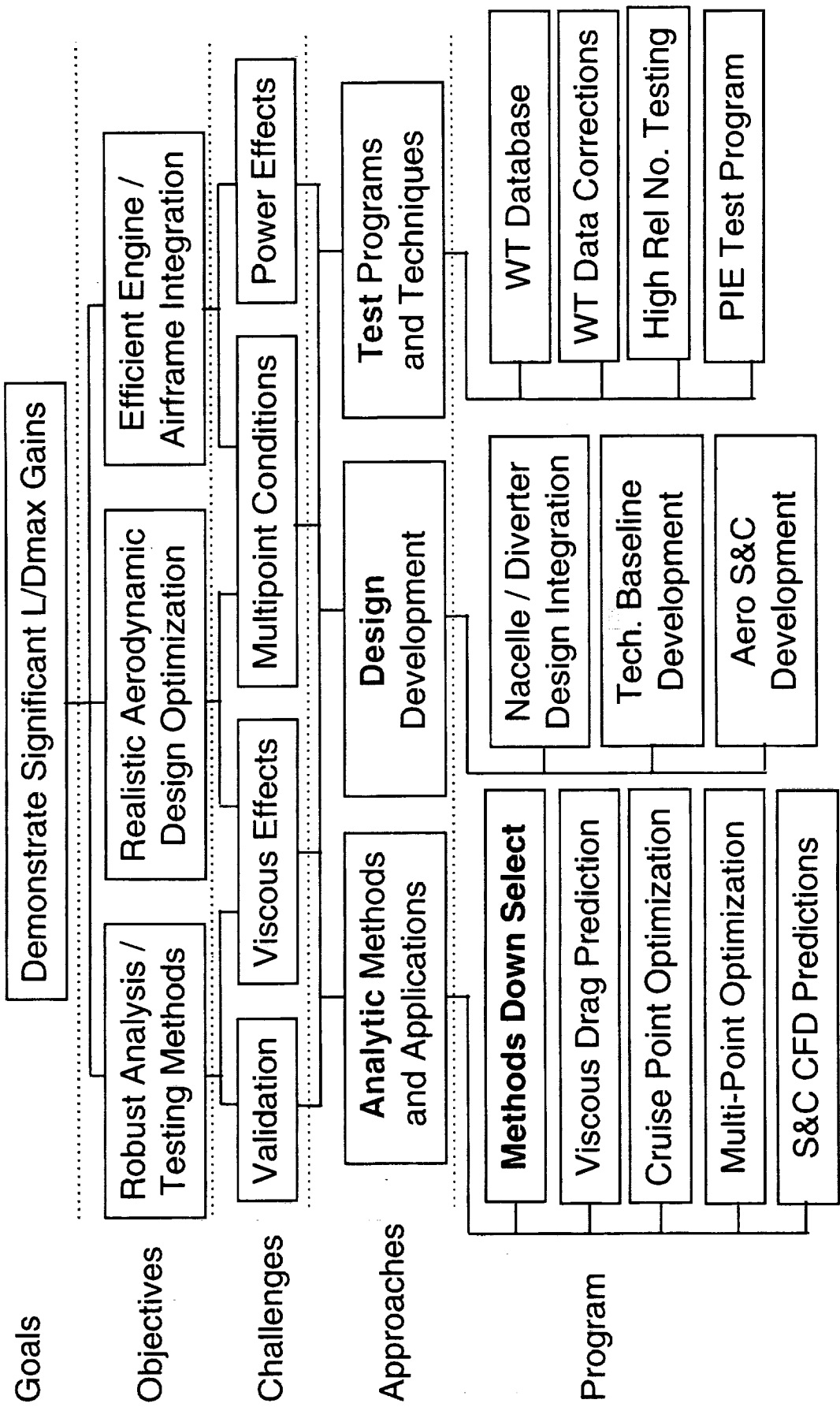
Mark J. Rimlinger, Sterling Software Inc

February 9, 1998

This page is intentionally left blank.

Configuration Aerodynamics Technology Development

Session 1: Analysis Methods and CFD Validation



Automatic Grid Generation Wish List

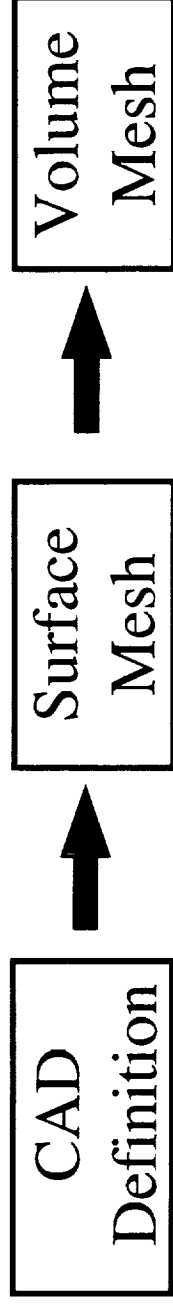
Geometry handling, including CAD clean up and mesh generation, remains a major bottleneck in the application of CFD methods. There is a pressing need for greater automation in several aspects of the geometry preparation in order to reduce set up time and eliminate user intervention as much as possible. Starting from the CAD representation of a configuration, there may be holes or overlapping surfaces which require an intensive effort to establish cleanly abutting surface patches, and collections of many patches may need to be combined for more efficient use of the geometrical representation. Obtaining an accurate and suitable body conforming grid with an adequate distribution of points throughout the flow-field, for the flow conditions of interest, is often the most time consuming task for complex CFD applications.

There is a need for a clean unambiguous definition of the CAD geometry. Ideally this would be carried out automatically by smart CAD clean up software. One could also define a standard piece-wise smooth surface representation suitable for use by computational methods and then create software to translate between the various CAD descriptions and the standard representation.

Surface meshing remains a time consuming, user intensive procedure. There is a need for automated surface meshing, requiring only minimal user intervention to define the overall density of mesh points. The surface mesher should produce well shaped elements (triangles or quadrilaterals) whose size is determined initially according to the surface curvature with a minimum size for flat pieces, and later refined by the user in other regions if necessary.

Present techniques for volume meshing all require some degree of user intervention. There is a need for fully automated and reliable volume mesh generation. In addition, it should be possible to create both surface and volume meshes that meet guaranteed measures of mesh quality (e.g. minimum and maximum angle, stretching ratios, etc.).

Automatic Grid Generation Wish List



- Unambiguous CAD definition of object surface
- Automatic generation of surface mesh with gradation of cell size based on surface curvatures and user defined density requirements
- Automatic generation of volume mesh that conforms to a prescribed surface mesh
- Guarantees of mesh quality for both surface and volume meshes

Modular Approach to Geometry Manipulation

Highly complex configurations are best handled using an unstructured mesh generation scheme with a modular approach in which the surface and volume meshes are generated independently. The modular approach offers improved accuracy and robustness over the previous method in which both an interior and exterior volume mesh were generated simultaneously, and the surface grid derived as a consequence of this procedure. The previous method lacked sufficient robustness to become an automated method since the resulting surface triangulation was usually initially flawed. The new grid generation approach presently under development creates surface and volume meshes independently. This should afford a more robust grid generation method with rigid control of the surface grid.

The new method uses a modular approach to generate volume meshes that match a prescribed surface triangulation by forming a Delaunay triangulation of the surface, outer flow-field boundaries and the points in the interior. The initial surface triangulation is re-established using edge/face swapping procedures.

Modular Approach to Geometry Manipulation

- Highly complex configurations are best handled by unstructured meshes using a modular approach
 - ➔ Volume and surface meshing are independent operations
 - ➔ Volume meshing matches a prescribed surface triangulation provided by the mesher

Technology for Tetrahedral Mesh Generation

Three unstructured mesh generation methods are in use today; Delaunay, moving or advancing front, and octree. Each method has its strengths and weaknesses. The primary advantages and disadvantages for each method will be summarized in the next chart.

The Delaunay method has been chosen for use with the AIRPLANE code since it offers the best choice for a truly automated method for highly complex geometries. The newly developed mesh generator for the AIRPLANE code (MESH3D) continues to employ a Delaunay based method as did the original grid generator (MESHPLANE).

Note, for planar conditions, the definition of a Delaunay triangulation requires that the circumcircle of each triangle contains no other points of the triangulation. This generalizes in an obvious way to three dimensions; a 3D triangulation is Delaunay if for each tetrahedron no points lie within the circumsphere defined by its four points.

Technology for Tetrahedral Mesh Generation

- **Current methods - Delaunay, Moving Front, and Octree (each has its strengths and weaknesses)**
- **Delaunay methods appear to offer the best choice for fully automated mesh generation**
- **MESH3D is a Delaunay based tetrahedral mesh generation module for volume meshing**

Triangulation Methods for Mesh Generation

The key advantages and disadvantages for these methods are given.

The Delaunay method has a well established mathematical basis that guarantees in 2D the existence of a constrained Delaunay triangulation (i.e. a triangulation that conforms with prescribed boundary edges). In 3D the theory is less well developed and the main difficulty in implementing this procedure in three dimensions is re-establishing the surface triangulation. The surface faces of the original surface grid are re-established by swapping edges and/or faces of tetrahedra. This becomes more difficult to accomplish for poorly shaped triangular faces, particularly those with angles near 180 degrees.

The main advantage of a moving front method is that it always begins marching from the surface boundary, which ensures that the surface grid is always maintained. The problem with this method is that there is no mathematical guarantee that a volume triangulation can be completed successfully. This can give rise to unfilled regions in the volume grid which can occur during the final stages when the front is collapsing onto itself. As the number of grid points increases, so does the chance of this mesh technique failing.

The quadtree(2D) or octree(3D) method is simple to implement. However, it is difficult to obtain high quality surface meshes due to the odd shaped triangles formed by the intersection of the (subdivided) mesh.

Triangulation Methods for Mesh Generation

<u>Method</u>	<u>Advantage</u>	<u>Disadvantage</u>
Delaunay	Fairly well developed theory	Re-establishing prescribed boundary faces for 3-D cases is difficult
Moving (or Advancing) Front	Always starts from a prescribed boundary definition	Almost no theory (mathematical guarantee) that a triangulation will succeed
Quadtree/Octree	Simple to implement	Difficult to obtain intersections of octree cubes with surface. Quality of surface triangulation can be poor

MESHPLANE

MESHPLANE, the tetrahedral mesh generation code, and FLOPLANE, the Euler flow solver, comprise the original AIRPLANE code. The two codes were first developed during the late 1980s when surface triangulation methods were not readily available.

Due to the unavailability of surface grid generation methods, MESHPLANE was developed to use sectional definitions of the configuration surface, whereby the surface grid was developed as part of the volume grid generation. The resulting surface grids were usually partially flawed after the initial triangulation. User expertise was needed in order to modify the sectional input data set and achieve accurate surface meshes.

MESHPLANE was used successfully for many years but it often required extensive user intervention and hence could not become a fully automated method.

MESHPLANE

- Originally developed in the late '80s when surface triangulation methods were NOT readily available
 - Boundary surface of aircraft given by a wire frame definition
- ➔ User has no direct control of boundary surface triangulation
- 1) User needs expertise in setting up appropriate wireframe data set
 - 2) Wireframe data set usually requires modification in order to achieve a satisfactory surface triangulation

Conclusion: Although MESHPLANE has been a reliable workhorse, it requires too much user interaction and cannot be made into an automated method.

MESH3D

MESH3D is designed to be a fully automated unstructured tetrahedral grid generation scheme. It requires a "water-tight" triangulated surface mesh from which it will re-establish the surface after a Delaunay triangulation of the volume mesh is completed. The surface is re-established by using an edge/face swapping procedure. The method of surface re-establishment works well for reasonable surface meshes, but difficulties can arise in establishing the surface faces when poor quality triangles are encountered.

A smooth gradation in mesh size from the fine surface grid to the coarse outer grid is provided with MESH3D.

On completion of the mesh, an optimization procedure is applied to find and remove poor quality tetrahedra by means of face/edge swapping procedures.

MESH3D has proven to be a reliable and fully automatic code for highly complex configurations provided the boundary surface triangulation has acceptable quality.

MESH3D

- Designed to be a fully automated tetrahedral mesh generator
- Creates a volume mesh to match a prescribed surface triang.
- Uses edge/face swaps to re-establish surface triangulation
- Bad quality surface triangulations (i.e. highly obtuse angles) can cause difficulties. Swapping diagonals and adding points to the boundary surface may be required in extreme cases
- Volume mesh has a smooth gradation in size of tetrahedra
- Quality of volume mesh is optimized by removing badly shaped tetrahedra

Conclusion: MESH3D is a reliable and automatic tetrahedral mesh generator for arbitrary domains provided the triangulation of the boundary surface has an acceptable quality.

Re-establishing Prescribed Boundary Surface

The procedure for re-establishing the surface boundary is a two step process. The first step is to establish all the edges of the original surface grid. This is accomplished by use of edge/face swapping wherever possible: if that fails, then an additional point is inserted on the missing edge. Additional points are rarely needed when reasonable quality surface meshes are provided.

The second step is to establish the boundary faces after all boundary edges have been established. In most cases, all boundary faces will be present in the mesh, but occasionally there are some boundary faces that need to be established. When a boundary face is not in the mesh there exists one or more mesh edges that pass through the triangle formed by the three boundary surface edges. In this situation, it is usually possible to recover the boundary face by an edge/face swap procedure. In stubborn cases for which edge/face swapping is not successful, a point is inserted at the face barycenter (centroid).

Re-establishing Prescribed Boundary Surface

- Check whether all boundary edges are present. If not, use edge/face swapping procedure. If an edge is still not established, insert a point on missing edge.
- Check whether all boundary faces are present. If not, use edge/face swapping procedure. If a face is still not established, insert a point at barycenter.

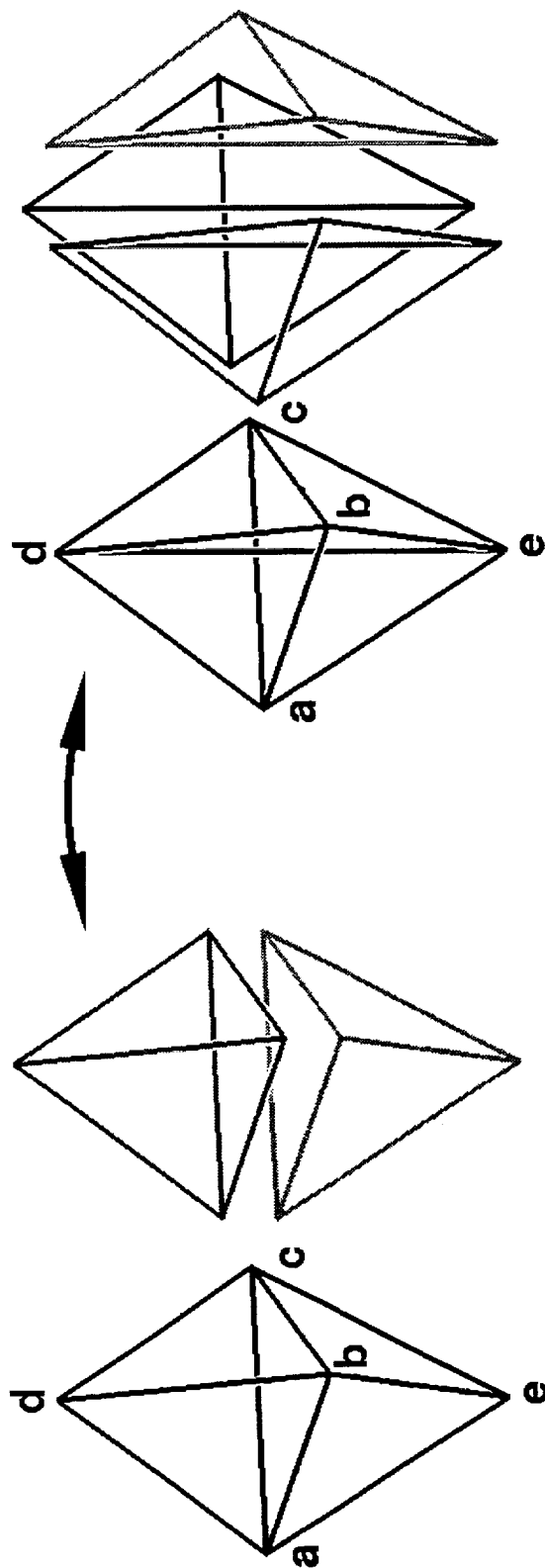
Edge/Face Swapping

It is possible for certain polyhedral configurations to be formed by different combinations of tetrahedra without changing the exterior triangulation. This is illustrated here for the simplest example consisting of either two tetrahedra with a common face (left hand figure) or three tetrahedra with a common edge (right hand figure). Since either possibility is compatible with the surrounding mesh of tetrahedra, one has the flexibility to choose the combination that is most favorable. For example, if the vertical edge shown in the right hand figure is a boundary surface edge but the initial Delaunay mesh contains the left hand combination of tetrahedra, a 2-to-3 tetrahedron swap will establish this boundary surface edge.

This procedure is also used during the mesh optimization stage. If, for example, one of the tetrahedra on the left hand side is extremely flat (e.g. the lower tetrahedron will be flat if the lowest vertex lies close to the plane of the common face) then the 2-to-3 tetrahedron swap will remove the bad tetrahedron and introduce three good quality tetrahedra.

The procedure can only be applied if the polyhedron formed by the tetrahedra is a convex configuration. When this particular configuration fails to be convex, it is often still possible to find other more complex combinations of tetrahedra for which a suitable swapping is feasible.

Edge / Face Swapping



Two Tetrahedra on Five Points Three Tetrahedra on Five Points

abcd, acbe

abed, bced, caed

Unstructured Mesh Generation - Present Status

MESH3D is presently quite capable of producing high quality volume meshes with suitable grid densities near the surface for Euler calculations.

The method is fully automated so that no user intervention is required except for providing the location of the outer flow-field boundaries.

The code has been tested on over 30 configurations, and has proven to be robust when reasonable quality surface grids are used.

MESH3D is sufficiently robust and reliable now to replace MESHPLANE as the mesh generation code for AIRPLANE.

Unstructured Mesh Generator

Present Status

- MESH3D generates high quality isotropic meshes suitable for solving the Euler equations of inviscid flow
- Generation of volume mesh requires no user intervention
- Code is robust and has been tested on numerous configurations
- MESH3D will now replace MESHPLANE as the tetrahedral mesh generator for use with the AIRPLANE code

Unstructured Mesh Generation - Current Research

MESH3D is currently being extended from an Euler mesh generator to a Navier Stokes mesh generator. Volume mesh points near the surface are placed normal to the boundary surface, giving a "structured" appearance to the mesh near the surface.

Higher precision arithmetic will be required when computing geometric primitives, such as the intersection of a face and an edge, for the Navier Stokes type meshes than is currently used for Euler meshes. In addition, extensive testing with a Navier-Stokes flow solver will be necessary to determine the accuracy of the solutions using highly stretched tetrahedral meshes for both laminar and turbulent flows. A laminar version of AIRPLANE has been written but has not been tested yet on a highly dense, high aspect ratio grid near the surface.

Unstructured Mesh Generation

Current Research

- NS tetrahedral mesh generator under development
- Mesh points are placed normal to boundary surface and tetrahedra adjacent to the boundary surface have a “structured” appearance
- High precision arithmetic is being incorporated into MESH3D to ensure accurate evaluation of geometric primitives
- Extensive testing with an NS flow solver is necessary to determine solution accuracy on highly stretched tetrahedral meshes for both laminar and turbulent flows

Unstructured Mesh Generation - Future Work

Although it was initially thought that unstructured surface grid generation algorithms were readily available, it turns out that the methods available are much more laborious than anticipated. Therefore, further investigation into more automated methods is needed (Gridgen) or improvements to VGRID are needed.

An unstructured mesh is well suited for the application of solution adaptive mesh refinement methods, and these techniques will be included into the production version of AIRPLANE.

Once the grid generation methods for AIRPLANE are sufficiently automated, an adjoint based design-by-optimization method will be developed.

Unstructured Mesh Generation

Future Work

- Improvement of surface meshing methods. Greater automation of surface mesh generation is needed
- Adaptive techniques for both Euler and NS (existing techniques are not reliable enough for use in a production code)
- Development of adjoint based optimization codes using unstructured meshes

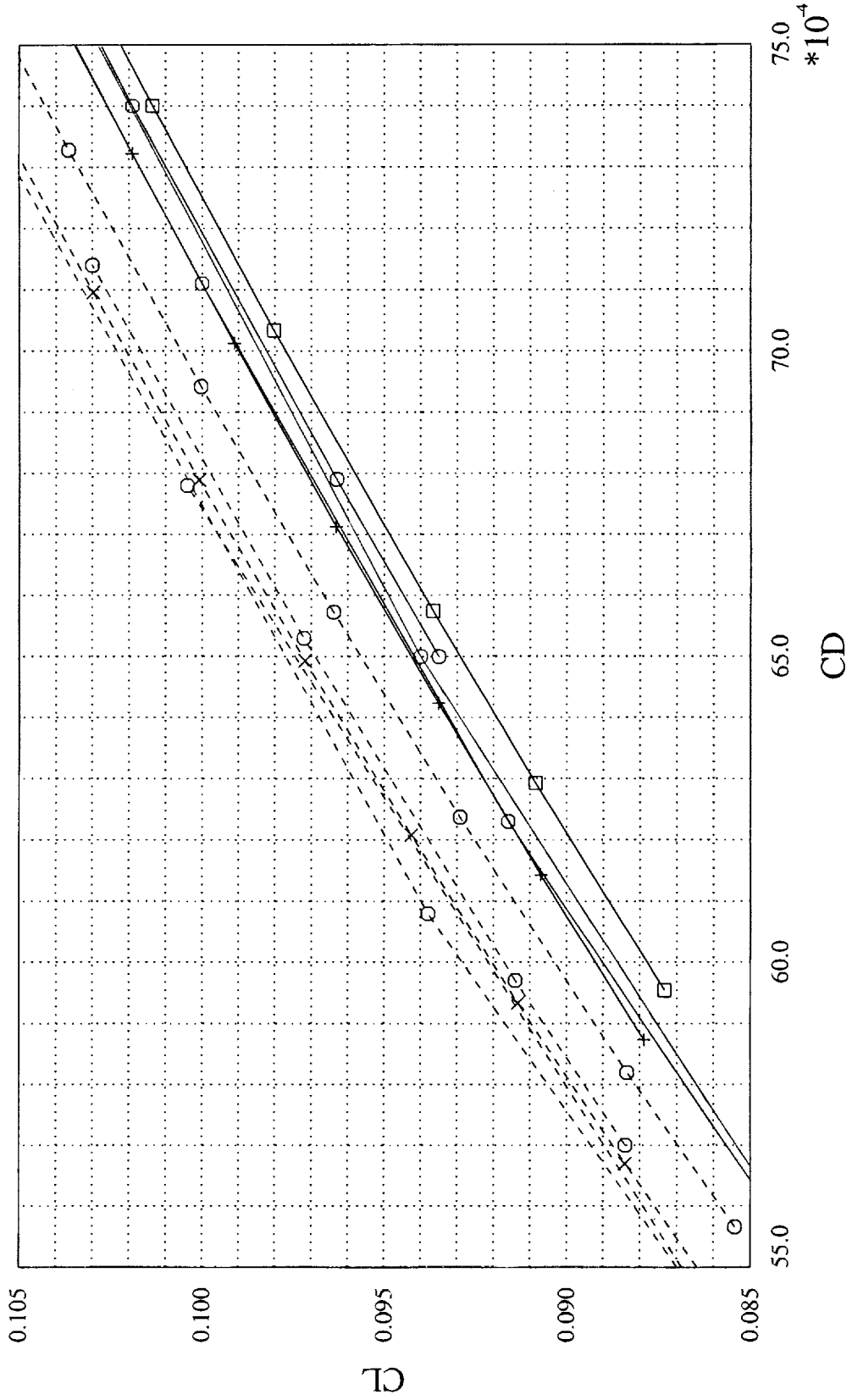
Euler Computations, Ames 01-03 vs. TCA, Wing/Body

The inviscid solutions from the analytical cross-checks for the baseline TCA and the Ames 01-03 wing/body configurations are shown. The computed values of the drag coefficient at a lift coefficient of 0.1 for all methods have a 2.0 and 1.4 drag count spread for the Ames 1-03 and the baseline TCA configurations, respectively. However, it is quickly noted that AIRPLANE is predicting a higher drag level than the other methods. In fact, if the AIRPLANE results were removed from the study, the remaining methods would be within 0.8 counts for both the Ames 1-03 and the baseline TCA configurations. This raises the question of why the AIRPLANE results are consistently predicting more drag than the other methods.

Euler Computations, Ames 01-03 vs. TCA, Wing/Body

M=2.4, entire fuselage

- | | | | |
|-------|---------------|-------|---------------|
| —□— | AIRPLANE TCA | --○-- | CFL3-D/E 1-03 |
| --○-- | AIRPLANE 1-03 | —○— | UPS/E TCA |
| —+— | FLO87-MB TCA | --○-- | UPS/E 1-03 |
| --*-- | FLO87-MB 1-03 | —○— | TRANAIR TCA |
| —○— | CFL3-D/E TCA | --○-- | TRANAIR 1-03 |

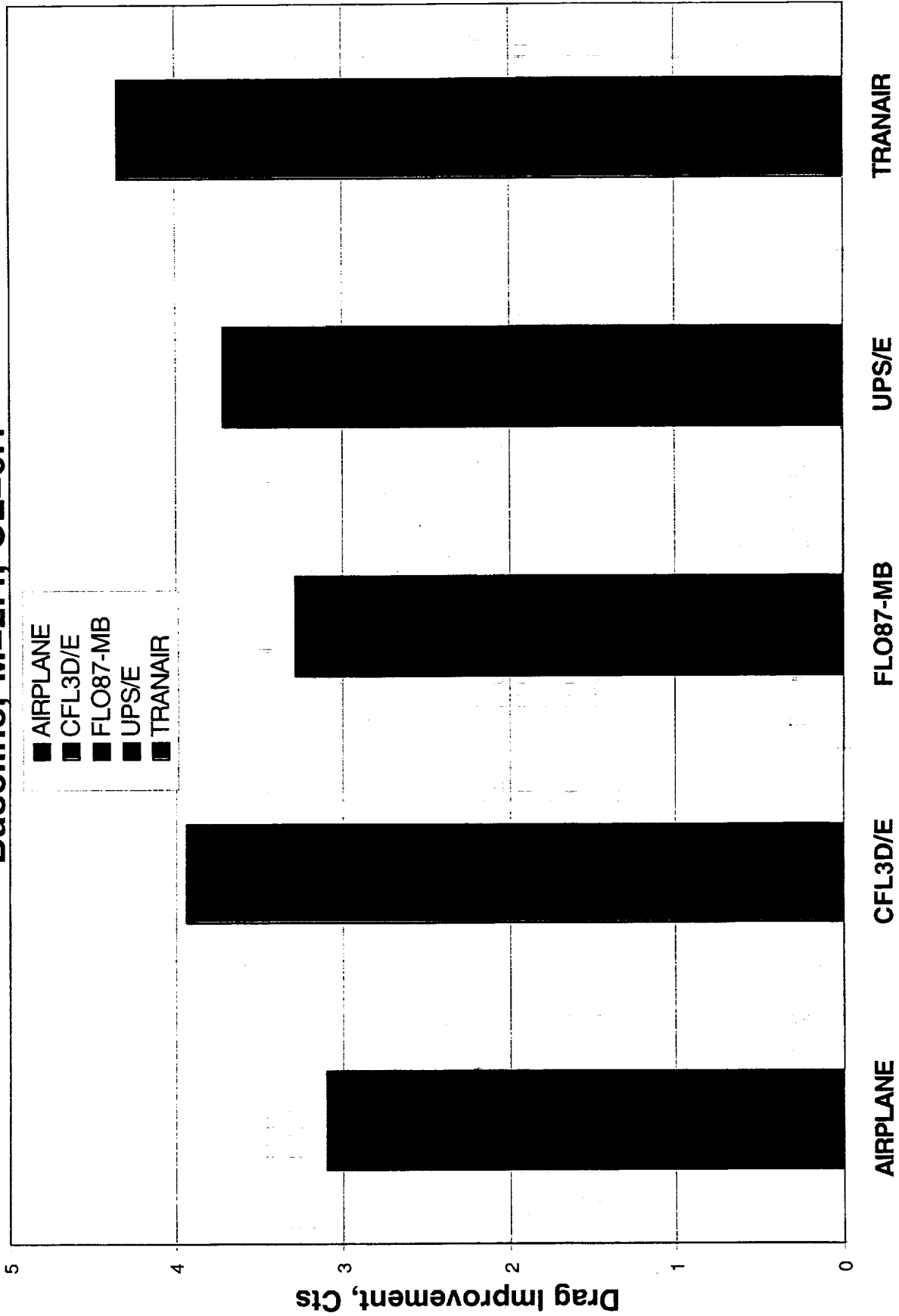


Ames 1-03 W/B Drag Increments Relative to the TCA Baseline, M=2.4, CL=0.1

The wing/body inviscid performance increments at cruise from the analytical cross-checks for the Ames 1-03 relative to the baseline TCA are shown. The improvements of all inviscid methods are within 1.25 counts.

The performance increment for AIRPLANE is in line with the other CFD results. In fact, the improvement suggested by AIRPLANE is within 0.18 counts of FLO87-MB.

Ames 1-03 W/B Drag Increments Relative to the TCA Baseline, $M=2.4$, $CL=0.1$



Ames 1-03 W/B/N/D Drag Increments Relative to the TCA Baseline, $M=2.4$, $CL=0.1$

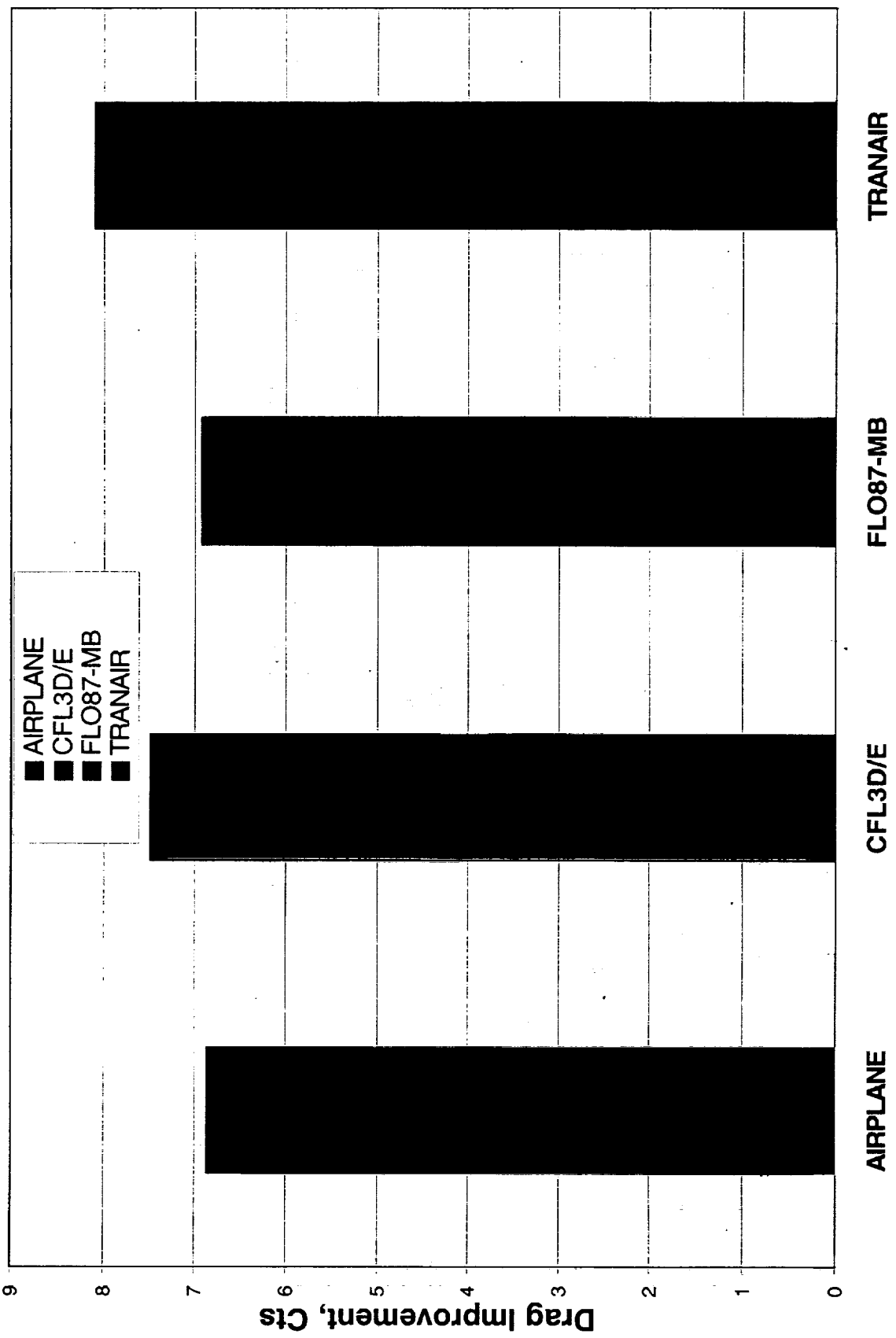
The wing/body/nacelle/diverter inviscid performance increments at cruise from the analytical cross-checks for the Ames 1-03 relative to the baseline TCA are shown. The improvements of all inviscid methods are within 1.23 counts.

The performance increment for AIRPLANE is in line with the other CFD results. In fact, the improvement suggested by AIRPLANE is within 0.05 counts of FLO87-MB.

The apparent discrepancy of the AIRPLANE code results relative to the other inviscid method is not found in terms of performance improvements. This is not surprising since AIRPLANE has repeatedly shown to provide good agreement with wind tunnel results in terms of performance improvements for several configurations tested as part of the HSR program. The fact that a warped surface grid with the same number and density distribution of grid points on the surface was used for both the baseline and 1-03 configurations should strengthen the credibility of the AIRPLANE performance improvement computations. For example, if the density of grid points is insufficient to capture a given flow phenomenon associated with one configuration then it will likely not capture it in the optimized configuration, and the relative performance gains should still be valid. However, if the optimized configuration has a performance gain that cannot be captured by the existing mesh, then the increment would have a discrepancy equal to the gain from that particular performance attribute.

The absolute drag level discrepancy that AIRPLANE displays relative to the other methods can now be studied with greater ease by making use of MESH3D. The ability of MESH3D to use triangulated surface grids as opposed to having to go back through CAD for additional sectional input as was needed for MESHPLANE makes it well suited for a grid convergence study. The automation of the volume gridding combined with the GridTool/VGRID method for obtaining unstructured surface grids allows for fairly rapid density modifications to the surface grids. Surface grid density changes are accomplished by increasing or decreasing the values of point and line sources (given by a nominal triangle size) within GridTool, and regenerating a surface grid with VGRID.

Ames 1-03 W/B/N/D Drag Increments Relative to the TCA Baseline, M=2.4, CL=0.1



LEADING EDGE GRID COMPARISON OF AIRPLANE/MESHPLANE AND FLO87-MB

An evaluation of the AIRPLANE grid as compared to FLO87-MB grid was the first step in determining the source of the increased drag level from the AIRPLANE computations. AIRPLANE was compared to FLO87-MB since FLO87-MB calculations had comparable drag levels as the other computations, and if refinement of the AIRPLANE mesh could produce similar drag levels as FLO87-MB then it would obviously agree with the other computations.

This figure shows the surface grid of the leading edge of the original AIRPLANE mesh generated using MESHPLANE, and the FLO87-MB structured surface grid. The FLO87-MB surface mesh has been triangulated by simply adding a diagonal to the quadrilateral surface grid. This was done to integrate drag using tools generated for unstructured meshes and to make a more comparable comparison of the structured and unstructured grids. The viewing region (centered at a spanwise location of 300 inches) and angle are held constant for accurate comparisons. The AIRPLANE mesh has 39,189 surface points and 578,678 total grid points whereas the FLO87-MB grid has 17,221 points and 936,740 total points. The MESHPLANE surface grid has more than twice the number of surface grid points than the FLO87-MB grid has, but the FLO87-MB grid has 1.6 times the number of points total. Obviously, the FLO87-MB grid has more points in the flow-field.

The AIRPLANE grid has comparable grid density in the leading edge region, in terms of grid lines going around the leading edge, but the AIRPLANE grid point spacing decays more rapidly aft of the leading edge than that of FLO87-MB. Note that the AIRPLANE grid has grid lines wrapping around the leading edge in a spanwise direction, whereas the FLO87-MB has grid lines wrapping in the streamwise direction. The AIRPLANE mesh clearly has more points in the spanwise directions. Tick marks are displayed below the leading edge to act as a "ruler" where the tick marks are placed 10 inches apart.

The pressure coefficients for AIRPLANE and FLO87-MB appear very similar, and are plotted to the same scale. The differences in the solutions are very slight and can not be seen by simply comparing qualitative quantities such as colored surface pressure contours.

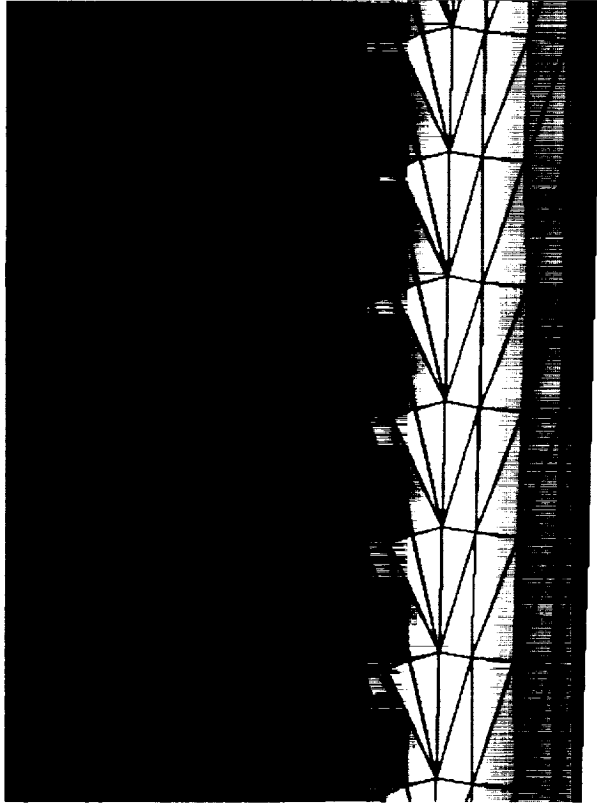
LEADING EDGE GRID COMPARISON

$M = 2.4$, $\alpha = 3.756$, $Z \sim 300$

C_p



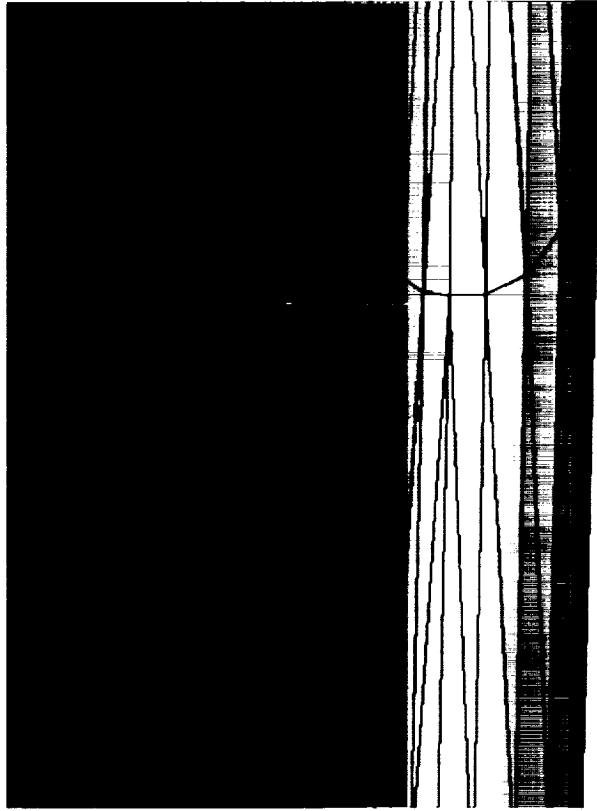
-0.16 -0.08 0.00 0.08 0.16 0.24



AIRPLANE: MESHPLANE

GRID 0: 39,189 surface points

578,678 total points



FLO87-MB (triangulated)

GRID 0: 17,221 surface points

936,740 total points

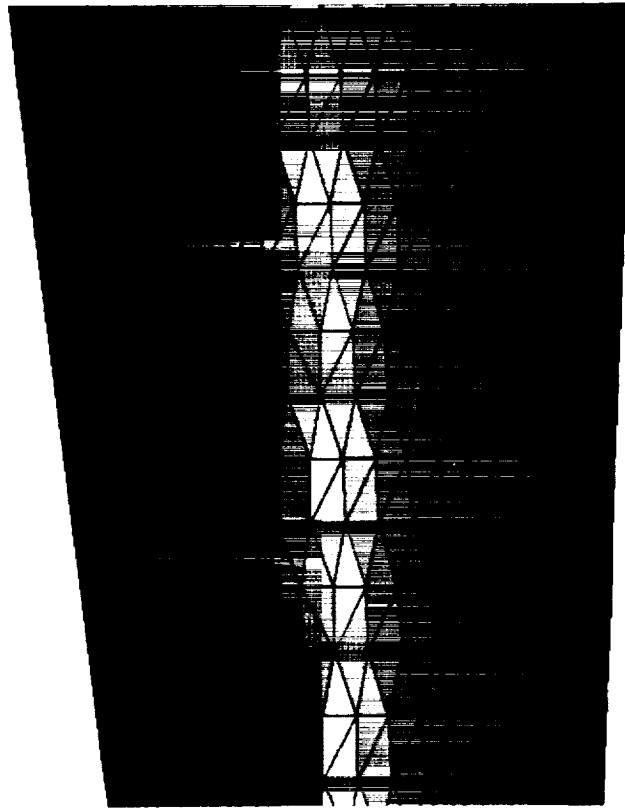
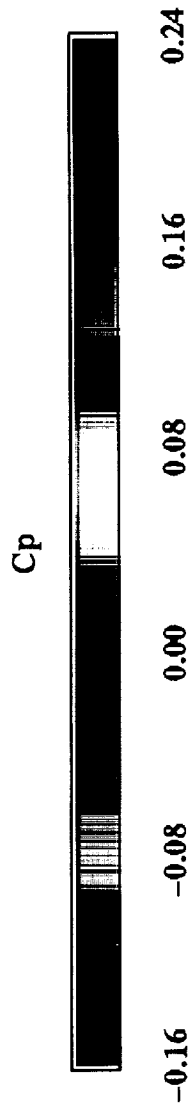
FOREBODY GRID COMPARISON OF AIRPLANE AND FLO87-MB

A comparison of the forebody grids, 500 inches from the nose, used with AIRPLANE and FLO87-MB is shown. The initial grid used by AIRPLANE appears to have a high quality surface mesh with an adequate number of grid points. In contrast, the FLO87-MB grid is coarse and highly skewed. The forebody grid from FLO87-MB is skewed since it uses a C-H topology, this makes very nice meshes around the leading edge of the wing, but leads to a very poor mesh around the body.

The tick marks displayed below the fuselage act as a "ruler" where the tick marks are placed 10 inches apart

FOREBODY GRID COMPARISON

M = 2.4, α = 3.756, X~500



AIRPLANE: MESHPLANE

GRID 0: 39,189 surface points

578,678 total points



FLO87-MB (triangulated)

GRID 0: 17,221 surface points

936,740 total points

AIRPLANE GRID/SOLUTION: GRID 0 - Cutting Plane Normal to Leading Edge at Z=300

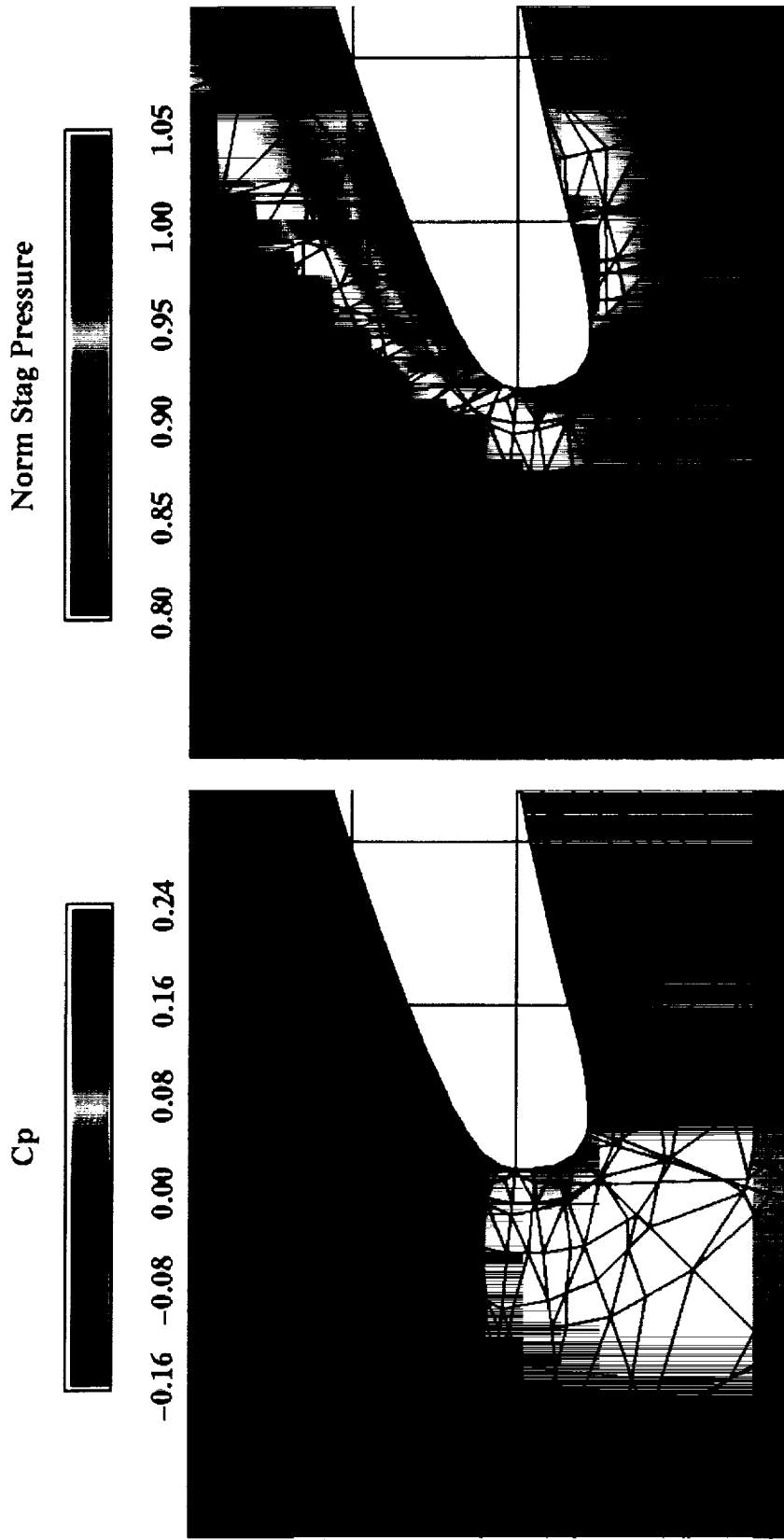
A cutting plane which slices through the unstructured tetrahedral mesh is used to display the volume grid near the leading edge. This cutting plane is oriented normal to the 71 degree swept inboard leading edge and passes through the leading edge at a spanwise location of 300 inches. The black "grid" lines indicate the sliced tetrahedral boundaries. A sliced tetrahedron can result in a point, line, triangle, or quadrilateral.

Based on the solution derived from the original AIRPLANE mesh obtained from MESHPLANE, the C_p and normalized stagnation pressure distributions are shown at Mach 2.4, alpha 3.756. The normalized stagnation pressure is equal to the ratio of total pressure divided by the freestream total pressure. Significant total pressure losses are observed on the upper surface just aft on the leading edge. Since there are no shock waves in the local flow-field, the stagnation pressure should be uniform. The losses in the total pressure are a result of excessive dissipation used to stabilize the solution. Note that scalar dissipation was used for this solution. This will be discussed later on when comparisons will be made with computations using Jameson's CUSP dissipation scheme.

Very negative pressure coefficients are observed in this region resulting from the flow expanding rapidly around the blunt leading edge. It is interesting to note that this region of expanding flow together with the orientation of the surface results in significant drag reductions to the configuration. This will be shown in subsequent figures.

A background grid is displayed inside the leading edge to act as a "ruler"; the grid lines are placed 10 inches apart.

AIRPLANE GRID/SOLUTION: GRID 0
Cutting Plane Normal to Leading Edge at Z = 300



AIRPLANE: MESHPLANE

M = 2.4, $\alpha = 3.756$

Ruler shows ten-inch increments

FLO87-MB GRID/SOLUTION: GRID 0 - Cutting Plane Normal to Leading Edge at Z=300

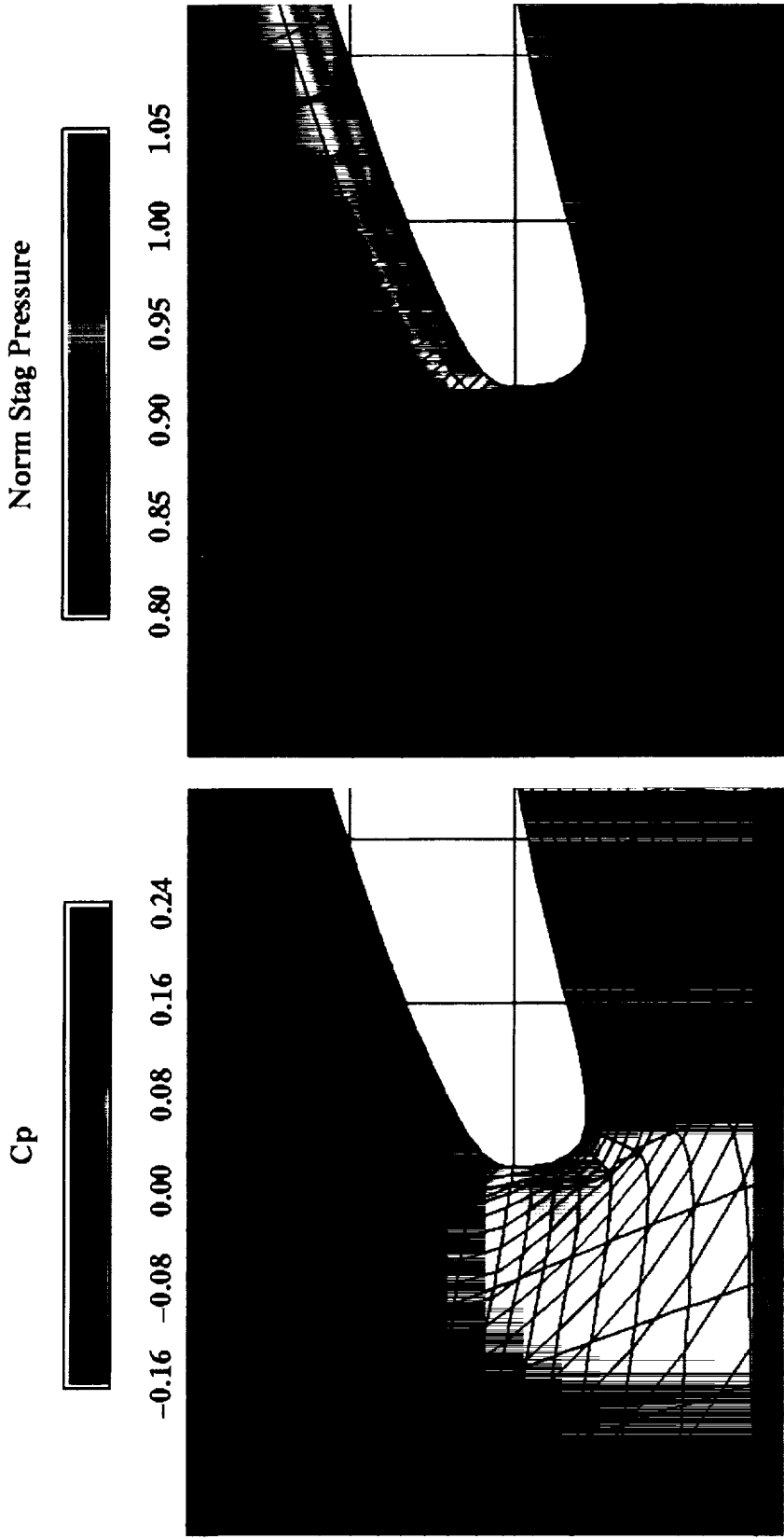
An identical cutting plane as used in the previous figure was used to slice through the tetrahedral FLO87-MB grid. The structured hexahedral FLO87-MB grid was turned into an unstructured tetrahedral grid by subdividing each hexahedron into six tetrahedra. This was carried out in order to use exactly the same graphics software that had been developed for unstructured grids.

The FLO87-MB grid has a similar number of surface points around the leading edge, but has a smoother gradation of points into the flow-field, where the surface grid density is maintained for a greater distance into the volume grid. However, since FLO87-MB is a structured mesh method there can be regions of unnecessarily refined grid in the far-field whenever it is not possible to coarsen the outer flow-field blocks. As a consequence, structured mesh methods are typically less efficient in the distribution of mesh points.

Note that this computation also used Jameson's scalar dissipation scheme, but the total pressure losses are confined to a smaller region than the AIRPLANE solution due to a less rapid decay of points from the surface.

FLO87-MB GRID/SOLUTION: GRID 0

Cutting Plane Normal to Leading Edge at Z = 300



FLO87-MB: Wing/Body Grid with Scalar Dissipation Model

M = 2.4, $\alpha = 3.756$

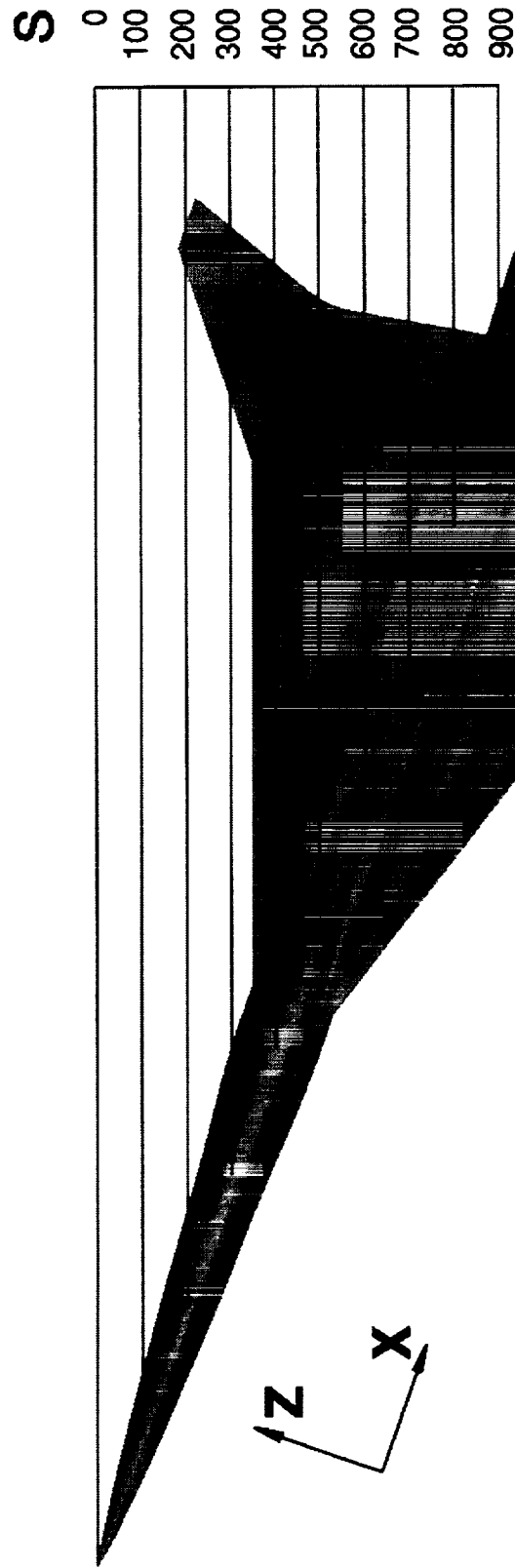
Ruler shows ten-inch increments

ACCUMULATED DRAG SAMPLING PLANES - Parallel to Inboard Wing Leading Edge

This figure illustrates the orientation and location of a series of cutting planes used to sum the drag coefficient from the nose of the aircraft as a function of S . S is defined as $X \cos(\lambda) - Z \sin(\lambda)$, where X is streamwise, and Z is spanwise. Each line of constant S represents a cutting plane in top view as shown. A drag build up comparison between AIRPLANE and FLO87-MB with the accumulated drag data sampled with cutting planes parallel to the leading edge angle will allow an accurate comparison of the drag characteristics attributed to the inboard leading edge.

**ACCUMULATED DRAG SAMPLING PLANES
PARALLEL TO INBOARD WING LEADING EDGE**

$$S = X \cos(\lambda) - Z \sin(\lambda)$$

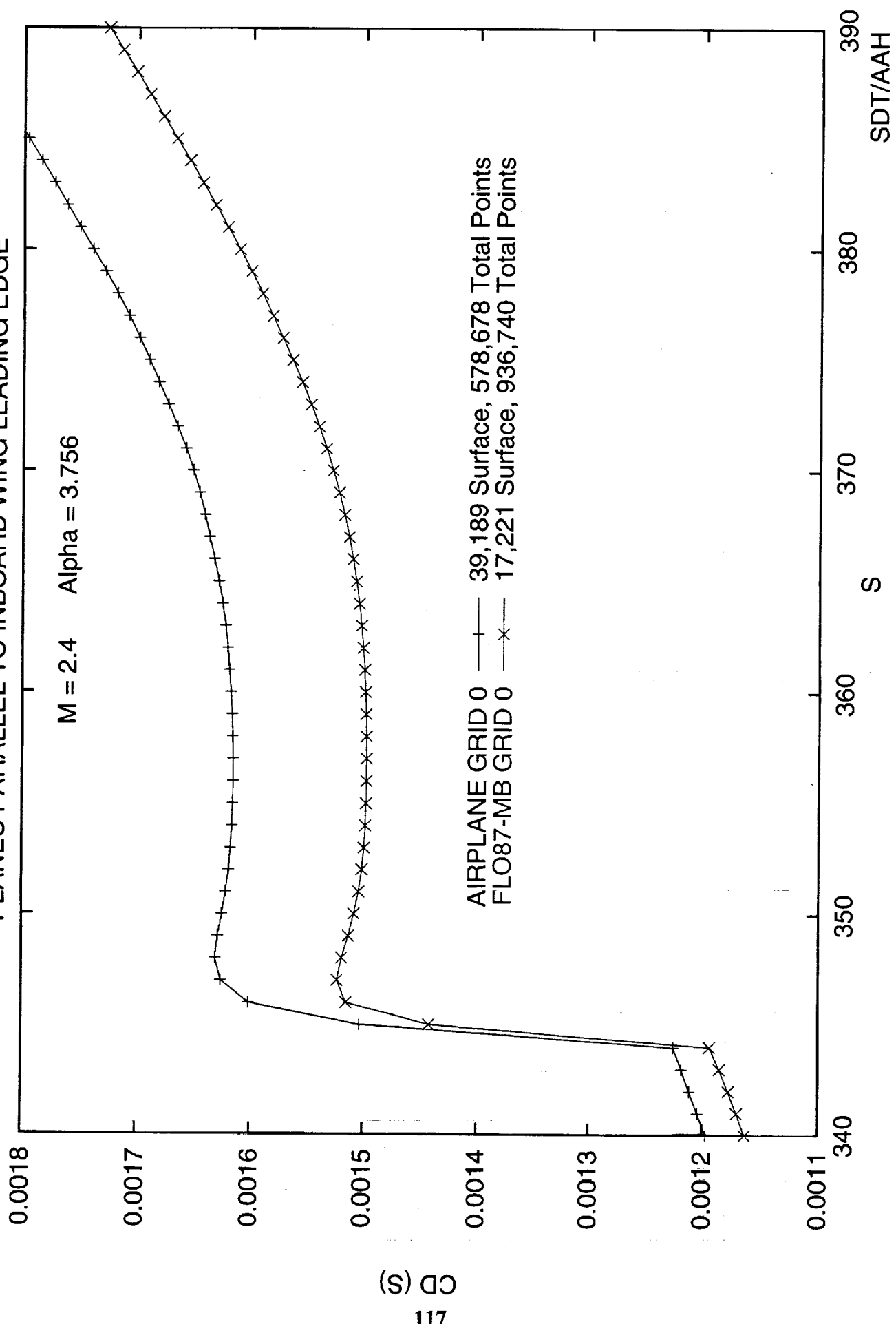


**$\lambda = 71$ deg is the sweep angle
 $S = 344.6$ at inboard leading edge**

ACCUMULATED DRAG COEFFICIENT - AIRPLANE Grid 0 vs. FLO87-MB Grid 0

This figure compares the accumulated drag coefficients computed by AIRPLANE and FLO87-MB at Mach 2.4, alpha 3.756. The drag is summed using sampling planes which are parallel to the inboard wing leading edge. This clearly indicates that the largest discrepancy in drag is associated with the leading edge, approximately 0.9 count. The value of 0.9 count is obtained after subtracting off the differences in forebody and supersonic wing drag immediately ahead of the leading edge (S=344.6). The drag discrepancy attributed to the forebody and a portion of the outboard wing is approximately 0.35 counts.

ACCUMULATED DRAG COEFFICIENT WITH SAMPLING
 PLANES PARALLEL TO INBOARD WING LEADING EDGE



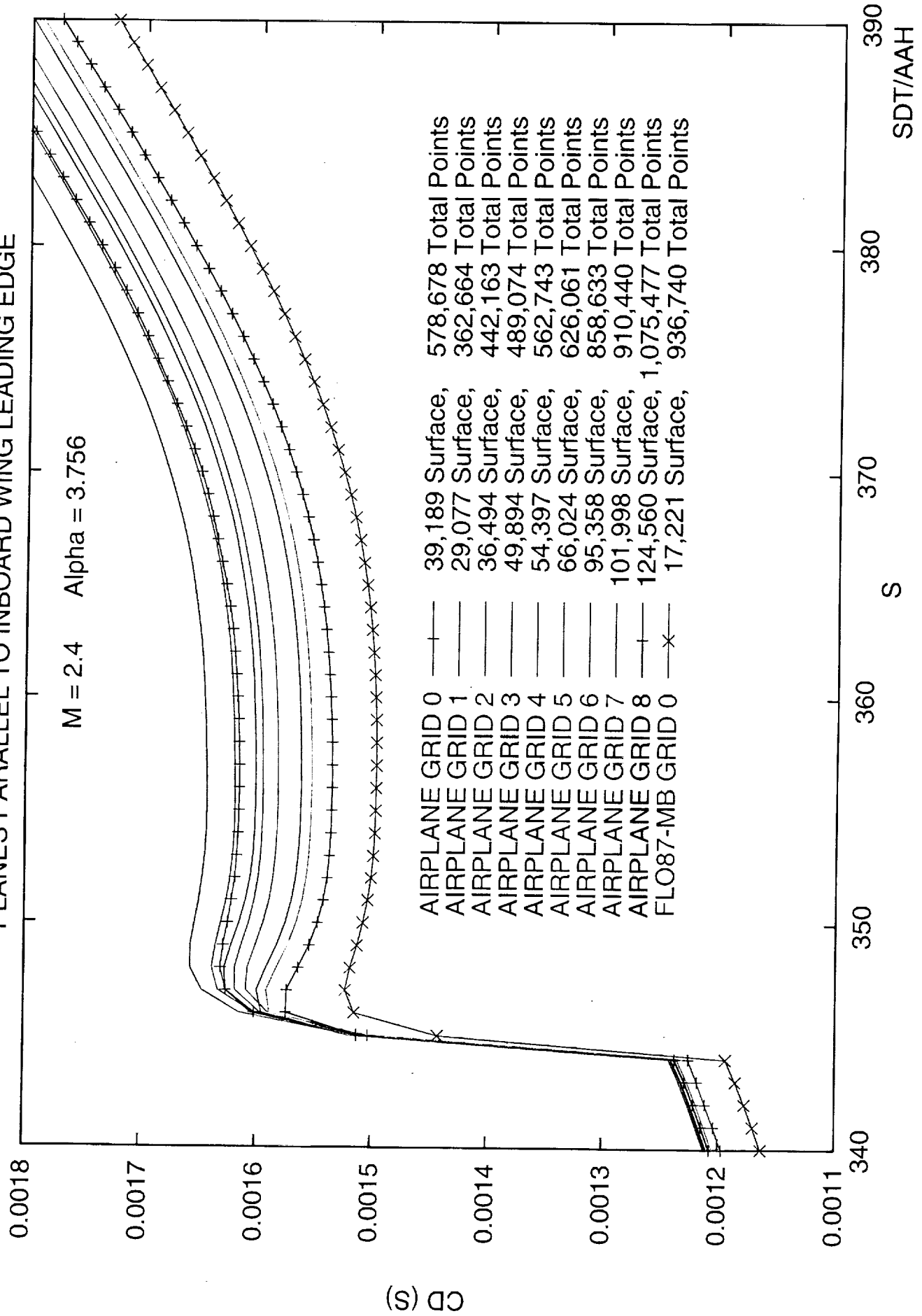
ACCUMULATED DRAG COEFFICIENT - AIRPLANE Grid 0-8 vs. FLO87-MB Grid 0

A series of eight surface grids of varying grid densities were generated using the Langley GridTool/VGRID software tools, and the volume grid generated using MESH3D. The accumulated drag for each of the eight solutions using MESH3D, and the initial solution generated using MESHPLANE, are compared to the FLO87-MB solution near the inboard leading edge. The accumulated drag coefficients directly aft of the inboard leading edge are decreasing in value with increasing number of mesh points in the MESH3D grids (grids 1-8) and approaching the FLO87-MB results. It would be expected that the drag coefficient would eventually remain unchanged with larger mesh sizes. Larger meshes were not generated due to the current lack of control in the placement of points near the surface in the volume grid with MESH3D. It is expected that the number of surface points used for grid 8 is more than sufficient to capture the flow characteristics, but the flow-field points near the surface need to be placed normal to, and closer to the surface.

The change in drag for the two grid extremes is over a count between the coarse grid 1 and refined grid 8. Also the more refined meshes are capturing leading edge suction that was not captured to this extent with FLO87-MB or AIRPLANE with the original MESHPLANE grid. This is observed by the drop in drag coefficient just aft of the leading edge in the more refined AIRPLANE grid computations. The changes to the forebody and outboard wing are relatively small for all the refined AIRPLANE meshes, and are within 0.1 counts.

The discrepancy between the most refined AIRPLANE grid (grid 8) aft of the leading edge is now of comparable value to the discrepancy at the forebody and outboard wing portion. The forebody grid of FLO87-MB is coarsely defined and somewhat skewed, whereas all the AIRPLANE grids have reasonably dense forebody grids with high quality surface grids. This now brings the FLO87-MB forebody results into question. Therefore we will investigate refinement of the FLO87-MB grid, and study an initial and a refined UPS solution.

ACCUMULATED DRAG COEFFICIENT WITH SAMPLING
 PLANES PARALLEL TO INBOARD WING LEADING EDGE



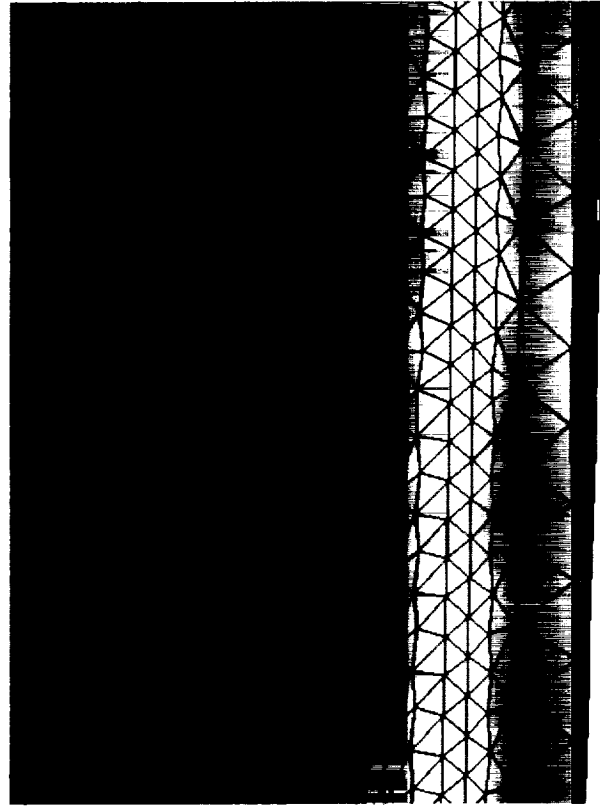
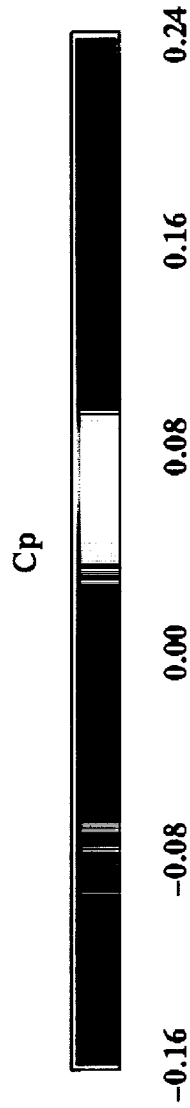
LEADING EDGE GRID COMPARISON - AIRPLANE/VGRID/GridTool Grid 1 and Grid 8

A comparison of the AIRPLANE leading edge surface grids generated by use of GridTool/VGRID for the two grid extremes, the coarsest grid (grid 1) and most refined grid (grid 8), are shown in the figure. The coarse grid clearly has an insufficient number of points to capture the curvature around the leading edge lower surface. The increased spacing in this region results from the stretching of the grid points in VGRID when the triangulated lower surface patch is projected onto the high curvature region of the leading edge. This was remedied in later grids by adding more patches around the leading edge. For example, the leading edge region for grid 8 was divided into 3 patches; a narrow patch placed directly at the leading edge, with surface normal facing forward, and two patches over each of the high curvature regions of the upper and lower "corners" of the leading edge. Thus the general orientation of the patch normals were pointing more or less in the general direction of the true surface to reduce stretching when the triangulated surfaces were projected to the true surface. Only two patches were used for the coarse grid (grid 1), an upper and a lower surface patch, resulting in an insufficient point density along the leading edge lower surface as shown.

The refined AIRPLANE grid (grid 8) is very dense. It has at least 2-3 times the number of points wrapping around the leading edge and approximately 20 times the density of points in the spanwise direction as the FLO87-MB grid (compare with chart 16). This grid also has increased density around the "corners" of the blunt wing leading edge, and should be of sufficient density to obtain accurate drag values around the leading edge.

LEADING EDGE GRID COMPARISON

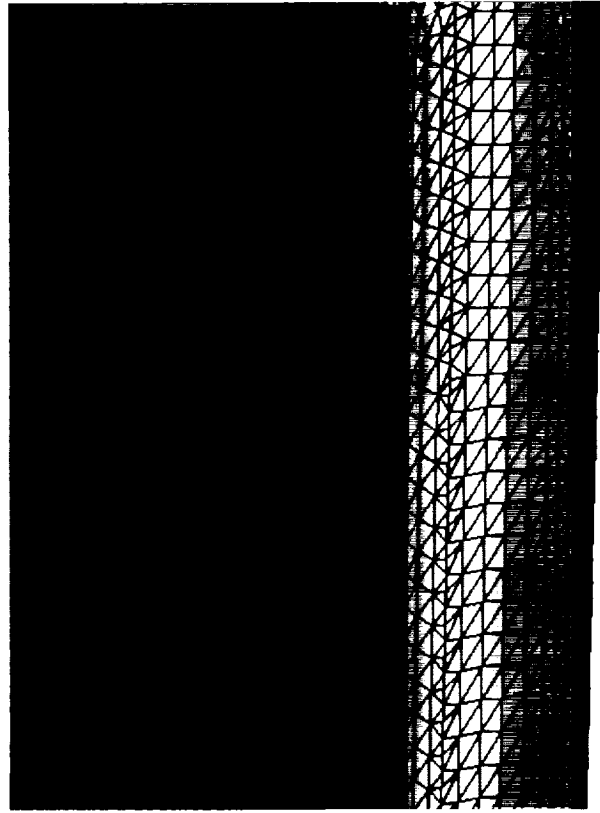
M = 2.4, α = 3.756, Z~300



AIRPLANE: VGRID/GridTool

GRID 1: 29,077 surface points

362,664 total points



AIRPLANE: VGRID/GridTool

GRID 8: 124,560 surface points

1,075,477 total points

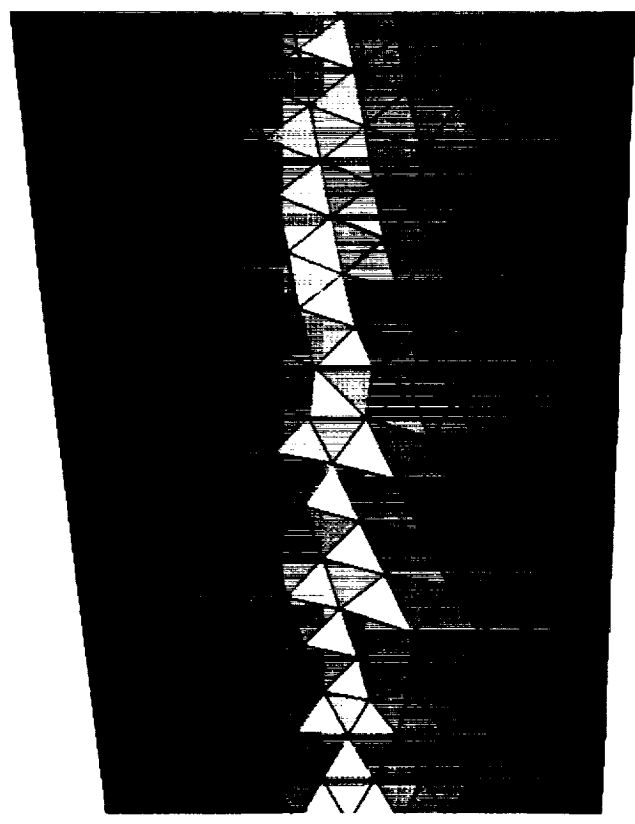
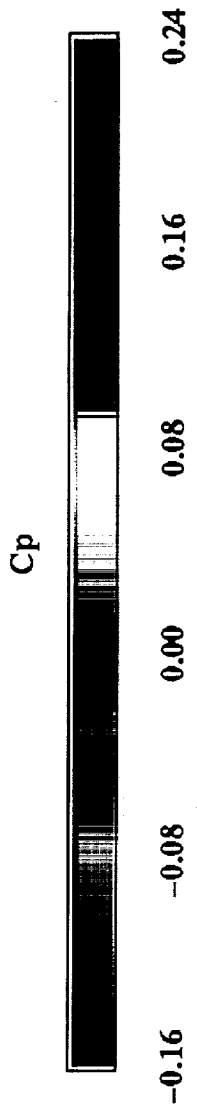
FOREBODY GRID COMPARISON - AIRPLANE/VGRID/GridTool Grid 1 and Grid 8

A comparison of the forebody surface grids generated by use of GridTool/VGRID for the two grid extremes, the coarsest grid (grid 1) and most refined grid (grid 8), are shown in the figure. Both grids exhibit high quality grids with smooth distributions of mesh points. The refined AIRPLANE grid (grid 8) has approximately twice the number of surface grid points as the coarse (grid 1), and 7 times the number of points of the FLO87-MB grid (compare with chart 17) in the forebody region.

The very coarse forebody grid used with FLO87-MB compared to the refined AIRPLANE grid further emphasizes that the FLO87-MB forebody grid needs refinement. An example of a very fine forebody grid is easily obtained from the parabolized Navier-Stokes code, UPS, which uses a marching scheme so that very dense meshes can be used without incurring large memory requirements. The coarse and highly skewed forebody grid used with FLO87-MB is now thought to produce less accurate solutions in this region than the refined AIRPLANE grid solutions.

FOREBODY GRID COMPARISON

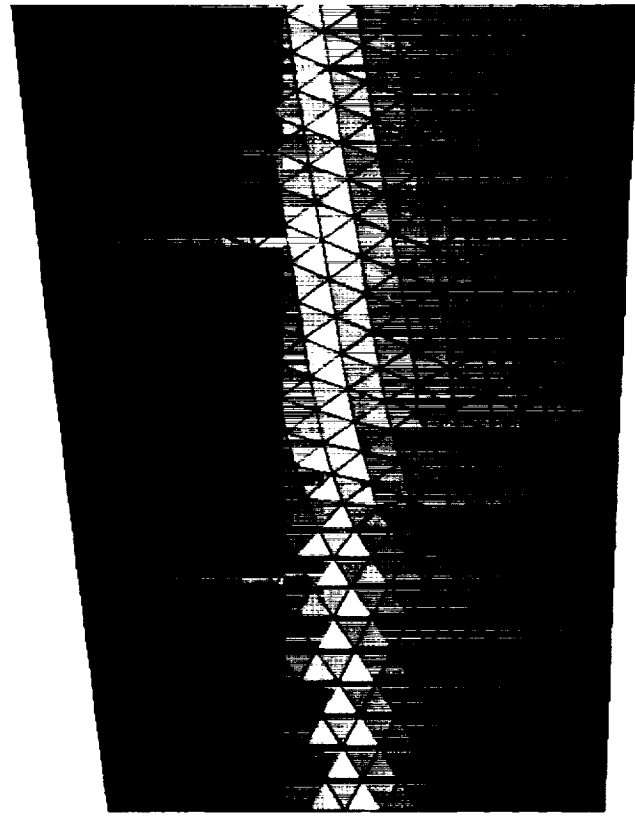
$M = 2.4$, $\alpha = 3.756$, $X \sim 500$



AIRPLANE: VGRID/GridTool

GRID 1: 29,077 surface points

362,664 total points



AIRPLANE: VGRID/GridTool

GRID 8: 124,560 surface points

1,075,477 total points

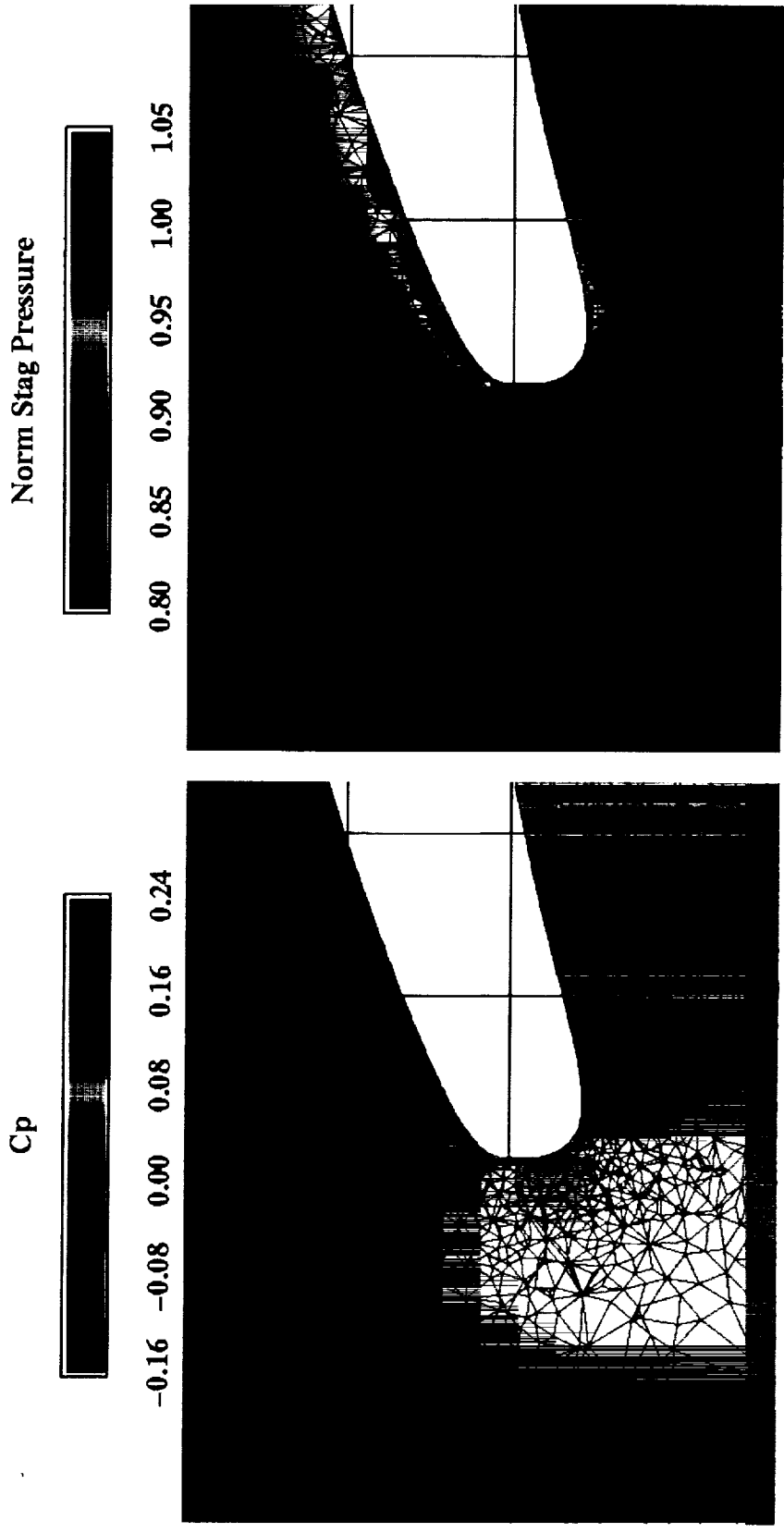
AIRPLANE GRID/SOLUTION: GRID 8 - Cutting Plane Normal to Leading Edge at Z=300

The volume grid and solution near the leading edge are shown for the refined AIRPLANE grid (grid 8). A smooth density gradation of volume points near the surface is observed with distance from the leading edge. The volume points nearest the surface are placed at a distance equal to the distance between neighboring surface points. The ability to place points in the volume grid normal to the surface was not yet included in MESH3D during the time of this study, but has recently been incorporated into the present version of the code. The present version will allow the user to specify the aspect ratio of the first cell off the surface, and the effects of clustering near the surface will be studied. It is thought that fewer surface points may be required if more extensive clustering near the surface is used.

The density of points in the volume grid for this refined grid now far exceeds the density of points for the FLO87-MB grid. Note that the increased density of surface and volume points has reduced the amount of stagnation pressure losses and distance which they extend into the flow-field. Although this AIRPLANE computation used the scalar dissipation scheme, the losses are less for this mesh than in the solutions with the original MESHPLANE mesh as might be expected given the increased density of mesh points.

AIRPLANE GRID/SOLUTION: GRID 8

Cutting Plane Normal to Leading Edge at Z = 300



AIRPLANE: VGRID/GridTool with Scalar Dissipation Model

$M = 2.4$, $\alpha = 3.756$

Ruler shows ten-inch increments

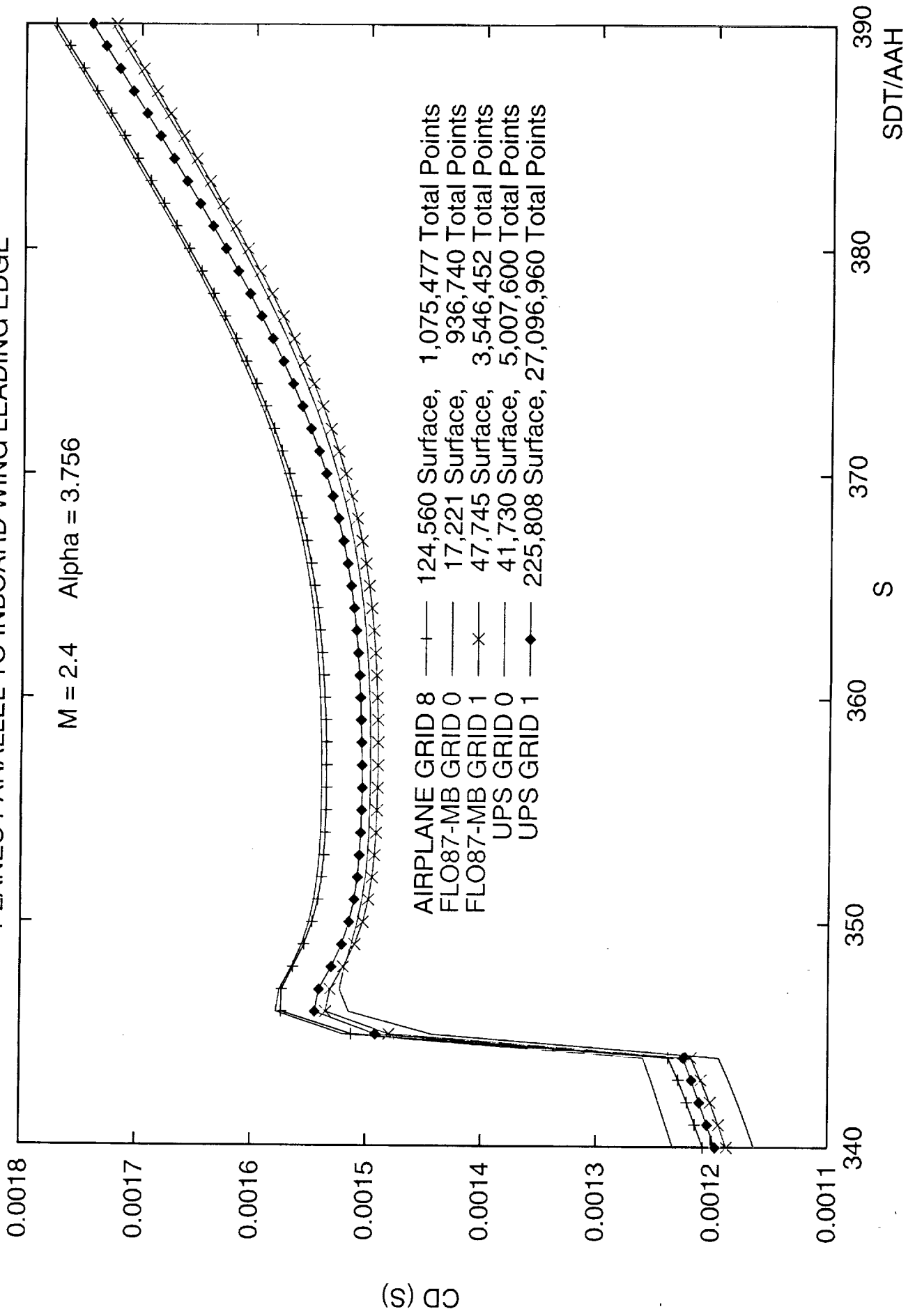
ACCUMULATED DRAG COEFFICIENT - AIRPLANE/FLO87-MB and UPS Solutions Using Initial and Refined Grids

The summed drag characteristics near the leading edge for a solution using a refined FLO87-MB mesh are shown. The mesh was doubled in two directions to increase the density of points on the fuselage, increasing the total number of mesh points by a factor of four. In addition, UPS solutions are now included in the study. Two UPS solutions are shown, one using the initial grid (grid 0) and the other using a refined grid (grid 1). The refined UPS mesh is extremely dense, it has twice the number of surface points as the refined AIRPLANE mesh, and 27 times the number of total points.

The FLO87-MB results after grid refinement are interesting. The change to the forebody drag is substantial, the refined grid has moved closer to the AIRPLANE result. The FLO87-MB solution using the initial grid had over a 0.5 count difference in forebody drag compared with the AIRPLANE solution using the refined grid. Now, the difference is approximately 0.22 counts. The changes to the drag at the leading edge remain the same, they shift upwards by the same increment as ahead of the leading edge, and are in closer agreement with AIRPLANE. Aft of the leading edge, the refined FLO87-MB solution captures additional suction that is captured by AIRPLANE and UPS. The additional suction can be seen where the two FLO87-MB solutions cross in the figure. The drag difference between the refined AIRPLANE and refined FLO87-MB solutions is approximately 0.7 counts at $S=390$.

The refined UPS results are in better agreement with the refined AIRPLANE solution on the forebody than with the refined FLO87-MB solution. The effect of refining the UPS solution was to reduce the forebody drag by approximately 1/3 of a count, this increment remains constant for the range of values shown in the figure. This implies that the only change to the UPS solution was from the forebody. The drag difference between the refined AIRPLANE and refined UPS solution is 1/3 of a count. The Euler CFD methods are beginning to converge upon the true inviscid solution for the Ames 01-03 configuration.

ACCUMULATED DRAG COEFFICIENT WITH SAMPLING
 PLANES PARALLEL TO INBOARD WING LEADING EDGE

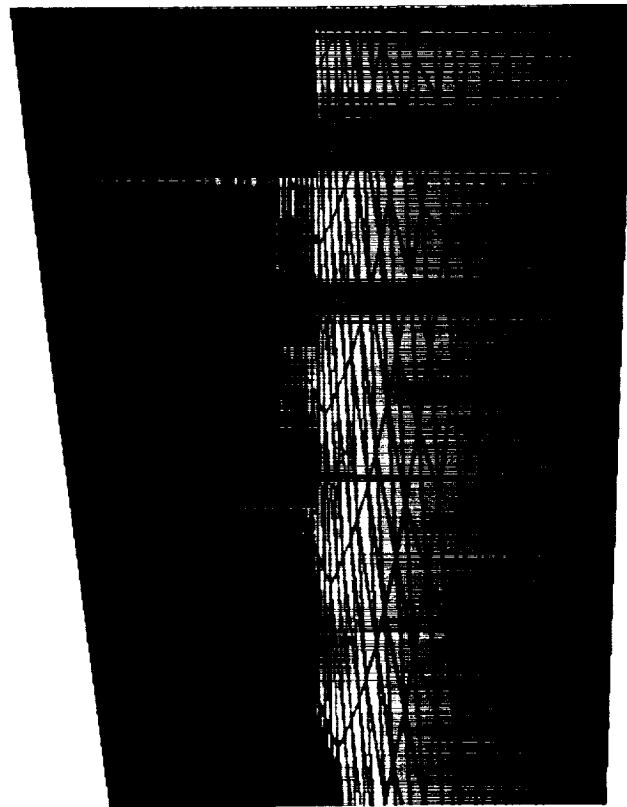
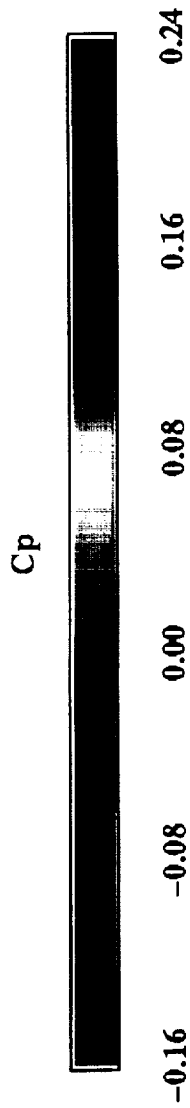


FOREBODY GRID COMPARISON - FLO87-MB and UPS with Refined Meshes

As previously stated, the FLO87-MB grid was refined in 2-directions (I and J) but only twice as dense on the wing surface because of the C-H topology and hence is four times as dense on the forebody surface as the initial grid. This grid is compared to the refined UPS forebody grid in the figure. The number of grid points shown in this figure reveals that FLO87-MB has approximately 1/6 the points displayed than the UPS grid has. Note that the AIRPLANE grid 8 forebody has approximately twice the number of points than FLO87-MB has (chart 24). Therefore, the FLO87-MB grid still has the coarsest forebody grid, and UPS grid has an extremely dense grid, far greater than one would think necessary to obtain an accurate Euler solution. However, the small memory requirements of a marching scheme can easily afford such a large number of surface points.

FOREBODY GRID COMPARISON

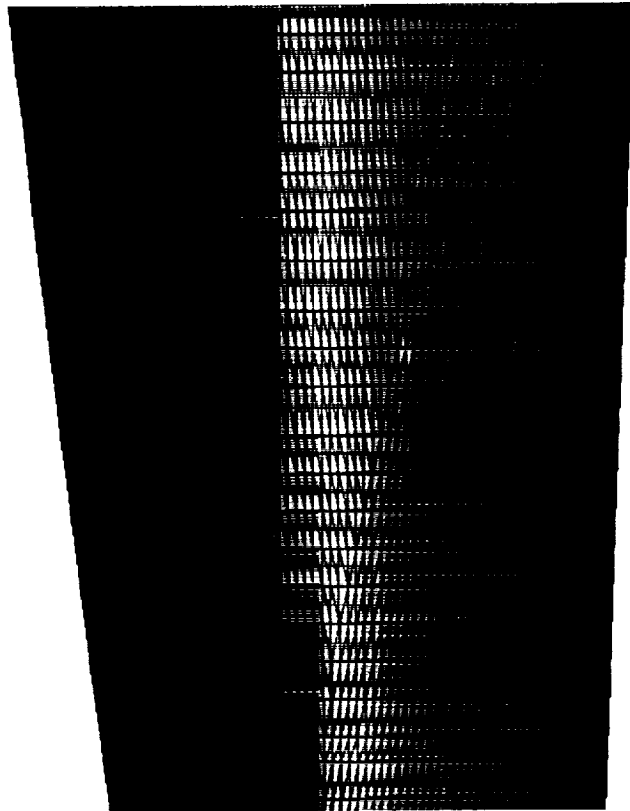
$M = 2.4$, $\alpha = 3.756$, $X \sim 500$



FLO87-MB (triangulated)

GRID1: 47,745 surface points

3,546,452 total points



UPS (triangulated)

GRID 1: 225,808 surface points

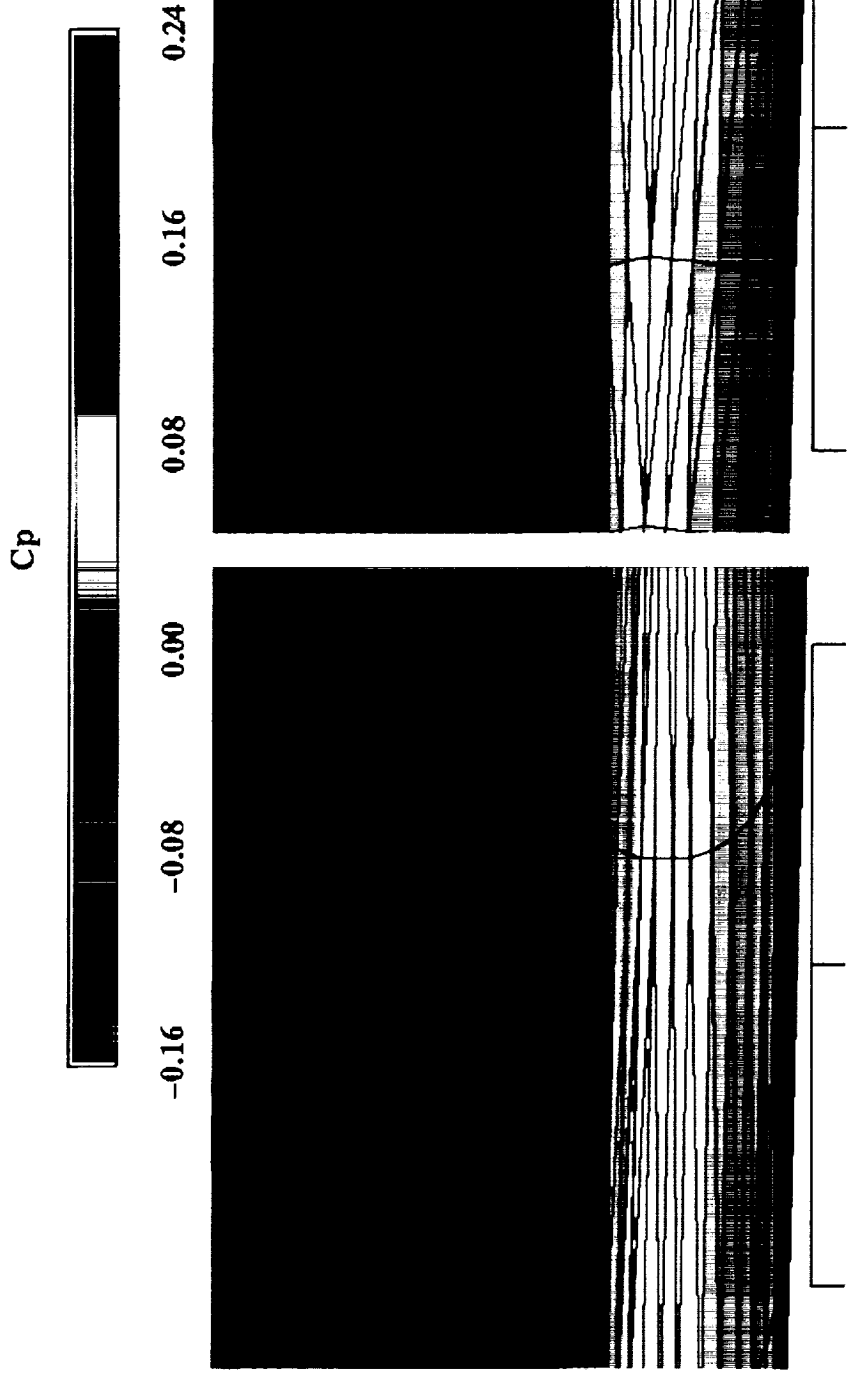
27,096,960 total points

LEADING EDGE GRID COMPARISON - FLO87-MB and UPS with Refined Meshes

The leading edge regions for the refined FLO87-MB and UPS grids are shown in the figure. The FLO87-MB grid is refined in the C direction on the wing so that twice the number of points wrapping around the leading edge are used (compare to chart 16). The refined UPS grid is slightly coarser than the FLO87-MB grid wrapping around the leading edge, but has slightly more spanwise points. The leading edge of the refined AIRPLANE grid is far denser than either the FLO87-MB grid or the UPS grid.

LEADING EDGE GRID COMPARISON

M = 2.4, $\alpha = 3.756$, Z~300



FLO87-MB (triangulated)

GRID1: 47,745 surface points

3,546,452 total points

UPS (triangulated)

GRID 1: 225,808 surface points

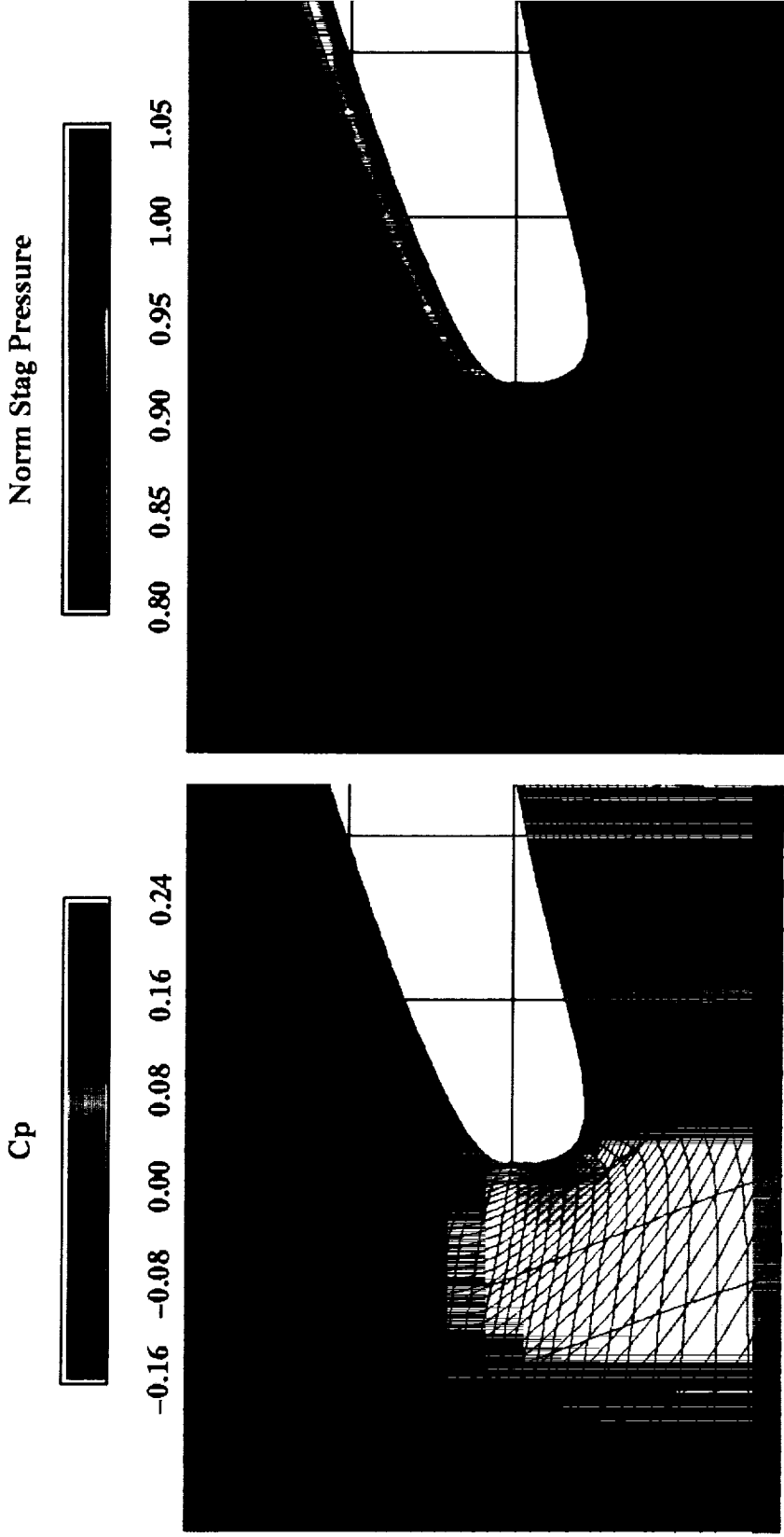
27,096,960 total points

FLO87-MB GRID/SOLUTION: GRID 1 - Cutting Plane Normal to Leading Edge at Z=300

The volume grid at the leading edge is displayed for the refined FLO87-MB grid. This grid has twice the number of points in the wrap-around C direction and twice the number of points in the vertical direction as did the original FLO87-MB mesh (compare with chart 19). The increase in grid density has reduced the stagnation pressure losses considerably. Note that the FLO87-MB solutions were obtained using Jameson's scalar dissipation scheme. The effects of the dissipation scheme will be discussed in more detail in the upcoming charts.

FLO87-MB GRID/SOLUTION: GRID 1

Cutting Plane Normal to Leading Edge at Z = 300



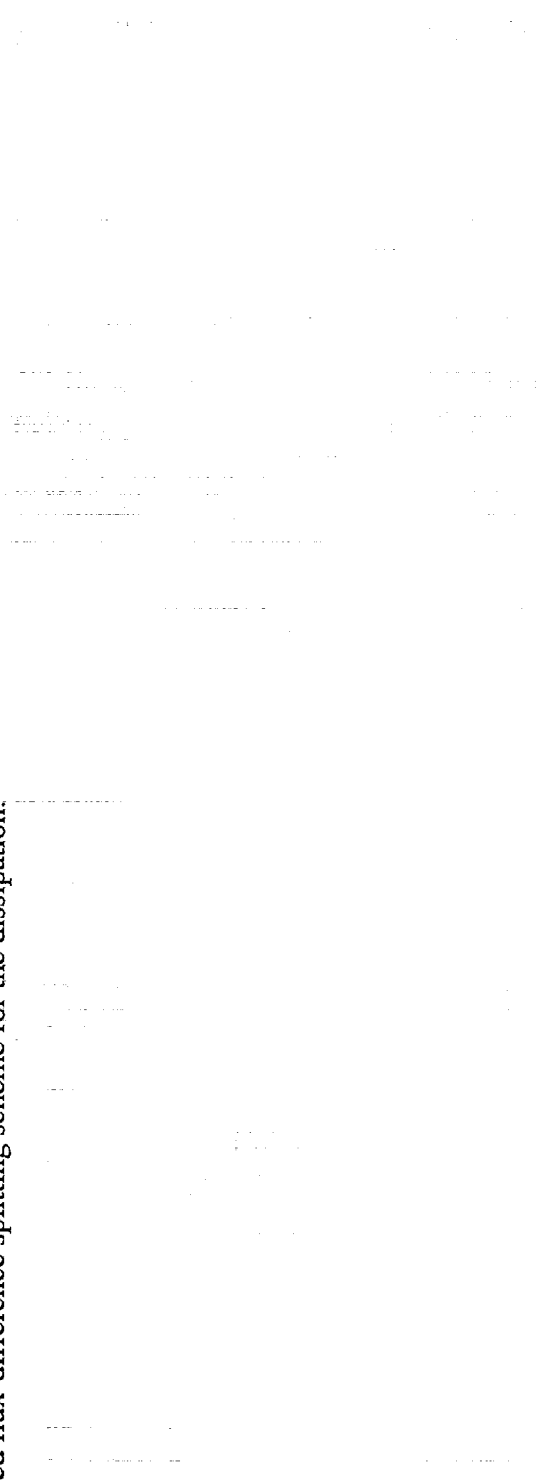
FLO87-MB: Wing/Body Grid with Scalar Dissipation Model

M = 2.4, $\alpha = 3.756$

Ruler shows ten-inch increments

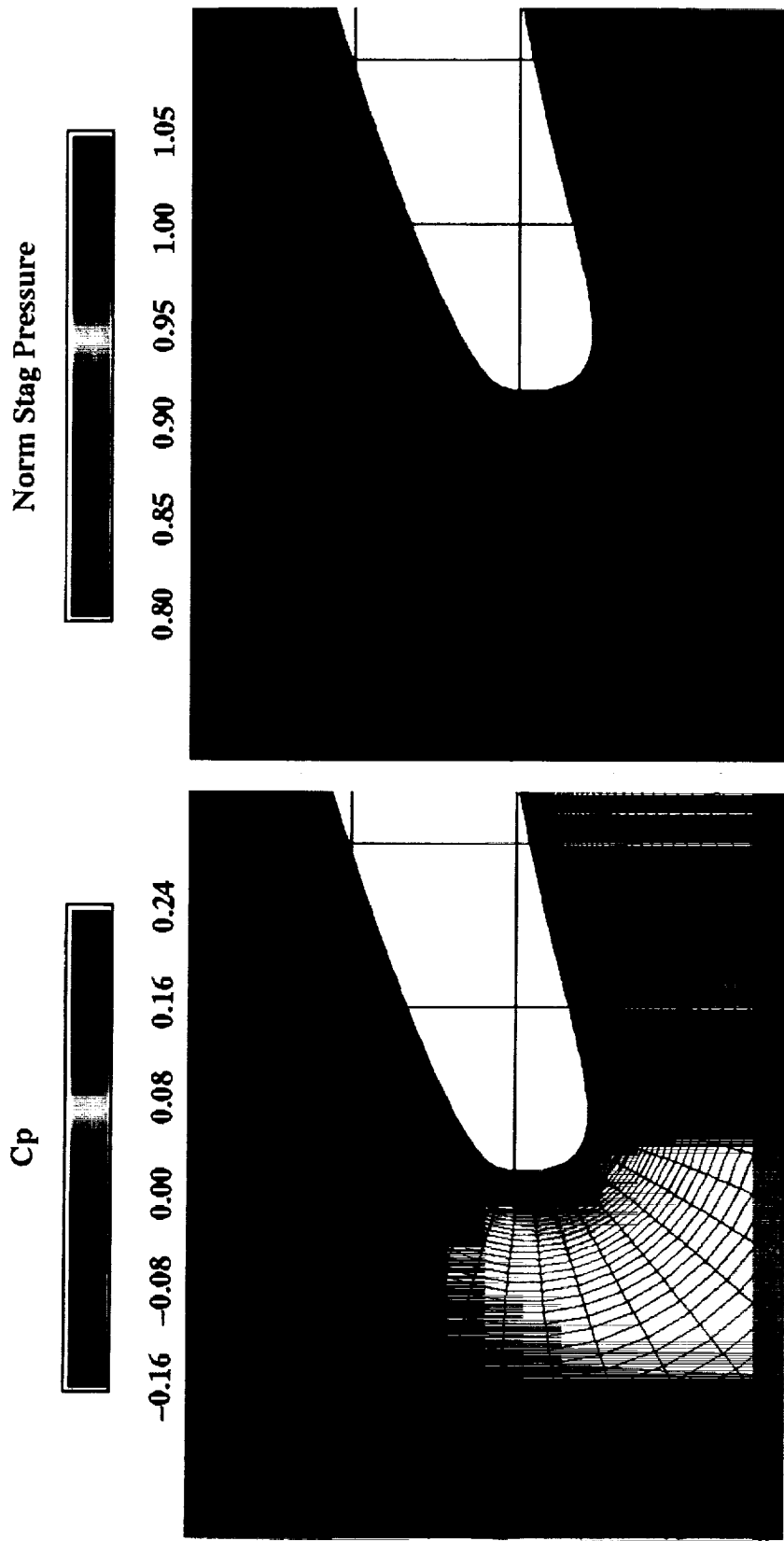
UPS GRID/SOLUTION: GRID 1 - Cutting Plane Normal to Leading Edge at Z=300

The volume grid at the leading edge is displayed for the refined UPS grid. This grid is extremely dense near the surface, reminiscent of a Navier-Stokes grid. The UPS solution appears to have none of the losses in total pressure that are seen in the AIRPLANE and FLO87-MB solutions. The very dense volume grid near the surface would reduce the likelihood of total pressure losses. The UPS solution uses a Roe based flux-difference splitting scheme for the dissipation.



UPS GRID/SOLUTION: GRID 1

Cutting Plane Normal to Leading Edge at Z = 300



M = 2.4, $\alpha = 3.756$

Ruler shows ten-inch increments

ACCUMULATED DRAG COEFFICIENT - Effect of CUSP Dissipation Scheme

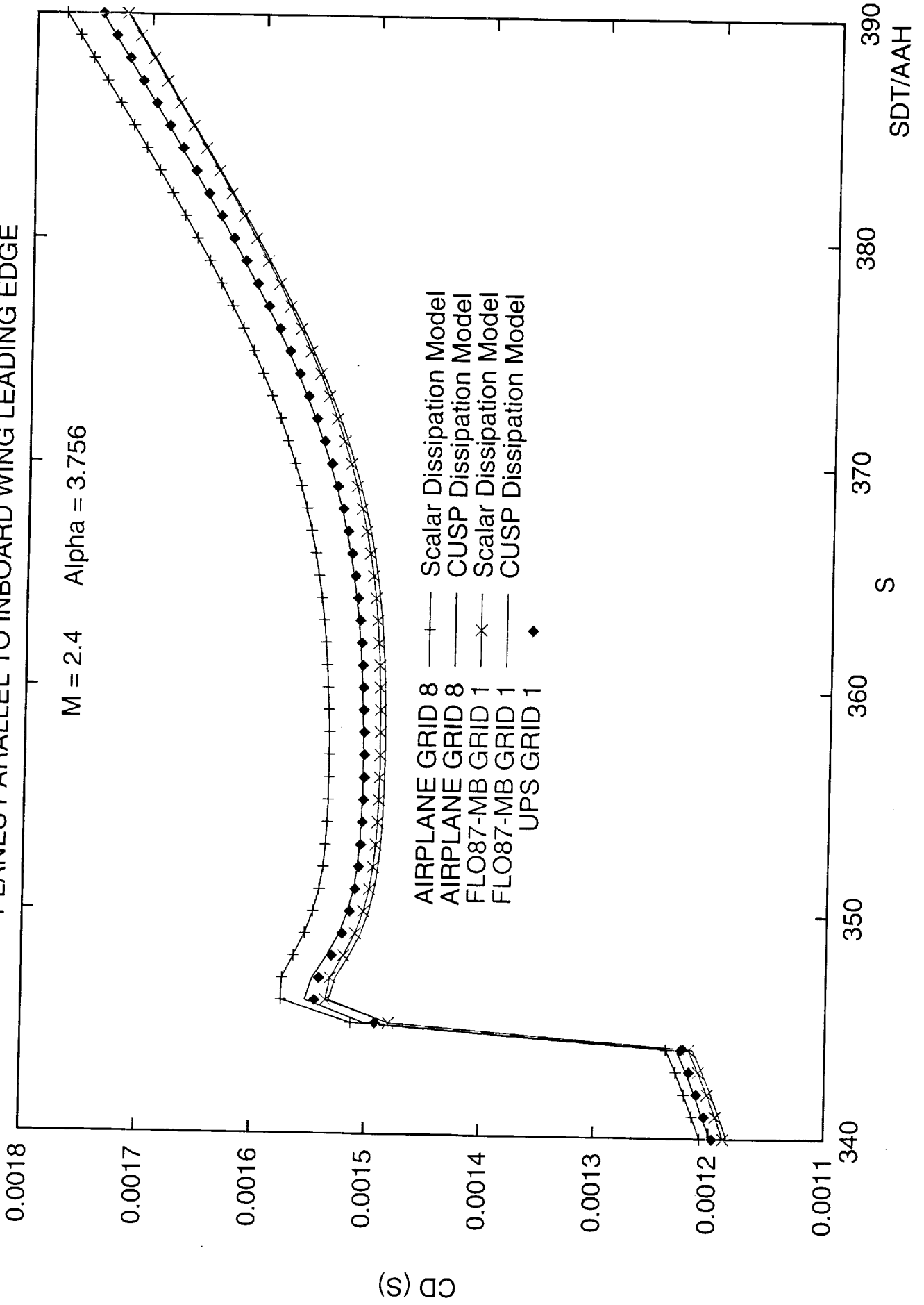
Several different artificial dissipation schemes have been proposed for the purpose of stabilizing CFD computations of the Euler equations and the Navier-Stokes equations. The presence of artificial dissipation can introduce significant errors in flow quantities such as the entropy and stagnation pressure. It is therefore desirable to select a dissipation scheme that achieves its objective while introducing the smallest possible error.

The classical Jameson dissipation scheme (i.e. scalar dissipation) uses fourth differences of the flow variables with a numerical value that scales with the magnitude of the largest wave component. The various upwind schemes use a characteristic decomposition that introduces artificial dissipation in each characteristic direction scaled by the corresponding wave speed.

The Jameson CUSP (convective upwind and split pressure) scheme applies upwinding to the convective terms while using a centered approximation to the pressure term. In addition, his formulation reduces the artificial dissipation contribution to the minimum that is strictly necessary. The net effect is that the CUSP scheme allows the possibility of shocks with a single internal point and at the same time greatly reduces the production of spurious entropy and erroneous stagnation pressure losses.

The AIRPLANE and FLO87-MB codes were re-run using the CUSP dissipation scheme with their respective refined meshes. The use of the CUSP scheme has resulted in fairly significant changes to the summed drag characteristics for the AIRPLANE code, but rather small changes were observed for the FLO87-MB code. The AIRPLANE forebody drag is reduced by less than 0.1 count, and by 0.2 counts at the leading edge using the CUSP scheme on the refined mesh. The AIRPLANE result using the CUSP scheme is now in excellent agreement with the refined UPS solution, looking almost like a faring through the UPS solution. Now the AIRPLANE and UPS solutions are essentially the same at $S=390$. The FLO87-MB results are within 0.2 counts of the AIRPLANE and UPS solutions.

ACCUMULATED DRAG COEFFICIENT WITH SAMPLING
 PLANES PARALLEL TO INBOARD WING LEADING EDGE

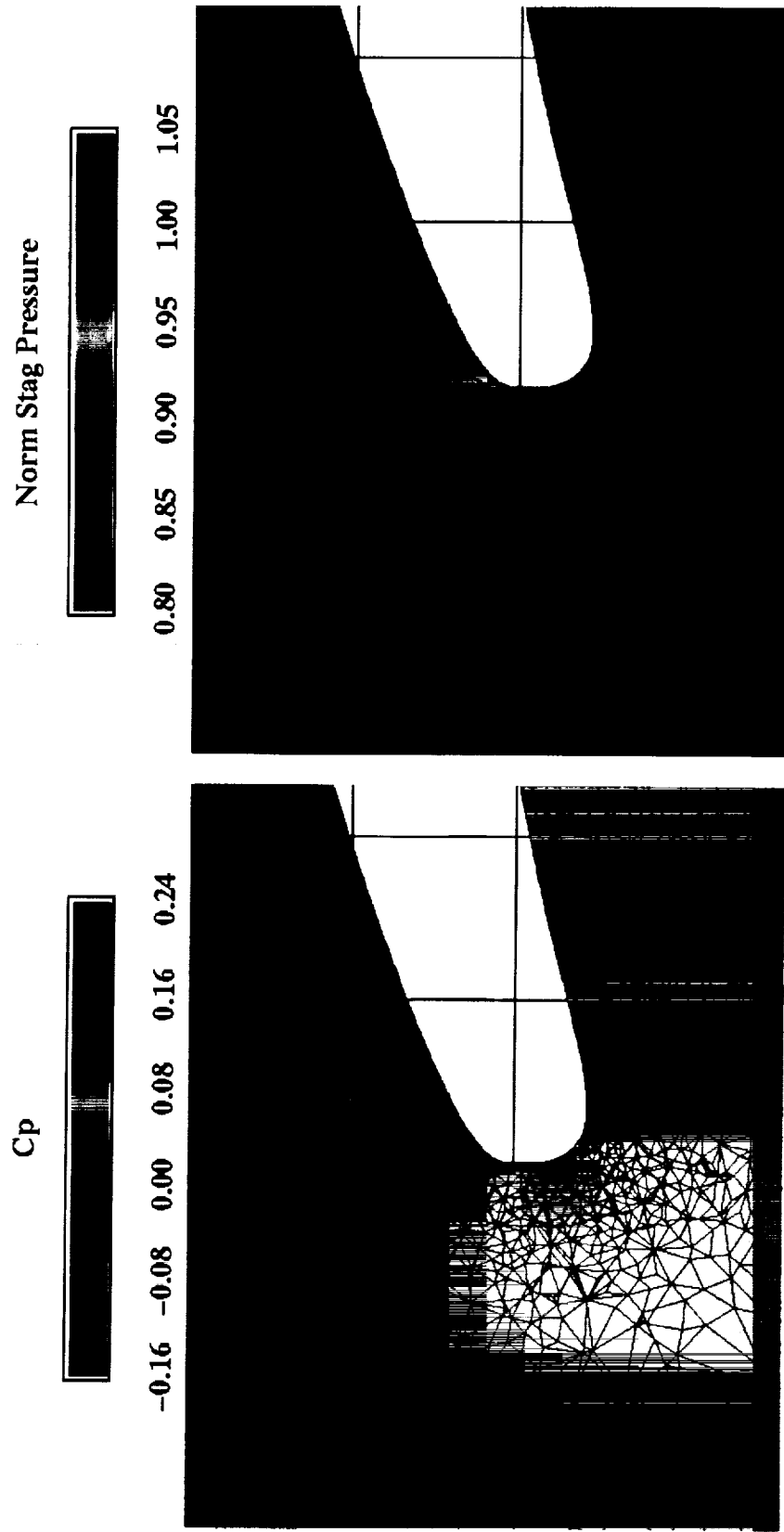


AIRPLANE GRID/SOLUTION: GRID 8 - CUSP Dissipation Scheme

This figure shows the AIRPLANE flow-field solution near the wing leading edge for the refined grid (grid 8) using the CUSP dissipation scheme. Use of the CUSP dissipation has substantially reduced the total pressure losses near the leading edge. (Compare with chart 25). This clearly indicates that the future mode of operation for the AIRPLANE solutions will be to use the CUSP dissipation scheme whenever possible. The CUSP dissipation scheme is currently only installed in the Cray C-90 version of the code, and will be incorporated into the parallel version as soon as possible.

AIRPLANE GRID/SOLUTION: GRID 8

Cutting Plane Normal to Leading Edge at Z = 300



AIRPLANE: VGRID/GridTool with CUSP Dissipation Model

M = 2.4, $\alpha = 3.756$

Ruler shows ten-inch increments

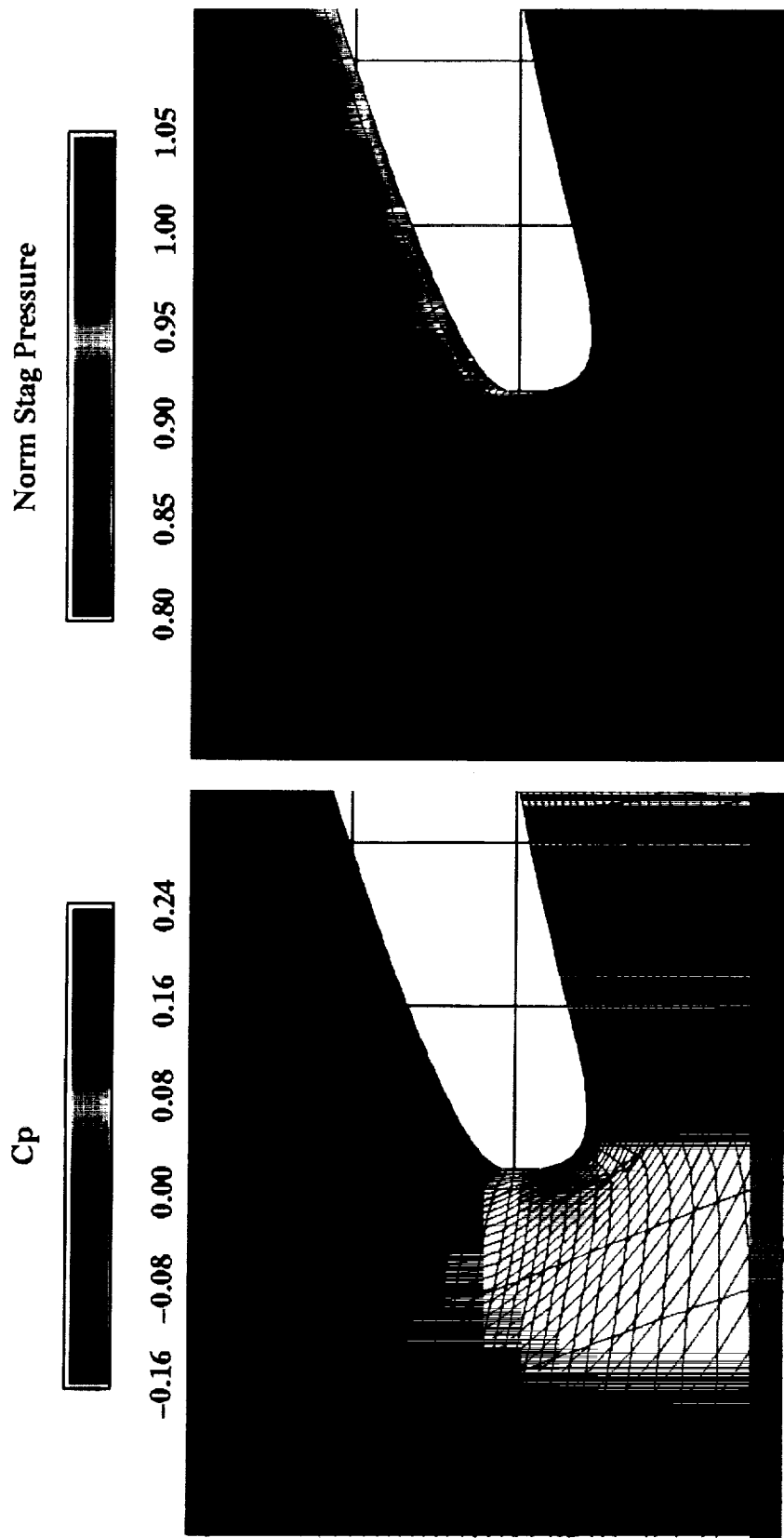
FLO87 GRID/SOLUTION: GRID 1 - CUSP Dissipation Scheme

This figure shows the FLO87-MB flow-field solution near the wing leading edge for the refined grid using the CUSP dissipation scheme. The use of the CUSP dissipation method has reduced the total pressure losses near the leading edge but not to the extent that the pressure losses were reduced with AIRPLANE. Compare this chart with charts 25, 29 and 32.

The reason for the considerable difference in the stagnation pressure losses is still under investigation. It is known that the AIRPLANE grid produced using the new mesh generator, MESH3D, is of high quality which no doubt contributes to this excellent result for the unstructured solver. Popular opinion would tend to favor a structured grid for accurate computation of sensitive flow variables such as stagnation pressure.

FLO87-MB GRID/SOLUTION: GRID 1

Cutting Plane Normal to Leading Edge at Z = 300



FLO87-MB: Wing/Body Grid with CUSP Dissipation Model

$M = 2.4$, $\alpha = 3.756$

Ruler shows ten-inch increments

Grid Convergence of Drag on Ames -103 W/B

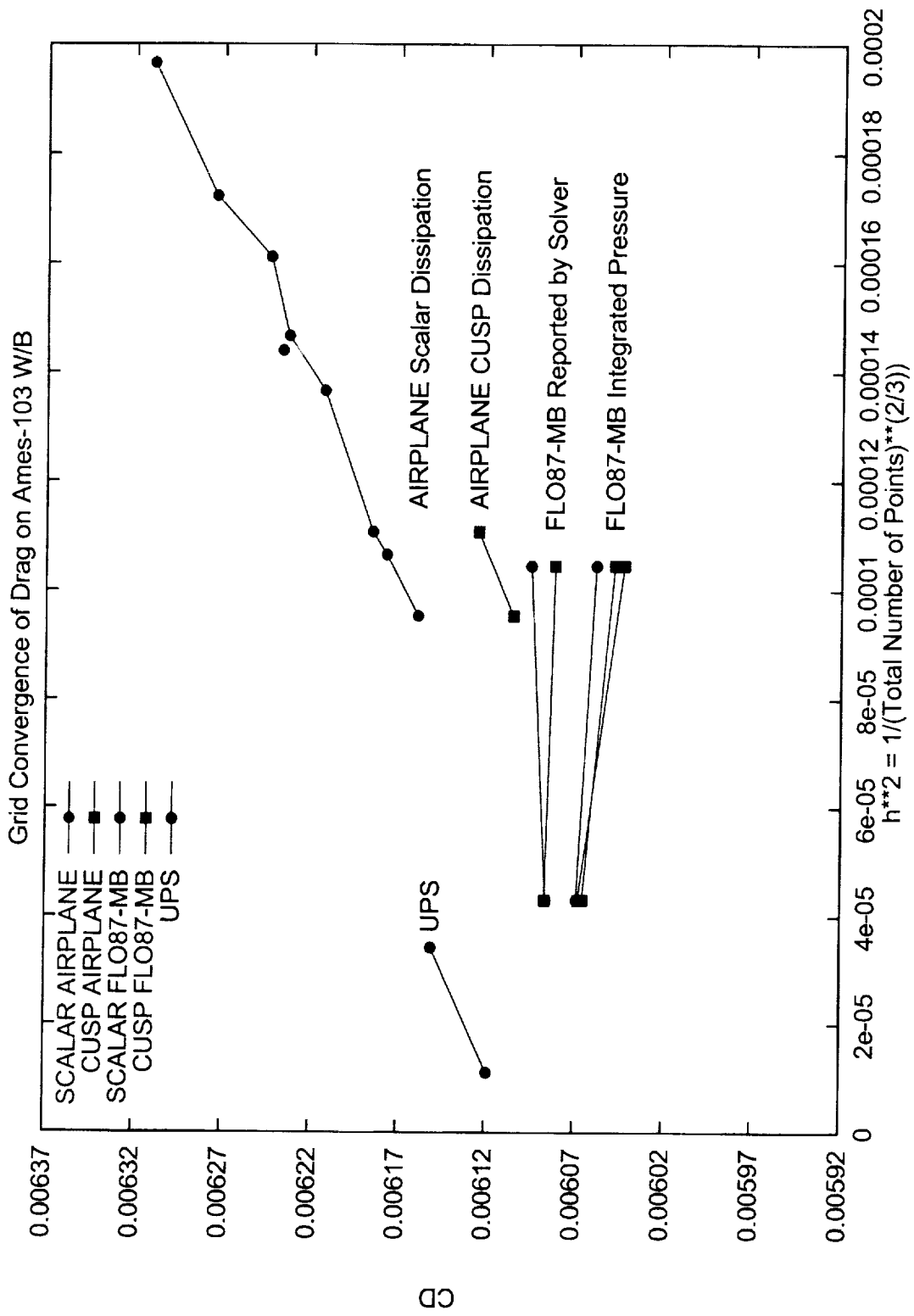
It is speculated that the error in the solution is proportional to h^{**2} , the average cell edge size squared. Since h is unknown we can approximate it using the inverse of the cube root of the total number of mesh points. The total drag coefficient is plotted as a function of h^{**2} in the figure. This also assumes that the solution error also affects the error in the drag computation to the same order.

The AIRPLANE solutions using the scalar dissipation scheme and meshes generated using MESH3D and GridTool/VGRID are shown by connected green dots. The various solutions for the range of differing mesh sizes plot in a nearly linear fashion. The isolated green dot represents the solution using the original MESHPLANE mesh, and is close to the solutions using the MESH3D grid generator.

Two AIRPLANE solutions were obtained using the CUSP dissipation scheme (using the grid 6 and grid 8 meshes). Although only two data points are plotted, the resulting line has a smaller slope than the two solutions obtained using the scalar dissipation scheme. This indicates that the CUSP dissipation scheme produces slightly more accurate solutions using fewer grid points.

The FLO87-MB solutions drag coefficients are shown using two methods of pressure integration. The forces from the flow solver are correct. The integrated pressures are not correct since the pressures on the surface are interpolated using an incorrect value of pressure. The solutions from the flow solver show a trend that suggests that the CUSP dissipation scheme can more accurately predict drag with fewer grid points. This conclusion is arrived at by a comparison of the absolute value of the slopes obtained using the two dissipation schemes. The absolute value of the slope computed using the CUSP scheme is less than that obtained using the scalar method, hence the drag is level is less effected by mesh size using the CUSP scheme.

The UPS drag computations are also shown. The refined grid solutions using the CUSP dissipation scheme for AIRPLANE and FLO87-MB, and the refined UPS solution all yield total drag values which are within 0.3 counts of each other.



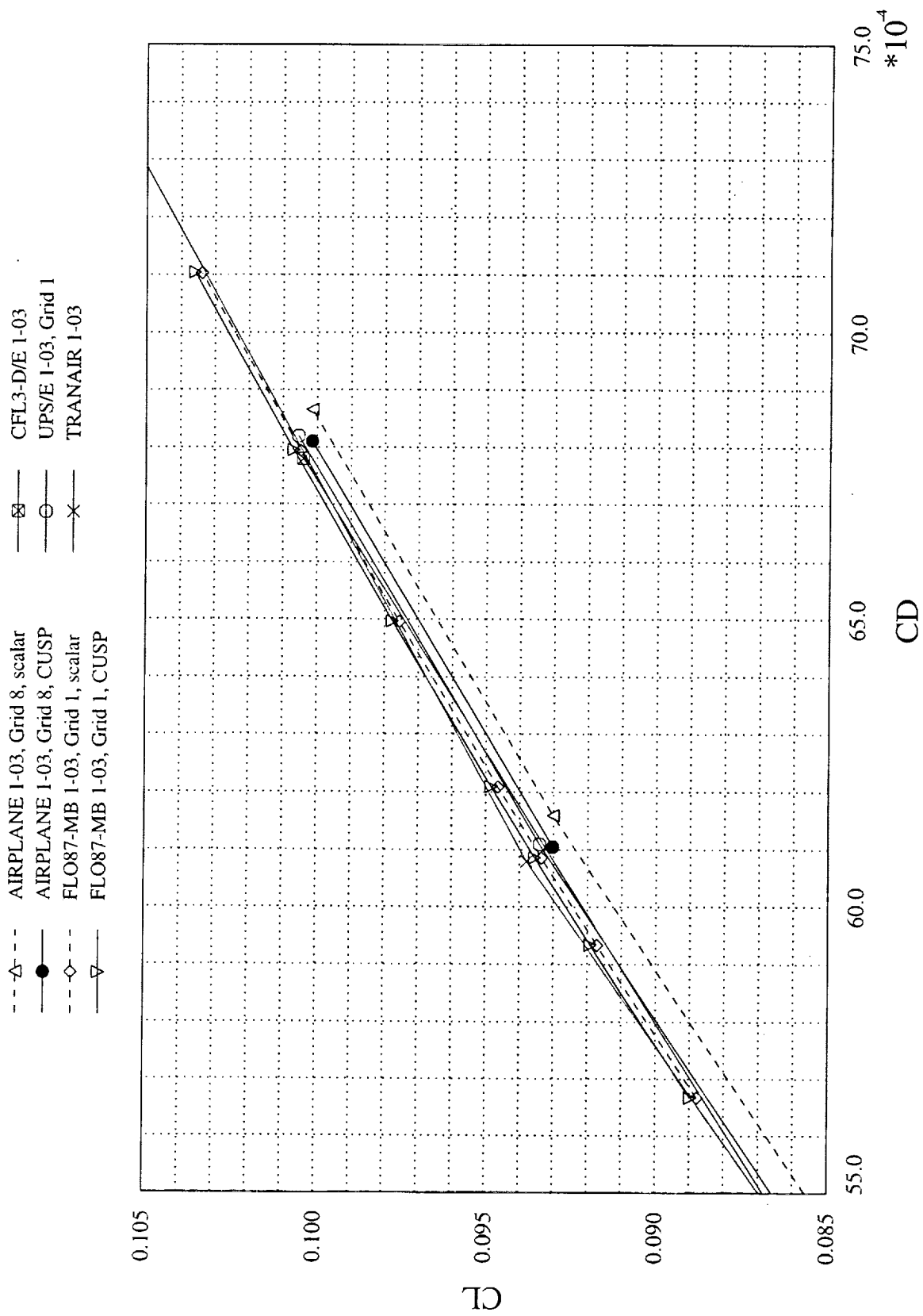
SDT/AAH

Euler Computations, Ames 01-03 Wing/Body (Refined grids, CUSP and Scalar dissipation)

The polar near cruise is plotted for the Ames 01-03 configuration using the most refined grids offering the greatest solution accuracy. The scalar dissipation results are shown for reference using AIRPLANE and FLO87-MB, but the CUSP dissipation results are more trusted. At a lift coefficient of approximately 0.093 there exists data points for all of the CFD codes. The spread in drag is about 1.5 counts at this lift. This is where the curves are most accurate since straight lines are used to connect the data points. The Ames solutions for AIRPLANE (CUSP), FLO87-MB (CUSP) and UPS are within 0.75 count of each other. This effect of the CUSP dissipation scheme on the AIRPLANE results is more favorable than expected, and as stated will be incorporated into the parallel version of the AIRPLANE code as soon as possible.

Euler Computations, Ames 01-03 Wing/Body (Refined Grids, CUSP and Scalar dissipation)

M=2.4, entire fuselage

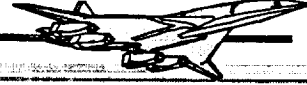


This page is intentionally left blank.

HSR

High Speed Research - Configuration Aerodynamics

Langley Research Center



High Reynolds Number Predictions for the Baseline Arrow Wing at Mach 2.48

Melissa Rivers (LaRC)

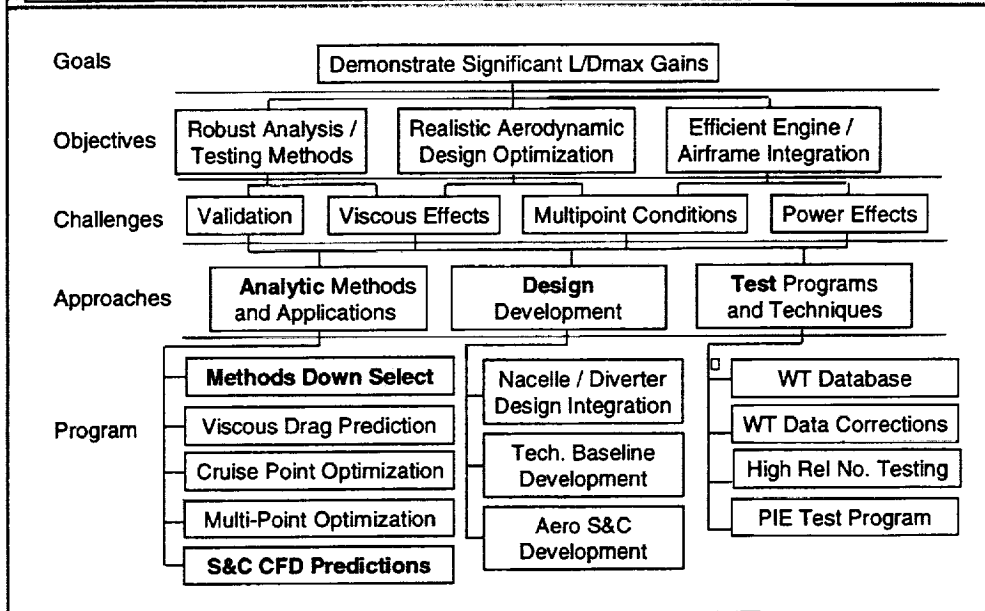
Richard Wahls (LaRC)

Aerodynamic Performance Workshop
HSR Annual Airframe Review
Los Angeles, CA
February 9 - 11, 1998

The NASA High Speed Research (HSR) Program is intended to establish a technology base enabling industry development of an economically viable and environmentally acceptable second generation high speed civil transport (HSCT). The objective of the Configuration Aerodynamics task of the program is the development of aerodynamic drag reduction, stability and control, and propulsion airframe integration technologies required to support the HSCT development process. Aerodynamic design tools are being developed, evaluated, and validated through ground based experimental testing. In addition, methods for ground to flight scaling are being developed and refined.

Configuration Aerodynamics Technology Development

Session 1: Analysis Methods and CFD Validation



Outline

- Objectives
- Approach
 - » Code description
 - » CFD matrix
- Computational results
 - » Turbulence model comparisons
 - » Angle-of-attack sweep results
 - » Reynolds number effect results
- Summary

As outlined above, this presentation describes the primary objectives of the project and the approach taken to meet the objectives. Next, the computational results from a turbulence model comparison, an angle-of-attack sweep, and a Reynolds number effect study are presented and compared to experimental data where available. A summary will complete the presentation.

Objectives

- Validation of a computational fluid dynamics (CFD) flow solver at a supersonic Mach number as a function of Reynolds number
- Enhanced understanding of data obtained in the supersonic high Reynolds number test in the PSWT

The main objective of this investigation was the validation of a computational fluid dynamics flow (CFD) solver at a supersonic Mach number as a function of Reynolds number. The investigation also provided an enhanced understanding of the data obtained in the supersonic high Reynolds number test in the Boeing Polysonic Wind Tunnel (PSWT).

Approach

- Developed a test matrix to complement the experimental study
 - » M2.4-7A arrow wing configuration
 - » Mach = 2.48
 - » $\alpha = -3$ to 3 deg
 - » Re = 5 to 15 million per foot
 - » Free and fixed transition configurations
- Used CFL3D flow solver
 - » Fully turbulent (some mixed turb. + lam and fully lam in progress)
 - » Single block C-O topology grid ($\sim 2.7 \times 10^6$ points, $y^+ \sim 1$)
 - » Convergence criteria
 - < 0.5 count C_D variation over 100 iterations
 - > 3 orders of magnitude residual reduction

The approach taken for this study was to first develop a test matrix which complemented the experimental study. The experimental study used the M2.4-7A arrow wing configuration at Mach 2.48, angles-of-attack ranging from -3 to 3 degrees and Reynolds numbers ranging from 5 to 15 million per foot. Both free and fixed transition configurations were tested.

A more detailed discussion of the experimental study is presented in a separate paper by Wahls, Rivers, Magee, and Novean in this workshop.

For the computational study, the flow solver known as CFL3D was used. All of the cases presented herein were run with the code modeling fully turbulent flow. A single block C-O topology grid with approximately 2.7 million grid points was used to model the M2.4-7A geometry. The convergence criteria for all solutions was less than half a count variation in drag over 100 iterations and at least 3 orders of magnitude residual reduction.

Approach (Cont.)

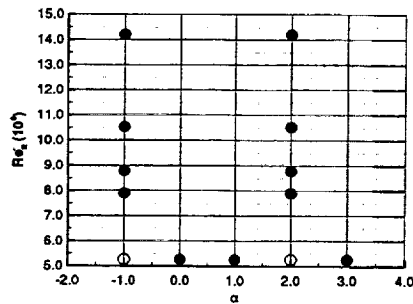
- Evaluated turbulence models, down selected to one for the full run matrix
 - » Spalart-Allmaras
 - » Baldwin-Lomax with Degani-Schiff modifications
 - » Baldwin-Barth
 - » Gatski/Speziale - not in production mode
 - » Mach 2.48, $Re_{\eta}=5.26 \times 10^6$, $\alpha=-1.0$ and 2.0 deg

For the turbulence model study, four different models were evaluated. The one-equation Spalart-Allmaras model, the algebraic Baldwin-Lomax with the Degani-Schiff modifications model, the one equation Baldwin-Barth model, and a preliminary version of the EASM Gatski/Speziale model. All turbulence models were tested at Mach 2.48, Reynolds number per foot of 5.26 million and at α 's of -1.0 and 2.0 degrees.

After all of the runs were completed for this study, the results from the four models were evaluated against the experimental data and one was chosen for the full run matrix.

Approach (Concluded)

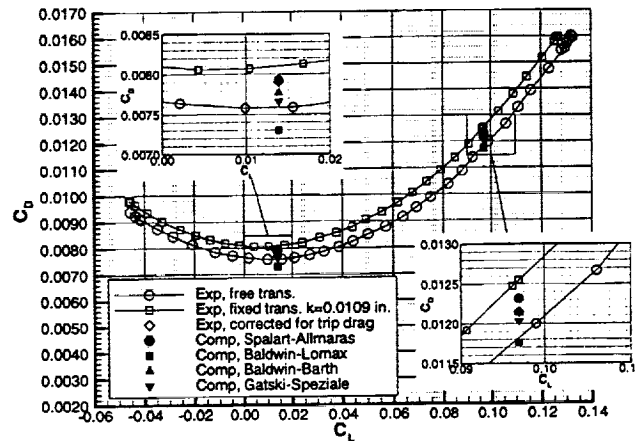
- Compared fully turbulent CFD solutions with experimental data
 - » Mach 2.48
 - » α sweep at $Re_{ft}=5.26 \times 10^6$
 - » Re sweep at $\alpha=-1.0$ (near C_{Dmin}) and $\alpha=2.0$ (cruise)



After the completion of the turbulence model study, an angle-of-attack sweep was performed at Mach 2.48 and $Re_{ft} = 5.26$ million. A Reynolds number sweep was also done at $\alpha=-1.0$ deg (near C_{Dmin}) and $\alpha=2.0$ deg (cruise C_L). The data from these sweeps were compared to the available experimental data.

Turbulence Model Study Results

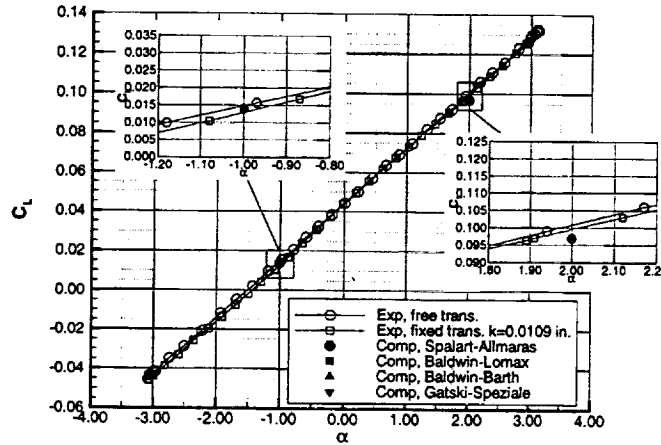
● $Re/ft = 5.26 \times 10^6$, Mach 2.48



This figure shows the drag polar for two experimental conditions and the four different turbulence models at Reynolds number per foot = 5.26 million and Mach 2.48. There is also one point on each of the enlarged figures showing an experimental value corrected for trip drag. The correction of the experimental data to fully turbulent conditions accounts for +1 count for a laminar leading edge run, and -2.9 and -5.0 counts of trip drag at $C_L=0.014$ and $C_L=0.097$, respectively. As the figure shows, Spalart-Allmaras agrees the best with the corrected data at $C_L=0.014$ (near C_{Dmin}), and Baldwin-Barth agrees the best with the corrected data at $C_L=0.097$ (near cruise), with Spalart-Allmaras over predicting the drag by only 2 counts.

Turbulence Model Study Results

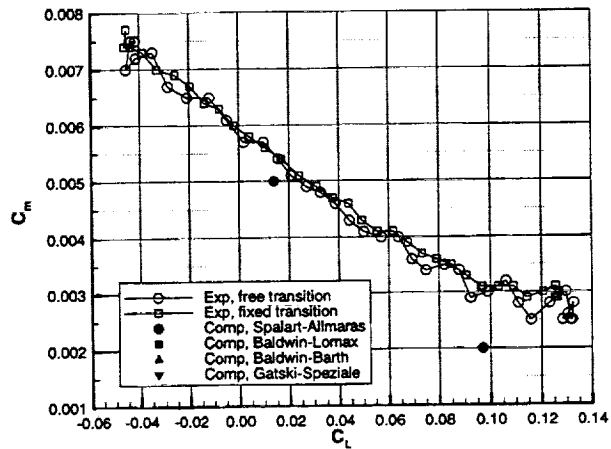
- $Re/ft = 5.26 \times 10^6$, Mach 2.48



This figure shows that at $\alpha = -1.0$ deg, all of the turbulence models predict the same lift, which is in between the free and fixed transition experimental data, as expected. At $\alpha = 2.0$ deg, all of the turbulence models again predict the same lift, which is lower than both the experimental values. The lower C_L prediction at $\alpha = 2$ deg is consistent with static aeroelastic deformation of the flexible wind tunnel model as compared to the rigid CFD geometry.

Turbulence Model Study Results

● $Re/ft = 5.26 \times 10^6$, Mach 2.48



All of the turbulence models predict the same pitching moment values at both $\alpha = -1.0$ and 2.0 deg. The slight rotation of the C_m/C_L curve seen is consistent with a flexible model (experiment) versus a rigid model (CFD).

Turbulence Model Study Conclusions

- $\alpha = -1.0$ tabulated results:

Exp/TM	C_l	C_D counts	C_{Dv} counts	C_m	Time for Comp., C-90 equiv. Hrs.
Exp. free trans.	0.014	75.90	58.7**	0.005	-
Exp. fixed trans.	0.013	80.90	58.7**	0.006	-
Exp. corrected	0.014	78.90	-	0.005	-
SA	0.014	79.30	58.10	0.005	1.82
BL/DS	0.014	73.00	51.90	0.005	1.66
BB	0.014	77.70	56.50	0.005	2.10
GS	0.014	76.60	55.20	0.005	2.36

** Theory

SA = Spalart-Allmaras

BL/DS = Baldwin-Lomax with
Degani-Schiff modifications

BB = Baldwin-Barth

GS = preliminary version of
Gatski/Speziale

- $\alpha = 2.0$ tabulated results:

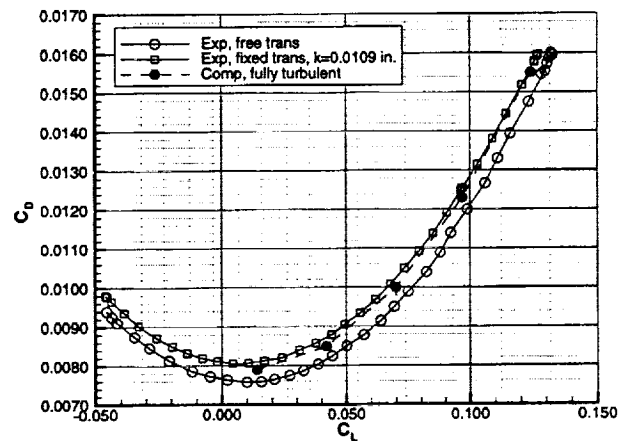
Exp/TM	C_l	C_D counts	C_{Dv} counts	C_m	Time for Comp., C-90 equiv. Hrs.
Exp. free trans.	0.097	118.20	58.7**	0.003	-
Exp. fixed trans.	0.097	125.50	58.7**	0.003	-
Exp. corrected	0.097	121.50	-	0.003	-
SA	0.097	123.20	57.70	0.002	1.83
BL/DS	0.097	117.60	52.20	0.002	1.71
BB	0.097	121.40	55.90	0.002	3.83
GS	0.097	120.30	54.70	0.002	2.50

- Spalart-Allmaras agreed the best at the C_{Dmin} condition with the corrected experimental fixed transition case; therefore it was used for the α sweep & Re effect study

The data presented herein is not corrected for static aeroelastics (i.e. model deformation), which has a minimal effect at C_{Dmin} ; therefore comparing at C_{Dmin} gives a cleaner comparison to “rigid” CFD. Using this reasoning and looking at the tabulated data for $\alpha = -1.0$ deg where Spalart-Allmaras comes the closest of the four models to matching the experimental corrected data in drag, Spalart-Allmaras was selected for further applications.

EFD and CFD Comparisons: α Sweep

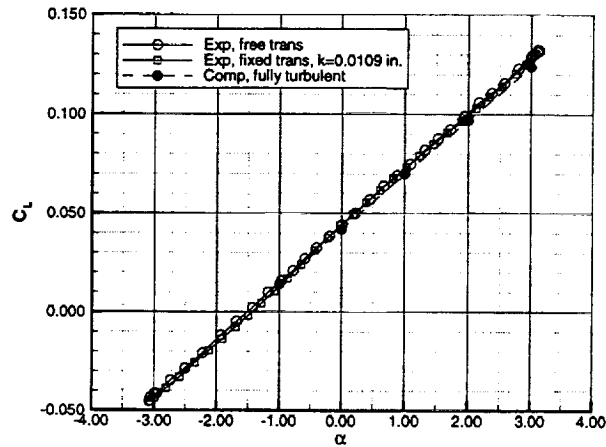
- $Re/ft = 5.26 \times 10^6$, Mach 2.48
- Exp. fixed transition not corrected for trip drag



This figure shows the drag polar for free and fixed transition experimental data and the computational data at Mach 2.48 and Reynolds number per foot of 5.26 million. The CFD results are between the fixed transition (not corrected for trip drag) and free transition data throughout the polar. As in the turbulence model study, correcting for trip drag improves the comparison.

EFD and CFD Comparisons: α Sweep

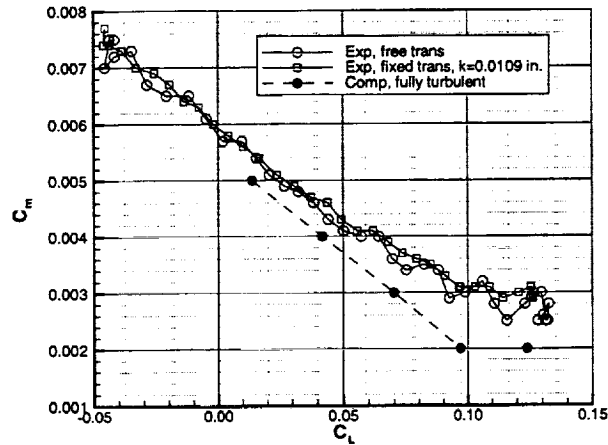
- $Re/ft = 5.26 \times 10^6$, Mach 2.48
- Exp. fixed transition not corrected for trip drag



This figure shows the lift curve for free and fixed transition experimental data and the computational data at Mach 2.48 and Reynolds number per foot of 5.26 million. The comparison between CFD and experimental fluid dynamics (EFD) is good throughout the polar.

EFD and CFD Comparisons: α Sweep

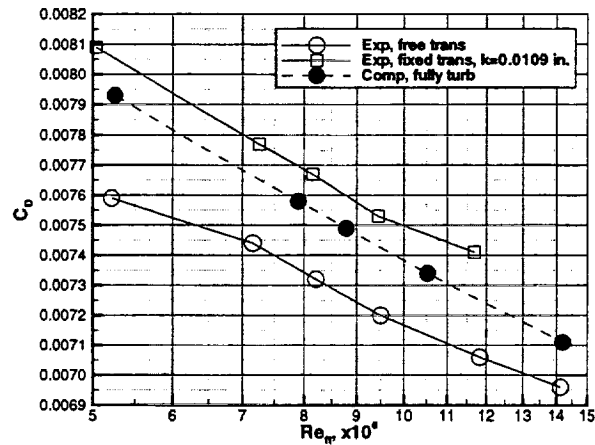
- $Re/ft = 5.26 \times 10^6$, Mach 2.48
- Exp. fixed transition not corrected for trip drag



This figure shows the pitching moment for free and fixed transition experimental data and the computational data at Mach 2.48 and Reynolds number per foot of 5.26 million. The CFD predicts a more nose-down pitching moment than the EFD but the CFD does pick up the slope change at $C_L=0.10$. The slight slope difference in the two C_m/C_L curves is again consistent with flexible model versus rigid CFD results.

Reynolds Number Effect Study

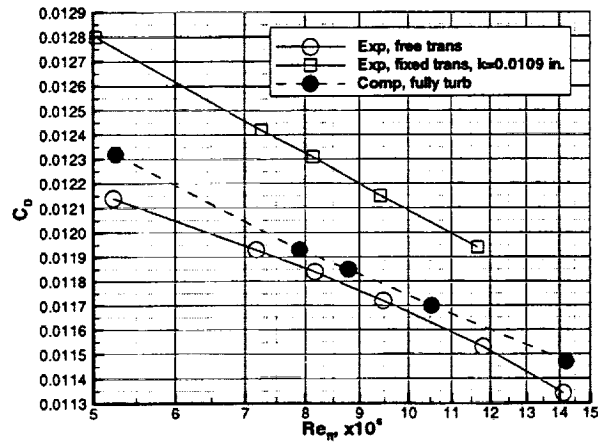
- Reynolds number effects on C_D , Mach 2.48, $\alpha = -1.0$ deg



This figure shows the Reynolds number effects on drag near C_{Dmin} ($\alpha = -1.0$ degrees) for both the experimental and computational data. The computational data is consistently about 1.5 counts below the fixed transition experimental data and 1.5 to 3 counts higher than the free transition experimental data. The free transition data appears to be approaching the fully turbulent CFD data near 15 million Reynolds number per foot.

Reynolds Number Effect Study

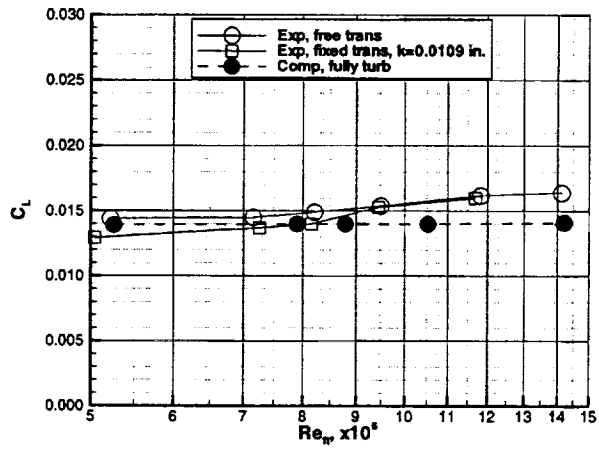
- Reynolds number effects on C_D , Mach 2.48, $\alpha=2.0$ deg



This figure shows the Reynolds number effects on drag near cruise ($\alpha=2.0$ degrees) for both the experimental and computational data. The computational data is 3-4 counts below the fixed transition experimental data and 0.5 to 1.5 counts higher than the free transition experimental data.

Reynolds Number Effect Study

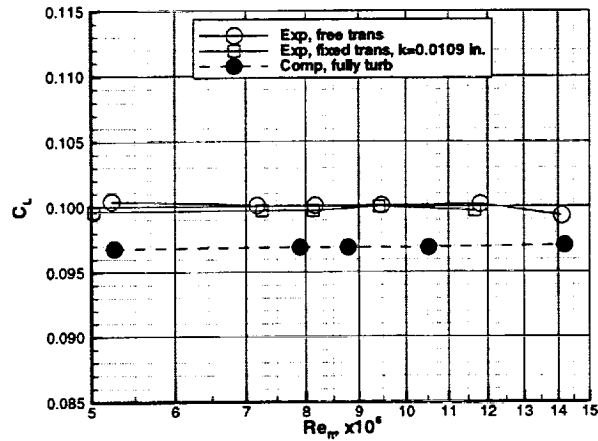
- Reynolds number effects on C_L , Mach 2.48, $\alpha=-1.0$ deg



This figure shows the Reynolds number effects on lift near C_{Dmin} ($\alpha=-1.0$ degrees) for both the experimental and computational data. This shows a minimal Reynolds number effect on lift over this small Reynolds number range (5 to 15 million per foot).

Reynolds Number Effect Study

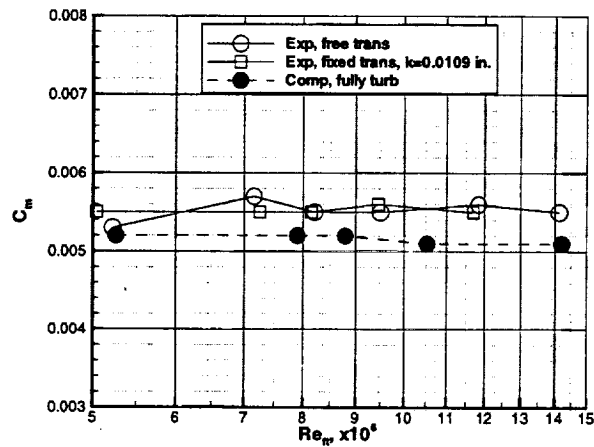
- Reynolds number effects on C_L , Mach 2.48, $\alpha=2.0$ deg



This figure shows the Reynolds number effects on lift near cruise ($\alpha=2.0$ degrees) for both the experimental and computational data. This figure shows a minimal Reynolds number effect on lift over this small Reynolds number range (5 to 15 million per foot). The computational data predicts the lift lower than the experimental data across the entire range of Reynolds numbers.

Reynolds Number Effect Study

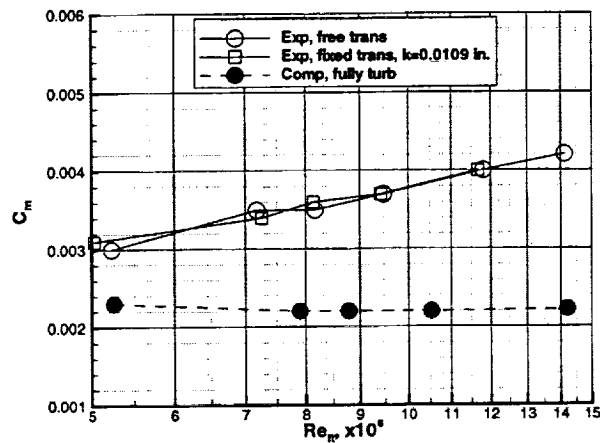
- Reynolds number effects on C_m , Mach 2.48, $\alpha=-1.0$ deg



This figure shows the Reynolds number effects on pitching moment near C_{Dmin} ($\alpha=-1.0$ degrees) for both the experimental and computational data. The basic pitching moment levels agree and there is a minimal Reynolds number effect on pitching moment over this small Reynolds number range (5 to 15 million per foot). This figure also shows that the aeroelastics are minimal near $C_L=0.0$.

Reynolds Number Effect Study

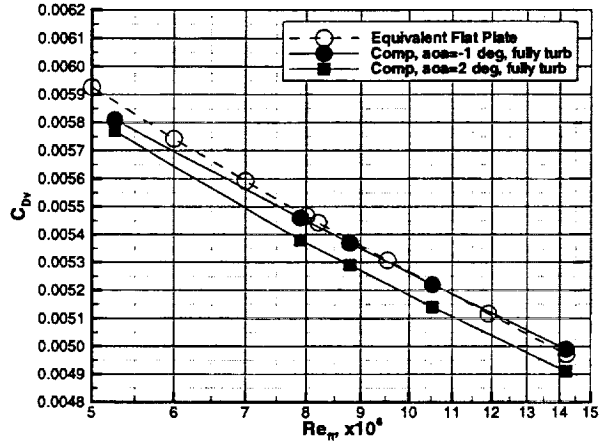
- Reynolds number effects on C_m , Mach 2.48, $\alpha=2.0$ deg



This figure shows the Reynolds number effects on pitching moment near cruise ($\alpha=2.0$ degrees) for both the experimental and computational data. This figure shows that there is minimal Reynolds number effects on pitching moment for this small range (5-15 million per foot). Also, the CFD predicts a different slope than the EFD, which can be accounted for by the fact that we are comparing a flexible experimental model with a rigid CFD model.

Reynolds Number Effect Study

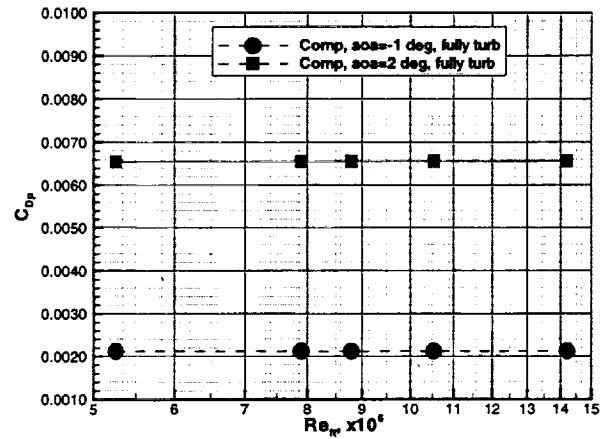
● Viscous drag, Mach 2.48



This figure shows the viscous drag component of the computational results at $\alpha = -1.0$ and 2.0 deg and the equivalent flat plate theory. The CFD and equivalent flat plate results agree well. The levels at C_{Dmin} ($\alpha = -1.0$ deg) agree well with a slight offset at cruise ($\alpha = 2.0$ deg). The Reynolds number effect trends agree at both conditions.

Reynolds Number Effect Study

● Pressure drag, Mach 2.48



This figure shows the pressure drag component of the computational results at $\alpha = -1.0$ and 2.0 deg. There are no Reynolds number effects on pressure drag over this small Reynolds number range.

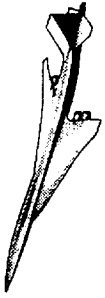
Summary

- **Method assessment**
 - » **Turbulence model study**
 - Baldwin-Barth and Spalart-Allmaras both performed well in this study
 - Chose Spalart-Allmaras for further use
 - » **Prediction**
 - Consistent results through α sweep
 - Fully turbulent results fall between experimental free and fixed transition results
 - Small or negligible Reynolds number effect on C_L and C_m over the small range of Reynolds numbers tested
 - Viscous drag results for CFD and equivalent flat plate agree well
- **Provided fully turbulent prediction to enhance understanding of experimental data and trip drag assessment**

To summarize, the turbulence model study showed that both Baldwin-Barth and Spalart-Allmaras performed well for this configuration at the tested conditions. The Spalart-Allmaras model compared the best near C_{Dmin} , where there is the least aeroelastic effects and it was used for the angle-of-attack sweep and Reynolds number effect study. The predictions gave consistent results throughout the angle-of-attack sweep. The fully turbulent results fall between the experimental free and fixed transition results and there is a small or negligible Reynolds number effect on C_L and C_m over the small range of Reynolds numbers tested. The viscous drag results for the CFD and equivalent flat plate results agreed well.

Finally, the results of this project provided a fully turbulent prediction to enhance the understanding of experimental data and trip drag assessment.

This page is intentionally left blank.



Applications of Parallel Processing in Configuration Analyses

**P. Sundaram, and James O. Hager
Configuration Aerodynamics
The Boeing Company, Long Beach**

&

**Robert T. Biedron
NASA Langley Research Center, Hampton, Virginia**

**HSR Airframe Technical Review
Los Angeles, California
February 9-13, 1998**



This page is intentionally left blank.

Applications of Parallel Processing in Configuration Analysis

P. Sundaram and James O. Hager
The Boeing Company
Long Beach, California 90807-5309

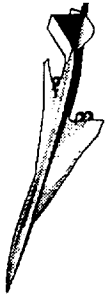
and
Robert T. Biedron
NASA Langley Research Center
Hampton, Virginia 23666

The paper presents the recent progress made towards developing an efficient and user-friendly parallel environment for routine analysis of large CFD problems. The coarse-grain parallel version of the CFL3D Euler/Navier-Stokes analysis code, CFL3Dhp, has been ported onto most available parallel platforms. The CFL3Dhp solution accuracy on these parallel platforms has been verified with the CFL3D sequential analyses. User-friendly pre- and post-processing tools that enable a seamless transfer from sequential to parallel processing have been written. Static load balancing tool for CFL3Dhp analysis has also been implemented for achieving good parallel efficiency. For large problems, load balancing efficiency as high as 95% can be achieved even when large number of processors are used. Linear scalability of the CFL3Dhp code with increasing number of processors has also been shown using a large installed transonic nozzle boattail analysis. To highlight the fast turn-around time of parallel processing, the TCA full configuration in sideslip Navier-Stokes drag polar at supersonic cruise has been obtained in a day. CFL3Dhp is currently being used as a production analysis tool.

Outline

This chart gives the outline of the topics covered in this presentation.

Outline



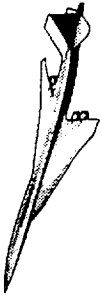
High Speed Aerodynamics, Long Beach

- Objectives
- Approach
- CFL3Dhp: coarse-grain parallelization
- Pre- and post-processing tools
- Load-balancing and scalability
- Summary

Objectives

The objectives of the parallel processing effort are listed in this chart. The primary objectives are to develop and apply the parallel processing technology for routine CFD analyses of large problems and to obtain the solutions with a significant reduction in wall time compared to a vector supercomputer. Satisfying these objective also reduces the reliance on the expensive vector supercomputers for CFD analyses.

Objectives



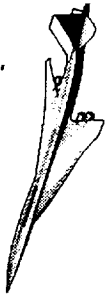
High Speed Aerodynamics, Long Beach

- Reduce cost and cycle time for CFD analyses
 - Decrease dependence on the high price-to-performance ratio vector supercomputers
 - Enable full configuration drag polar in a day
- Develop capability to solve CFD problems that are too large for sequential supercomputers, e.g., Cray C-90
- Utilize parallel computers to harness large CPU power required for analysis with quick turn-around

Approach

The approach taken is to use the parallel version of the CFL3D analysis code, called CFL3Dhp, and to demonstrate the advantages of parallel processing compared to vector supercomputing. As a first step, CFL3Dhp was ported onto several parallel platforms and the CFL3Dhp solutions obtained on these platforms were validated against those obtained using CFL3D run on serial machines. Since the primary advantage of parallel systems is the availability of large number of processors, several tools were developed to achieve high parallel efficiency and a user-friendly parallel analysis process. To emphasize the need for the parallel processing capability, solutions were obtained to analysis problems that were too large for a Cray C-90.

Approach



High Speed Aerodynamics, Long Beach

- Port CFL3Dhp onto various parallel platforms
- Validate CFL3Dhp (parallel version) results with CFL3D (serial version) results
- Improve the analysis process
 - Develop parallel efficiency enhancement tools
 - Develop user-friendly pre- and post-processing utilities for parallel CFD analysis
- Use CFL3Dhp to obtain solutions for problems too large for Cray C-90

CFL3Dhp: Coarse-Grain Parallelization

NASA LaRC initiated the development of a parallel version of the CFL3D code. CSC developed an early version of CFL3Dhp during 1996. The philosophy used in the code parallelization are given in the chart. Boeing Long Beach (BLB) obtained the code and worked on it in collaboration with NASA LaRC to render it a powerful analysis tool. Several limitations in the original code have been removed, and the code now has a number of desirable features. These include (a) a single restart file generation, (b) the minimum distance search is performed in parallel.

CFL3Dhp: Coarse-Grain Parallelization



High Speed Aerodynamics, Long Beach

- Coarse-grain parallel version of CFL3D from NASA LaRC
 - Minimum modifications to CFL3D code
 - Nodes communicate via Message Passing Interface (MPI) protocol
 - Host node performs task assignment and manages the overall I/O operations
 - Task nodes perform the actual computations
- Single restart file written by the host node
- Field equation turbulence model distance computations done by individual nodes in parallel

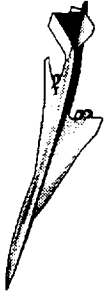
CFL3Dhp Code Portability

Portability of a parallel code to variety of platforms is necessary for its effective use. CFL3Dhp uses embedded C-preprocessor code to enhance portability. The *ifdef* constructs automatically modifies the real variable precision definition and architecture dependent system calls. For example, the following *ifdef* construct uses the logical FLUSHFLAG value and branches off to the correct segment of the code to make the appropriate system call to flush the processor buffer in the event of an abnormal termination of the code.

```
#ifdef FLUSHFLAG
    call flush_(5)
    call flush_(noutp)
    call flush_(nouts)
#else
    call flush(6)
    call flush(noutp)
    call flush(nouts)
#endif
```

C-preprocessor *ifdefs* are also used to modify the MPI calls that are specific to each parallel platform based on the processor real-variable word length. In this case, the *ifdef* argument is automatically defined using an architecture query in the makefile.

CFL3Dhp Code Portability



High Speed Aerodynamics, Long Beach

- Easy portability to many parallel platforms using C-preprocessor directives
 - Same code for sequential or parallel processing
 - Automatic single/double precision handling
 - Architecture dependent MPI and system calls

Environments and Platforms Supported

This chart describes the various parallel platforms and environment that are supported by the CFL3Dhp parallel code. It encompasses a large spectrum of today's parallel architectures.

Large shared memory vector multiprocessors, such as the Cray C-90 and J-90, can perform do-loop level fine-grain parallel computations as well as mimic host/node coarse-grain parallel tasks. CFL3Dhp runs on these systems in the multithreaded multitask mode. TCA wing/body, and wing/body/flaps computations were performed using CFL3Dhp on such a platform.

Workstations clusters are an effective means of extracting large CPU resource at minimal cost. CFL3Dhp has been tested on both Silicon Graphics Inc. (SGI) and Hewlett-Packard (HP) workstation clusters for wing/body analyses. The bottlenecks here are the poor network speeds and the cluster heterogeneity.

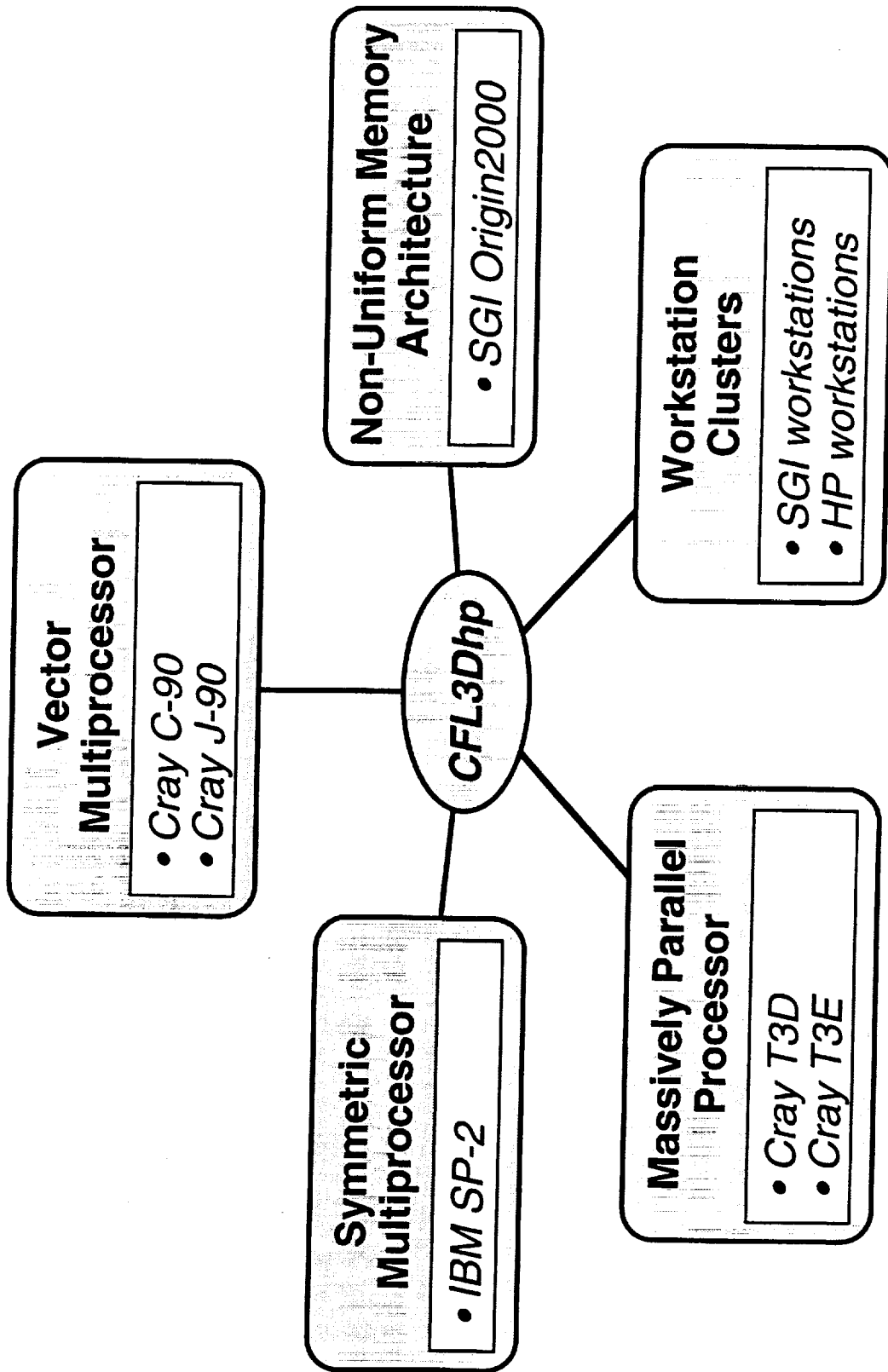
Cache-based distributed-memory parallel computers, called scaleable symmetric multiprocessors, are primarily tightly connected commodity workstations. These platforms, such as IBM SP-2 with hundreds of processors, provide much more computational power than a vector supercomputer at a fraction of the cost. CFL3Dhp has been used for TCA wing/body and wing/body/nacelle/diverter Navier-Stokes solutions on the IBM SP-2 for code validation studies.

The Non-uniform (distributed/shared memory) computer, SGI's Origin 2000, supports both coarse-grain and fine-grain parallelization. Here, the data resident in a specific processor's memory is accessible from any other processor with insignificant memory latency. CFL3Dhp has been used on the Origin 2000 to obtain TCA full configuration in sideslip Navier-Stokes solutions.

Massively parallel architectures such as the Cray T3E where the processors are interconnected in a 3-D torous are attractive for parallel applications requiring hundreds of processors. Scaleable performance of CFL3Dhp has been demonstrated on Cray T3E.

Environments and Platforms Supported

High Speed Aerodynamics, Long Beach



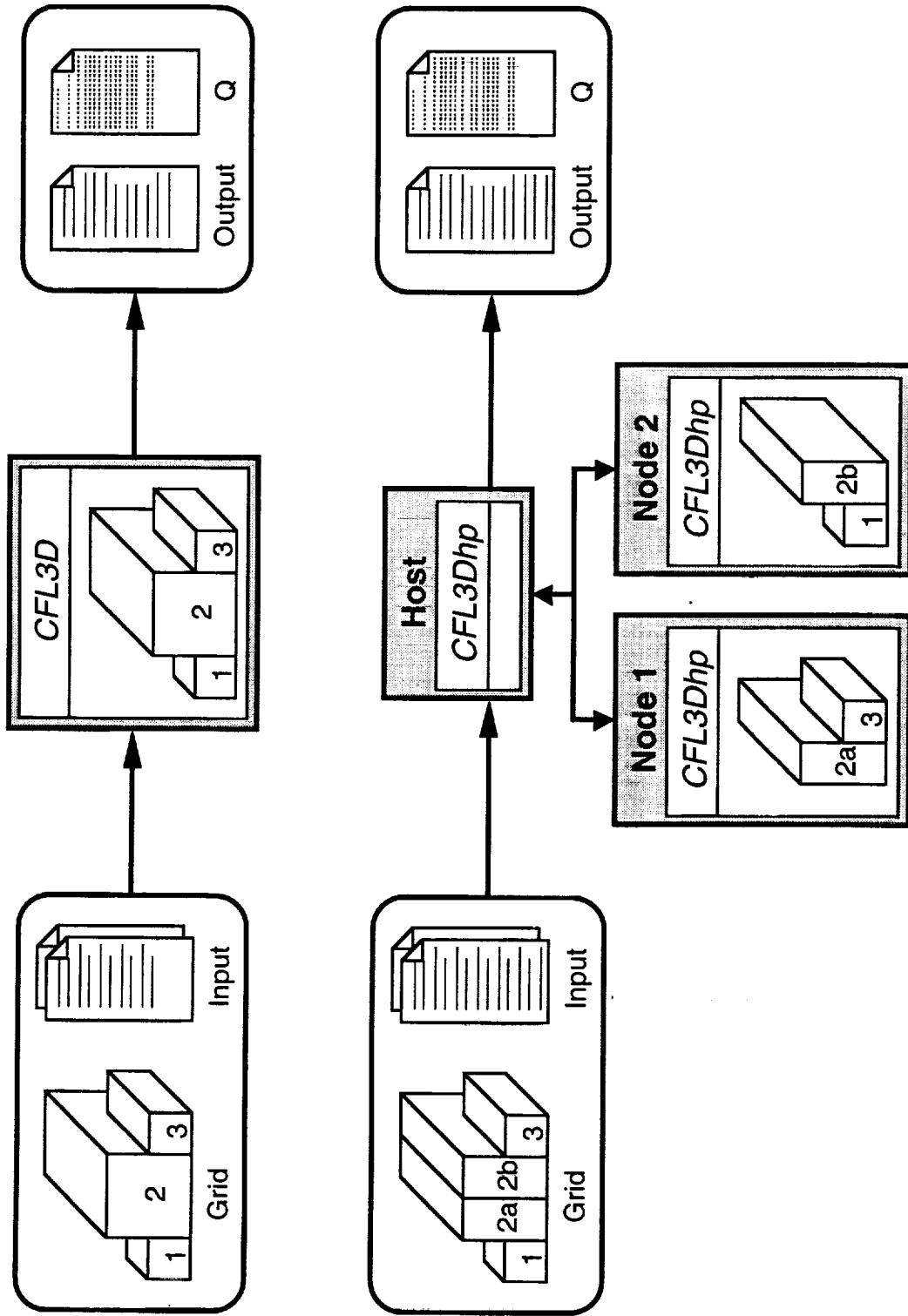
CFL3Dhp Requires External Block Splitting

The top part of the block diagram shows how CFL3D is run on a serial computer. In sequential processing on a shared memory serial supercomputer, the size of the grid block is not an issue. The coarse-grain host/node parallel programming paradigm used in CFL3Dhp implies that each processor performs computations on the data assigned to it based on the block-to-processor mapping. For parallel processing, a single block grid must be split in order to map the grid onto more than one processor. The bottom part of the block diagram shows the coarse-grain parallel implementation of CFL3Dhp for a multiblock grid. In a multiblock grid CFD analysis, the grid shall be mapped onto a given number of processors for parallel processing. Typically, the size of these grid blocks may vary by a large extent and the large grid blocks may be too large for the memory available in a processor. When the processor memory is limited, as in most parallel platforms, it is necessary to split the large grid blocks. An advantage of the grid block splitting is that it allows a larger number of processors to do the work and this reduces the work load per processor resulting in a faster turn-around. It will be shown later that splitting the grid blocks also improves parallel efficiency. However, this splitting also introduces additional block boundaries which slightly worsens the solution convergence rate and also increases the inter-processor communication. The advantages of being able to use a large number of processors far outweighs the slight increase in the iteration count needed to achieve the same level of convergence as the un-split grid.

CFL3Dhp Requires External Block-Splitting



High Speed Aerodynamics, Long Beach



Pre- and Post-Processing Tools

The input file for CFL3Dhp is similar to its serial version counterpart. The problem with splitting the grid is that the input files have to re-created for the split grid. Also, since the blocks that contain non point-matched surfaces are sometimes split, there is an additional complexity in the input file preparation. BLB has developed a suite of tools to improve the process of using CFL3Dhp when grid blocks must be split.

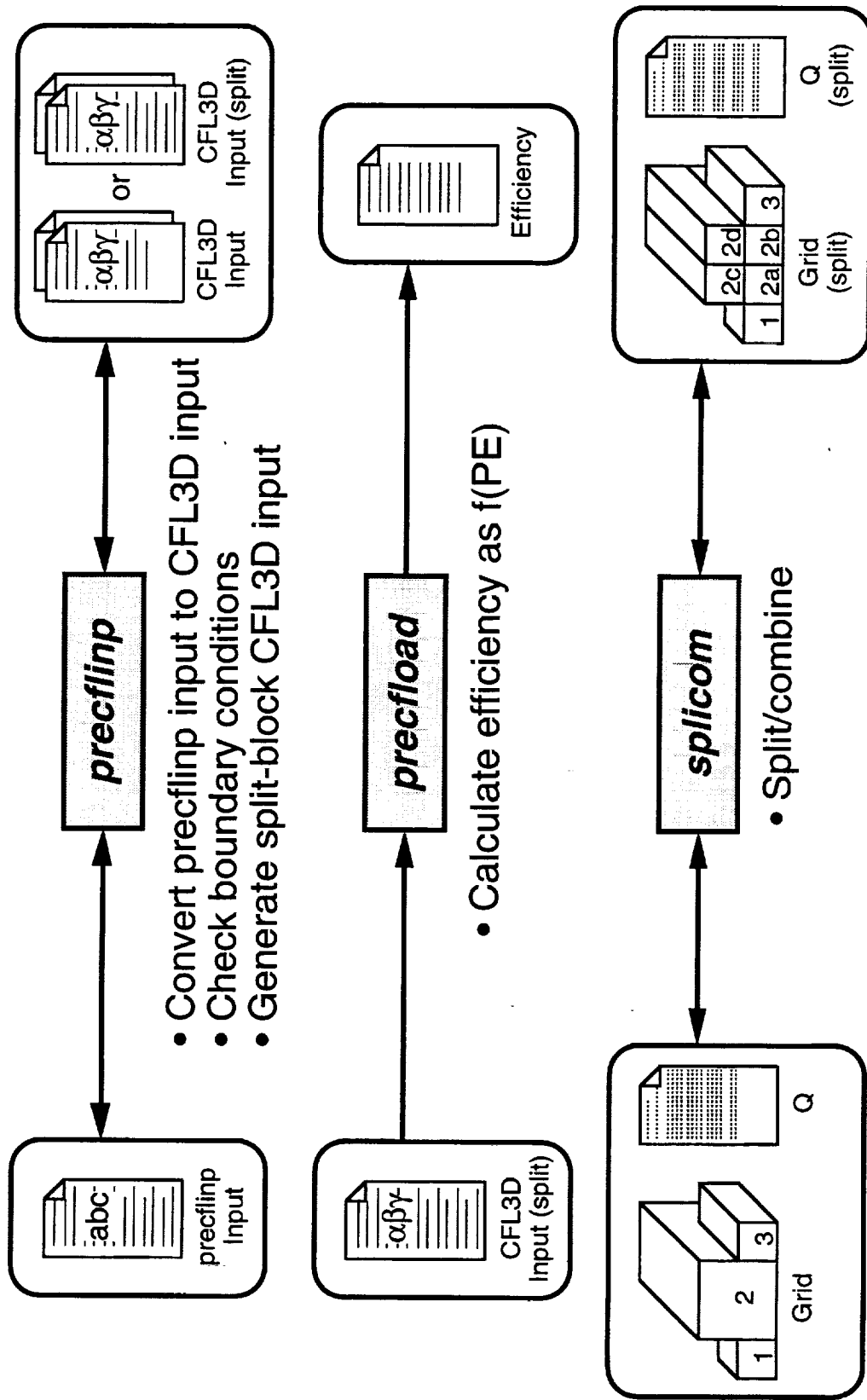
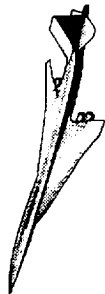
The *preclinp* utility is an input file preprocessor. It was originally developed to create a CFL3D input file. It was extended to also create a CFL3D input file when the blocks are split.

As in CFL3D, the parallel version of *precl3d* outputs the parameters needed for CFL3Dhp in addition to determining the work array sizes required for the block-to-processor mapping associated with the total number of processors used for the split block. The *preclload* utility calculates the load and the load-balancing efficiency for all block-to-processor mappings ranging from one processor to the total number of grid blocks. Here, load is the number of points mapped to a processor and the definition of load-balancing efficiency is given in the next chart. The load for each mapping is given in order to determine whether the processor has enough memory available for the mapping. The number of processors that optimizes the parameters such as the processor load, load-balancing efficiency, and throughput is chosen for a computation.

Splicom splits and combines grid files and solution files using the same input file as *preclinp*. When the grid blocks are split, the number of blocks that contain the solid surfaces can become large. This is a post-processing nightmare, particularly with the present GUI-based visualization packages, for visualizing the surface flow quantities. To avoid this, the *Splicom* combines the split grid and solution back to the original un-split blocks. Both the grid and solution file split blocks can be combined.

Pre- and Post-Processing Tools

High Speed Aerodynamics, Long Beach

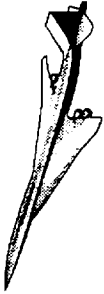


Parallel Efficiency

Achieving good load-balancing and scalability are vital for achieving high parallel efficiency. The Load on a processor is defined as the number of points mapped onto it. In this study, only static load-balancing is considered. Load-balancing is performed by mapping grid blocks to processors such that all the processors have nearly equal number of points. Load-balancing efficiency is a goodness measure of the load-balancing. On a distributed memory parallel computer limited by processor memory constraints, the maximum number of grid points per processor cannot exceed a value (e.g., for CFL3Dhp, the per processor grid points for Baldwin-Lomax turbulence models should be $< 200,000$ on the IBM SP-2 with a processor memory of 128 Mbytes). The *precfload* utility described in the previous chart maps the grid blocks to different number of processors and calculates the load-balancing efficiency for each of this mapping.

Scalability is a measure of speedup increase with increase in number of processors. Linear scalability is achieved when speedup increases at the same rate as the PE increase. number of processors used for the computations. PEs with the same load-balancing efficiency should be used when scalability is evaluated.

Parallel Efficiency



High Speed Aerodynamics, Long Beach

- Load-balancing efficiency and scalability are vital for high parallel efficiency
- If PE is the number of processors, load-balancing efficiency is:

$$\eta = \frac{1}{PE} \sum \frac{\text{Local Load}}{\text{Max. Load}} ; \text{ Max. Load} = \max(\text{Local Load}(i)), i = 1, PE$$

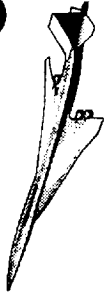
- Scalability is a measure of speedup increase with increase in PE

CFL3Dhp Navier-Stokes Solutions

To demonstrate the power of parallel processing, two large analysis problems are shown. The first problem is a Navier-Stokes solution for TCA full configuration in sideslip at supersonic cruise. The original grid has 42-blocks with 13.6 million points. For this problem, the serial CFL3D code requires 4 Gigabytes of core memory. This memory requirement is much higher than the single-processor memory allowed (2.4 Gigabytes) on the Cray C-90. To emphasize the capability of parallel processing, the Navier-Stokes polar for this problem was obtained using CFL3Dhp in a day on a Cray T3E.

The second problem is the Reference H transonic nozzle boattail drag calculations. The original grid has 37 blocks with 9.5 million grid points. Navier-Stokes solution for this problem requires several thousands of iterations. Parallel computing, using CFL3Dhp, with a large number of processors produced the solution in less than a week of wall time.

CFL3Dhp Navier-Stokes Solutions



High Speed Aerodynamics, Long Beach

- TCA full configuration in sideslip N-S solutions
 - 42-block 13.6 million grid points
 - Required memory is 4 GB
 - Polar obtained in a day
- Ref. H transonic 2-D nozzle boattail N-S calculations
 - 37-block 9.6 million grid points; need 3 GB memory
 - Took excess of 10,000 iterations to converge
 - Solution obtained in a week

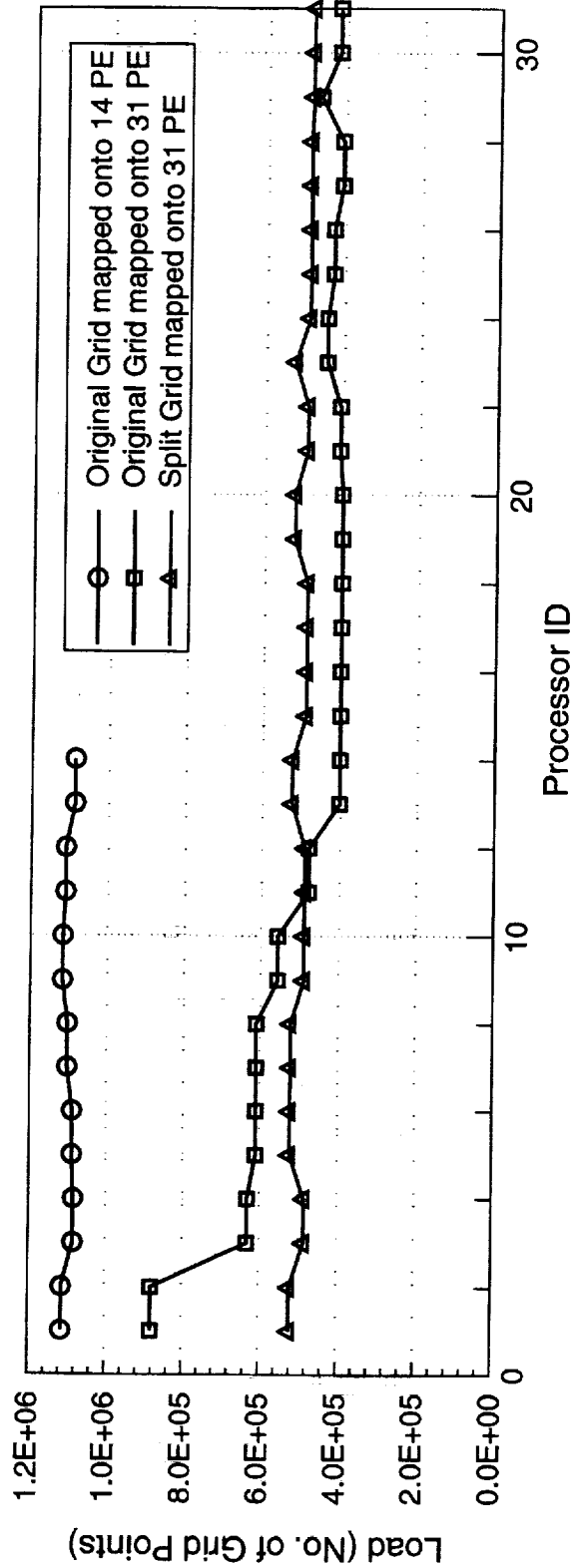
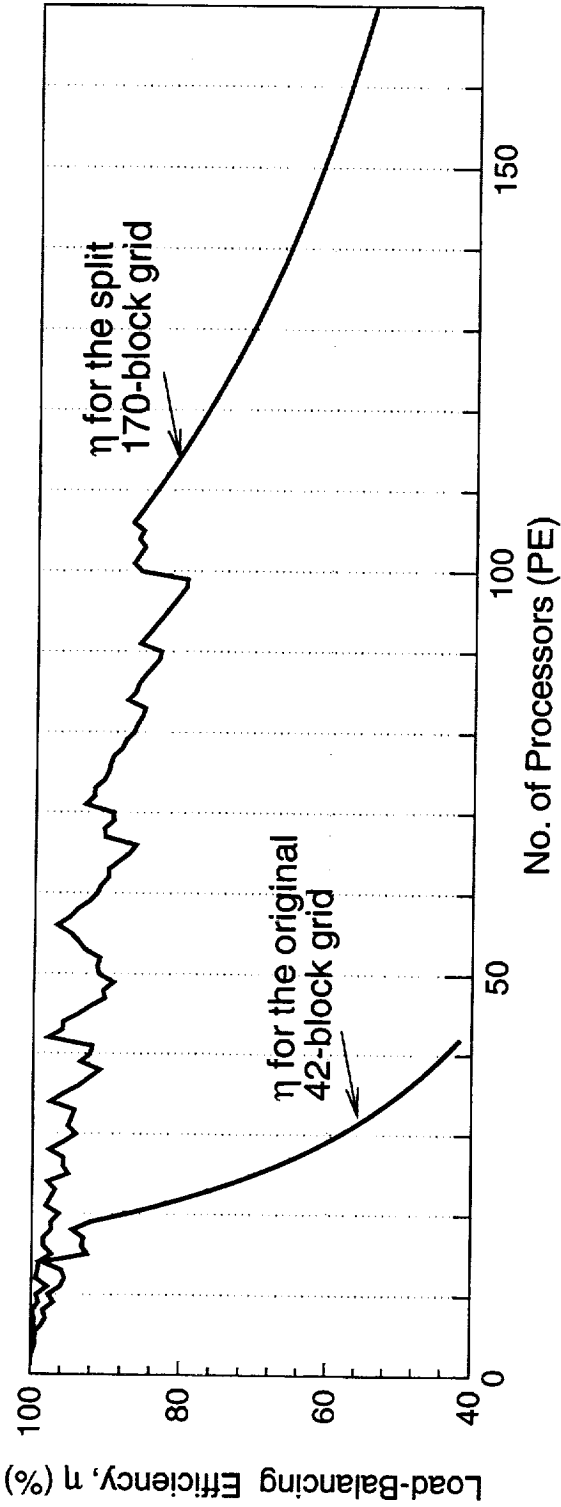
Load-Balancing Efficiency and Processor Load

This chart shows the load-balancing efficiency and the processor load distribution for the 42-block TCA full configuration in sideslip grid (13.6 million points). The efficiency curve for the 42-block grid shows that mapping this grid directly onto 42 processors would yield a poor load-balancing efficiency of only 42%. Mapping the 42-block grid onto 31 processors of the SGI Origin 2000 system (32 total processors) gives only 52% efficiency. The load corresponding to this mapping shows that two of the 31 processors have nearly double the load of the last 18 processors which stay idle while the two processors with the high load are busy.

The 42-block red efficiency curve also shows that mapping the grid on to 14 processors gives nearly 97% load-balancing efficiency. The load distribution for this mapping is given by the red circle symbols. This mapping, although efficient, uses only 14 processors for computations and hence takes long wall-time for completing the solution. It would be desirable to use more number of processors to increase throughput and maintain high load-balancing efficiency. To achieve this, it is necessary to split the blocks so that there is more flexibility to map the blocks to the processors compared to the original 42-block grid. Indeed, by splitting this grid into 170 blocks and mapping it onto 31 nodes, nearly 95% efficiency has been achieved. The nearly uniform processor loads corresponding to this mapping is given by the green square symbols. It can also be seen that the same split grid can be mapped onto 106 processors (on IBM SP-2 or Cray T3E) and still achieve nearly 90% efficiency which would significantly reduce the wall-time for obtaining the solution.

Load-Balancing Efficiency and Processor Load

High Speed Aerodynamics, Long Beach



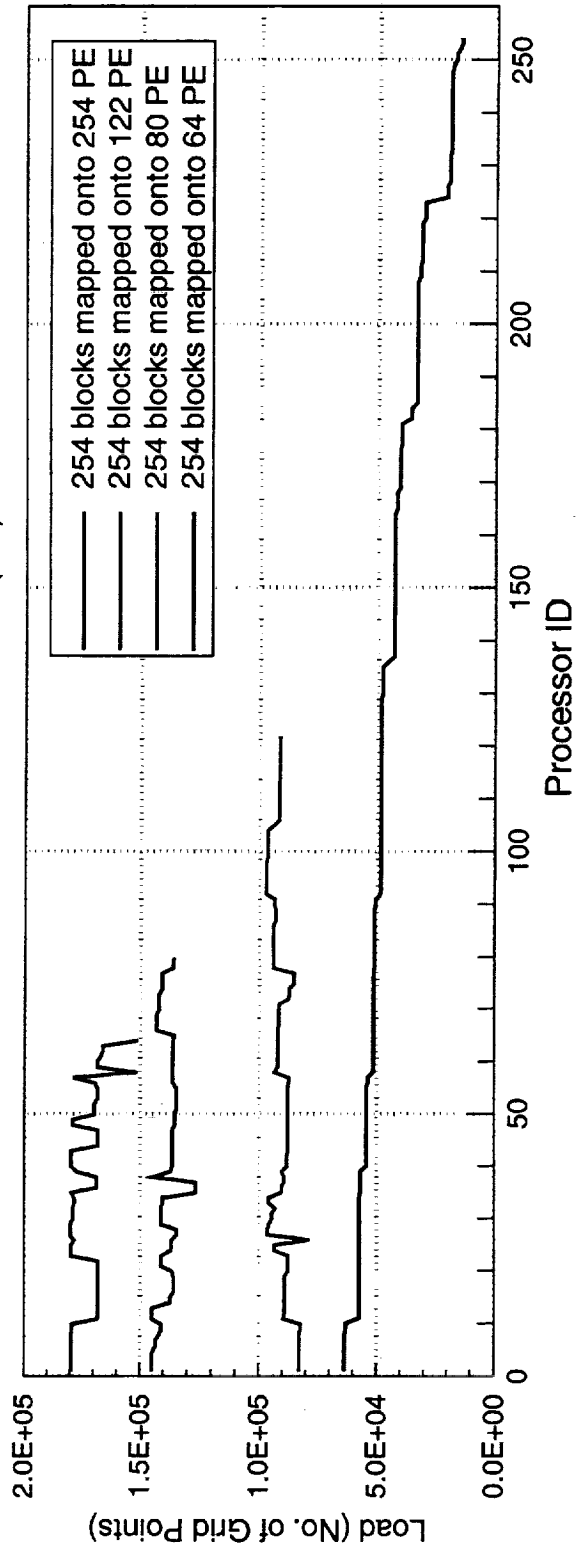
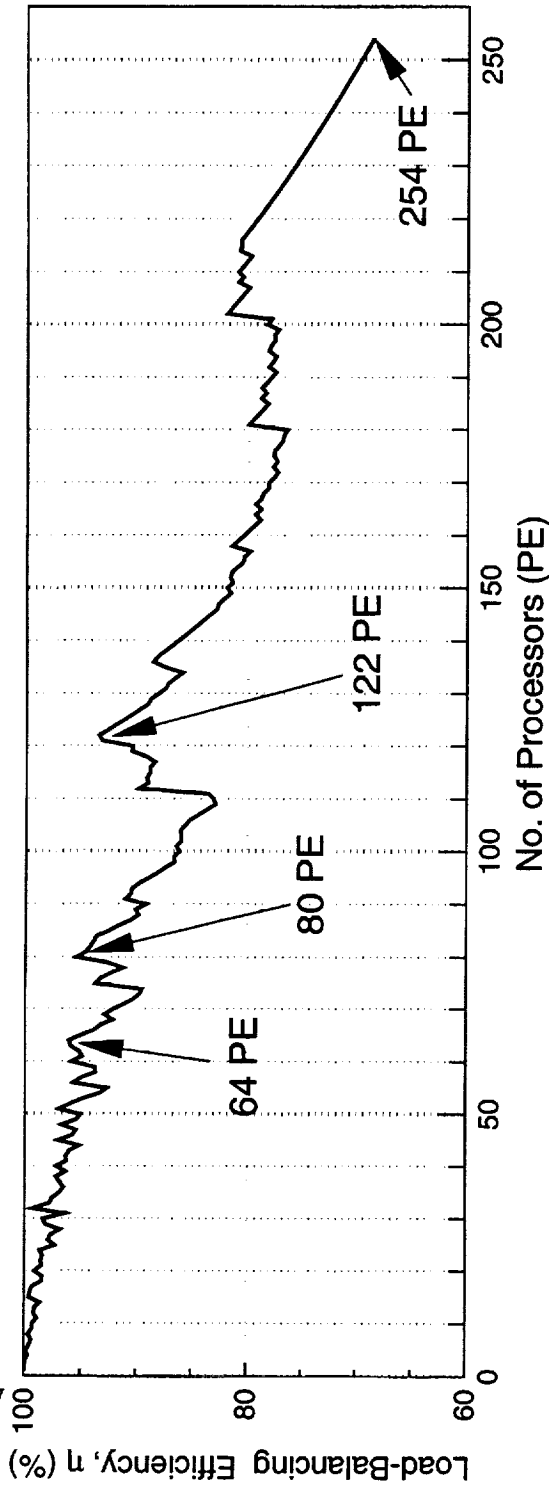
Load-Balancing Efficiency and Processor Load

In this chart, the importance of block splitting to achieve high parallel efficiency is reiterated. The original grid is a 37-block installed transonic nozzle boattail grid with 9.5 million points. This grid is split into 254 blocks to improve parallel efficiency. The load-balancing efficiency and the load distribution for the split grid are shown. As pointed out in the chart, mapping the split grid onto 64, 80, and 122 PE produces more than 94% efficiency. This indicates that 122 PE can be used for very fast turn-around time. Based on this observation, a parallel scalability study was performed for this problem using CFL3Dhp, and will be discussed in the next chart.

Load-Balancing Efficiency and Processor Load Distributions



High Speed Aerodynamics, Long Beach

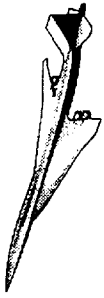


CFL3Dhp Scalability

To evaluate the scalability of the CFL3Dhp code, the transonic Navier-Stokes analysis of an installed nozzle boattail grid with 254 blocks is chosen. The efficiency curve (shown in the previous chart) of the various block-to-processor mapping indicates that mapping this grid onto 122, 80, 64, and 48 processors produce nearly equal load-balancing efficiency.

The table shows that increasing the number of processors from 64 to 122 maintains the CPU time taken per processor to complete one iteration. In addition, the wall time needed for completing 10000 iterations of the solutions is given. As a reference, the estimate for a single-processor Cray C-90 are also shown. Note that the C-90 run would take a wall-time of nearly 20 days even if it runs non-stop. In contrast, the 122 PE solution can be completed within a few days.

CFL3Dhp Scalability



High Speed Aerodynamics, Long Beach

- Transonic nozzle boattail N-S solution at $Re_c = 40 \times 10^6$
- 37-block, 9.6 million point grid split into 254 blocks

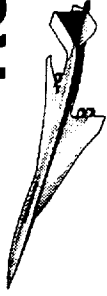
PE	CPU/PE/iter (minutes)	Wall time for 10^4 iter (Hrs)
122	31.7	43.30
80	29.4	61.25
64	29.3	78.30
1 (C-90*)	2.9	484

* required memory = 400 Mw

Room for Performance Improvement

Good load-balancing efficiency does not guarantee good overall efficiency. In fact, CFL3Dhp runs much below the processor's Mflop rate. In the process of examining the reasons for the poor performance of the CFL3Dhp code on the current cache-based parallel platforms, it was noted that the processors were waiting for data from the memory. These memory fetch operations are generally slow due to latency. In CFL3Dhp, these memory fetch operations were too frequent and had long strides because of the loop constructs in CFL3Dhp code preserved the CFL3D loops which was optimized for vector processors. Efforts to correct this involves reordering of the arrays as well as the nested do-loop orders. It is anticipated that making these improvements in the CFL3Dhp code can nearly double the present code performance on these parallel platforms.

Room for Performance Improvement



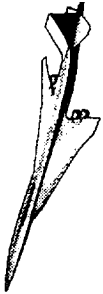
High Speed Aerodynamics, Long Beach

- CFL3Dhp runs much below processor's Mflop rate
 - Most available parallel platforms are cache-based
 - Vector loops are inefficient for cache-based systems
- CFL3Dhp is not cache-friendly
 - Too many memory misses and long memory strides
 - Data is fetched from memory and not available in the cache from earlier memory fetch
- Suggested improvement
 - Reorder arrays and remove vector loops
 - Multitask within nodes (if possible)

Summary

In summary, CFL3Dhp has rapidly grown out of its infancy to become a production code. It is very easy to port and it runs on most available parallel platforms. The pre- and post-processing tools developed at BLB provides a user-friendly environment for parallel processing. Several CFD analysis problems that are too large for the Cray C-90 have been tackled using the CFL3Dhp code. Several ways of improving the code performance on parallel platforms have been successfully implemented. Additional modifications that could make the code cache-friendly are suggested. Efforts in this direction are either currently underway or will have to be continued.

Summary



High Speed Aerodynamics, Long Beach

- CFL3Dhp has been ported onto most parallel platforms
- User friendly CFL3Dhp analyses are made possible by the pre- and post-processing tools developed at BLB
- Splitting of grid blocks improves load balancing
- CFL3Dhp scales well on the platforms tested
- Navier-Stokes mini-polar for full configuration in sideslip has been obtained within a day using CFL3Dhp
- Parallel processing using CFL3Dhp has expanded our capability to rapidly perform very large CFD analyses

This page is intentionally left blank.



TCA Full Configuration Performance and S&C Characteristics

Grant L. Martin, Raul Mendoza, Paul Kubiak, and
Shreekant Agrawal

Configuration Aerodynamics
The Boeing Company, Long Beach

HSR Airframe Technical Review
Los Angeles, California
February 9-13, 1998



This page is intentionally left blank.

TCA Full Configuration Performance and S&C Characteristics

Grant L. Martin, Raul Mendoza, Paul Kubiатko, and Shreeкant Agrawal
Long Beach, California 90807-5309

During the past year, Boeing Long Beach has made major strides in Computational Fluid Dynamics (CFD) analysis of increasingly complex HSCT configurations using both serial and parallel computational platforms.

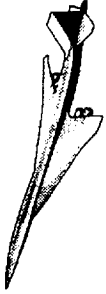
Presented herein are full configuration Euler and Navier-Stokes solutions obtained using CFL3D on the NAS C-90, J-90, IBM SP-2, Cray T3E, and SGI Origin2000. Solutions were obtained for the 1.675% TCA wing/body (W/B), wing/body/empennage (W/B/E), wing/body/nacelle/diverter (W/B/N/D), and the full configuration (W/B/N/D/E). Other CFL3D full configuration computations were performed on the 1.5% Modular Controls Model to assess the longitudinal and lateral-directional characteristics of the TCA at $M_\infty=2.4$. Limited full configuration predictions were obtained at $M_\infty=0.9$.

In order to validate the predicted force and moments, a number of comparisons are made between predicted results and the available test data from the NASA Langley Unitary Plan Wind Tunnel (UPWT) and the transonic 16' TT facility.

Outline

In this report, we investigate flow over the TCA full configuration (W/B/N/D/E) using CFL3D. After the objectives have been established, descriptions of the flow analysis tools and computer platforms used to run the codes are given. The test data used in the measured and predicted comparisons will then be described. Both Euler and Navier-Stokes solutions were computed for selected cases. In each presentation of results, a description of the geometry is given, followed by a description of the grid. The results include W/B, W/B/E, W/B/N/D, and W/B/N/D/E for the TCA with closed aftbody and W/B, W/B/N/D, and W/B/N/D/E for the 1.5% TCA Controls Model 20. Since no test data exists for the 1.675% TCA configuration with closed aftbody, computations were performed to predict component build-up. Limited full configuration transonic results will then be presented. The report closes with an important conclusion on the capability of supersonic and transonic analysis of full configuration longitudinal and lateral-directional predictions.

Outline



High Speed Aerodynamics, Long Beach

- Objectives
- Description of flow analysis and platforms
- Test data
- Supersonic results
 - 1.675% TCA performance build-up (closed aftbody)
 - » W/B, W/B/E, W/B/N/D, and W/B/N/D/E
 - 1.5% TCA Model 20 controls model (flared aftbody)
 - » W/B/N/D/E
- Transonic results
 - 1.5% TCA Model 20 controls model (flared aftbody)
 - » W/B/N/D/E
- Summary and conclusions

Objectives

As the HSR program advances, greater detail and more complexity will need to be addressed for HSCT analyses. For the program to be successful, good engineering judgement based on accurate analysis of the complete configurations must be made. Thus, it becomes important to validate the analysis tools. There are three main objectives of this work. The first is to demonstrate the capability of the full configuration computations; the second is to assess the quality of the performance and S&C predictions; and the third is to gain an understanding of the aerodynamic performance impact due to the addition of component such as the nacelles and empennage.

Objectives



High Speed Aerodynamics, Long Beach

- Demonstrate full configuration (W/B/N/D/E) computations using nonlinear flow solver at $M_\infty=2.4$
 - Performance predictions
 - S&C assessments
 - Understand the effects of the addition of various components (i.e., empennage, nacelles, etc.)
- Assess the accuracy of full configuration force and moment predictions at $M_\infty=0.9$

Flow Analysis and Computer Platforms

The nonlinear flow solver, CFL3D in the Euler and Navier-Stokes modes, was used in simulations of flows over TCA configurations. CFL3D version 4.1 was used on the Cray C-90 and J-90 computers. In addition, a parallel version, CFL3Dhp, was used on the SGI Origin2000, IBM SP-2, and Cray T3E. CFL3D uses an upwind Roe's flux-differencing scheme to solve either the Euler or Navier-Stokes equations on patched, structured, multiblock grids. A number of convergence accelerators are programmed in CFL3D to reduce CPU time. Here, grid sequencing and multigrid were actively used.

Flow Analysis and Computer Platforms



High Speed Aerodynamics, Long Beach

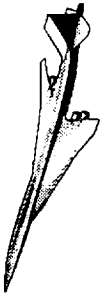
- **CFL3D Flow Solver**
 - Serial version
 - » Cray C-90 and J-90
 - Parallel version
 - » SGI Origin2000, IBM SP-2, and Cray T3E

- **Flat-plate skin friction**
 - Added to predicted Euler pressure drag
 - Van Driest II

Test Data

In order to validate the predicted force and moments, a number of comparisons were made to the available test data from the NASA Langley UPWT and the transonic 16' TT facility. The chart below shows the model, flow parameters, and test number for the test data used in the comparisons.

Test Data



High Speed Aerodynamics, Long Beach

- **1.675% TCA Model 2a (performance model)**
 - UPWT Test 1671
 - » $M_\infty=2.4$, $Re=4 \times 10^6/\text{ft}$
- **1.5% TCA Model 20 (modular controls model)**
 - UPWT Test 1677
 - » $M_\infty=2.4$, $Re=3 \times 10^6/\text{ft}$
 - 16' TT Test 488
 - » $M_\infty=0.9$, $Re=4 \times 10^6/\text{ft}$

Supersonic Results

This section presents results for the 1.675% TCA performance build-up with closed aftbody. The full configuration TCA is shown below.

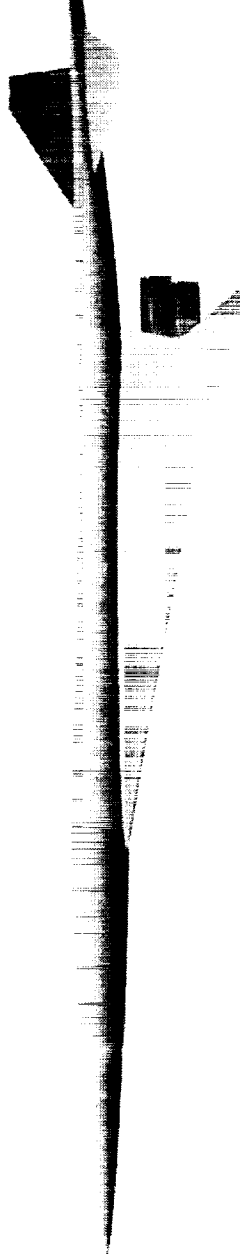
Supersonic Results



High Speed Aerodynamics, Long Beach

1.675% TCA performance build-up (closed aftbody)

$M_\infty = 2.4$, $Re = 4 \times 10^6 / ft$



1.675% TCA Predictions

This chart is an outline for the 1.675% TCA results.

1.675% TCA Predictions



High Speed Aerodynamics, Long Beach

- TCA grids
- Force build-up
 - $M_\infty=2.4$, $Re=4 \times 10^6/\text{ft}$
- No test data exists for closed aftbody
 - predict component build-up only
- CFL3D and Model 2a test data for W/B/N/D (truncated aftbody)
- Predicted full configuration Cp contours

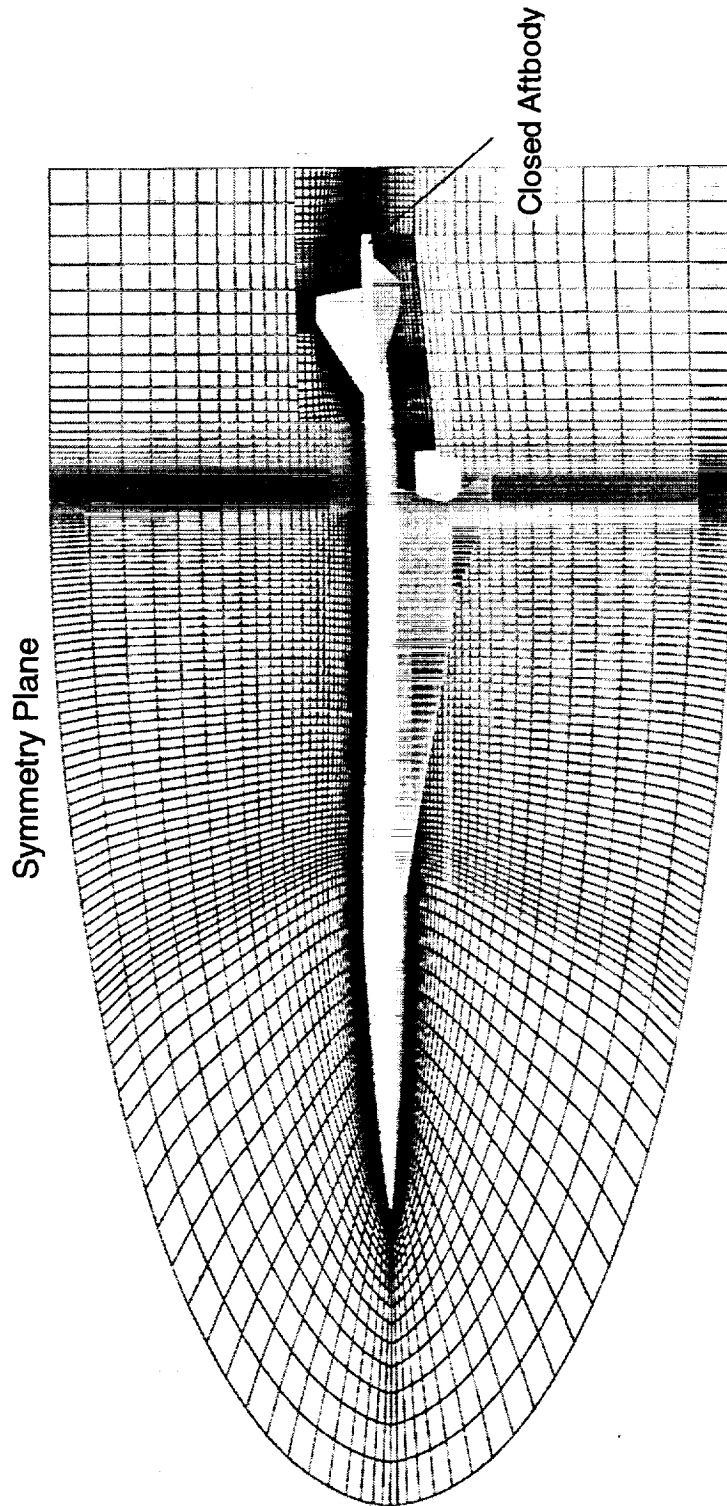
TCA Supersonic Grids

The CFL3D flow solver used structured grids for all configurations. The W/B supersonic Euler grid had a C-O topology with 97, 301, and 41 points in the spanwise, streamwise, and normal directions, respectively. The multiblock grids for W/B/E, W/B/N/D, and W/B/N/D/E were kept as modular as possible so that components could be removed and added with ease. For example, the W/B/E grid was created from the W/B/N/D grid. Six blocks surrounding the nacelles of the W/B/N/D grid were removed and replaced with a single block. Additionally, the aft end was replaced with three zones using an H-O topology; one zone covering the lower surface of the horizontal tail, a second one covering the upper surface of the horizontal tail, and a third one covering the vertical tail. All structured Navier-Stokes grids were built from the corresponding Euler grids with additional points in the normal direction clustered near the surface for a y^+ of ~ 1.5 . The W/B/N/D/E Euler grid had 21 blocks with 3.5 million points, while the Navier-Stokes grid had 6.7 million points. The 21 blocks represent the left side of the TCA configuration. This chart shows the symmetry plane for the full configuration Euler grid. The different colors represent different blocks. The angle-of-attack sweep predictions used the 21-block grid with a symmetry plane boundary condition.

TCA Wing/Body/Nacelle/Diverter/Empennage Euler Grid



High Speed Aerodynamics, Long Beach
21 Blocks, 3.5 Million Grid Pts.



TCA Drag Build-up (Closed Aftbody)

This section presents the TCA drag build-up for the closed aftbody configurations at $M_\infty = 2.4$, $C_L = 0.10$, and $Re = 4.0 \times 10^6 / ft$. The Navier-Stokes results were obtained using the Baldwin-Lomax turbulence model. All Euler results are complemented with the flat-plate skin-friction estimate for the corresponding geometries, where the skin-friction coefficient was determined by the Van Driest II method. It is important to note that the internal forces have been removed from the nacelle ducts for W/B/N/D and W/B/N/D/E configurations. Since no test data has been obtained for the closed aftbody configuration, only numerical predictions are presented.

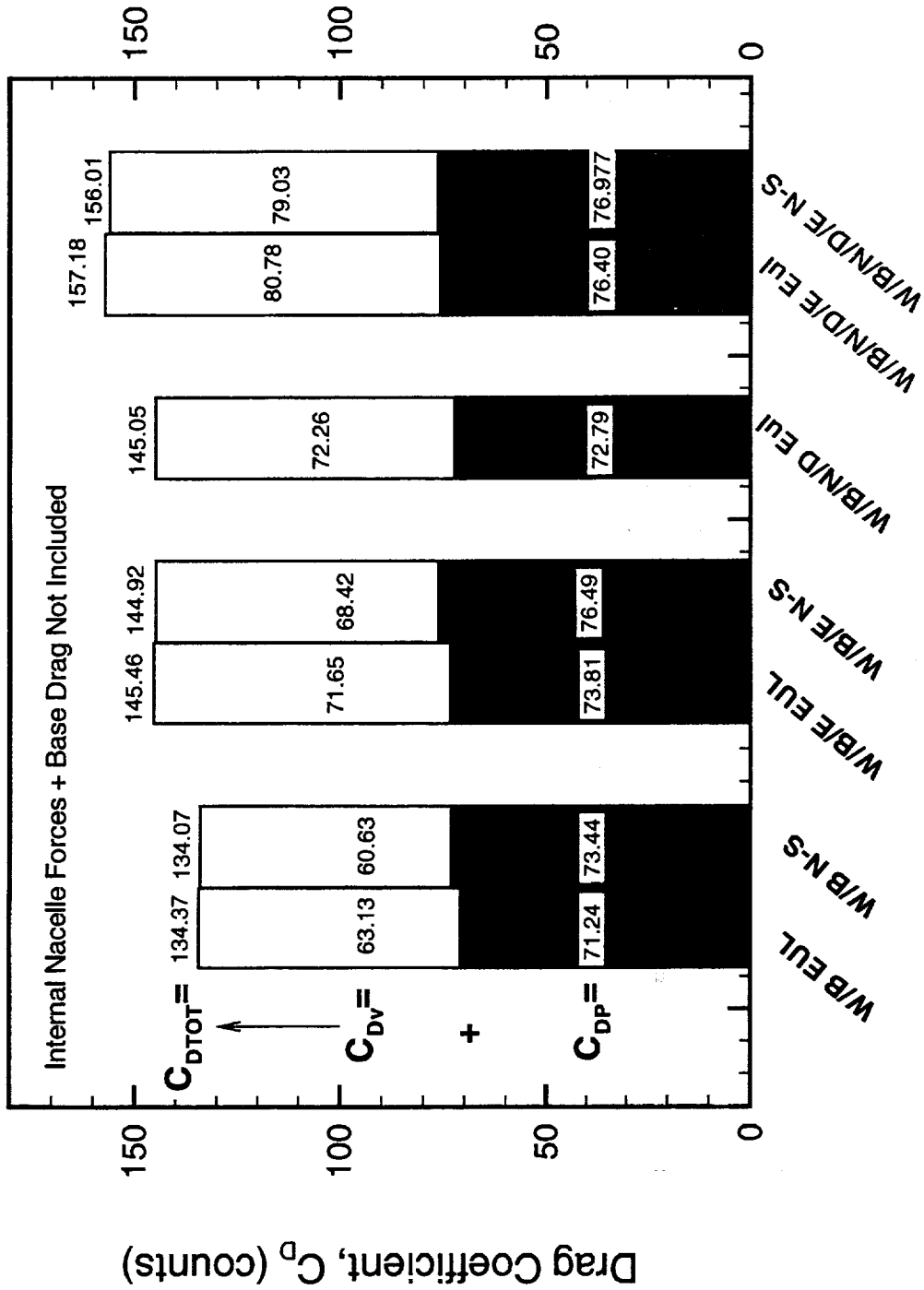
The figure below shows a breakdown of drag in terms of its pressure and skin-friction components. The W/B Euler and Navier-Stokes pressure drag values, C_{Dp} , are 71.24 and 73.44 cts., respectively. This difference is unexpected since previous Euler and Navier-Stokes-based C_{Dp} predictions for W/B have been very close to each other. However, in those calculations, the aftbodies were not closed. Likewise for the W/B/E configuration, Euler and Navier-Stokes pressure drag values differ. In this case, the Navier-Stokes prediction is 2.7 cts. higher. For the full configuration, the Euler and Navier-Stokes results predict similar levels of pressure drag, $C_{Dp} \sim 77$ cts.

1.675% TCA Drag Build-up (Closed Aftbody)



High Speed Aerodynamics, Long Beach

CFL3D, $M_\infty=2.4$, $C_L=0.1$, $Re=4 \times 10^6/ft$



Configuration



TCA Predicted Nacelle Installation Drag

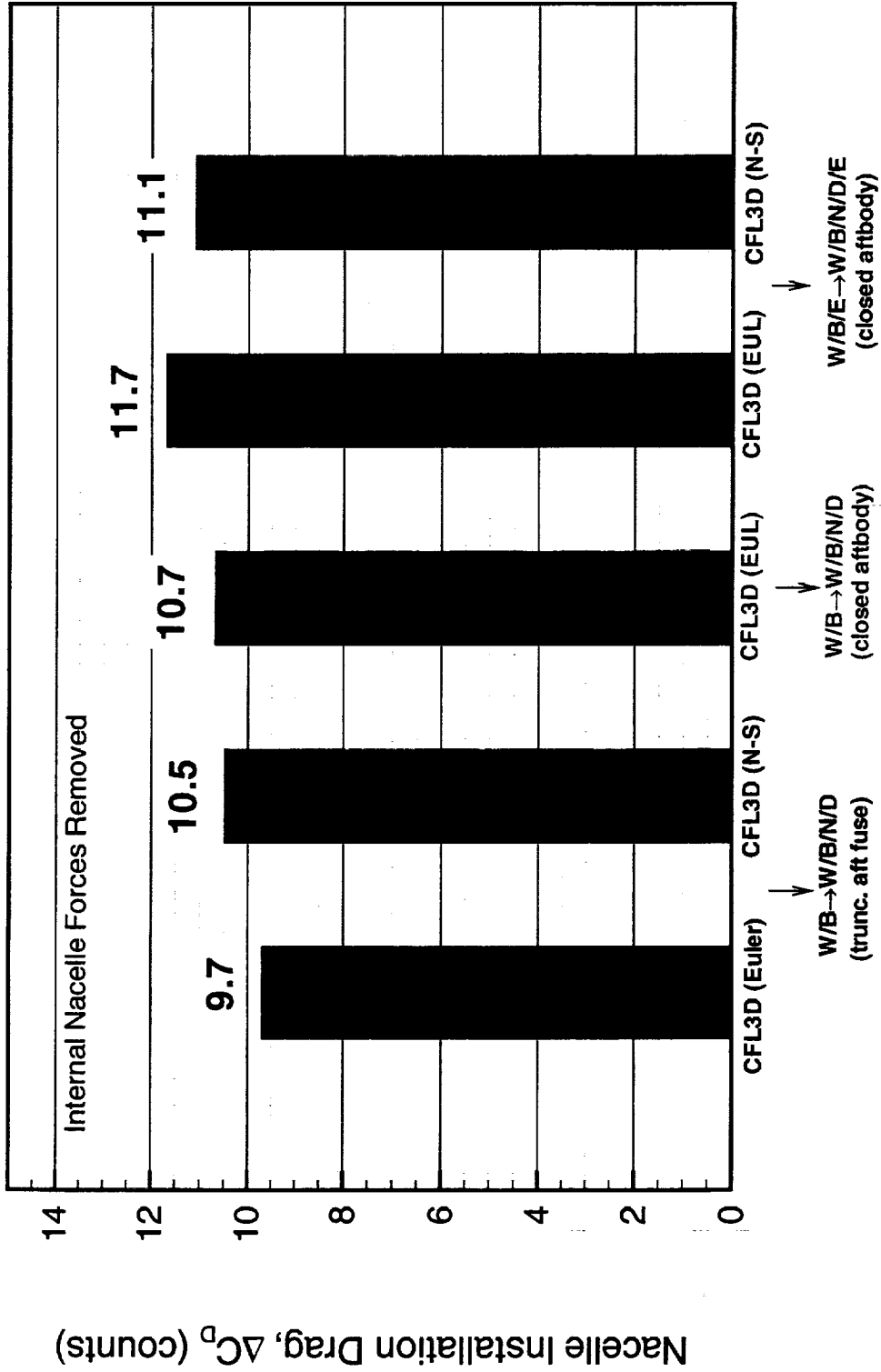
The predicted nacelle installation drag results are shown below. In this figure, results for the truncated aftbody configuration are also included. The CFL3D Euler and Navier-Stokes solutions for the truncated aftbody predict 9.7 and 10.5 cts., respectively. The remaining three bars show the nacelle installation drag for the closed aftbody configurations. Note that the nacelle installation drag is slightly higher (~ 1 ct.) with the empennage-on configuration.

1.675% TCA Predicted Nacelle Installation Drag



High Speed Aerodynamics, Long Beach

$$M_\infty = 2.4, C_L = 0.10, Re = 4 \times 10^6 / ft.$$



TCA Predicted Emp. Drag (Closed Aftbody)

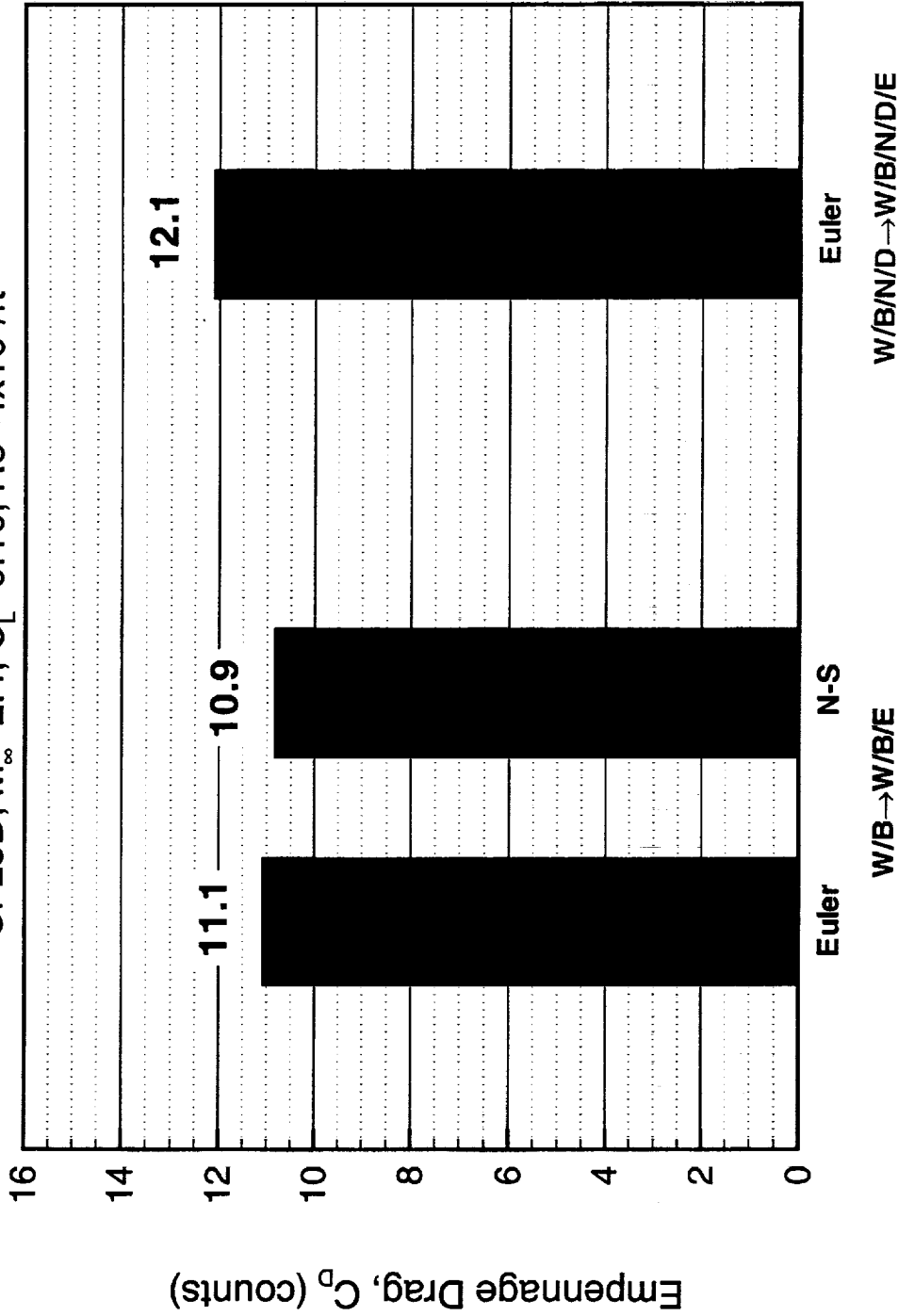
The predicted drag increments from the Euler and Navier-Stokes solutions on the W/B and W/B/E are 11.1 and 10.9 cts., respectively. The predicted drag increment from the Euler solutions on the W/B/N/D and W/B/N/D/E is 12.1 cts. At $C_L=0.10$ the different configurations do not cruise at the same angle-of-attack. This results in different empennage drag increments.

TCA Predicted Empennage Drag (Closed Aftbody)



High Speed Aerodynamics, Long Beach

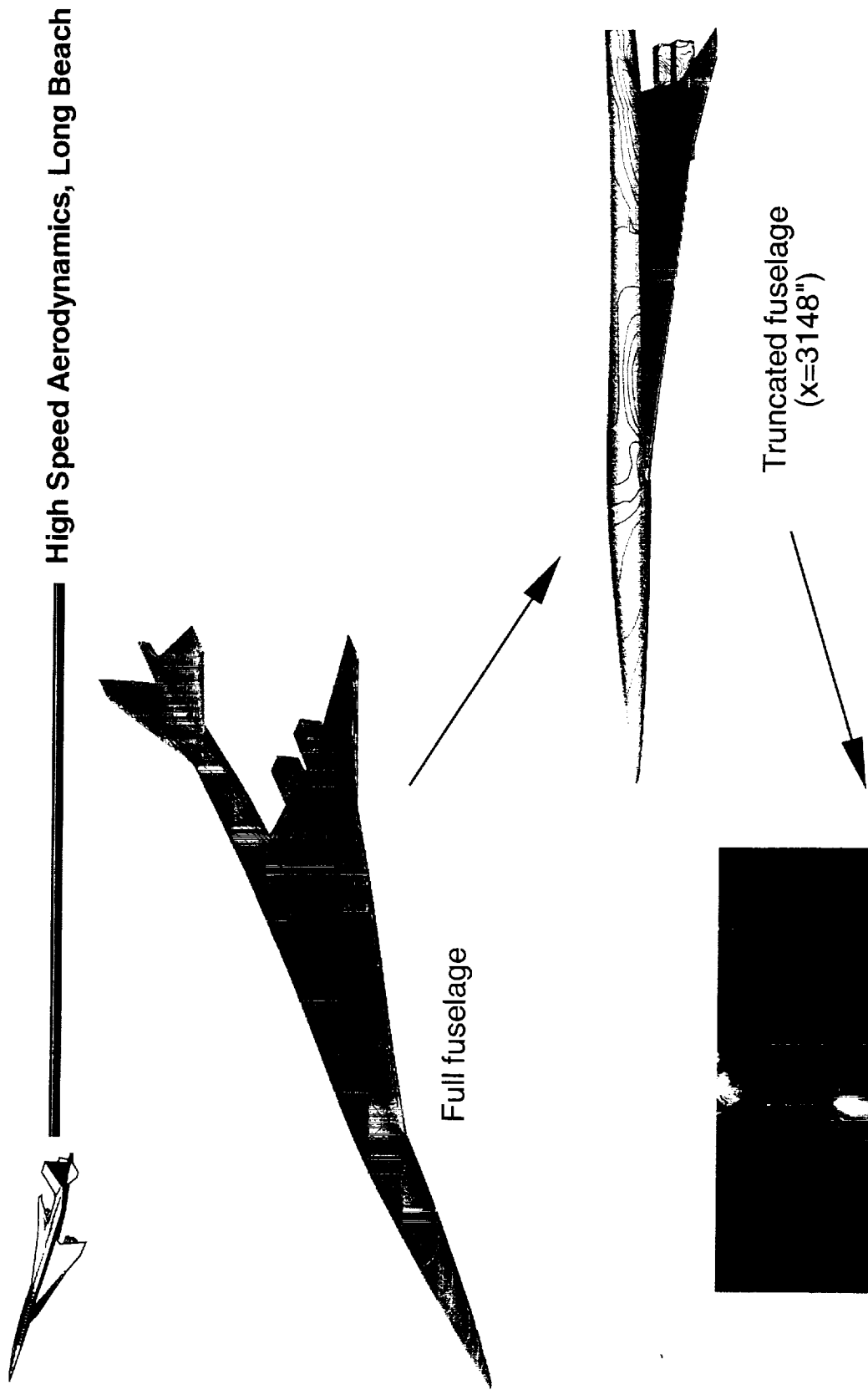
CFL3D, $M_\infty=2.4$, $C_L=0.10$, $Re=4 \times 10^6/\text{ft}$



Comparison of 1.675% TCA Predicted & Experimental Results

Since no test data exists for the closed aftbody configurations, some confidence in the CFD results can be gained by examining the data for the 1.675% TCA performance model (Model 2a) which had a truncated aftbody. The CFL3D predictions were therefore obtained by integrating forces up to $x=3148''$ location, where the aftbody was truncated on Model 2a.

Comparison of 1.675% TCA Predicted & Exp. Results



Comparison of Predicted and Measured Drag Polars

The Mach 2.4 Euler and Navier-Stokes-based drag predictions using CFL3D are compared to the test data below. A flat-plate skin-friction drag estimate of 70.2 cts. has been added to the Euler calculations. The Euler and Navier-Stokes solutions over-estimate the drag by approximately 3 and 2 cts., respectively. A trip drag estimate varying with C_L and ranging from 3 to nearly 7 cts. has been removed from the wind-tunnel data.

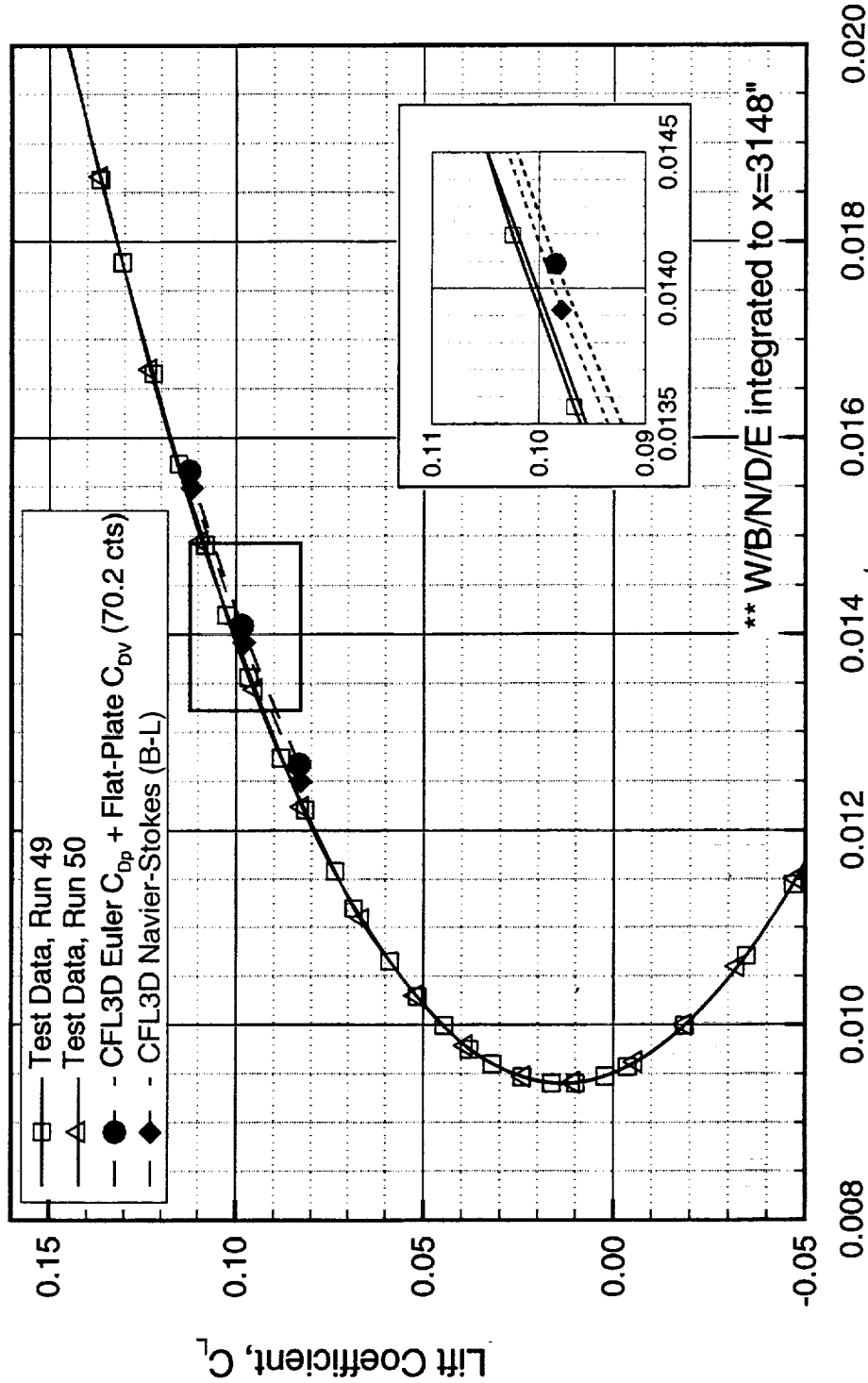
Comparison of Predicted and Experimental Drag Polars



High Speed Aerodynamics, Long Beach

TCA Wing/Body/Nacelle/Diverter Configuration**, (Trunc. Aftbody)

Langley Test 1671, UPWT-2, $M_\infty = 2.4$, $Re = 4 \times 10^6$ /ft, Trip Drag Removed



Lower Surface Pressure Contours

Lower surface pressure contours are shown on the full TCA configuration with closed aftbody at $M_\infty=2.4$, $\alpha=3.5^\circ$, and $Re_c=6.36 \times 10^6$. The predicted lower surface Cp contours show the complex shock interactions in the nacelle region.

Pressure Contours on the TCA Full Configuration
CFL3D N-S (B-L), $M_\infty = 2.4$, $C_L = 0.1$, $Re_c = 6.36 \times 10^6$

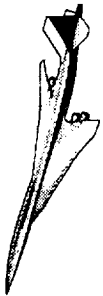


GLM

Supersonic Results

The 1.5% TCA modular controls model results are presented in the next few charts.

Supersonic Results



High Speed Aerodynamics, Long Beach

1.5% TCA Model 20 controls model (flared aftbody)

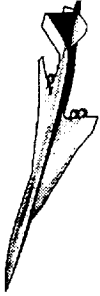
$M_\infty=2.4$, $Re=3 \times 10^6/\text{ft}$

1.5% HSR TCA Modular Controls Model

A view of the 1.5%-scale TCA modular controls model in the NASA Langley UPWT is shown in this chart. The TCA modular controls model was tested in the NASA Langley 4-ft UPWT, test section #1, from November 5 to December 5, 1996. During the wind-tunnel entry, designated as Test 1677, the model was tested at $M_\infty = 2.4$ and 2.7. The boundary layer trip applied to the TCA Model 20 used trip dots which were 0.0012" high and spaced 0.2" after every other trip dot was removed. Trip dots appeared on the fuselage nose, wing, nacelles, horizontal, and vertical tails.

The 1.5%-scale TCA modular controls model is a scaled representation of the current HSR TCA configuration with an aftbody and tails that have been modified to accept an aft-sting support. This model is equipped with both truncated and extended aft-bodies, removable forebody chines (strakes), nacelles, deflectable outboard leading- and full-span trailing-edge flaps, variable-incidence horizontal stabilizers with deflectable elevators, and a deflectable rudder. Data was obtained on the TCA model for various combinations of truncated and extended aft-bodies, nacelles, vertical and horizontal tails, and forebody chines. Data was also obtained for deflected outboard leading-edge flaps, trailing-edge flap deflections, various stabilizer incidence angles, and deflected elevator and rudders. Pitch polars were obtained for all configurations, and yaw polars were obtained on appropriate configurations.

1.5% TCA Modular Controls Model #20



High Speed Aerodynamics, Long Beach

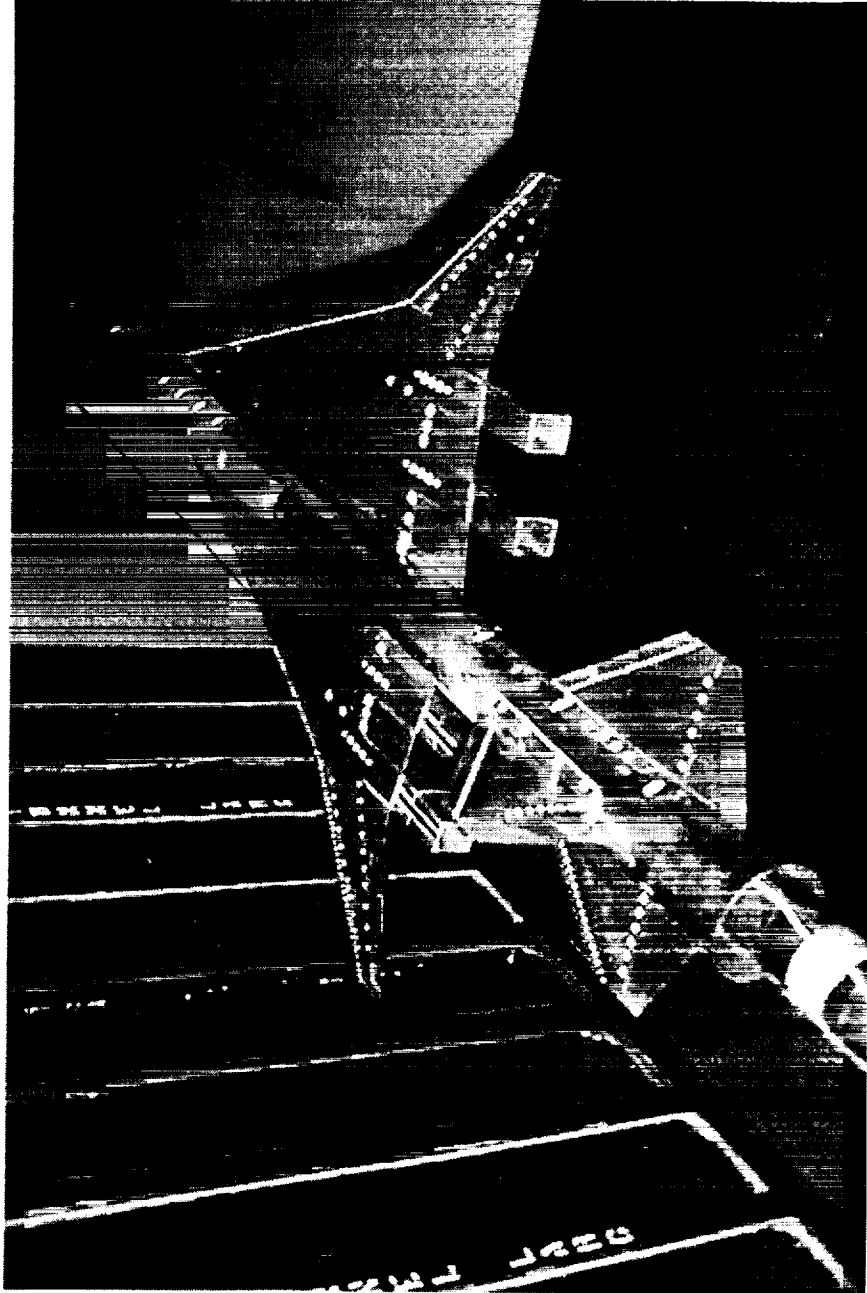
- TCA model & grids
- $M_\infty = 2.4$, $Re = 3 \times 10^6 / ft$ solutions
 - W/B/N/D/E (flared aftbody)
 - predicted and measured force comparisons
 - » angle-of-attack & sideslip sweeps
 - » surface Cp's and streamlines
- $M_\infty = 0.9$, $Re = 4 \times 10^6 / ft$ solutions
 - W/B/N/D/E (flared aftbody)
 - predicted and measured force comparisons
 - » angle-of-attack sweep

This page is intentionally left blank.

1.5% TCA Modular Controls Model

High Speed Aerodynamics, Long Beach

Flared Aftbody with Tails
NASA Langley Unitary Plan Wind Tunnel



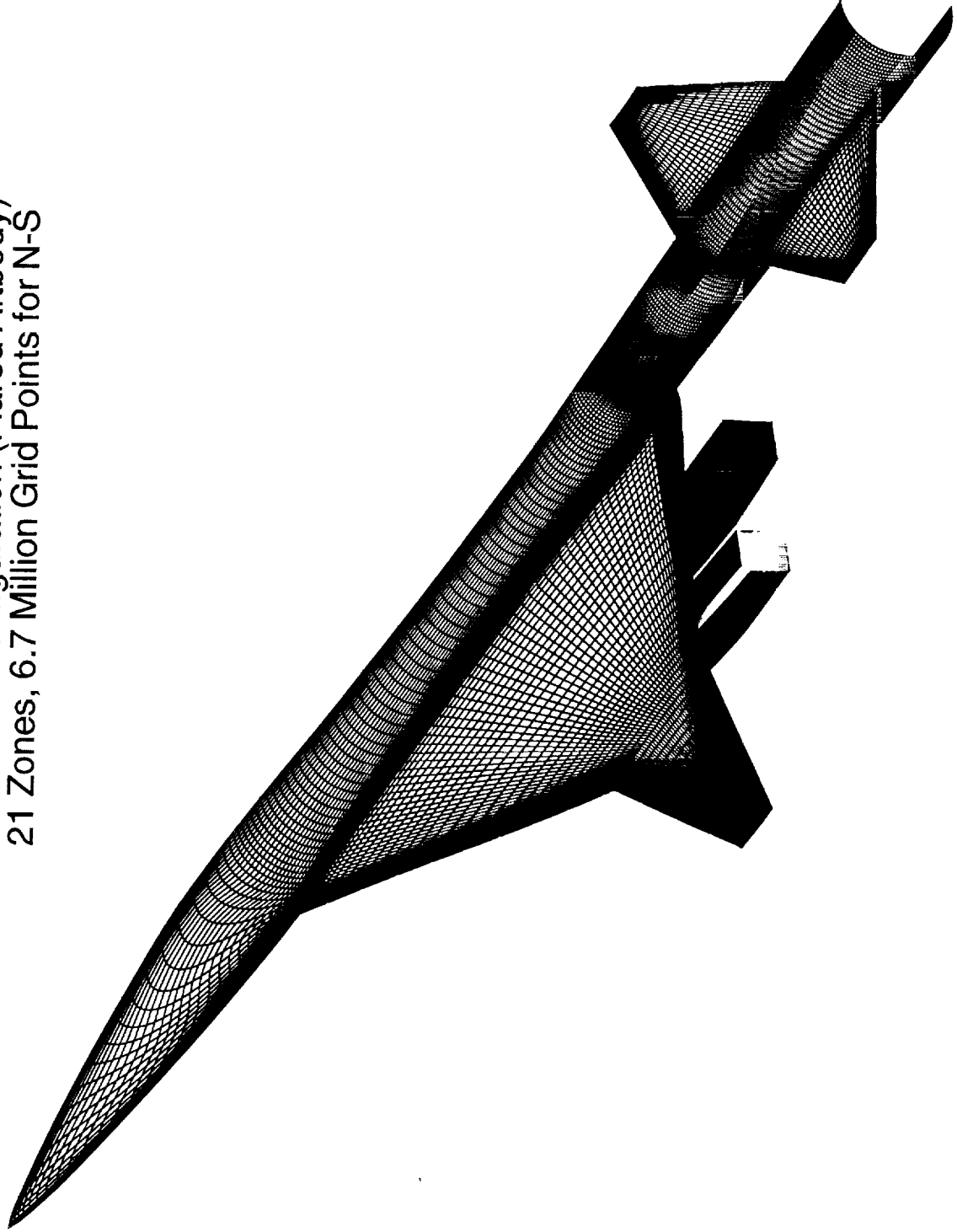
1.5% TCA Modular Controls Model

Since the flow is symmetric at $\beta=0^\circ$ conditions, only 21 blocks are needed for the alpha sweeps (half of the grid only). This results in the full configuration Euler and Navier-Stokes grids having 3.5 and 6.7 million points, respectively. This chart shows the surface grid for the full configuration. The different colors represent different blocks.

1.5% TCA Modular Controls Model

High Speed Aerodynamics, Long Beach

W/B/N/D/E Configuration (Flared Aftbody)
21 Zones, 6.7 Million Grid Points for N-S



1.5% TCA Modular Controls Model

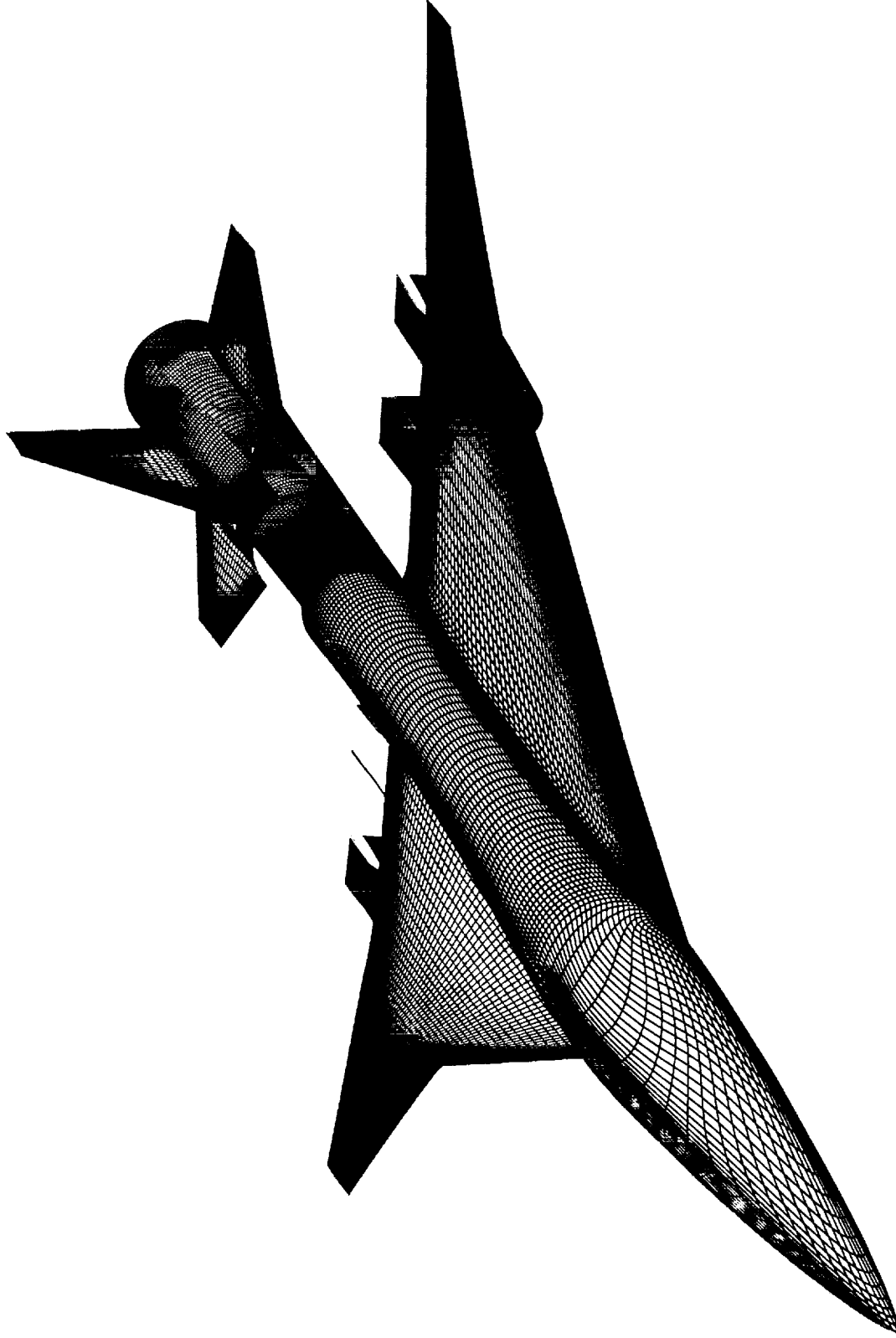
For the non-zero β , both left and right half of the airplane are needed. This results in a grid with 42 blocks and 13.4 million pts. for Navier-Stokes calculations. This chart shows the surface grid for the full configuration which was used to compute forces for the sideslip cases.

1.5% TCA Modular Controls Model



High Speed Aerodynamics, Long Beach

W/B/N/D/E Configuration (Flared Aftbody)
42 Zones, 13.4 Million Grid Points for N-S



Comparison of Predicted and Measured Lift Curves

Force results for the full configuration with the flared aftbody are shown in the next several figures. The test data, Run 57, is shown below with and without the modified cavity pressure correction.

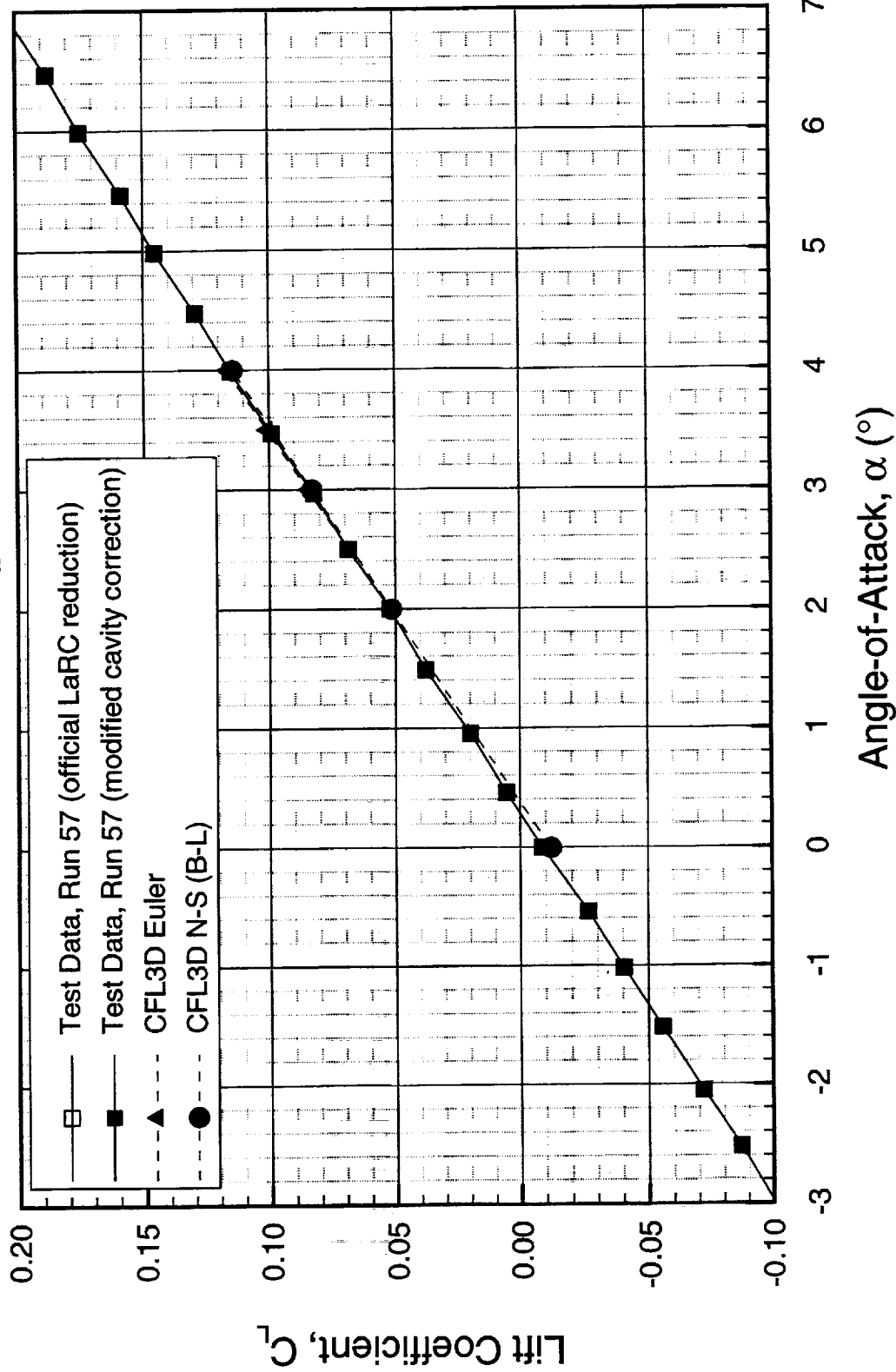
Comparison of Predicted and Experimental Lift Curves



High Speed Aerodynamics, Long Beach

1.5% TCA Controls Model, W/B/N/D/E Configuration (Flared Aftbody)

LaRC Test 1677, UPWT, $M_\infty=2.4$, $Re=3 \times 10^6$ /ft



Magnitude of the Cavity Pressure Correction on Drag

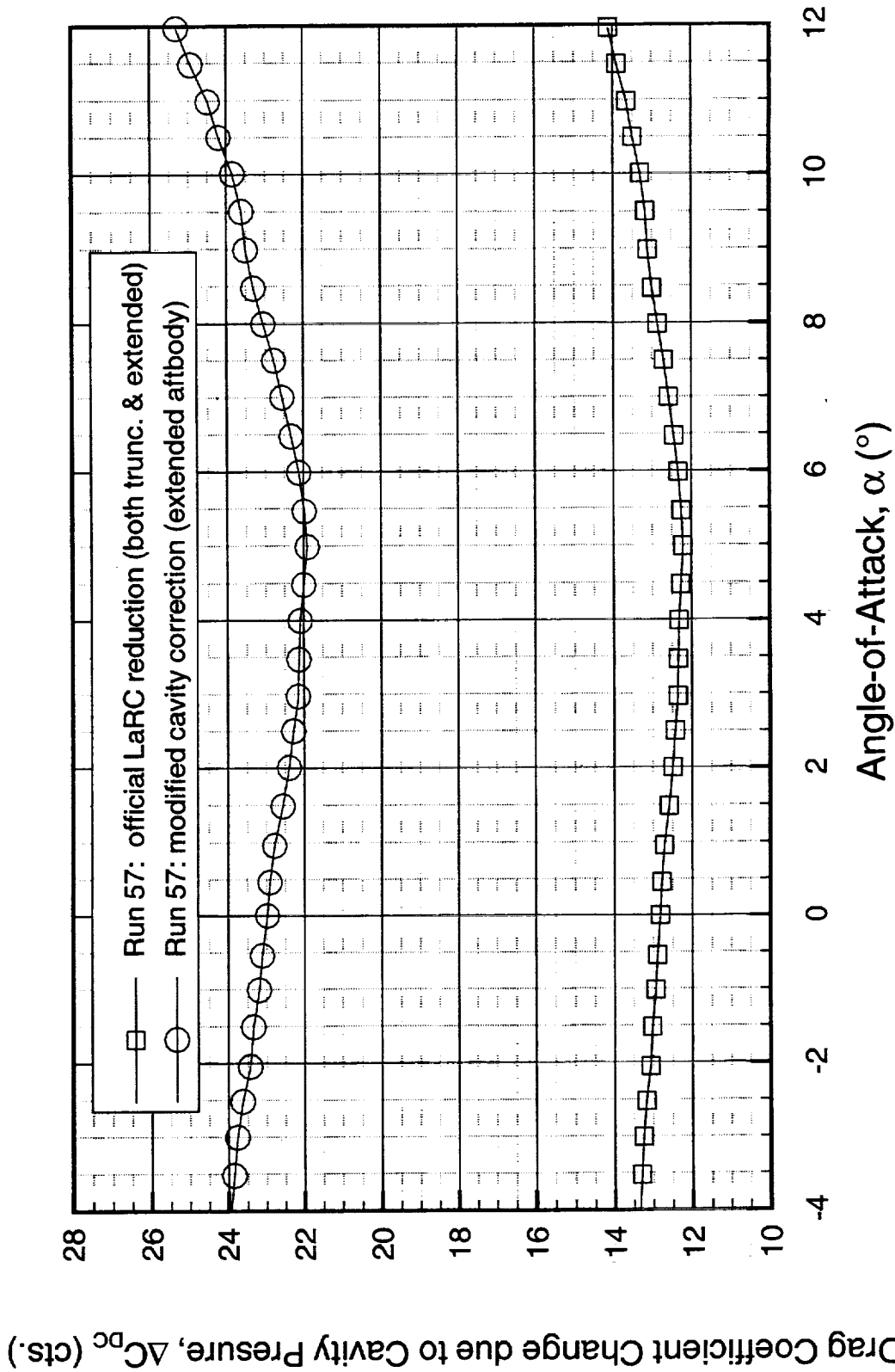
In order to prevent binding of the model on the sting and balance, the inner diameter of the aft fuselage has to be greater than the outer diameter of the sting and balance. This results in a base pressure region in the aft fuselage chamber and a measured increase in drag of the model. This spurious effect is removed from the data through the cavity pressure correction. The difference of the average cavity pressure and static pressure multiplied by the body cavity area generates a cavity pressure force which exerts itself in the axial direction. A cavity area of 2.8 in² was used in the official LaRC data reduction. From the model drawings, the authors determined that the base cavity area should have been 5.1 in². The chart below shows the magnitude of the cavity pressure correction on drag for the official reduced data and the modified cavity correction. The shift of ~10 cts. results in a larger cavity pressure drag.

Magnitude of the Cavity Pressure Correction on Drag

HSCT Aerodynamics, Long Beach

1.5% TCA Controls Model, W/B/N/D/E Configuration

LaRC Test 1677, UPWT, $M_\infty=2.4$, $Re=3 \times 10^6$ /ft



Comparison of Predicted and Measured Drag Polars

CFL3D Euler under-predicted the test data (with modified cavity correction) by ~3 cts. at $C_L = 0.10$. A flat-plate skin-friction drag estimate of 90.2 cts. has been added to the CFL3D Euler predictions. The Navier-Stokes solution under-predicts the test data (with modified cavity correction) by ~2 cts. at $C_L = 0.10$. Since a trip drag study was not conducted during this test, a trip drag correction has not been applied to the test data.

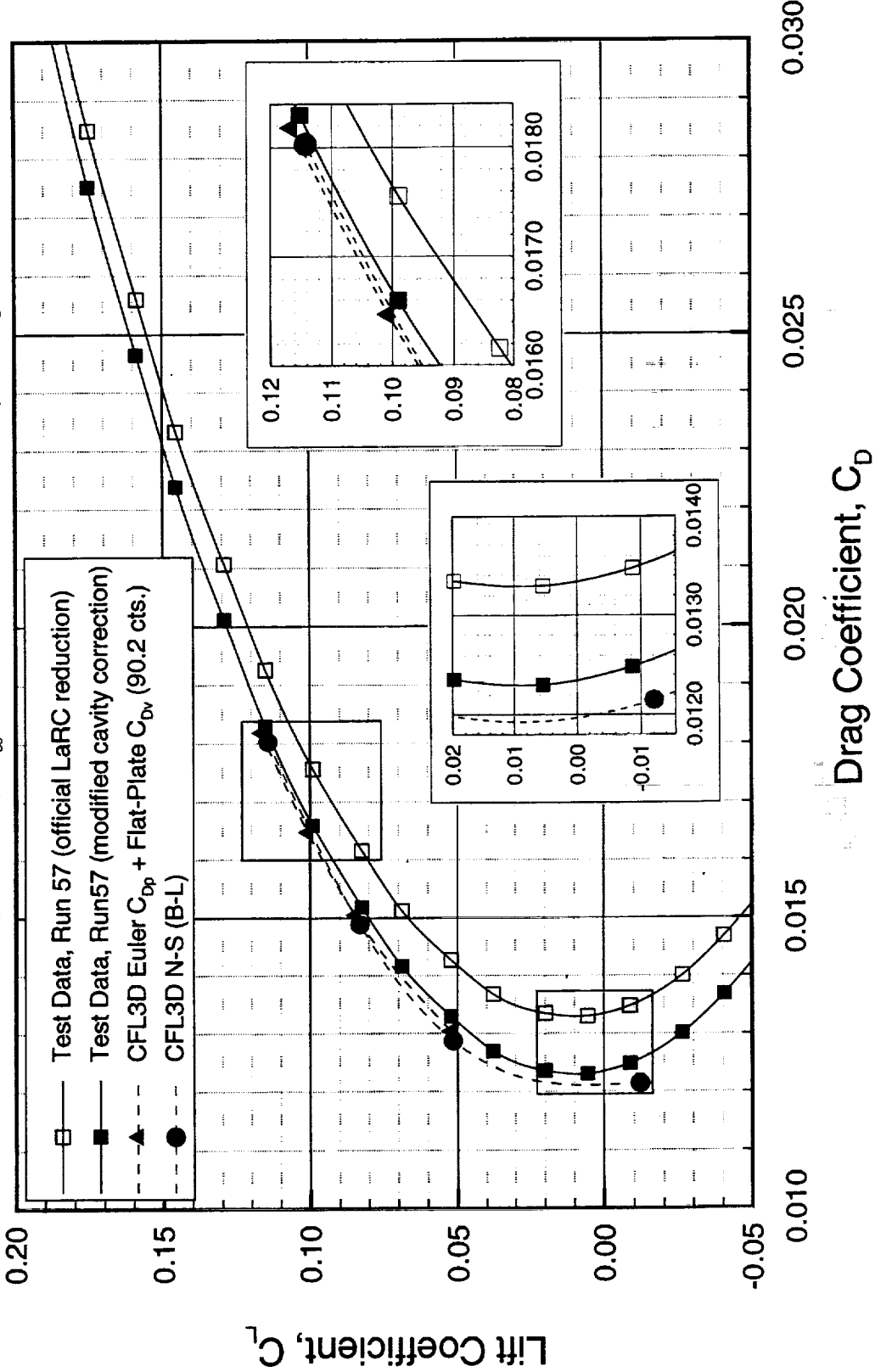
Comparison of Predicted and Measured Drag Polars



High Speed Aerodynamics, Long Beach

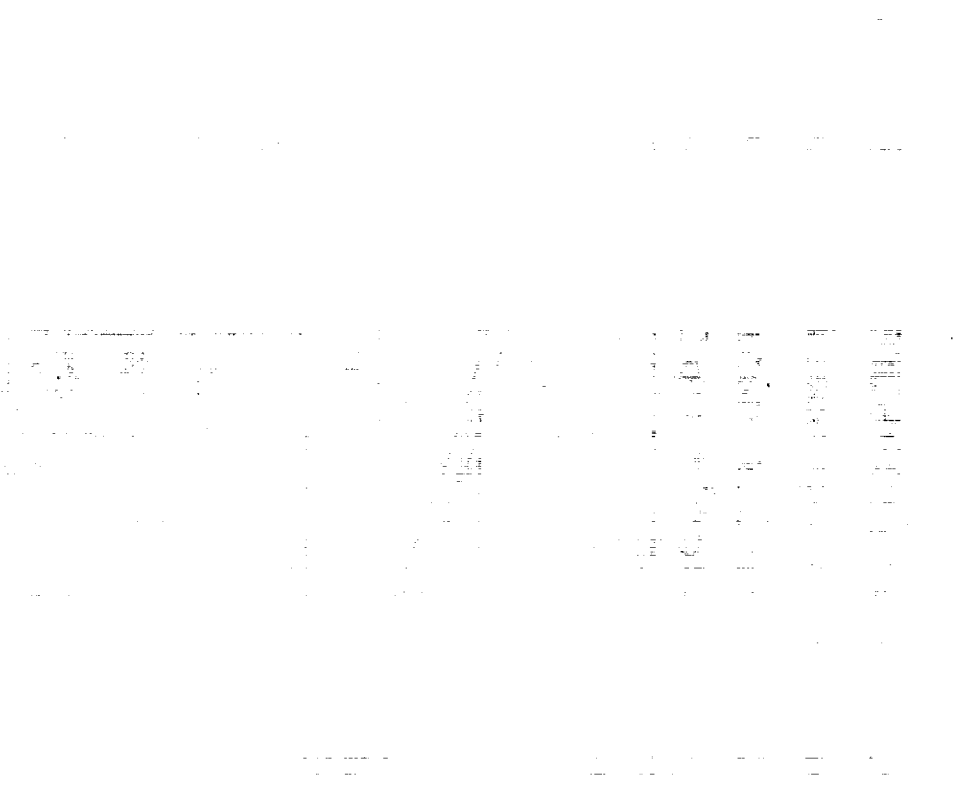
1.5% TCA Controls Model, W/B/N/D/E Configuration (Flared Aftbody)

LaRC Test 1677, UPWT, $M_\infty=2.4$, $Re=3 \times 10^6$ /ft, Trip Drag Not Removed



Comparison of Predicted and Measured L/D

The predicted and measured lift-to-drag ratios are compared in the following figure. The under-prediction in drag by both numerical schemes produce slightly higher lift-to-drag ratios at $C_L = 0.10$. It is important to note that the wing, fuselage, nacelles, and empennage had trip dots and no trip drag has been removed from the test data.

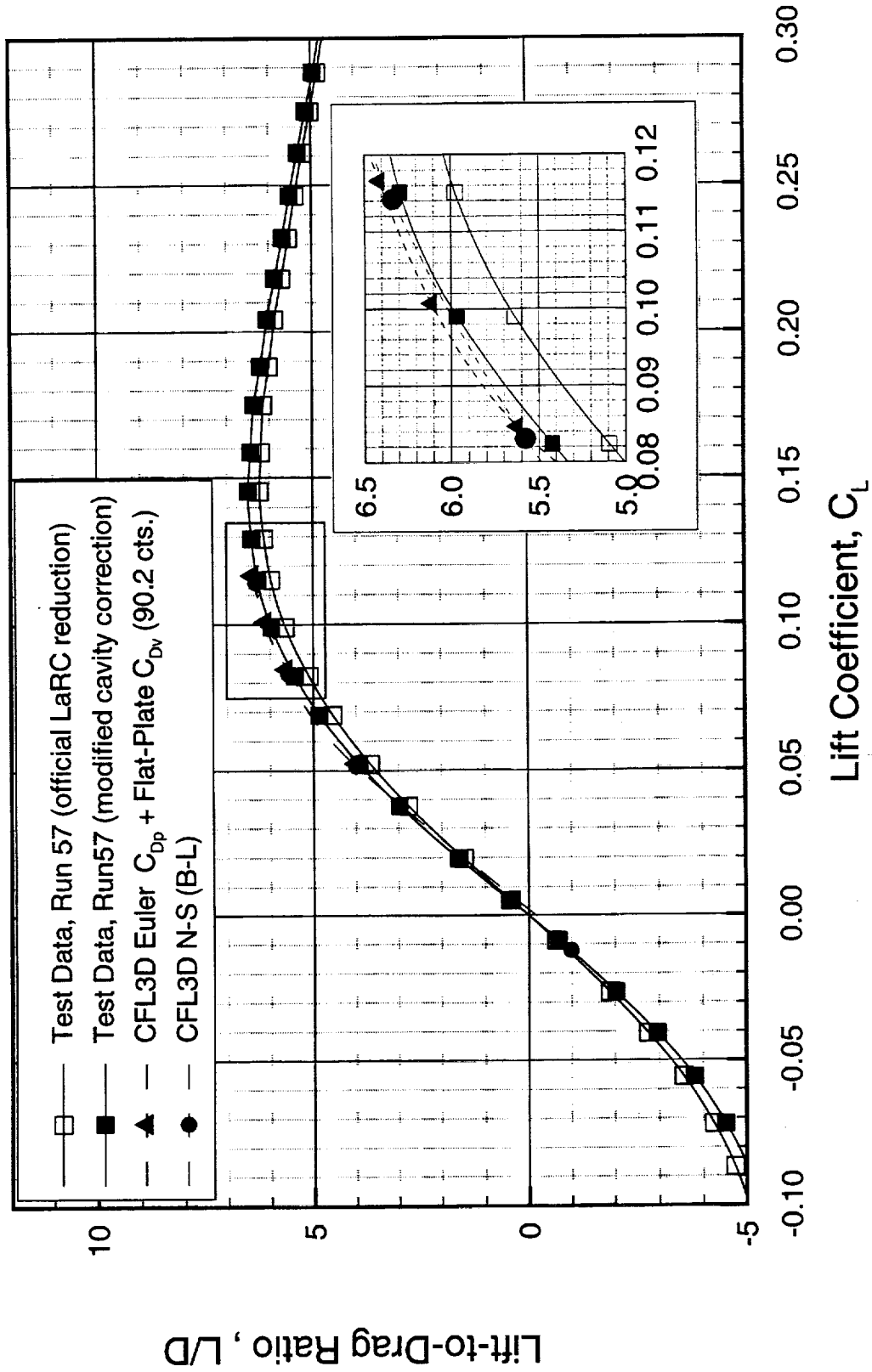


Comparison of Predicted and Experimental L/D



High Speed Aerodynamics, Long Beach

1.5% TCA Controls Model, W/B/N/D/E Configuration (Flared Aftbody)
 LaRC Test 1677, UPWT, $M_\infty=2.4$, $Re=3 \times 10^6$ /ft, Trip Drag Not Removed



Comparison of Predicted and Measured Pitching Moments

The comparison between predicted and measured lift coefficient versus pitching moment slope for the full configuration is presented in the following figure. Pitch stability is predicted very well from the CFL3D Navier-Stokes calculations.

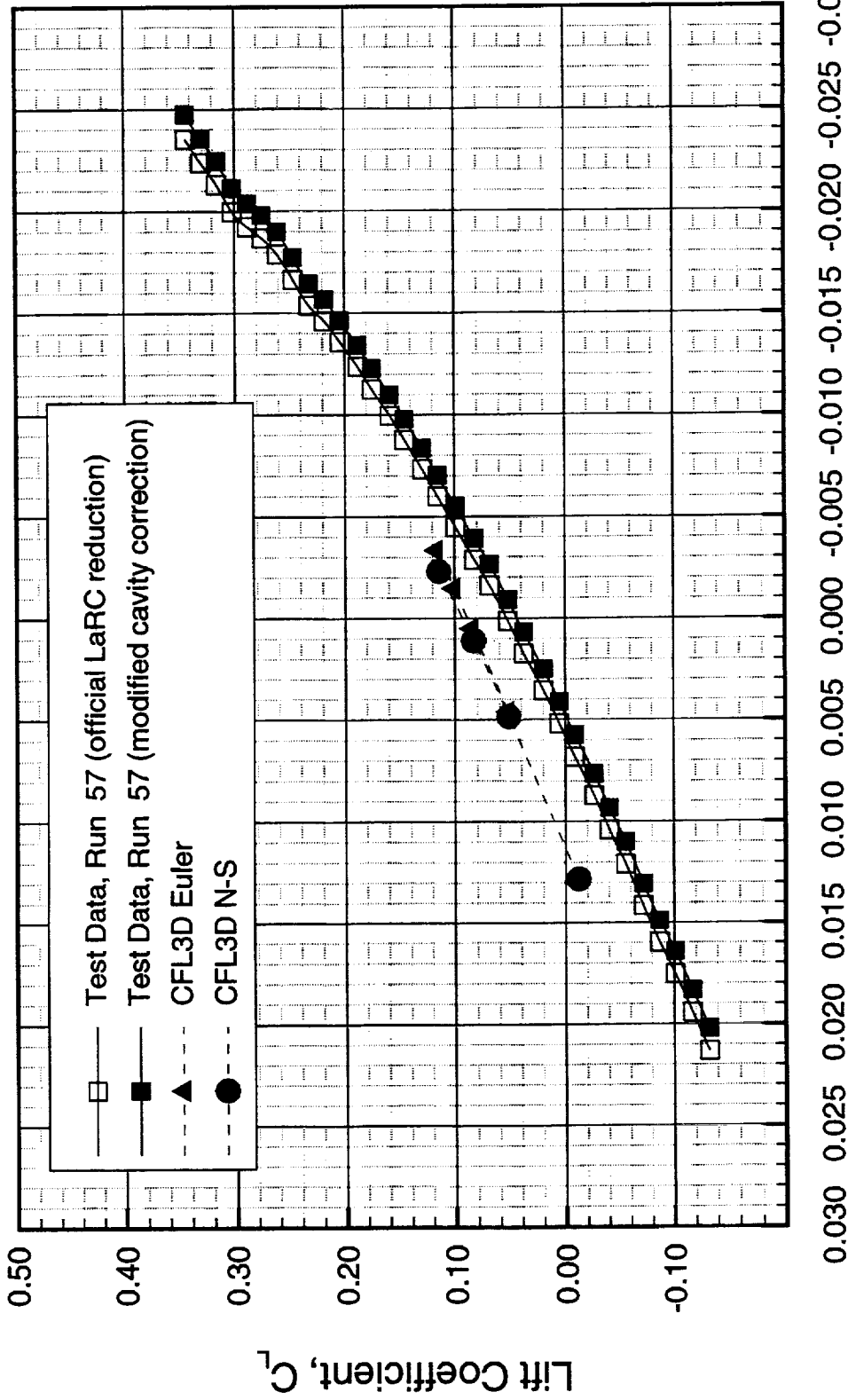
Comparison of Predicted and Measured Pitching Moments



High Speed Aerodynamics, Long Beach

1.5% TCA Controls Model, W/B/N/D/E Configuration (Flared Aftbody)

LaRC Test 1677, UPWT, $M_\infty = 2.4$, $Re = 3 \times 10^6 / ft$



Pitching Moment, C_M



This page is intentionally left blank.

Supersonic Results



High Speed Aerodynamics, Long Beach

1.5% TCA Model 20 controls model (flared aftbody)

$$M_{\infty}=2.4, Re=3 \times 10^6/\text{ft}$$

Sideslip solutions (α 's 0° & 4°)

Comparison of Predicted and Measured Rolling Moments ($\alpha=0^\circ$)

The predicted and measured rolling moments for the W/B/N/D/E with flared aftbody are compared below. The CFL3D N-S predicted rolling moment, C_l , exhibits some of the same non-linear characteristics with sideslip angle seen in the test data. The lateral stability derivative, $C_{l\beta}$, is predicted very well. The offset in the test data at $\beta=0$ is usually attributed to tunnel flow angularity or model asymmetry.

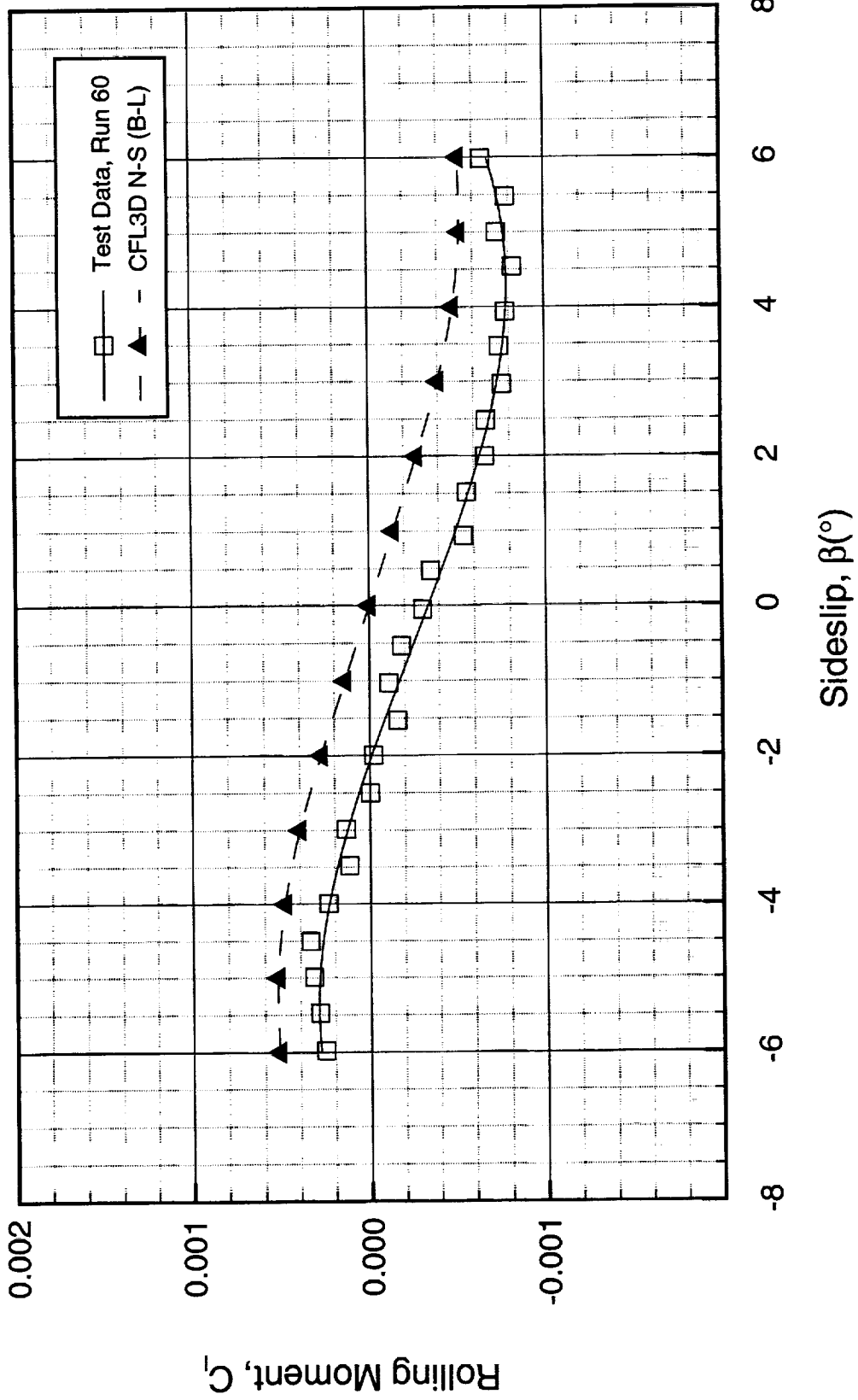
Comparison of Predicted and Measured Rolling Moments



High Speed Aerodynamics, Long Beach

1.5% TCA Controls Model, W/B/N/D/E Configuration

LaRC Test 1677 and CFL3D N-S (B-L), $M_\infty=2.4$, $\alpha=0.0^\circ$, $Re=3.0 \times 10^6/\text{ft}$



Comparison of Predicted and Measured Yawing Moments ($\alpha=0^\circ$)

The CFL3D N-S predicted C_n and the test data show good correlation in terms of magnitude and trend, although the predicted directional stability derivative, $C_{n\beta}$, is slightly less than the test data indicates.

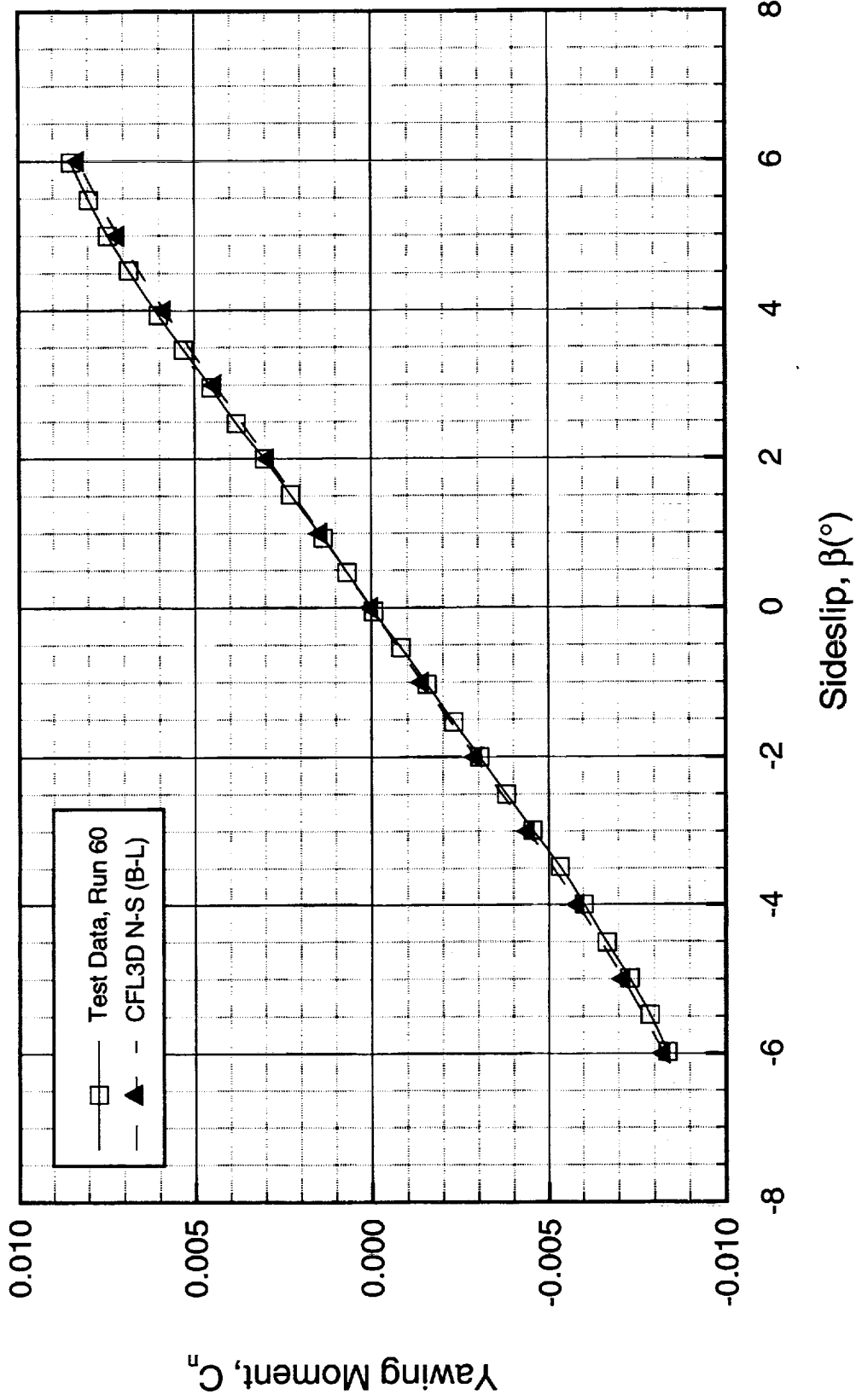
Comparison of Predicted and Measured Yawing Moments



High Speed Aerodynamics, Long Beach

1.5% TCA Controls Model, W/B/N/D/E Configuration

LaRC Test 1677 and CFL3D N-S (B-L), $M_\infty=2.4$, $\alpha=0^\circ$, $Re=3.0 \times 10^6$ /ft



Comparison of Predicted and Measured Side Force ($\alpha=0^\circ$)

The CFL3D N-S predicted C_Y has the correct trend, but the stability derivative, $C_{Y\beta}$, is significantly under-predicted. This discrepancy is currently being investigated.

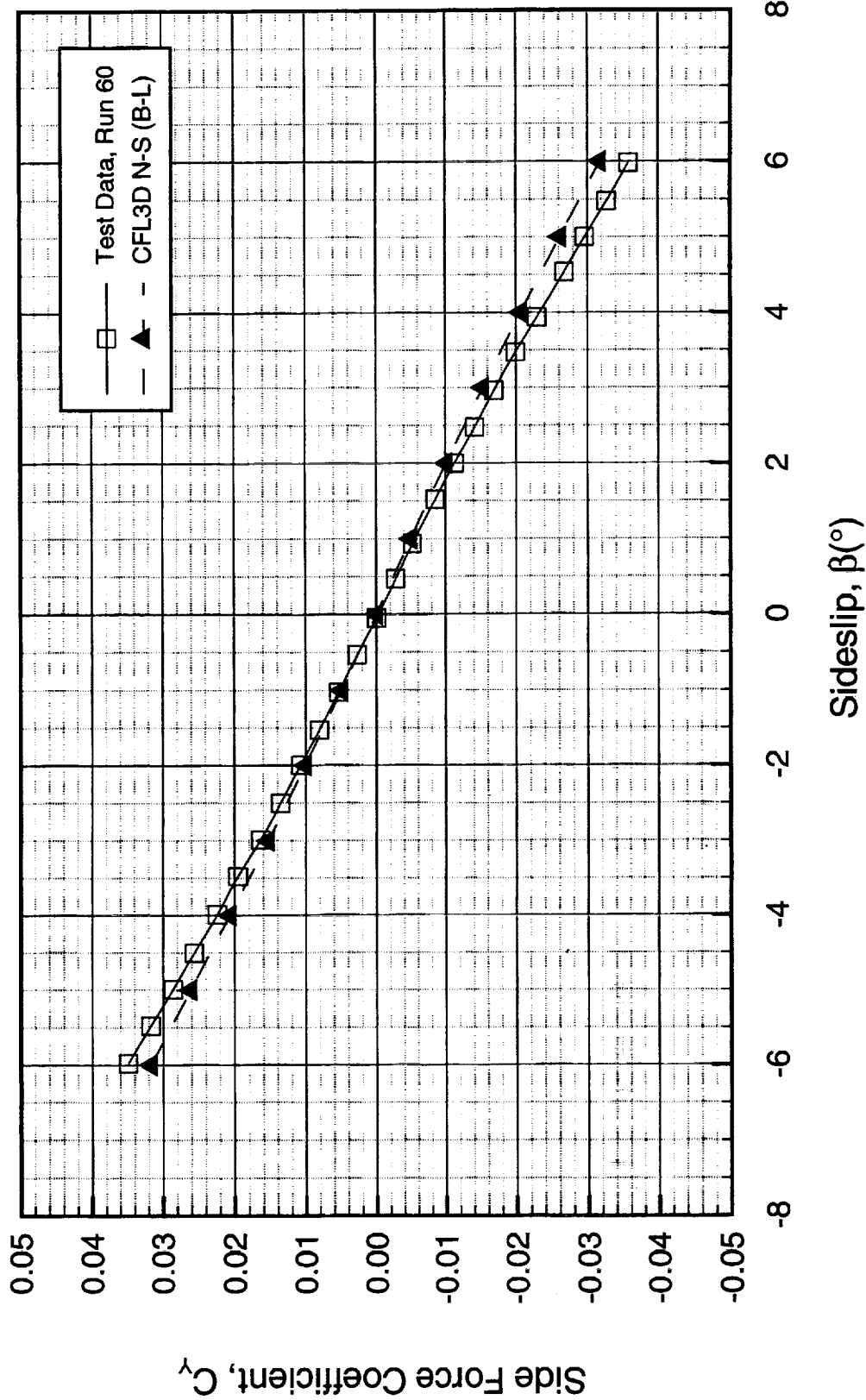
Comparison of Predicted and Measured Side Forces



High Speed Aerodynamics, Long Beach

1.5% TCA Controls Model, W/B/N/D/E Configuration

LaRC Test 1677 and CFL3D N-S (B-L), $M_\infty=2.4$, $\alpha=0.0^\circ$, $Re=3.0 \times 10^6$ /ft



Comparison of Predicted and Measured Lateral-Directional Characteristics

The next several figures show the β -sweep results for $\alpha=4^\circ$. Overall, the comparison with test data is similar to that discussed previously at $\alpha=0^\circ$. However, the predicted directional stability is under-predicted more than at $\alpha=0^\circ$.

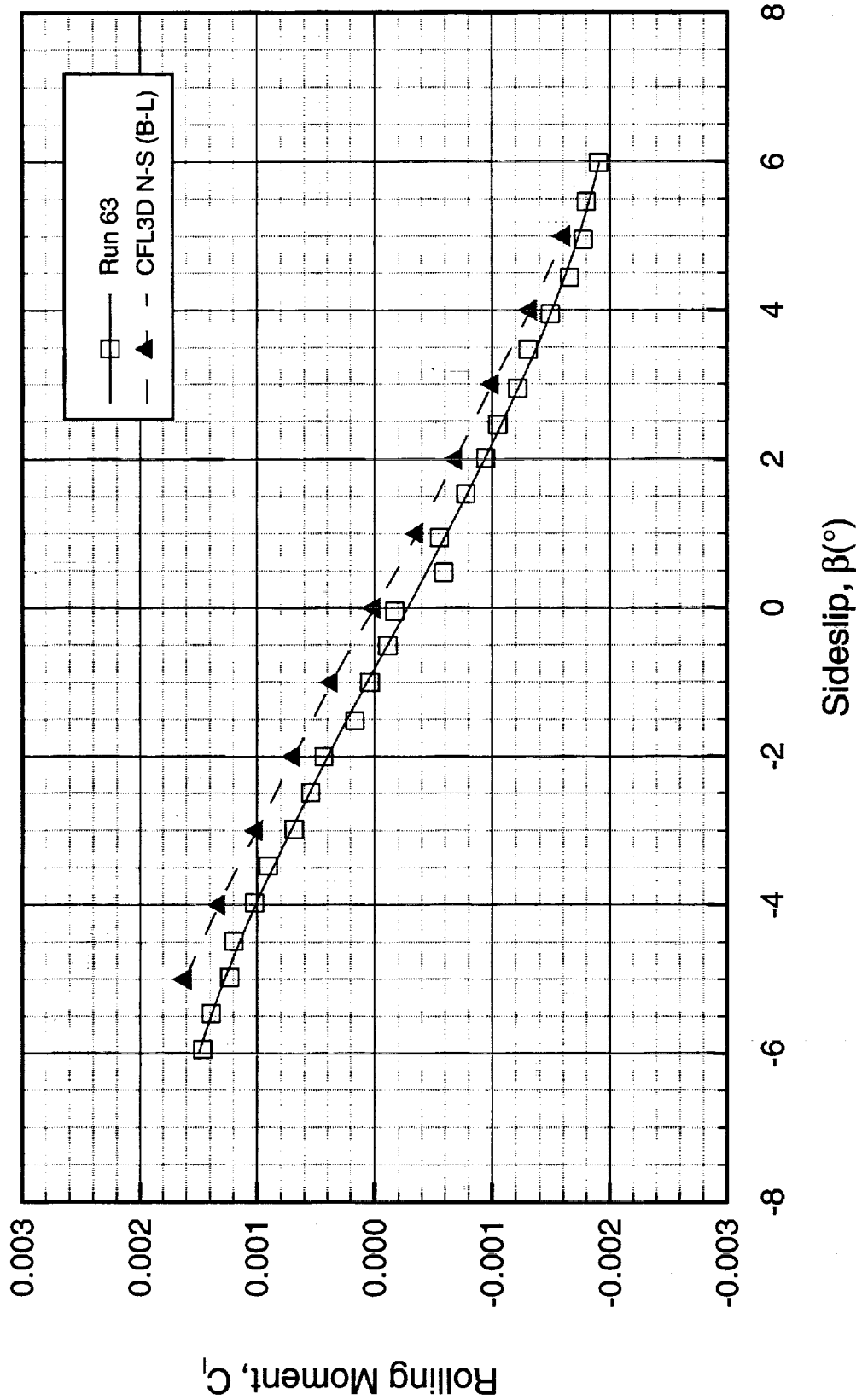
Comparison of Predicted and Measured Rolling Moments



High Speed Aerodynamics, Long Beach

1.5% TCA Controls Model, W/B/N/D/E Configuration

LaRC Test 1677 and CFL3D N-S (B-L), $M_\infty=2.4$, $\alpha=4.0^\circ$, $Re=3.0 \times 10^6/\text{ft}$



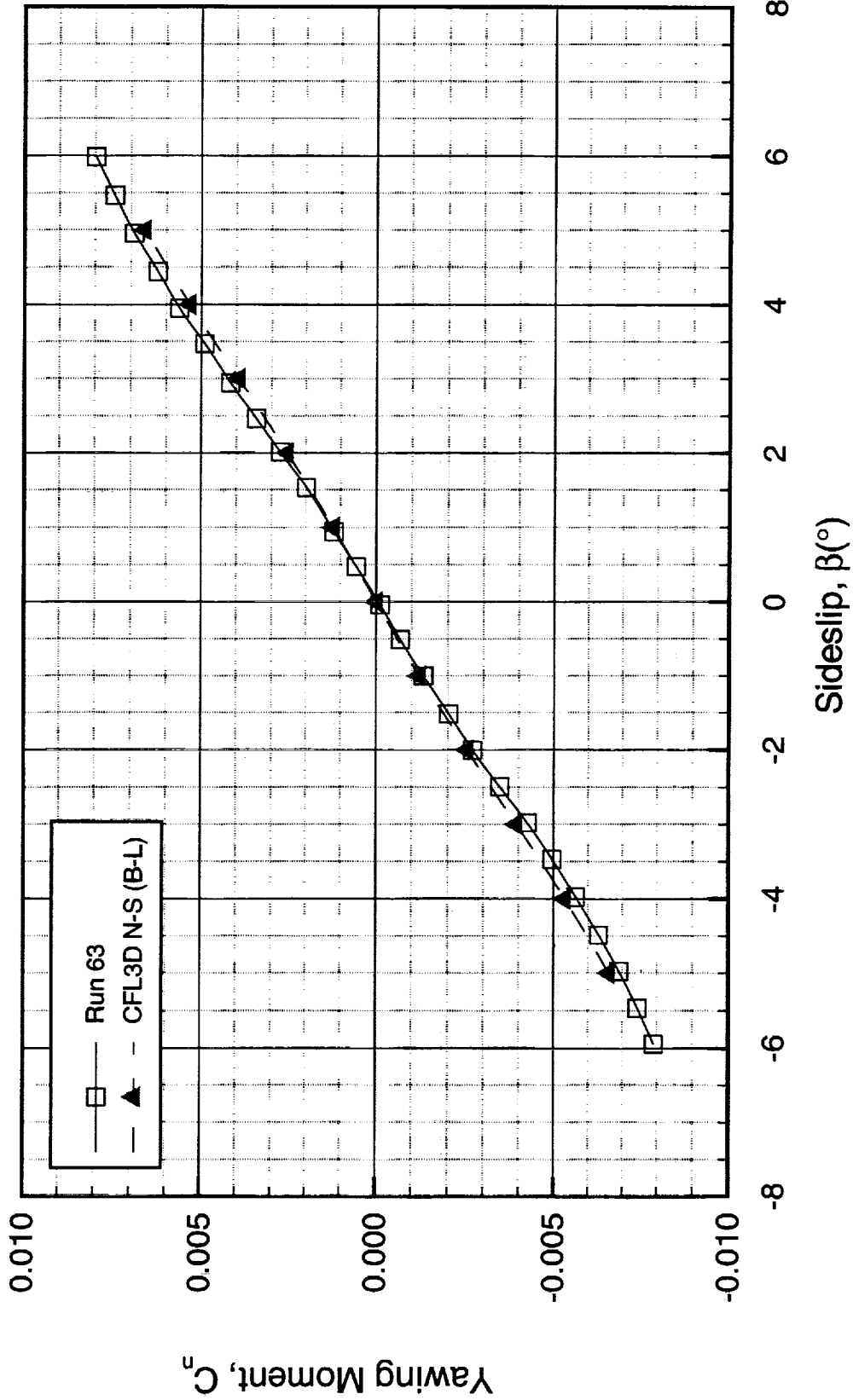
Comparison of Predicted and Measured Yawing Moments



High Speed Aerodynamics, Long Beach

1.5% TCA Controls Model, W/B/N/D/E Configuration

LaRC Test 1677 and CFL3D N-S (B-L), $M_\infty=2.4$, $\alpha=4^\circ$, $Re=3.0 \times 10^6/ft$



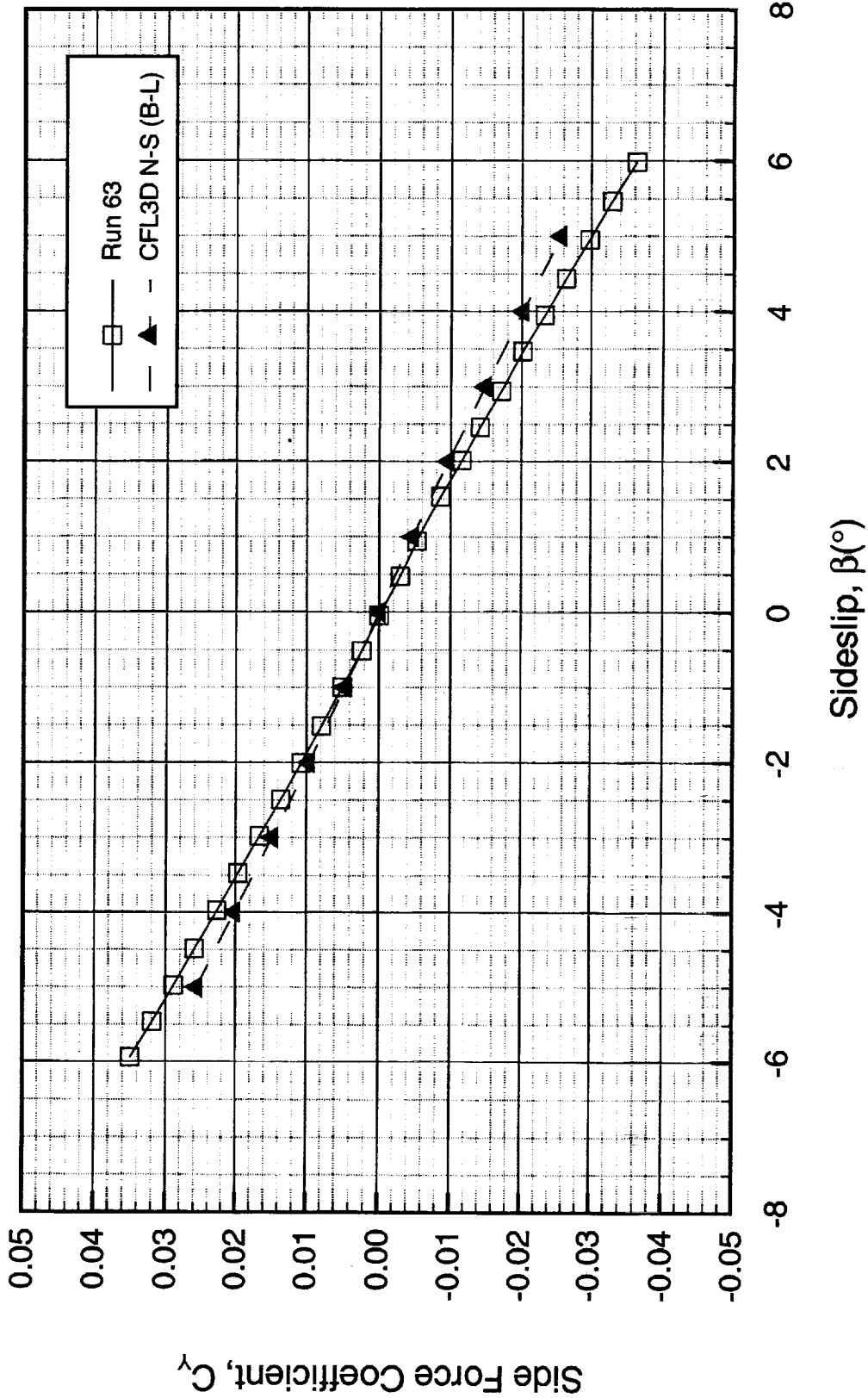
Comparison of Predicted and Measured Side Forces



High Speed Aerodynamics, Long Beach

1.5% TCA Controls Model, W/B/N/D/E Configuration

LaRC Test 1677 and CFL3D N-S (B-L), $M_\infty=2.4$, $\alpha=4.0^\circ$, $Re=3.0 \times 10^6/ft$



Upper Surface Pressures (W/B/N/D/E)

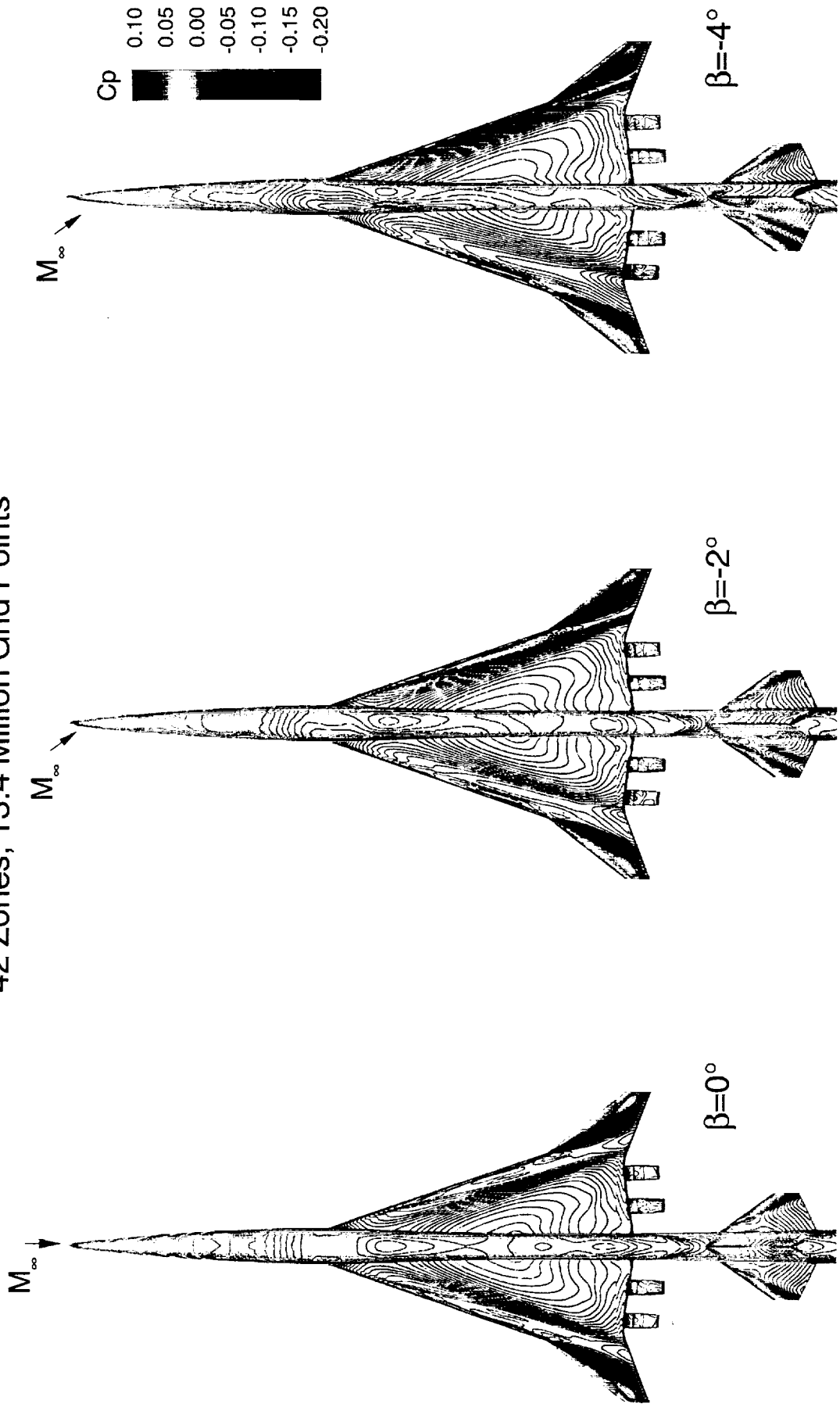
Upper surface pressure contours, as predicted by CFL3D Navier-Stokes, are shown below at $\alpha=4^\circ$ and $\beta=0^\circ$, -2° , and -4° . The asymmetric pressures are evident for the non-zero- β solutions. There is a compression on the port (left) side of the horizontal tail at $\beta=-2^\circ$ which increases in strength with β .

Upper Surface Pressures on the 1.5% TCA Modular Controls Model



High Speed Aerodynamics, Long Beach

CFL3D N-S (B-L), $M_\infty=2.4$, $\alpha=4.0^\circ$, $Re=3 \times 10^6$ /ft
42 Zones, 13.4 Million Grid Points



Upper Surface Streamlines (W/B/N/D/E)

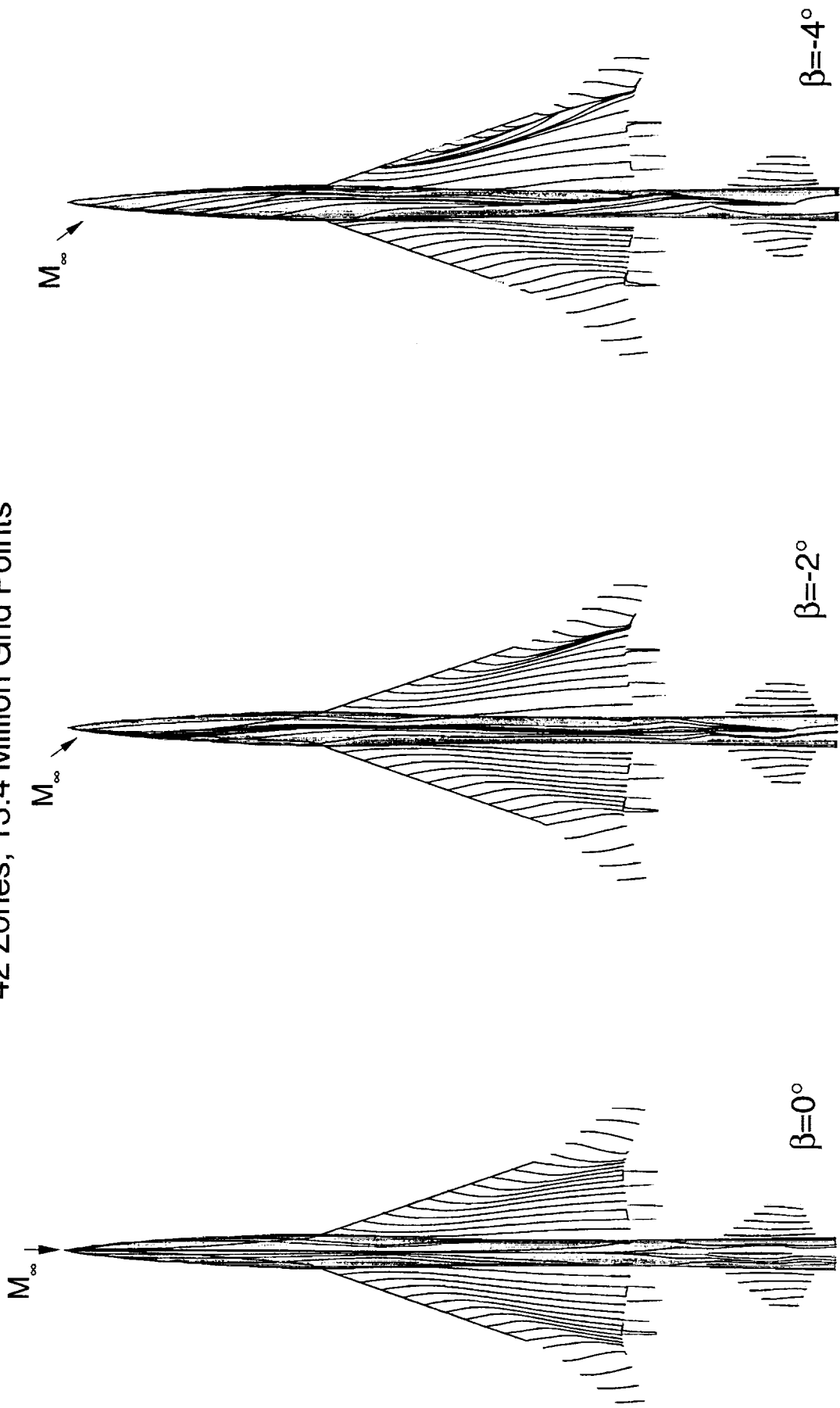
The asymmetric surface streamlines are evident for the non-zero- β solutions for the upper surface. The upper surface streamlines for $\beta = -4^\circ$ show evidence of separation on the starboard (right) wing.

Upper Surface Streamlines on the 1.5% TCA Modular Controls Model



High Speed Aerodynamics, Long Beach

CFL3D N-S (B-L), $M_\infty=2.4$, $\alpha=4.0^\circ$, $Re=3 \times 10^6$ /ft
42 Zones, 13.4 Million Grid Points



Lower Surface Pressures (W/B/N/D/E)

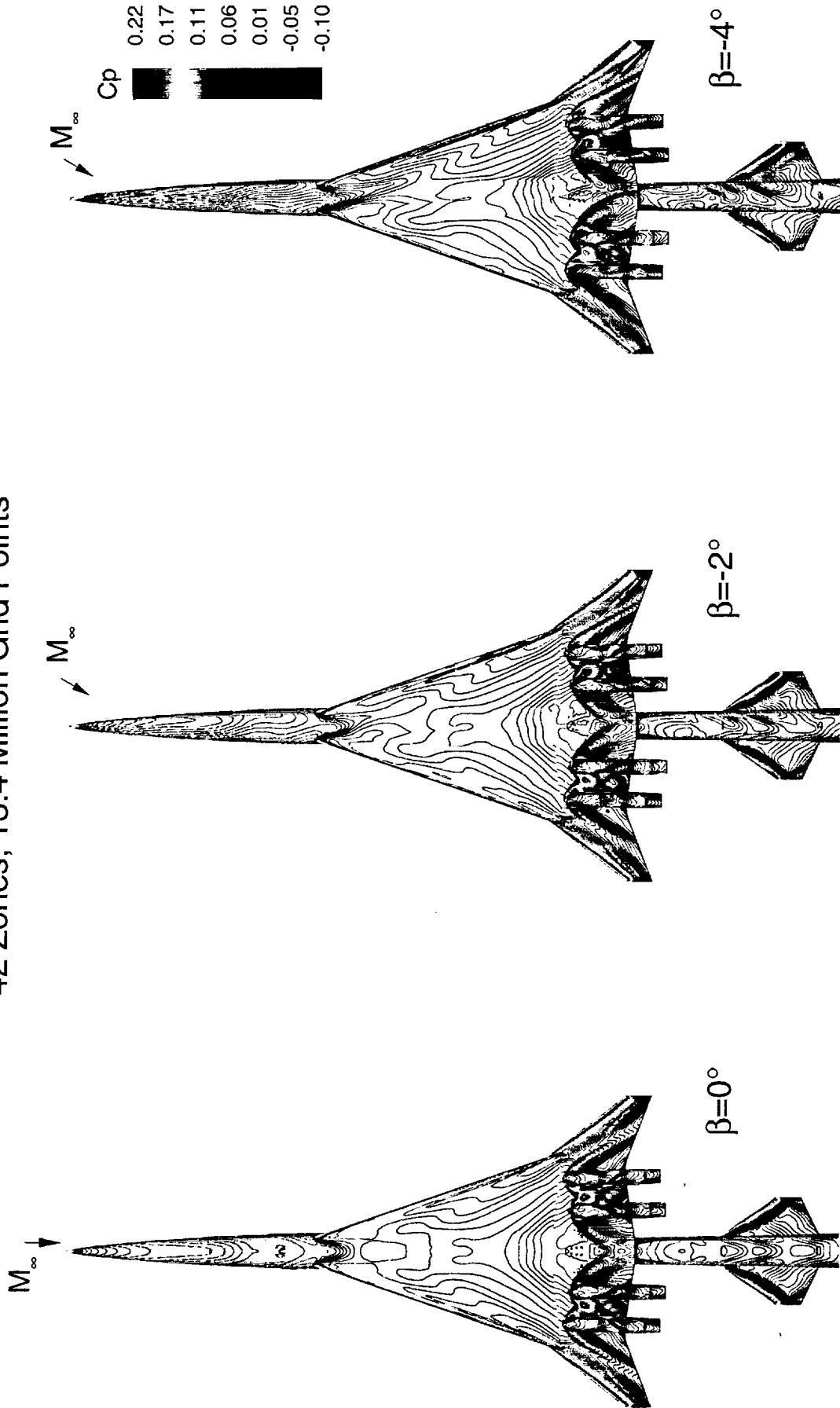
Lower surface pressure contours, as predicted by CFL3D Navier-Stokes, are shown below at $\alpha=4^\circ$ and $\beta=0^\circ$, -2° , and -4° . The asymmetric pressures are evident for the non-zero- β solutions. The lower surface pressures show the complex shock interaction in the nacelle region. The strength of the shocks on the outboard side of both port (left) nacelles increases with increasing β .

Lower Surface Pressures on the 1.5% TCA Modular Controls Model



High Speed Aerodynamics, Long Beach

CFL3D N-S (B-L), $M_\infty=2.4$, $\alpha=4.0^\circ$, $Re=3 \times 10^6$ /ft
 42 Zones, 13.4 Million Grid Points



Lower Surface Streamlines (W/B/N/D/E)

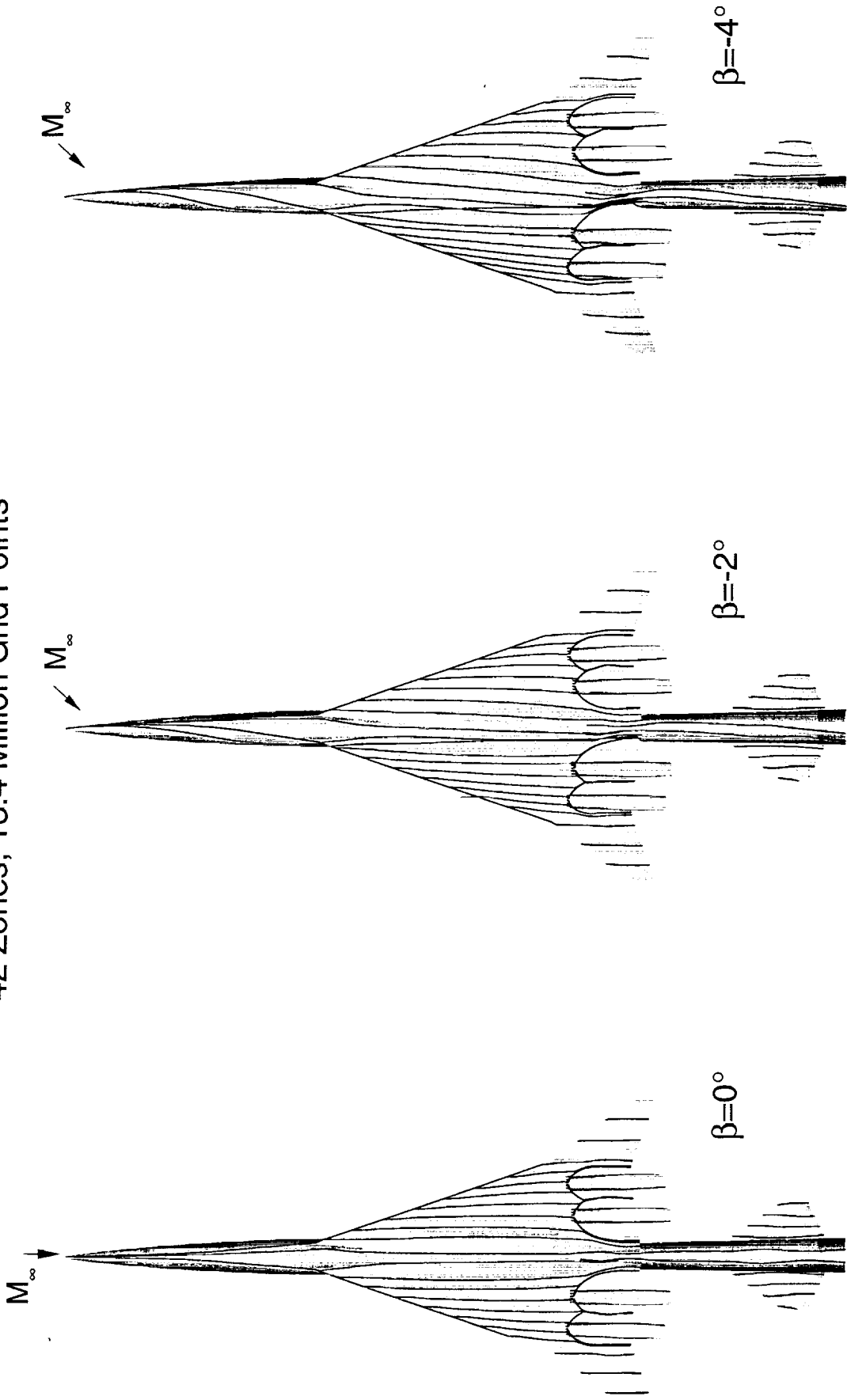
The spanwise flow over the lower surface is evident in the figure below.

Lower Surface Streamlines on the 1.5% TCA Modular Controls Model



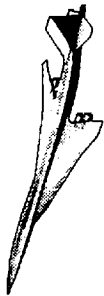
High Speed Aerodynamics, Long Beach

CFL3D N-S (B-L), $M_\infty=2.4$, $\alpha=4.0^\circ$, $Re=3 \times 10^6/\text{ft}$
42 Zones, 13.4 Million Grid Points



This page is intentionally left blank.

Transonic Results



High Speed Aerodynamics, Long Beach

1.5% TCA Model 20 controls model (flared aftbody)

$M_\infty=0.9$, $Re=4 \times 10^6/\text{ft}$

1.5% TCA Model 20 (W/B/N/D/E), $M_\infty=0.9$

The 1.5% TCA Model 20 W/B/N/D/E transonic grid at the symmetry plane is shown below. The transonic Euler grid was created by taking the existing supersonic grid, shown in red below, and adding a transonic “cap” to the original supersonic grid. The addition of the transonic “cap” added 17% more grid pts. to the existing supersonic grid.

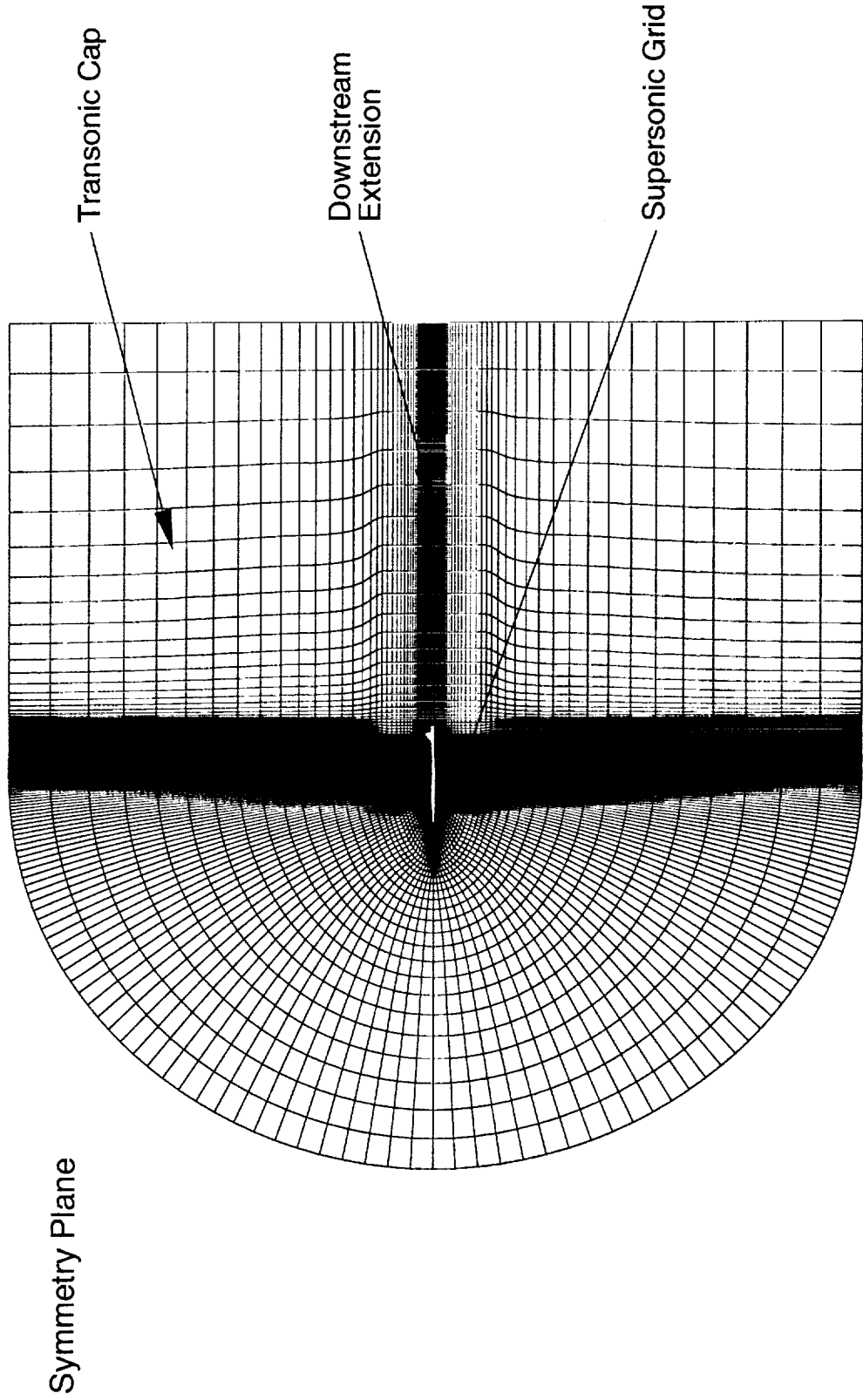


1.5% TCA Modular Controls Model

High Speed Aerodynamics, Long Beach

W/B/N/D/E Configuration (Flared Aftbody)

23 Zones, 4.2 Million Grid Points for Transonic Euler Computations



Comparison of Predicted and Measured Lift Curves

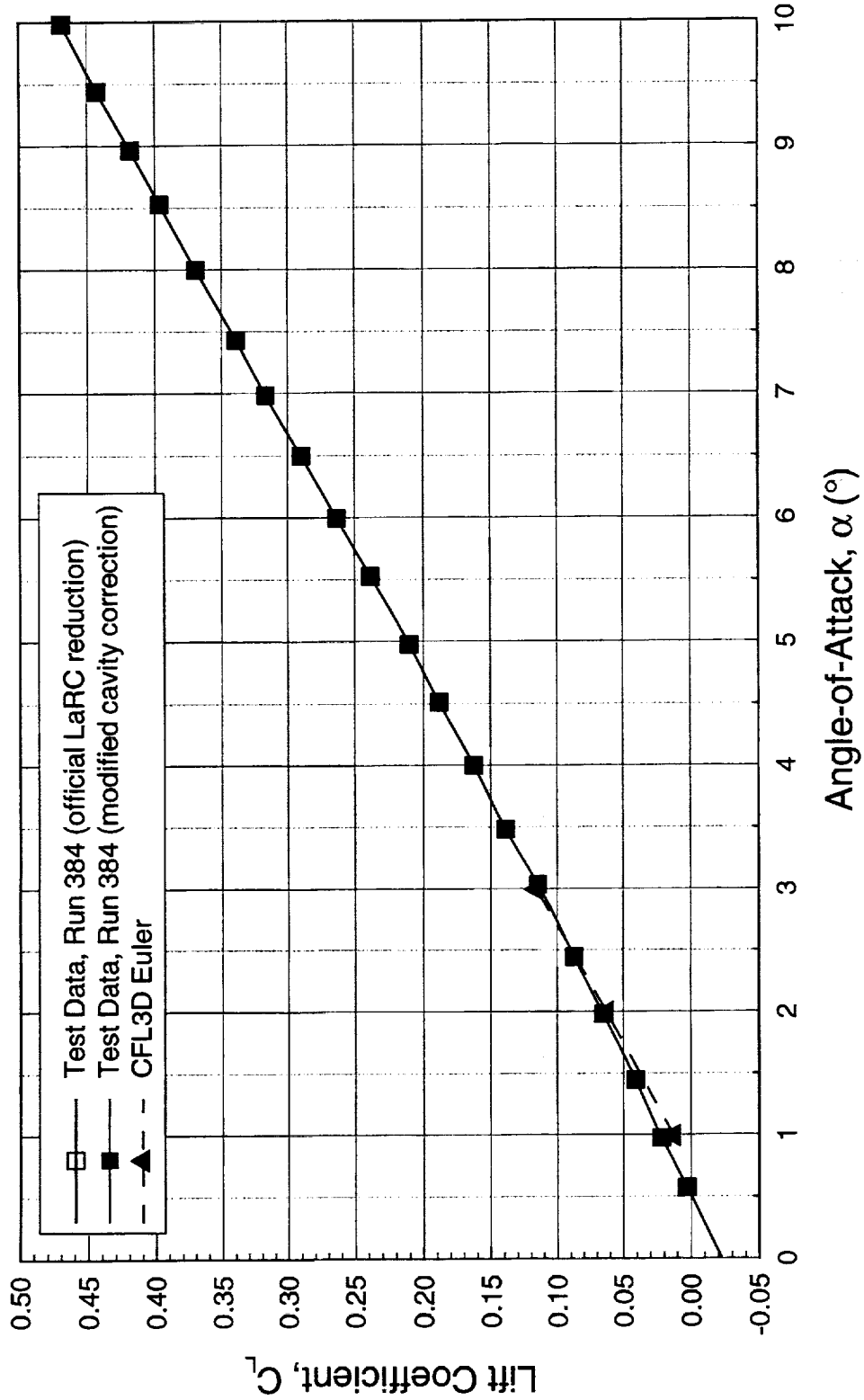
Force predictions are compared with the test data in the next several figures for Model 20 W/B/N/D/E configuration at $M_\infty=0.9$ and $Re=4 \times 10^6/ft$. CFL3D Euler over-estimates the lift curve slightly relative to the test data, as seen in numerous other cases in the past.

Comparison of Predicted and Measured Lift Curves

High Speed Aerodynamics, Long Beach

1.5% TCA Modular Controls Model, W/B/N/D/E Configuration (Flared Aftbody)

LaRC Test 488, 16' TT, $M_\infty = 0.9$, $Re = 4.0 \times 10^6$ /ft



Comparison of Predicted and Measured Drag Polars

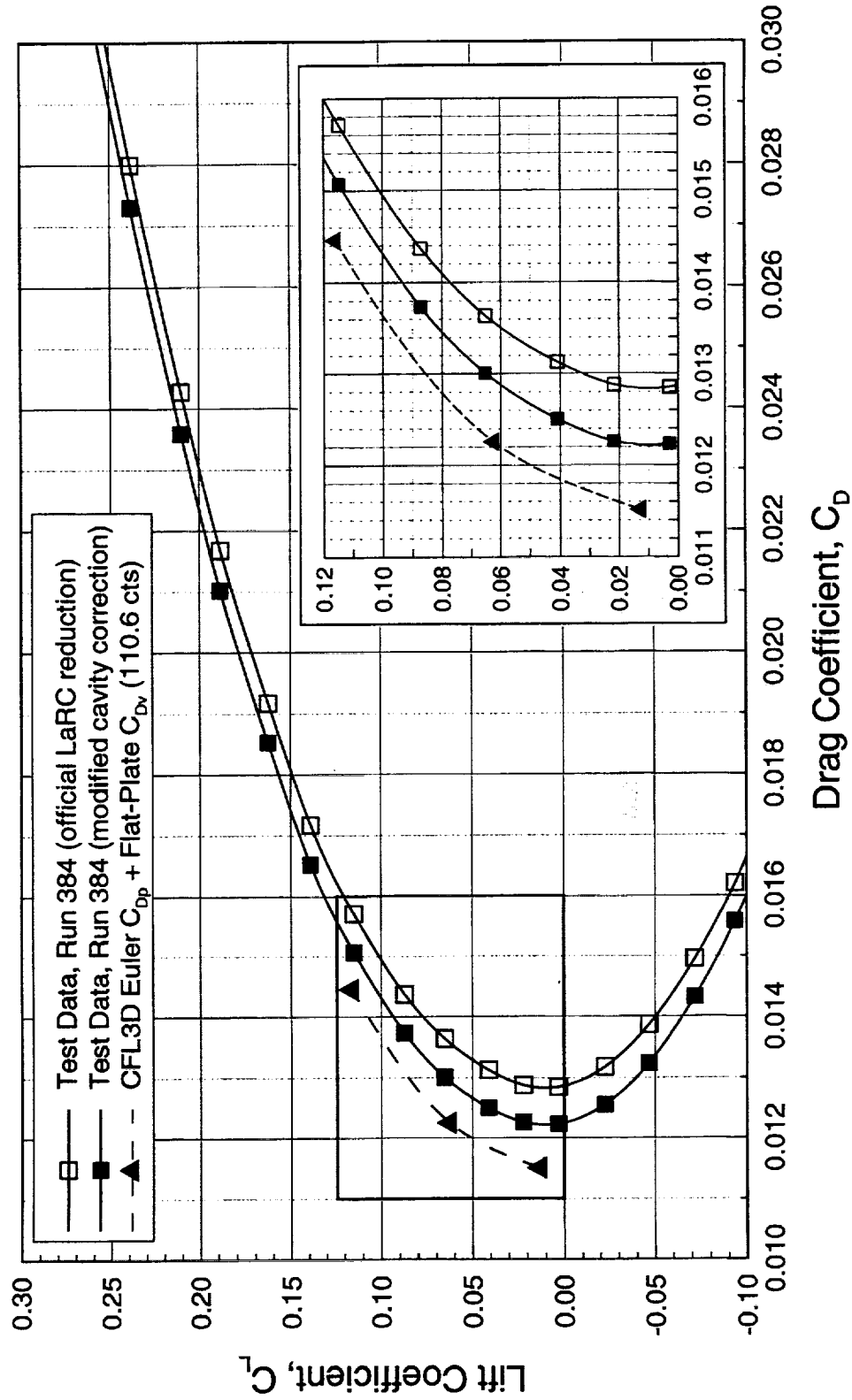
The Euler plus flat plate C_{Dv} (≈ 110.6 cts.) predictions under-estimate the drag value (with modified cavity correction) by ~ 7 cts at $C_L = 0.10$. The cruise C_L for $M_\infty = 0.9$ is 0.18. Since a trip drag study was not conducted during this test, a correction for the trip drag has not been applied to the test data.

Comparison of Predicted and Measured Drag Polars



High Speed Aerodynamics, Long Beach

1.5% TCA Modular Controls Model, W/B/N/D/E Configuration (Flared Aftbody)
 LaRC Test 488, 16' TT, $M_\infty = 0.9$, $Re = 4.0 \times 10^6$ /ft, Trip Drag Not Removed



Comparison of Predicted and Measured Pitching Moments

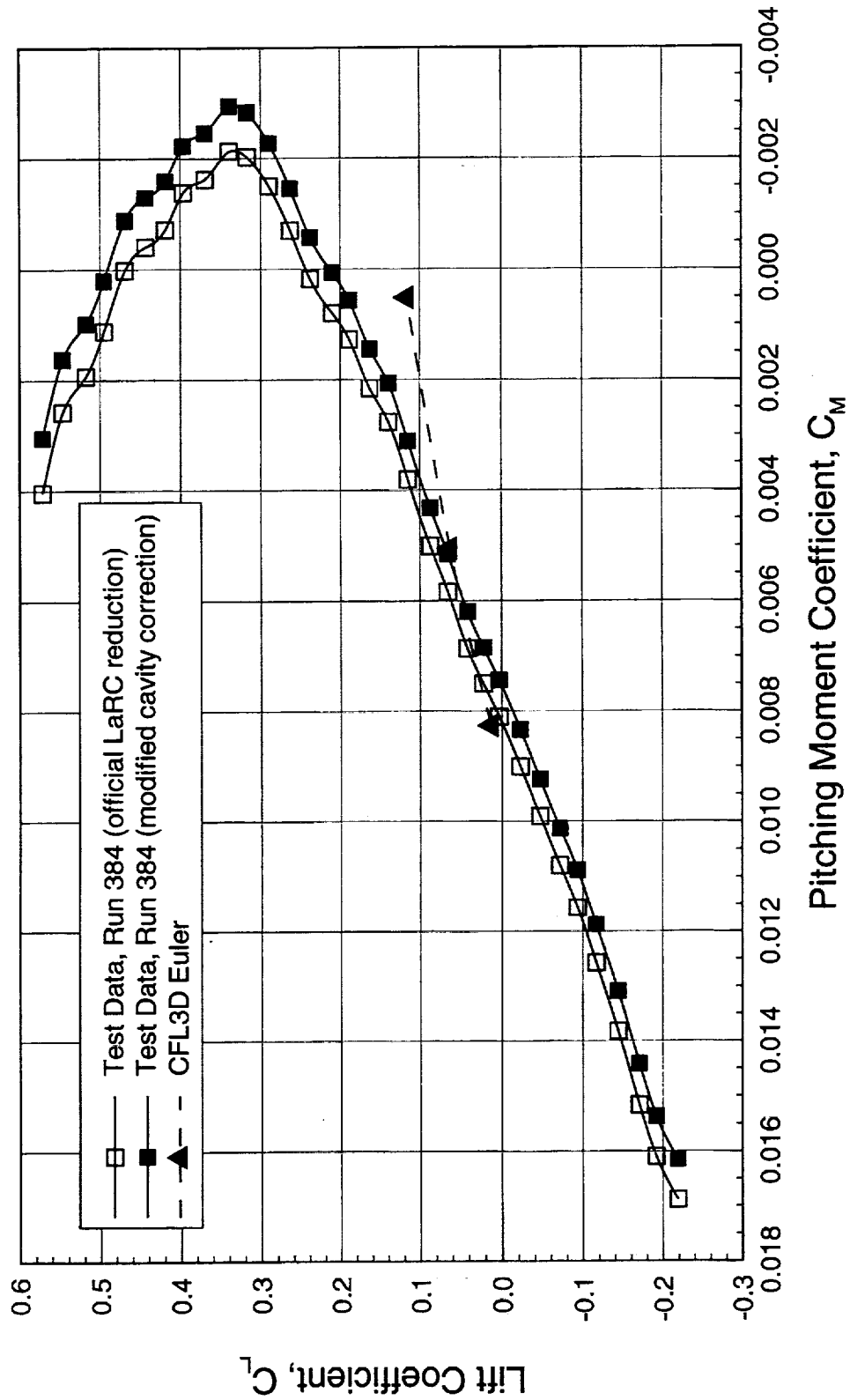
The CFL3D Euler prediction for the W/B/N/D/E pitching moment is shown below. The W/B/N/D/E moment curve shows a stable configuration up to C_L 's of 0.3. The Euler predictions indicate more longitudinal stability than the test data.

Comparison of Predicted and Measured Pitching Moments

High Speed Aerodynamics, Long Beach

1.5% TCA Modular Controls Model, W/B/N/D/E Configuration (Flared Aftbody)

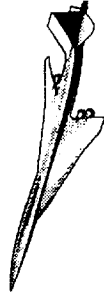
LaRC Test 488, 16' TT, $M_\infty = 0.9$, $Re = 4.0 \times 10^6/ft$



Summary & Conclusions

Full configuration HSCCT solutions in sideslip were obtained using the nonlinear flow solver CFL3D. Overall, there was good agreement between the predicted CFL3D force and moments and the test data for the 1.5% TCA modular controls model at supersonic speeds. This agreement is extremely important in order to validate the analysis tools used for the complex configurations. Full configuration CFL3D Euler solutions were also demonstrated at transonic speeds. The current computer resources available appear to be sufficient to produce full configuration Euler and Navier-Stokes solutions.

Summary & Conclusions



High Speed Aerodynamics, Long Beach

- Performed full configuration Navier-Stokes sideslip solutions
- TCA (closed aftbody) results obtained on W/B, W/B/E, W/B/N/D, and W/B/N/D/E configurations
- Good agreement between CFD and wind-tunnel for full configuration 1.5% TCA modular controls model at supersonic speeds
- $M_{\infty}=0.9$ Navier-Stokes analysis underway
- Current computer resources available appear to be sufficient to produce full configuration Euler and Navier-Stokes solutions

This page is intentionally left blank.

Unstructured Grid Euler Method Assessment for Aerodynamic Performance Prediction of the Complete TCA Configuration at Supersonic Cruise Speed

Farhad Ghaffari

**Aero- & Gas- Dynamics Division
NASA Langley Research Center**

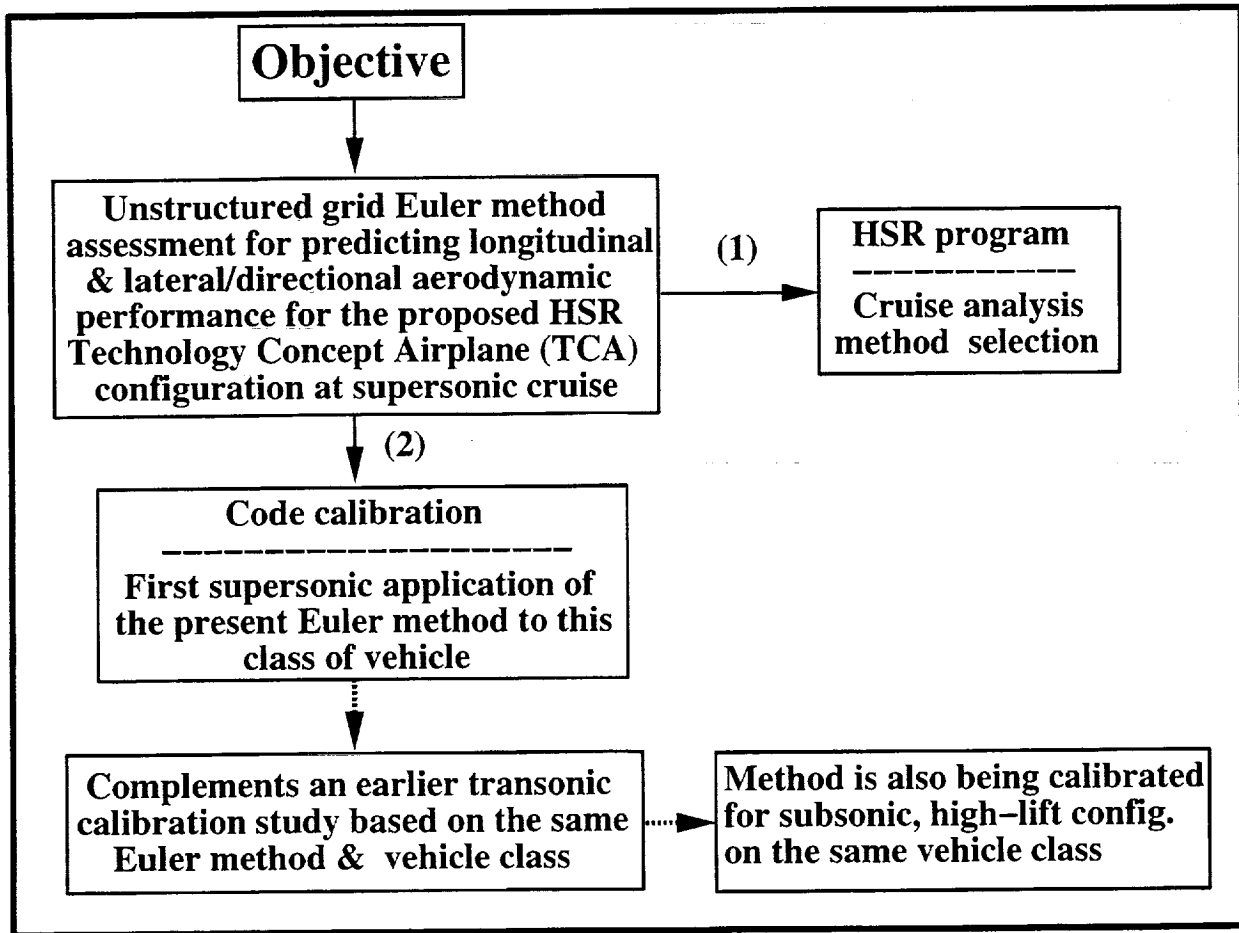
**High Speed Research Program
Biannual Airframe Technical Review
Los Angeles, February 9-13, 1998**

Unstructured grid Euler computations, performed at supersonic cruise speed, are presented for a proposed high speed civil transport configuration, designated as the Technology Concept Airplane (TCA) within the High Speed Research (HSR) Program. The numerical results are obtained for the complete TCA cruise configuration which includes the wing, fuselage, empennage, diverters, and flow through nacelles at Mach 2.4 for a range of angles-of-attack and sideslip. The computed surface and off-surface flow characteristics are analyzed and the pressure coefficient contours on the wing lower surface are shown to correlate reasonably well with the available pressure sensitive paint results, particularly, for the complex shock wave structures around the nacelles. The predicted longitudinal and lateral/directional performance characteristics are shown to correlate very well with the measured data across the examined range of angles-of-attack and sideslip. The results from the present effort have been documented into a NASA Controlled-Distribution report which is being presently reviewed for publication.

-- OUTLINE --

- **Objective**
- **Computational Approach & Attributes**
 - ➔ **Numerical Model Approach**
 - ➔ **Selected Computational Flow Matrix**
 - ➔ **Typical Computational Grid**
 - ➔ **Numerical Method & Typical Convergence**
- **Results & Discussion**
 - ➔ **Longitudinal Aerodynamic Analysis**
 - ➔ **Lateral/Directional Aerodynamic Analysis**
- **Concluding Remarks**
- **What's Next?**

This chart shows the outline of this presentation.



The primary objective of the present effort is to evaluate an unstructured grid Euler method for predicting the longitudinal and lateral/directional performance characteristics of the TCA configuration at the design supersonic cruise Mach number of 2.4. Due to the inviscid nature of the present analysis, the evaluation emphasis is placed on the method's ability to predict the aggregate forces and moments acting on the configuration accurately and not necessarily the detail flow physics. In spite of this fact, some representative samples of the predicted flow structures will be presented.

The results from this effort contribute to two activities; 1)– the HSR tools & methods development, where a variety of CFD technologies are being evaluated for their potential utilization in the early phase of the configuration design and aerodynamic analysis, and 2)– the code calibration. The latter code calibration effort at supersonic speed would complement the prior investigations where the aerodynamic prediction capabilities of the same methodology were evaluated at both transonic as well as subsonic speeds for this vehicle class.

Experimental Wind-Tunnel Model and Numerical Model for TCA

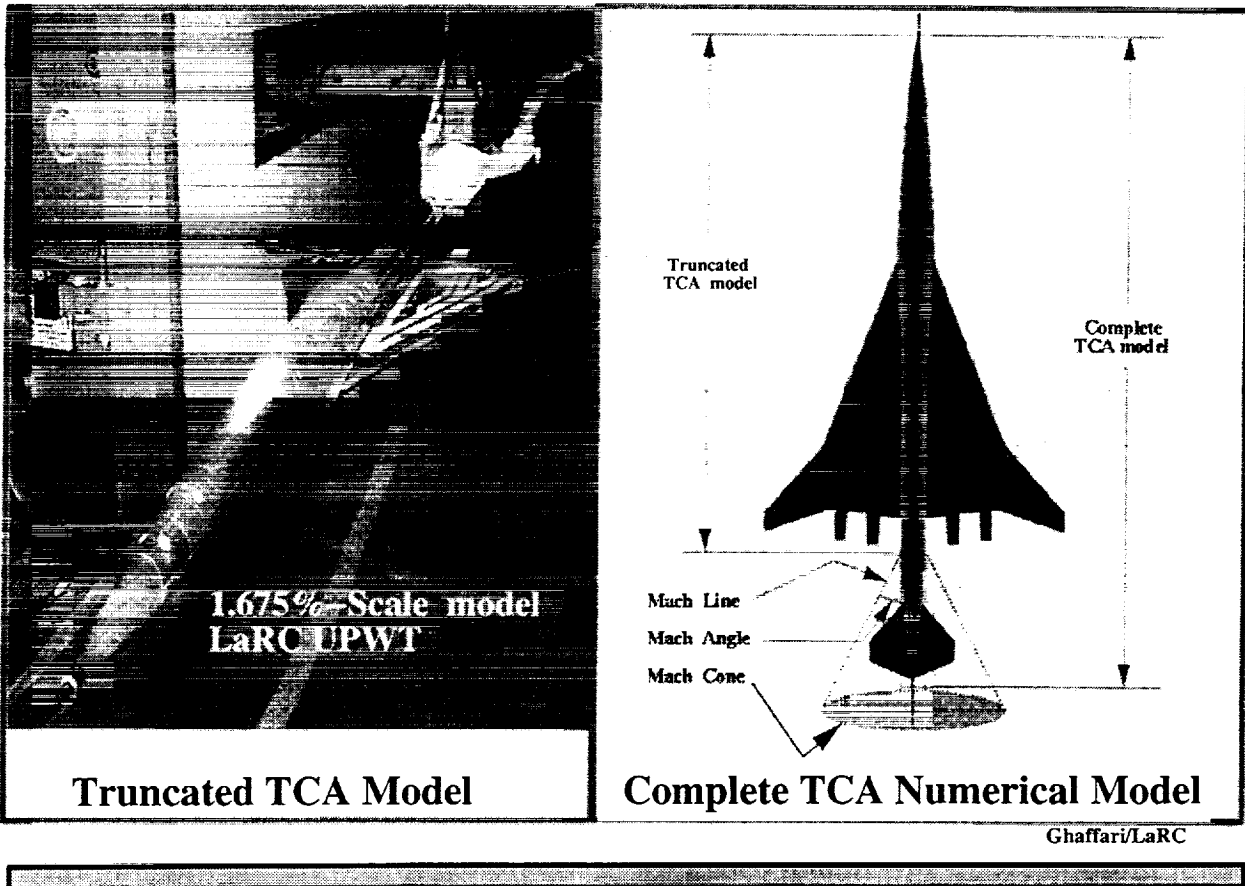
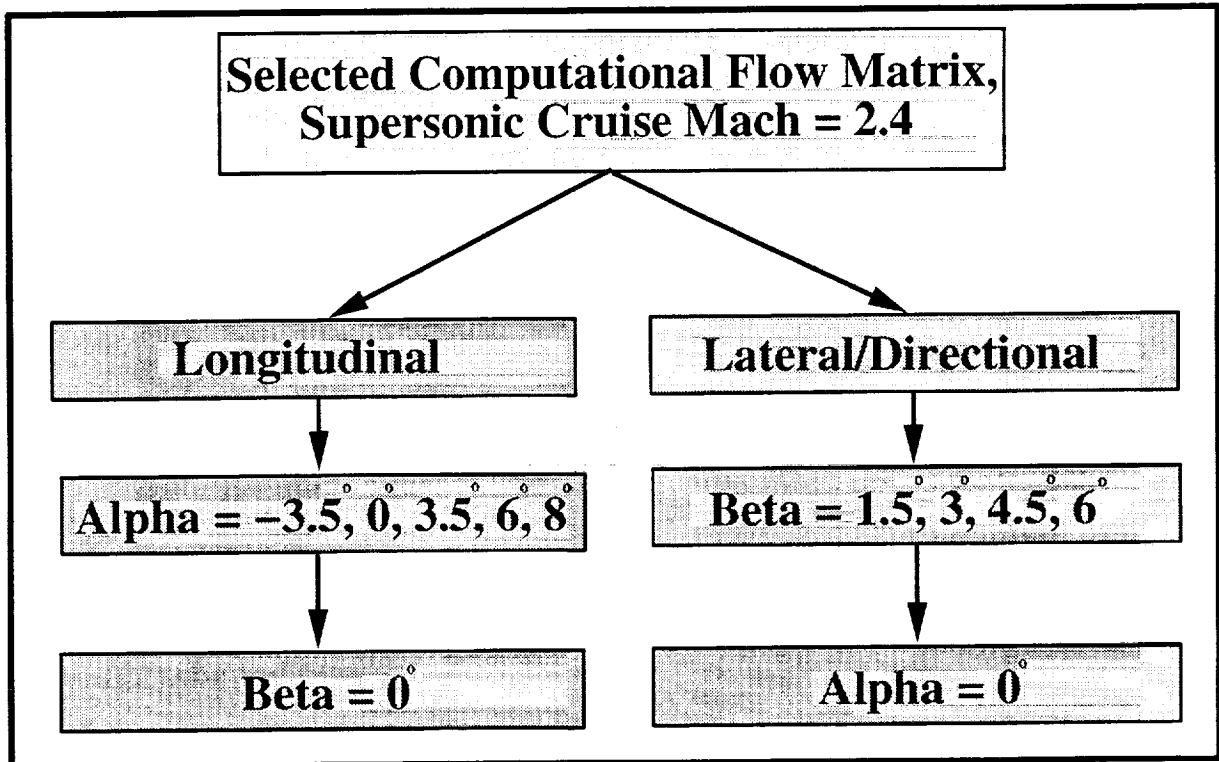


Figure on the left shows a photograph of the sting mounted "truncated TCA model" as installed in the NASA Langley Research Center (LaRC) Unitary Plan Wind Tunnel (UPWT). The truncated (aft-fuselage/empennage removed) TCA model, consisting of wing/fuselage/nacelle/diverter combinations, was primarily tested to obtain the aerodynamic performance data for supersonic cruise conditions. The figure on the right shows the present numerical model including the aft-fuselage/empennage components. Although, the experimental data have been obtained with the truncated TCA model, provision has been made for extracting complementary aerodynamic characteristics from the present numerical analysis of the complete TCA model. This provision is based on an assumption, derived from the fundamental supersonic aerodynamic principle, that simply states that any flow disturbance caused by a source in a supersonic medium does not propagate upstream beyond its Mach cone. Based on this principle, it is assumed in the present numerical approach that any flow disturbance caused by the presence of the empennage is confined to a Mach cone originated from the longitudinal station where the empennage is truncated from the wind tunnel model. The approximate shape of this Mach cone, having a semi-vertex angle of 24.6 degree (i.e., $\sin^{-1}(1/\text{Mach}) = \sin^{-1}(1/2.4) = 24.6$ degree), is schematically shown over the complete TCA numerical model planform in the above figure on the right hand-side.

There are two clear advantages associated with modeling the complete TCA configuration. The obvious advantage is the efficient utilization of the computer resources, i.e., one computational solution provides results for both the complete TCA model and the truncated TCA model. The second advantage is that the computational results for the complete TCA model provide valuable aerodynamic performance predictions for which no experimental data presently exist within the HSR program. Though not presented in this paper, the validity of the computational results for the truncated TCA model, extracted from the complete TCA numerical simulation, have been fully addressed through a set of separate numerical analysis representing the actual sting-mounted truncated TCA model. The latter analysis is included in the final NASA Controlled-Distribution form publication which is presently being reviewed.



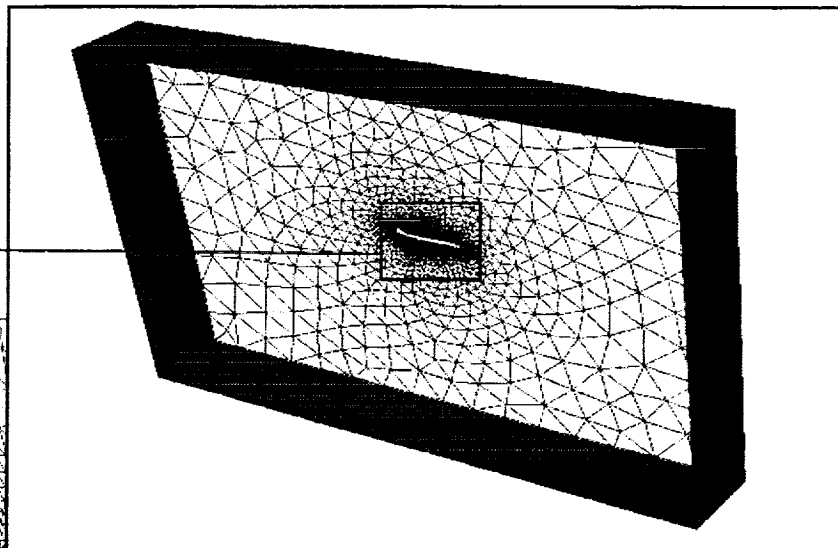
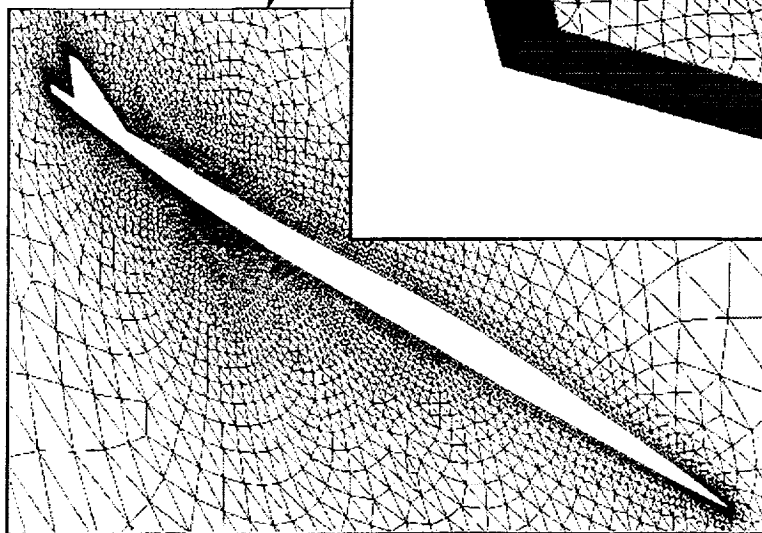
Preliminary analysis of the available experimental data from UPWT was conducted to identify the conditions for the present numerical investigation. This chart shows the selected computational matrix for the longitudinal (an alpha sweep at zero sideslip) and lateral/directional (a beta sweep at zero alpha) aerodynamic analysis at the design supersonic cruise Mach number of 2.4.

Computational Grid Domain for the Complete TCA

Grid sensitivity study led to:

of cells ~ 670,000

of faces ~ 1,400,000



Farfield boundaries:

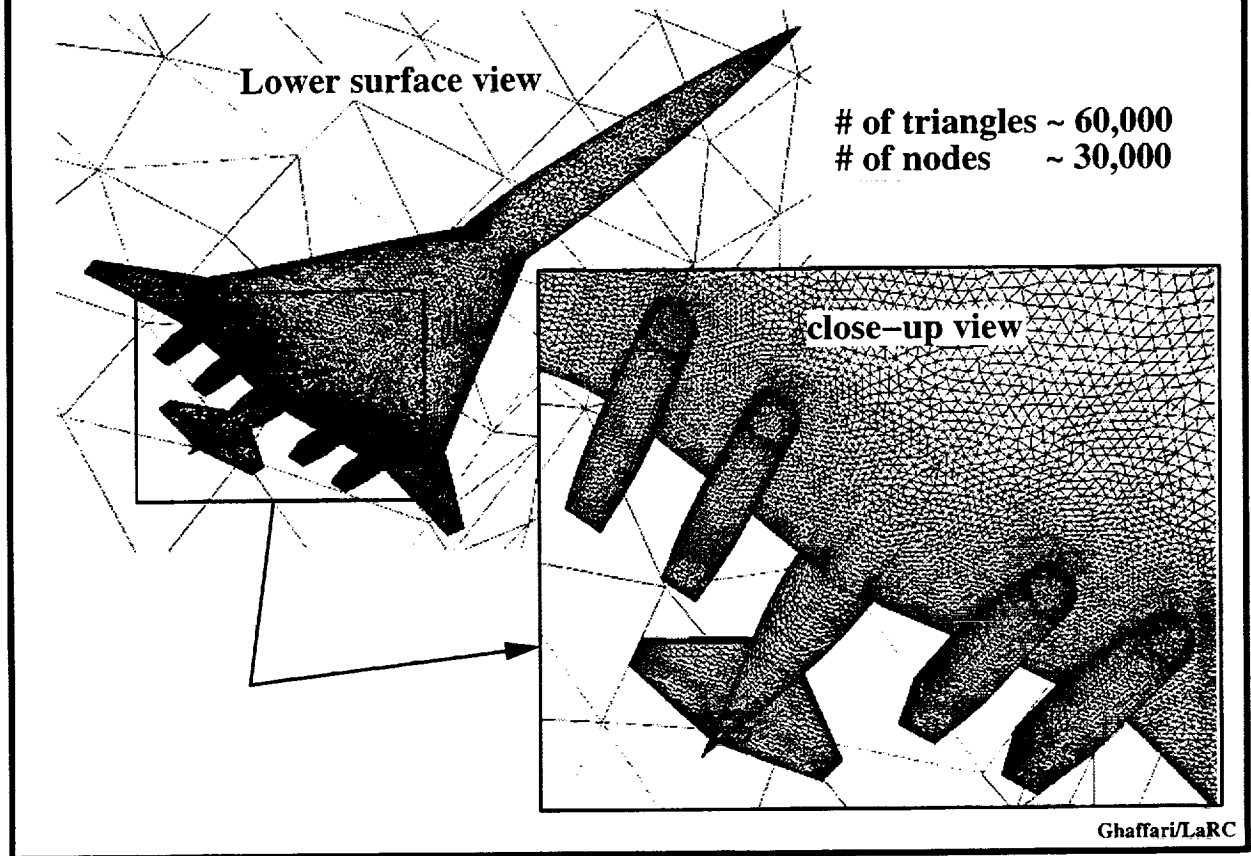
Upstream	~ $11 \bar{c}$
Downstream	~ $14 \bar{c}$
Radial-up/down	~ $9 \bar{c}$
Radial-side	~ $4 \bar{c}$

Ghaffari/LaRC

A grid sensitivity analysis was conducted to study the effect of grid resolution on solution convergence and the aerodynamic performance predictions. This analysis indicated that the baseline grid, consisting of about 670,000 cells, was sufficient to simulate the inviscid flow about the complete TCA configuration with the same degree of accuracy as the solutions obtained on a grid that was twice as fine (i.e., about 1.3 million cells). The degree of solution accuracy between the baseline and the fine grid was assessed for the surface and off-surface flow characteristics as well as the integrated forces and moments across the examined range of angle-of-attack (i.e., -3.5, 0, 3.5, 6, and 8 degree). Though not included in this paper, the complete results and analysis from this grid sensitivity study are included in a NASA Controlled-Distribution report which is currently being reviewed for publication.

The above figure shows the farfield boundary faces for the computational domain and the grids in the configuration plane-of-symmetry. The computational domain farfield boundary dimensions are also shown in the above figure as multiples of the wing mean aerodynamic chord (\bar{c}). It should be noted that this grid, and in particular the upstream farfield boundary extension, was defined in such a way that it could be used to compute the flow at both supersonic as well as transonic speeds.

Computational Surface Grid for the Complete TCA



This chart shows the lower surface view of the computational grid and a close-up view of the surface triangles around the nacelles. The baseline computational grid consisted of about 60,000 surface triangles to discretize one-half of the complete TCA numerical model. Complementary to the experimental test, the interior surfaces of the nacelles are modelled to simulate flow through propulsion effects.

Computational Methodologies

-- TetrUSS --

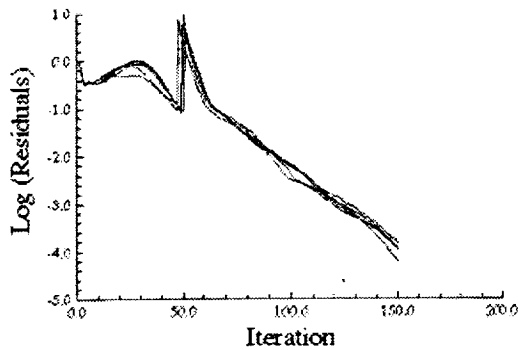
Developed at NASA Langley Research Center

- **GridTool**
 - CAD ---> Surface patch
 - NonUniform Rational B-Spline (NURBS)
- **VGRID**
 - Surface patch ---> Surface/volume-tetrahedral mesh
 - Advancing Front Technique
- **USM3D**
 - Upwind-biased, cell center, finite volume approach
 - Implicit time integration (Gauss-Siedel)
 - Convergence acceleration with local time stepping
 - Flux Difference Splitting approach (Roe's scheme)
- **VPLOT3D**
 - Solution postprocessing (Not used in this study)

This chart shows the salient features of the computational methodology, known as TetrUSS, which is being evaluated in the present analysis. TetrUSS package includes: GridTool, to discretize primarily the surface geometry; VGRID, to generate flow field grids; USM3D, to solve the flow; and VPLOT3D, to postprocess the solutions (not used in the present analysis).

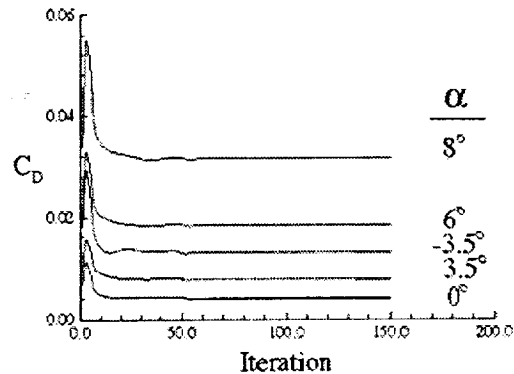
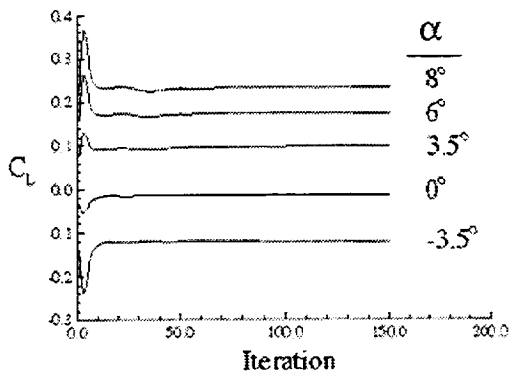
Convergence Characteristics and Typical Method Performance for Complete TCA

Supersonic cruise configuration; $\beta = 0^\circ$, $M_\infty = 2.4$



Typical solution attributes:

- Took about 1/2 hrs of Cray C-90
- Requires about 120MW of memory
- All solutions based on 2nd order FDS



This chart shows the solution convergence characteristics for the complete TCA configuration, using the baseline grid, across the examined range of angles-of-attack. A typical solution convergence for the longitudinal analysis is achieved with about 150 iterations where the total residuals are dropped by approximately 3 to 4 orders of magnitude and reduced the oscillations in lift and drag coefficients to a negligible level. All computations are performed on the Cray-C90 class computer with a typical case requiring about 120-MegaWords of memory and about 1/2-CPU hours to achieve the above nominal convergence characteristics. All solutions are based on second-order, flux-difference-splitting (FDS2) algorithm.

-- Results & Discussion --

Longitudinal analysis

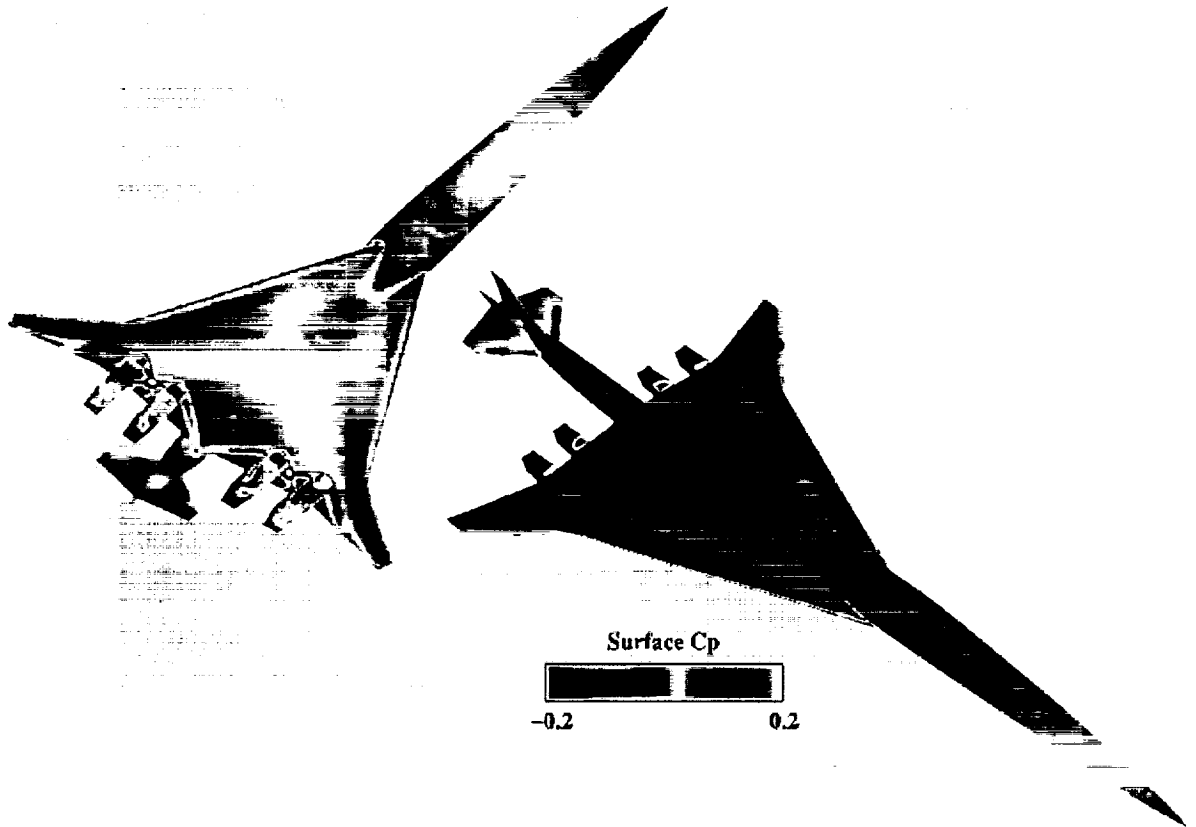
- **Typical flow features**
 - **Surface pressure contours**
 - **Correlation with PSP data**
 - **Off-surface flow structures**
- **Force & moment analysis**
 - **Drag correction to Euler predictions**
 - **Correlation with data**

Lateral/directional analysis

- **Typical surface pressure contours**
- **Forces & moments predictions – correlation with data**

Longitudinal aerodynamic analysis is presented next which includes results for typical flow features followed by integrated forces/moment analysis and correlations with experimental data.

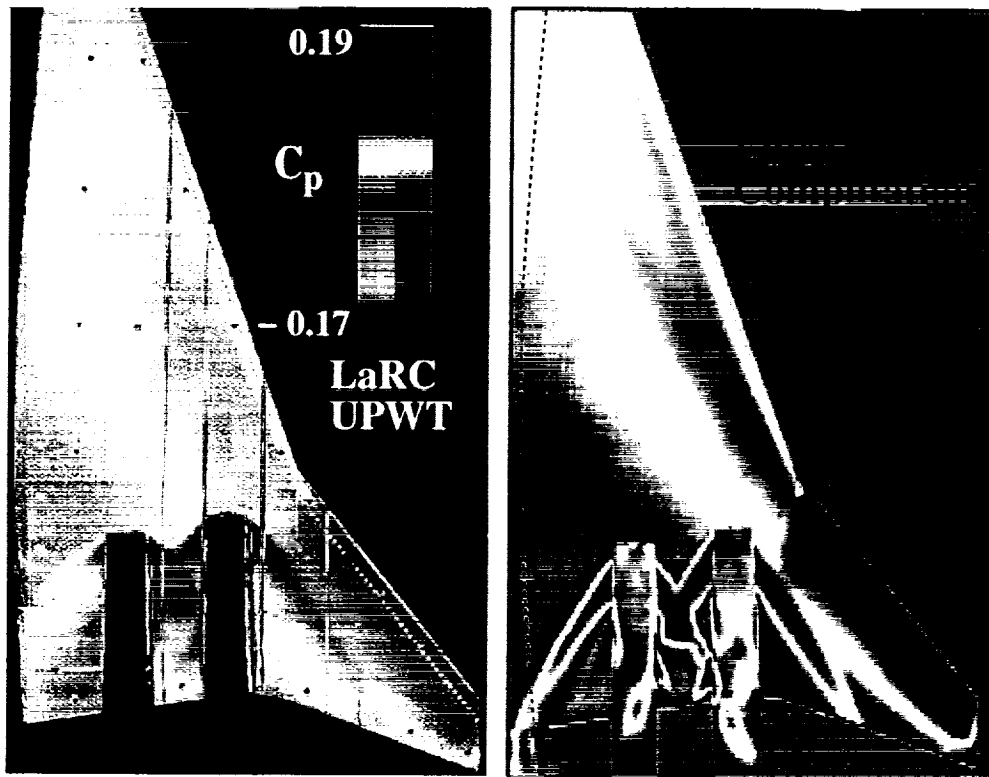
Surface Cp Prediction for the Complete TCA Configuration Flow through propulsion cruise geometry; $\text{Alpha}=3.5^\circ$, $\text{Mach}=2.4$



Ghaffari/LaRC

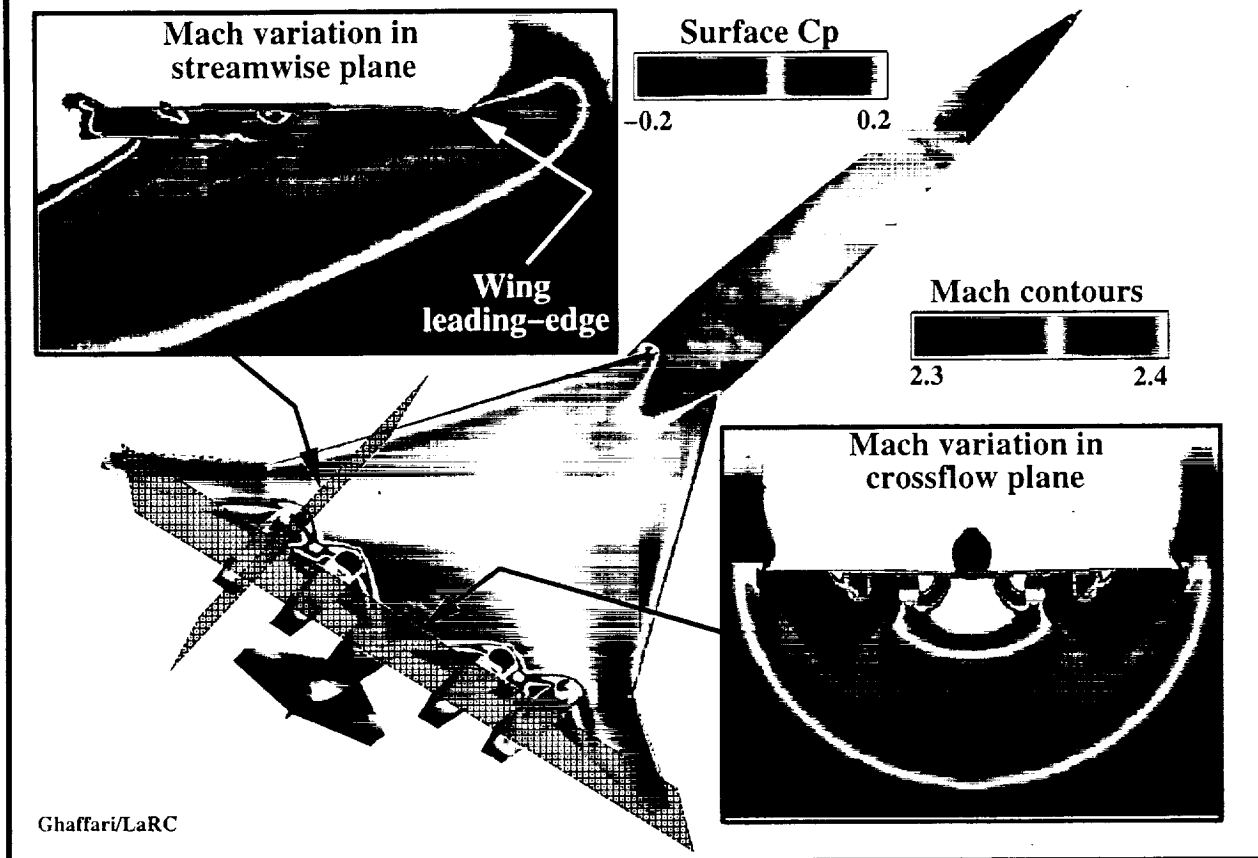
Typical surface Cp distributions computed for the complete TCA configuration are shown here from two different vantage points. The computed lower surface Cp distribution can be characterized by the flow compression around the nose apex region, the inboard/outboard wing leading edges and a complex shock wave structure around the engine nacelles. The shock waves are emanated from both the inboard and the outboard leading-edges of the nacelle diverters. The upper surface Cp contours reveal a fairly benign distribution over the forebody and a region of flow expansion that runs parallel to the inboard wing leading-edge which extends onto the wing outboard panel. The upper surface Cp distribution also indicates a slight flow expansion around the leading edges of the outboard wing, along with a region of compression around the horizontal-tail leading-edges.

Surface C_p Prediction for the Complete TCA and Correlation with PSP
Unstructured Grid Method (TetrUSS); $M = 2.4$, $\text{Alpha} = 3.5^\circ$, $R_{ft} = 4 \times 10^6$



A limited amount of Pressure Sensitive Paint data were acquired on the truncated TCA model during the UPWT test. Typical PSP data obtained over the wing lower-surface of the TCA supersonic cruise configuration (i.e., no-control surface deflection) at 3.5 degree angle-of-attack and Mach number of 2.4 is presented on the left hand-side of the above figure. Complementary to the PSP results, the surface C_p computed for the same configuration and flow conditions is shown from the same vantage point on the right hand-side. The computational result is actually extracted from the same numerical solution that was shown in the previous figure, except the pressure range and the corresponding color map have been changed to match that of the PSP data. The results indicate that the two main flow features highlighted by a region of flow compression under the wing outboard section as well as the complex shock wave structures around the nacelles have been predicted reasonably well. Note that the diffusive nature of the PSP shock waves which are, in general, located further upstream than those of the predictions are attributed to the lack of viscous modelling in the present Euler numerical analyses.

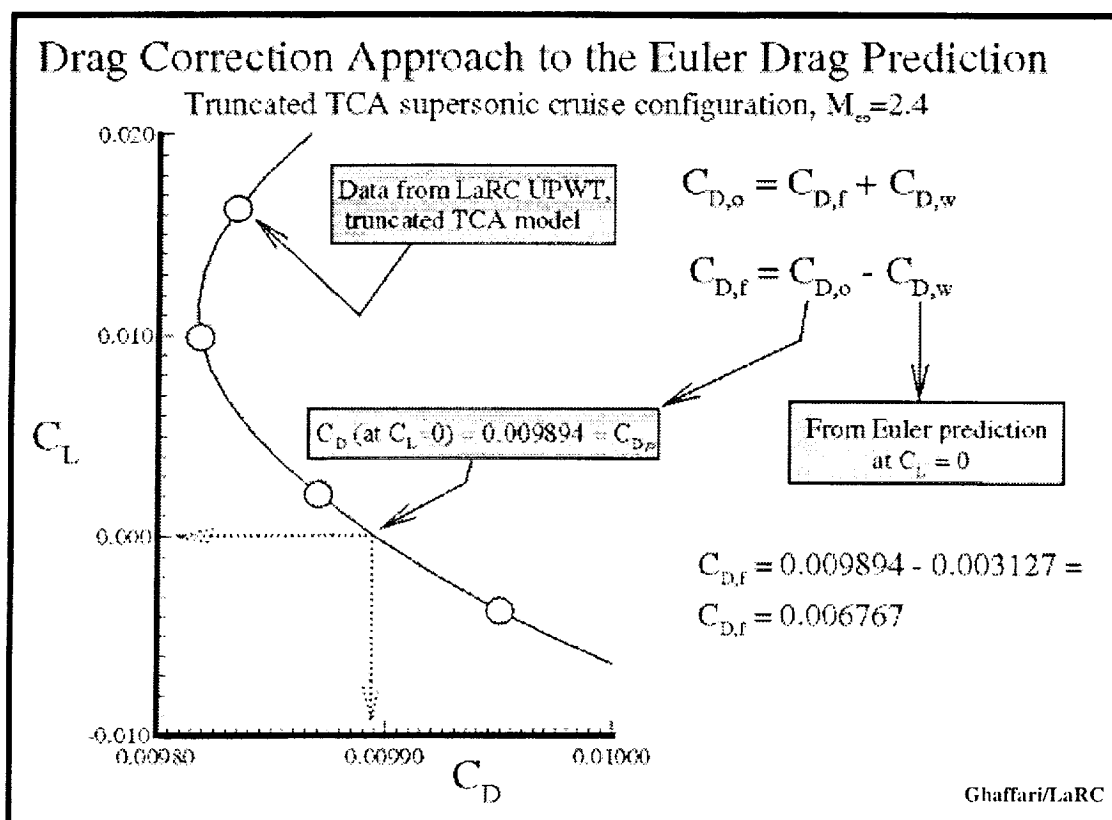
Surface Cp & Off-Surface Mach Predictions for the TCA Flow through propulsion cruise geometry, $\alpha=3.5^\circ$, Mach=2.4



Typical off-surface flow features, highlighted by Mach number variation in a cross-flow & streamwise planes, in conjunction with the surface Cp distribution are shown in this chart for the complete TCA configuration. To accentuate the flow features in & around the nacelles, the Mach number variation in both the cross-flow & streamwise planes are contoured over a compressed range of 2.3 to 2.4. Over this contour range, the Mach numbers exceeding 2.4 (i.e., free-stream cruise Mach) are shown in white, while, Mach numbers below 2.3 are shown in black color indicating a slower moving flow relative to the free-stream.

The Mach variation in the cross-flow plane, longitudinally located slightly aft of the engine inlets, indicates a speed range in excess of the free-stream cruise Mach for essentially the entire upper surface and a region between the two inboard nacelles. The Mach variation in the cross-flow plane also indicates a compression region wrapped around the outboard nacelles and an extension toward the outboard wing leading-edges. Furthermore, the off-surface extension of the shock waves emanated from the inboard nacelle diverter (i.e., inboard legs close to the configuration plane-of-symmetry) is also shown to bend outboard and impinge on the exterior side of the inboard nacelles.

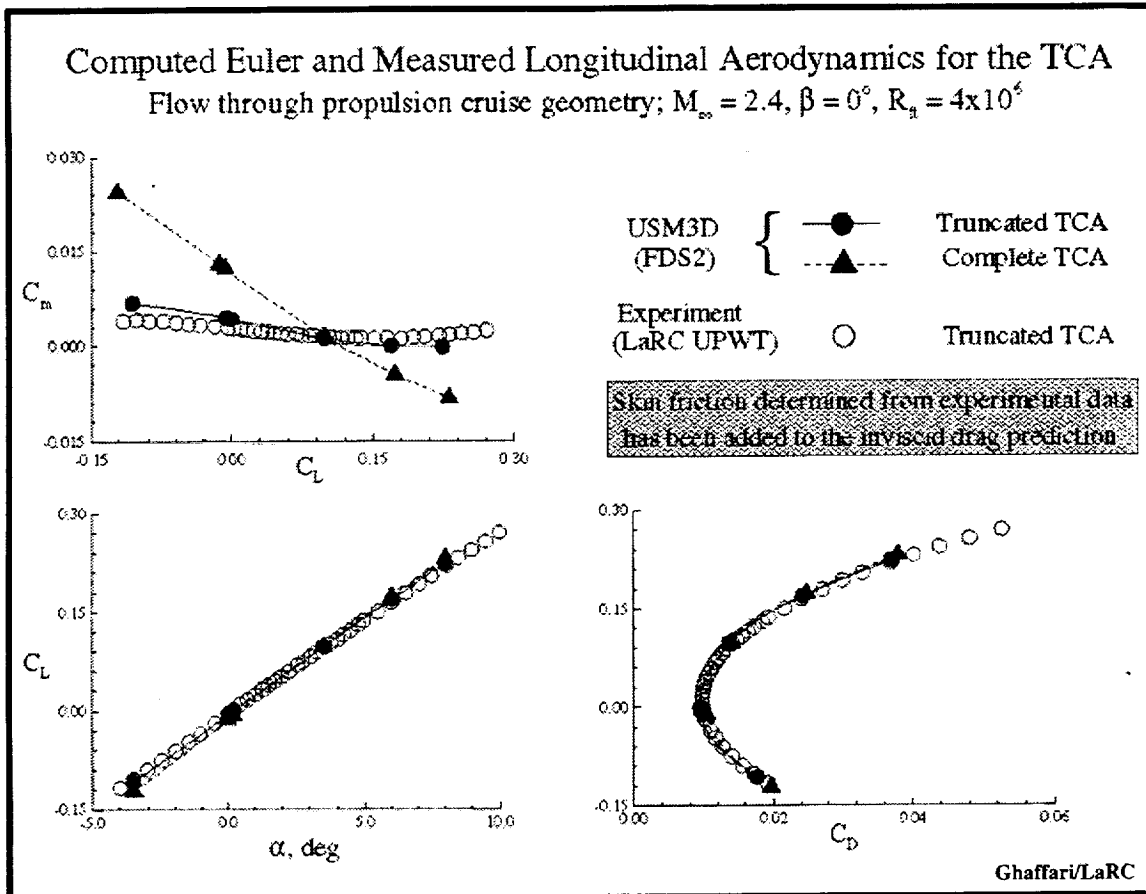
The Mach variation in the streamwise plane (parallel to the configuration plane-of-symmetry), located at a station that roughly cuts through the starboard mid-outboard nacelle is presented in the upper left of the figure. The Mach variation clearly shows a region of flow compression around the wing leading-edge followed by another one just ahead of the nacelle inlet. The outboard nacelle interior flow structure reveals a series of shock waves that bounce back and forth, creating regions of flow expansion and compression on the interior surfaces of the nacelle.



In general, there are two aerodynamic phenomena contributing to the total drag (C_D) force exerted on an airborne vehicle, the viscous (or the skin friction) component ($C_{D,f}$) and the pressure drag (or the drag-due-to-lift or vortex drag) component ($C_{D,p}$). In supersonic flow, the pressure drag consists of both the drag-due-to-lift ($C_{D,l}$) and the wave drag ($C_{D,w}$) components. Hence,

$$C_D = C_{D,f} + C_{D,p} = C_{D,f} + C_{D,l} + C_{D,w}$$

Conventional approach is taken to correct the drag coefficients predicted by the present Euler analysis to account for the viscous component of the total drag coefficient. This correction is required primarily due to the inviscid nature of the present Euler analysis and the inherent limitation of the corresponding equations to only predict the pressure components of the total drag. This conventional approach is based on determining the total drag coefficient at zero lift (i.e., $C_{D,o}$) using the experimental drag polar curve. This approach is adopted and the $C_{D,o}$ determined, as shown in the above plot, to be 98.94 drag counts. However, the determined $C_{D,o}$ is not only the drag contribution due to viscosity but it also includes the wave drag component. In an effort to isolate the wave drag component from the determined $C_{D,o}$, an Euler solution was obtained at an angle-of-attack of 0.2° which was found to correspond to the experimental zero-lift data. It is assumed that the pressure drag coefficient predicted by the Euler method is solely the wave drag component with no contribution from drag-due-to-lift. The resulting wave drag coefficient is computed to be 31.27 counts. As a result, the skin friction contribution to the total drag can now be determined by subtracting the computed wave drag at zero lift from the determined $C_{D,o}$ as shown in the above figure. The skin friction coefficient, found to be 67.67 counts (assumed to remain constant with both the angle-of-attack and sideslip angle) is used to correct all the drag coefficient predictions in the present Euler analysis.



The computed longitudinal aerodynamic characteristics are presented here for both the complete and the truncated TCA configuration, along with the measured experimental data for the truncated TCA model at supersonic cruise Mach number of 2.4. The results for the computed lift coefficients clearly indicate minimal effects due to the additional empennage loads at 3.5° alpha (i.e., close to the configuration design cruise angle-of-attack). However, as expected for off-design angles-of-attack, the additional load from the presence of the empennage on lift becomes more pronounced, i.e., increase in C_L for alpha $> 3.5^\circ$ and decrease in C_L for alpha $< 3.5^\circ$. Although the latter effects on C_L are relatively small, the corresponding impact on the pitching moment is considerable due to the long moment arm. The results indicate that the additional load from the empennage presence to be minimal at the design cruise angle-of-attack of 3.5° , cause a pitch down for alpha $> 3.5^\circ$, and cause a pitch up for alpha $< 3.5^\circ$. Furthermore, the empennage load increments on the computed drag coefficients appear to be small over the examined range of flow conditions.

The correlation between the predictions and the experimental data for the truncated TCA configuration indicate good agreement for the pitching moment, lift and drag coefficients across the examined angle-of-attack range.

-- Results & Discussion --

Longitudinal analysis

- **Typical flow features**
 - **Surface pressure contours**
 - **Correlation with PSP data**
 - **Off-surface flow structures**
- **Force & moment analysis**
 - **Drag correction to Euler predictions**
 - **Correlation with data**

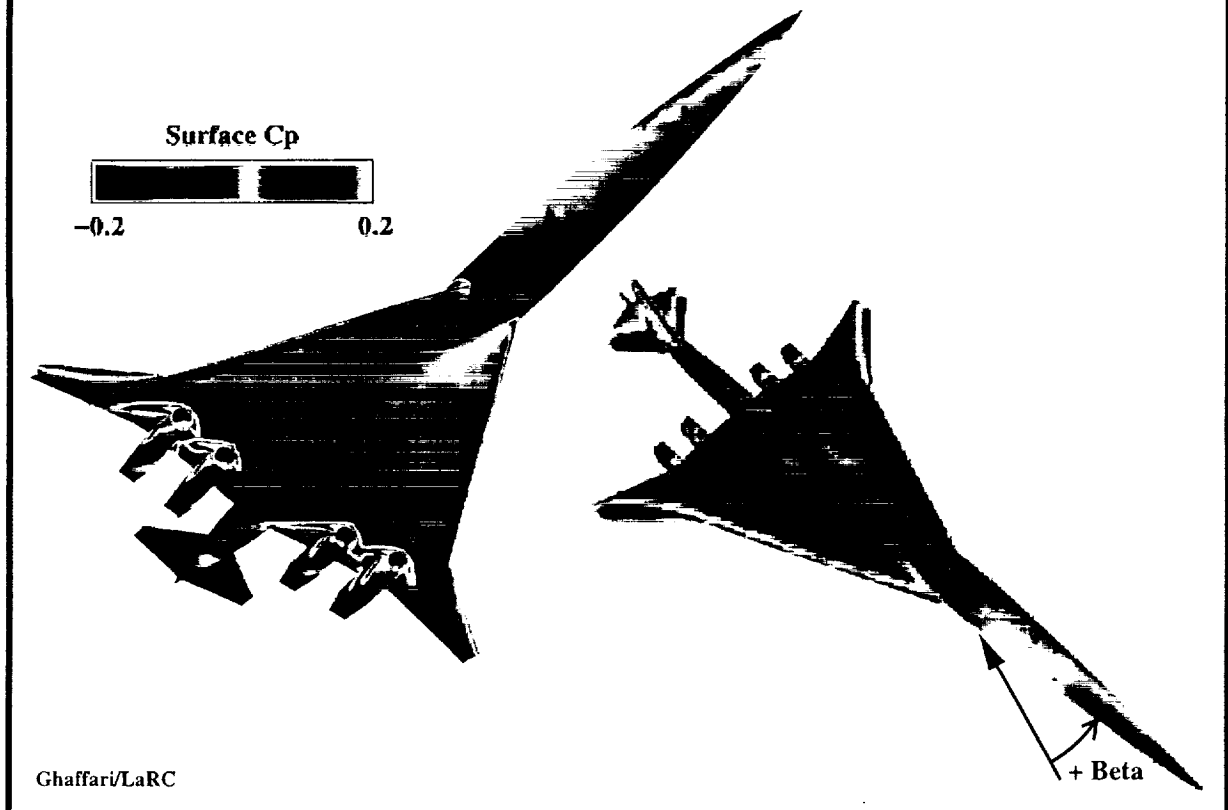
Lateral/directional analysis

- **Typical surface pressure contours**
- **Forces & moments predictions – correlation with data**

Lateral/directional aerodynamic analysis is presented next which includes results for typical surface pressure contours followed by integrated forces/moments and correlations with experimental data.

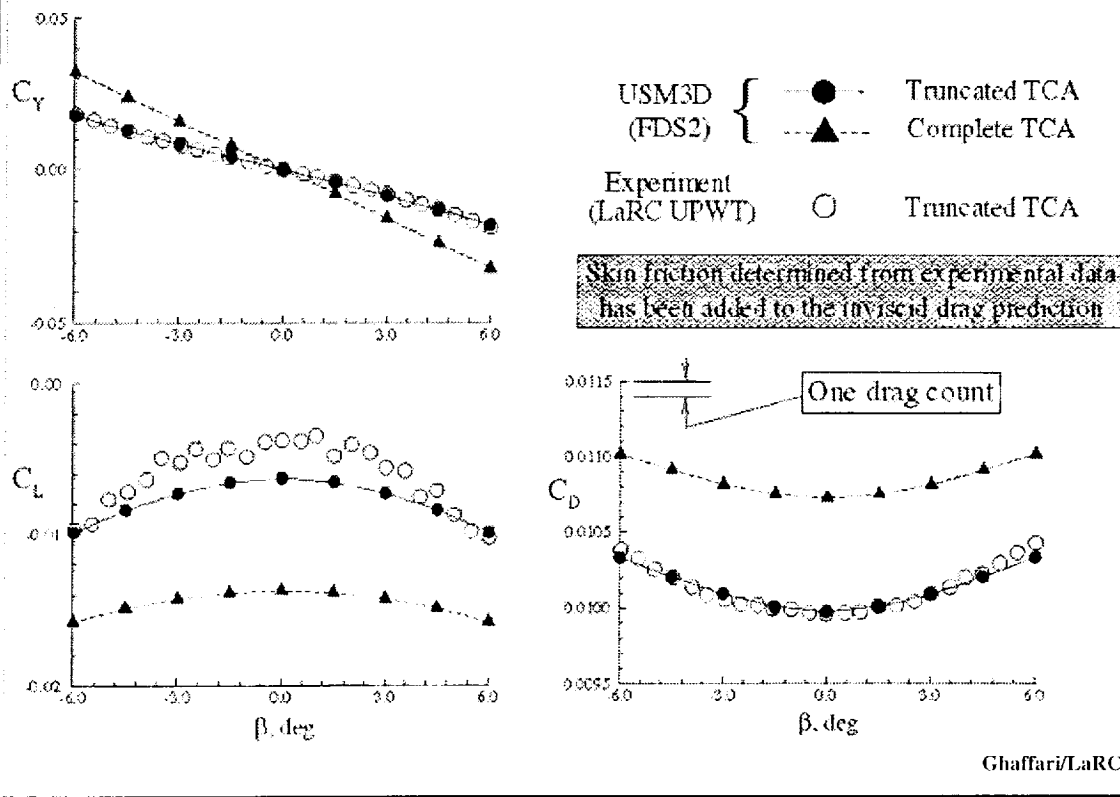
Surface Cp Prediction for the Complete TCA Model

Flow through propulsion cruise geometry, $\text{Alpha} = 0^\circ$, $\text{Beta} = 3^\circ$, $M = 2.4$



Typical upper & lower surface Cp contours computed at a finite sideslip angle are shown in this figure from similar vantage points and contour range consistent with the earlier results presented for the longitudinal analysis. The results clearly show the expected asymmetrical load distribution on both the upper and lower surface. The lower surface pressure contours indicate a region of expansion ($C_p \sim -0.2$) that runs roughly parallel to the starboard leading-edge of the inboard wing, whereas, the pressure contours around the port-side leading-edge of the inboard wing show a fairly benign attached flow condition. The upper surface Cp contours indicate a uniform distribution over the majority of the wing with a narrow band of compression along the starboard leading-edge of the inboard wing which expands over onto the outer wing panel. In addition, the computed upper surface pressure contours over the horizontal tails also show a large region of compression just aft of the leading edges, particularly on the starboard side.

Computed Euler and Measured Aerodynamic Forces at Sideslip for the TCA
 Flow through propulsion for cruise geometry; $\alpha = 0^\circ$, $M_\infty = 2.4$, $R_n = 4 \times 10^6$



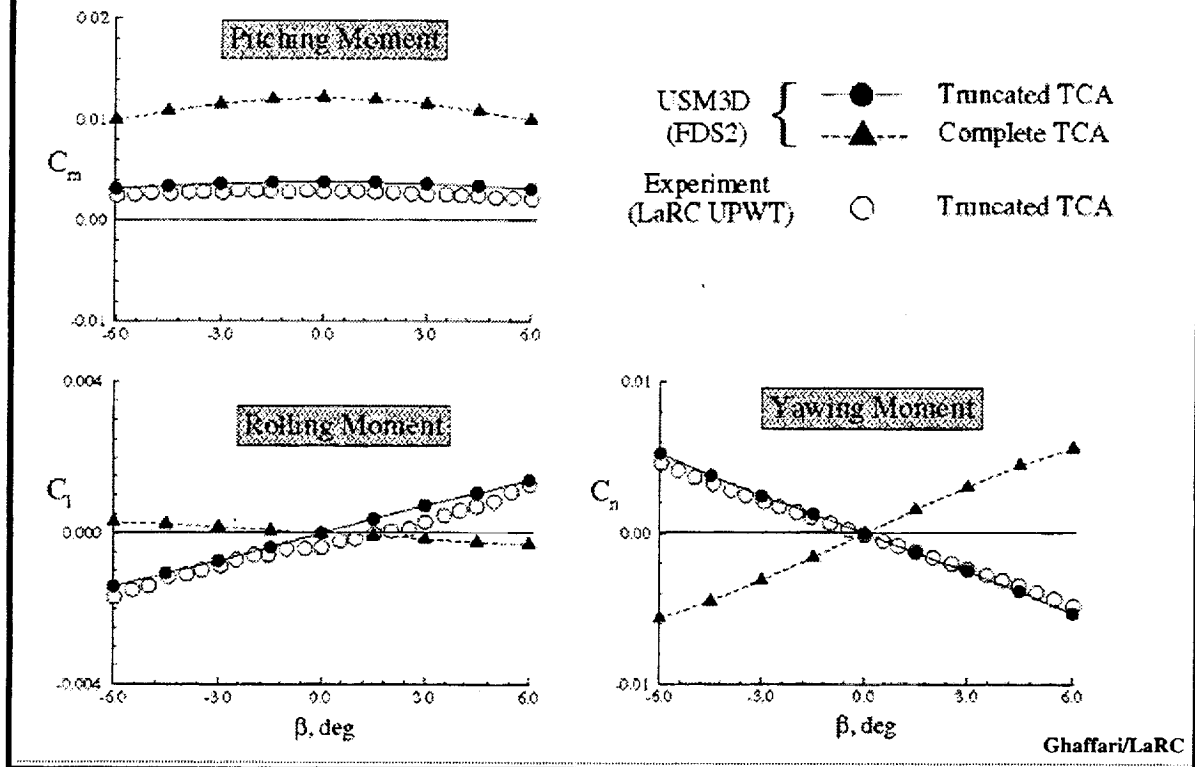
The overall aerodynamic force characteristics computed for the complete TCA configuration across the examined range of sideslip angles at zero-degree angle-of-attack and supersonic cruise Mach number of 2.4 are shown in this figure. The experimental data for the truncated TCA model along with complementary results extracted from the full TCA numerical simulation (i.e., with appropriate component integration to only account for the truncated TCA geometry) are also included in the figure. Note the small scales in these plots, particularly in the measured lift coefficients which clearly illustrate the scattering of the data, as a function of sideslip angle, contributing to the overall asymmetrical lift distribution about the zero-degree sideslip angle (i.e., positive and negative sides).

The predicted side-force coefficients for the truncated TCA configuration are in excellent agreement with the experimental data, both in terms of magnitude and trends, across the examined range of sideslip angles. In general, the sideforce coefficients vary in a fairly linear fashion with sideslip angle and the corresponding change in the slope for the complete TCA configuration can mainly be attributed to the asymmetrical load distribution on the vertical-tail.

The computed lift coefficients for the truncated TCA configuration correlate very well with the measured data across the examined sideslip range. The presence of the empennage also appears to cause a nearly constant decrease to the overall lift coefficient for all the sideslip angles considered in the present study.

Similar to the lift coefficients, the computed drag coefficients for the truncated TCA configuration also correlate very well with the experimental data and that the empennage presence cause nearly a constant increase in the overall drag coefficients (~ 7 drag counts) across the examined sideslip angles.

Computed Euler and Measured Aerodynamic Moments at Sideslip for the TCA
 Flow through propulsion cruise geometry; $\alpha = 0^\circ$, $M_\infty = 2.4$, $R_n = 4 \times 10^6$



The computed and measured aerodynamic moment characteristics for the truncated TCA configuration across the examined range of sideslip angles are presented in this figure. Complementary numerical predictions for the complete TCA configuration are also included for comparison. In general, there is an excellent correlation between the numerical predictions and the measured data for the aerodynamic moment characteristics of the truncated TCA configuration across the examined range of sideslip angles. As expected, the aerodynamic moments predicted for the complete TCA configuration clearly indicate a dramatically different characteristics than those of the truncated TCA model. These differences in the moment characteristics are primarily due to the presence of the empennage components. For example, the results indicate a sign reversal in the yawing and rolling moments which can primarily be attributed to the presence of the vertical and horizontal tails. Furthermore, the pitch-up moment characteristics for the complete TCA configuration can be mainly be attributed to the negative load contributions due to the empennage presence. It should also be noted that the asymmetrical lift distribution in the measured data, for positive and negative sideslip angles discussed in the previous chart, is the primary cause of the nonlinearities in the rolling moment distribution. Such nonlinearities in the measured rolling moment distribution are evident as they deviate from a fairly linear character of the computed results, in particular, around zero and the positive sideslip range.

--- Concluding Remarks ---

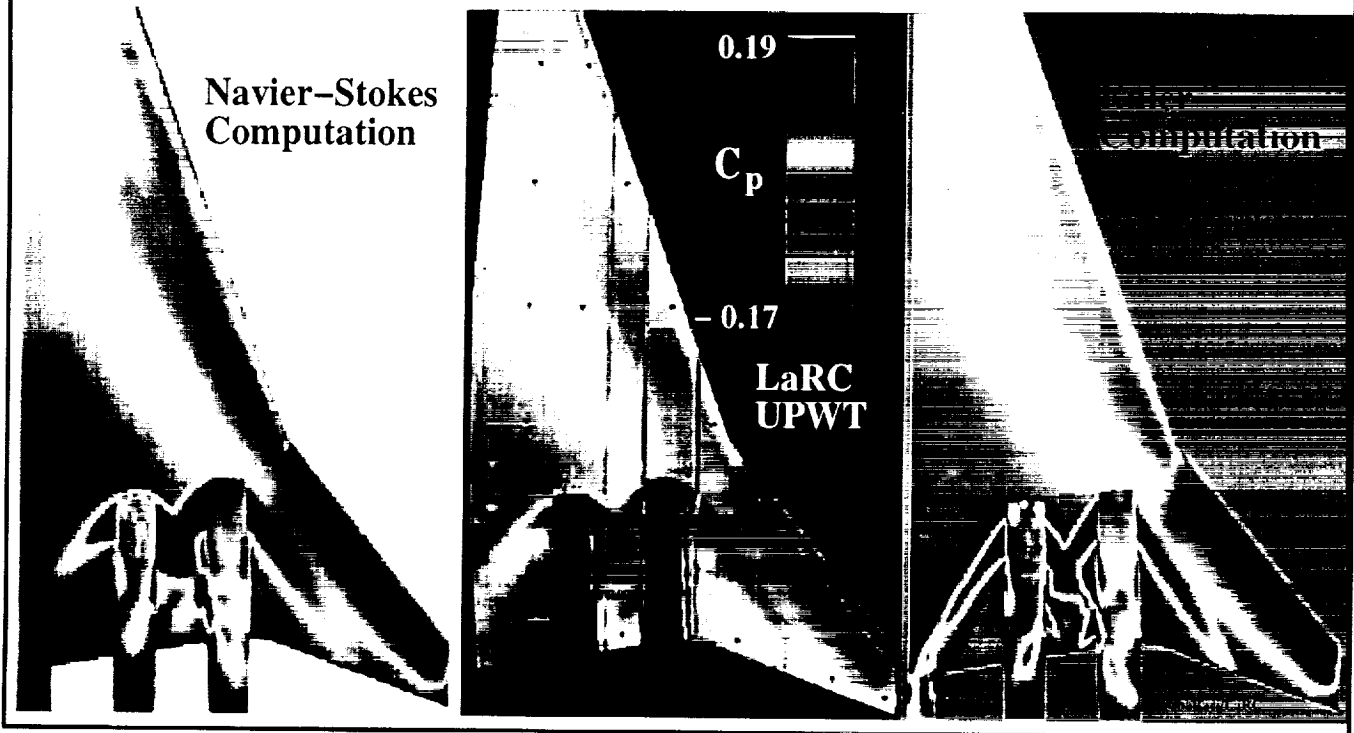
- **TCA longitudinal aerodynamic characteristics for supersonic cruise are accurately predicted by the present unstructured grid Euler method**
- **TCA lateral/directional aerodynamic predictions agree very well with experimental data**
- **Predicted nacelles shock-wave structures correlate reasonably well with Pressure Sensitive Paint data**
- **Computational method produced consistent results across the examined range of conditions without any convergence difficulties**
- **Completed the documentation – Presently being reviewed**

What's next?

The numerical results clearly demonstrate that the present unstructured grid Euler method is a viable tool that can be used, with confidence, for the aerodynamic analysis of the high-speed-civil-transport class of vehicle in the early configuration design cycle. The present analysis also indicates that the method is robust and produces consistent solutions across the examined range of flow conditions without any convergence difficulties. Where would we like to go next from the present Euler analysis?

Well, to Navier-Stokes flow simulation.

**Surface Cp Prediction for the Complete TCA and Correlation with PSP
Unstructured Grid Method (TetrUSS); $M = 2.4$, $\text{Alpha} = 3.5^\circ$, $R_{ft} = 4 \times 10^6$**



The lessons learned from the present Euler analyses were used to extend the computations to simulate the viscous flow over the same configuration for cruise conditions. Advancing-layers method was used to add grids in the viscous region to resolve the boundary-layer flows. This effort has already been initiated and preliminary results indicate good correlations with experimental data. A representative result for the computed wing lower-surface pressure distribution is shown here to complement the present Euler analysis. The Navier-Stokes result clearly show an improvement over the Euler flow predictions for simulating the shock waves around the nacelles. Also note that the viscous effects appear to have minimal impact on other regions of the wing lower-surface pressure distribution.

This page is intentionally left blank.

Unstructured Navier–Stokes Analysis of Full TCA Configuration

Neal T. Frink and Shahyar Z. Pirzadeh
NASA Langley Research Center
Hampton, VA

HSR Airframe Technical Review
Los Angeles, CA

February 9–14, 1998

Outline

- Motivations
- Milestone and approach
- Overview of the unstructured-grid system
 - The *TetrUSS* system
 - Navier-Stokes capability
- Results on full TCA W/B/N/D/E configuration
- Concluding remarks
- Future directions

TetrUSS

Motivation for Investigating USG Methodology

The carrot:

- Earlier use of advanced CFD codes in design process
- Reduced Design Cycle Time

Approach:

- Investigate unstructured-grid (USG) CFD methodology
- Exploit flexibility of tetrahedral cells

Immediate benefits:

- Viscous & inviscid grids generated in days by non-specialists
- Accurate, robust flow solvers

Challenges:

- More computer memory intensive than structured-grid methods
- Confidence in Navier-Stokes solution on tetrahedral cells
- Limited experience base

HSR Configuration Aerodynamics 4.3.1 – Subtask 1 NASA LaRC

Milestone: MS 4–2: Rigid Full Configuration F&M (6/1/97)

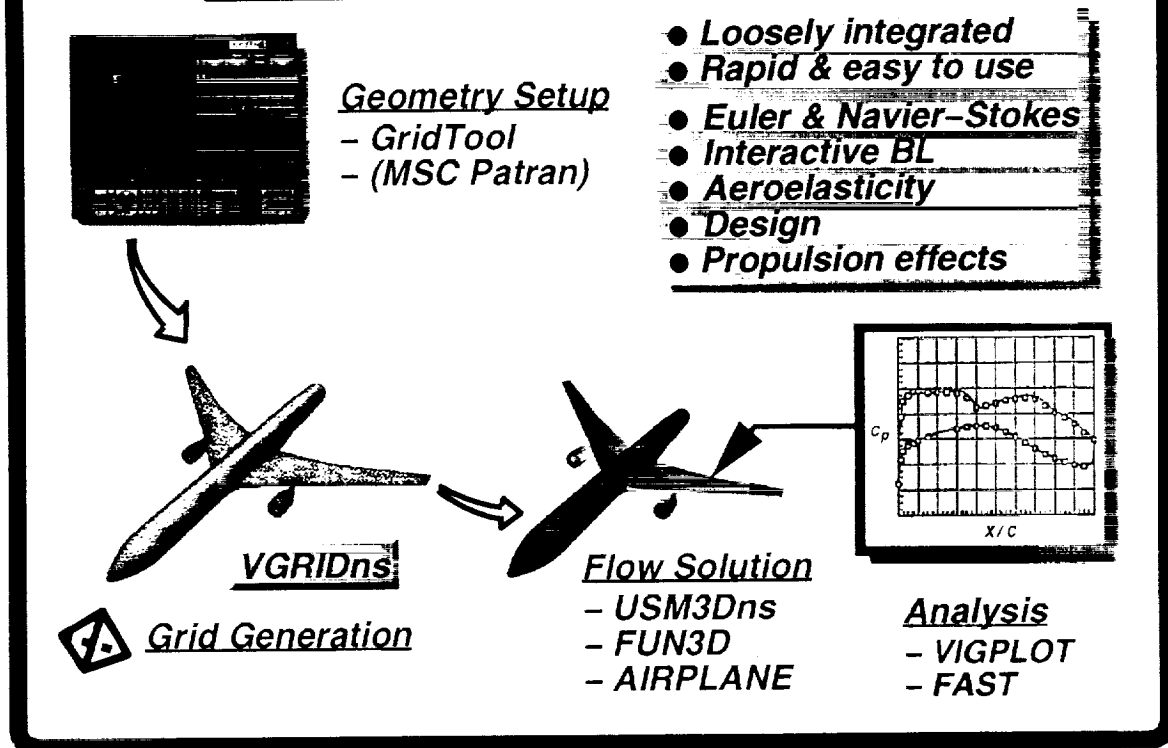
- Assess inviscid and viscous USG CFD for TCA W/B/N/D/E at supersonic cruise conditions
- Comparisons with F&M with TCA wind tunnel data from MS 3–8

Approach:

- Apply the *TetrUSS* unstructured-grid codes to compute full TCA configuration Navier–Stokes solutions
- Compare to PSP, surface C_p , and F&M data from NASA UPWT for truncated TCA W/B/N/D configuration

The TetrUSS System

Tetrahedral Unstructured Software System



TetrUSS is a loosely integrated set of software forming a complete aerodynamic analysis package. The primary components of *TetrUSS* are GridTool, VGRIDns, USM3Dns, and VIGPLOT. Other codes have been adapted within the system by various users as evidenced by the additional software listings on the slide.


The process begins with geometry setup which is performed by the GridTool code. GridTool reads in the surface geometry from various sources, e.g. IGES, PLOT3D, GRIDGEN, etc. on which mathematical surface patches are constructed. The user also prescribes cell-spacing information by way of source elements. A VGRIDns input file is output along with boundary condition information. VGRIDns then generates a triangular surface grid and tetrahedral volume grid on which the flow solution is obtained with USM3Dns. The solution is analyzed graphically with the VIGPLOT code.

The system can solve both the Euler and Navier-Stokes equations, and has additional useful engineering capabilities such as interactive boundary layer, aeroelasticity, design, and propulsion boundary conditions.

More details are presented for VGRIDns and USM3Dns in the next few slides.

VGRID/VGRIDns – Salient Features

● Inviscid Grids (VGRID)

- Tetrahedral Unstructured "Euler" grids
- Based on the Advancing-Front Method (AFM)
- Elliptically smooth grids
- Restart capability
- Local remeshing  (POSTGRID)

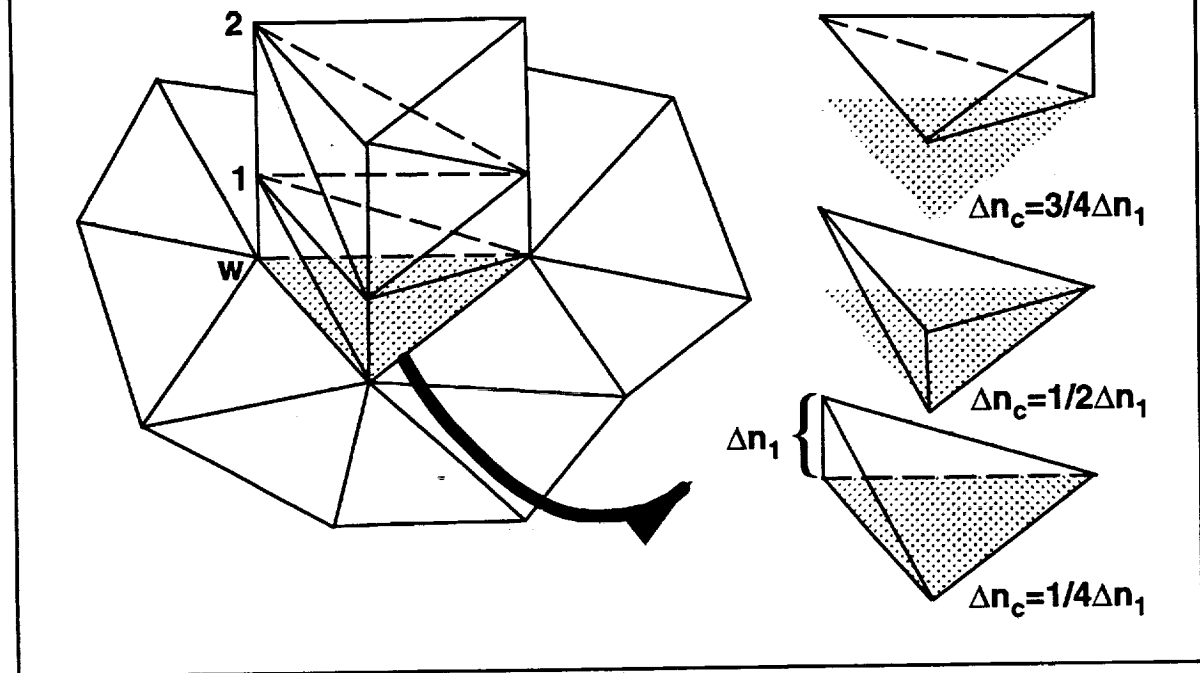
● Viscous/Inviscid Grids (VGRIDns)

- Thin-layer tetrahedral "Navier-Stokes" and "Euler" grids
- Based on the AFM and Advancing-Layers Method (ALM)
- Anisotropic grid stretching

This slide lists the salient features of the VGRID/VGRIDns tetrahedral grid generator. VGRID is the prior "inviscid" version, whereas VGRIDns is an extended version which includes a thin-layered 'viscous' grid generation capability.

Two very important advances within VGRIDns is the "Advancing-Layers Method" (ALM) and multi-directional anisotropic stretching. More information on these two features are described in the following slides.

Inherent "Structure" of Thin-Layered Tetrahedral Grids

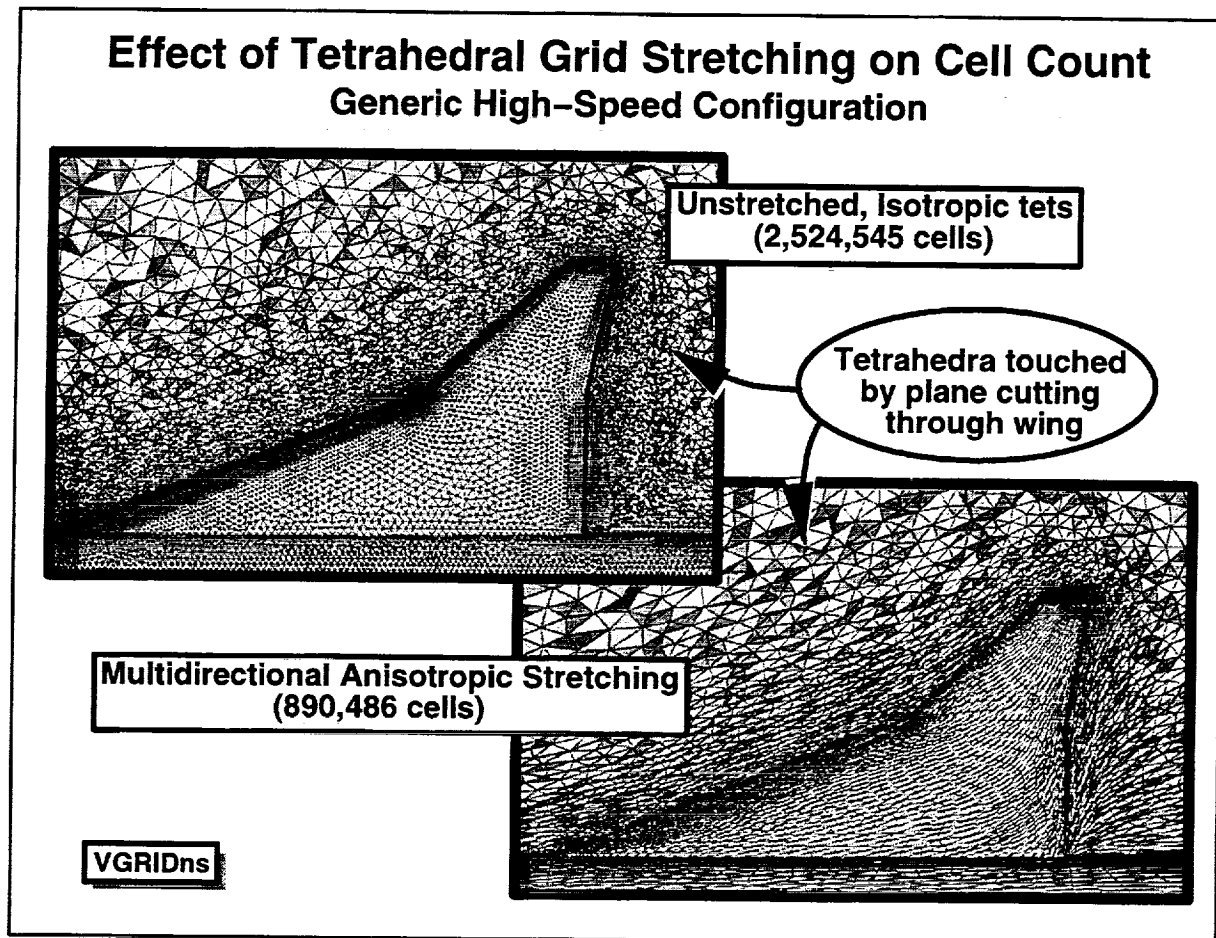


The requirements for 'viscous' grid generation are

- 1) highly-stretched tetrahedral to resolve the boundary layer
- 2) precise control of normal point distribution
- 3) smooth transition to isotropic grid outside of boundary layer
- 4) accommodate sharp corners and cavities, and 'close' surfaces
- 5) retain the flexibility and automation of the classic Advancing-Front Method.

Thin-layered Navier-Stokes grids are generated by a new approach called the Advancing-Layers Method (ALM) as illustrated in this slide. Once a surface triangulation has been generated, direction vectors are determined along which the viscous layers are advanced. The distribution of points along these vectors is dictated by a user-prescribed stretching function. The resulting layers consist of well-ordered layers of tetrahedral cells as depicted in the figure. Within each "layer" are three tetrahedral cells. Each layer of cells will march outward until it is told to stop by the global background grid, or if it is about to collide with an approaching front. The entire process is fully automatic and robust.

Effect of Tetrahedral Grid Stretching on Cell Count Generic High-Speed Configuration



Unstructured flow solvers require relatively large memory compared to structured-grid codes due to their general indexing data structure. Thus, keeping grid sizes to manageable levels become a major issue for addressing viscous problems. The use of classic omni-directional clustering with isotropic cells is a very inefficient utilization of cells because of excessive clustering in regions of low gradients. Our experience has been that attempting to solve the Navier-Stokes equations on complex geometries with isotropic surface grids is impractical on most current computers.

This limitation has been overcome with multi-directional anisotropic stretching. For example, on the Generic High-Speed Configuration in the slide, the upper figure illustrates isotropic clustering near the leading- and trailing-edges. (This figure shows the surface triangulations on a double-delta wing and cylindrical fuselage, and the volume tetrahedra intersected by a plane cutting through the wing and fuselage.) Note the desirable chordwise clustering at the leading edge, but an undesirable spanwise clustering along the leading edge. The result is a large grid with over 2.5 million cells. In the lower figure, cell stretching is applied along the wing edges and fuselage. This results in a factor of 3 reduction in cells while retaining the cell clustering in the critical directions. Our experience has been that there is no noticeable degradation of solution accuracy if proper stretching is utilized. This feature has had a major impact on opening the way toward practical computation of unstructured-grid Navier-Stokes solutions on complex geometries.

USM3Dns – Salient Features

- **Tetrahedral cell-centered, finite volume**
- **Time integration:**
 - Implicit Point GS & Explicit RK
 - Local time stepping convergence acceleration
- **Euler and Navier–Stokes**
 - Spalart–Allmaras turbulence model with Wall Function
- **Upwind flux functions**
 - Roe’s Flux Difference Splitting
 - Van Leer’s Flux Vector Splitting
 - Superbee and MinMod flux limiters
- **Computer resources:**
 - Memory: Implicit – 175 words/cell, Explicit – 45 words/cell
 - CRAY Multitasking: Efficiency of 6 out of 10 processors
 - Workstation: SUN, SGI, HP, Convex
- **Parallel processing with zonal grids (under testing)**

The salient features of USM3Dns are listed in this slide. It is important to note that USM3Dns is a tetrahedral *cell-centered* scheme where the tetrahedral cell forms the underlying computational element. This is in contrast to most unstructured-grid work which utilizes a *node or vertex based approach* where the unknowns are computed within computational elements surrounding the nodal locations. This distinction is important since a given grid has between 5 and 5.5 more tetrahedra than nodes. Thus, for comparable spatial resolution, a tetrahedral node-centered scheme will require a 'finer' grid than a tetrahedral cell-centered scheme.

Another important feature of USM3Dns is the use of a wall function which is coupled with the Spalart–Allmaras turbulence model. The wall function eliminates the need to grid-resolve the near-wall region of the boundary layer, thereby reducing memory requirements and decreasing solution stiffness which impedes convergence.

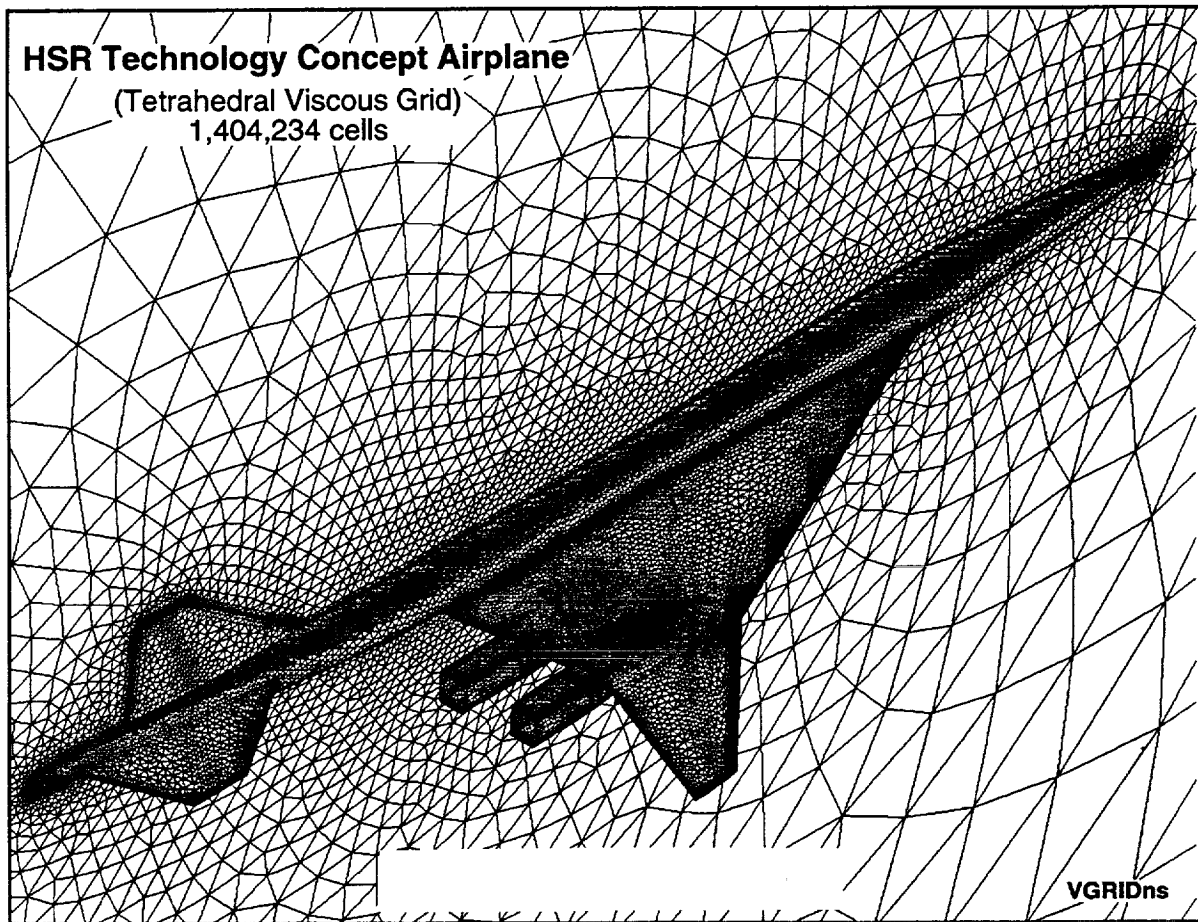
USM3Dns has also been multitasked for the Cray supercomputers and yields a substantial reduction in wallclock time for a solution. Work is near completion on a version of USM3Dns for parallel processing machines and loosely coupled workstations.

Characteristics for TCA W/B/N/D/E TetrUSS Results

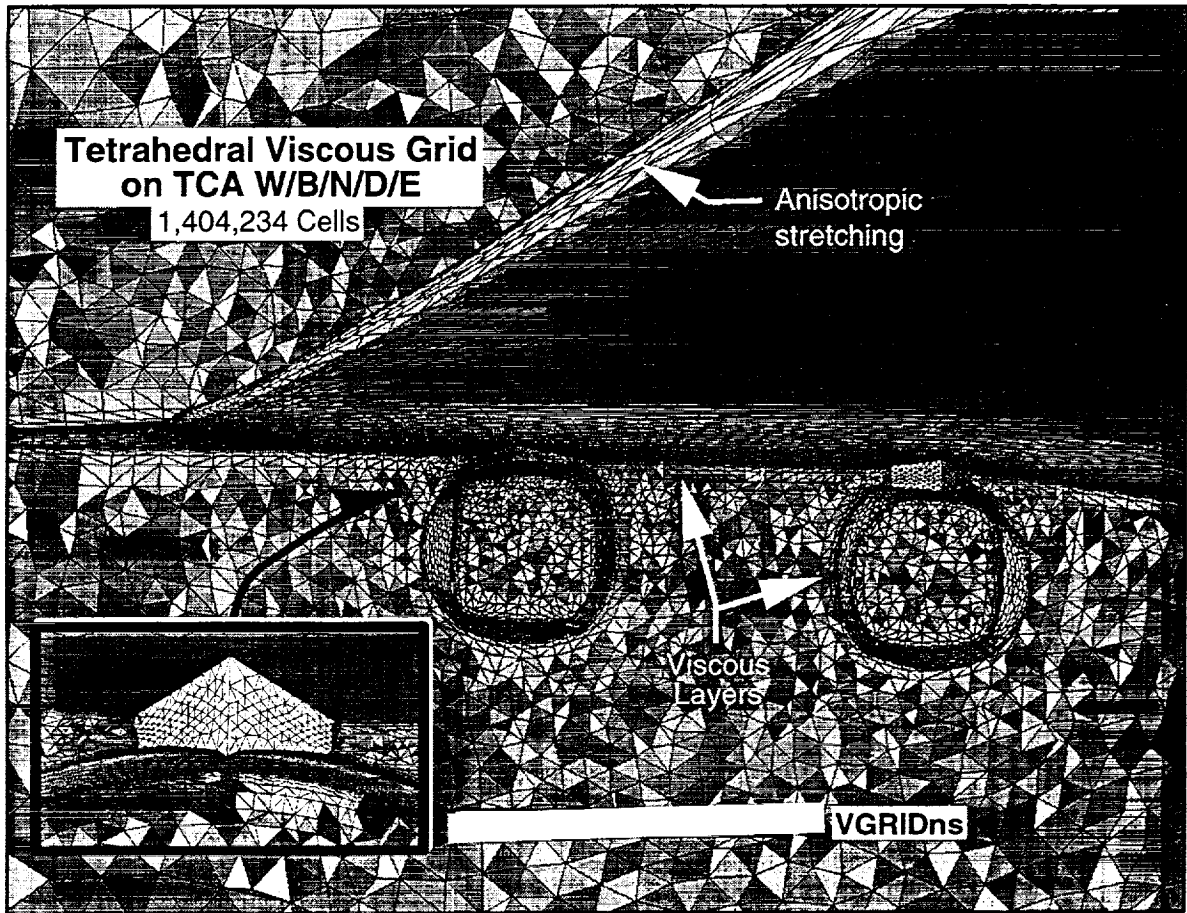
- Thin-Layer Tetrahedral Grid
 - 1,404,234 cells (789,396 cells in 'viscous' layer)
 - Approx. 18 tetrahedra across mid-chord BL
- Flow conditions
 - Mach=2.4, $\alpha=3, 3.5, \& 4$ deg., $Re_c=6.4$ million
- Flow model
 - Full Reynolds-averaged Navier-Stokes
 - Spalart-Allmaras turbulence model
 - Wall function with $y^+ \cong 50$
- Resource requirements
 - Initial grid generation time: 7 to 10 days (est.)
 - modifications, e.g. relocating nacelle: ~1/2 to 1 day
 - Flow solution time: 22 Cray C90 hours
(4 hours wall-clock with multitasking)
 - Memory: 250MW

The characteristics of the following TCA solution results are listed. A grid of 1.4 million tetrahedra surrounds the entire TCA W/B/N/D/E configuration with over one-half of the cells residing in the 'viscous' layer. By using the wall function, the grid was sized to have approximately 18 tetrahedra across the mid-chord boundary layer with the first node off of the surface placed at a y^+ of 50. The wall function is utilized to determine the wall viscous stresses used by the numerical scheme for solving the Navier-Stokes equations.

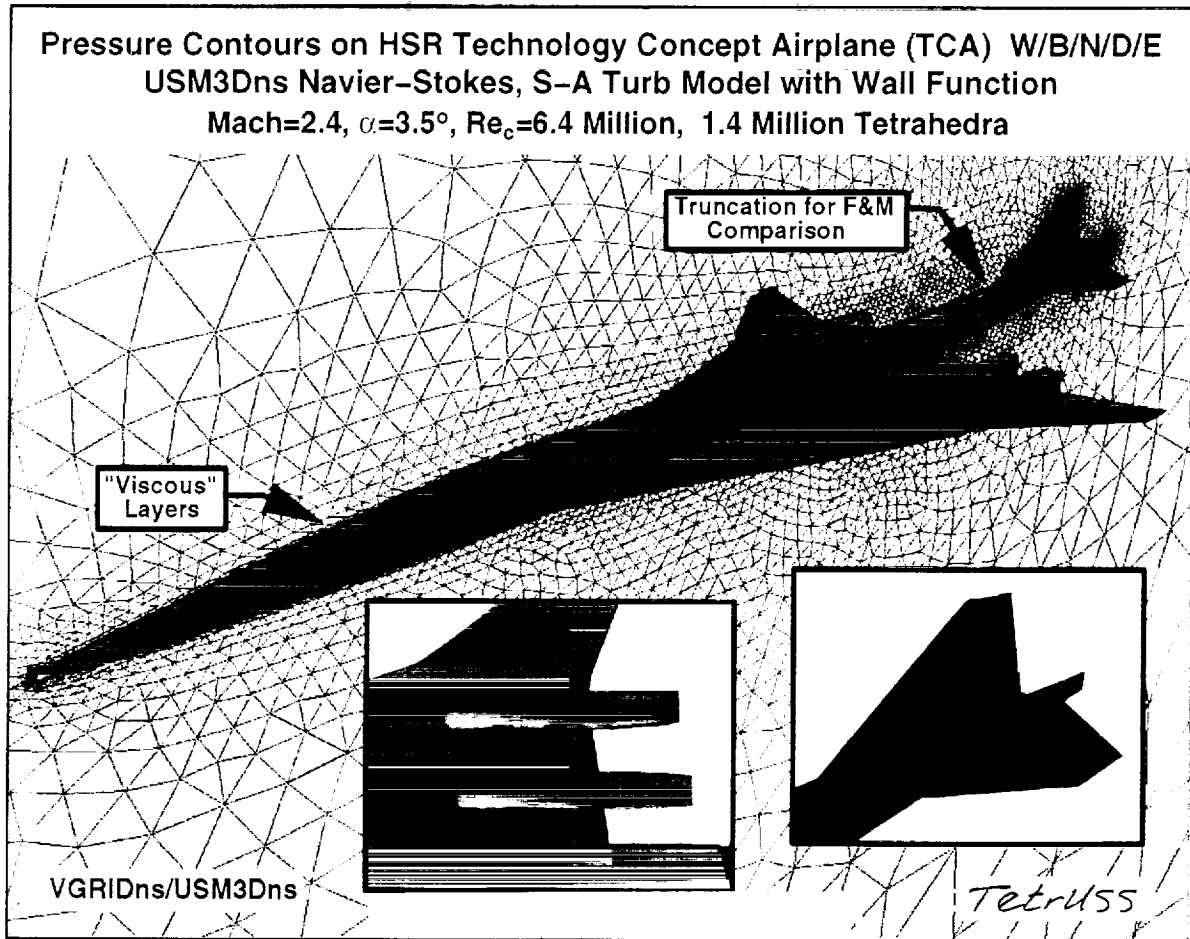
Supersonic solutions were run for three angles of attack at a wind-tunnel Reynolds number. Each solution was turned around in 4 hours wallclock time on the NAS Cray C90, once the job execution commences..



This slide shows the surface and symmetry plane triangulation for the configuration. Note the thin-layer viscous clustering along the fuselage/symmetry plane boundary. The nacelles were modeled as open flow-through channels as was constructed on the wind-tunnel model.



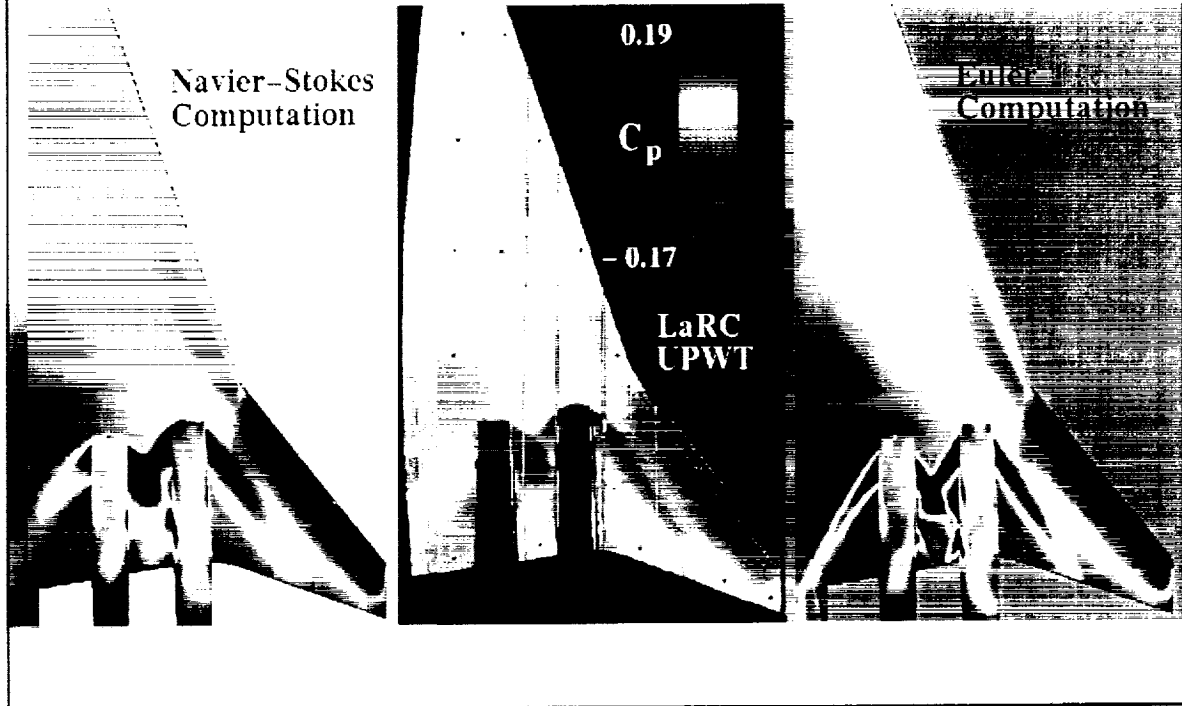
More detail is shown for the viscous tetrahedral grid on the TCA W/B/N/D/E. The view is looking aft along the under surface of the wing. The background are volume tetrahedra intersected by a plane cutting through the wing and nacelle/diverters. Note the thin-layered tetrahedra near the surface, and within the nacelle/diverter gap in the inset. Anisotropically stretched cells are also evident along the leading edge.



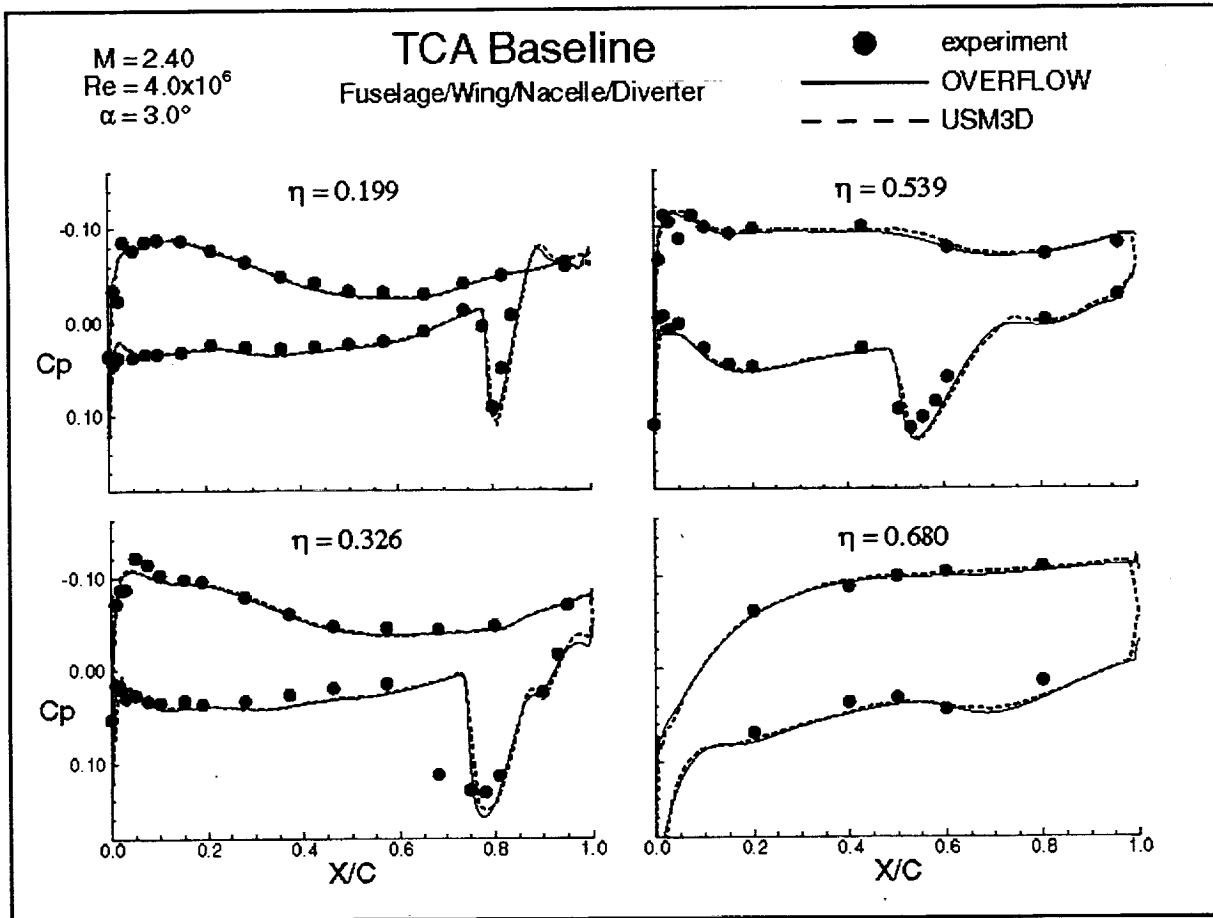
This slide displays the surface pressure contours at Mach=2.4 and angle-of-attack=3.5°. Details of the shock interactions between the nacelles and on the empennage are shown in the insets. The viscous layers are evident in the symmetry plane grid.

While the computations were performed on the full W/B/N/D/E configuration, a separate force and moment integration was also obtained on the truncated geometry ahead of the "blue" section. This integration corresponds to the UPWT Test 1671 TCA W/B/N/D model geometry. Since the computation was performed at Mach=2.4, the effect of the empennage will not be felt in the truncated integration, thus, enabling direct correlations with experiment to be performed.

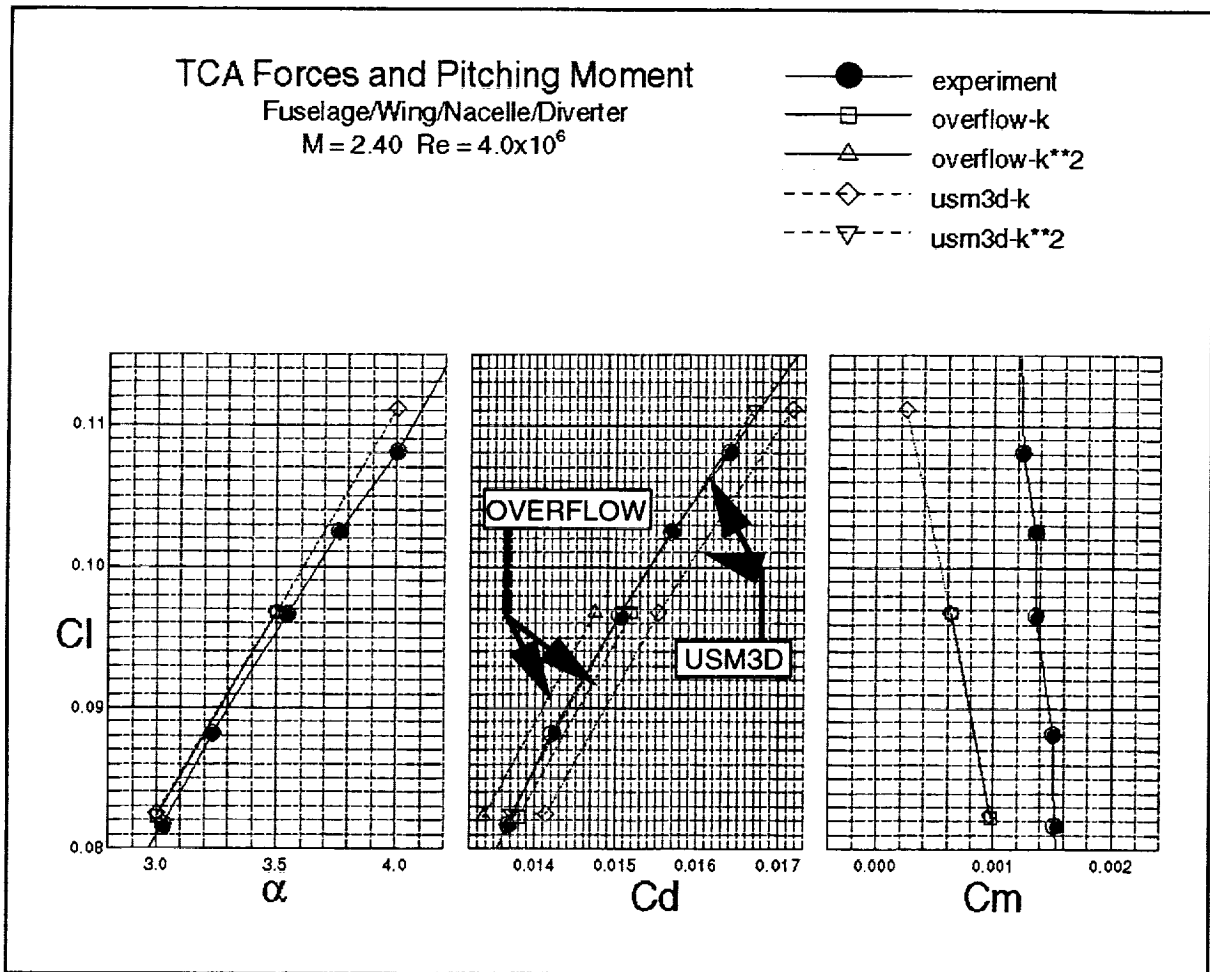
Surface C_p Prediction for the Complete TCA and Correlation with PSP
Unstructured Grid Method (TetrUSS); $M = 2.4$, $\alpha = 3.5$, $R_{\eta} = 4 \times 10^6$



A qualitative correlation of surface pressure is shown between the Navier-Stokes TetrUSS solution and experimental Pressure-Sensitive Paint (PSP) data obtained from UPWT. The colors of the PSP data are modified to closely match that from the computations. Note that the shock structures in the Navier-Stokes computation is in excellent qualitative agreement with the PSP data. An Euler computation result is also included for reference to illustrate the necessity for full Navier-Stokes modeling. The Euler result exhibits the stronger and sharper shock structures expected for inviscid flows.



This slide shows four longitudinal C_p distributions at span stations from 20- to 68-percent semispan. A comparison with an established structured-grid code, OVERFLOW, is also included. The general agreement of the computations with experimental data are good. The agreement between the unstructured USM3D and structured OVERFLOW solutions is also very good. This figure helps to establish more confidence in the relatively new unstructured Navier-Stokes methodology.



This slide presents a comparison of structured and unstructured force and moment solutions with experimental data from UPWT Test 1671. Examining the CL vs. alpha and CL vs. CM comparisons first, note that both the OVERFLOW and USM3D results agree very well with each other, but neither agree with the data. It has been demonstrated in structured-grid calculations by Boeing Long Beach that the disagreement with the data is due entirely to aeroelastic effects. Furthermore, the effect of aeroelasticity on CL vs. CD is only to slide the data point along the curve. Thus, comparisons can be made for drag using the present rigid configuration results.

The force and moment results include corrections for nacelle base pressure. Trip-drag corrections are not included in the experimental data, but are added to the computational drag by two approaches; the k and k -squared methods. The configuration drag is predicted by both the structured and unstructured flow solvers to within the tolerance of the trip-drag correction. The USM3Dns drag estimate falls directly on the data for the three angles of attack with the k -squared correction, whereas the OVERFLOW estimate is very close with the k correction.

Concluding Remarks

- Evaluated the *TetrUSS* unstructured-grid codes for the Navier-Stokes analysis of full TCA W/B/N/D/E at supersonic cruise conditions
 - constructed pure tetrahedral, viscous grid with VGRIDns
 - solved N-S equations with wall function coupled with S-A turbulence model
 - partial integration of pressures for comparison with UPWT data
- Demonstrated accuracy and robustness for tetrahedral-based N-S
 - grid generation from scratch in 7 to 10 days
 - resource requirements and accuracy comparable to structured code
 - good agreement with PSP, pressure, and F&M data, and with OVERFLOW structured-grid code

The presented results have demonstrated the strong potential of the unstructured Navier-Stokes capability of *TetrUSS* for accurately computing the force and moment characteristics of the full TCA configuration. The primary advantages of this technology is the rapid grid generation on the order of days, and modifications within hours.

Future TetrUSS Capabilities

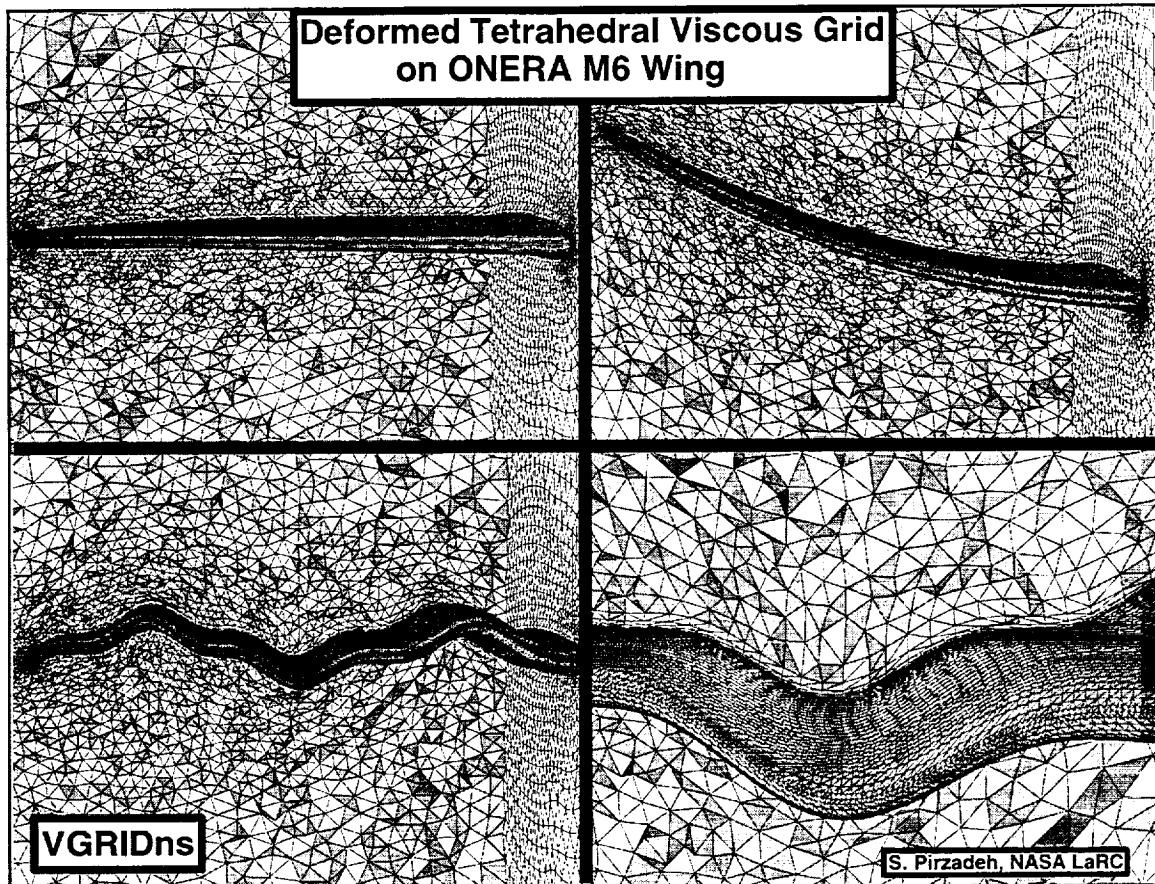
- Advanced two-equation turbulence models (Started Nov. 1997)
- Solution adaptive grids (Started Oct. 1997)
- Aeroelastic Navier–Stokes (In progress)
- Customer requested, but not scheduled
 - low Mach number preconditioning (needed soon)
 - incompressible
 - time accuracy
 - moving grids
 - wake capturing

Work is currently underway to implement linear and non-linear k-epsilon turbulence models into USM3Dns. The models have been installed and are undergoing testing.

Work is also progressing toward a solution adaptive grid capability. While initial results are forthcoming, this capability should mature over the next year.

Progress is being made toward aeroelastic Navier–Stokes capability. The missing piece is the viscous grid movement scheme. More will be said about this on the next slide.

There have been a number of customer requests for important additional capability which have not been pursued due to limited resources.



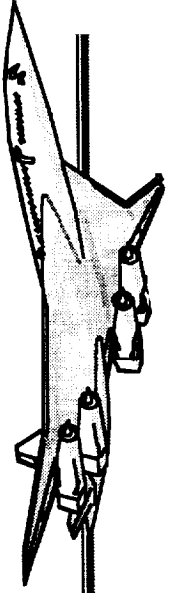
As stated in the previous slide, the only missing component in the *TetrUSS* aeroelastic process is the methodology for deforming 'viscous' grids. An approach has been developed which permits significant arbitrary movement while maintaining the integrity of the original viscous layers.

This is illustrated for the ONERA M6 wing in the slide. The volume grid is visualized using tetrahedra intersected by a plane which intersects the midchord of the wing. This is useful for the qualitative assessment of the effects of deformation on the thin-layered cells. Note that for the wing in bending or arbitrary deformation the cells are well behaved and of high quality. This advancement is relatively new and will be tested with USM3Dns in the near future.

This page is intentionally left blank.

HSR

High Speed Research



**Configuration Aerodynamics ITD Team
Year End Technical Review**

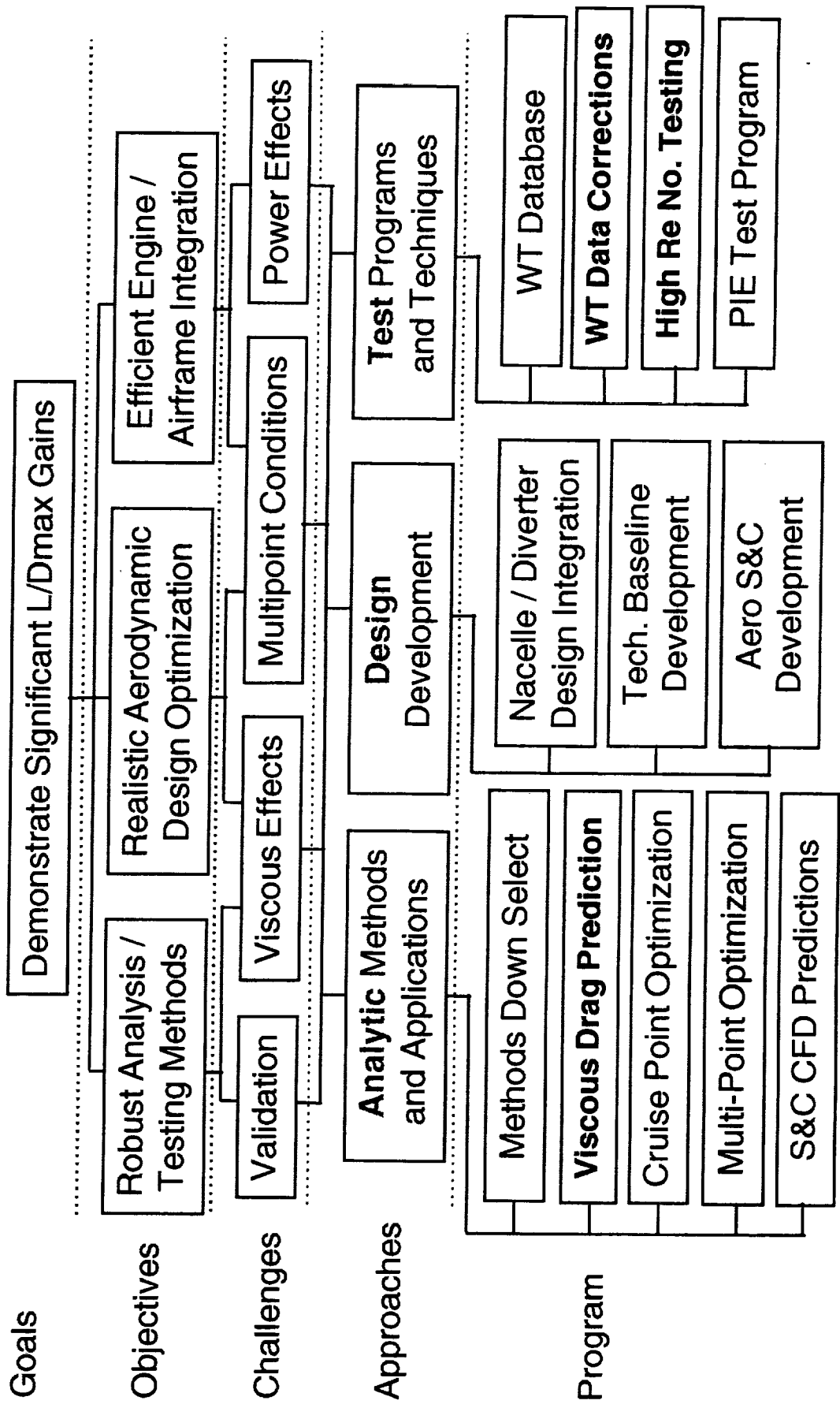
February 9 - 11, 1998

Session 2: Viscous Drag Predictions and Testing Methods

Session Chairman: Robert Kulfan

Configuration Aerodynamics Technology Development

Session 2: Viscous Drag Predictions and Testing Methods



Configuration Aerodynamics Technology Development

Viscous Drag Predictions : ISSUES AND NEEDS

- Accurate predictions of CF are required to validate total drag predictions of HSCT configurations
- CFD predictions of CF differ between codes and vary with the different turbulence models.
- Need to validate extrapolation of wind tunnel drag levels to full scale conditions
- Need quality test data to support CF prediction validation studies

Configuration Aerodynamics Technology Development

Testing Methods: ISSUES AND NEEDS

- Assess, improve, control wind tunnel data accuracy
- Trip technique to simulate full scale conditions in low Reynolds No. W.T.
- Trip technique and trip drag corrections for WT evaluation of high performance wing designs.
- Validated internal drag correction method for simple flow through nacelles
- Evaluate the use of calibrated nacelles for internal drag corrections
- Wind tunnel to wind tunnel data comparisons. Do we get the same results?
- Understand effects of model aeroelastics on WT test data? Do we need to correct the test data?
- Improved flow visualization techniques to determine transition location, and to determine if a trip is effective
- Unique testing methods (eg. PIE, Aft-body closure)

NASA Ames Research Center

**Skin Friction Drag Predictions: Summary
of CFD Cross Checks, Wing/Body**

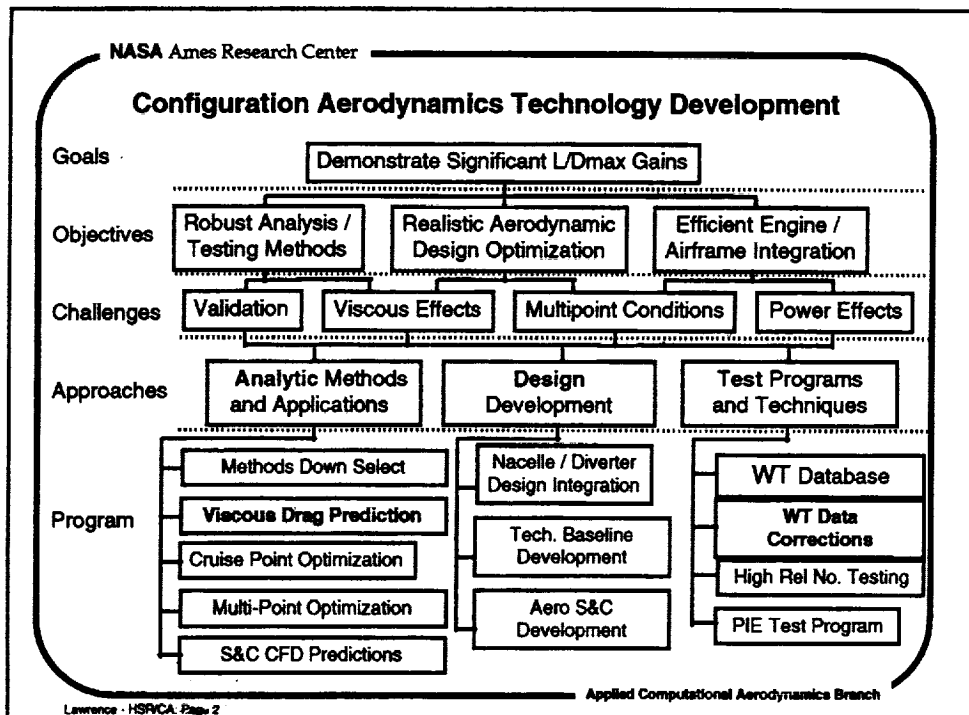
Scott Lawrence and Goetz Klopfer

NASA Ames Research Center

**HSR Airframe Technical Review
Los Angeles, CA
February 9-13, 1998**

Applied Computational Aerodynamics Branch

A summary of skin friction drag predictions computed for the TCA and three optimized wing/body configurations during the analytical cross-checks exercise is presented.



This work pertains mainly to the prediction of skin friction drag, but also involves the evaluation of CFD methods and processes for skin friction drag prediction.

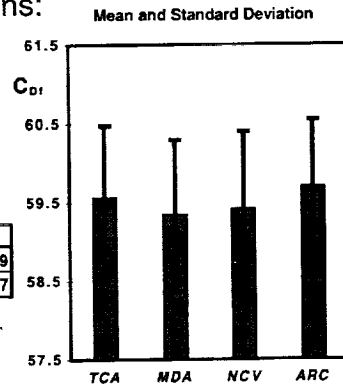
Introduction

➤ **Basic skin friction drag questions:**

- Accurate absolute predictions?
- Accurate trends?

➤ **All available W/B CFD results:**

	<i>TCA</i>	<i>MDA</i>	<i>NCV</i>	<i>ARC</i>
C_f	59.56	59.34	59.42	59.69
σ	0.93	0.97	0.99	0.87



➤ **Approach:**

Identify and quantify sources of skin friction variations using UPS and OVERFLOW codes

Applied Computational Aerodynamics Branch

The objective of the present study was to address the questions of: 1) how reliably or consistently the Navier-Stokes methods and processes used by the various organizations can predict integrated skin friction drag, and 2) how well the methods can predict trends within a family of optimized configurations.

As a first step, all available skin friction drag predictions were accumulated to obtain a mean and standard deviation for the TCA baseline and each of the optimized configurations. It is observed that the optimization process has had little effect on the predicted skin friction drags. The variation in the mean that is observed is dwarfed by the standard deviations.

In order to understand the reasons for the relatively large spreads in the computed results, a number of auxiliary computations have been performed using the UPS and OVERFLOW codes in an effort to identify and quantify potential sources of the variations.

Solution Methods

Type	Code	Organization	Tinf	Turbulence
CFD	UPS	ARC	151	BL
CFD	CFL	Boeing-LB	151	BL
CFD	UPS	ARC	217	BL
CFD	OVERFLOW	ARC	217	SA92
CFD	UPS	ARC	151	SA92
CFD	UPS	ARC	217	SA92
CFD	OVERFLOW	ARC	217	SA93
CFD	UPS	ARC	151	SA93
CFD	UPS	ARC	217	SA93
CFD	OVERFLOW	Boeing-Seattle	151	SA93
	Scimmer-Short	ARC	ALL	Flat Plate
	van Driest II	ARC	ALL	Flat Plate

► Nomenclature

- Turbulence model:
 - BL: Baldwin-Lomax
 - SA92: Original Spalart-Allmaras
 - SA93: Modified S-A (w/ fv3 term)
- Freestream temperature, Kelvin

All of the solution approaches accounted for in this study are shown in this table, along with two well known flat plate methods. Three turbulence models are used in the various methods: Baldwin-Lomax, the original Spalart-Allmaras one-equation model, and the modified Spalart-Allmaras model. The NASA Ames solutions were originally computed with an erroneous (with respect to the wind tunnel test) freestream temperature.

Significant Friction Drag-Related Parameters

- > Grid
 - Surface-normal grid stretching can affect
 - Finite-difference flow solver (OVERFLOW needs $GF = 1$ at wall)
 - Any post-processor
 - Surface-normal spacing ($y^+ < 1$)
 - Number of surface-normal grid points in boundary layer (30-40 pts)
- > Turbulence model
- > Freestream temperature

During our experience analyzing these types of configurations, several numerical parameters affecting predicted skin friction drag have become evident. These include, of course, a number of grid-related parameters, such as stretching factor at the wall, wall-normal spacing at the wall, and total number of grid points in the boundary layer. Of these, only the first will be discussed at any length in this paper. The others have been discussed in earlier papers and/or are well understood and the methods involved in this study were fairly consistent in choosing these parameters.

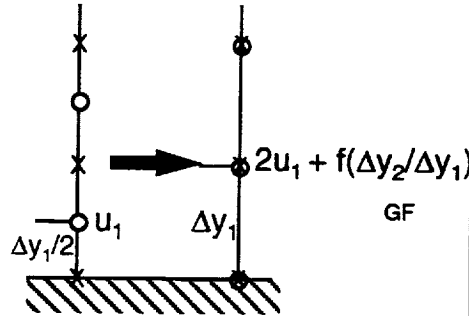
The next most important parameter observed in these computations is the choice of turbulence model. This will be discussed at some length here.

Finally, the freestream temperature was observed to be somewhat more important than expected.

Grid Effect on Post-Processing, UPS

- > Errors are introduced by using averaged variables

- > Example:
GF = 1.1 \Rightarrow $\Delta C_{Df} = 3.5\%$



- > Non-averaged UPS friction drag estimates are approximately 2 counts higher than averaged (W/B)

Grid stretching at the surface has been known for some time to affect the prediction of skin friction by finite-difference codes such as OVERFLOW. Recently, a significant error was discovered in the post-processing for skin friction of the finite-volume code UPS. The error was introduced through the use of solution variables that had been averaged onto the primary grid points. For example, a grid with a growth rate at the wall of 10% was observed to introduce a 3.5%, or 2 counts, error in integrated skin friction drag. All UPS results presented in this paper have been computed based on non-averaged solution variables.

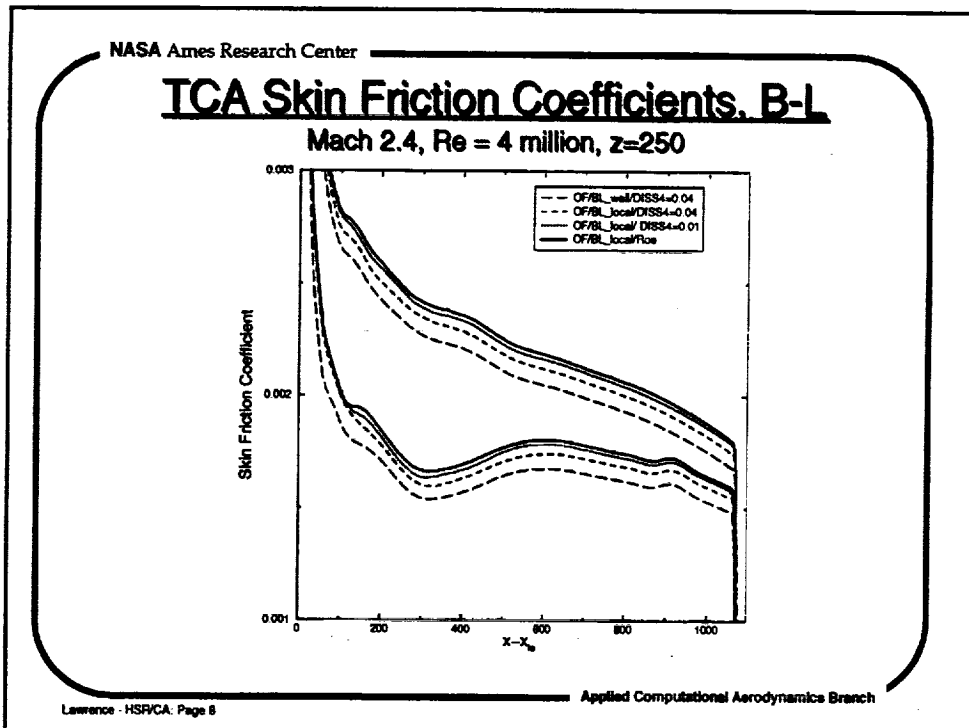
Turbulence Model Sensitivities

Model	Parameter
Baldwin-Lomax	Algorithm Dissipation
Spalart-Allmaras, Modified (SA93)	Re, Grid
Spalart-Allmaras, Original (SA92)	Grid

Applied Computational Aerodynamics Branch

Lawrence - HSRCA: Page 7

Results of the TCA cross checks as well as flat plate test cases have indicated these sensitivities of the Baldwin-Lomax algebraic and Spalart-Allmaras one-equation turbulence models. As will be described, the Baldwin-Lomax model was observed to be especially sensitive to algorithm dissipation, and the Spalart-Allmaras model appears to be somewhat more sensitive to grid coarseness. Most importantly, the modified S-A model has been observed to be difficult to trip to full turbulence at low Reynolds numbers. This effect is significant at wind tunnel Reynolds numbers.



The sensitivity of the Baldwin-Lomax model to algorithm dissipation is displayed in this figure. Chordwise skin friction coefficients for the TCA configuration computed from four different OVERFLOW solutions are shown. The solutions were computed using: 1) the baseline Baldwin-Lomax model with the default OVERFLOW dissipation model (scalar dissipation with $DIS2 = 2$, $DIS4 = 0.04$), 2) a B-L model modified to include compressibility effects by simply evaluating y^+ using local flow properties and the default OVERFLOW dissipation, 3) the compressible Baldwin-Lomax model with a reduced value of $DIS4 = 0.01$, and 4) compressible Baldwin-Lomax with the Roe upwind scheme. The Baldwin-Lomax model is quite sensitive to the overshoot in the velocity profile that is associated with the scalar dissipation model in OVERFLOW. As the overshoot is reduced, the turbulence length scale produced by the model is increased, as is the computed skin friction. In terms of integrated skin friction drag, a spread of approximately four counts of drag is observed.

Spalart-Allmaras Production Terms

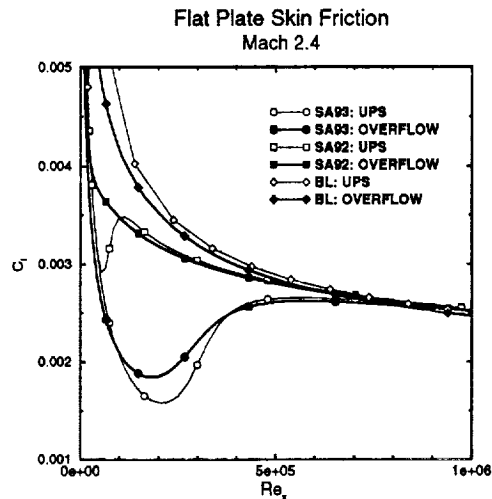
➤ Original Model:

$$S' = S + \nu f_{v2}/(\kappa d)^2$$

➤ Modified Model:

$$S' = f_{v3}S + \nu f_{v2}/(\kappa d)^2$$

- positive S'
- more robust
- better convergence
- delays onset of fully turbulent flow



Lawrence - HSR/CA, Page 9

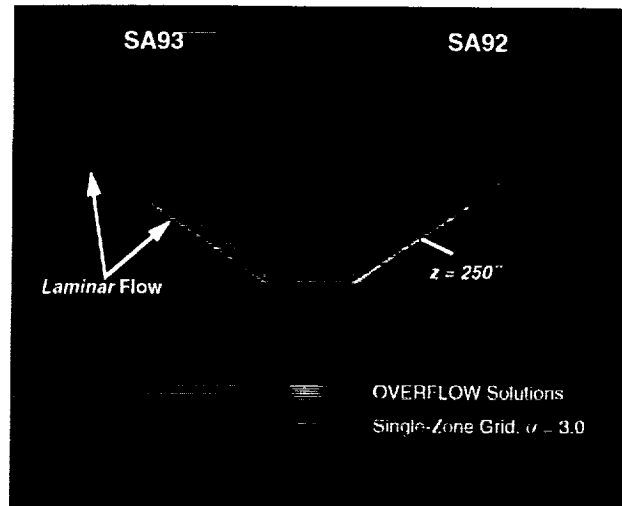
Applied Computational Aerodynamics Branch

The Baldwin-Lomax model sensitivity is somewhat moot, because the only solutions computed during the cross-check exercise using the Baldwin-Lomax model were computed using upwind schemes which should preclude the types of errors displayed in the previous slide. However, the Spalart-Allmaras sensitivities were observed to be important sources of uncertainty in the computed skin friction drags.

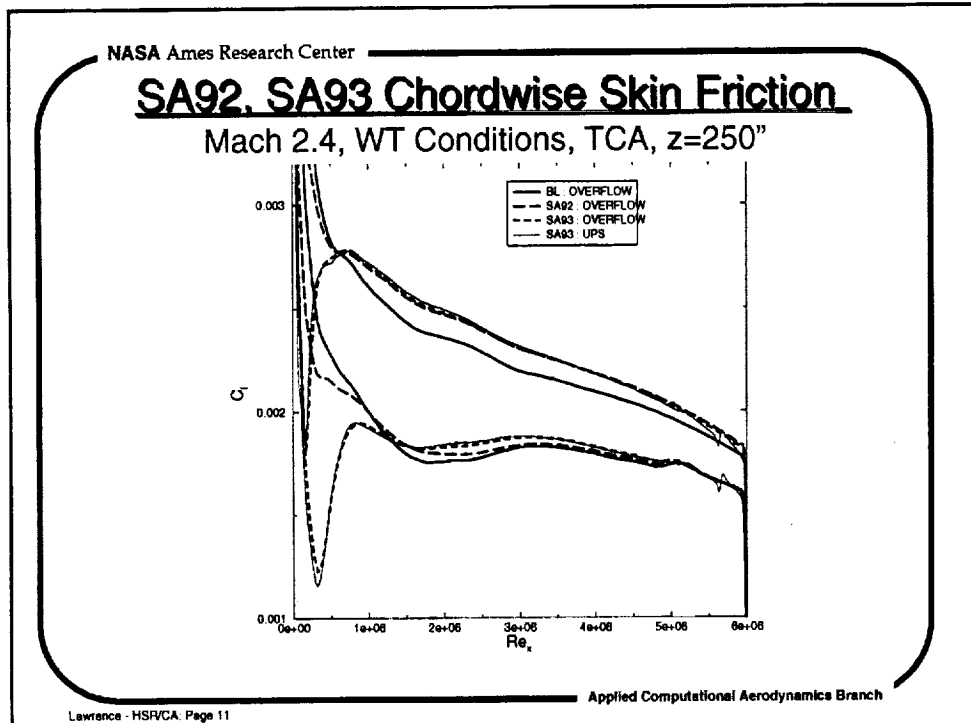
The tendency of the modified model to damp turbulence at low Reynolds numbers is shown in the figure to the right. Results from both UPS and OVERFLOW are shown as computed on substantially different grids. The effect is observed to be relatively implementation-independent as well as grid insensitive. The original model is observed to be essentially fully turbulent from the leading edge. The modification was originally developed to improve the robustness of the model by insuring that the production term remained positive throughout the boundary layer profile.

SA92, SA93 Skin Friction Distributions

Mach 2.4, WT Conditions, TCA



The upper surface of the TCA wing/body is mapped by local skin friction coefficient in this figure. A streak of relatively laminar-like skin friction is observed to run nearly the entire length of the wing leading edge. A streak is also present on the lower surface but is somewhat narrower. The black lines indicate a spanwise station of $z=250$ inches (full scale).



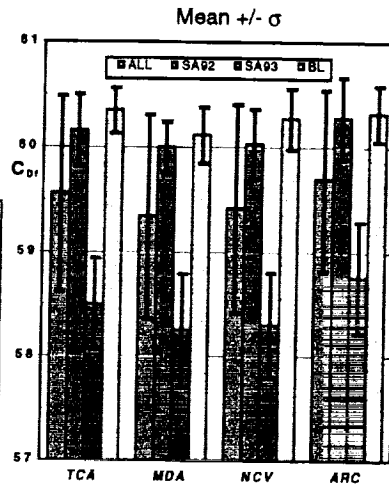
Chordwise skin friction distributions are shown for the z=250" spanwise cut as computed with OVERFLOW using the Baldwin-Lomax model, the original Spalart-Allmaras model (SA92), and the modified Spalart-Allmaras model (SA93). In addition, UPS results computed using the SA93 model are included to, again, indicate the implementation-independence of the effect. The region of laminar-like skin friction is observed to be quite sizable, and is comparable, in terms of Reynolds number, to that observed in the flat plate case. The difference in the size of the laminar run between the upper and lower surfaces is exhibited here.

Turbulence Modeling: Integrated Drag

WT Conditions, Mach 2.4

- SA93 consistently 1.5-2 cts below other models
- Consistent trends, SA93 shows slightly more variation

	Configuration			
C_{Df}	59.56	59.34	59.42	59.69
C_{Df}	60.16	60.00	60.03	60.22
C_{Df}	58.51	58.26	58.31	58.76
C_{Df}	60.36	60.12	60.27	60.33



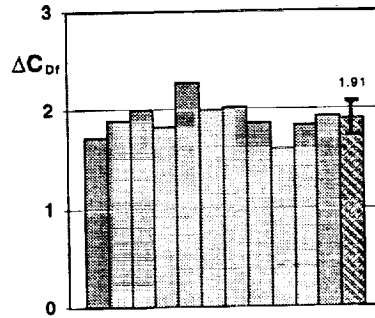
Lewrence - HSR/CA Page 12

Applied Computational Aerodynamics Branch

This figure shows the effect of turbulence model on integrated skin friction drag on each of the four wing/body configurations. Here it is seen that the SA93 model produces friction drag predictions consistently 1.5-2.0 counts lower than those produced by the other, "fully turbulent", models. This characteristic is shown to be responsible for much of the spread observed in the solutions. Results for each turbulence model show deviations less than half of the global values, except for some results of the SA93 model, which are slightly more than half. In addition to showing more deviation for each configuration, results obtained with the SA93 model show somewhat more sensitivity to configuration than those obtained with the other models. This is, perhaps, to be expected because the transition location appears to be at least a little bit sensitive to local flow conditions.

Laminar Flow Correction

- OVERFLOW and UPS solutions, all configurations
- Laminar flow effect evaluated for each case
 $\Delta C_{Df}^L = C_{Df,SA92} - C_{Df,SA93}$
- UPS tends to predict slightly higher laminar flow effect
- Results (function of Re_L):
 - Mean = 1.91cts
 - Std Dev = 0.16 cts



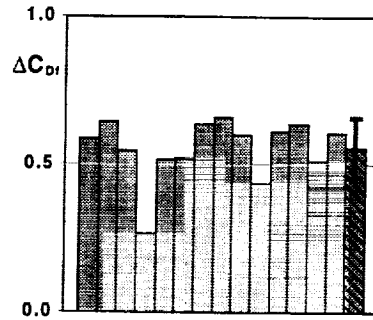
Code	Tin1	TCA	MDA	NCV	ARC	All Configs
OVERFLOW	217	1.72	1.83	1.94	1.60	1.77
UPS	217	1.89	2.28	2.03	1.85	2.01
UPS	151	2.01	2.00	1.87	1.91	1.95
						1.91
						0.16

Applied Computational Aerodynamics Branch

In order to simplify comparison of the various results, it was thought to be useful to obtain an estimate of the average laminar run-related friction drag decrement. This was done by performing dual sets of computations where only the turbulence model was varied between the two. The difference in skin friction drag was determined for each matching pair. These changes in CDf are shown in the bar chart to the right and in the table at the bottom of this chart. UPS results tended to predict a slightly higher effect (slightly longer laminar runs) than OVERFLOW.

Temperature Corrections

- > UPS solutions for all configurations, all turbulence models
- > OVERFLOW spot checks
- > Freestream T effect evaluated for each case
 $\Delta C_{Df}^T = C_{Df,151} - C_{Df,217}$
- > Results:
 - Mean = 0.56 cts
 - Std Dev = 0.1 cts



Temperature Variation	TCA	MDA	NCV	ARC	All Configs
OVERFLOW SA92		0.59		0.61	0.60
UPS BL	0.52	0.65	0.66	0.64	0.61
UPS SA93	0.52	0.55	0.50	0.53	0.55
UPS SA92	0.64	0.27	0.44	0.80	0.49

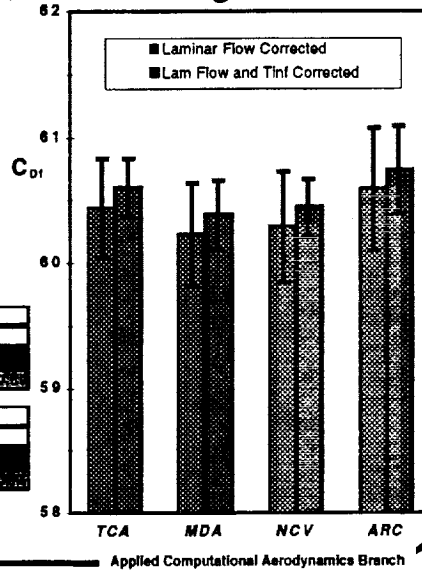
A similar procedure was applied to correct the Ames OVERFLOW results for the use of an incorrect freestream temperature. UPS solutions were computed for each configuration using each of the three turbulence models at $T_{inf}=151K$ and $T_{inf}=217K$. OVERFLOW computations were performed using the SA93 model for two of the configurations to spot check the UPS results. It was determined that slightly more than half a count of friction drag could be attributed to the use of the higher freestream temperature, with the lower temperature producing the higher friction drag coefficient.

Corrected Friction Drags

- Mean values for laminar flow and T_{inf} corrections added to all SA93 and $T_{inf}=217$ results, respectively
- Result: σ reduced by a factor of 3-4

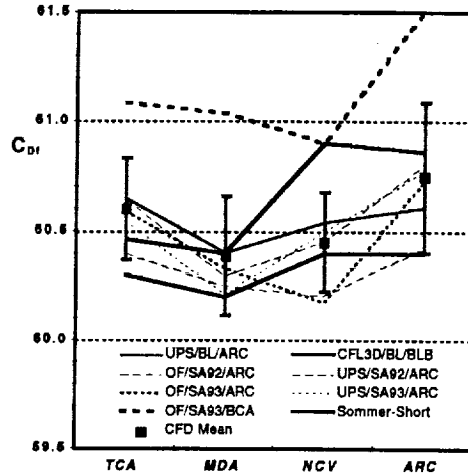
Laminar Flow Corrected				
	TCA	MDA	NCV	ARC
Mean C_{Df}	60.44	60.23	60.29	60.66
Std Dev	0.12	0.12	0.12	0.12

Laminar Flow and Temperature Corrected				
	TCA	MDA	NCV	ARC
Mean C_{Df}	60.60	60.38	60.45	60.78
Std Dev	0.04	0.04	0.04	0.04



The correction for laminar flow was added to each of the friction drag predictions produced by the SA93 turbulence model. The global average was then recomputed and the results are tabulated above and charted as the blue bars in the chart to the right. Note: the UPS results computed using the incorrect freestream temperature have been removed at this point. The temperature correction was then applied to the Ames OVERFLOW results and the final collection of friction drags was averaged and tabulated above and as the red bars the chart. The standard deviations obtained from this global average of corrected results is a factor of three to four lower than that of the raw data, and are now nearly at the same level as is observed for pressure drag.

Corrected Drags: All Solutions



Notes:

- OVERFLOW solution sets show different trends than UPS, CFL3D (NCV solutions)
- Boeing/Seattle OVERFLOW solution 0.3-0.5 cts outside σ
- Correlations (w.r.t. CFD Mean)

UPS/BL/ARC	0.787
CFL/BL/BLB	0.569
OF/SA92/ARC	0.894
UPS/SA92/ARC	0.988
OF/SA93/ARC	0.902
UPS/SA93/ARC	0.928
OF/SA93/BCA	0.873
Sommer-Short	0.376
Van-Driest	0.335

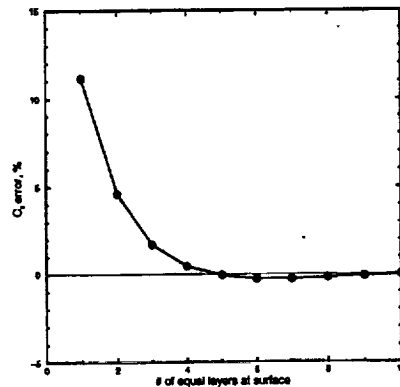
Each of the corrected solution sets are plotted here along with the global average (+/- one standard deviation), and the results of using the flat plate method of Sommer and Short.

OVERFLOW results can be seen to deviate somewhat from the results of UPS and CFL3D in terms of trends. Most noteworthy is the outlying result obtained at Boeing-Seattle using OVERFLOW. This will be discussed further in the next two slides. Correlations were computed for each solution set (i.e., each method applied to the configuration set) in an attempt to quantify the level of consistency to which the trends were predicted. The CFD solutions were observed to correlate better with each other than with the flat plate methods. This is thought to be an indication that the optimization process, though inviscid, is producing some skin friction improvements in an average sense, i.e., relative to total wetted area. The flat plate methods scale, to a large extent, with the surface wetted area.

Surface Normal Stretching Effects

- > "Glitch" in viscous terms associated with discontinuity in $y_{\xi\xi}$ (finite-difference, e.g., OVERFLOW)
- > Growth Factor, $gf > 1$ at the wall effectively creates discontinuity in $y_{\xi\xi}$
- > Effect on surface shear decays rapidly with y

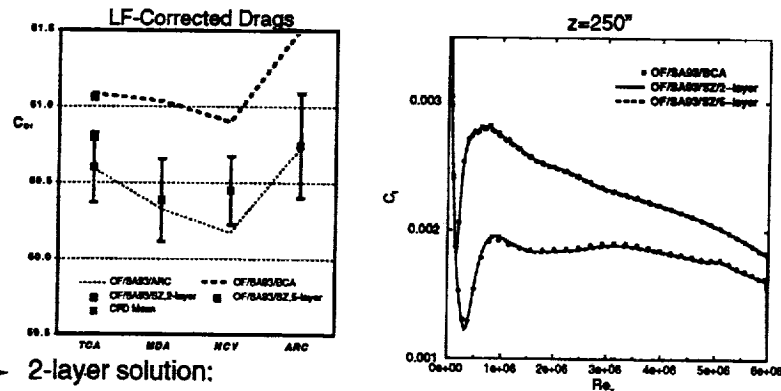
Skin Friction at $Re_x = 10^6$
Mech 2.4 Flat Plate Boundary Layer



Applied Computational Aerodynamics Branch

Lawrence - HSRCA, Page 17

Significant friction drag differences were observed between the OVERFLOW solutions generated at Ames and at Seattle using the same turbulence model, correcting for freestream temperature. Since similar algorithm parameters were used for the solutions, the difference in gridding is probably the source of the variance. It is known that OVERFLOW is very sensitive to wall stretching in the prediction of wall shear. This is illustrated in the figure above showing the skin friction coefficient at $Re_x = 1$ million for 10 different grids. The grids all have a stretching rate throughout the boundary layer of approximately 20%, but they differ in where the stretching begins. The horizontal axis indicates the number of equally spaced grid layers on the surface, starting with the case of stretching applied right at the wall. In this most extreme case, the skin friction is elevated relative to the 10-layer case by more than 11%. The predictions improve rapidly to where, with four equal layers, the prediction is within 1% of the "converged" result. It is believed that the Seattle solution was computed on a grid with three equally spaced layers at the wall. The character of this chart is thought to be fairly general, but the level of the errors is a function of Reynolds number.

Grid Stretching Effect on TCA W/BMach 2.4, WT Conditions, $\alpha=3.0$ 

► **2-layer solution:**

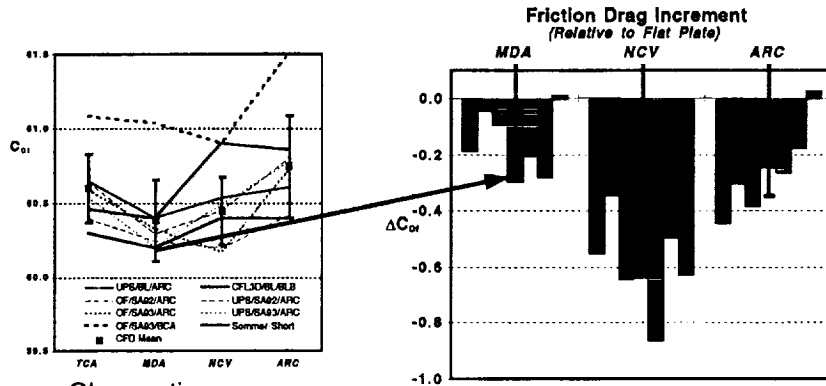
- slightly elevated local skin friction relative to 5-layer
- integrated drag increase is small but significant relative to σ
- very good agreement with Boeing-Seattle soln. in terms of local and integrated skin friction

Lawrence - HSPVA, Page 18

Applied Computational Aerodynamics Branch

To investigate the effect on a wing/body configuration, OVERFLOW was applied with a single-zone, C-O topology grid for the TCA. This grid was reclustered in two ways: with 2.5 equal layers and with 5.5 equal layers. The half indicates that the stretching ramps up to 20% over two cells, rather than jumping immediately, as do the grids of the other OVERFLOW solutions. Solutions were run using the SA93 model. The integrated skin friction drags for the two cases were corrected for laminar flow using the same correction used for the other SA93 results and are plotted above with the other OVERFLOW results. Local skin friction coefficients at the mid-inboard span station of $z=250$ " are plotted to the right for the single-zone solutions in comparison with the solution from Boeing/Seattle. The effect is small, but a discernible difference is observed, with the 2.5-layer case giving better agreement with the Seattle solution. The integrated drags, similarly, show a reduction with increased equal layers that is small, but is significant relative to the standard deviation. The grid used for the Seattle solution also had spacing at the wall that is generally 30% greater than that of the Ames solution. Finally, the Ames grid contains regions, especially near the wing/body intersection, that are anti-stretched, i.e., spacing decreases with distance from the wall, for a few points off the wall. This might be expected to reduce the local skin friction in these areas. These latter two effects have not been investigated, but are of a nature that, if resolved, would be expected to bring the OVERFLOW solutions closer together.

Increments and Trends



- > Observations:
 - NCV shows most improvement in skin friction relative to surface area.
 - N-S trends agree better with each other than with flat plate.
- > Conclusion:
 - Optimization can reduce skin friction to a level that is measurable by N-S.

Finally, in an effort to establish the extent to which the N-S codes can be relied on to predict trends, friction drag increments are plotted above. The bar chart shows the friction drag increments as differenced from the increment predicted by the flat plate method of Sommer and Short. The chart indicates that the NCV wing/body shows the most improvement, relative to flat plate, of the three configurations. In nearly all cases, the increments are large relative to the associated standard deviation of the friction drag predictions.

Summary

- N-S parameters relevant to friction drag prediction have been identified.
- N-S skin friction drag results have been accumulated and sorted by relevant parameters.
- "Corrections" have been developed for the laminar run associated with the SA93 turbulence model and for freestream temperature differences.
 - note: SA93 laminar flow correction is a function of freestream Re
- Corrected friction drags have been generated for "apples-apples" comparison.
- Trends evaluated based on corrected drags.

Various elements of the present study are outlined here. It should be highlighted that the correction to the SA93 results for laminar run is strictly Reynolds number dependent. At flight Reynolds numbers, the correction would be negligible.

Conclusions

- > N-S methods, carefully applied, can produce results that are consistent to within 0.5 counts.
- > This level of consistency is sufficient to predict general trends in average skin friction reduction generated by inviscid optimization.

Issues

- > Spalart-Allmaras transition
- > OVERFLOW "features"
 - sensitivity to wall stretching
 - matrix dissipation option

Conclusions based on the results presented here are stated above. The effects associated with the modified Spalart-Allmaras turbulence model appear to be sufficiently consistent that, by accounting for them through a laminar run friction drag correction, the various N-S methods produce results consistent to within +/- 0.35 counts. There appears to be potential for significant reductions in this value with further study of higher-order grid effects. As it stands, however, this value is lower than the friction drag improvements, relative to flat plate theory, that have been predicted by the N-S methods.

This page is intentionally left blank.



HSR Configuration Aero Final Review FY 97



HSCT High Speed Aerodynamics

TCA and Symmetric Model Viscous Drag Predictions

Max Kandula
Dynacs Engineering Co. Inc.
Renton, WA 98055

HSR Airframe Technical Review
Los Angeles, CA
February 9-13, 1998

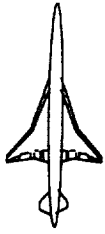


This page is intentionally left blank.



Acknowledgement

- Chris Vegter (Boeing HSCT)
 - Sym TCA loft, Flat plate integrated drag forces
- Steve Chaney (Boeing HSCT)
 - TCA baseline grids & solutions
- Bob Patton (Boeing HSCT)
 - local dynamic pressure computation approach
- David Kerlick (Boeing Information & Support Services)
 - drag.c program (local skin friction coefficient)
- Tim Haynes (Dynacs)
 - drag.c program mods : consulting



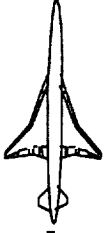
Objectives

A CFD analysis with the OVERFLOW code was carried out to determine the viscous drag for the symmetric TCA wing/body configuration (angle of attack $\alpha=0$ deg) at wind tunnel Reynolds number (Mach 0.7 through 2.4) and at flight Reynolds number (Mach 0.9 through 2.4). Detailed local and chordwise averaged skin friction coefficients were computed at two selected Mach numbers ($M=0.9$ and 2.4). The predicted viscous drag, local and averaged sskin friction coefficients were compared with the flat plate theories (based on two-dimensional boundary layer theories) of Sommer-Short and Frankl-Voishel. Skin friction coefficients were evaluated for the baseline TCA configuration at $M=0.9$ and $M=2.4$ at both flight and wind tunnel Reynolds number and corresponding to cruise angles of attack. The purpose of the study was to establish the accuracy of the flat plate skin friction theories for HSCT applications.



Objectives

- **Compute CFD viscous drag on Symmetric & Baseline TCA W/B**
 - range of Mach number (transonic & supersonic)
 - range of Reynolds number (flight & WT Re)
- **Compare CFD solutions with Flat Plate Theories**
 - component viscous drag (wing & body)
 - wing local skin-friction coefficient
 - wing chordwise-averaged skin friction coefficient
- **Assess Flat Plate Skin Friction Theory for W/B Configuration**
 - effect of Reynolds number
 - effect of Mach number
 - effect of local dynamic pressure
 - effect of pressure gradient
 - effect of flow three-dimensionality



Flow Conditions

For the skin friction study, OVERFLOW Navier-Stokes solution were obtained for the symmetric TCA at $\alpha = 0$ deg for both flight and wind tunnel Reynolds number over a range of freestream Mach number. The flight Reynolds numbers considered were 1.64×10^6 ($M=0.9$), 3.00×10^6 ($M=0.95$), 1.1×10^7 ($M=1.2$), and 1.97×10^7 ($M=2.4$). The wind tunnel Reynolds numbers included 5.57×10^6 ($M=0.7$), 6.04×10^6 ($M=0.9$), 6.2×10^6 ($M=1.07$), 1.2×10^7 ($M=1.5$), 1.8×10^7 ($M=2.1$), and 2.4×10^7 ($M=2.4$). The flight Reynolds numbers for the baseline TCA were 1.64×10^6 ($M=0.9$), and 1.95×10^6 ($M=2.4$). The wind tunnel Reynolds numbers for the TCA included 6.1×10^6 ($M=0.9$), and 6.4×10^6 ($M=2.4$).





Flow Conditions

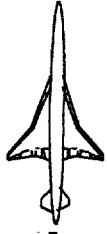
- Symmetric TCA at $\alpha=0$ deg
 - Mach Number: 0.7-2.4
 - Reynolds Number: $6E6-300E6$

- Baseline TCA at cruise α
 - Mach Number: 0.9 & 2.4
 - Reynolds Number: $6E6-195E6$



HSR Configuration Aero Final Review FY97

HSCT High Speed Aerodynamics



Approach

The necessary loft geometry for the symmetric TCA wing/body were obtained from Chris Vegter of Boeing HSCT. Based on this geometry, surface grids for the body and the wing were generated using AGPS. The AGPS command files developed for the TCA as obtained from Steve Chaney (Boeing HSCT) were modified for this purpose. Volume grids were then generated using HYPGEN code and PEGSUS code. The same surface grids were used for the generation of volume grids for both the flight Reynolds number and the wind tunnel Reynolds number. The wall spacing for the two Reynolds numbers were however different, and were based on the y^+ requirements for the flow resolution. The flow solutions were obtained from the OVERFLOW code with the Spalart-Allmaras (SA) one-equation turbulence model. Multi-gridding (three grids) procedure was employed to accelerate convergence. For the baseline TCA, the grids and the flow solutions corresponding to cruise angles of attack were obtained from Steve Chaney (Boeing HSCT Aerodynamics). These solutions were again based on the SA turbulence model, and multi-gridding.

36

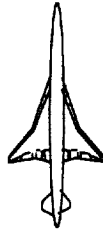
The local skin friction coefficients were based on either freestream dynamic pressure, or the local dynamic pressure. Skin friction coefficients based on the local dynamic pressure serve to more accurately correlate the flat plate theories, and identify the areas where local dynamic pressure effects are important. Local skin friction coefficient distributions were obtained with the aid of drag.c (c-language) program that has been acquired from David Kerlick of Boeing Information and Support Services. The local dynamic pressure was computed on the assumption that the surface cp computed by the viscous OVERFLOW solution is approximately the same as the local static pressure at the boundary layer edge, and that outside the boundary layer the flow is everywhere isentropic with the total pressure remaining constant. This approach (as suggested by Bob Patton of Boeing HSCT Aerodynamics) afforded a great simplification in quantifying the local dynamic pressure, and is quite convenient as compared to the estimation of boundary layer edge conditions for computing local dynamic pressure.

The two flat plate theories considered are those of Sommer-Short and Frankl-Voishel. The flat plate theories considered were based on the extension of incompressible formulations, and on adiabatic wall temperature.



Approach

- **OVERFLOW CFD Analysis**
 - Surface grids: **AGPS**
 - Volume grids: **HYPGEN & PEGSUS**
 - Turbulence model: **Spalart-Allmaras**
 - local friction coeff.: **drag.c program**
 - based on freestream dynamic pressure (qinf)
 - based on local dynamic pressure (qloc)
 - **local dynamic pressure: from computed surface cp**
 - constant cp inside the boundary layer
 - isentropic flow outside the boundary layer
 - $q_{loc}/q_{inf} = f(\gamma, Minf, cp) \rightarrow 1$ as cp $\rightarrow 0$
- **Flat Plate Theories (2-Dimensional flow, adiabatic wall)**
 - **Sommer-Short (1955) : iterative**
 - **Frankl-Voishel (1943) : non-iterative**



Skin Friction Study with Sym TCA

Surface and Volume Grids for the Sym TCA Wing/Body

The necessary loft geometry for the TCA symmetric TCA wing/body has been obtained from Chris Vegter of Boeing HSCT. Based on this geometry, surface grids for the body and the wing have been generated using AGPS (Boeing proprietary). The AGPS command files developed for the TCA as obtained from Steve Chaney (Boeing HSCT) have been modified for this purpose. The leading edge and trailing edge chordwise grid spacing for the wing were taken as 0.005 percent local chord and 0.5 percent local chord respectively.

Volume grids were built with the aid of HYPGEN hyperbolic grid generator. The communication between the volume grids was established by the help of PEGSUS code. The wake grids for the wing and the collar, originally obtained from HYPGEN hyperbolic grid generator, have been relaxed by SMOGRID smoothing routine. This figure shows the surface grid for the symmetric TCA wing/body. This figure shows the wing/body surface grid for the symmetric TCA

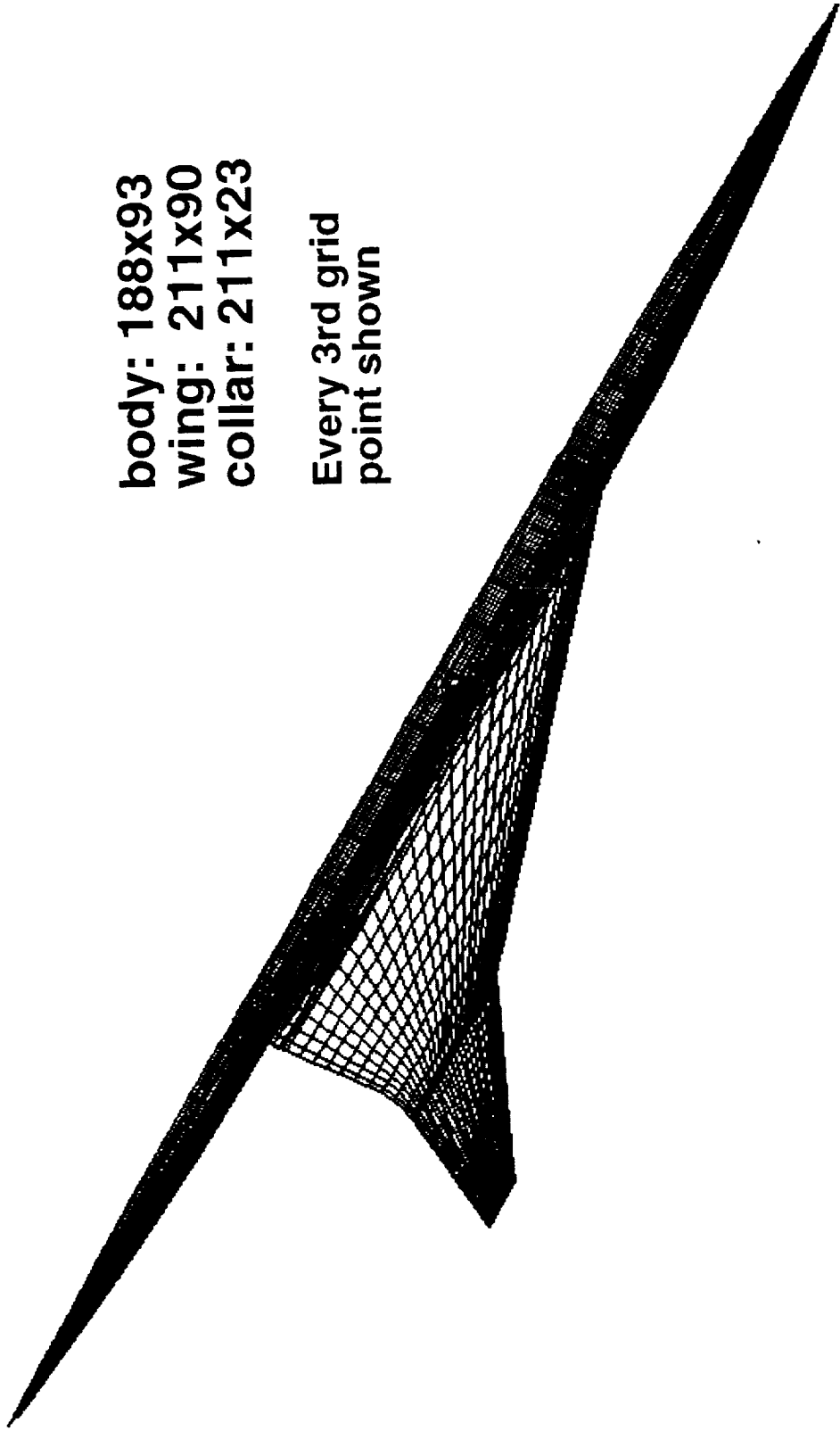
For the flight Reynolds number volume grid system, the first cell distance from the wall was taken as 0.0006 in to provide a value of $y^+=1$ at $M=2.4$. This resulted in values of $y^+=2$ at $M=0.9$, and $y^+=$ about 3 for the Mach number range of 0.95 to 1.8. In the case of wind tunnel Reynolds number, the first cell distance was taken as 0.0004 in (full scale), so that the y^+ values were 0.3 at $M=2.4$ and 0.7 at $M=0.7$.



Symmetric TCA Wing/Body Surface Grid

body: 188x93
wing: 211x90
collar: 211x23

Every 3rd grid
point shown

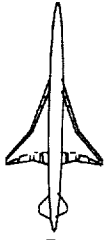




BOEING

HSR Configuration Aero Final Review FY97

HSCT High Speed Aerodynamics



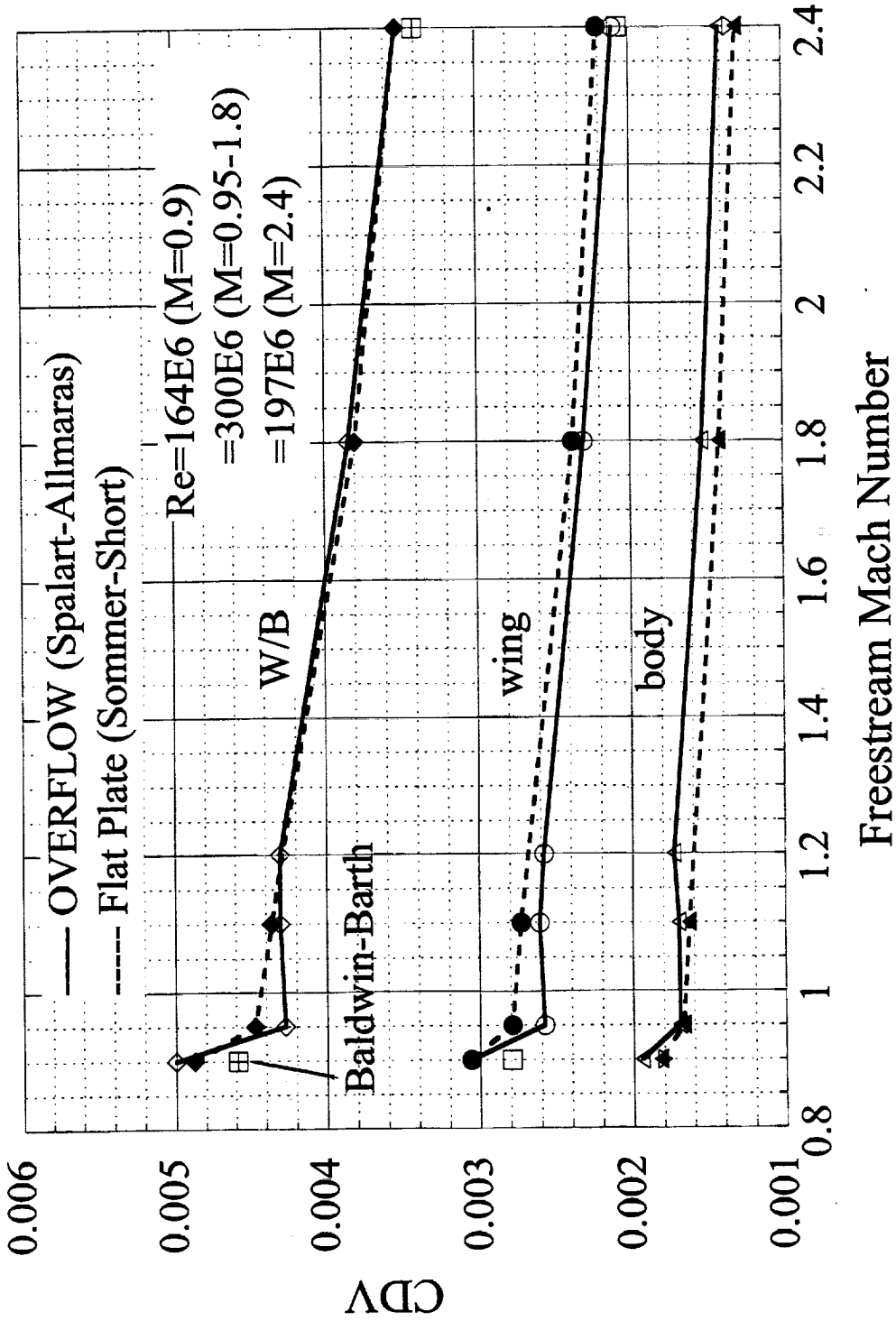
Comparison of Sym TCA Skin Friction Drag at Flight Reynolds Number

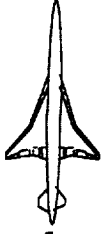
OVERFLOW solutions with the Spalart-Allmaras (SA) one-equation turbulence model have been obtained for the symmetric TCA skin-friction drag at flight Reynolds number for freestream Mach numbers of 0.9, 0.95, 1.1, 1.2, 1.8, and 2.4. The corresponding flight Reynolds numbers are 164E6 at $M=0.9$, 300E6 at $M=0.95$, 1.1, 1.2 and 1.8, and 195E6 at $M=2.4$. In order to understand the sensitivity of the viscous drag with respect to the turbulence model considered, some additional solutions have been obtained with the Baldwin-Barth (BB) one-equation turbulence model at two selective Mach numbers ($M=0.9$ and 2.4).

Shown here is a comparison of the skin-friction drag from OVERFLOW and the flat plate theory (Sommer-Short) at flight Reynolds number. The flat plate drag predictions were provided by Chris Vegter of Boeing HSCT Aerodynamics. At flight conditions, the OVERFLOW solution with the SA model agrees well with the flat plate theory over the entire Mach number range (except at $M=0.95$). The difference in the component viscous drag from the two methods is within one count in the entire Mach number range, except at $M=0.95$ where the departure is about two counts. In general except at $M=0.95$, the body viscous drag from OVERFLOW is about one count higher than that from the flat plate theory, and the wing viscous drag one count less than that from the flat plate theory. The total viscous drag for the wing-body combination from the two methods is also within one count except at $M=0.95$. The total viscous drag from the BB model is seen to match that from the SA model at $M=2.4$, but is considerably below that from the SA model (by 4 cts) and the flat plate theory (by 3 cts) at $M=0.9$. The difference at $M=0.9$ is primarily due to departures in the predicted viscous drag for the wing.



Sym TCA Skin Friction Drag at Flight Reynolds Number





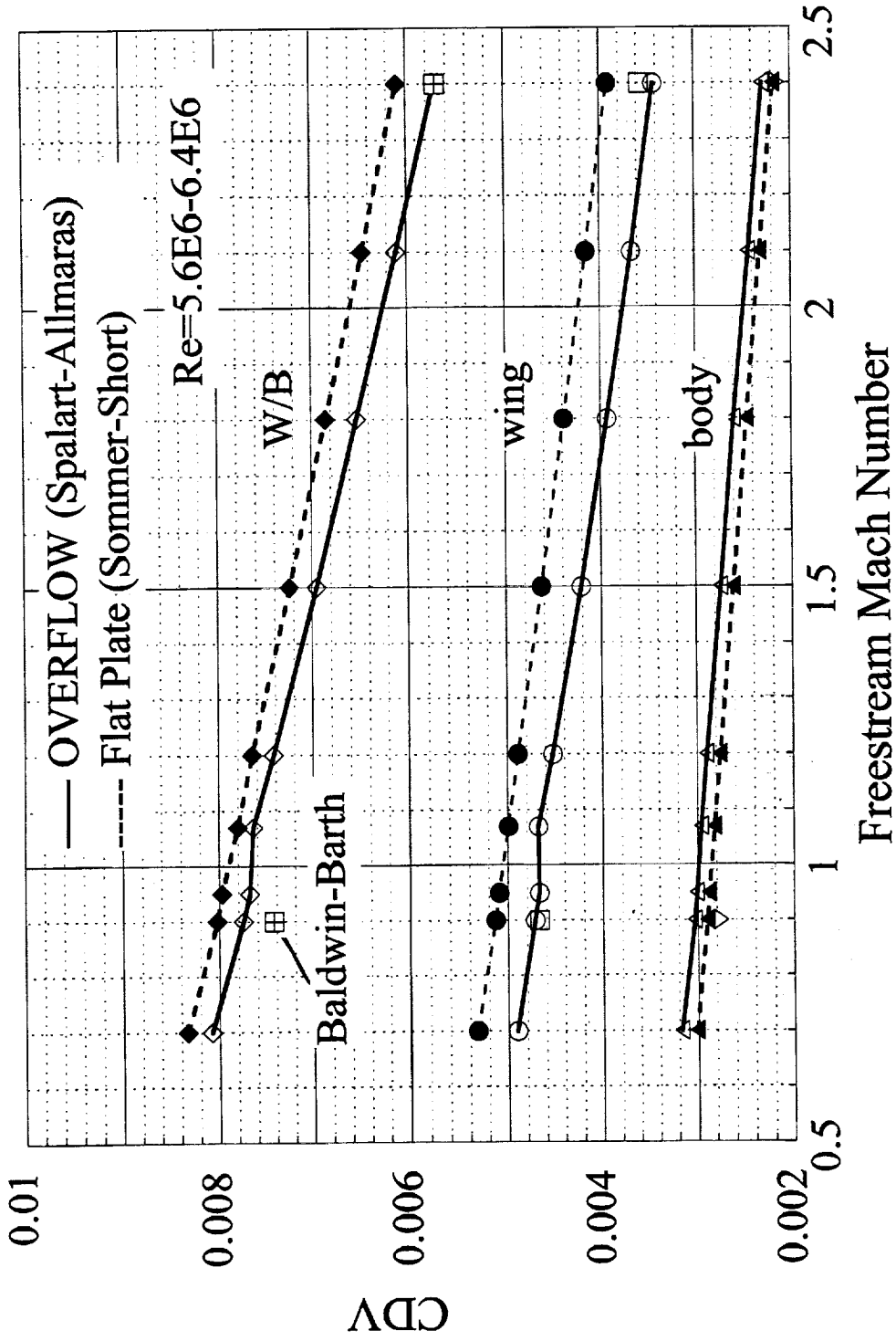
Comparison of Sym TCA Skin Friction Drag at Wind Tunnel Reynolds Number

Symmetric TCA viscous flow solutions from OVERFLOW with Spalart-Allmaras (SA) one-equation turbulence model at the wind tunnel Reynolds number of 6E6 have been obtained. These solutions correspond to various Mach numbers in the range of $M=0.7$ through 2.4 ($M=0.7, 0.9, 0.95, 1.07, 1.2, 1.5, 1.8, 2.1$ and 2.4), and complement those at flight Reynolds number. In order to understand the sensitivity of the viscous drag with respect to the turbulence model considered, some additional solutions have been obtained with the Baldwin-Barth (BB) one-equation turbulence model at two selective Mach numbers ($M=0.9$ and 2.4).

This plot shows a comparison of the OVERFLOW solutions and the flat plate theory at the wind tunnel Reynolds number. The total wing/body viscous drag from the OVERFLOW code with the SA model is about three to four counts below the flat plate theory over the entire Mach number range studied ($M=0.7$ to 2.4). The solution with the BB model for the total viscous drag is seen to be close to that with the SA model at $M=2.4$, but at $M=0.9$ is about four counts below that from the SA model, and six counts below the flat plate theory. The component comparisons suggest that the SA model yields wing viscous drag that is about four to five counts below the flat plate theory, and the body viscous drag about 1.5 counts above that from the flat plate theory. On the other hand, the BB model predicts total viscous drag close to the SA model at $M=2.4$, but about 3.5 counts below the SA model at $M=0.9$. The model differences at $M=0.9$ are primarily due to departure in the predicted body viscous drag.



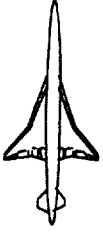
Sym TCA Skin Friction Drag at Wind Tunnel Reynolds Number





HSCT High Speed Aerodynamics

HSR Configuration Aero Final Review FY97



Skin Friction Results for Sym TCA at M=0.9 and Flight Reynolds Number

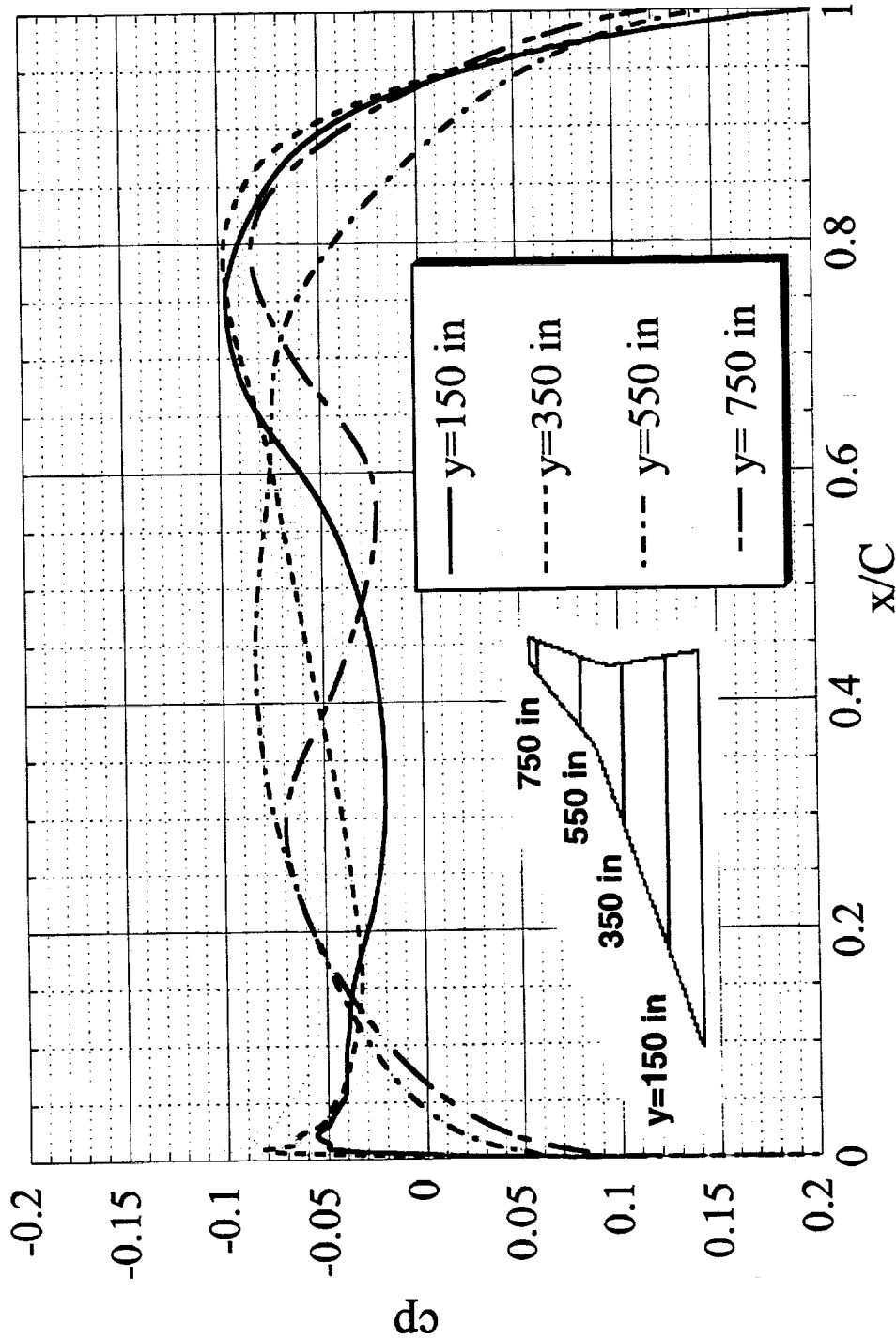
Predicted chordwise Surface cp for the Sym TCA at M=0.9 and Flight Re

This plot displays the chordwise surface cp at M=0.9 and flight Re of 164E6 at several span stations of the inboard wing (y=150 in and 350 in) and the outboard wing (y=550 in and 750 in).



HSCT High Speed Aerodynamics

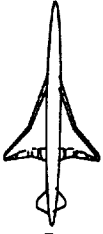
Sym TCA Wing ($M=0.9$, $\alpha=0$ deg, $Re=164E6$)





HSR Configuration Aero Final Review FY97

HSC T High Speed Aerodynamics



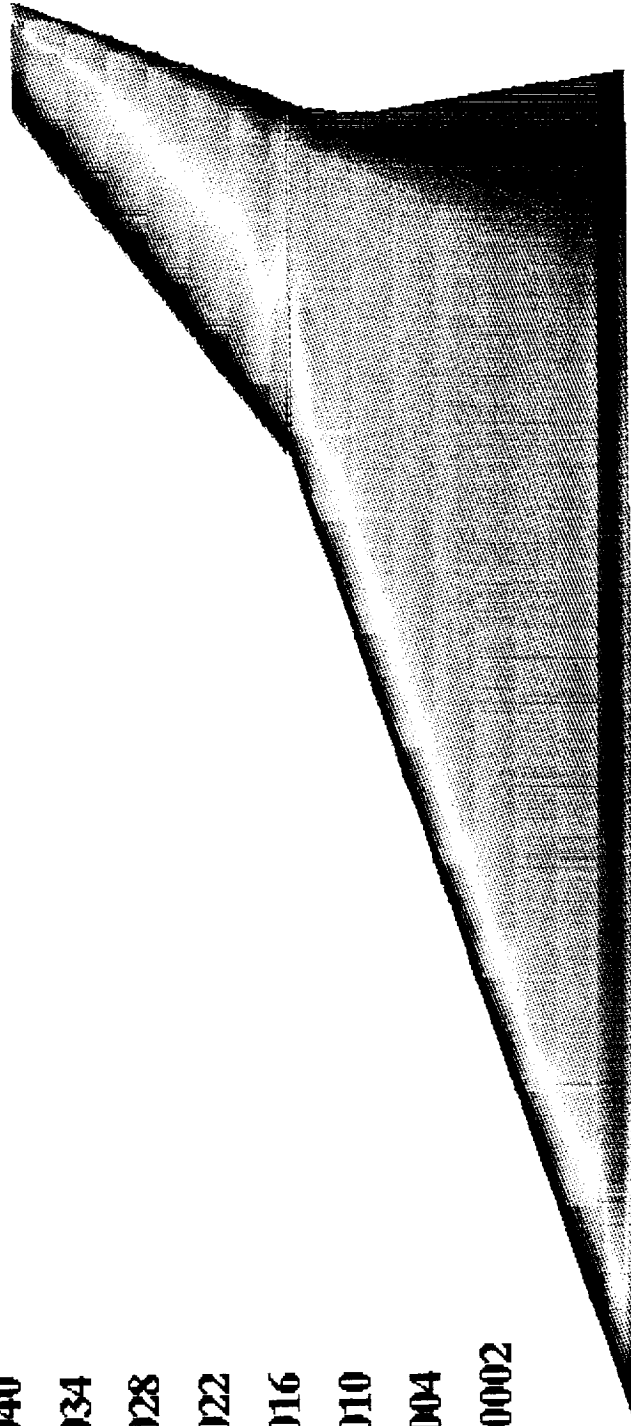
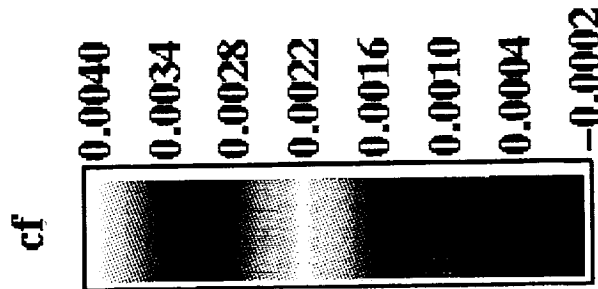
Surface of distribution for the Sym TCA at $M=0.9$ and Flight Re

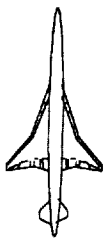
Shown here is the distribution of local c_f (based on q_{inf}) on the wing surface for the symmetric TCA at $M=0.9$ and flight Reynolds number.



HSCT High Speed Aerodynamics

**Sym TCA (M=0.9, alpha=0 deg, Re=164E6)
Wing Skin Friction Coefficient (OVERFLOW)**





Comparison of Local cf for the Sym TCA at M=0.9 and Flight Re

The local chordwise cf distributions from the OVERFLOW solution at some selective span stations of the inboard wing ($y=150$ in and 350 in) and the outboard wing ($y=550$ in and 750 in) have been presented in this figure. The local cf from OVERFLOW based on both freestream dynamic pressure (q_{inf}) and local dynamic pressure (q_{loc}) are displayed. The predictions of cf (based on freestream dynamic pressure) from the flat plate theories of Sommer-Short (SS) and Frankl-Voishel (FV) have also been shown for comparison. The FV correlation predicts higher cf than that from the SS correlation. The drop in the cf from OVERFLOW near the trailing edge is connected with a rapidly rising adverse pressure gradient in that region. The results also exhibit the deviations in the local cf based on q_{inf} and that based on q_{loc} , indicating the effect of local dynamic pressure.

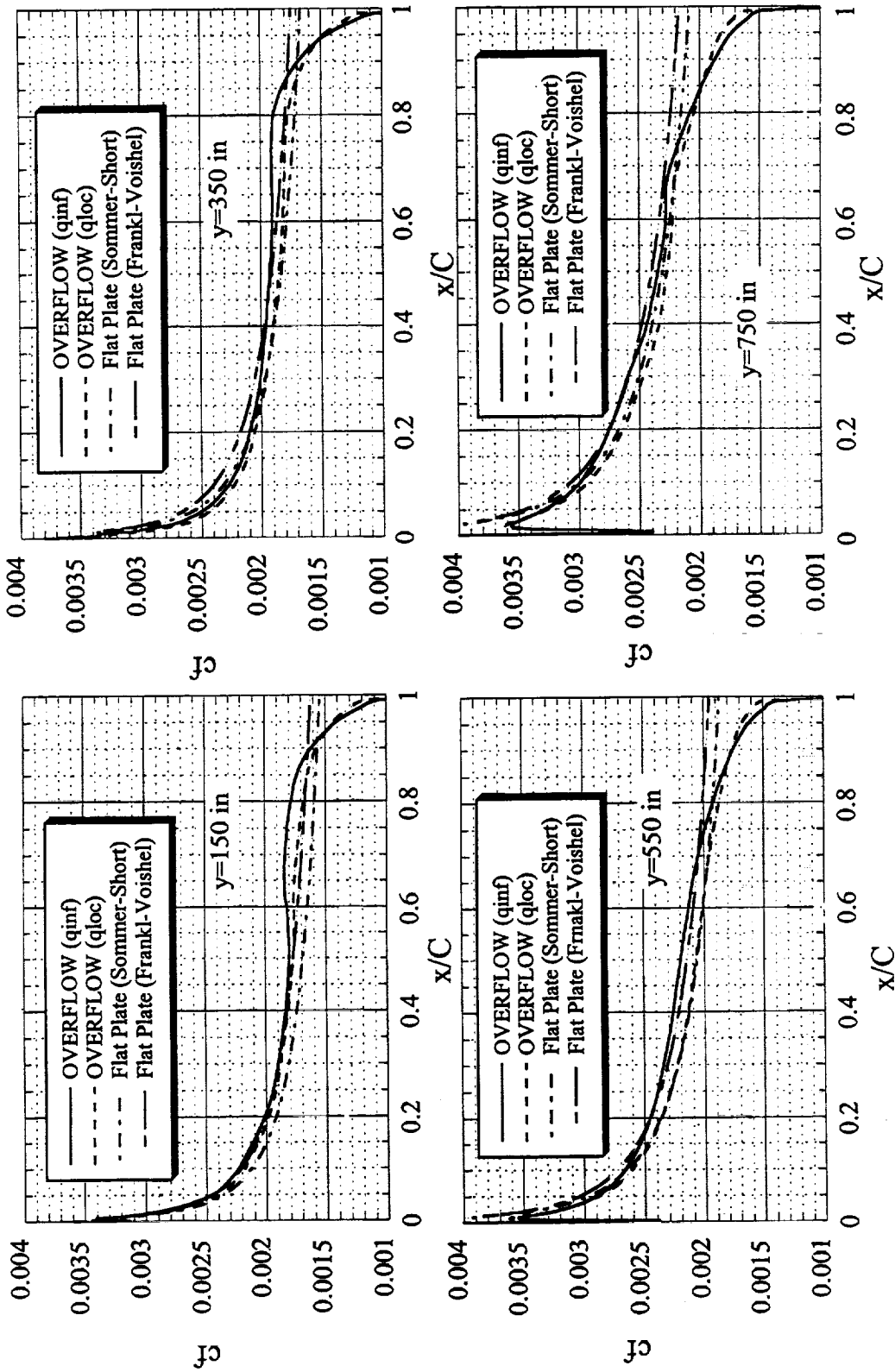


HSCT High Speed Aerodynamics

HSR Configuration Aero Final Review FY97



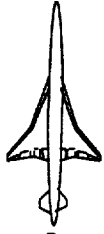
Comparison of Local Skin Friction Coefficient
Sym TCA ($M=0.9$, $\alpha=0$ deg, $Re=164E6$)





HSCT High Speed Aerodynamics

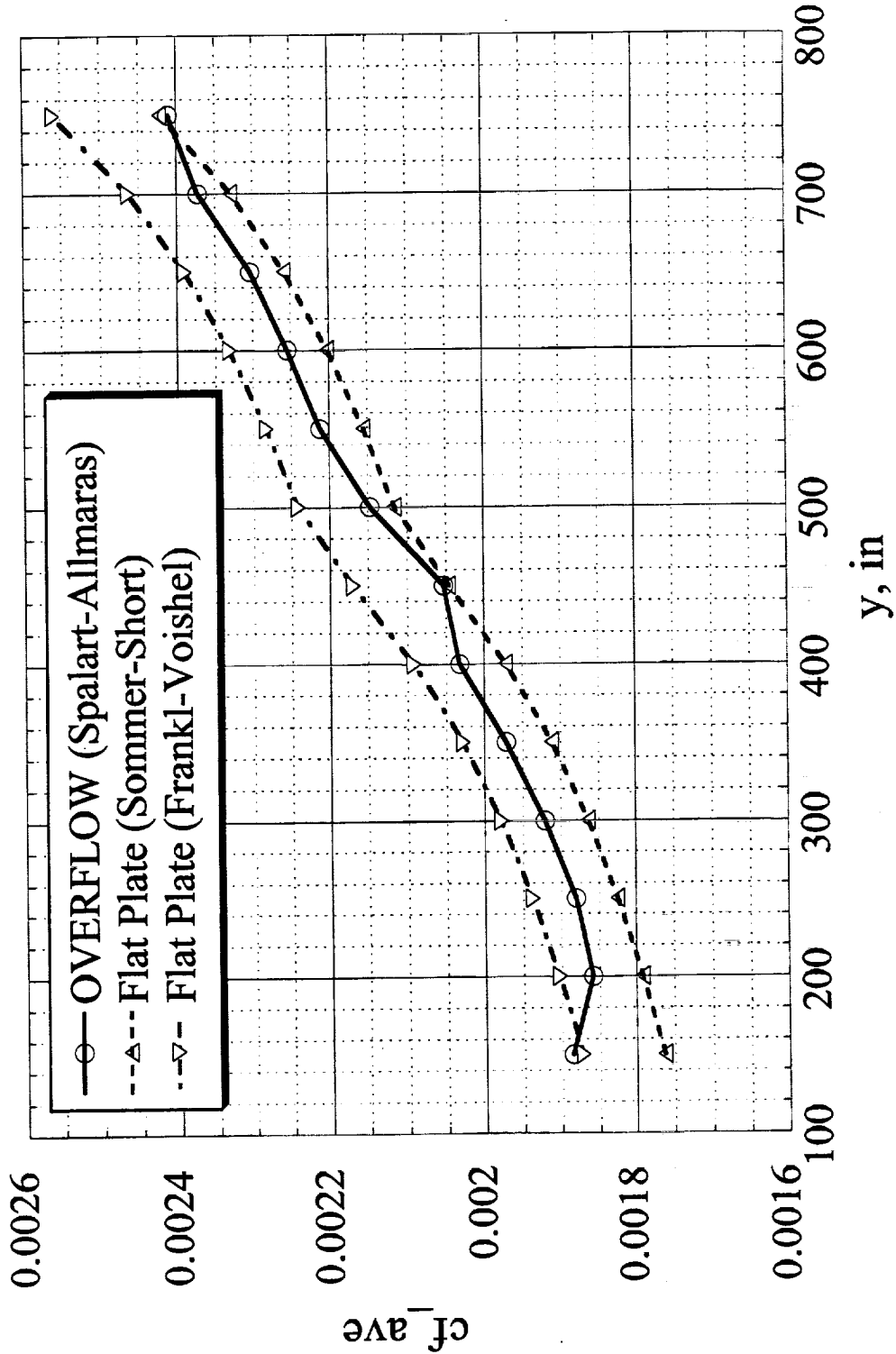
HSR Configuration Aero Final Review FY97



Comparison of Average c_f for the Sym TCA at $M=0.9$ and Flight Re

A comparison of the average c_f based on q_{inf} is presented here. Excellent agreement is seen between the OVERFLOW predictions and the flat plate correlations over the entire wing span. At this Mach number and Re , the OVERFLOW solution falls between the values represented by the two flat plate correlations, except at $y=150$ in and $y=750$ in. It is observed that the local dynamic pressure effects do not exert any appreciable effect on the wing average c_f at these flow conditions. The results suggest that the average c_f increases spanwise nearly linearly, with the highest occurring near the wing tip region.

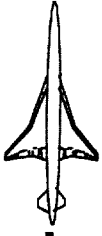
Sym TCA Wing ($M=0.9$, $\alpha=0$ deg, $Re=164E6$)





HSCT High Speed Aerodynamics

HSR Configuration Aero Final Review FY97



Skin Friction Results for Sym TCA at M=2.4 and Flight Reynolds Number

Predicted Surface cp for the Sym TCA at M=2.4 and Re=195E6

Shown here is the surface cp computed from OVERFLOW.

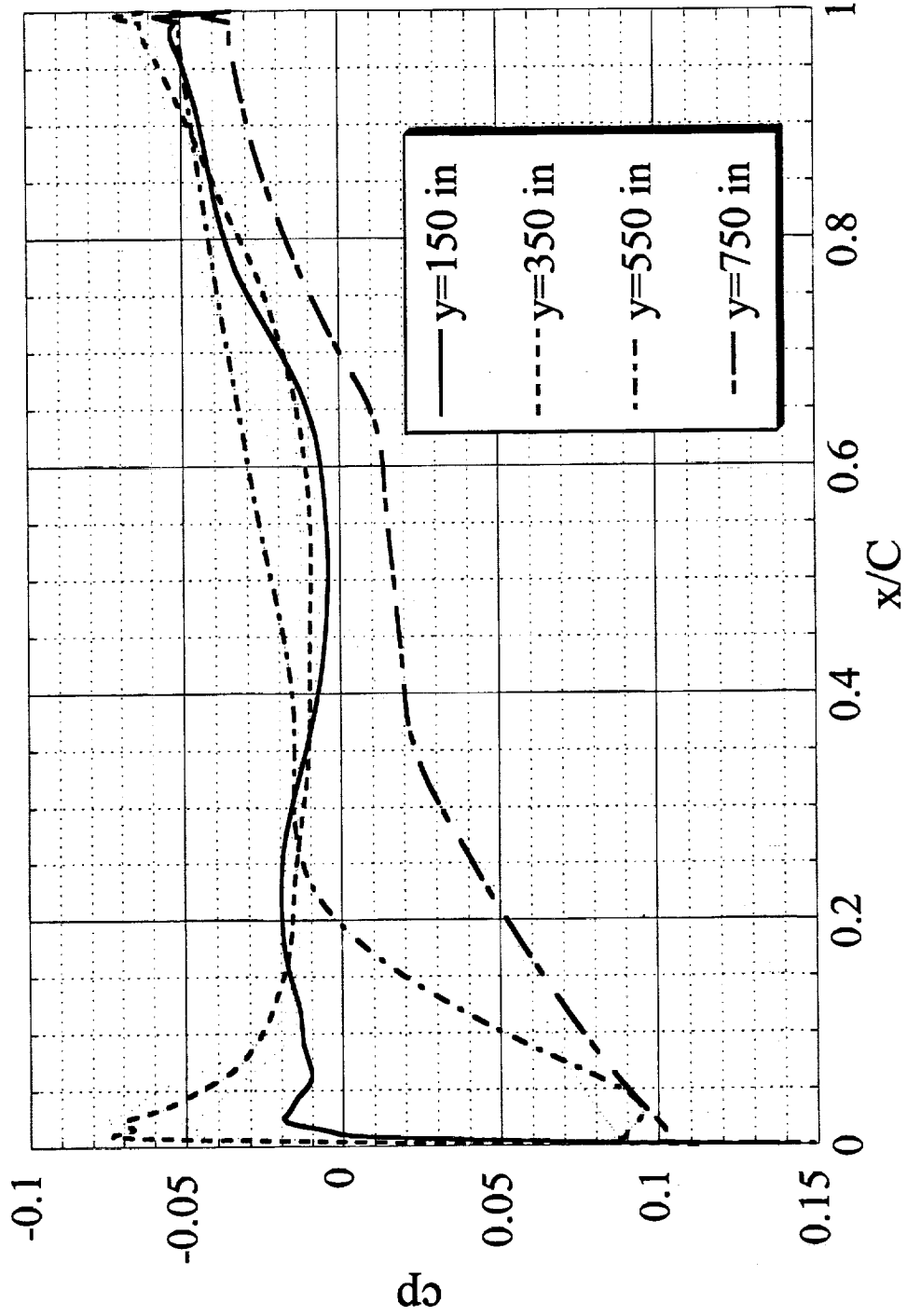


HSCT High Speed Aerodynamics

HSR Configuration Aero Final Review FY97



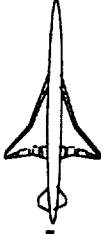
Sym TCA Wing ($M=2.4$, $\alpha=0$ deg, $Re=195E6$)





HSR Configuration Aero Final Review FY97

HSCT High Speed Aerodynamics



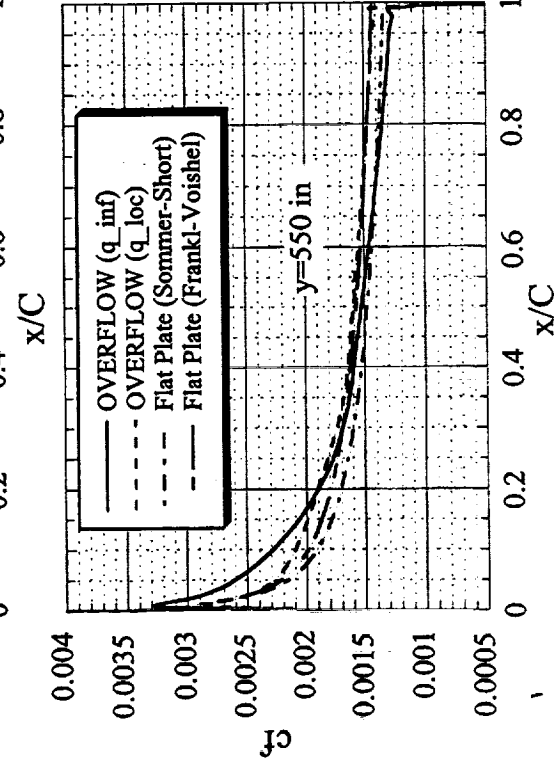
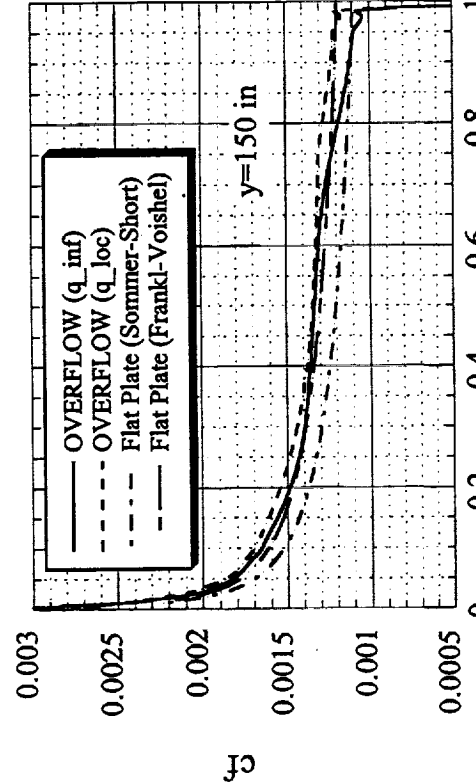
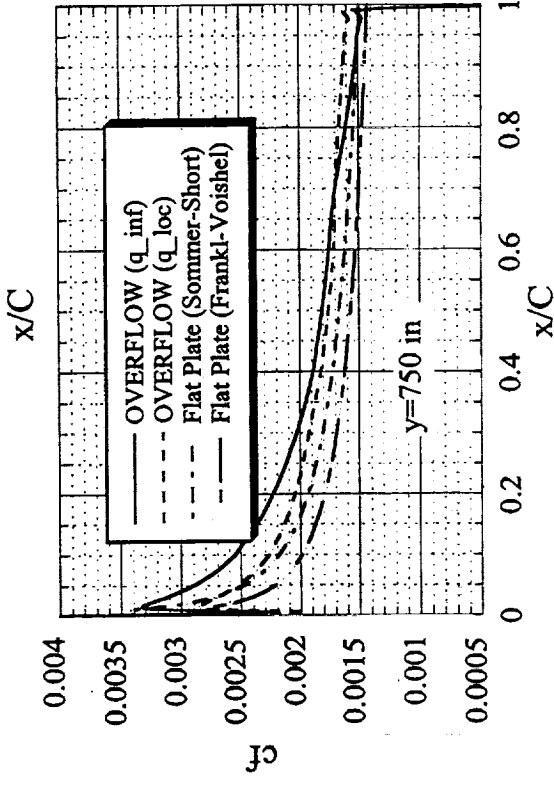
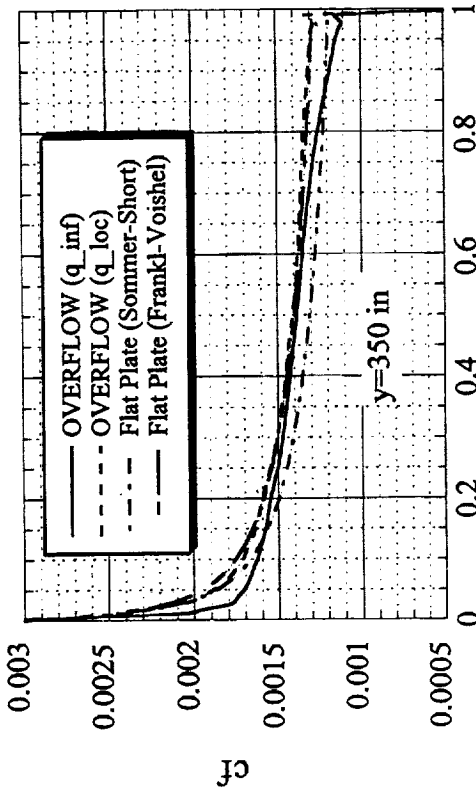
Comparison of Local c_f for the Sym TCA at $M=2.4$ and $Re=195E6$

This figure displays the comparisons of local c_f with the flat plate theories at $y=150$ in, 350 in, 550 in and $y=750$ in respectively. In general, the local c_f based on q_{loc} agrees more closely with the flat plate theories than that based on q_{inf} . Local dynamic pressure effects on the local c_f begin to be important at $y=350$ in near the leading edge of the inboard wing. The chordwise extent in which local dynamic pressure influence is present is seen to increase with the span coordinate, reaching up to 40 percent of the chord at $y=750$ in near the wing tip.



HSCT High Speed Aerodynamics

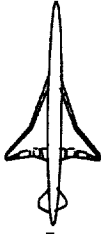
**Comparison of Local Skin Friction Coefficient
Sym TCA (M=2.4, alpha=0 deg, Re=195E6)**





HSR Configuration Aero Final Review FY97

HSCT High Speed Aerodynamics

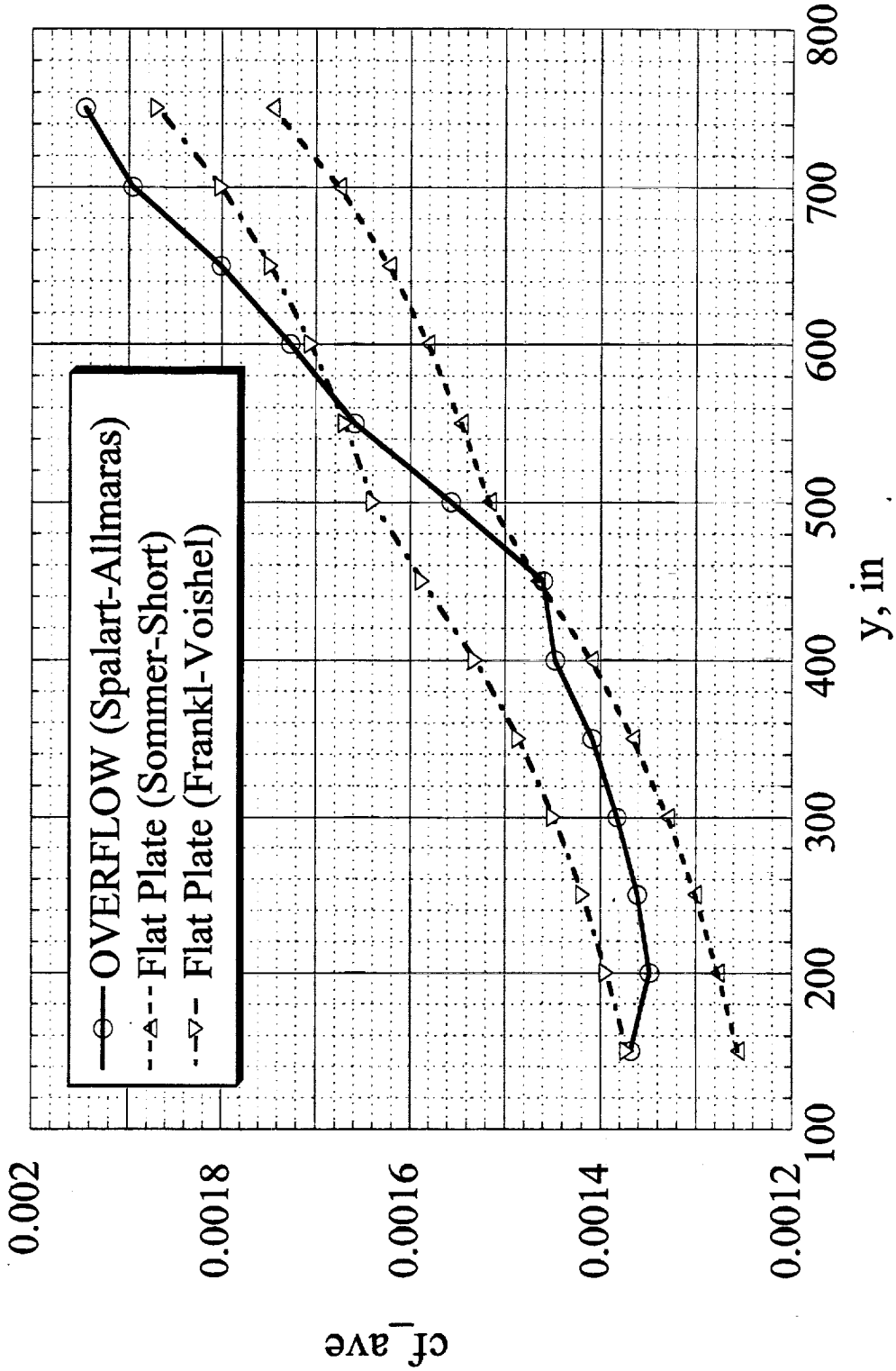


Comparison of Average of for the Sym TCA at $M=2.4$ and $Re=195E6$

The averaged c_f plotted along the span coordinate shows that for the inboard wing region the OVERFLOW solution falls midway between the two flat plate correlations; however for the outboard wing the OVERFLOW solution is somewhat overestimated for y in excess of 550 in, due to the local dynamic pressure effects present in the outboard wing region as evidenced by the local c_f distributions.



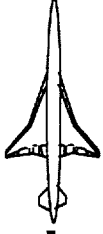
Sym TCA Wing ($M=2.4$, $\alpha=0$ deg, $Re=195E6$)





HSR Configuration Aero Final Review FY97

HSCT High Speed Aerodynamics



Skin Friction Results for Sym TCA at M=0.9 and Wind Tunnel Reynolds Number

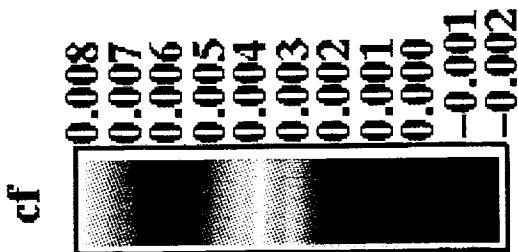
Surface of distribution for the Sym TCA at M=0.9 and Wind Tunnel Re

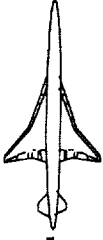
Shown here is the distribution of local c_f (based on q_{inf}) on the wing surface for the symmetric TCA at $M=0.9$ and wind tunnel Reynolds number of 6E6. Regions of low c_f near the leading edge are due to laminar-turbulent transition. This transition occurs both on the inboard wing and the outboard wing, regardless of the nature of the leading edge. The physical distance of this transition is fairly uniform along the span of the inboard wing and the outboard wing.



**Sym TCA (M=0.9, alpha=0 deg, Re=6.04E6)
Skin Friction Coefficient (OVERFLOW)**

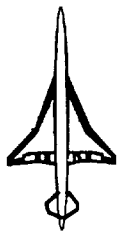
Wing Surface





Comparison of Local c_f for the Sym_TCA at $M=0.9$ and $Re=6.04E6$

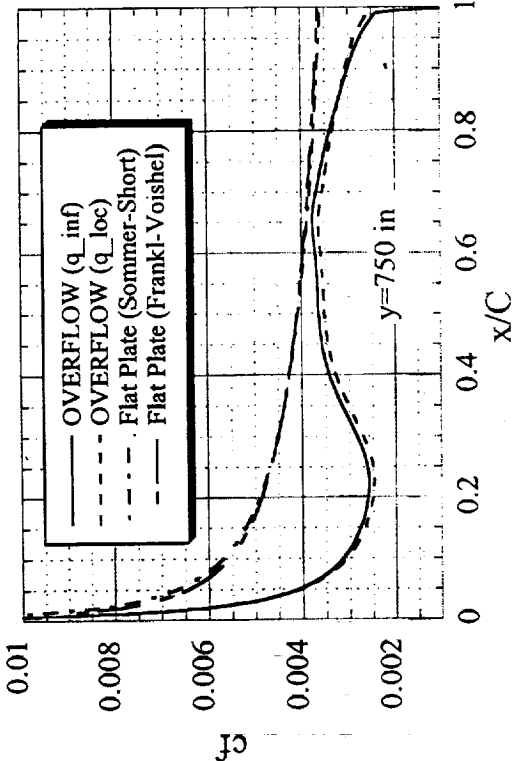
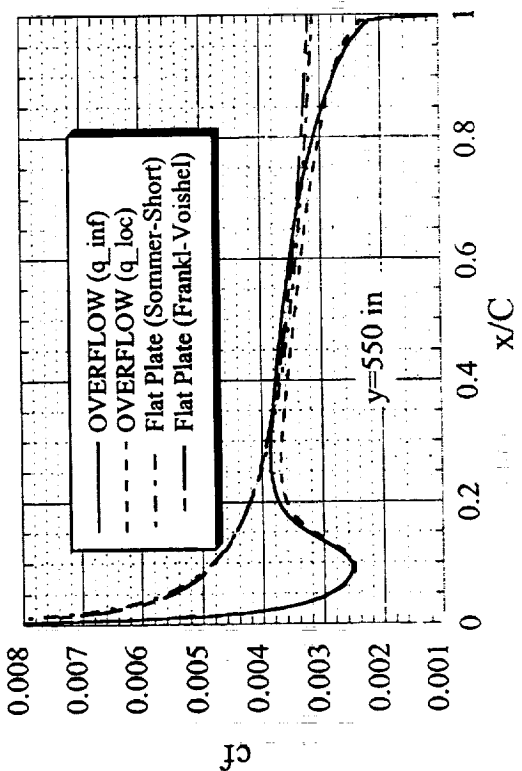
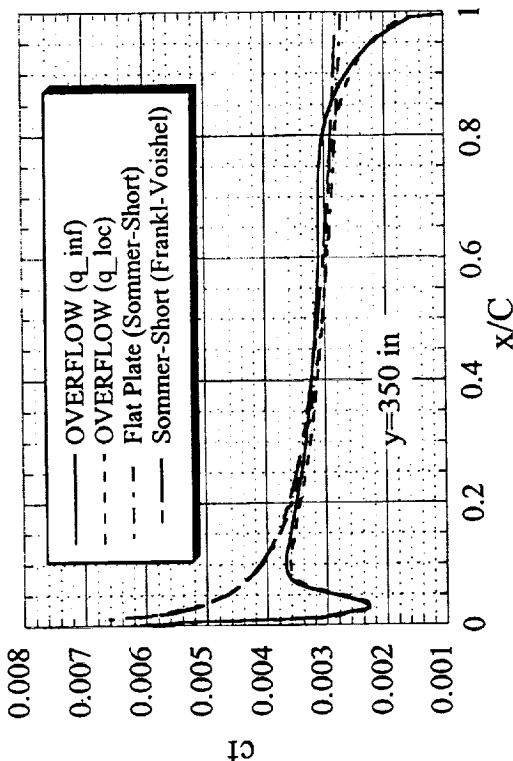
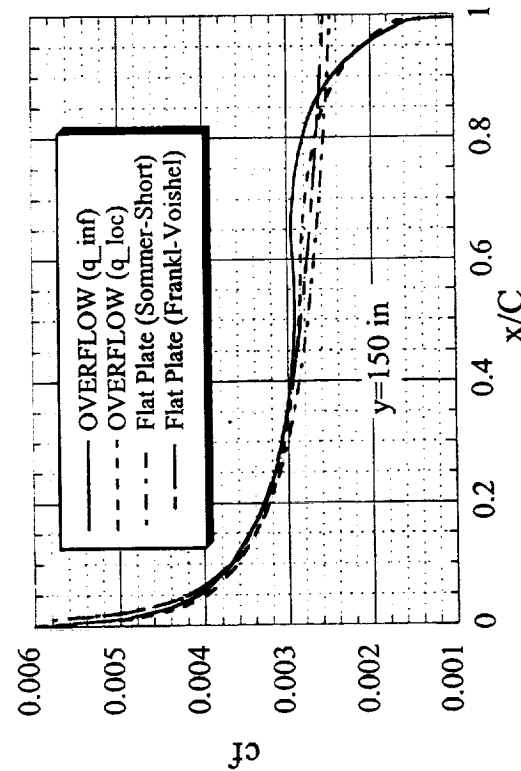
The local chordwise c_f distributions from the OVERFLOW solution for $M=0.9$ and $Re=6.04E6$ at four selective span stations of $y=150$ in, 350 in, 550 in and 750 in are presented in this figure. Local c_f values are based on the freestream dynamic pressure (q_{inf}) and also on the local dynamic pressure (q_{local}). The predictions of local c_f (based on q_{inf}) from the flat plate theories of Sommer-Short (SS) and Frankl-Voishel (FV) have also been shown for comparison. The FV correlation predicts c_f somewhat higher than that from the SS correlation, as in the case of flight $Re=164E6$. The drop in the c_f from OVERFLOW near the trailing edge is linked to a rapidly rising adverse pressure gradient in that region. For $y=350$ in and further outboard, an undershoot in the local c_f near the leading edge is predicted by OVERFLOW, regardless of the nature of the wing leading edge geometry (rounded inboard, sharp outboard). Although the level of the maximum dip is relatively unchanged with the span distance, the chordwise extent of the dip is seen to widen considerably with the spanwise coordinate, with the dip extending to as high as 50 percent of the chord near the tip region ($y=750$ in). The dip in the local c_f is believed to be a consequence of laminar-turbulent transition (even though the oncoming flow is turbulent) of the boundary layer predicated by the Spalart-Allmaras turbulence model at the wind tunnel Reynolds number. Such a transition has been observed at the flight Reynolds number $Re=164E6$ also, but it is less important as it is restricted to a very narrow region in the immediate vicinity of the leading edge. A significant undershoot in c_f near the leading edge with the SA model at wind tunnel Re has also been reported by Scott Lawrence of NASA Ames (Scott also notes that near the leading edge, the c_f from Baldwin-Lomax algebraic model produces higher c_f than that from the SA model). Beyond the transition region, the OVERFLOW predictions are in agreement with the flat plate predictions, except near the trailing edge. As the local c_f based on q_{inf} and q_{loc} are close to one another, and differ considerably from the flat plate values, it may be concluded that the low Reynolds number effects on the local c_f are more pronounced than those of the dynamic pressure.



HSCT High Speed Aerodynamics

Comparison of Local Skin Friction Coefficient

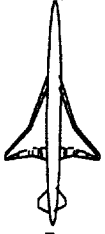
Sym TCA ($M=0.9$, $\alpha=0$ deg, $Re=6.04E6$)





HSR Configuration Aero Final Review FY97

HSCT High Speed Aerodynamics



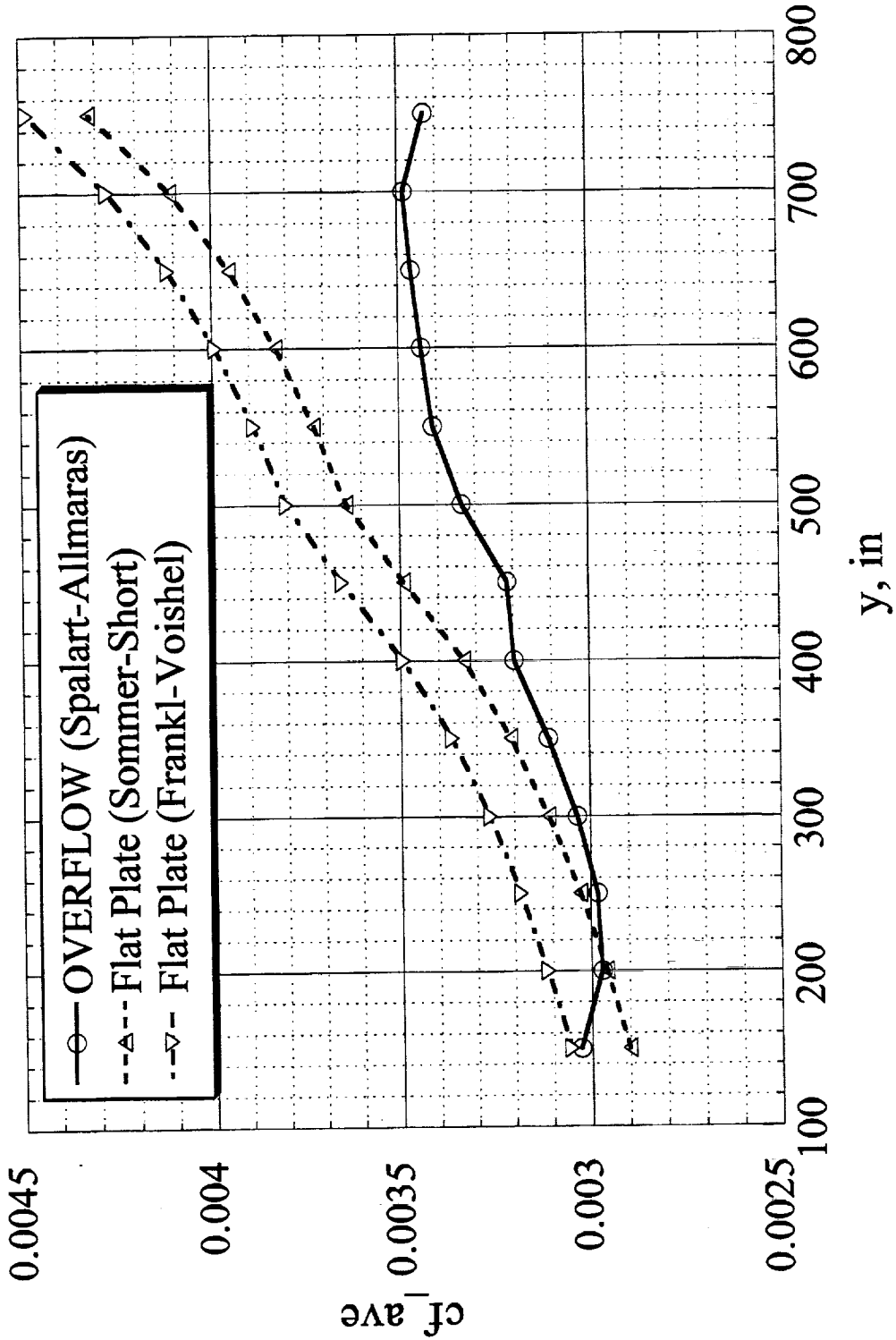
Comparison of Average c_f for the Sym TCA at $M=0.9$ and $Re=6.04E6$

A comparison of the average c_f (based on q_{inf}) c_{f_ave} as a function of the span coordinate y is presented here. The c_{f_ave} predicted by OVERFLOW is seen to be somewhat comparable to the flat plate theories only below about $y=300$ in, but for y in excess of about 300 in, the OVERFLOW prediction falls below the flat plate calculations, with the deviation increasing with y . This marked deviation is a result of the undershoot in the local c_f due to laminar-turbulent transition computed by OVERFLOW, as discussed earlier.



HSCT High Speed Aerodynamics

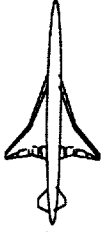
Sym TCA Wing (M=0.9, alpha=0 deg, Re=6.04E6)





HSR Configuration Aero Final Review FY97

HSCT High Speed Aerodynamics



Skin Friction Results for Sym TCA at M=2.4 and Wind Tunnel Reynolds Number

The corresponding results at M=2.4 and wind tunnel Re of 6.4E6 are summarized in the following figures. In general the results and comparisons at M=2.4 are similar to those noted for the M=0.9 case, with the local dip in cf being again the distinguishing factor. At M=2.4, the local dynamic pressure effects, that were present near the forward portion of the outboard wing at flight Reynolds number, appear to be engulfed by the laminar-turbulent transition undershoot predicted at the wind tunnel Reynolds number.

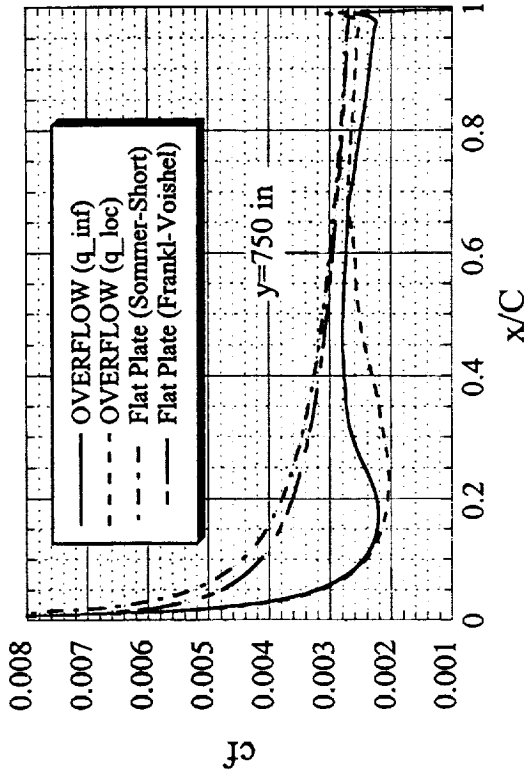
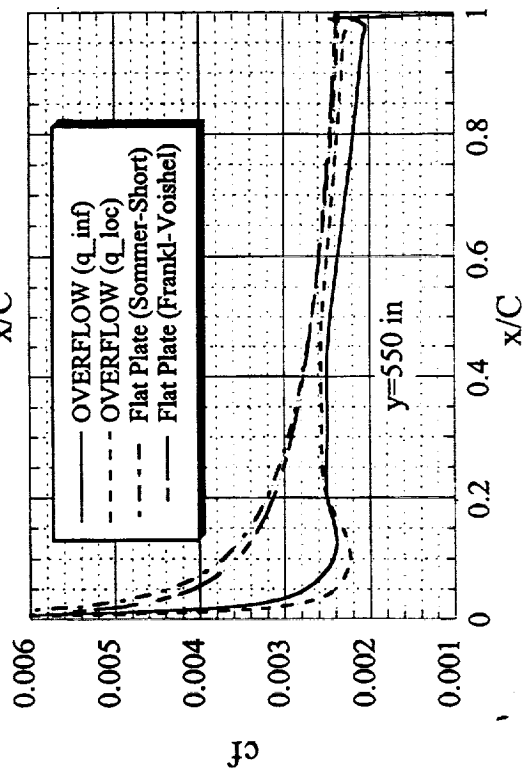
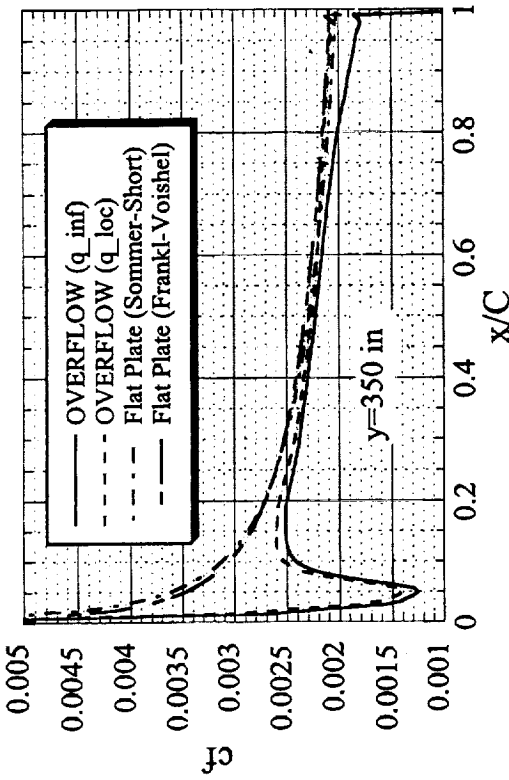
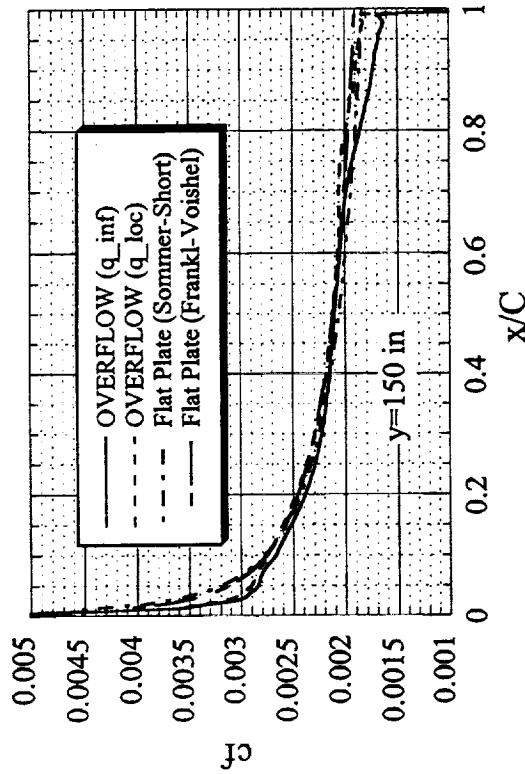


HSR Configuration Aero Final Review FY97



HSCT High Speed Aerodynamics

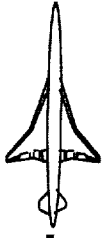
Comparison of Local Skin Friction Coefficient
Sym TCA ($M=2.4$, $\alpha=0$ deg, $Re=6.36E6$)





HSCT High Speed Aerodynamics

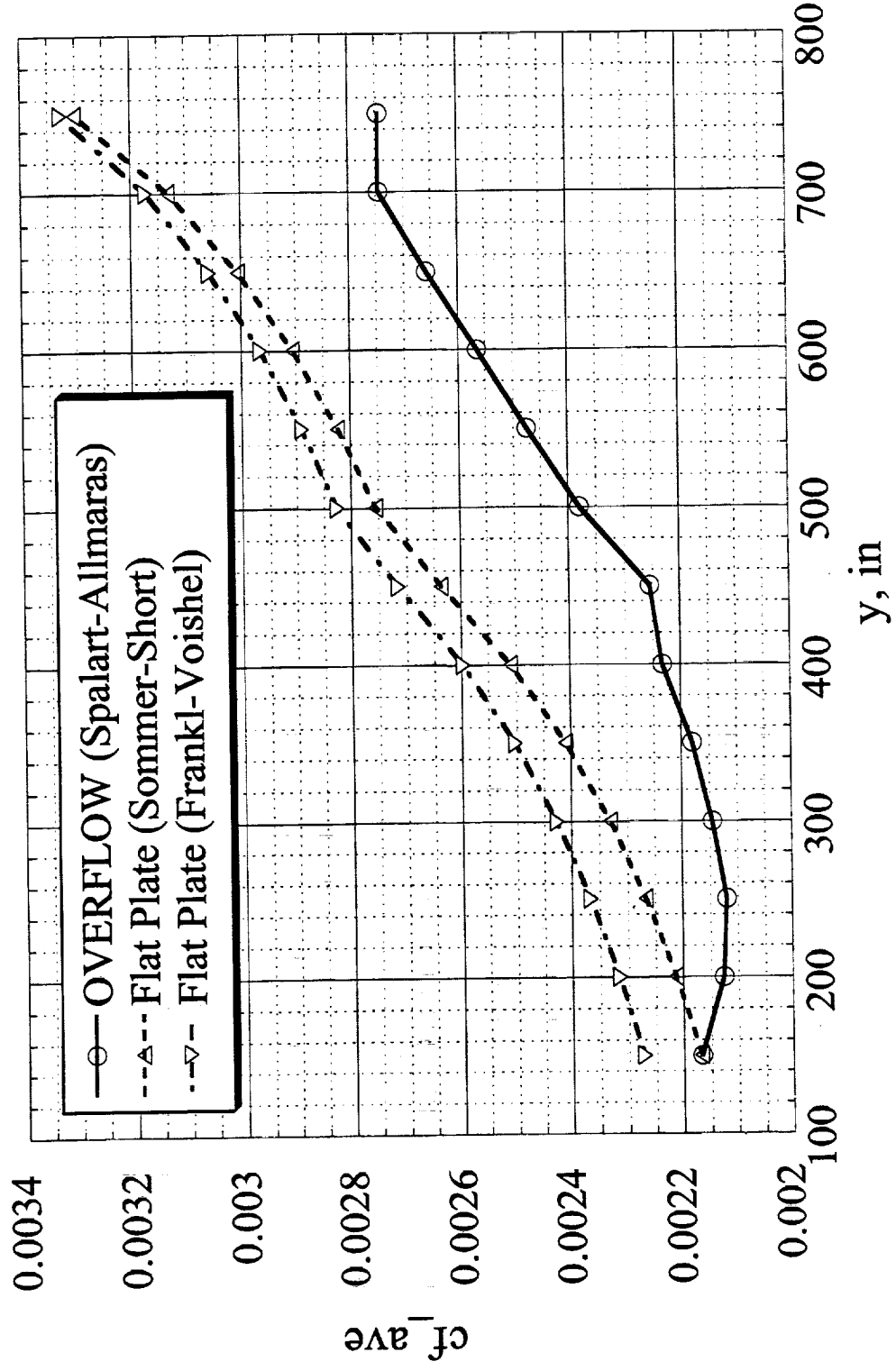
HSR Configuration Aero Final Review FY97



---This page is left intentionally blank---



Sym TCA Wing (M=2.4, alpha=0 deg, Re=6.36E6)





Skin Friction Study with Baseline TCA

All the TCA grid and flow solutions for the baseline case ($M=0.9$ and 2.4 at both flight and wind tunnel Re) were obtained from Steve Chaney (Boeing HSCT High Speed Aerodynamics), and correspond to cruise angles of attack ($\alpha=3.7$ deg at $M=0.9$, and $\alpha=3$ deg at $M=2.4$). The value of the first cell distance from the wall was based on a requirement of $y^+=1$. For example, at $M=2.4$ the first cell distance was taken as 0.0006 in at flight Re , and 0.013 in (full scale) at the wind tunnel Reynolds number.

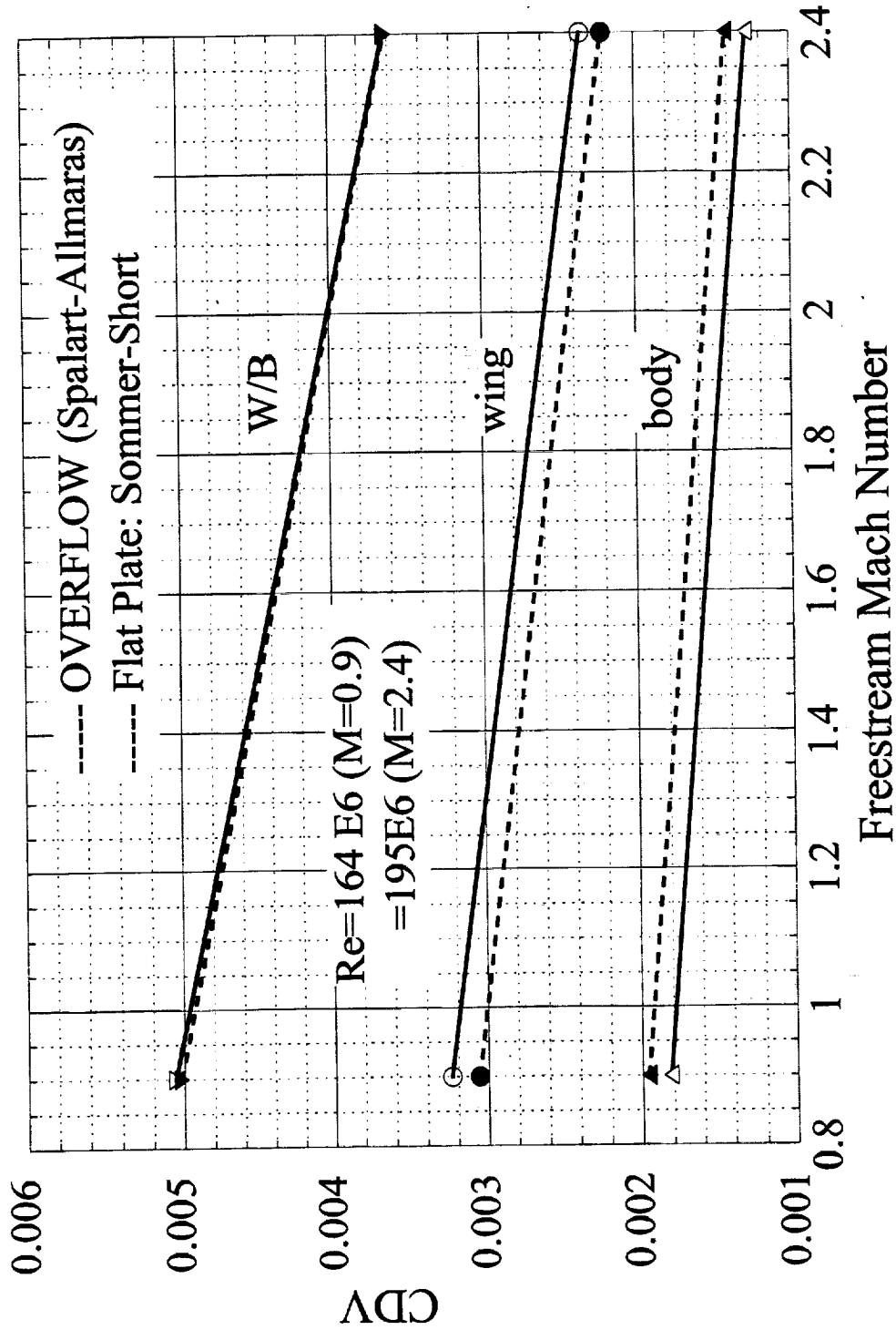
Comparison of Skin Friction Drag for the TCA at Flight Reynolds Number

OVERFLOW solutions with the Spalart-Allmaras (SA) one-equation turbulence model have been obtained for the baseline TCA skin-friction drag at flight Reynolds number for freestream Mach numbers of 0.9 and 2.4 . The corresponding flight Reynolds numbers are $164E6$ at $M=0.9$, and $195E6$ at $M=2.4$.

Shown here is a comparison of the skin-friction drag from OVERFLOW and the flat plate theory (Sommer-Short) at flight Reynolds number. The flat plate drag predictions were provided by Chris Vegter of Boeing HSCT Aerodynamics. At flight conditions, the OVERFLOW solution with the SA model agrees well with the flat plate theory at both $M=0.9$ and 2.4 , the difference in the component viscous drag from the two methods being within one count in the entire Mach number range. The body viscous drag from the OVERFLOW is about two counts higher than that from the flat plate theory, and the wing viscous drag two counts higher than that from the flat plate theory. The trend for the component viscous drag comparisons (for the body and the wing) are opposite to that found for the symmetric TCA at flight Reynolds number.



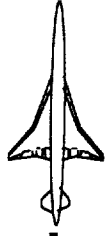
TCA Skin Friction Drag at Flight Reynolds Number





HSR Configuration Aero Final Review FY97

HSCT High Speed Aerodynamics



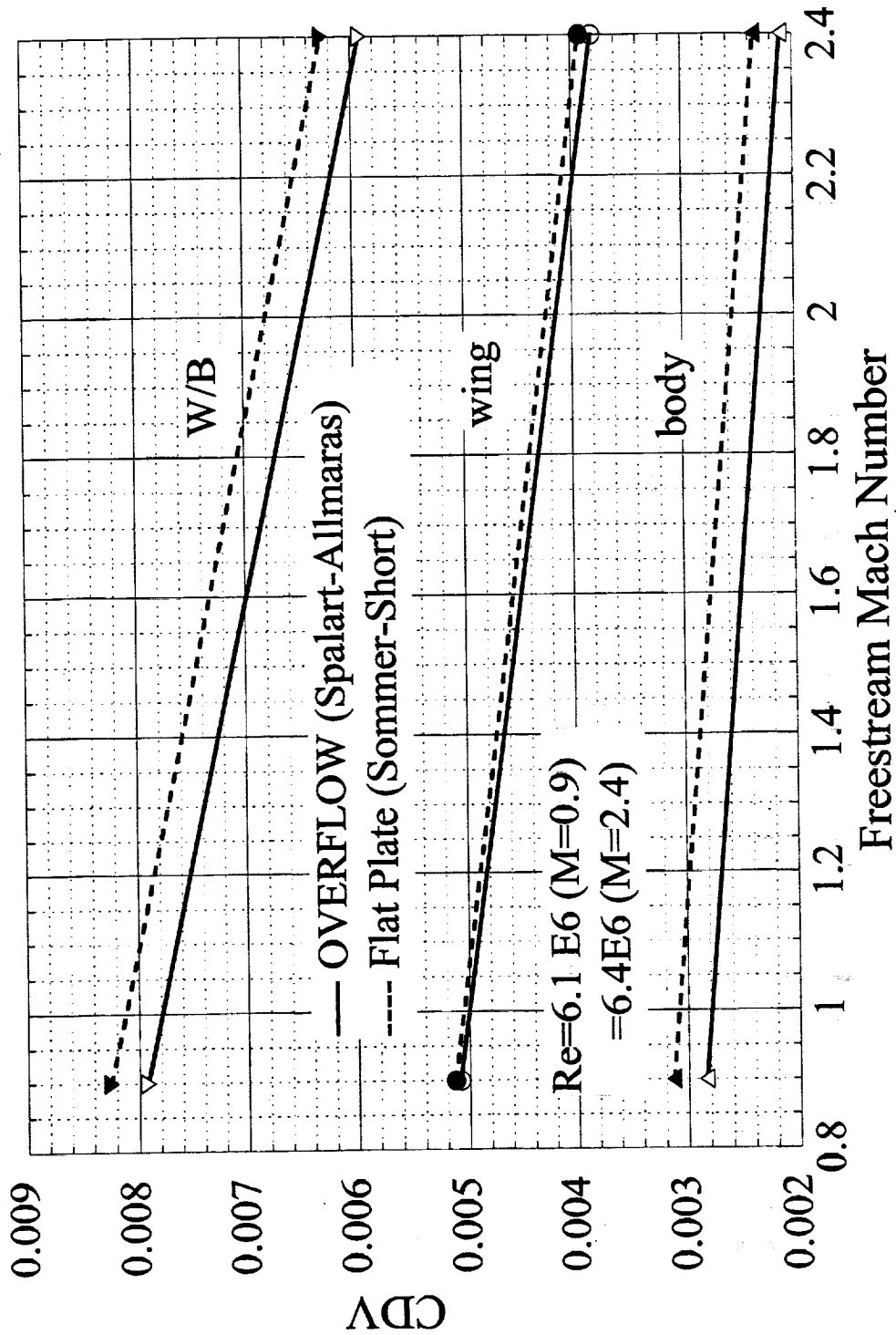
Comparison of Skin Friction Drag for the TCA at Wind Tunnel Reynolds Number

Symmetric TCA viscous flow solutions were obtained from OVERFLOW with Spalart-Allmaras (SA) one-equation turbulence model at the wind tunnel Reynolds number at $M=0.9$ and 2.4. The wind tunnel Reynolds numbers are $6.1E6$ at $M=0.9$ and $6.4E6$ at $M=2.4$. In order to understand the sensitivity of the viscous drag with respect to the turbulence model considered, some additional solutions have been obtained with the Baldwin-Barth (BB) one-equation turbulence model. at two selective Mach numbers ($M=0.9$ and 2.4).

This plot shows a comparison of the OVERFLOW solutions and the flat plate theory at the wind tunnel Reynolds number. The total wing/body viscous drag from the OVERFLOW code with the SA model is about three to four counts below the flat plate theory. The component comparisons suggest that the SA model yields wing viscous drag that is about one count below the flat plate theory, and the body viscous drag about three counts below that from the flat plate theory.



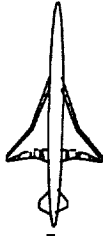
TCA Skin Friction Drag at Wind Tunnel Reynolds Number





HSCT High Speed Aerodynamics

HSR Configuration Aero Final Review FY97



Skin Friction Results for TCA at M=0.9 and Flight Reynolds Number

A comparison of the OVERFLOW and the flat plate predictions for the TCA at M=0.9 at flight Reynolds number and alpha=3.7 deg is summarized in the following figures.

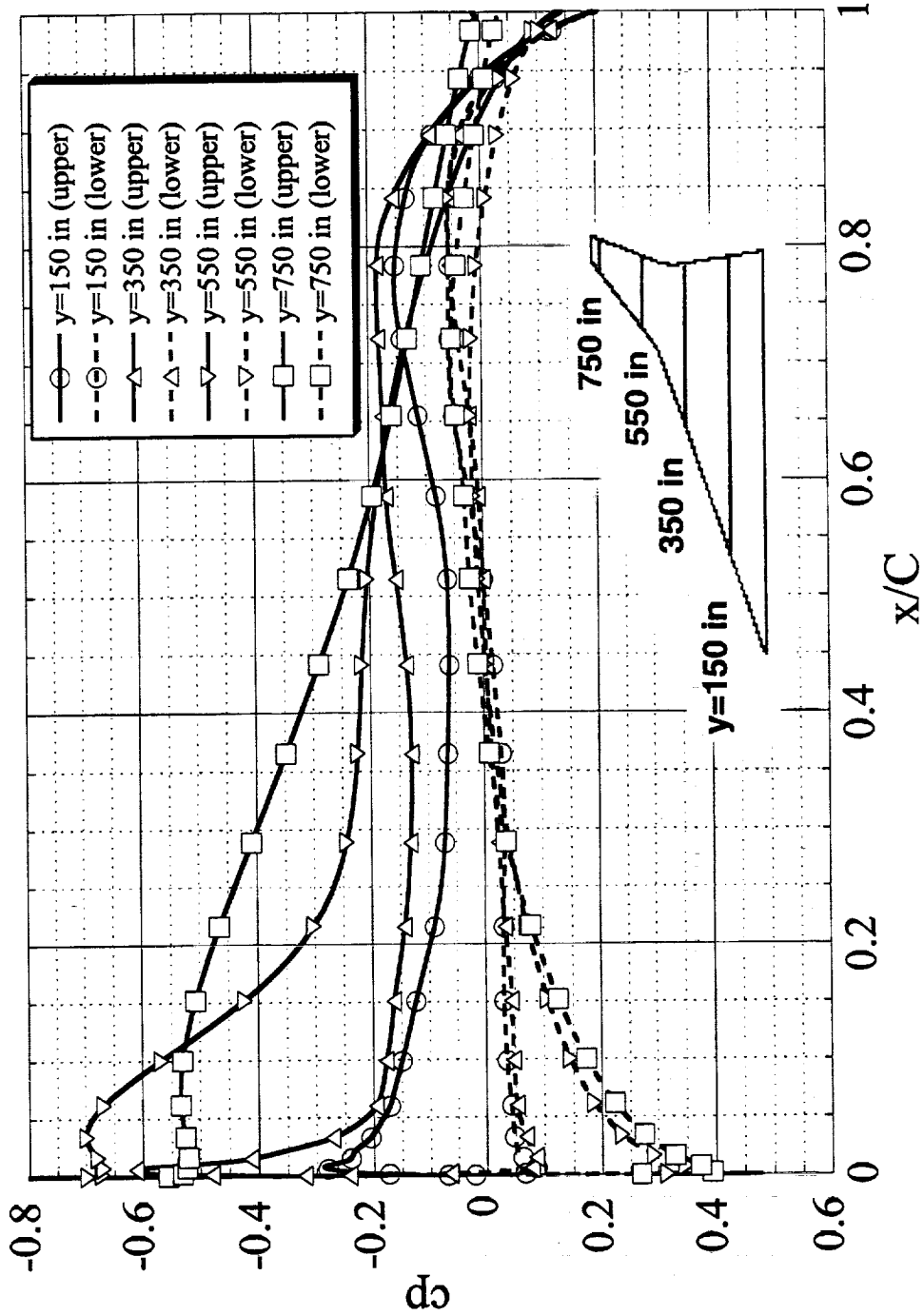
Predicted Surface cp for the Baseline TCA at M=0.9 and Re=1.64E6

The chordwise wing surface cp for the baseline TCA (M=0.9, alpha=3.7 deg, Re=1.64E6) from the OVERFLOW solution for various span stations is indicated in this plot.



HSCT High Speed Aerodynamics

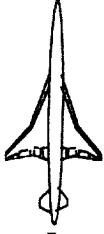
TCA Wing ($M=0.9$, $\alpha=3.7$ deg, $Re=164E6$)





HSCT High Speed Aerodynamics

HSR Configuration Aero Final Review FY97



Comparison of Local c_f for TCA at $M=0.9$ and $Re=164E6$

The following figures display a comparison of the local c_f for the TCA at $M=0.9$ and $Re=164E6$, given by OVERFLOW and the flat plate theories. The results from OVERFLOW and the flat plate theories agree well for the inboard wing ($y=150$ in and $y=350$ in), the local c_f predicted by the OVERFLOW for the upper surface is found to be substantially lower than the flat plate predictions for the outboard wing ($y=550$ in, and $y=750$ in). Flow visualization via surface streamlines has shown the existence of spanwise flow (three-dimensional flow) on the outboard wing upper surface, which tends to lower c_f in the drag direction. Computations with local c_f based on the magnitude of the skin friction vector for $y=550$ in and $y=750$ in have improved the upper surface results somewhat, but are still considerably underpredicted relative to the flat plate predictions. From the results of local c_f for the outboard wing, it may be inferred that the effect of flow three-dimensionality on the local c_f is more pronounced than that of local dynamic pressure.

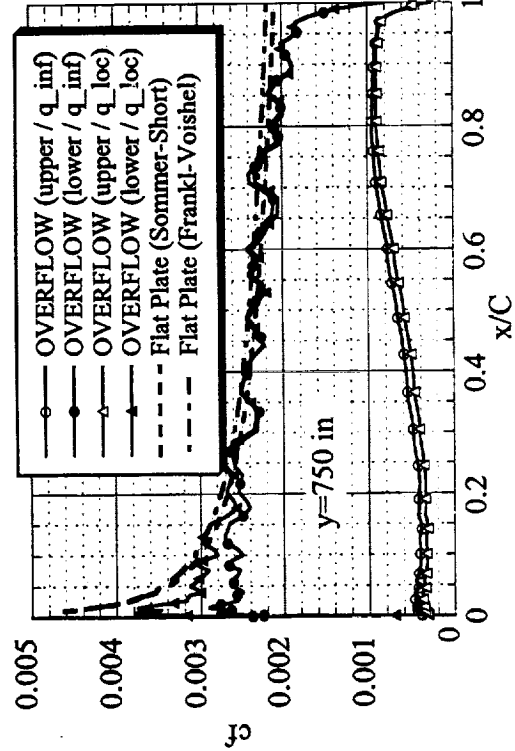
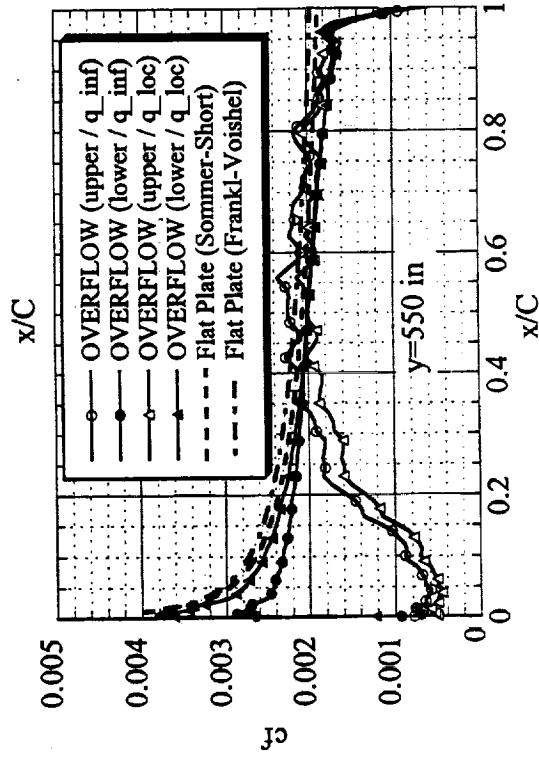
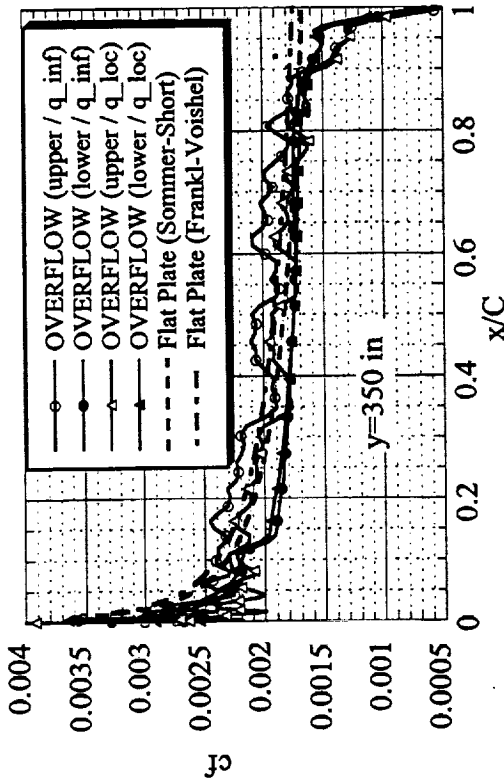
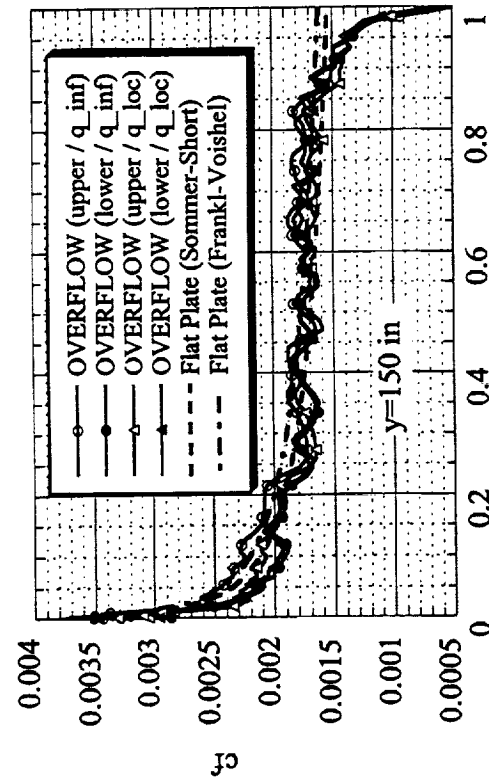


HSR Configuration Aero Final Review FY97



HSCT High Speed Aerodynamics

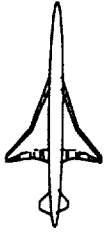
Comparison of Local Skin Friction Coefficient
TCA Wing ($M=0.9$, $\alpha=3.7$ deg, $Re=164E6$)





HSCT High Speed Aerodynamics

HSR Configuration Aero Final Review FY97



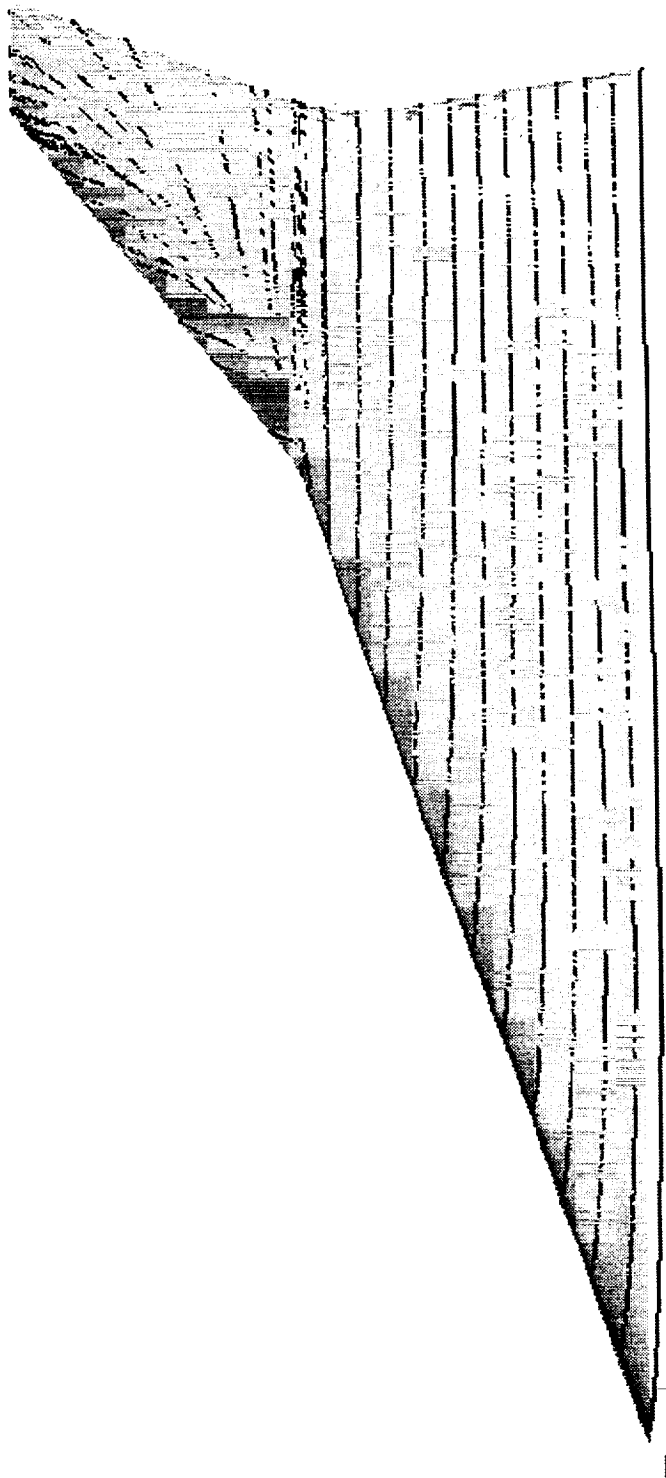
---This page is left intentionally blank---





HSCT High Speed Aerodynamics

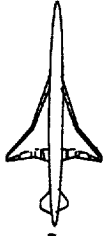
**TCA Wing ($M=0.9$, $\alpha=3.7$ deg, $Re=164E6$)
Surface Streamlines (OVERFLOW)
Wing Upper Surface**





HSCT High Speed Aerodynamics

HSR Configuration Aero Final Review FY97



Comparison of Average c_f for TCA at $M=0.9$ and $Re=1.64E6$

Shown here is a comparison of the c_{f_ave} as a function of the span coordinate. The discrepancy in the predictions from the OVERFLOW and the flat plate theories for the outboard wing upper surface is due to the three-dimensional flow effects discussed above. On the wing lower surface, the relatively small departure in the c_{f_ave} from OVERFLOW and the flat plate theories is attributable to the effect of local dynamic pressure.

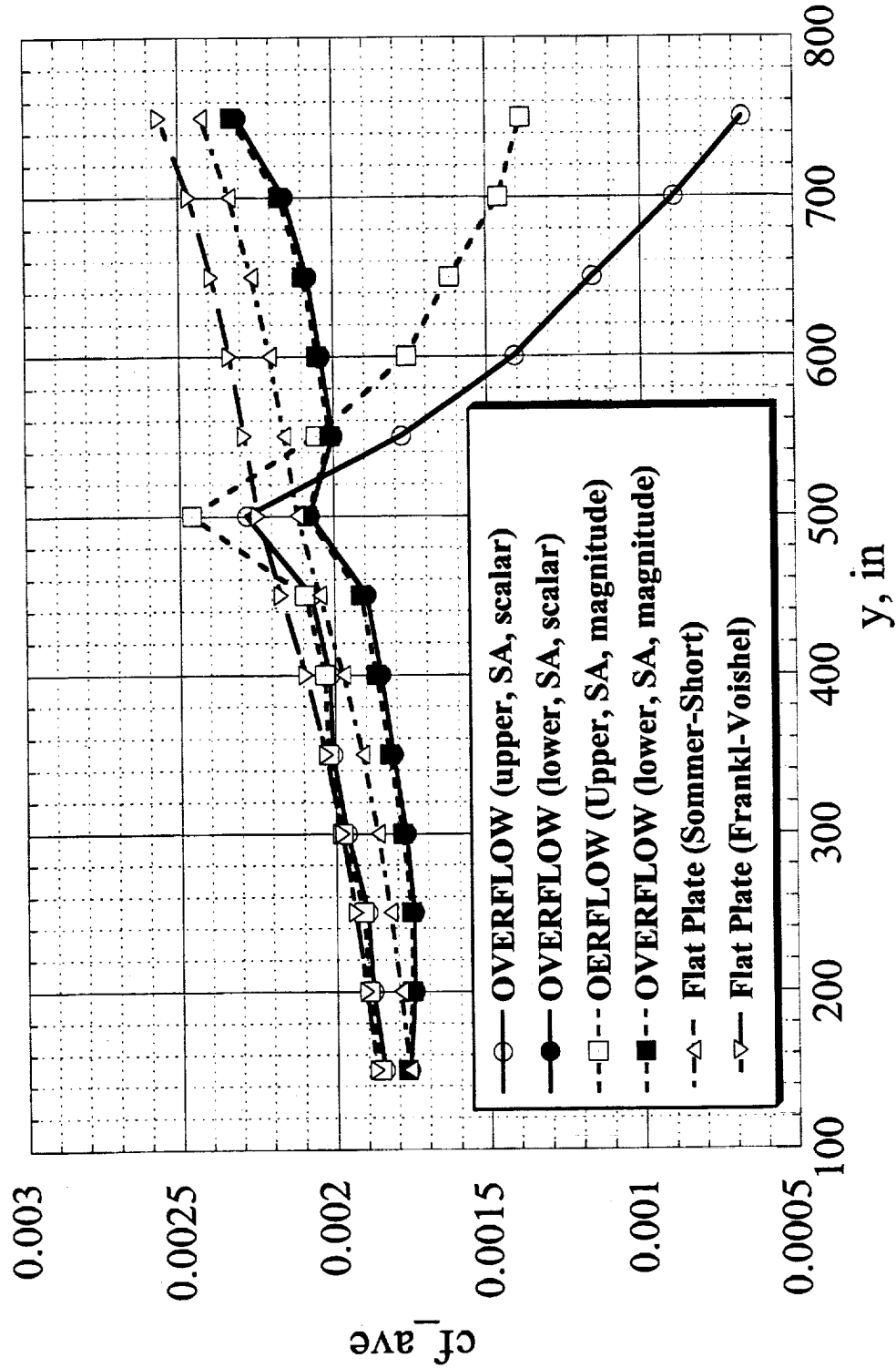


HSCT High Speed Aerodynamics

HSR Configuration Aero Final Review FY97



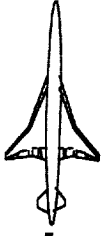
TCA Wing (M=0.9, alpha=3.7 deg, Re=164E6)





HSR Configuration Aero Final Review FY97

HSCAT High Speed Aerodynamics



Skin Friction Results for TCA at M=2.4 and Flight Reynolds Number

The following figures illustrate the comparisons of skin friction coefficient for the baseline TCA at M=2.4, $\alpha=3$ deg and flight $Re=195E6$.

Predicted Surface c_p for the TCA at M=2.4 and $Re=195E6$

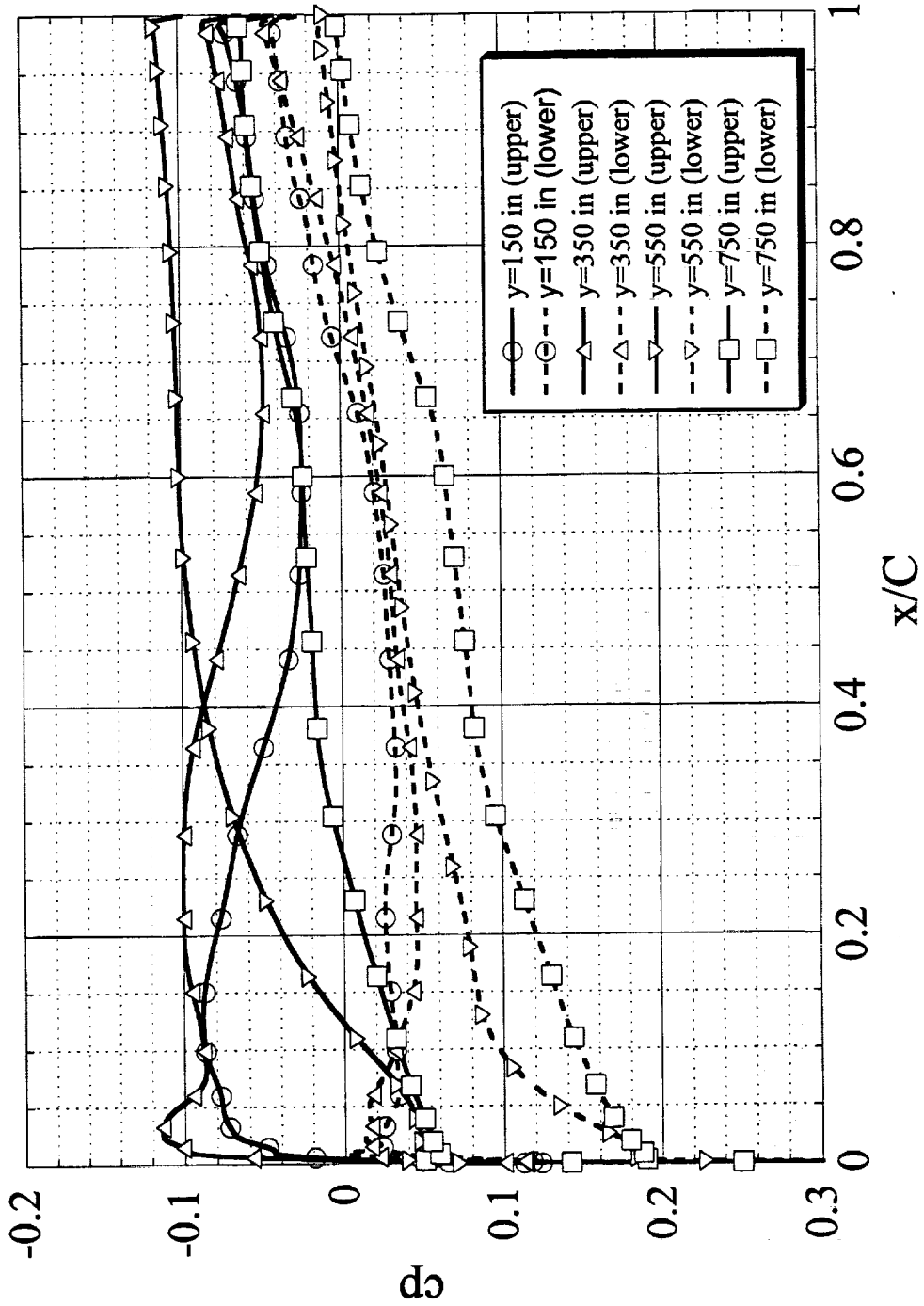
This figure shows the chordwise surface pressure distribution for the TCA at M=2.4 and flight Reynolds number of 195E6 at various span stations of the inboard wing ($y=150$ in and 350 in) and the outboard wing ($y=550$ in and 750 in).

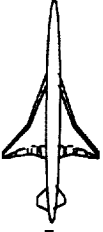




HSCT High Speed Aerodynamics

TCA Wing ($M=2.4$, $\alpha=3\text{deg}$, $Re=195E6$)





Comparison of Local c_f for TCA at $M=2.4$ and $Re=195E6$

Shown here are the results of local c_f for the TCA wing at $M=2.4$, $\alpha=3$ deg and flight $Re=195E6$ at various span stations as obtained from the OVERFLOW code. The OVERFLOW solutions for the local c_f are compared with the flat plate theories of Sommer-Short and Frankl-Voishel. For all span stations, the c_f based on q_{inf} from OVERFLOW for the lower surface is higher than that for the upper surface. This trend is a consequence of the differing surface pressure distributions on the upper and the lower surface of the wing. While the c_f based on q_{inf} for the upper and lower surface differ from the flat plate predictions, the c_f based on q_{local} are found to be close to the flat plate theories, implying that the local dynamic pressure effects have become important.

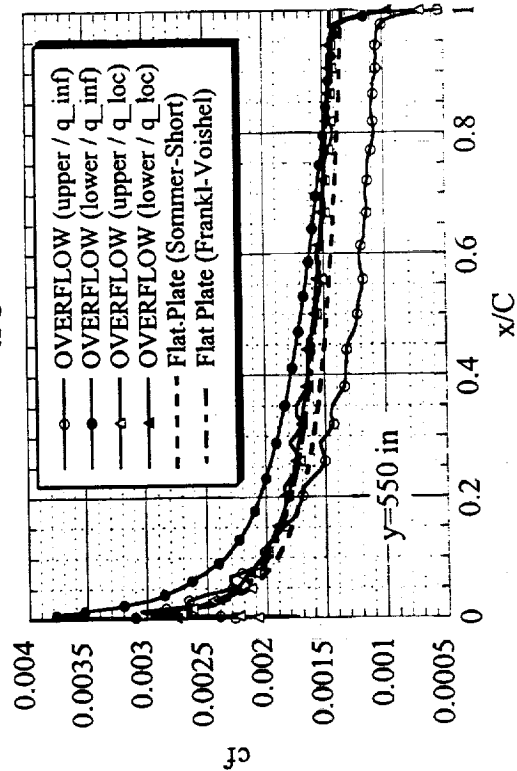
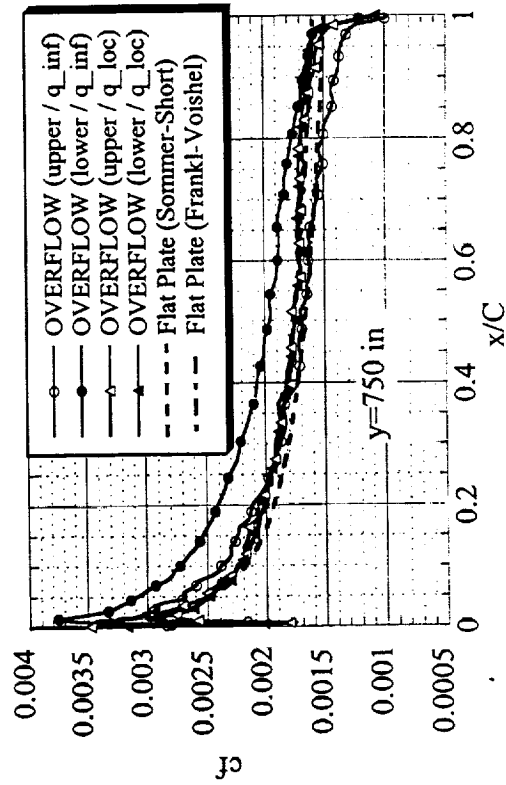
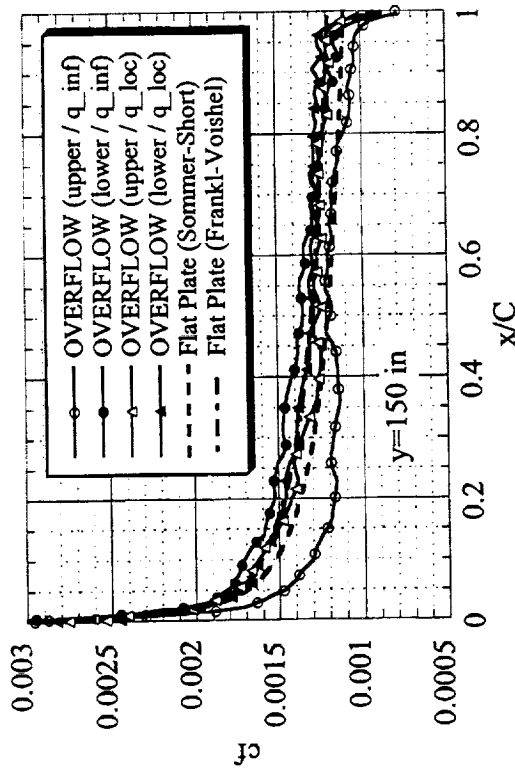
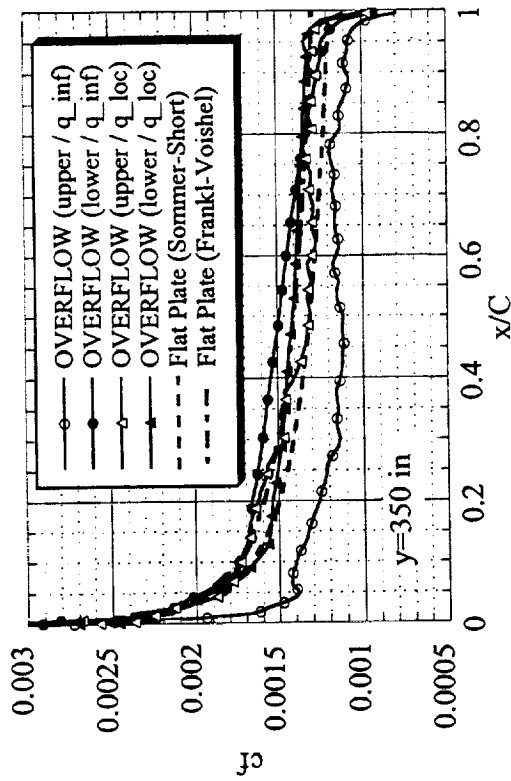


HSR Configuration Aero Final Review FY97



HSCT High Speed Aerodynamics

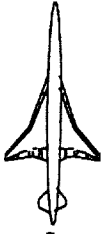
Comparison of Local Skin Friction Coefficient
TCA Wing ($M=2.4$, $\alpha=3$ deg, $Re=195E6$)





HSCT High Speed Aerodynamics

HSR Configuration Aero Final Review FY97

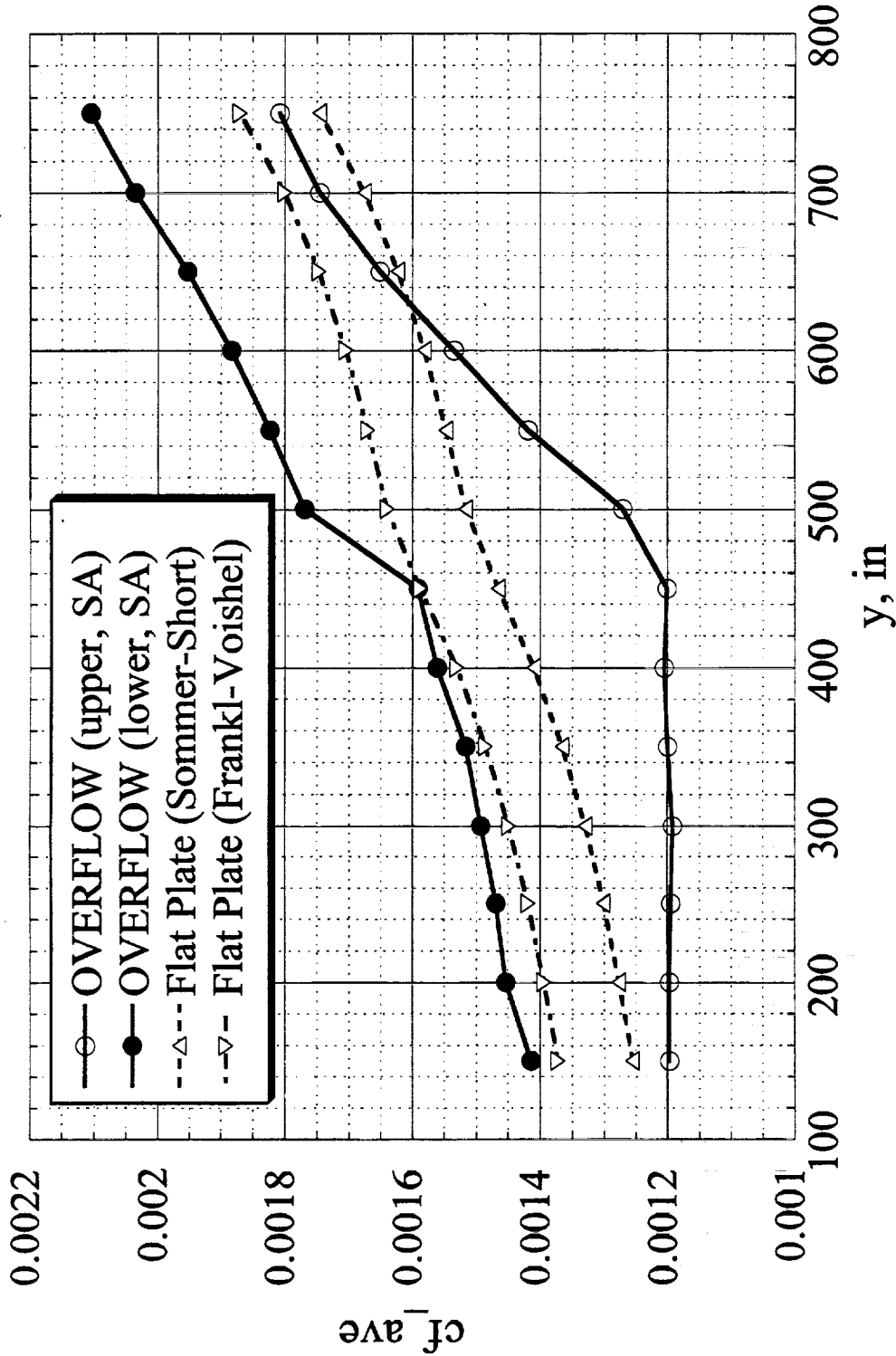


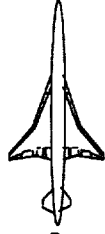
Comparison of Average c_f for TCA at $M=2.4$ and $Re=195E6$

The plot of c_{f_ave} with y suggests that the flat plate predictions are generally bounded by the OVERFLOW predictions for the upper and lower surface, and are close to the mean value of the c_{f_ave} for the upper and the lower surfaces.



TCA Wing (M=2.4, alpha=3 deg, Re=195E6)



**Skin-Friction Results for TCA at M=0.9 and Wind Tunnel Reynolds Number**

Skin friction coefficient distributions were evaluated for the baseline TCA wing at the wind tunnel Reynolds number at $M=2.4$ ($Re=6.36E6$), and $M=0.9$ ($Re=6.1E6$). The OVERFLOW solutions are based on the Spalart-Allmaras (SA) one-equation turbulence model. A comparison of the OVERFLOW and the flat plate predictions for the TCA at $M=0.9$ at $\alpha=3.7$ deg and wind tunnel $Re=6.1E6$ is summarized below.

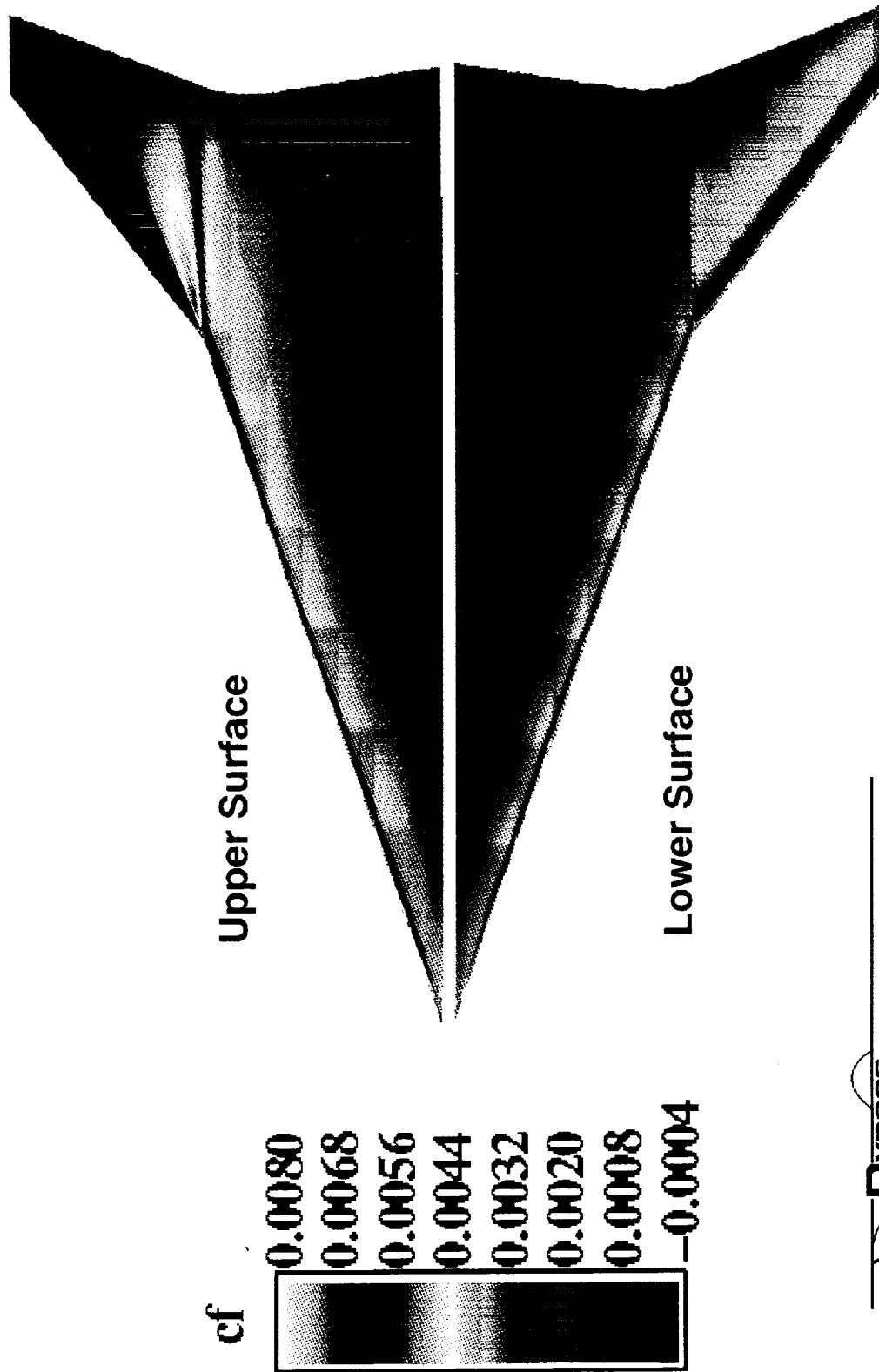
Surface c_f for the TCA at M=0.9 and $Re=6.1E6$

The surface c_f distribution at $M=0.9$ and wind tunnel Re reveal laminar-turbulent transition on the lower surface, and flow three-dimensionality on the upper surface.



HSCAT High Speed Aerodynamics

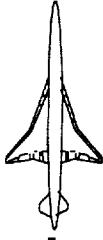
TCA Wing (M=0.9, alpha=3.7 deg, Re=6.1E6) Skin Friction Coefficient (OVERFLOW)





HSR Configuration Aero Final Review FY97

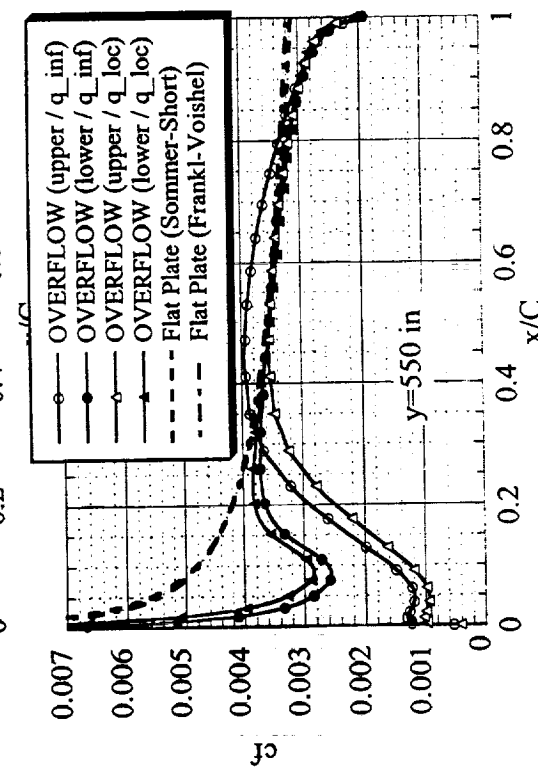
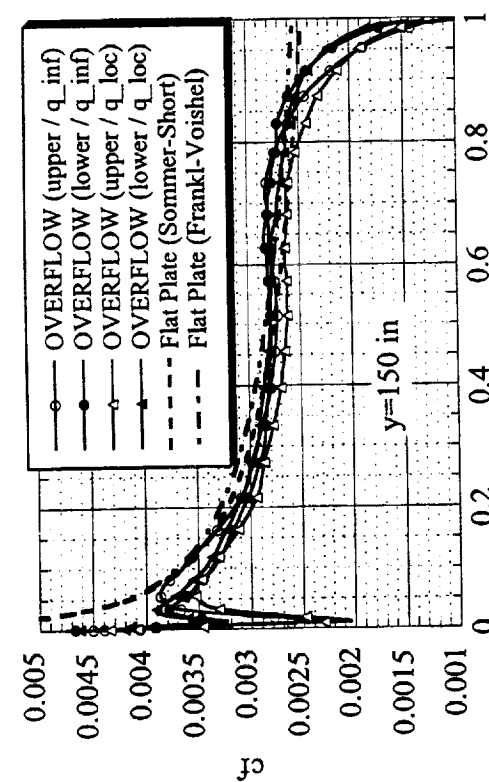
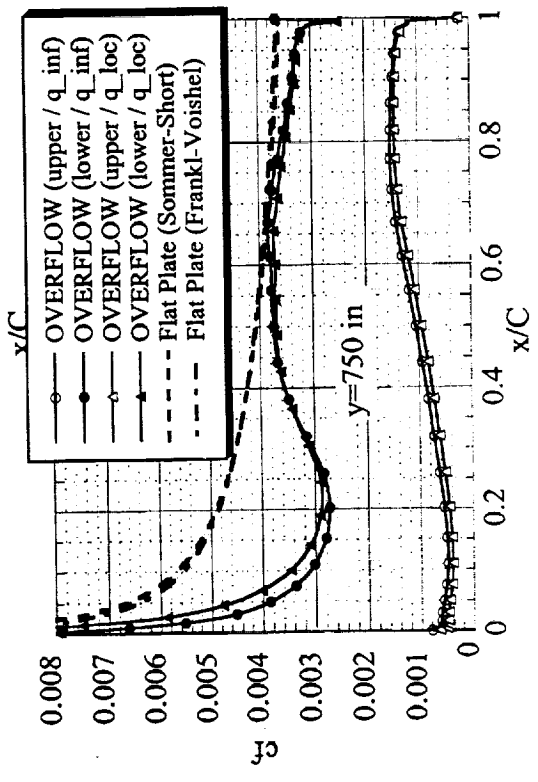
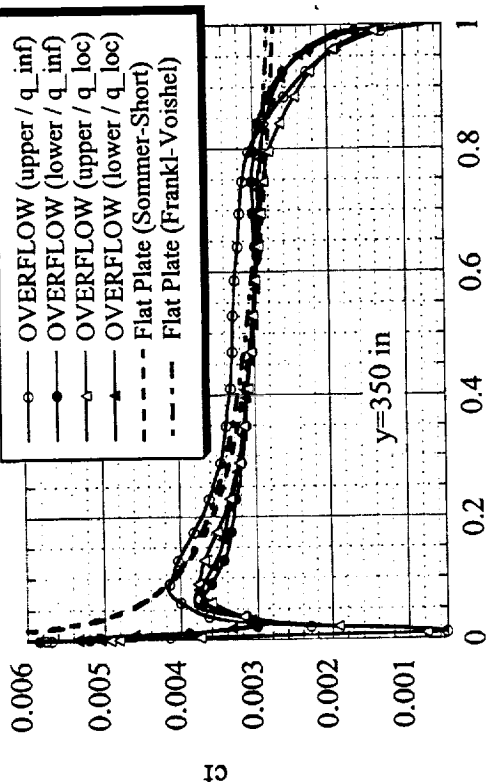
HSCT High Speed Aerodynamics



Comparison of Local cf for TCA at $M=0.9$ and $Re=6.1E6$

While the OVERFLOW solution and the flat plate theories for the local cf agree for the inboard wing region, the cf predicted by OVERFLOW for the upper surface is found to be substantially lower than the flat plate predictions for the outboard wing. Flow visualization via surface streamlines has revealed that there is spanwise flow (three-dimensional flow) on the outboard wing upper surface, which tends to diminish cf in the drag direction. Computations with local cf based on the magnitude of the skin friction vector for $y=550$ in and $y=750$ in have improved the upper surface results somewhat, but are still considerably underpredicted relative to the flat plate theory.

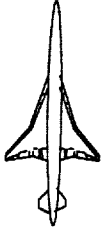
Comparison of Local Skin Friction Coefficient
TCA Wing ($M=0.9$, $\alpha=3.7$ deg, $Re=6.1E6$)





HSCT High Speed Aerodynamics

HSR Configuration Aero Final Review FY97

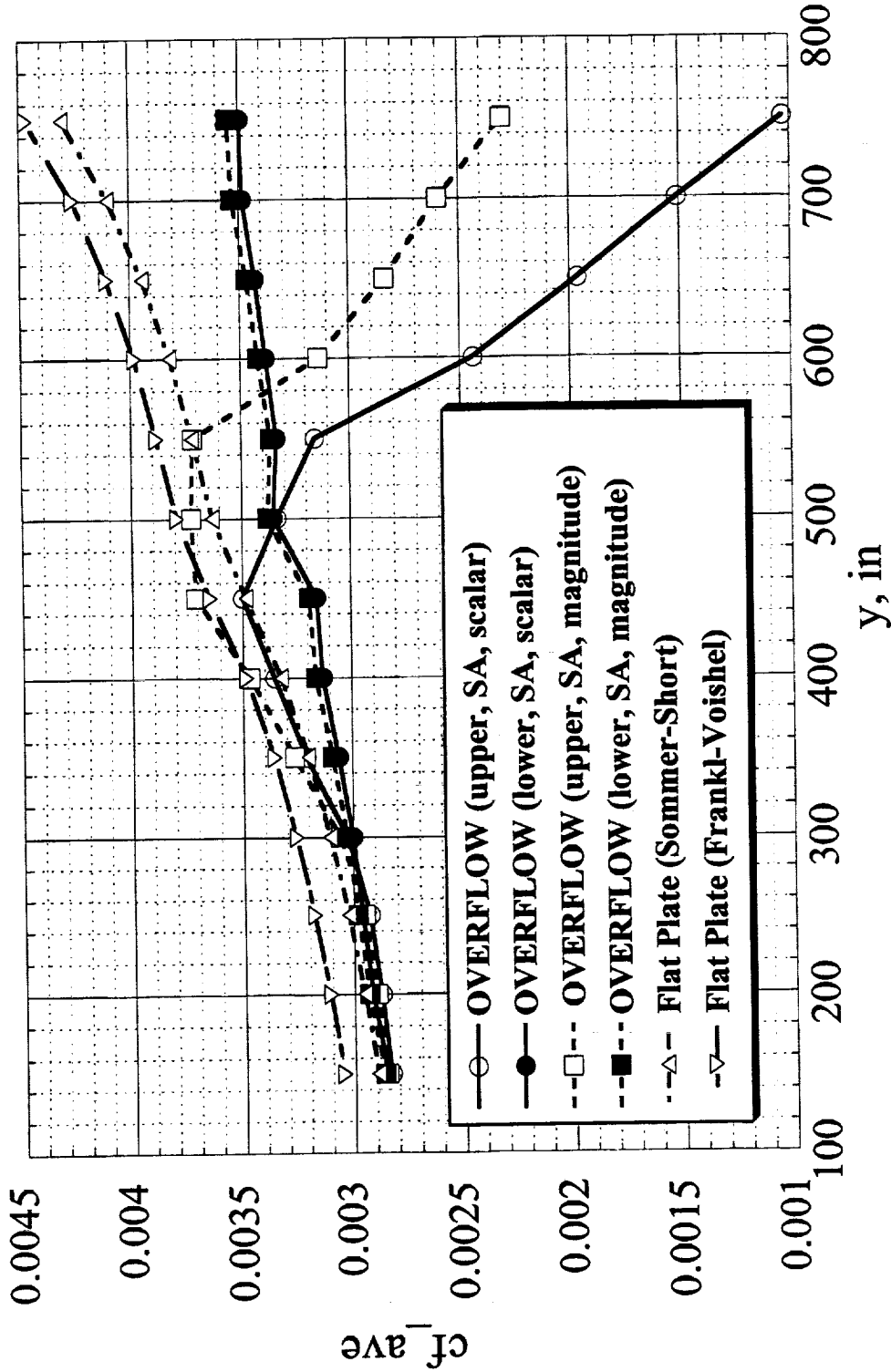


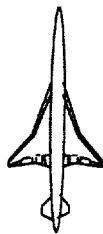
Comparison of Average c_{f_ave} for TCA at $M=0.9$ and $Re=6.1E6$

This plot displays the comparison of the c_{f_ave} as a function of the span coordinate. Since the flat plate theories are based on two-dimensional boundary layer flow, it is plain that the discrepancy in the predictions from the OVERFLOW and the flat plate theories for the outboard wing upper surface is primarily due to the three-dimensional flow effects discussed above. A similar drop in the c_{f_ave} for the outboard wing region has been noted for the TCA at $M=0.9$ and at flight Reynolds number. Flow transition is responsible for the deviation between the OVERFLOW and the flat plate results for the wing lower surface. Flow three-dimensionality is seen to have a more pronounced effect on the c_{f_ave} than flow transition.



TCA Wing (M=0.9, alpha=3.7 deg, Re=6.1E6)

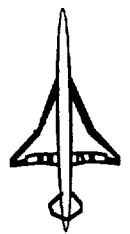


**Skin-Friction Results for TCA at M=2.4 and Wind Tunnel Reynolds Number****Comparison of Local c_f for TCA at M=2.4 and $Re=6.36E6$**

Shown here is a comparison of local c_f for the TCA wing at M=2.4, $\alpha=3$ deg and flight $Re=6.36E6$ with the flat plate theories of Sommer-Short and Frankl-Voishel. For all span stations, the c_f based on q_{inf} from OVERFLOW for the upper surface is found to be lower than that for the lower surface. This trend follows from the differing surface pressure distributions on the upper and the lower surface of the wing. While the c_f based on q_{inf} for the upper and lower surfaces differ from the flat plate predictions, the c_f based on q_{local} is found to be closer to the flat plate theories, implying that the local dynamic pressure effects have become important. The local undershoot in c_f is related to the laminar-turbulent transition described by the SA turbulence model at wind tunnel Reynolds number. Such a transition was noted earlier for the symmetric TCA at wind tunnel Reynolds number. A more detailed study of this laminar-turbulent transition at low Reynolds number is under progress with reference to OVERFLOW solutions for flat plate geometry. This case (configuration and flow conditions) thus represents a situation in which both laminar-turbulent transition and local dynamic pressure have important effect on the local c_f distribution.

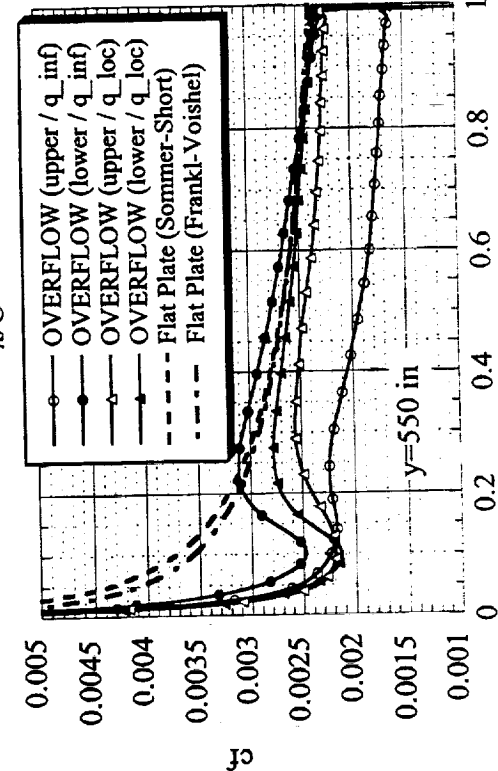
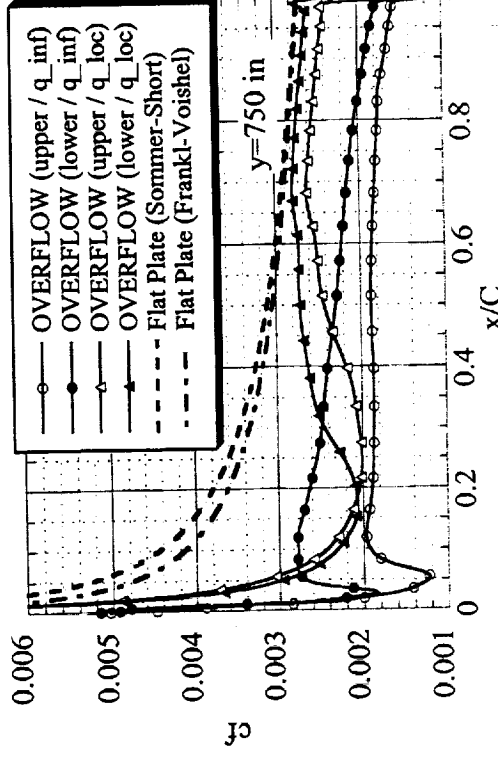
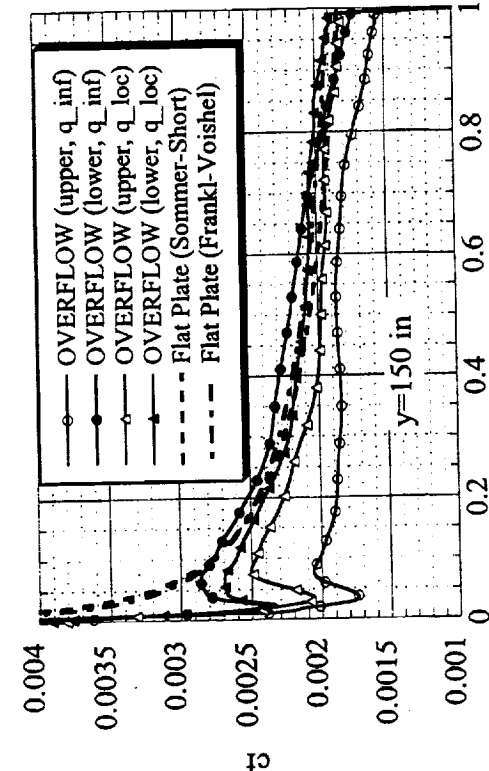
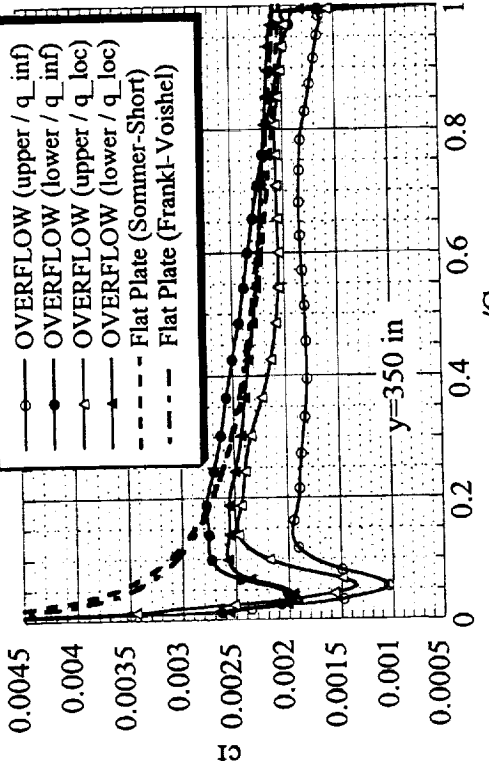


HSR Configuration Aero Final Review FY97



HSCT High Speed Aerodynamics

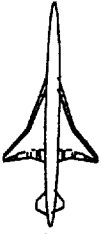
Comparison of Local Skin Friction Coefficient TCA Wing ($M=2.4$, $\alpha=3$ deg, $Re=6.36E6$)





HSCT High Speed Aerodynamics

HSR Configuration Aero Final Review FY97

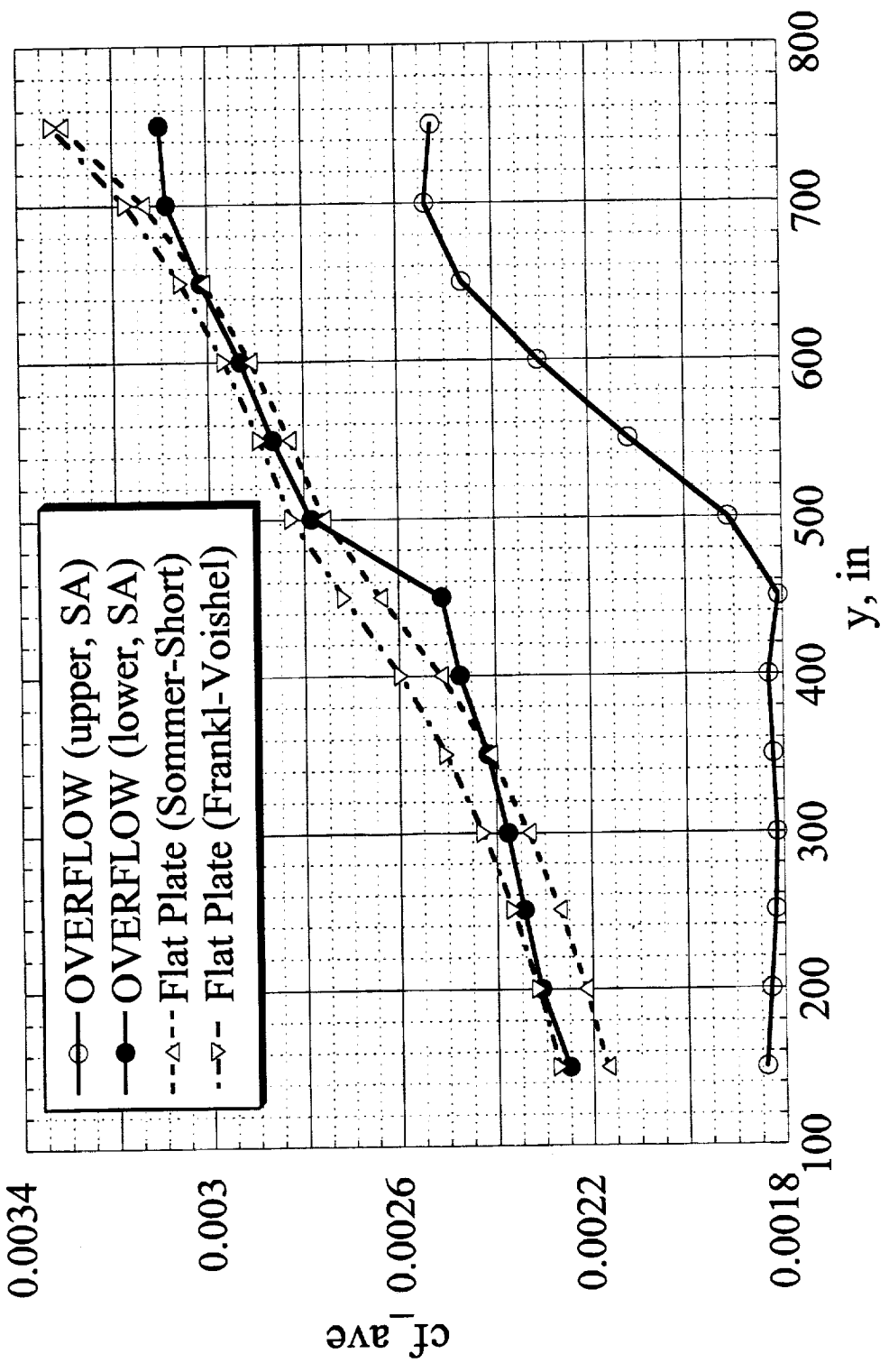


Comparison of Average cf for TCA at $M=2.4$ and $Re=6.36E6$

This figure depicts a comparison of the average cf for the TCA at $M=2.4$ and $Re=6.36E6$. While the cf_{ave} for the lower surface from OVERFLOW is comparable to the flat plate theories, the value of cf_{ave} from OVERFLOW for the upper surface is considerably below the flat plate computations. This trend is due to the laminar-turbulent transition on the upper surface, as discussed earlier with reference to the local cf . The results also suggest that the cf_{ave} for the upper surface of the inboard wing is relatively uniform.



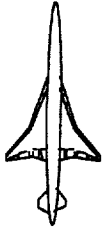
TCA Wing (M=2.4, alpha=3 deg, Re=6.36E6)





HSCT High Speed Aerodynamics

HSR Configuration Aero Final Review FY97



---This page is left intentionally blank---





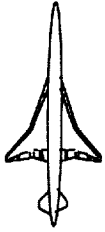
Conclusions

- For the Sym TCA at flight Re, local and average wing cf from OVERFLOW (SA model) agree well with flat plate correlations, with the W/B viscous drag matching within 1 ct.
- For the Sym TCA at WT Re, wing local cf from OVERFLOW shows laminar-turbulent transition undershoot, with the W/B viscous drag (3-4 cts) below that from flat plate theory.
- For the TCA at WT Re, laminar-turbulent transition in the wing local cf from OVERFLOW is also noted.
- For the TCA at M=0.9, local cf from OVERFLOW for the outboard wing upper surface falls well below the flat plate theory due to three-dimensional flow.
- Local dynamic pressure effects on the wing local cf become more important at M=2.4 than at M=0.9.
- Flow three-dimensionality, flow transition, local dynamic pressure and pressure gradient influence the local cf in a decreasing order.



HSCT High Speed Aerodynamics

HSR Configuration Aero Final Review FY97



---This page is left intentionally blank---



Recommendations

- **The incorporation of local dynamic pressure into flat plate theory will improve the predictions of the wing local skin friction coefficient.**
- **Flat plate theory should also take into account the effect of laminar-turbulent transition on the wing at wind tunnel Reynolds number.**
- **The laminar-turbulent transition on the wing at wind tunnel Re, predicated by OVERFLOW with the Spalart-Allmaras turbulence model, needs further examination with regard to two-equation turbulence models ($k-\omega$ & $k-\epsilon$).**

This page is intentionally left blank.



High Speed Aerodynamics, Long Beach

Feasibility Study of a TCA Symmetric Model for Accurate Skin-Friction Measurements

Raul Mendoza and P. Sundaram

Configuration Aerodynamics
The Boeing Company

HSR Airframe Technical Review
Los Angeles, California
February 9-13, 1998



This page is intentionally left blank.

Feasibility Study of a TCA Symmetric Model for Accurate Skin-Friction Measurements

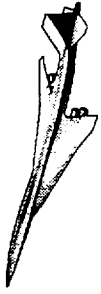
Raul Mendoza and P. Sundaram
The Boeing Company
Long Beach, California 90807-5309

Computational results from different CFD codes have been observed to produce significant differences in viscous drag predictions for HSCT configurations. Therefore, the HSR Configuration Aerodynamics (CA) community has proposed testing a TCA symmetric model in an effort to obtain wind-tunnel data useful in the validation of Navier-Stokes viscous drag predictions. This paper presents some initial computations to assess the feasibility of such a model and help define an appropriate test program.

Outline

This paper investigates the merits of conducting a wind-tunnel test on a TCA symmetric W/B model. First, the motivation and primary objective of such a test will be established. Then the approach for the proposed symmetric model program will be discussed. After the computational grid and the flow analysis tools are described, computational results at zero angle-of-attack will be presented. The TCA symmetric W/B configuration was analyzed at both, wind-tunnel and flight Reynolds numbers. Euler and Navier-Stokes solutions were obtained at various freestream Mach numbers. The effect of Reynolds number on zero-lift drag was also studied. Conclusions drawn from this study will then be given. Before closing, testing issues and model limitations will be discussed. And finally, some recommendations for the proposed wind-tunnel test will be offered.

Outline



High Speed Aerodynamics, Long Beach

- Motivation and objective
- Approach to symmetric TCA program
- Flow analysis tools
- Computational grid
- Computational results
- Conclusions
- Test issues and model limitations
- Recommendations

Motivation and Objective

It is, in general, assumed that CFD is accurate in computing pressure drag because predictions agree with each other to within two counts for TCA W/B and W/B/N/D configurations. Skin-friction drag, however, seems to be the major uncertainty in current CFD methods. Viscous drag estimates from different Navier-Stokes codes vary by as much as six counts for TCA W/B and W/B/N/D configurations. For this reason, a symmetric TCA wind-tunnel test has been proposed. The primary objective of this test would be to obtain experimental data useful in the calibration of Navier-Stokes codes for accurate viscous drag predictions.

Motivation and Objective

High Speed Aerodynamics, Long Beach



Motivation:

- High confidence in CFD predictions for pressure drag
 - Codes agree to within 2 counts of each other for TCA W/B and W/B/N/D configurations
- High uncertainty in CFD predictions for skin-friction drag
 - Estimates vary by as much as 6 counts for TCA W/B and W/B/N/D configurations

Primary objective of symmetric TCA program:

- Calibration of CFD codes for accurate skin-friction drag predictions

Approach to Symmetric TCA Program

In order to successfully accomplish the objective of the proposed symmetric model program, a comprehensive CFD analysis must be conducted first to help define the scope of the wind-tunnel test. It may also be prudent to create a detailed plan prior to testing, trying to anticipate possible sources of trouble during the test (such as lack of trip effectiveness).

The proposed wind-tunnel model would be built based on the TCA W/B configuration with no nacelles. It would be a mid-wing design with the same planform and volume as the TCA. However, the wing would have neither camber nor twist, and the fuselage would have a cylindrical shape with no camber. Even though some of the important features present in an HSCT design would be lost with these simplifications, the model would still be more realistic than, for instance, an ogive body.

Testing a symmetric model (with a symmetric sting) at zero angle-of-attack offers several advantages. First, it minimizes the effects of aeroelasticity due to model deformations. At $\alpha = 0^\circ$, a symmetric model produces no lift, and therefore, the drag due to lift is zero. Thus, ideally, the total drag of such a model at zero angle-of-attack consists of only a skin-friction drag component and a pressure drag contribution. In addition, the flow on a symmetric model at $C_L = 0$ is expected to be attached (unlike the flow on a cambered model, which usually exhibits some lower-surface separation near zero-lift).

To investigate the variation of drag with freestream Mach number, as well as the effects of Reynolds number, this model would need to be tested in different NASA and industry facilities such as NASA Langley's Unitary Plan Wind Tunnel (UPWT) or the National Transonic Facility (NTF), Boeing's Supersonic Tunnel (BSWT) in Seattle, or the Polysonic Wind Tunnel (PSWT) in St. Louis. The data collected from this series of wind-tunnel tests would then be used to validate skin-friction drag predictions from the various Navier-Stokes codes used in the HSR program.

Approach to Symmetric TCA Program



High Speed Aerodynamics, Long Beach

- Conduct CFD analysis to help define a wind-tunnel test program
- Build symmetric model based on TCA with wing/body twist and camber removed
- Test model at zero α :
 - No drag due to lift
 - No aeroelastic effects
 - Attached flow
- Test model at various M_∞ and over a wide range of Re in different NASA and industry facilities:
 - UPWT, NTF, BSWT, PSWT
- Validate Navier-Stokes skin-friction drag predictions

Flow Analysis Tools

CFL3D was the flow solver used throughout this study. The serial version of the code was run on the Cray C-90 computer, while the parallel version was used on the IBM SP-2 and the Cray T3E machines. The code was exercised in both the Euler and Navier-Stokes modes. Even though several turbulence models are available, only the Baldwin-Lomax model was used because it is very robust and, being an algebraic model, it is relatively inexpensive. Multigridding and grid sequencing were two of the techniques utilized to accelerate convergence.

Skin-friction drag estimates from flat-plate theory were computed to supplement the CFL3D Euler drag calculations. Two different ways of computing the equivalent flat-plate skin-friction predictions were used: the van Driest II method, which has been used at Boeing Long Beach for a long time, and the Sommer-Short formulation, which is preferred by Boeing Seattle. Both methods require the freestream Mach number and the Reynolds number as inputs. In addition, the Sommer-Short formulation needs the freestream temperature. In both cases the flow is assumed to be compressible and fully turbulent. Also, the flat plate is taken to be smooth and adiabatic. No attempt is made to account for form drag in the flat-plate calculations.

Flow Analysis Tools



High Speed Aerodynamics, Long Beach

- Flow solver:
- CFL3D serial version 4.1 on Cray C-90
 - CFL3D parallel version on IBM SP-2 and Cray T3E
 - Euler and Navier-Stokes (Baldwin-Lomax) modes
 - Convergence acceleration:
 - Multigridding
 - Grid sequencing

Flat-plate theory for skin-friction:

- van Driest II
- Sommer-Short

Computational Grid

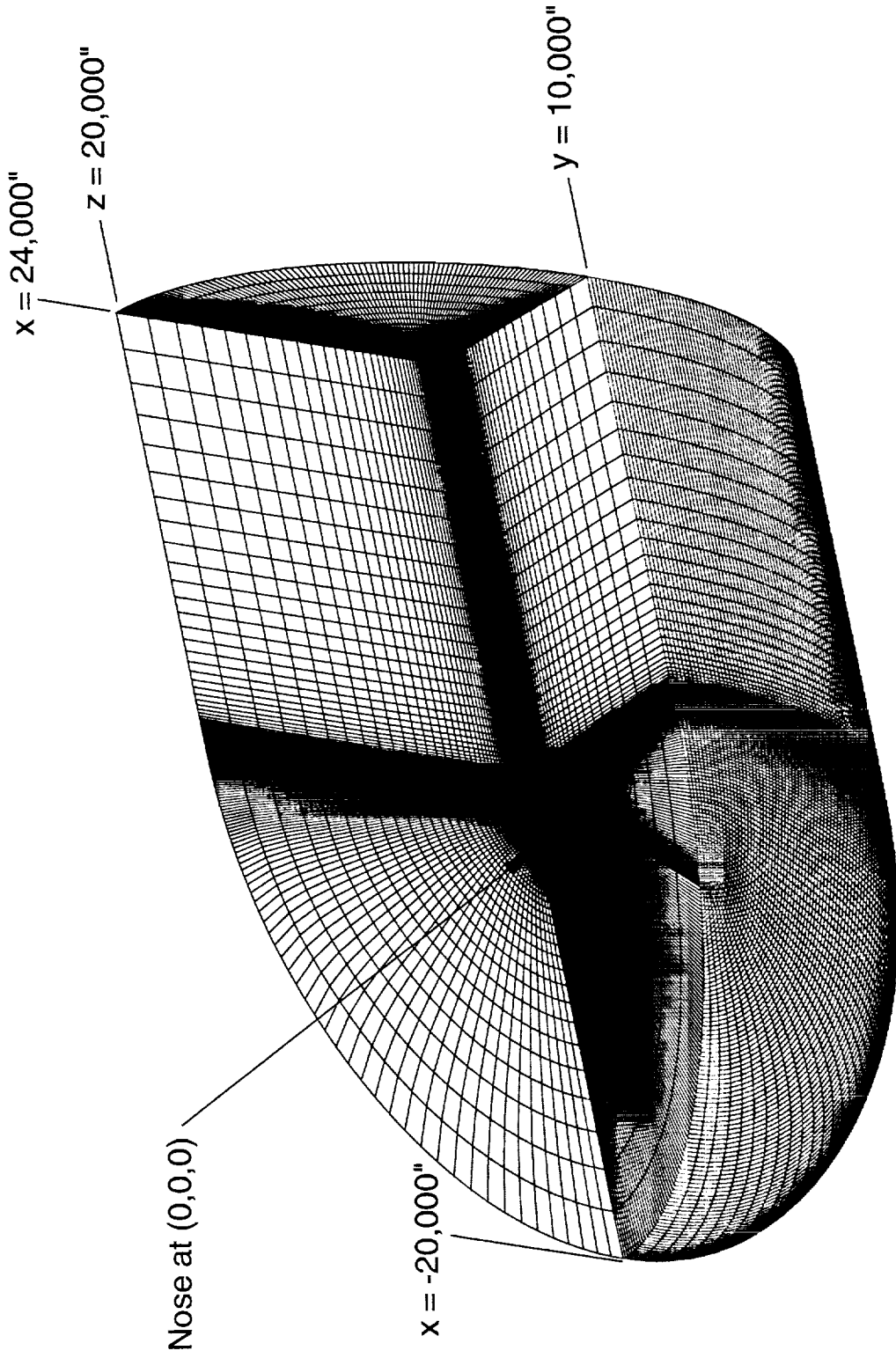
A typical volume grid used during this study is shown here. This is a structured, single-block W/B grid with a C-O topology. There are a total of 329 points in the streamwise direction and 97 points in the spanwise direction. The grid used for all the Euler calculations had 65 points in the normal direction for a total of 2.1 million points. On the other hand, a different Navier-Stokes grid was used every time the flow conditions changed significantly. The Navier-Stokes grids were constructed from the Euler grid by adding 24 cells in the normal direction and clustering the points near the surface appropriately for different Reynolds numbers. Thus, the Navier-Stokes grids increased to 89 points in the normal direction resulting in a total of 2.8 million points. The volume grids extend more than five body lengths in all directions, except in the spanwise direction where the grid extends by more than 12 semispans. This type of grid was found to be adequate for all computations performed, including the transonic calculations. A 1.675% model with a closed airbody was used in the CFD computations.

Volume Grid for the TCA Symmetric W/B Configuration

High Speed Aerodynamics, Long Beach

Euler: C-O Grid (329 x 65 x 97), 2.1 Million Points

Navier-Stokes: C-O Grid (329 x 89 x 97), 2.8 Million Points



Computational Results

In order to study the variation of zero- α drag with freestream Mach number, two Mach number sweeps were performed. One was done at a typical wind-tunnel Reynolds number of $4 \times 10^6/\text{ft}$ (or $Re_c = 6.36 \times 10^6$, based on the mean aerodynamic chord). A second Mach sweep was performed at flight Reynolds numbers, which were varied with M_∞ according to the TCA flight schedule. The effects of Reynolds number on zero- α drag were also evaluated at $M_\infty = 0.5$.

Computational Results



High Speed Aerodynamics, Long Beach

- Variation of zero- α drag with M_∞ at:
 - Wind-tunnel Reynolds number ($Re_c = 6.36 \times 10^6$)
 - Flight Reynolds numbers (vary with M_∞)
- Variation of zero- α drag with Reynolds number at $M_\infty = 0.5$

Computational Results (Case 1)

The next few charts illustrate the variation of zero- α drag with Mach number at the wind-tunnel Reynolds number of $Re_c = 6.36 \times 10^6$. First, Navier-Stokes skin-friction drag results and flat-plate estimates will be compared. Next, a comparison of Navier-Stokes and Euler pressure drag predictions will be presented. In addition, predictions for total drag will be shown. Finally, the effects of truncating the aftbody on pressure drag for the wind-tunnel model at $M_\infty = 0.5$ will be estimated.

Computational Results (Case 1)



High Speed Aerodynamics, Long Beach

- Variation of zero- α drag with M_∞ at wind-tunnel Reynolds number ($Re_c = 6.36 \times 10^6$):
 - Viscous drag (N-S vs. equivalent flat-plate theory)
 - Pressure drag (N-S vs. Euler)
 - Total drag (N-S vs. Euler + flat-plate)
 - Effect of truncating the aftbody on pressure drag for wind-tunnel model at $M_\infty = 0.5$

Variation of Viscous Drag with Mach Number

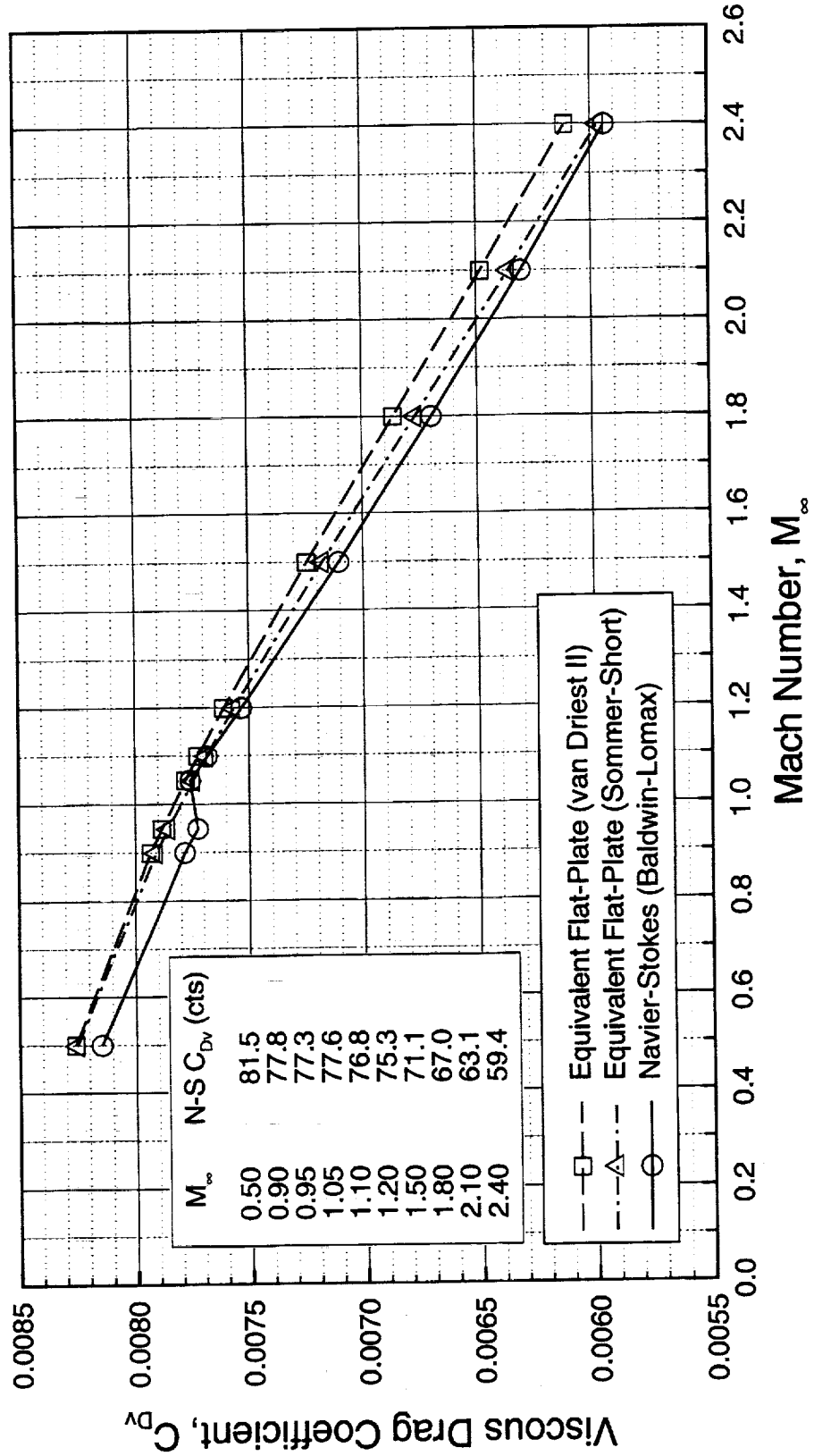
This chart presents the variation of viscous drag with Mach number at $Re_c = 6.36 \times 10^6$ and zero angle-of-attack for Mach numbers ranging from 0.5 to 2.4. Three different sets of drag predictions are shown. The data represented by the squares correspond to the equivalent flat-plate skin-friction drag estimates from the van Driest II formulation. The triangles represent the flat-plate skin-friction drag results, as predicted by the Sommer-Short formulation. Finally, the CFL3D Navier-Stokes predictions are represented by the circles. At low Mach numbers the flat-plate estimates agree very well with each other. But as the Mach number increases, the flat-plate methods start to deviate from each other. It can be seen that both flat-plate formulations overpredict the Navier-Stokes results for practically the entire range of Mach numbers considered. However, at high Mach numbers, the Sommer-Short predictions show better agreement with CFL3D Navier-Stokes than the van Driest II estimates. Also, the Navier-Stokes curve shows a discontinuity in the vicinity of Mach 1.0 that the flat-plate results do not display. This discontinuity is probably due to the shock/boundary layer interaction that, of course, flat-plate theory cannot capture.

Variation of Viscous Drag with Mach Number

High Speed Aerodynamics, Long Beach



TCA Symmetric W/B Configuration at $\alpha = 0^\circ$, $Re_c = 6.36 \times 10^6$
 CFL3D, Navier-Stokes (Baldwin-Lomax)



Variation of Pressure Drag with Mach Number

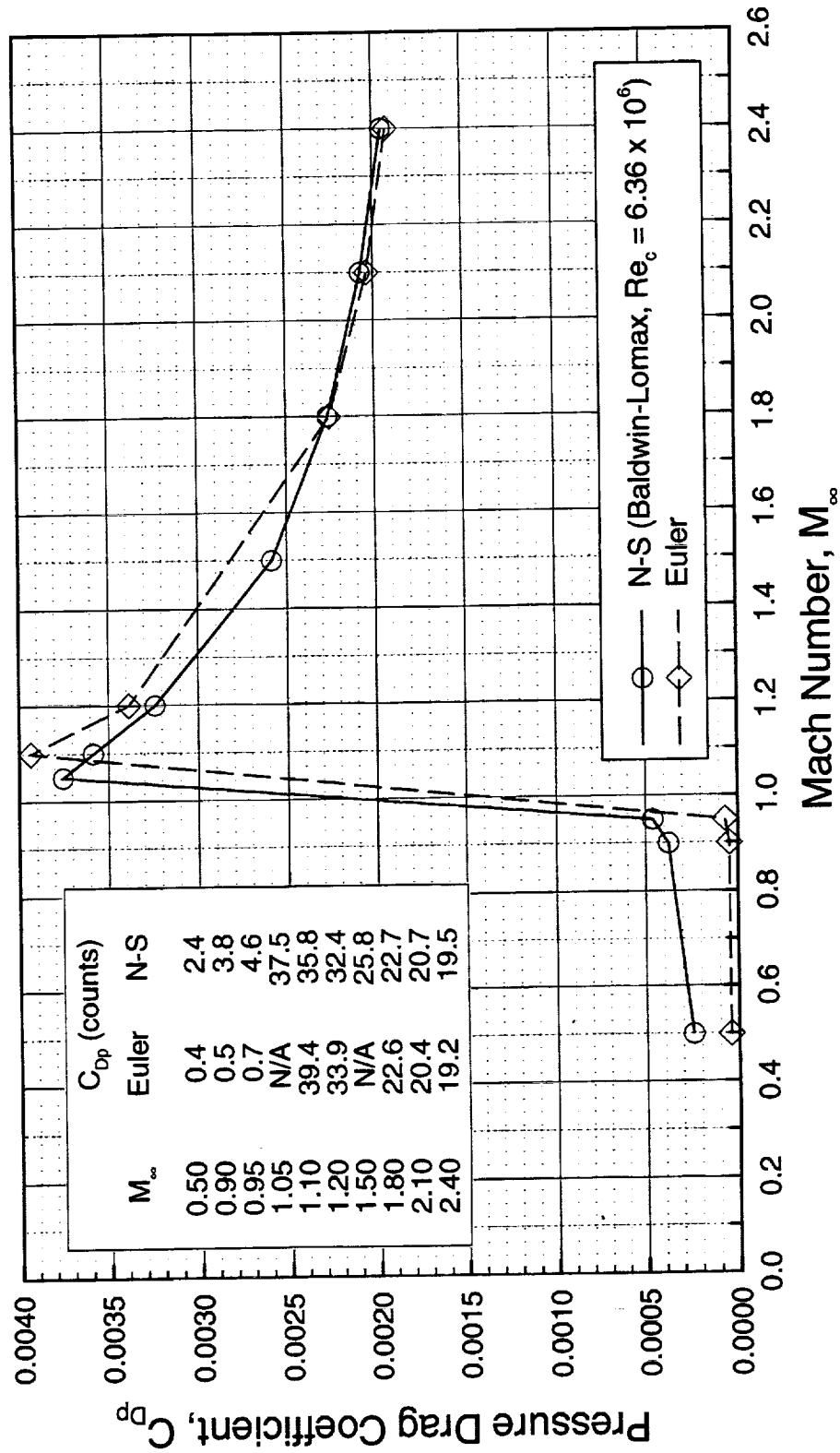
Pressure drag as a function of Mach number is shown in this chart. Both, Euler and Navier-Stokes ($Re_c = 6.36 \times 10^6$) results are presented. Ideally, the zero-lift drag of a closed body in subsonic, inviscid flow should be zero. However, at $M_\infty = 0.5$ (for instance), CFL3D Euler produced an inviscid drag of 0.4 counts at zero-lift (the computed lift was in the order of 10^{-9}). Several attempts were made to bring the computed value closer to the theoretical value, but a quick grid refinement study indicated that even for infinitely small grid spacing, CFL3D Euler would predict a finite amount of drag. However, the important thing to note from this chart is the increase in subsonic pressure drag that results from switching from inviscid solutions to viscous computations. At $M_\infty = 0.5$, for instance, the pressure drag goes from 0.4 counts (Euler) to 2.4 counts (Navier-Stokes). At $M_\infty = 0.95$, there is an increase in pressure drag of almost 4 counts. These results clearly show the effects of viscosity on pressure drag. It is evident that even at subsonic speeds the total drag is not just viscous drag. There is a pressure drag component (i.e., form drag), which is a result of the presence of the boundary layer. Although small, this component is not negligible. In this case, at $M_\infty = 0.5$, the pressure drag component computed by CFL3D Navier-Stokes represents almost 3% of the total drag of the symmetric model. At high Mach numbers, the Euler results predict the Navier-Stokes solutions fairly well.

Variation of Pressure Drag with Mach Number

High Speed Aerodynamics, Long Beach



TCA Symmetric W/B Configuration at $\alpha = 0^\circ$
 CFL3D, Euler and Navier-Stokes (Baldwin-Lomax)



Variation of Total Drag with Mach Number

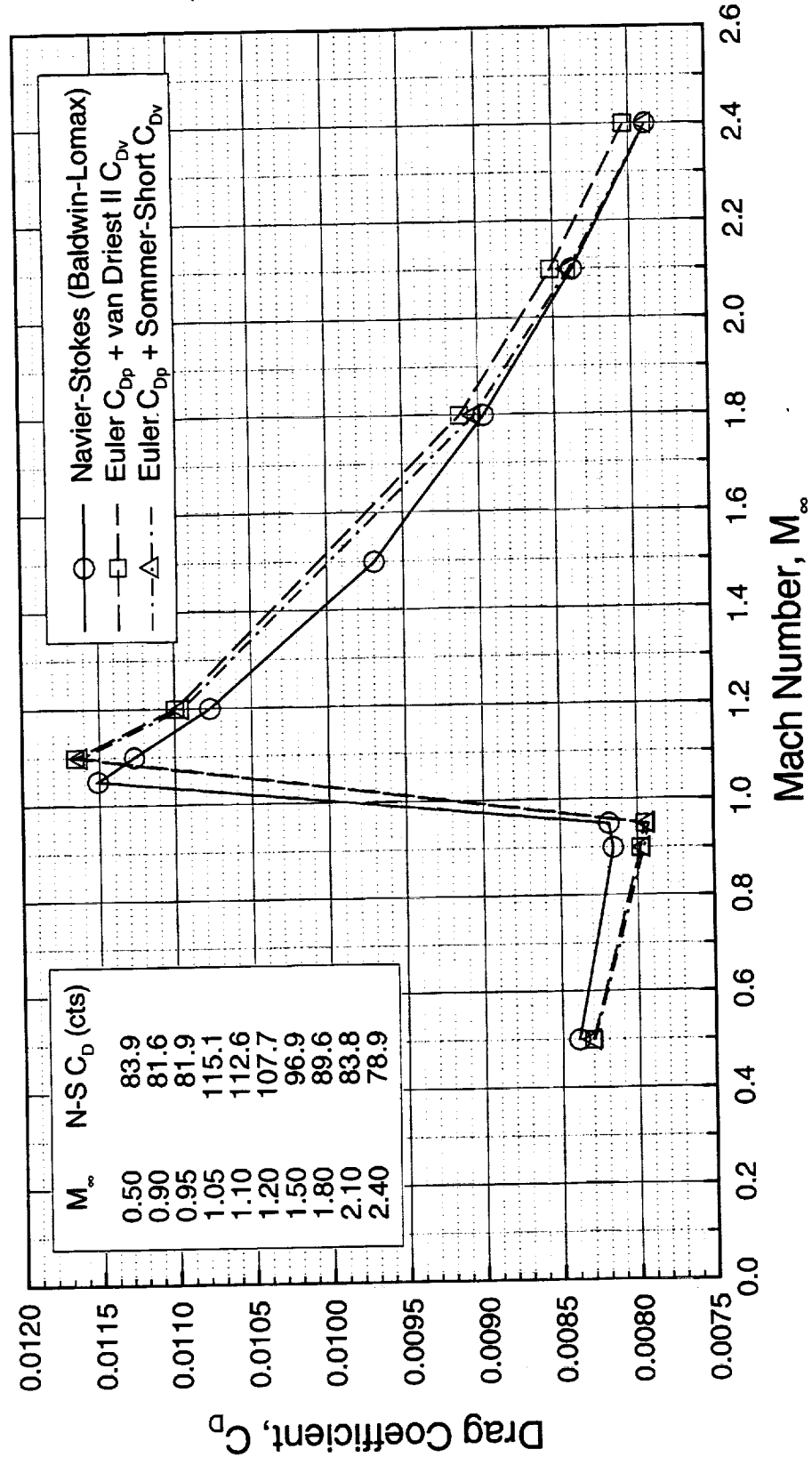
The total drag is shown in this figure. Flat-plate skin-friction drag estimates have been added to the Euler pressure drag. All three curves shown here lie within 2 counts of each other, except near Mach 1.1, where the difference is about 4 counts.

Variation of Total Drag with Mach Number



High Speed Aerodynamics, Long Beach

TCA Symmetric W/B Configuration at $\alpha = 0^\circ$, $Re_c = 6.36 \times 10^6$
 CFL3D, Euler and Navier-Stokes (Baldwin-Lomax)



Effect of Truncating the Aftbody on C_{Dp}

All the computations shown so far were performed using a fuselage with a closed aftbody. However, in a wind-tunnel test, the aftbody needs to be truncated to accommodate the sting. Pressure drag estimates for the symmetric W/B configuration with a closed and a truncated aftbody are listed in this chart (both values were obtained from the same CFD solution, but in the latter case, force integration was performed only up to the truncation station to simulate a truncated aftbody). Both Euler and Navier-Stokes calculations show that the additional drag component that results from truncating the aftbody is approximately one count at $M_\infty = 0.5$. Thus, the Navier-Stokes pressure drag goes up from almost 3% to about 4% of the total drag at $Re_c = 6.36 \times 10^6$.

Effect of Truncating the Aftbody on C_{Dp}



High Speed Aerodynamics, Long Beach

TCA Symmetric W/B Configuration

CFL3D, $M_\infty = 0.5$, $\alpha = 0^\circ$

	Pressure Drag C_{Dp} (cts)		
	Closed Aftbody	Truncated* Aftbody	ΔC_{Dp} (Truncated - Closed)
Euler	0.4	1.5	1.1
Navier-Stokes (Balwin-Lomax, $Re_c = 6.36 \times 10^6$)	2.4	3.3	0.9

*force integration to $x = 3148$ in. (full scale)

Computational Results (Case 2)

The effects of Mach number on zero- α drag at flight Reynolds numbers will be presented next. Again, the equivalent flat-plate estimates for skin-friction drag will be compared to Navier-Stokes predictions. Pressure drag estimates from Euler and Navier-Stokes runs will also be compared. Total drag predictions will be presented as well. Finally, a summary chart comparing different drag predictions at $M_\infty = 0.9$ will be shown.

Computational Results (Case 2)



High Speed Aerodynamics, Long Beach

- Variation of zero- α drag with M_∞ at flight Reynolds numbers:
 - Viscous drag (N-S vs. equivalent flat-plate theory)
 - Pressure drag (N-S vs. Euler)
 - Total drag (N-S vs. Euler + flat-plate)
 - Summary of drag predictions at $M_\infty = 0.9$

Variation of Viscous Drag with Mach Number

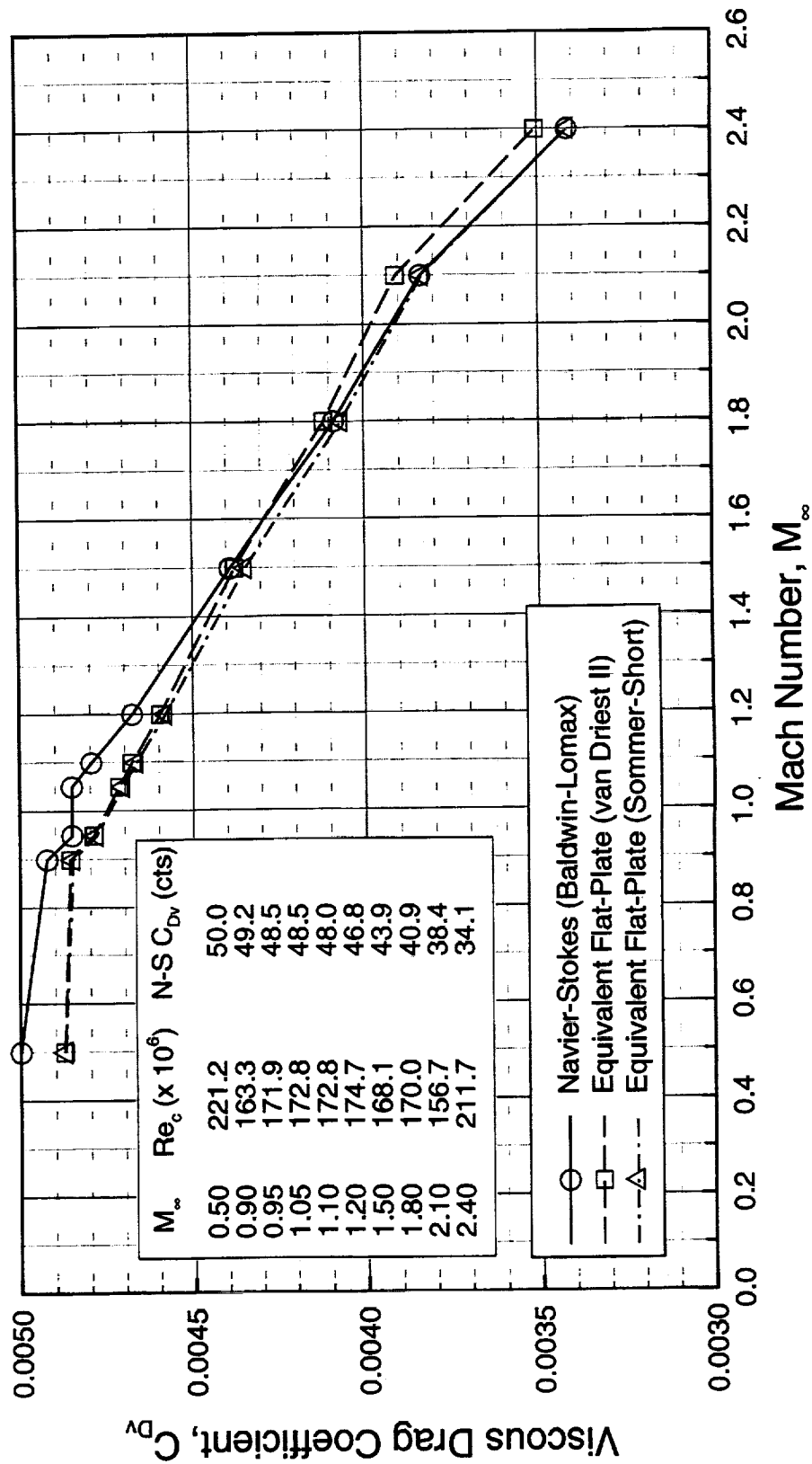
Viscous drag at flight Reynolds numbers is presented in this chart as a function of Mach number. Once again, the flat-plate skin-friction drag estimates show excellent agreement with each other at low speeds, but they start to deviate from each other beyond Mach 1.0. Flat-plate theory underpredicts the Navier-Stokes results at subsonic and low supersonic Mach numbers. However, for Mach numbers greater than 1.6, the van Driest II formulation overpredicts the Navier-Stokes computations. The Sommer-Short predictions, on the other hand, get closer to the Navier-Stokes results as the Mach number increases to 2.4. The Navier-Stokes result for this case also exhibits the same type of discontinuity near Mach 1.0 previously observed in the Navier-Stokes results for wind-tunnel conditions. This discontinuity is, again, believed to be caused by the shock/boundary layer interaction that CFL3D detects and flat-plate theory does not.

Variation of Viscous Drag with Mach Number

High Speed Aerodynamics, Long Beach



TCA Symmetric W/B Configuration at $\alpha = 0^\circ$, Flight Reynolds Numbers
CFL3D, Navier-Stokes (Baldwin-Lomax)



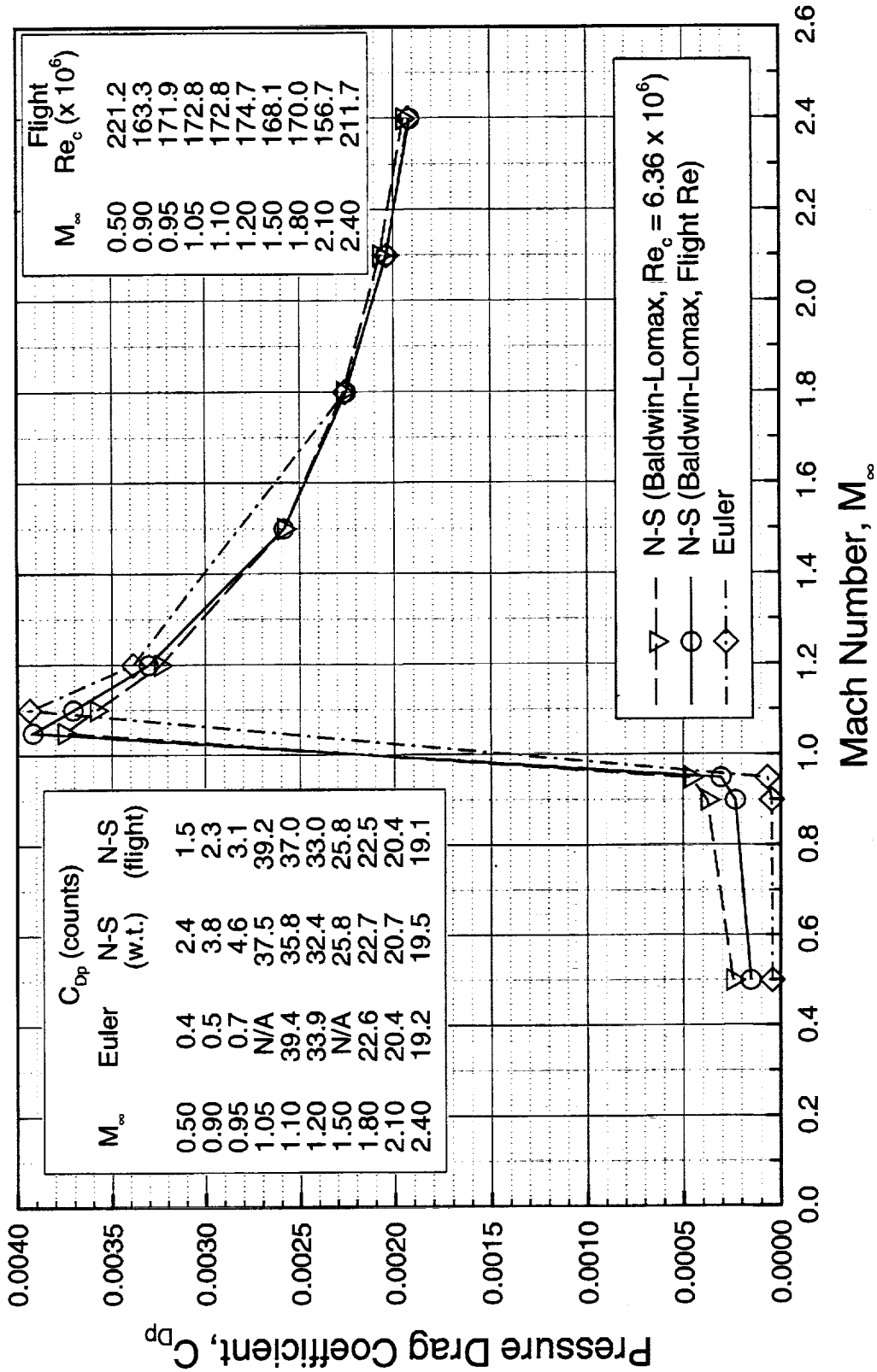
Variation of Pressure Drag with Mach Number

The pressure drag variation as predicted by CFL3D is illustrated in this figure. Euler and Navier-Stokes (Baldwin-Lomax) solutions are presented. The data corresponding to wind-tunnel conditions are shown here for comparison purposes. As expected, the displacement effects of the boundary layer cause the Navier-Stokes computations to predict more pressure drag than the Euler calculations for Mach numbers less than one. Also, the lower the Reynolds number, the thicker the boundary layer and the higher the pressure (form) drag. So, for $M_\infty < 1$, the pressure drag obtained for the wind-tunnel Reynolds number is seen to be higher than the pressure drag computed for the flight Reynolds numbers. At $M_\infty = 0.5$, for example, the pressure drag increases by almost one count when the Reynolds number decreases from $Re_c = 221.2 \times 10^6$ to $Re_c = 6.36 \times 10^6$. At $M_\infty = 0.95$, the drag increment between flight and wind-tunnel conditions is 1.5 counts. At high Mach numbers, however, the Reynolds number effects do not seem to be as significant. For $M_\infty > 1.8$, all three curves agree to within less than 0.5 counts of each other.

Variation of Pressure Drag with Mach Number

High Speed Aerodynamics, Long Beach

TCA Symmetric W/B Configuration at $\alpha = 0^\circ$
 CFL3D, Euler and Navier-Stokes (Baldwin-Lomax)



Variation of Total Drag with Mach Number

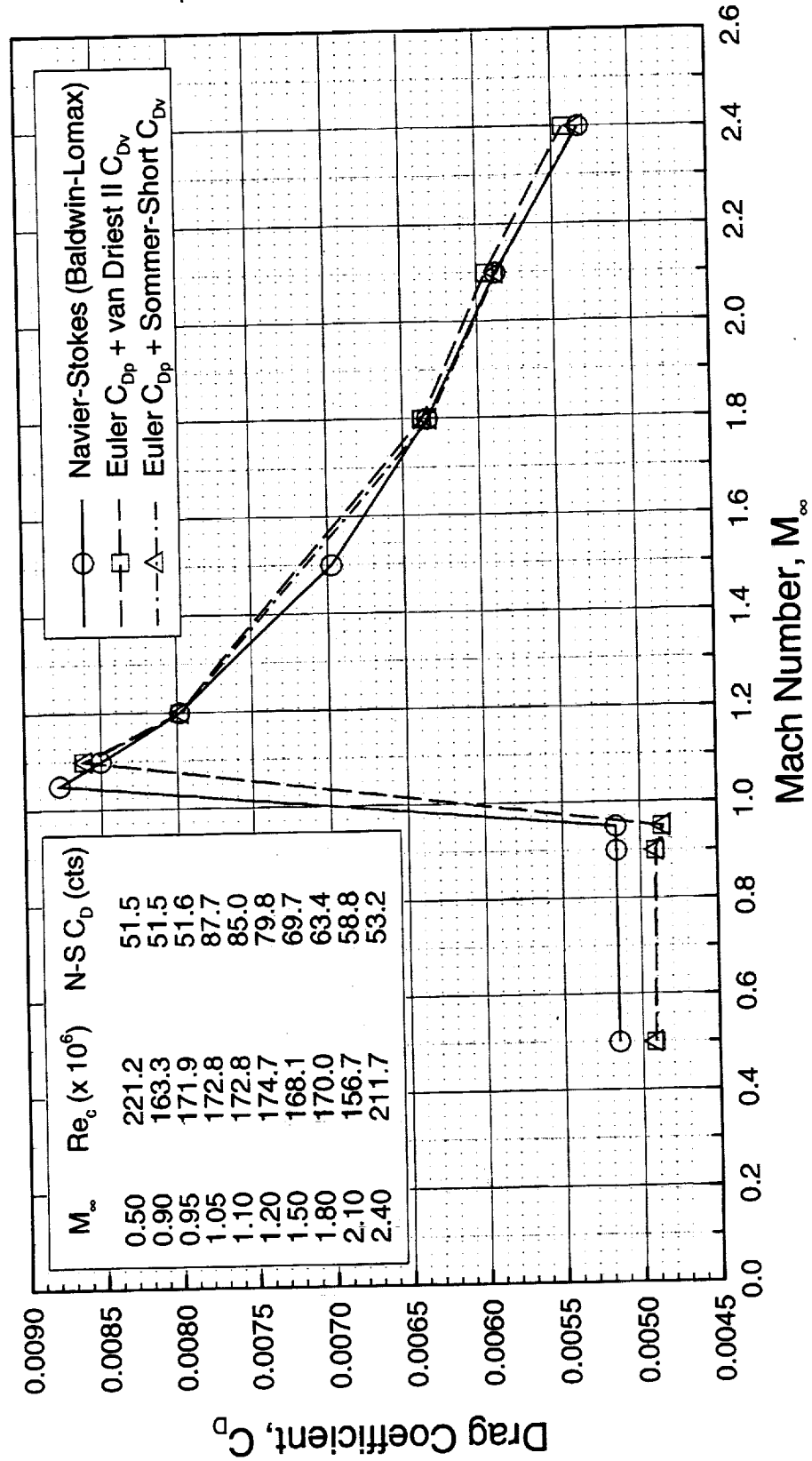
This figure illustrates the variation of total drag with Mach number at flight Reynolds numbers. Navier-Stokes (Baldwin-Lomax) results are presented along with Euler solutions with both the van Driest II and Sommer-Short skin-friction drag. For subsonic Mach numbers, the difference between the Navier-Stokes predictions and the Euler-based drag is about 2.5 counts. In the supersonic regime, all three curves agree to within one count of each other.

Variation of Total Drag with Mach Number



High Speed Aerodynamics, Long Beach

TCA Symmetric W/B configuration at $\alpha = 0^\circ$, Flight Reynolds Numbers CFL3D, Euler and Navier-Stokes (Baldwin-Lomax)



Summary of Drag Predictions at $M_\infty = 0.5$

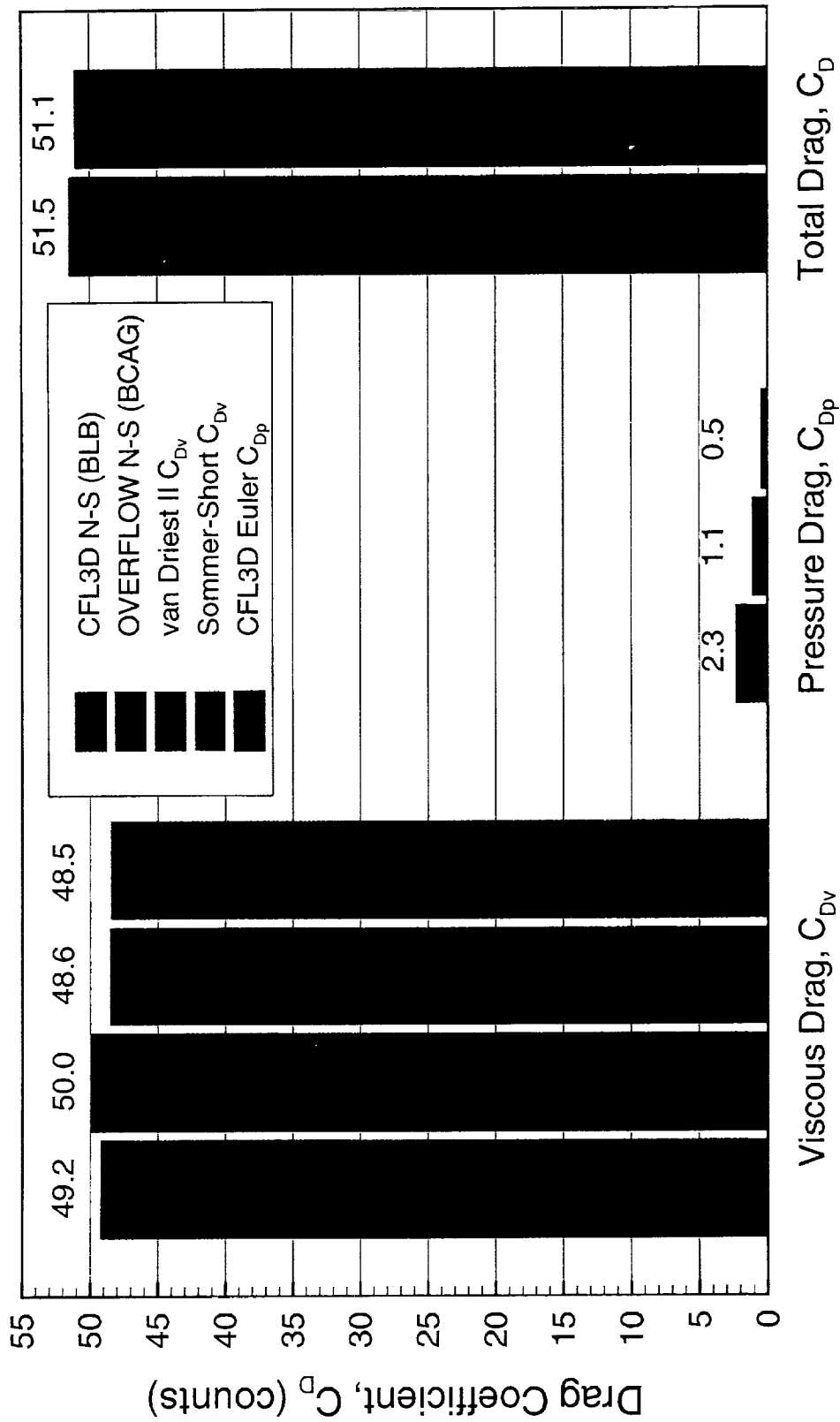
A summary of drag predictions for the TCA symmetric W/B configuration at $M_\infty = 0.9$, $Re_c = 163.3 \times 10^6$, and $\alpha = 0^\circ$ is presented in this chart. Four different methods were used to compute the viscous drag: CFL3D N-S (Baldwin-Lomax), OVERFLOW N-S (Spalart-Allmaras), and the van Driest II and the Sommer-Short formulations for flat-plate skin-friction. (The OVERFLOW results were obtained from BCAG's monthly technical report.) The CFL3D and OVERFLOW predictions for viscous drag differ by almost 1 count. The flat-plate estimates are in closer agreement with CFL3D than OVERFLOW. CFL3D N-S predicts a pressure drag of 2.3 counts, which is more than 1 count higher than the OVERFLOW N-S value and almost 2 counts higher than the CFL3D Euler prediction. A pressure drag of 2.3 counts represents 4.5% of the total drag. The total drag values predicted by the two CFD codes are in fairly good agreement, with the CFL3D prediction being 0.4 count higher.

Summary of Drag Predictions at $M_\infty = 0.5$

High Speed Aerodynamics, Long Beach



TCA Symmetric W/B Configuration at $\alpha = 0^\circ$, $Re_C = 163.3 \times 10^6$



Computational Results (Case 3)

The effects of Reynolds number on zero- α drag are assessed in the next three charts. Navier-Stokes (Baldwin-Lomax) calculations have been performed at $M_\infty = 0.5$ for Reynolds numbers from 6.36×10^6 to 300×10^6 . First, flat-plate and Navier-Stokes viscous drag predictions will be compared. Then, the variation of pressure drag with Reynolds number will be shown. Finally, total drag as a function of Reynolds number will be presented.

Computational Results (Case 3)



High Speed Aerodynamics, Long Beach

- Variation of zero- α drag with Reynolds number at $M_\infty = 0.5$:
 - Viscous drag (N-S vs. equivalent flat-plate theory)
 - Pressure drag (N-S)
 - Total drag (N-S vs. Euler + flat-plate)

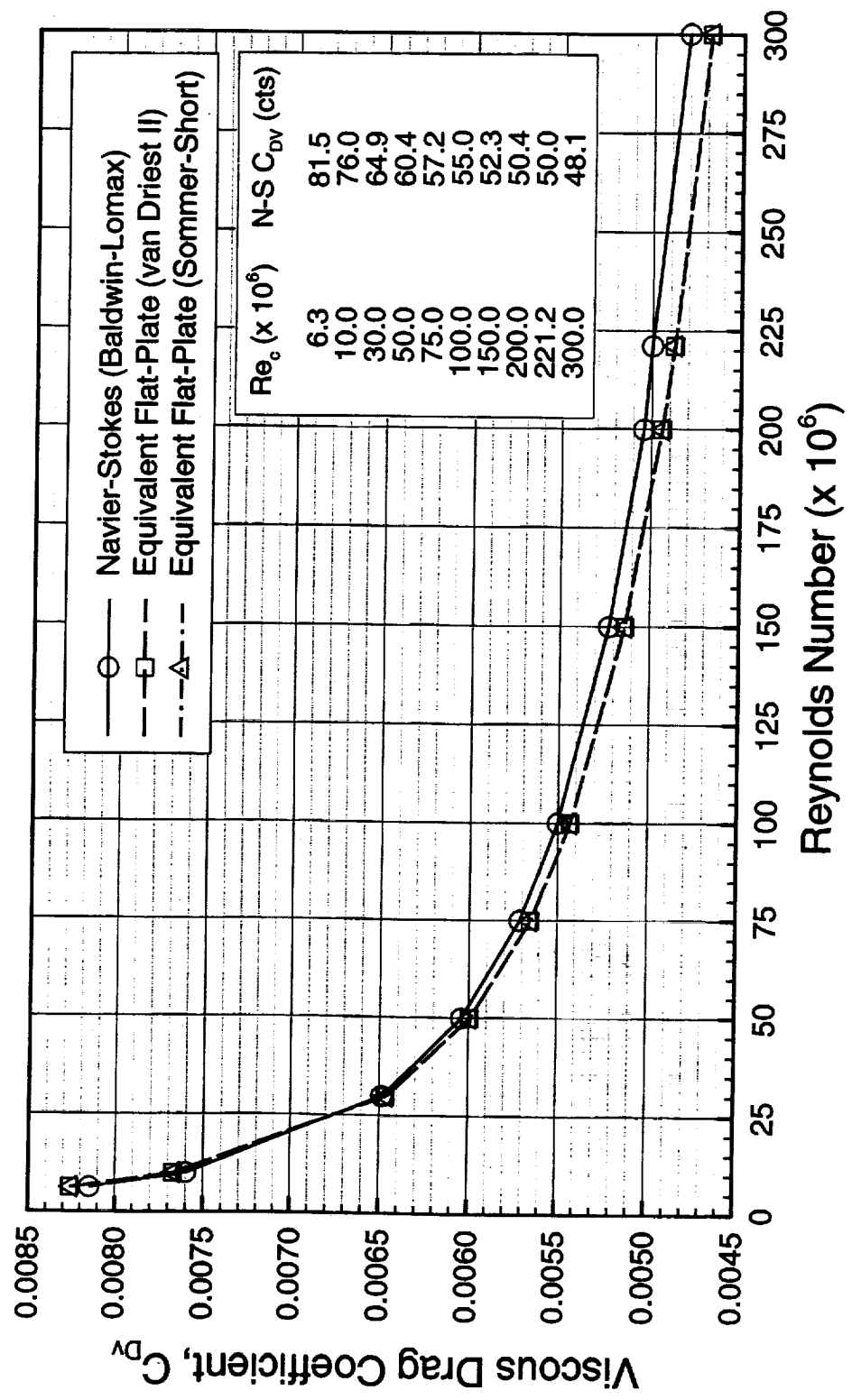
Variation of Viscous Drag with Reynolds Number

This chart shows the variation of viscous drag at $M_\infty = 0.5$, as predicted by CFL3D and the van Driest II and Sommer-Short formulations for estimating flat-plate skin-friction drag. At this low Mach number, the flat-plate formulations agree very well with each other. For Reynolds numbers less than approximately 25×10^6 , flat-plate theory estimates are higher than the CFD results. For Reynolds numbers greater than about 25×10^6 , flat-plate estimates underpredict the CFL3D viscous drag. The disagreement between CFD and flat-plate theory grows as the Reynolds number increases.

Variation of Viscous Drag with Reynolds Number

High Speed Aerodynamics, Long Beach

TCA Symmetric W/B Configuration at $\alpha = 0^\circ$, $M_\infty = 0.5$
 CFL3D, Navier-Stokes (Baldwin-Lomax)



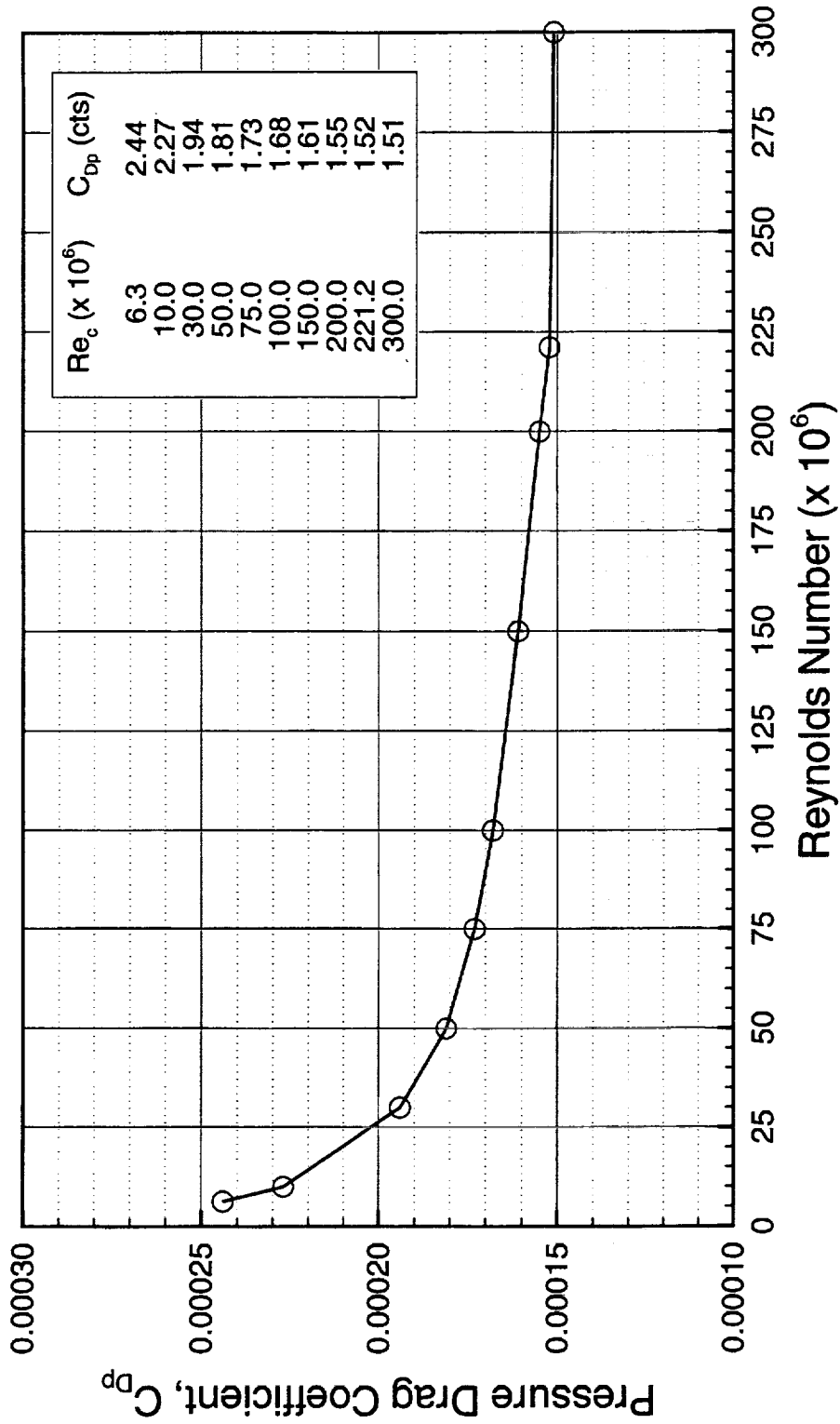
Variation of Pressure Drag with Reynolds Number

It is often assumed that the effects of Reynolds number on pressure drag are negligible. However, this figure shows that there is almost a one-count difference in pressure drag from a wind-tunnel Reynolds number of $Re_c = 6.36 \times 10^6$ to a flight Reynolds number of $Re_c = 221 \times 10^6$.

Variation of Pressure Drag with Reynolds Number

High Speed Aerodynamics, Long Beach

TCA Symmetric W/B Configuration at $\alpha = 0^\circ$, $M_\infty = 0.5$
 CFL3D, Navier-Stokes (Baldwin-Lomax)



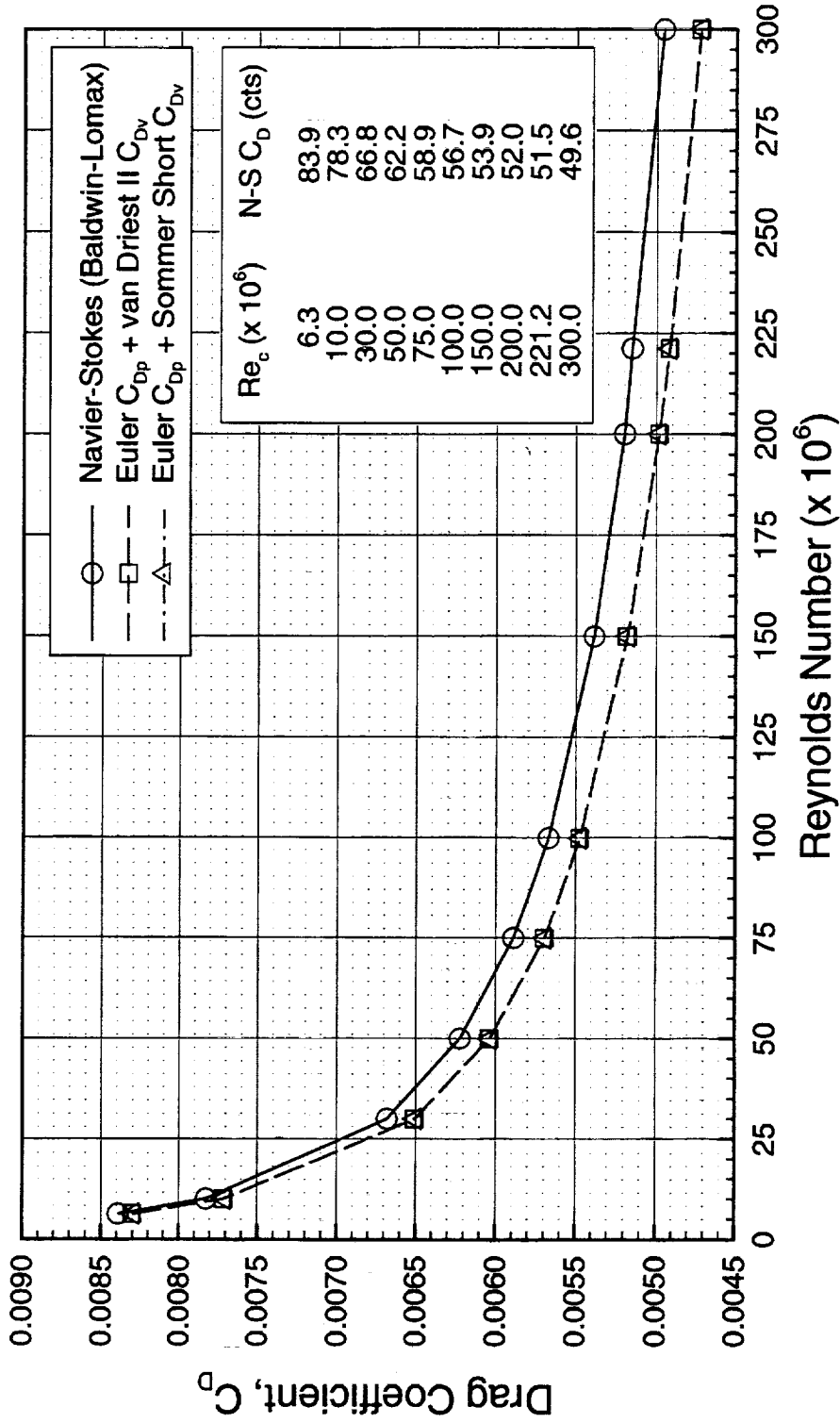
Variation of Total Drag with Reynolds Number

The variation of total drag as predicted by CFL3D Navier-Stokes and CFL3D Euler with the van Driest II and Sommer-Short formulations is shown in this chart for Reynolds numbers ranging from 6.36×10^6 to 300×10^6 . The Navier-Stokes results are underpredicted by the Euler calculations with flat-plate skin-friction drag estimates for the entire range of Reynolds numbers computed. This deviation amplifies as the Reynolds number increases.

Variation of Total Drag with Reynolds Number

High Speed Aerodynamics, Long Beach

TCA Symmetric W/B Configuration at $\alpha = 0^\circ$, $M_\infty = 0.5$
 CFL3D, Euler and Navier-Stokes (Baldwin-Lomax)

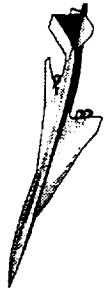


Conclusions

In conclusion, it has been demonstrated that even for subsonic Mach numbers the total drag cannot be assumed to be just skin-friction drag. There is a pressure drag component due to the displacement effects of the boundary layer that cannot be neglected. At $M_\infty = 0.5$ and $Re_c = 6.36 \times 10^6$, for instance, there are 2.4 counts of pressure drag that constitute close to 3% of the total drag for the symmetric W/B configuration with a closed aftbody. Also, there is an additional pressure drag that originates from the need to truncate the aftbody of a wind-tunnel model to accommodate the sting. This increases the pressure drag to 3.3 counts, or about 4% of the total drag at these flow conditions.

Therefore, an accurate determination of viscous drag cannot be obtained from force measurements because the axial force measured in the wind tunnel includes viscous and pressure drag components. CFD predictions still need to be relied upon to isolate the viscous drag from the total drag.

Conclusions



High Speed Aerodynamics, Long Beach

- Total drag is not just skin-friction drag:
 - pressure drag due to displacement effects of boundary layer
 - additional pressure drag component from truncated fuselage
- Absolute viscous drag cannot be measured accurately

Test Issues and Model Limitations

As with any wind-tunnel test, several issues need to be considered regarding the symmetric TCA test program. For instance, current supersonic wind tunnels do not generate fully turbulent flow on a model. Therefore, trip dots are required to trip the boundary layer in order to better simulate flight conditions. However, the addition of trip dots affects the drag of the wind-tunnel model. Determining the drag associated with trip dots is a potential source of substantial errors. Also, the lack of trip dot effectiveness can lead to inaccurate drag estimations. There are also significant uncertainties associated with the fact that the aftbody of a wind-tunnel model has to be truncated in order to accept the sting and balance.

But even assuming that the symmetric TCA program is a success, a symmetric W/B model does not address some important real-world issues. Being able to make accurate drag predictions for such a model does not necessarily mean that predictions will be correct for a more realistic configuration having camber and twist and flying at $C_L \neq 0$. Additionally, the proposed model includes only wing and body. But the nacelles have a large influence on the shock/boundary layer interaction and, therefore, have a significant impact on the drag polar. It is necessary to focus on a more realistic HSCT model in addition to a symmetric model.

Test Issues and Model Limitations



High Speed Aerodynamics, Long Beach

Test issues:

- Boundary layer transition/trip drag
- Open vs. closed aftbody
 - Cavity drag
 - Base drag
 - Sting effects

Limitations of a symmetric model:

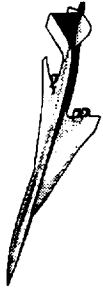
- No twist/camber
- No nacelle/diverter

Recommendations

Although a symmetric model may not address all the necessary issues, it is realized that wind-tunnel data is needed for code validation. Therefore, even though it does not appear to be possible to measure absolute values of skin-friction drag in the tunnel, the following recommendations are suggested.

Since there is a fairly good confidence in CFD pressure drag predictions, it is proposed that estimates of absolute skin-friction drag be obtained by removing the Navier-Stokes pressure drag from the wind-tunnel drag. Nevertheless, in an attempt to reduce the uncertainties associated with the above procedure, it is recommended that incremental skin-friction drag be computed instead. This would be accomplished by subtracting the change in the Navier-Stokes pressure drag from the change in wind-tunnel drag between two different Reynolds numbers. A third recommendation would be to measure local skin-friction values for a more direct comparison with CFD results (even if this means increased complexity and cost). Finally, it is recommended that the test be conducted in facilities capable of high unit Reynolds numbers so that trip drag uncertainties are minimized or eliminated and partial laminar flow on the model does not become an issue.

Recommendations

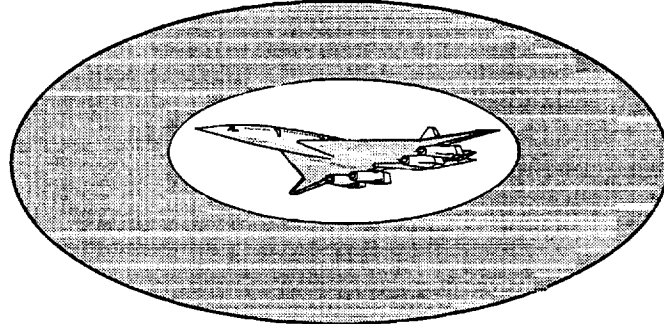


High Speed Aerodynamics, Long Beach

- Estimate absolute skin-friction drag values
 - Remove CFD pressure drag from the wind-tunnel drag:
$$C_{Dv} = (C_D)_{w.t.} - (C_{Dp})_{N-S}$$
- Compute incremental skin-friction drag
 - Calculate the change in viscous drag between two Reynolds numbers:
$$\Delta C_{Dv} = (\Delta C_D)_{w.t.} - (\Delta C_{Dp})_{N-S}$$
- Measure local skin-friction values to validate CFD
- Test model in facilities capable of high unit Reynolds numbers

This page is intentionally left blank.

**Historic Background on Flat Plate Turbulent
Flow Skin Friction and Boundary Layer Growth**



HSR Airframe Technical Review

**Los Angeles, California
February 9 - February 13, 1998**

**Robert M. Kulfan
Boeing Commercial Airplane Group**

Topics

- Early Skin Friction Compressibility Prediction Attempts
- Skin Friction Prediction Validation Studies
- Prediction of Flat Plate Turbulent Layer Growth
- Summary / Conclusions

Recent CFD validation studies have shown significant variations in viscous drag predictions between the various methods used by the NASA and industry HSCT organizations. The methods include Navier Stokes CFD codes in which the viscous forces are part of the solutions, and predictions obtained from the different fully turbulent flow flat plate skin friction drag equations used by the various organizations.

The initial objective of this study was to provide an experimental database of fully turbulent flow skin friction measurements on flat plate adiabatic surfaces at subsonic through supersonic Mach numbers and for a wide range of Reynolds numbers. The database could then be used as the initial step in resolving the differences in the viscous predictions.

This database, (Ref 1), was originally assembled in 1960 from selected experiments conducted prior to that time period. The criteria used to select the appropriate test data are described in the reference. Data were also found on turbulent boundary layer velocity profiles and it was therefore possible to analyze other boundary layer properties such as shape factor, displacement thickness and boundary layer thickness.

The data presented in this note was scanned from the figures in the report and then digitized using a highly accurate PC screen digitizer. The digitized data will be released in a report early in 1998.

In the process of extracting the data, statistical analyses were made between the test data and the corresponding predictions of various fully turbulent flat plate skin friction prediction methods. An improved method of predicting compressible turbulent skin friction drag was developed.

Boundary layer profile data measurements are also included along with a new method for predicting boundary layer growth characteristics. These include approximate velocity profile representation, boundary displacement thickness, and boundary layer thickness.

Why the Interest in Flat Plate Turbulent Boundary layers ?

- First Step in Evaluating Navier Stokes Prediction Methods
- Help Sort Out Appropriate Turbulence Models
- Good Estimate of Viscous Drag of HSCT Type Configurations (Easy, Quick , Robust and Accurate)
- PD Drag Prediction Methods
- Extrapolation of Wind Tunnel Data to Flight Conditions
- δ Predictions Used to Size Diverter Height
- δ^* plus CF Predictions Used to Calculate Spillage and Internal Drag of Flow-Through Nacelles
- Quick Estimate of Surface Temperature
- Provides Physical Insight into Viscous Flow Characteristics

It is felt that the first step in validating the viscous drag predictions of any Navier Stokes code is to make sure that predictions of the local and average skin friction drag and boundary layer must match the "simple" flat plate measured test data over the range of Mach numbers and Reynolds for which the codes will be used. This process will help to evaluate the applicability of the various turbulence models.

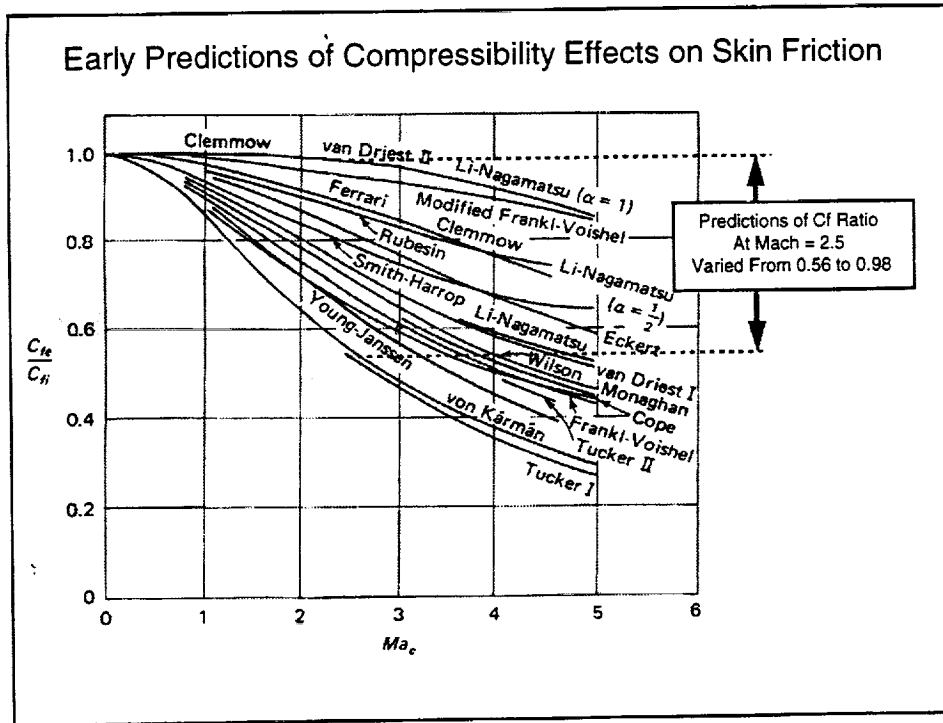
Because HSCT configurations have rather thin wings, slender bodies and low cruise lift coefficients, experience has shown that flat plate skin friction calculations provide good estimates of the viscous drag of HSCT type configurations. The predictions are easy, quick, robust and quite accurate.

The current PD viscous drag prediction methods are based on flat plate skin friction drag calculations. Currently wind tunnel data is extrapolated to flight conditions using flat plate friction drag predictions.

Flat plate estimates of the boundary layer thickness are used as the preliminary criteria for specifying the boundary layer diverter height for the HSCT nacelle installations. Boundary layer displacement thickness predictions together with CF calculations are used to calculate the spillage and internal drag of wind tunnel flow through nacelles.

Local skin friction calculations corrected for local dynamic pressure effects can be used to estimate local surface temperatures.

The boundary layer thickness information presented in this note also provides some physical insight in to the fundamental features of turbulent flat plate flow.



The initial objective of the study in Reference 1, was to determine the most appropriate semi-empirical method for accounting for compressibility effects on flat plate skin friction drag.

Chapman and Kester in Reference 5, after a study of approximately 20 theoretical methods being proposed at that time, found at Mach 2.5, calculated values of the ratio of compressible skin friction drag to incompressible skin friction drag, ($C_{f,c}/C_{f,i}$), varied from 0.98 to 0.56 depending upon which method was used. Whereas measured values for this ratio varied from about 0.67 to 0.65 over a Reynolds range of 5.5×10^6 to 8.5×10^7 . The different predictions are shown in the above figure from Reference 2.

In order to establish the validity of the skin friction coefficient relation; an extensive survey was made in Reference 1, to gather reliable experimental data from many independent sources. A rigid set of criteria was adopted as a means of selecting data for a systematic study. This was done to insure that the test conditions closely approximate the theoretical model, and that both the measurement and reduction techniques were such as to yield accurate information.

The most significant of these requirements were:

1. Use only of data obtained by direct force measurements. Reference 9, 16, 25 and 26 discuss the relative merits of various skin friction measurement techniques. The general conclusion is that the most accurate data are obtained by direct force measurements.
2. The flow over the experimental model was to be properly tripped to satisfy the condition of fully turbulent flow.
3. Measurements were to be made at stations far enough downstream of the trips to allow the flow to reach a "naturally" turbulent character.
4. Experimental results were to be presented in terms of the properly determined effective turbulent length.

Reference Temperature Approach

- Incompressible Skin Frictions Equations Can be Used to Calculate Compressible Skin Friction if an "Appropriate" Reference Temperature is Used To Calculate ρ and μ in the equations:

eg: $C_{fi} = 0.295 [\log(\text{Re}_x)]^{-2.45}$ ---- Modified Schultz-Grunow Eqn

$$C_f = \frac{\rho^*}{\rho_\infty} C_{fi}^* \quad \text{Re}_x^* = \text{Re}_x \frac{\rho^* \mu_\infty}{\rho_\infty \mu^*}$$

- Assuming the Static Pressure is Constant Across the Boundary Layer:

$$\frac{\rho^*}{\rho_\infty} = \frac{T_\infty}{T^*}$$

- The Compressible Skin Friction Equation becomes:

$$C_f = 0.295 \frac{T_\infty}{T^*} \left[\log \left(\text{Re}_x \frac{T_\infty \mu_\infty}{T^* \mu^*} \right) \right]^{-2.45}$$

It is perhaps worth emphasizing the empirical nature of what is called "theory" in this report and the necessity, therefore, that this theory should be compared with data from more than one source. The basis of the theory selection was; first, it had to agree, of course, with test data within the scatter of that data, and secondly, it had to be based on good physical reasoning. All of the theoretical flat plate formulations involve disposable constants that have been determined empirically. Thus, as is the rule for all empirical formulae, the theory should be, strictly speaking, only be applied where it has been justified by experiment; however, because there is a physical basis to this theory, it is believed that some extrapolation should be permissible. This is equally true for current Navier Stokes CFD codes where viscous flow effects are determined using various turbulence models which approximate the flow phenomena.

Statistical analyses of the differences between the flat plate theory and the test data will be used to establish both the consistency of the test data, and the adequacy of the theoretical predictions. This will allow more effective use of the data for use in CDF viscous drag prediction validation studies.

All of the skin friction theories shown in the previous figure were developed by assuming that compressible turbulent skin friction drag could be obtained using well known incompressible skin friction equations by evaluating all of the fluid properties that appear in the incompressible equations at some appropriate reference temperature, T^* . This assumption parallels the analytical transformation methods that had been used in laminar boundary compressible flow analyses.

The assumption of an effective reference temperature in essence implies that the turbulent boundary shape and height are not strongly affected by Mach number. This will be further examined in this paper.

Methods Used To Determine a Reference Temperature

- Similar to Laminar Flow Transformation
- For Adiabatic Wall Conditions The Reference Temperature Equation is of the Form:

$$\frac{T^*}{T_\infty} = 1 + Kr \cdot r(\sigma - 1)M_\infty^2$$

- "Constant" Kr Determined By:
 - Wall Temperature (Correction Too Large)
 - Determined Experimentally -- Sommer / Short
 - Correlation of Experimental Cf data -- Kulfan; Spaulding / Chi; White
 - Velocity Averaged Enthalpy Across the Boundary Layer -- Monaghan
 - Semi-Analytic -- Van Driest

Numerous ideas were for an appropriate reference were proposed by the various researchers. This accounts for the widely differing predictions of compressibility effects on skin friction drag as shown in Figure 4. Some of the early concepts used to define the reference temperature equation coefficients are shown in the figure.

These include:

- Use of the surface temperature ----this provided too large a compressibility correction
- Determined experimentally by specially designed experiments, --- Sommer / Short (Ref 12)
- Determine by correlation of Cf predictions with test data. --- Spaulding / Chi (Ref 2), White (Ref 2), Kulfan (shown later in this report).
- Velocity averaged enthalpy across a boundary layer ---- Monaghan (Ref 27)
- Semi-analytic formulations -- Van Driest (Ref 2)

Current Approach

- Use Existing Local Skin Friction Data to Validate Incompressible Equation
- Selected "Quality" Data from Many Sources
- Statistical Analysis to Assess Scatter of Data and Consistency of Predictions
- Use Selected Reference Temperature Equation(s) to Transform Experimental Values of "Rex" and "Cf" to Equivalent Incompressible Values.
- Statistical Analysis to Assess Scatter of the Experimental Data and the ability of the Reference Temperature to Convert the Measured Friction Data to Equivalent Incompressible Values.
- Apply to Selected Reference Temperature equation(s) to Existing CF Data as Additional Verification

Cf ----- Local Skin Friction Coefficient
CF ----- Average Skin Friction Coefficient

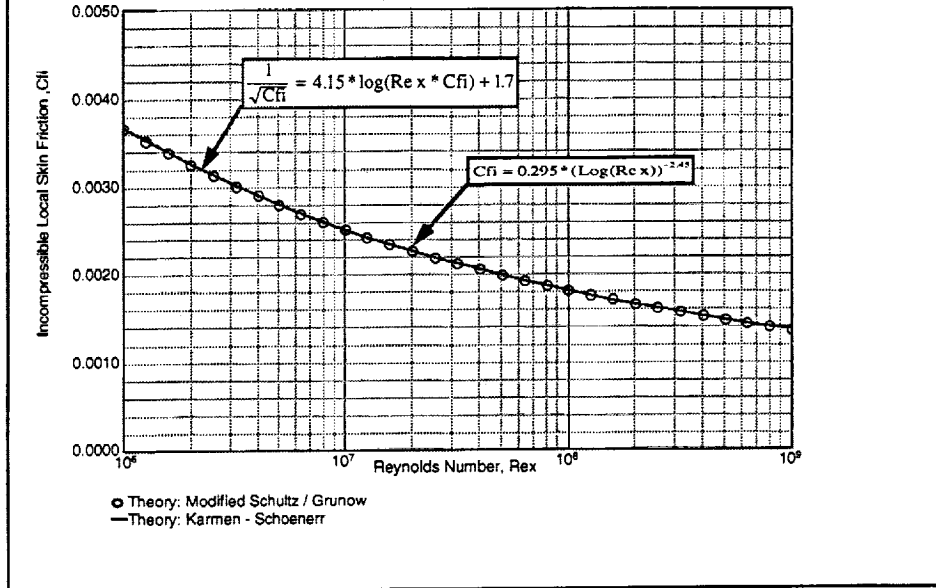
In the current study the reference temperatures selected for evaluation included: the Monaghan mean enthalpy equation, and the Sommer / Short equation. Previous studies have shown both to provide accurate assessments of compressible skin friction. The Sommer / Short method is the current method used in Boeing Seattle PD methods.

Experimentally, it is much easier to obtain force measurements of local skin friction drag than of average skin friction drag. Consequently, the initial step in the current evaluation process was to compare incompressible local skin friction data with the most generally accepted incompressible skin friction equations. Data from many different sources were used.

The selected reference temperature were then used to transform measured compressible local skin friction data to equivalent incompressible Cf and Reynolds numbers. Statistical analyses of the transformed compressible friction data were compared with the incompressible predictions, to assess the adequacy of the selected reference temperatures to account for the compressibility effects.

Subsequently, the same process was then applied to available average skin friction data.

Comparison of Incompressible Local Skin Friction Predictions



The most widely accepted in compressible local skin friction equation is the Karmen / Schoenherr equation:

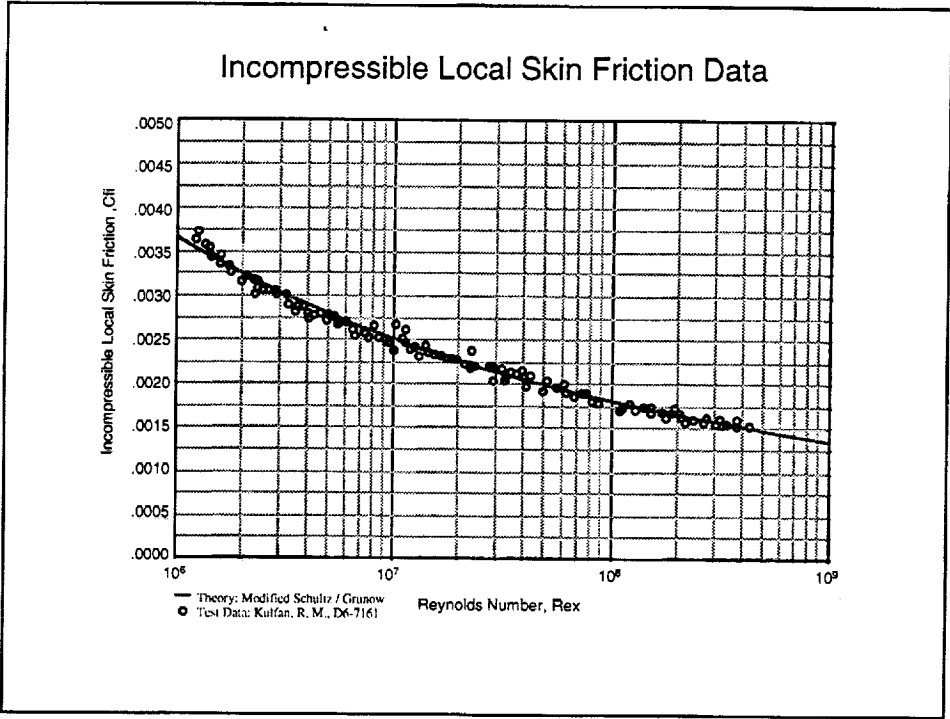
$$\frac{1}{\sqrt{C_{fi}}} = 4.15 \cdot \log(\text{Re } x \cdot C_{fi}) + 1.7$$

This is compared in this figure with the less sophisticated modified Shultz / Grunow equation.

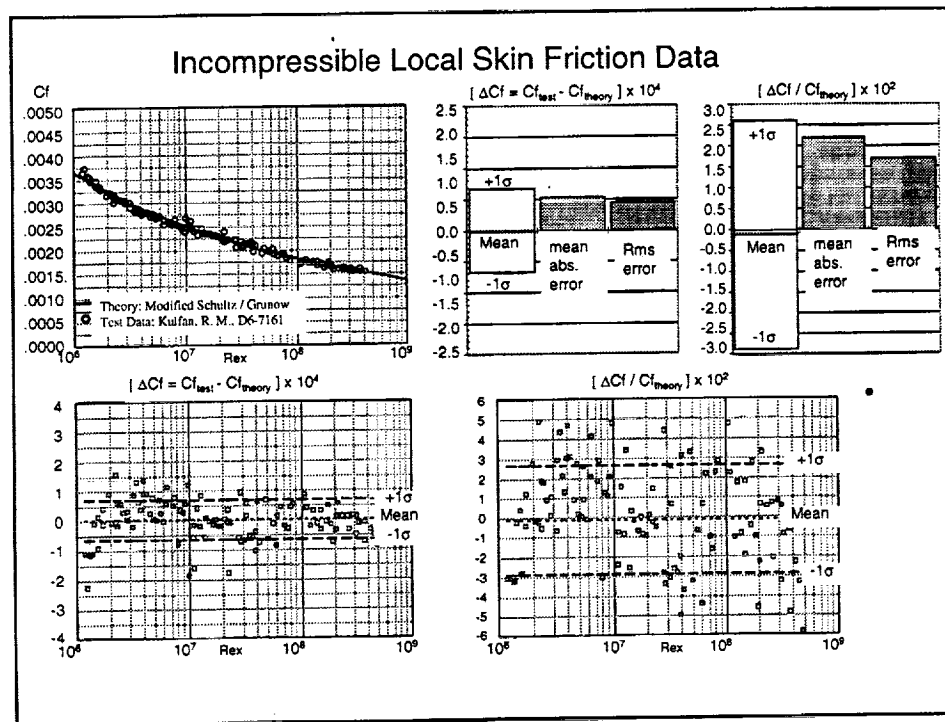
$$C_{fi} = 0.295 \cdot (\text{Log}(\text{Re } x))^{-2.45}$$

The modification was simply replacing the standard constant “0.288” by “0.295”.

The “mean” difference between the Cf values calculated by the Karmen-Schoenherr equation and by the modified Shultz-Grunow equation was -0.0000031 over the complete Reynolds number range. The standard deviation was calculated to be 0.00000452. Consequently, the simpler Shultz / Grunow equation was used in the current study.



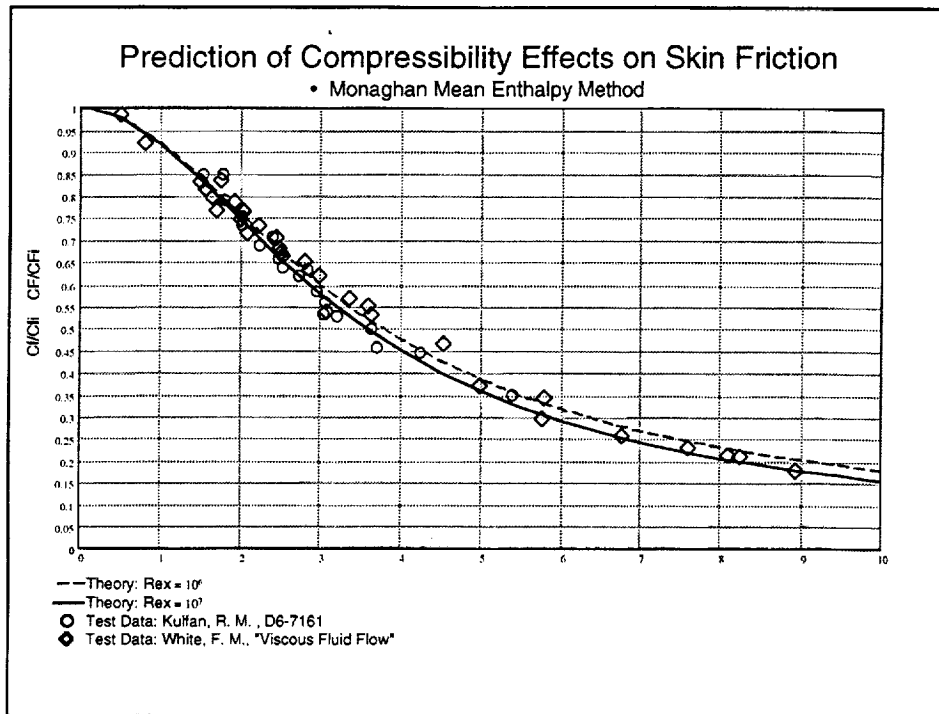
This figure compares measured incompressible local skin friction data from References 15, 25 and 39. The test data appears to scatter about the theoretical predictions for the entire Reynolds number range of the test data.



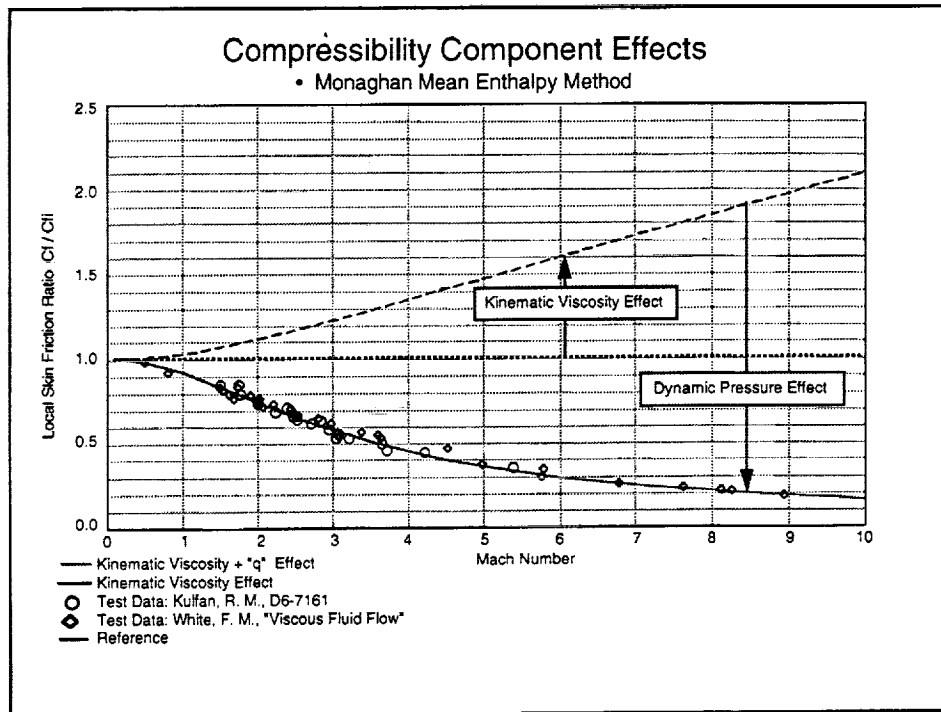
Statistical analysis of the differences between the test data and corresponding C_f predictions shows that the mean of the differences is $\Delta C_f = -.00000671$ which corresponds to an average difference of 0.13%. The standard deviation of data about the mean is approximately 0.7 counts of drag ($\Delta C_f = 0.000067$) which corresponds to 2.8% of the corresponding predicted value.

The constant 0.288 in the original Shultz / Grunow equation would result in a mean difference between the test and theory of - 2.6%

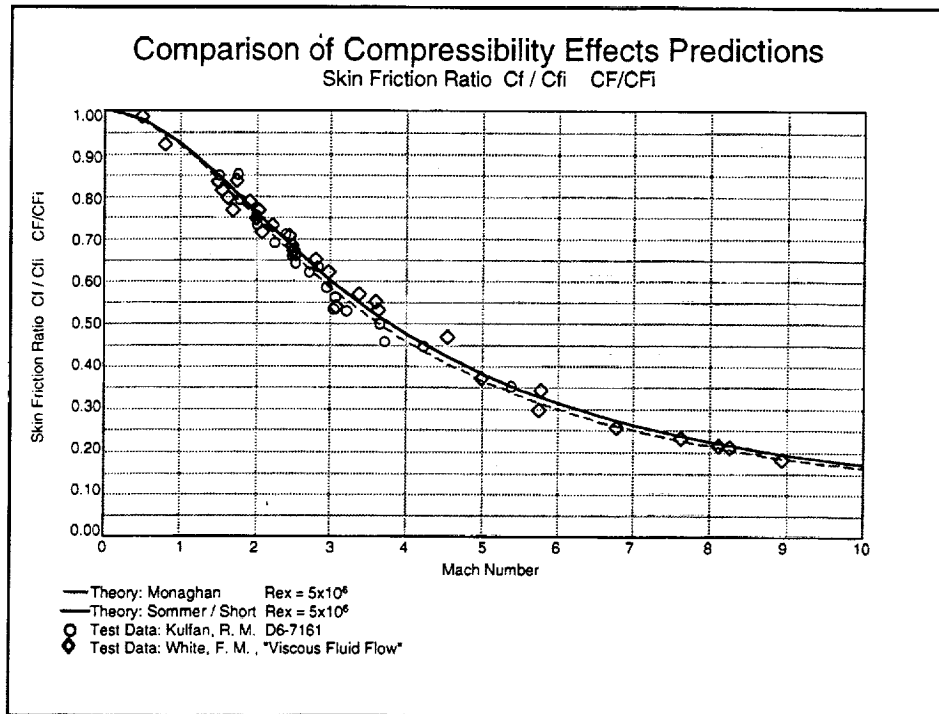
The modified Shultz / Grunow equation therefore appears to provide an accurate estimate of incompressible local skin friction coefficient over the entire range of Reynolds Numbers covered by the test data.



This figure includes comparisons of the predicted effects of Mach number on the ratio of compressible skin friction to incompressible skin friction at the same Reynolds. The experimental data are from thirteen independent experiments. The sources of the test data are given in References 1 and 2. The test data correspond to Reynolds number between 10^6 and 10^7 . The theoretical predictions shown in the figure were obtained using the Monaghan T^* equation. The predictions appear to match the Mach number trends quite well.



This figure shows the elements of the compressibility corrections. The reference temperature reduces the kinematic viscosity and therefore decreases the effective Reynolds number. This increases the effective skin friction coefficient. The dynamic pressure effect associated with reduction in effective density overpowers the kinematic viscosity and results in the reduced skin friction coefficient when corrected back to free stream reference conditions.

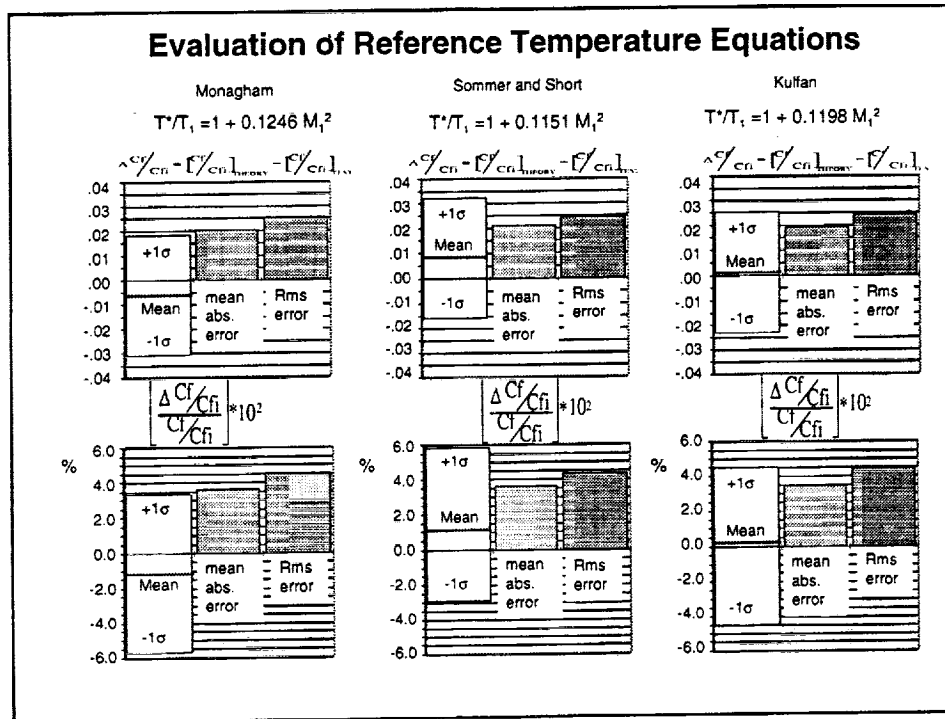


This compares the compressible skin friction predictions obtained using the Monaghan T^* equation with the predictions obtained using the Sommer-Short T^* equation.

The Sommer-Short T^* equation results in compressible skin friction values consistently higher than predicted using the Monaghan method. It was for this reason that the Boeing US SST program switched from the Monaghan method to the Sommer-Short method.

The full scale SST performance predictions were obtained from wind tunnel data corrected to full scale conditions. Wind tunnel skin friction drag is higher than the full scale conditions. Using higher skin friction values calculated by the Sommer-Short method resulted larger skin friction corrections. This resulted in higher L/D assessments for the SST.

Evaluation of Reference Temperature Equations



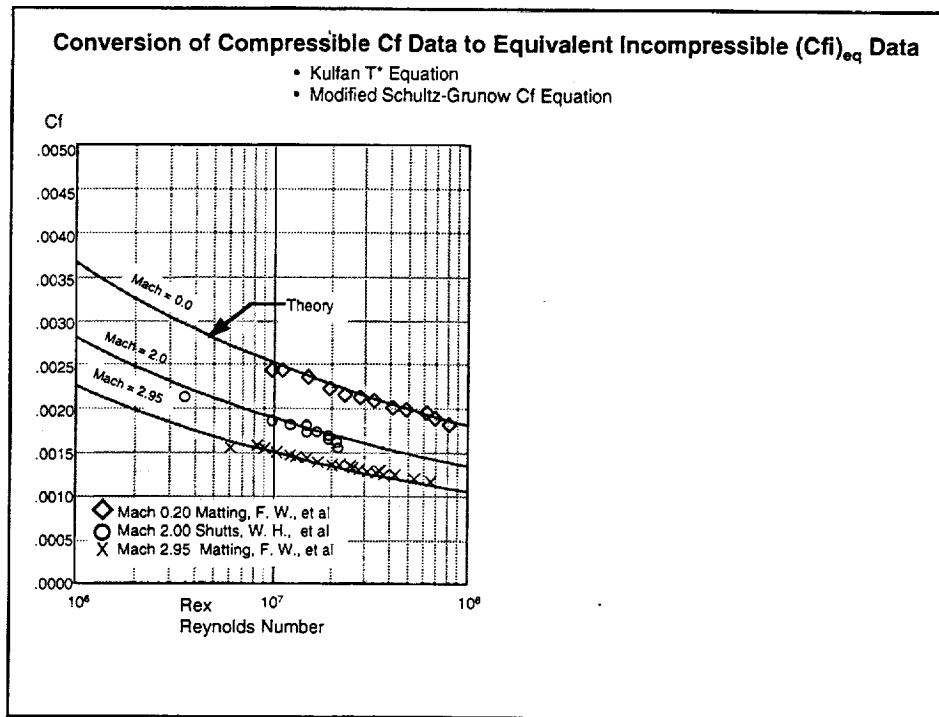
Statistical analyses of the differences between C_f predictions and the corresponding test data are shown in this figure. The theoretical predictions were obtained using three different T^* equations.

The "scatter" in the test - theory increments are essentially equal. The mean of the differences between the test and theory, however differs between the predictions obtained using the different T^* equations.

The "mean" of the theory - test differences obtained using the Monaghan T^* equation is approximately 1% low. The "mean" of the theory - test differences obtained using the Sommer-Short T^* equation is approximately 1% high. The constant for the Kulfan T^* equation was therefore chosen to be the average of the Sommer-Short and the Monaghan constants.

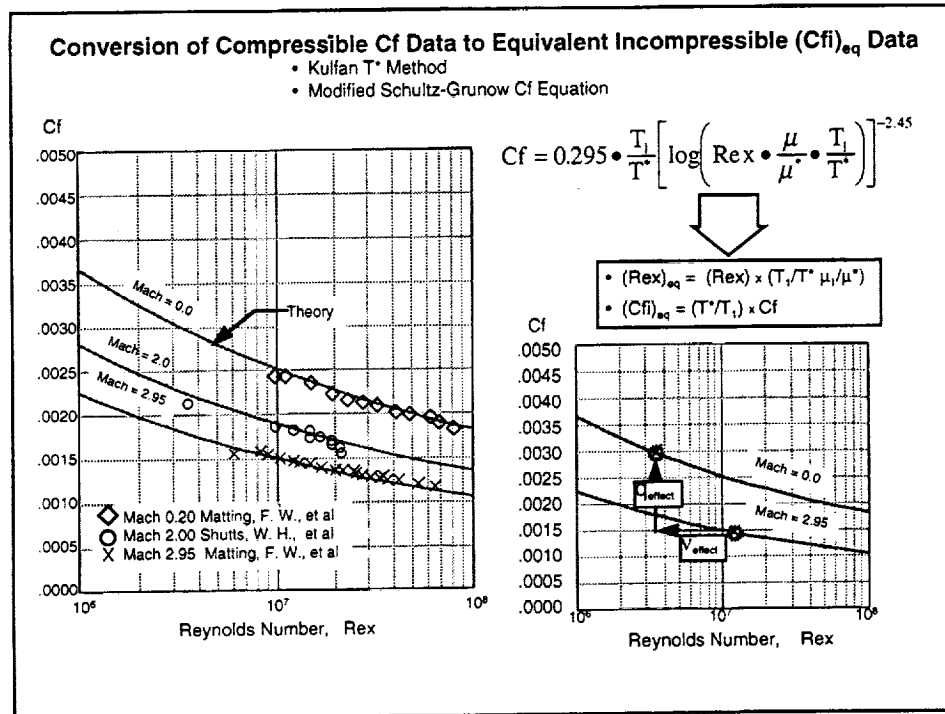
This essentially resulted in a mean error between the test data and the theoretical predictions of zero.

The test data scatter about the mean has a standard deviation of about 4.5%. This large scatter is in part due to the variations of Reynolds number of the test data. The Reynolds number for the test data 10^6 to 10^7 .



This figure contains comparisons of theoretical predictions of C_f with test data for three Mach numbers from 0.0 to approximately 3.0.

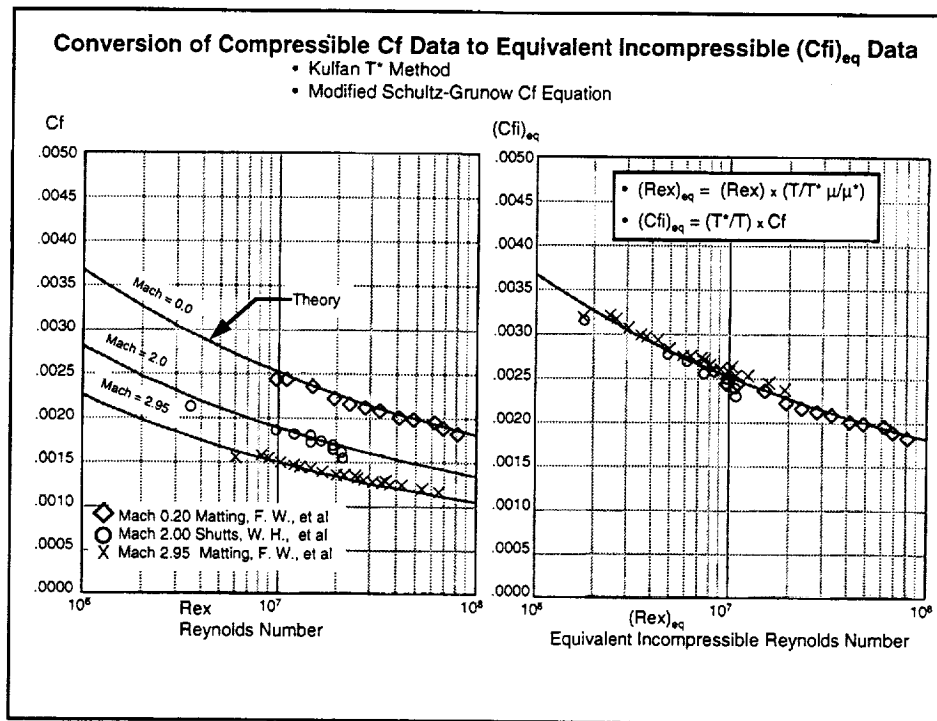
The theory in this figure used the Kulfan T* equation.



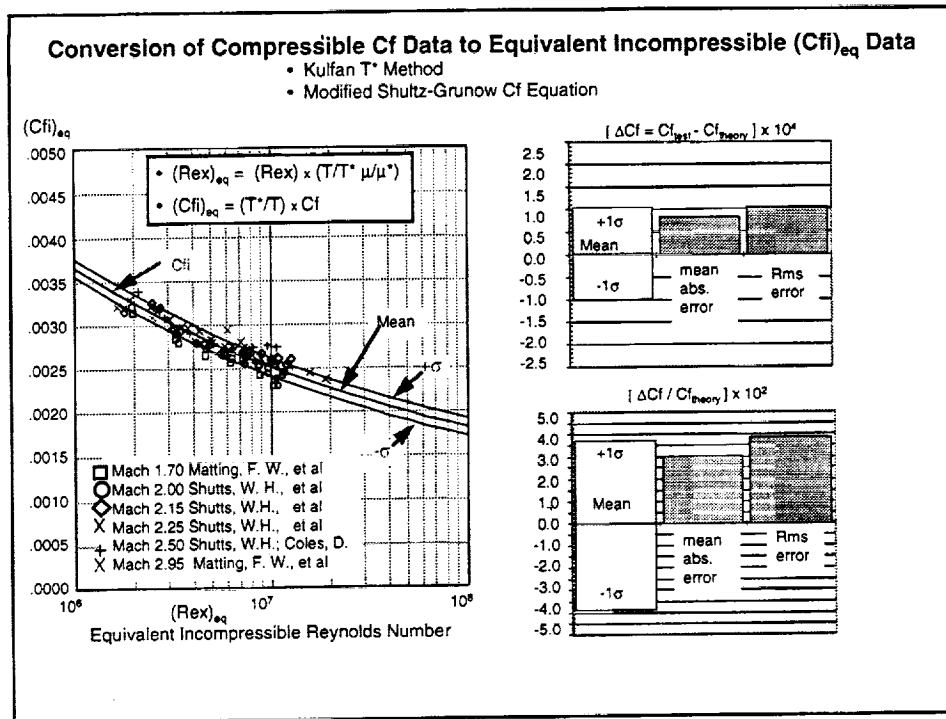
In order to assess the accuracy of the C_f predictions to account for compressibility or Mach number effects, the test data were converted to equivalent incompressible values of C_{fi} and Reynolds number.

An example of this transformation is shown in the Figure.

The Equivalent incompressible Reynolds number is less than the actual test Reynolds number. The equivalent incompressible skin friction coefficient is higher than the actual measured skin friction coefficient.



This transformation procedure, as shown in the Figure, “collapses” all of the test data about the incompressible skin friction curve. This approach can provide a convenient means to assess the accuracy of the theoretical methods to account for compressibility effects simultaneously over a range of Mach numbers and Reynolds numbers.



This shows transformed experimental data for six different sets of test data obtained at Mach numbers from 1.7 to 2.95. The incompressible Mach number data from the previous plot has not been included in the above figure since it is desired to assess the ability of the different T* equations to account for Mach number effects on skin friction.

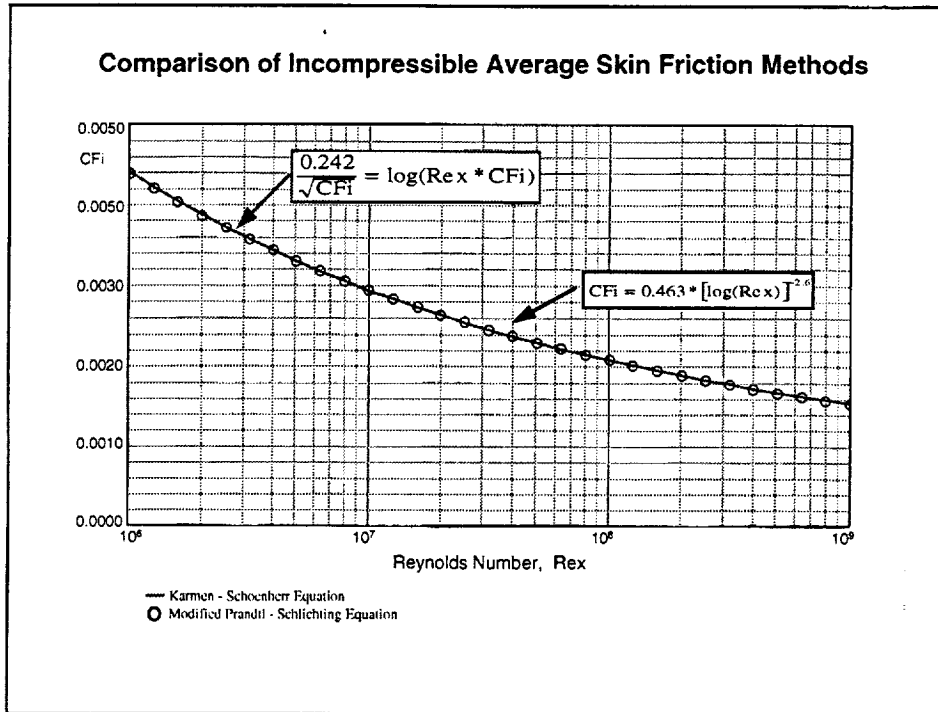
The figure includes the statistically determined differences between the transformed equivalent incompressible skin friction and the modified Shultz-Grunow theoretical Cf predictions. The Kulfan T* equation was used for the transformation process. The "mean" of the differences between the transformed skin friction data and the incompressible Cf predictions is essentially

The "scatter" of the test has a standard deviation of about 1 drag count ($\Delta Cf \sim 0.0001$). This corresponds to about a 3.8% scatter of the test data about the theoretical Cf predictions over the entire Reynolds number range and Mach number conditions represented by the test data.

The table below shows the results obtained different T* equations. On the average, the Monaghan predictions tend to underestimate the test data by about 0.3 counts or 1.2% and the Sommer-Short predictions are about 0.3 counts high corresponding to about 1.0%. The Kulfan T* method provides the best estimate of the compressibility effects.

	Monaghan T* Eqn.		Sommer-Short T* Eqn		Kulfan T* Eqn.	
	ΔCf (counts)	$\Delta Cf / Cf$ (%)	ΔCf (counts)	$\Delta Cf / Cf$ (%)	ΔCf (counts)	$\Delta Cf / Cf$ (%)
Mean	-.301	-1.2	.308	1.00	.00071	.085
σ	1.022	3.8	.985	3.0	1.066	4.0

The "scatter" in the compressible theoretical - experimental transformed skin friction increments are only slightly higher than the scatter in the incompressible data shown in figure 10. (0.7 counts versus 1 count). This is most likely because the transformation to equivalent Cf amplifies the magnitude of the Cf values and hence the absolute differences.



The most widely accepted incompressible local skin friction equation is the Karmen / Schoenherr equation:

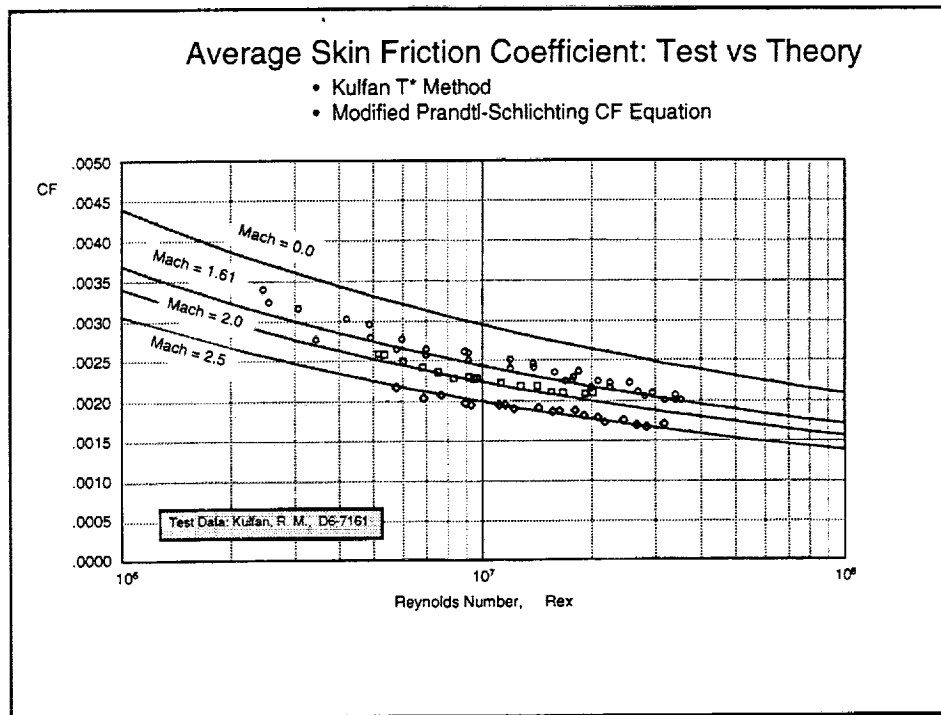
$$\frac{0.242}{\sqrt{C_{f_i}}} = \log(Re_x \cdot C_{f_i})$$

This is compared in this figure with the less sophisticated modified Prandtl / Schlichting equation.

$$C_{f_i} = 0.463 \cdot (\text{Log}(Re_x))^{-2.6}$$

The modification was simply replacing the standard constant “0.460” by “0.463”. The mean difference between the C_f values calculated by the Prandtl-Schlichting equation and by the Karmen-Schoenherr equation was -0.0000013 over the complete Reynolds number range. The standard deviation was calculated to be 0.00000678. Consequently, the simpler modified Prandtl-Schlichting equation was used in the current study.

It is interesting that though out their technical careers, Prandtl and Von Karmen often tackled the same fluid dynamic problem. Their results almost always differed in the analytical formulations and the form of the equations describing the flow phenomena. Computed results were always within a few percent of each other.

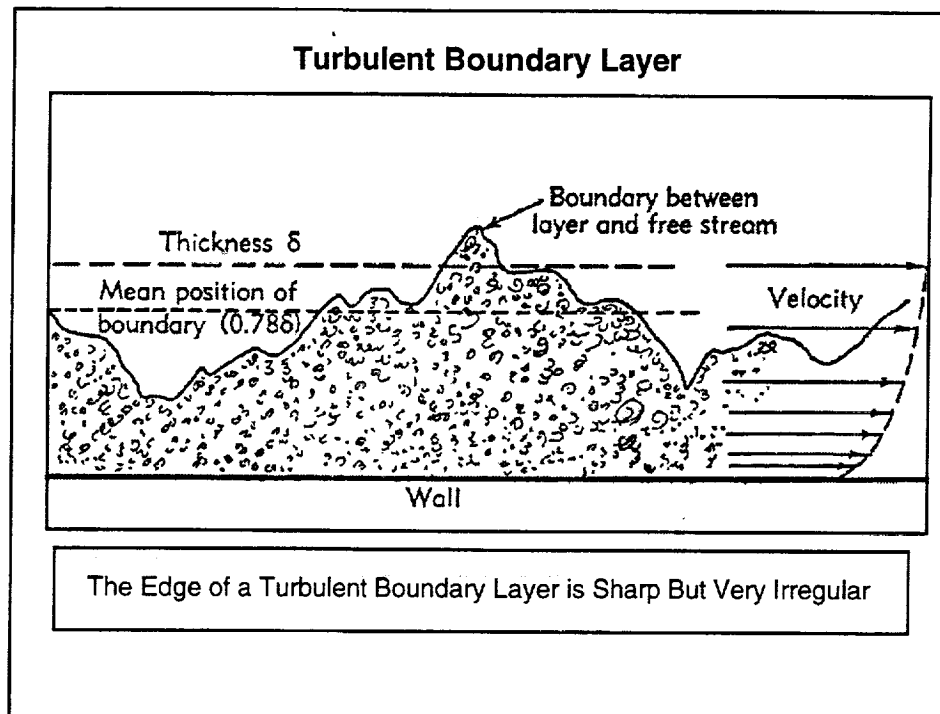


Comparisons between theoretical and experimental average skin friction data are shown in the figure. The lack of additional test data is attributed to the difficulty in obtaining average skin friction data by direct force measurements. Most often, average skin friction data are obtained by application of the momentum integral equation to boundary layer velocity profile measurements. The uncertainties of the interference between the pitot probes used for the measurements and the surface introduces errors that are difficult to correct.

The data shown in the Figure for Mach 2.0 and Mach 2.5, were obtained from force measurements on the cylindrical portion of a cone-cylindrical body of revolution. The Mach 1.61 data were obtained with an ogive - cylinder body of revolution. Three dimensional effects are considered to be small on the cylindrical sections. However determining the "effective origin" for the flow over the cylindrical can certainly introduce substantial errors.

The theoretical predictions match the Mach 2.0 and Mach 2.5 data quite well. Theory underestimated the friction drag at Mach 1.6. This is believed to be due to a bias in the test data.

The results of the data correlations shown in this paper indicate that comparisons with local skin friction data is the best approach to evaluate any methods for prediction of flat plate skin friction drag.



In the current HSCT studies estimates of the boundary layer height are used to specify the height of the boundary layer diverter to keep the inlet from ingesting portions of the boundary layer.

During the course of the investigation described in Reference 1, experimental measurements of velocity profiles were found. It was also then possible to study the growth characteristics of a turbulent boundary layer over a flat plate. A method was developed to predict the growth of a turbulent boundary layer on a flat plate. This method has been revised in the current study.

The edge of a turbulent boundary layer bounded by a free stream of negligible turbulence has a sharp but very irregular outer limit as shown above. The velocity tends to approach the free stream velocity asymptotically. Hence the definition of the thickness of a turbulent boundary layer is subject to many variations. A common definition of the edge of the boundary layer, δ , is the height at which the velocity is equal to some percentage of the free stream value. Typically a value of 0.995 is used.

Parameters Used to Characterize the Growth of a Boundary Layer

- Boundary Layer Thickness, δ
- Displacement Thickness, δ^*

$$\delta^* = \int_0^{\delta} \left[1 - \frac{\rho}{\rho_{\infty}} \frac{u}{U_{\infty}} \right] dy$$

- Momentum Thickness, θ

$$\theta = \int_0^{\delta} \frac{\rho}{\rho_{\infty}} \frac{u}{U_{\infty}} \left[1 - \frac{u}{U_{\infty}} \right] dy$$

- Shape Factor, H

$$H = \delta^* / \theta$$

Because of the asymptotic nature of a turbulent boundary layer, other parameters are often used to characterize the boundary layer growth. These include the displacement thickness, δ^* , the momentum thickness, θ , and the shape factor H.

The displacement thickness defines the amount that the flow streamlines diverge around the surface because of the boundary. Calculations of the displacement thickness are used in the estimation of the spillage characteristics and the internal drag of flow-through nacelles on wind tunnel models.

The momentum thickness on a flat plate is directly related to the average skin friction coefficient as:

$$\theta = (X C_F)/2$$

One technique used to determine average skin friction on a flat plate to measure the velocity profile, integrate the experimental velocity profile to obtain q . Then the average skin friction coefficient is calculated using the above equation.

The shape factor, H, is often used to predict the separation tendency of a boundary layer with an adverse pressure gradient.

Calculation Of Boundary Layer Characteristics

1. Approximate Velocity Profile as:
$$\frac{u}{U_{\infty}} = \left(\frac{y}{\delta}\right)^{\frac{1}{N}}$$

2. Determine "N" Experimentally

3. Calculate δ^* From :
$$\delta^* = \theta * H_i * \left(\frac{H}{H_i}\right)$$

$$\theta = \frac{X * CF}{2}$$

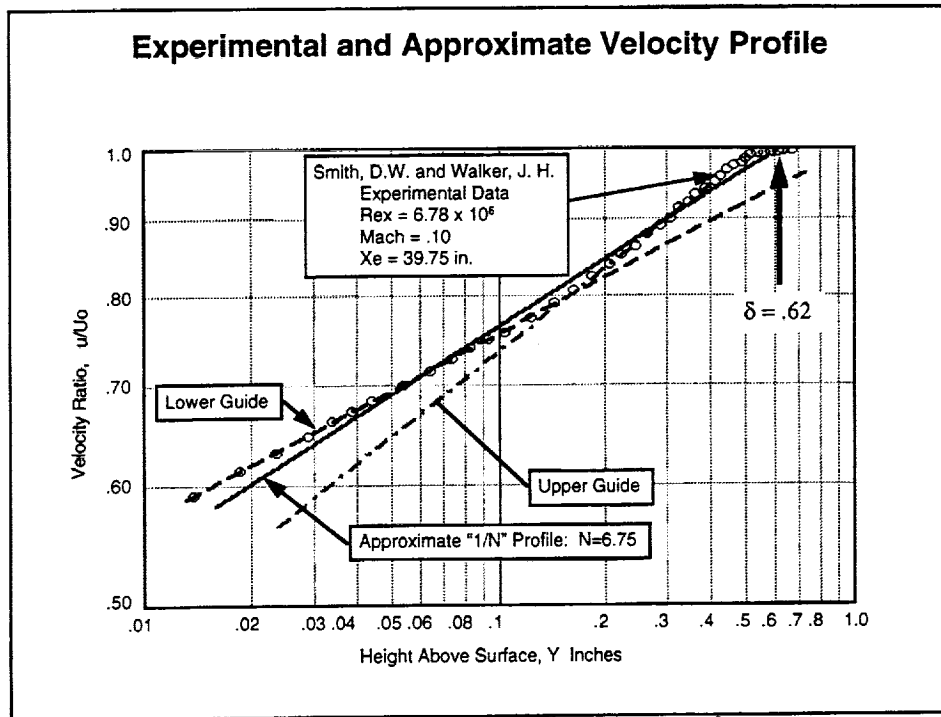
4. Calculate δ From :
$$\frac{\delta^*}{\delta} = \int_0^1 \left[1 - \frac{\rho}{\rho_{\infty}} \left(\frac{y}{\delta}\right)^{\frac{1}{N}} \right] d\left(\frac{y}{\delta}\right)$$
 and
$$\delta = \frac{\delta^*}{\left(\frac{\delta^*}{\delta}\right)}$$

Often in boundary layer studies, it is convenient to represent the velocity profile by a power law relation of the form:

$$\frac{u}{U_{\infty}} = \left(\frac{y}{\delta}\right)^{\frac{1}{N}}$$

This approximate form of the turbulent boundary velocity profile has been used to develop a four step process for predicting the boundary layer thickness. The boundary layer thickness is defined as the height at which the velocity is essentially equal to the free stream velocity.

The elements incorporated in the process for calculating the boundary layer thickness are summarized above, and will be discussed in greater detail in subsequent figures.



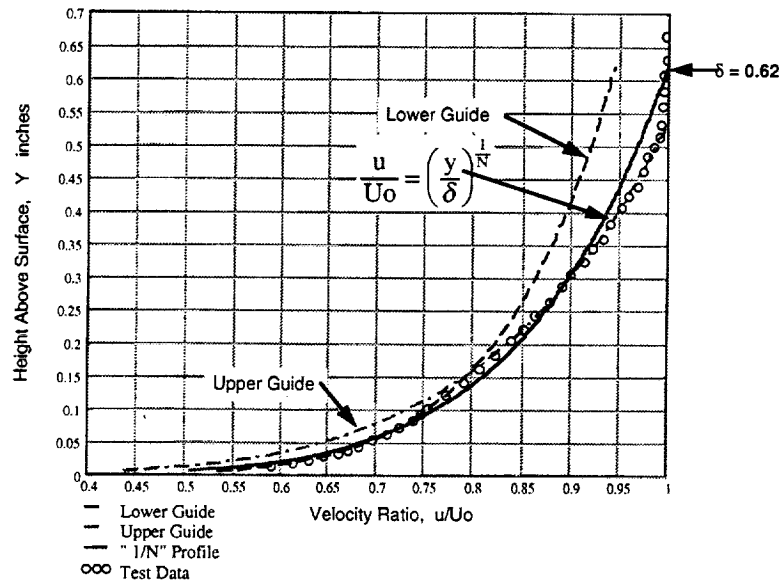
The disposable constant for the empirical equation has been determined from correlations of a large number of measured velocity profiles from six independent sources.

This figure is a typical logarithmic plot of experimental profile measurements and shows the approximate velocity profile representation. Plots such as this indicate that the region on the boundary layer near the surface, and the upper portion can each be represented by a distinct straight lines. This is indeed as it should be, since a more accurate description of a turbulent boundary layer requires the use of two functions.

These include the "law of the Wall" which applies near the surface and the "Law of the Wake" which applies to the intermediate/outer portion of the boundary layer, (References 16,19,23 28,29). These straight lines were used to systematically select a mean line representation of the entire boundary layer.

The velocity profile exponent "N" is determined by the slope of the mean line. The corresponding value of the boundary layer thickness, δ , is defined as the height where the mean line intersects the value of $u/U_o = 1.0$

Experimental and Approximate Velocity Profiles



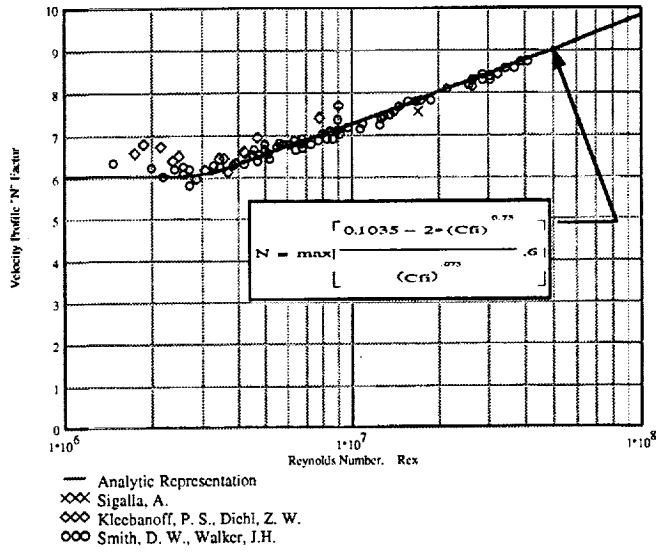
This is a conventional plot of the velocity profile data shown in the previous chart. The various boundary layer growth characteristics were calculated from the measured velocity profile data and also using the approximate "power law" velocity profile. The results are summarized in the table below.

	Measured Profile	Approximate Profile	"Error" %
δ^+	0.0803	0.0801	-0.25
θ	0.0592	0.0613	3.5
H	1.357	1.307	-3.7

The approximate velocity profile "matched" to fit the experimental velocity profile by the process described on the previous page, does provides a good approximation to the turbulent boundary layer growth characteristics.

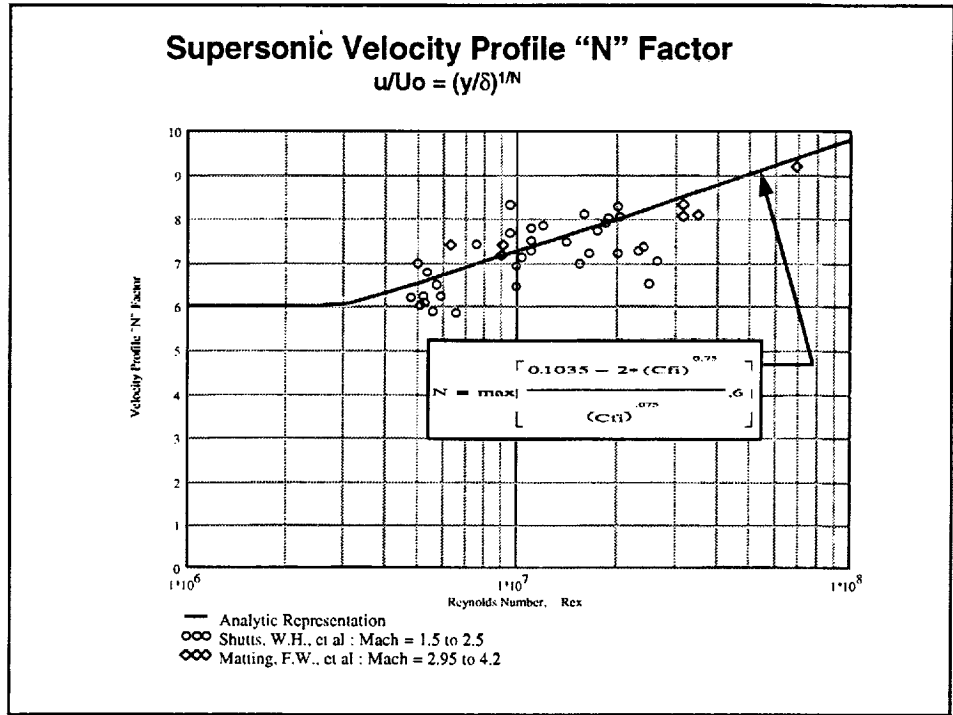
Incompressible Velocity Profile "N" Factor

$$u/U_0 = (y/\delta)^{1/N}$$



Incompressible velocity profile data from a number of independent sources were used to determine "appropriate" values of N to represent a turbulent boundary layer. The results as shown in this figure, indicate that the value of " N " is strongly dependent on Reynolds number.

The equation shown in the figure was developed in the current study to represent the effect of Reynolds number on " N " as determined from the experimental data.

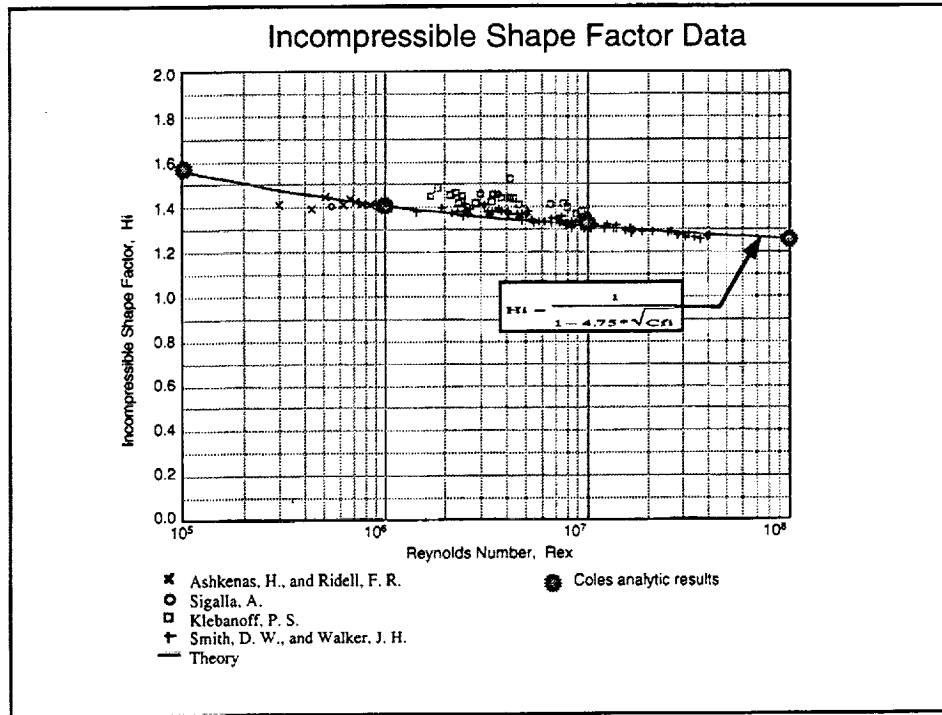


The data in this figure are values of "N" determined from compressible boundary layer measurements for a number of Mach numbers from 1.5 to 4.2. The compressible values of "N" appear to scatter about the empirical equation that was developed from the incompressible velocity profile data.

Thus it appears that the shape of a turbulent depends on Reynolds number but is independent of Mach number.

This result should not be surprising for it is implied by the concept of the reference temperature approach to calculate supersonic skin friction drag. Skin friction depends on the shape of the boundary layer as well as the density and viscosity in the boundary. The reference temperature method as defined earlier in this note assumes that compressibility only changes the effective values of density and viscosity. Hence, Mach number doesn't change the velocity profile shape.

Developing an analytic expression for "N" was the second step in the process for developing a method to predict the boundary layer thickness.



In incompressible flow the boundary layer displacement thickness and momentum thickness equations are:

$$\delta^* = \int_0^{\infty} \left[1 - \left(\frac{u}{U_{\infty}} \right) \right] dy$$

$$\theta = \int_0^{\infty} \frac{u}{U_{\infty}} \left[1 - \left(\frac{u}{U_{\infty}} \right) \right] dy$$

$$H = \delta^* / \theta$$

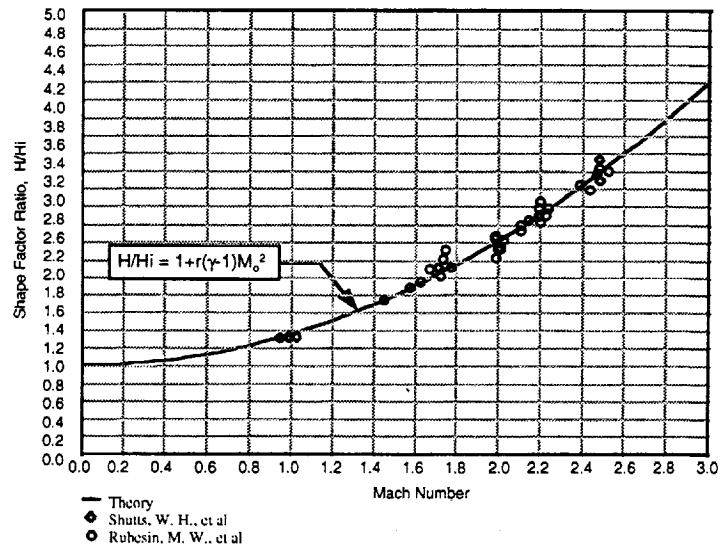
In incompressible flow, the value of H for a flat plate turbulent flow is a unique function of the "shape" of the boundary layer.

In principal, the variation of H with Reynolds number could be determined from the approximate velocity profile shape and the empirical equation for "N". As previously shown, the approximate velocity profile shape provides a very good estimate for δ^* . The values for both θ and H calculated using the approximate velocity profile are not as accurate. Consequently, it was decided to use an equation for H developed by Clauser (presented in Ref 28) based on a more sophisticated representation of the boundary layer based on the "velocity defect" concept. Experimental values of the incompressible shape factor, H_i , are compared with a modified version of Clauser's equation in which the constant 4.75 replaced Clauser's original value of 4.31.

Also shown in the figure are analytic values for H_i calculated by Coles (presented in Ref 35) using "log" wall relations for the boundary layer.

Mach Number Effect on Boundary Layer Shape Factor

Reynolds Number = 4×10^6 to 30×10^6



Following Monaghan (Ref 27), the shape factor for the turbulent boundary layer on a flat plate can be related to the incompressible value H_i , the free stream temperature T_∞ , the wall temperature T_w , and the recovery temperature T_r , by the equation:

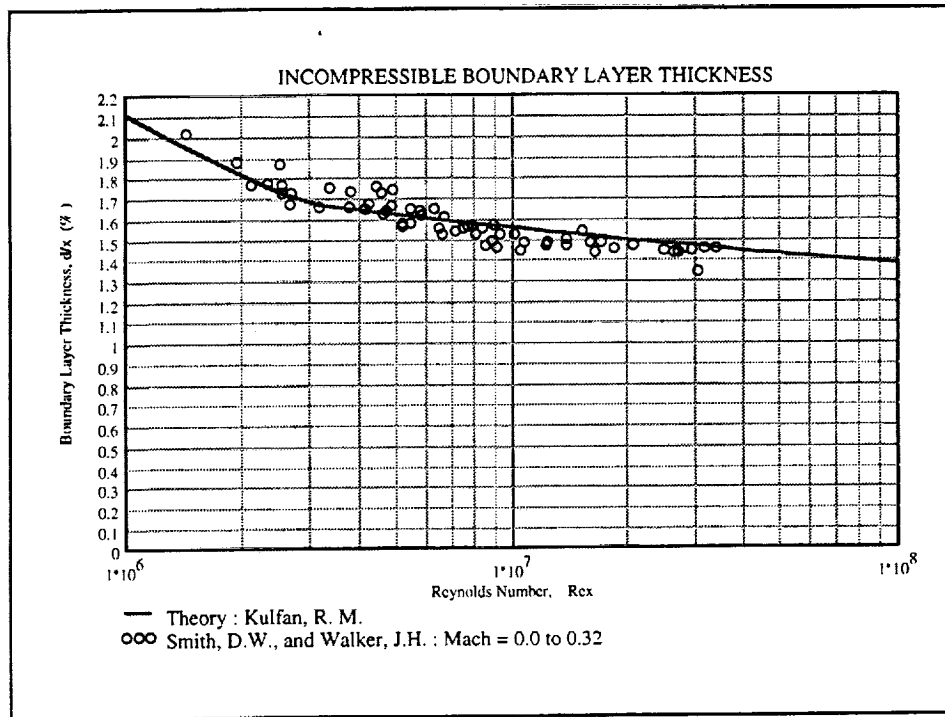
$$\frac{H}{H_i} = 1 + \left| \frac{T_w}{T_\infty} - 1 \right| + \left| \frac{T_r}{T_\infty} - 1 \right|$$

For an insulated surface this equation becomes:

$$\frac{H}{H_i} = 1 + r(\gamma - 1)M_\infty^2$$

Experimental data shown in the figure appears to validate this equation. Hence, the shape factor for fully turbulent flat plate flow can be calculated as the product of two factors. One factor depends only on Reynolds number and the second factor depends only on Mach number.

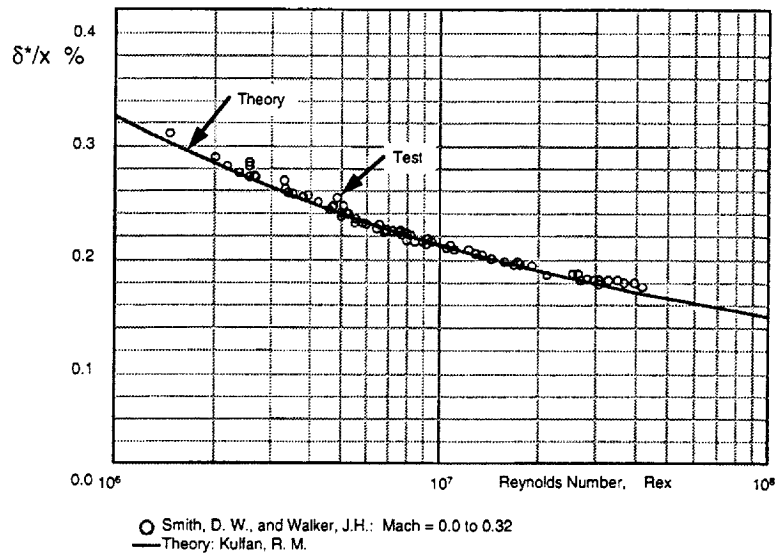
The equation implies that boundary layer displacement effects become much larger than the momentum thickness as Mach number increases.



We now have developed all the ingredients to calculate the boundary layer thickness for fully turbulent flat plate flow using the process shown in figure 23.

Calculations of the variation of incompressible flat plate boundary layer thickness are compared with test data from reference 1. The theoretical predictions obtained using this process closely matches the test data.

Incompressible Boundary Layer Displacement Thickness

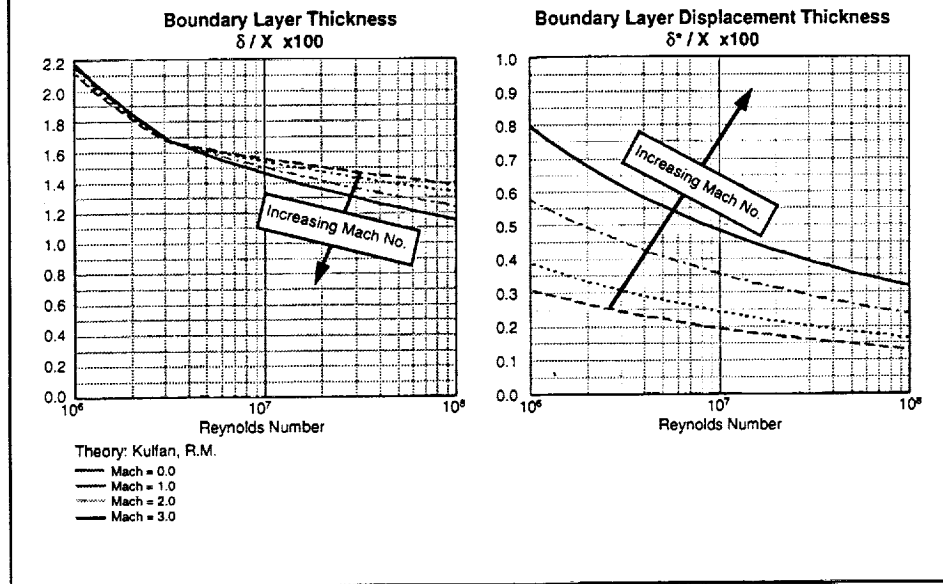


The boundary layer displacement thickness can be calculated by the shape factor equations and the average flat plate skin friction coefficient as:

$$\frac{\delta^*}{X} = \frac{H_i}{2} \frac{H}{H_i} CF$$

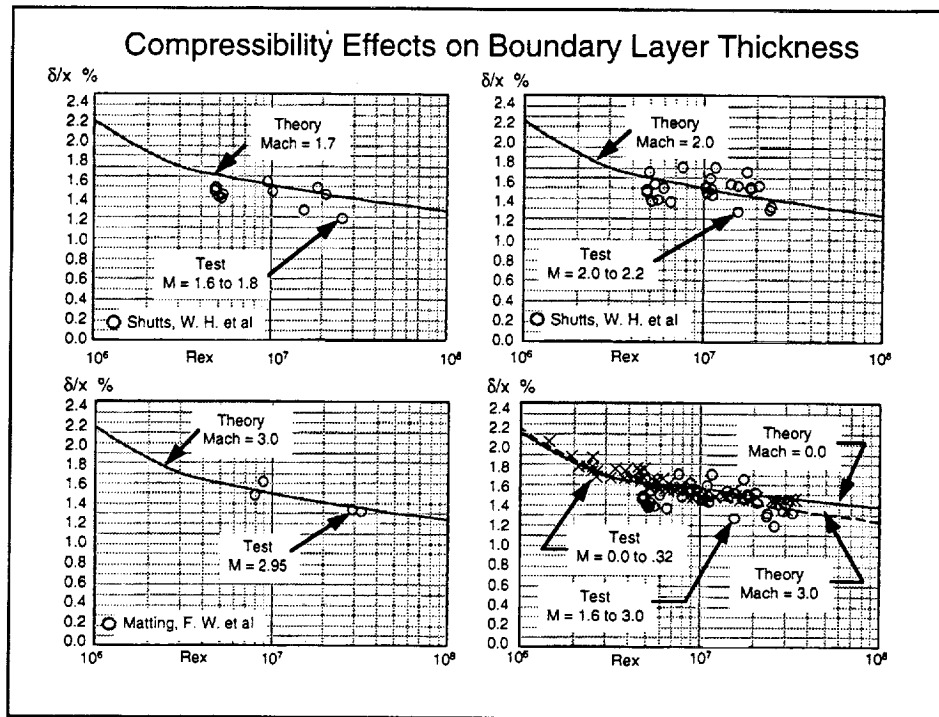
Predictions of incompressible displacement thickness are compared with test data in the figure. The agreement between the theory and the test data is quite good.

Compressibility Effects on Boundary Layer Thickness



Boundary layer thickness and displacement thickness have been calculated for a range of Reynolds numbers and Mach numbers from 0 to 3 using the methods presented in this paper.

The overall boundary layer thickness is seen to be relatively insensitive to Mach number. The boundary layer displacement thickness, however, grows rapidly as Mach number increases.



Compressible boundary layer thickness predictions are compared with test data in this Figure for Mach numbers of 1.7, 2.0 and 3.0. Although there is quite a bit of data scatter, the data appears to validate the boundary layer thickness predictions.

The fourth figure contains the incompressible data from the previous figure and the three sets of compressible data. This appears to substantiate the conclusion that the thickness of a turbulent boundary layer is indeed relatively insensitive to Mach number.

Conclusions

- Modified Incompressible Equations and Improved T^*/T Method Predict "Mean" of Available Flat Plate Skin Friction Drag Measurements
- New Methods Presented That Appear to Provide Good Estimates of Boundary Layer Thickness and Displacement Thickness
- Compressibility Effects Have Very Little Effect on The Shape or Height of the Turbulent Flat Plate Velocity Profile.
- Boundary Layer Displacement Thickness Increases Rapidly With Mach Number
- Comparisons of Navier Stokes CFD Predictions of Flat Plate Turbulent Skin Friction Drag and Boundary Layer Growth, With the Test Data and / or Theory Presented in This paper, is considered to be a Necessary and Vital Step to Validating the Codes For HSCT Viscous Drag Predictions .
- Need Additional / Quality Experimental CF Data:
 - Locate Available Existing Data
 - Symmetric Model Tests
 - Segmented Axisymmetry Body of Revolution
 - Utilize TU-144 Flight Test Data
 - ???

The modified incompressible CF equations and the improved T^* equation presented in the paper appear to consistently match the test better than the other flat plate CF methods currently in use on the HSCT program. It is recommended that the methods presented here, be adapted as the official HSCT flat plate calculation methods.

The boundary layer thickness, and displacement thickness calculations methods presented in this paper seem to be validated by the existing data.

Compressibility effects have little effect on either the shape or height of a turbulent boundary layer. The displacement thickness however varies rapidly with increasing Mach number.

Comparisons of Navier-Stokes predictions, of the skin friction drag and boundary layer growth characteristics for fully turbulent flat plate flow, with the theory and/or test data presented in this paper is considered to be a necessary and vital step in validation of the CFD codes for HSCT viscous drag predictions. This is just the first step in the total validation process that may also include comparisons with data from tests of a symmetric HSCT type configuration, or data from tests of a long segmented cone/cylinder body, and utilization of the newly acquired TU-144 flight test data.

REFERENCES

Each reference listed below contains one or more of the following criteria (as denoted by the letter in the brackets):

- A. Extensive experimental measurement and data reduction techniques.
- B. Presentation or discussion of analytical techniques.
- C. Experimental data.
- D. Extensive bibliography.

1. Kulfan, Robert M., "Turbulent Boundary Layer Flow Past a Smooth Adiabatic Flat Plate", Boeing Document D6-7161, May 1961 [B,C,D]
2. White, Frank M. VISCOUS FLUID FLOW, Mc Graw - Hill Book Company, 1974, [B,C,D]
3. Wegener, Winkler, Sibulkin. "A Measurement of Turbulent Boundary Layer Profiles and Heat Transfer Coefficients at Mach 7.0", Journal of Aero-nautical Sciences, Vol.20, No.3, 1953. [A,C]
4. Chapman and Kester. "Measurement of Turbulent Skin Friction on Cylinders in Axial Flow at Subsonic and Supersonic Velocities," Journal of Aeronautical Sciences, Vol.20, No.7, 1953. [A,B,C,D]
5. Chapman and Kester. "Turbulent Boundary Layer and Skin Friction Measurements in Axial Flow along Cylinders at Mach Numbers between 0.5 and 3.6." NACA TN 3097. [A,B,C,D]
6. Naleid, J. F. "Experimental Investigation of the Impact Probe Method of Measuring Local Skin Friction at Supersonic Speeds in the Presence of an Adverse Pressure Gradient." Defense Research Laboratory Report. D.R.L. - 432, CF - 273. [A,C]
7. Sibulkin, M. "Boundary Layer Measurements at Supersonic Nozzle Throats." Journal of Aeronautical Sciences, April, 1957. [A,C]
8. Winkler, E. M., Cha, M. H. "Experimental Investigations of the Effect of Heat Transfer on Hypersonic Turbulent Boundary Layer Skin Friction." Journal of Aero/Space Sciences, February, 1959. [A,C]
9. Shutts, W. H., Hartwig, W. H., and Weiler, J. E. "Final Report on Turbulent Boundary Layer and Skin Friction Measurements on a Smooth, Thermally Insulated Flat Plate at Supersonic Speeds." Defense Research Laboratory Report. D.R.L. - 364, C.M. - 823. [A,C,D]
10. Coles, Donald. "Measurements of Turbulent Friction on a Smooth Flat Plate in Supersonic Flow." Journal of Aeronautical Sciences, Vol.21, No.7, July, 1954. [A,C]

REFERENCES(Continued)

11. Korkegi, Robert H. "Transition Studies and Skin Friction Measurements on an Insulated Flat Plate at a Mach Number of 5.8." *Journal of Aeronautical Sciences*, Vol.25, No.2, February, 1956. [A,C]
12. Sommer, Simon C., and Short, Barbara J. "Free Flight Measurements of Skin Friction of Turbulent Boundary Layer Skin Friction in the Presence of Severe Aerodynamic Heating at Mach Numbers from 2.8 to 7.0." *NACA TN 3391*, March, 1955. [A,B,C]
13. Sommer, Simon C., Short, Barbara J. "Free Flight Measurements of Skin Friction of Turbulent Boundary Layers with High Rates of Heat Transfer at Supersonic Speeds." *Journal of Aeronautical Sciences*, June, 1956. [A,B,C]
14. Rubesin, M. W., Maydew, R. C., and Varga, S. A. "An Analytical and Experimental Investigation of Skin Friction of the Turbulent Boundary Layer on a Flat Plate at Supersonic Speeds." *NACA TN 2305*, February, 1951. [A,B,C]
15. Matting, F. We, Chapman, D. R., Nyholm, J. R., Thomas, A. G. "Turbulent Skin Friction at High Mach Numbers and Reynolds Numbers." *PROCEEDINGS OF THE 1959 HEAT TRANSFER AND FLUID MECHANICS INSTITUTE*. Stanford University Press, 1959. [A,B,C,D]
16. Dhawan, Satish. "Direct Measurements of Skin Friction." *NACA Report 1121*, 1953. [A,B,C,D]
17. Czarnecki, K. R., Sevier, J. R., and Carmel, N. M. "Effects of Fabrication 'type Roughness on Turbulent Skin Friction at Supersonic Speeds." *NACA TN 4299*. [A,C]
18. Fenter, F. W., and Stalmach, C. J., Jr. "The Measurement of Local Turbulent Skin Friction at Supersonic Speeds by Means of Surface Impact Pressure Probes." *Defense Research Laboratory Report. D.R.L. - 392, CM - 878*, October, 1957. [A,B,C,D]
19. Kuethe, A.M., and Schetzer, J. D., *FOUNDATIONS OF AERODYNAMICS* John Wiley and Sons, Incorporated, . New York, 1959. [B]
20. Nielsen, J. N. *MISSILE AERODYNAMICS*. New York, McGraw-Hill Book Company Inc., 1960. [B,C]
21. Liepmann H. W., and Roshko, A., *ELEMENTS OF GASDYNAMICS*, John Wiley and Sons, Inc., New York 1957. [B,D]
22. Shapiro, A. H. *THE DYNAMICS AND THERMODYNAMICS OF COMPRESSIBLE Flow*. Vol.11, New York, The Ronald Press Company, 1954. [B,C]

REFERENCES(Continued)

23. Schlichting, H. BOUNDARY LAYER THEORY. New York, Pergamon Press, 1955. [B,D]
24. Hilsenrath J. et al. TABLES OF THERMAL PROPERTIES OF GASES. National Bureau of Standards Circular 564, November, 1955.
25. Smith, D. W., and Walker, J. H. "Skin Friction Measurements in Incompressible Flow." NACA TN 4231, 1958. [A,C]
26. Matting, F. W., Chapman, D. R., Nyholm, J. R., Thomas, A. G. "Turbulent Skin Friction at High Mach Numbers and Reynolds Numbers in Air and Helium." NASA R-82. [A,B,C,D]
27. Monaghan, R. J. "On the Behavior of Boundary Layers at Supersonic Speeds." I.A.S. - R A. S Proceedings, 1955. [B,D]
28. Lin, C. C. TURBULENT FLOWS AND HEAT TRANSFER. Vol.5, Princeton Series on High Speed Aerodynamics and Jet Propulsion. Princeton University press, 1959. [B,D]
29. Thwaites, B. "Incompressible Aerodynamics." Oxford at the Clarendon Press, 1960. [B,D]
30. Klebanoff, P.S., and Diehl, Z. E. "Some Features of Artificially Thickened Fully Developed Boundary Layers with Zero Pressure Gradient." NACA Report 1110, 1952. [A,C,D]
31. Simon, P. C. and Kowalski, K. L. "Charts of Boundary Layer Mass Flow and Momentum for Inlet Performance Analysis Mach Number Range, 0.2 to 5.0." NACA TN 3583, November, 1955. [B]
32. Ashkenas, H., and Riddell, F. R. "Investigation of the Turbulent Boundary Layer on a Yawed Flat Plate." NACA TN 3383, 1955. [A,B,C]
33. Klebanoff, P.S. "Characteristics of Turbulence in a Boundary Layer with Zero Pressure Gradient." NACA Report 1247, 1955. [A,B,C]
34. Sigalla, A. "Experiments with Pitot Tubes for Skin Friction Measurements." British Iron and Steel Research Association Report P/2/58, List 92, 1958. [A,C]
35. Duncan, W. J., Thom, A. S., Young, A. D., MECHANICS OF FLUIDS, American Elsevier Publishing Co. New York, 1970. [A,B,C,D]
36. Erickson, W. D. "Real-Gas Correction Factors for Hypersonic Flow Parameters in Helium." NASA TN D-462, September, 1960.

REFERENCES(Continued)

37. Eckert, E. R. G. et al: "Prandtl Number, Thermal Conductivity, and Viscosity of Air-Helium Mixtures." NASA TN D-533, September, 1960.
38. Czarnnecki, K. R. et al: "Investigation of Distributed Surface Roughness on a Body of Revolutions at a Mach Number of 1.61." NACA TN 3230, June, 1954. [A,C]
39. Smith, D. W., and Walker, J. H. "Skin Friction Measurements in Incompressible Flow." NACA TR R-26, 1959. [A,C,D]
40. Eckert, Z. R. G. "Simplified treatment of the Turbulent Boundary Layer along a Cylinder in Compressible Flow." Journal of Aeronautical Sciences, January, 1952. [B]

HSR
High Speed Research

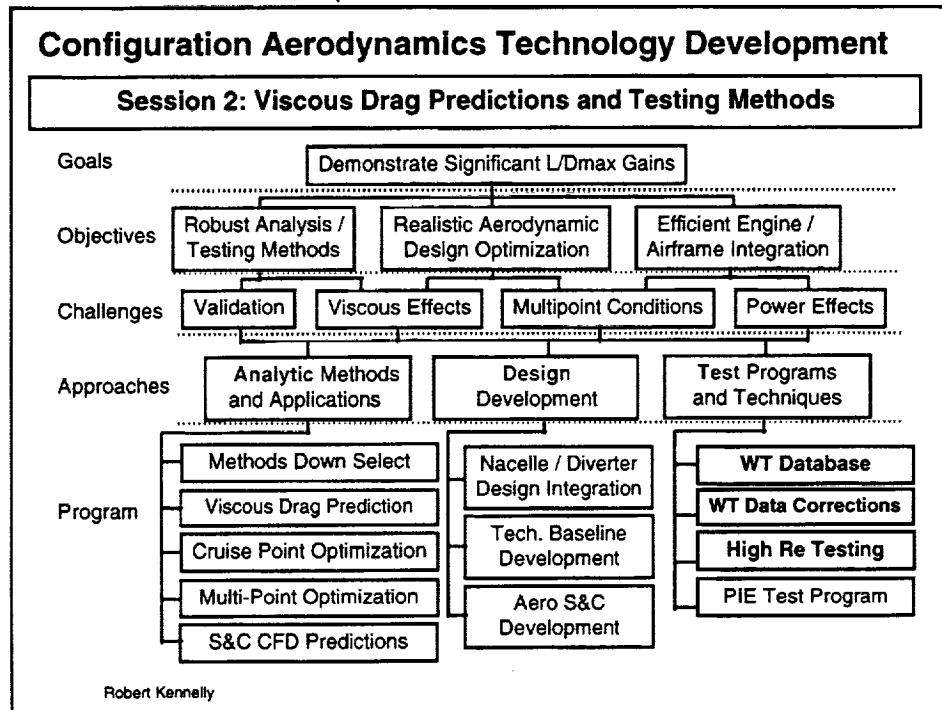


CA Testing Workshops: Process, Issues, Results

Robert A. Kennelly, Jr.
NASA Ames Research Center

Los Angeles, CA
February 9–13, 1998

Robert Kennelly



The Configuration Aerodynamics test team has met for weekly telecons since August 1996, and its members have worked together on a number of tests. But the group wished to gather and exchange thoughts away from the heat of battle, and their collective wish was granted on a trial basis in the spring of 1997. The CA ITD team authorized an informal workshop to be held at Ames Research Center for the purpose of addressing some of the concerns which had arisen in the course of testing the Tech Concept and its predecessors. This was the first time that team members from all four sites had been able to meet together to concentrate on testing issues.

Outline

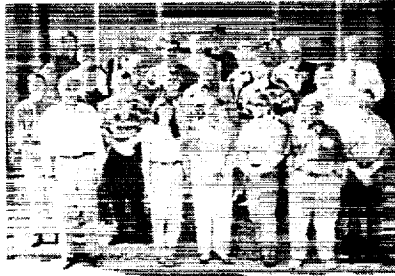
- **Process**
 - Who, what, where, when, why...
- **Issues**
 - General confab in 1st workshop
 - Reviewed NCV test in 2nd
- **Results**
 - Selected topics in more detail
 - » Low-speed trip dot testing
 - » Alternate trip configurations
 - » Trip drag & laminar run correction
 - Future "grit drag" tests

Robert Kennelly

This presentation will describe the organization and conduct of the workshops, list the topics discussed, and conclude with a more-detailed examination of a related set of issues dear to the presenter's heart.

Because the current HSCT configuration is expected to have (mostly) turbulent flow over the wings, and because current CFD predictions assume fully-turbulent flow, the wind tunnel testing to date has attempted to duplicate this condition at the lower Reynolds numbers attainable on the ground. This frequently requires some form of artificial boundary layer trip to induce transition near the wing's leading edge. But this innocent-sounding goal leads to a number of complications, and it is not clear that present-day testing technology is adequate to the task. An description of some of the difficulties, and work underway to address them, forms the "Results" section of this talk. Additional results of the testing workshop will be covered in presentations by other team members.

Workshop Process

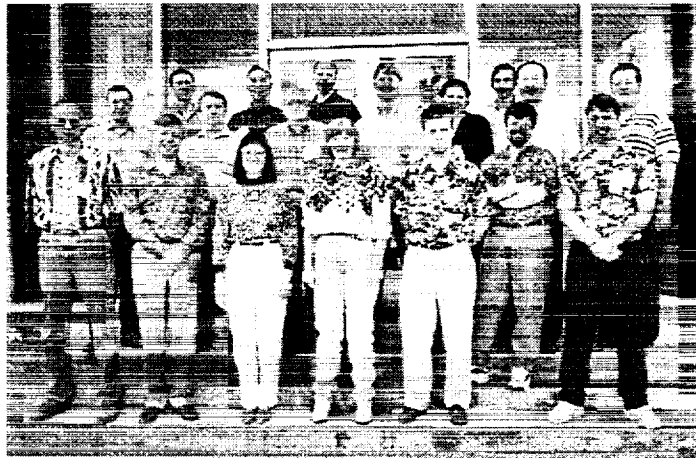


May '97 workshop

- NASA & Industry PDW's, plus invited gurus (30 participants in all)
- Short fuse, good response from all organizations
- *Lots of discussion!*
- Structure for interaction between PDW's & ITD
- Informal "Notes" volumes delivered in one month

Robert Kennelly

Major Progress in Loud Attire



November '97 workshop participants

Robert Kennelly

Shown above is the somewhat more intimate group which gathered for the second workshop, which was also held at Ames Research Center. Improved pre-event coordination resulted in a striking display of colorful shirts.

Workshop Products

- **May '97 Workshop**
 - Quote: "This was the first workshop I've been to that actually was a workshop!"
 - Memo to ITD with consensus items, and a prioritized list and timetable of proposed work for FY98 and beyond
 - Several of these projects were funded and are now underway
- **November '97 Workshop**
 - Summary presentation to ITD of a "6-month" plan to address NCV vs. TCA performance shortfall
 - Collective brainstorming produced a number of lines of attack for follow-up testing during early '98
 - Two volumes of notes and reference materials distributed

Robert Kennelly

We didn't just talk—a prioritized list of suggestions to the ITD team was produced during the first workshop, and a short-range plan to address questions raised by the recent NCV test was presented to the ITD team at the conclusion of the second.

Published volumes with copies of the presentations, background references (which proved quite useful), and notes from the discussions were distributed to participants and the ITD team members shortly after the workshops.

Acknowledgements

- **The active involvement of our guests was much appreciated by all the participants**
- **Invited guests:**
 - **Seetharam Chintamani, Jim Crowder, Jim Daugherty, Mike Hensch, Ray Hicks, Paul Vijgen, Russ Westphal**
 - **Tonja Krutckoff, Pradip Parikh, Chih-Fang Shieh**
- **Facilitator: Dave Lund (1st workshop)**
- **Co-hosts & scribes: Mina Cappuccio, Aga Goodsell**

Robert Kennelly

Workshop Issues

- The 1st workshop included “works-in-progress”, tutorials, and talks on specific issues
- Presentations coordinated by session chairpersons
- Everybody took a crack at trip drag for Test #1679; nobody was entirely pleased with their results!

Topic

Overview of recent tests at LaRC
Test process at UPWT & 16-ft
Statistical treatment of WT data
Reporting
Transition detection
Trip drag correction
Discussion with invited guests
Future directions

Session Chair

Cappuccio
Goodman
Mejia
Novean
Goodsell
Magee
Mejia
Wahls

Robert Kennelly

One useful result of the joint effort at estimating “grit drag” for Model 2b (the TCA baseline performance model) was the realization that no approach was clearly superior. It was helpful to get this contentious issue out into the open.

The Session Chairs played a vital role in coordinating the presentations on the various topics; we would not have fared as well as we did without this level of organization.

Workshop Issues, con't.

- **The 2nd workshop was smaller, shorter, and focused on NCV testing issues**
- **Much tighter schedule: the ITD demanded that we present a plan of action on the second afternoon**
- **Topics (all covered in one day!):**
 - Overview of CFD predictions
 - Results of NCV test
 - Computed laminar & turbulent streamlines
 - QA results for models 2b and NCV
 - Results of Polysonic WT high-Re tests
 - Boundary layer stability
 - Trip dot study
 - CFD skin friction overview
 - Upcoming tests
- **Consensus: Don't neglect fundamentals!**

Robert Kennelly

Workshop Results

- **Test procedures, uncertainty, reporting**
 - Better communication within our far-flung group
- **Transition detection**
 - Best sublimation photos to date; documented technique
 - General agreement on interpretation of photos (incl. gurus)
- **B'layer trips**
 - Fundamental work underway with WSU (low speed)
 - Less intrusive trip techniques (high speed)
- **Corrections to WT data**
 - Laminar run: work in progress on estimation using new code
 - Trip drag remains problematic; additional testing planned
 - Analyze experiment more accurately with CFD?

Robert Kennelly

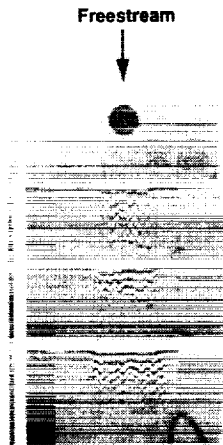
Although some progress has been made, correction for the drag associated with artificially tripping the boundary layer remains problematic. The highlighted elements above form the core of the "grit drag" discussion to follow. The central issues are "how to characterize the boundary layer state?" and "how to correct for the measures required to achieve it?"

Selected Outcome Threads

- (1) Low-speed trip dot investigation**
- (2) Alternate trip techniques**
- (3) Trip drag & flat-plate skin friction analysis**

Robert Kennelly

(1) Low Speed Test: Trip Dots at Expanded Scale



Robert Kennelly

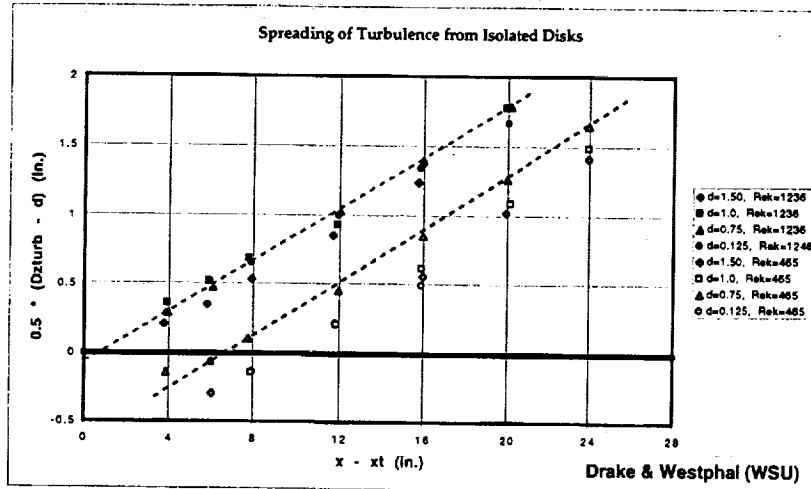
- Joint research with WSU
- Low-speed flow, enlarged dot geometry
- Matches Re (but not Ma)
- Study skin friction using Oil Film Interferometry (local C_f proportional to fringe spacing)
- Investigate dot shapes & spacing, wire, beads
- Looking for alternative trip configurations, C_f bias, *understanding*

It's not easy to trip the boundary layer at Mach 2.40, especially in the presence of a strongly-favorable pressure gradient. Achieving this efficiently (with minimum disturbance to the flowfield under test) and at a reliably-known location is harder. Sublimation images from supersonic testing revealed a variety of features, some the familiar result of the increased stability of compressible flows and some new. This work, being conducted at Washington State University in collaboration with NASA Ames, is an overdue, systematic examination of the use of cylindrical roughness elements ("trip dots") as boundary layer trips.

Oil Film Interferometry is an optical technique for measuring local skin friction (see References). In the composite image above, the spreading zone of turbulence downstream of a large-scale trip dot is revealed by the widely-spaced interference fringes in a film of transparent oil exposed to the air stream. This novel application of the technique permits both qualitative and quantitative examination of trip dot performance over a wide range of parameters. The Reynolds number matches that used in high-speed testing in the LaRC UPWT, but compressibility effects are absent in this laboratory tunnel.

A poster with a number of OFI images is available from the author.

Spreading of Turbulence from Dots



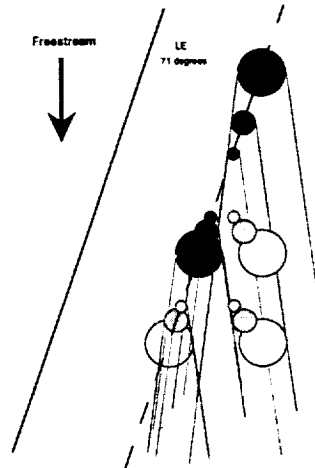
Robert Kennelly

The experimental set-up consists of a 4-ft chord flat plate with beveled edge in the 2- by 2-ft test section of the WSU low-speed tunnel. The plate is covered with strips of black paint-backed Mylar, which provides the optically smooth surface required for interference between monochromatic light reflecting from the air-oil and oil-Mylar interfaces. The trip dots are located at about 6 in from the leading edge of the plate, where $Re(x) = 100,000$.

The data presented above show that the characteristic turbulence spreading angle behind different (isolated) dots is the same regardless of dot height or diameter—only the origin of the spreading varies. The edges of the turbulent region were measured from photographs of oil film patterns. The plot shows how the width of the pattern increases with distance downstream of the trip location.

(2) High Speed Test: Alternate Trip Configurations

- **Smaller dots, more closely spaced**
 - approx. same turbulent area
 - less "blockage", smaller correction
 - extrapolate to zero width!
- **Usual dots, larger pitch on highly-swept LE's**
 - less "blockage", smaller correction
- **Others?**
- **Test at LaRC UPWT in Dec. 1998**



Robert Kennelly

If, as appears to be the case from the low-speed experiments, the aspect ratio of the dots does not significantly affect their efficacy, some alternative arrangements suggest themselves. It turns out that a pattern of smaller-than-usual dots (dark red and blue in the sketch), somewhat more closely spaced, can be chosen to induce transition at the same average streamwise distance as the customary configuration (dark green). The "blockage" is, however, less: the projected frontal area of the dots is reduced as they are made smaller, even though they must also be packed more densely. (Compare the dark pattern with the adjacent light-colored disks to see the relative spacing.) Such an approach may prove to be more efficient, even if it does not eliminate trip drag entirely. Perhaps more significant is the possibility of a meaningful extrapolation to zero dot width, which would permit estimation of "grit drag" in an entirely new way.

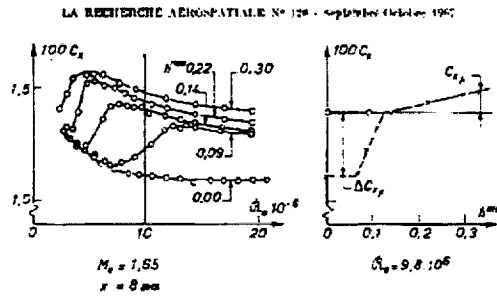
Another, related, approach would be to use the same "trip tape" technique as at present, but remove two out of three dots (rather than every other dot). The average transition point would move back slightly, but again the blockage would be reduced (see downstream dot clusters in the sketch).

(3) Trip Drag is NOT a New Problem!

- **Braslow, et al.**
- **Other supersonic cruise tests**
 - Vaucheret: Symmetric model tested in the ONERA S-2 WT (Modane, FR)
 - Daugherty, et al: XB-70 model tested in Ames 9- by 7-ft
- **HSR experience to date doesn't match very well**
 - Hard to get prompt transition, especially where flow expands rapidly around blunt inboard LE (TCA is bad; NCV worse)
 - No "drag plateau" observed
 - Estimates of trip drag are large (up to 6 counts)
 - Sensitive to extrapolation technique (and no way to resolve the issue one way or the other!)

Robert Kennelly

X. Vaucheret (mid 1960's)

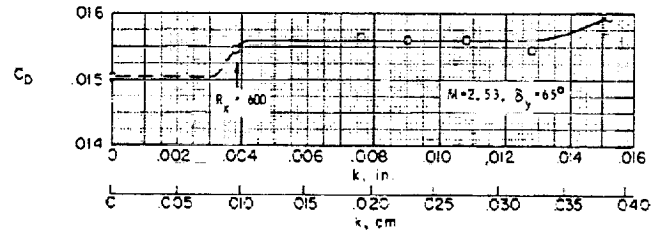


- **Ma (here) = 1.65, Re = 9.8 million/m, symmetrical sections, zero angle-of-attack**
- **Trip consisted of a single row of glass beads**
- **Drag “plateau” found after correcting for laminar flow**

Robert Kennelly

Xavier Vaucheret, working in France in the 1960's, observed the same difficulties as the test team does at present in tripping the flow on supersonic models, including the delayed trip observed in sublimation patterns. But the technique he describes for evaluating trip drag is a new one to HSR: he corrects for laminar run (based on flow visualization, and using a flat plate model for the viscous drag) and then asserts that the trip drag is the excess drag above the drag plateau observed for the smaller trip heights.

XB-70 Test (late 1970's)



Daugherty, et al. (Ames)

- **Ma (here) = 2.53, Re = 4 million/ft, sharp LE sections**
- **Transition observed at or near the grit strip**
- **Drag “plateau” observed; zero trip drag for k up to about 0.013 in**

Robert Kennelly

James Daugherty also obtained a “drag plateau” in tests of an XB-70 model in the Ames 9- by 7-ft Supersonic Wind Tunnel. Turbulent flow was obtained promptly at the trip location, so no correction for laminar run was required.

“Whad’da they got we ain’t got?”

- **Gently-favorable pressure gradient?**
 - TCA trips promptly on outboard panel for modest dots, and natural transition on inboard, lower surface is quite near the LE
 - Problem area is inboard suction surface
- **Similar pressure distribution on the entire wing?**
 - Partially addressed in Test #1679 where only the upper, inboard dots were varied—not the whole solution
- **Use of distributed roughness (grit) or individual glass beads**
 - Already looking into alternate trips—we’ll see if it matters...
- **Correction for laminar run, or no need for it**
 - Delayed transition not well modeled at present by CFD
 - We need a revised experimental approach!

Robert Kennelly

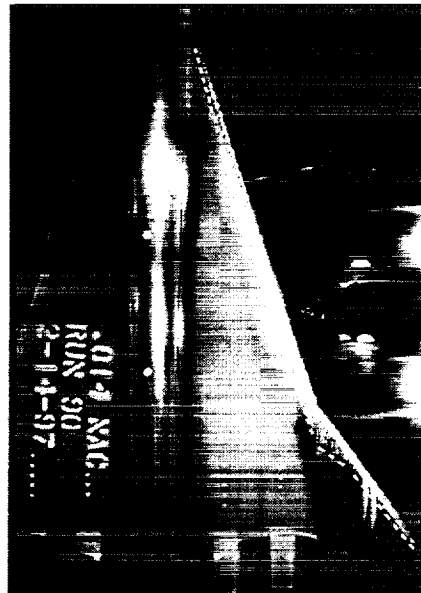
Part of the solution to the trip drag problem consists of understanding why we even have a problem—at least two previous experiments found that they had little or no dot drag at the conditions tested. So what’s different? The most likely culprit would seem to be the pressure distribution on the upper, inboard wing surface—it’s strongly favorable, in contrast (we suspect) to both the symmetrical French configuration and the wedge-flat-wedge airfoil of the XB-70. Gently-favorable pressures require an artificial trip, but it needn’t be as high for prompt effect.

The effect of different trip configurations (individual glass beads in Vaucheret’s work and distributed glass beads in Daugherty’s) will be examined as part of the work at WSU and in an upcoming HSR high-speed test.

Another contributing factor is that we have not yet analyzed our TCA data for the effect of laminar run. Indeed, the apparent trip drag may well be much smaller when this is taken into account.

Sublimation Photo (TCA)

- $k = 0.012''$ dots, cruise alpha
- Ineffective trip inboard (and near planform break)
- Outboard panel behaves differently from inboard
- Significant laminar flow (ΔCD several counts?)
- Note delayed turbulent spreading (compare with WSU low-speed results)

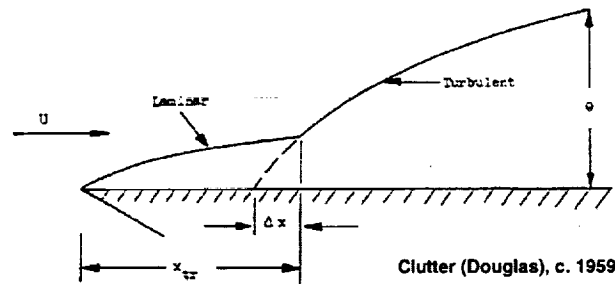


Goossens, et al.

Robert Kennelly

Example of sublimation flow visualization from Test #1679 showing Model 2b's upper surface at 3.5° angle-of-attack, Mach 2.40, Reynolds number 4 million/ft. The dotted yellow line indicates the transition front estimated from a digitally-enlarged view.

Cdf: New Code, Old Method



- Flat plate, compressible, specified wall temperature
- Iteratively matches laminar & turbulent momentum thicknesses at a specified x-location
- Drag areas (D/q) are summed over all elements; normalized by S_{ref} to yield CD for configuration
- Modular FORTRAN 90 code, several C_f methods

Robert Kennelly

Informal investigation turned up several codes and a handbook method which partially addressed the laminar run correction, but no off-the-shelf method was fully satisfactory. A new program, Cdf, was created using ideas gleaned from the other approaches. A complete configuration may be represented as a collection of rectangular "flat plates", each characterized by a length, wetted area, and transition location. The computed drag is normalized by a specified reference area.

The laminar methods presently available are both based on the Blasius solution, with compressibility effects accounted for using the reference temperatures of Eckert and Sommer & Short. Two turbulent methods are also included, those of van Driest (method II) and Prandtl-Schlichting with Sommer & Short's reference temperature. The code is highly modular and additional formulae are easily incorporated. Cdf has been distributed to the other CA experimental groups, and has been successfully compiled and run on several platforms.

Sample Cdf Applications

- **Immediate transition at dots rather than at LE**
 - Simple correction for all WT data; do this much at least!
 - Worth about +0.9 counts in TCA baseline test at UPWT
- **Laminar run CD correction à la Vaucheret**
 - TCA baseline test (in progress—Aga Goodsell)
- **Free transition in high-Re facilities**
 - Some laminar flow remains even at highest Re; must be accounted for (in progress—Kevin Mejia)
- **Non-equilibrium temperatures in blow-down WT?**
 - Compare T_{wall} extremes: room temp. vs. adiabatic wall
 - Predicted spread is up to 2 counts (cold day, warm model, short run); perhaps we should monitor model temperature?
- **Eventually need to validate against CFD**

Robert Kennelly

The new code permits us to approximately correct for laminar run by assuming laminar boundary layer flow from the LE to the trip location or to the actual transition point, if known. Preliminary measurements suggest that the correction may be as large as 6 counts in the LaRC UPWT. Some such correction is also needed when testing in high pressure blow-down tunnels—portions of the outboard wing remain laminar up to the highest Reynolds numbers tested to date.

Because the skin friction methods embodied in Cdf permit specification of “wall” temperature, the code can also be used to estimate the impact of non-equilibrium model temperature. In a worst case analysis, the viscous drag in a blow-down tunnel on a very cold day could be up to 1 or 2 drag counts high. This suggests that we should try to look at model temperature during a blow to see whether adiabatic wall conditions obtain by the time data acquisition begins.

This flat plate approach is not the final word in laminar run correction. It would be desirable to use Navier-Stokes analysis to provide estimates which include the (possibly significant) effects of pressure distribution on the skin friction near the leading edge.

Future Tests

- **Alternate trip configurations in UPWT (Dec. '98)**
- **High-Reynolds number facilities**
 - Polysonic (St. Louis) has imprecise angle-of-attack, questionable flow quality (upgrades later this year)
 - BSWT (Seattle) doesn't go low enough to overlap UPWT Re
 - Can't get fully-turbulent flow in either tunnel with available models/balances/stings (yet, anyway)
 - Test planned for May '98; decision soon...

Robert Kennelly

Upcoming tests related to transition, grit drag, and laminar run corrections are being planned for the LaRC UPWT at Reynolds numbers up to 5 million/ft and at one of the industry blow-down facilities capable of up to about 15 million/ft. The Model 2b wing/body (TCA baseline performance model) will be used with a variety of trip configurations in conjunction with flow visualization and, possibly, local C_f measurements using oil film interferometry.

Summary

- **The informal get-togethers by PDW's were welcomed by the participants**
- **Around-the-table format was effective for background talks and for focused discussion**
- **A number of lines of inquiry emerged and are being pursued:**
 - Low-speed trip dot investigation
 - Systematic testing of alternative trip configurations
 - Trip drag and laminar run correction methodology
- **Many of the presentations to come will elaborate on ideas presented & discussed in the workshops**

Robert Kennelly

SELECTED REFERENCES

- Braslow, Albert L., Raymond M. Hicks, and Roy V. Harris, Jr. 1966. "Use of Grit-Type Boundary-Layer-Transition Trips on Wind-Tunnel Models." NASA TN D-3579.
- Daugherty, James C. 1979. Wind-Tunnel/Flight Correlation Study of Aerodynamic Characteristics of a Large Flexible Supersonic Cruise Airplane (XB-70-1), vol. I. NASA Technical Paper 1514.
- Kennelly, Robert A., Jr., Russell V. Westphal, George G. Mateer, and Julie Seelen. 1995. "Surface Oil Film Interferometry on a Swept Wing Model in Supersonic Flow" in J. P. Crowder, ed. Flow Visualization VII. New York: Begell House, Inc.
- Tanner, L. H., and L. G. Blows. 1976. "A Study of the Motion of Oil Films on Surfaces in Air Flow, With Application to the Measurement of Skin Friction." J. Phys. E: Sci. Inst., vol. 9, pp. 194-202.
- Vaucheret, Xavier. 1967. "Déclenchment Artificiel de la Transition en Supersonique." La Recherche Aéronautique, no. 120, pp. 25-32.

This page is intentionally left blank.

HSR

High Speed Research - Configuration Aerodynamics

Langley Research Center



High Reynolds Number Assessment of Boundary Layer Transition Trip Drag at Mach 2.48 on an HSCT Configuration

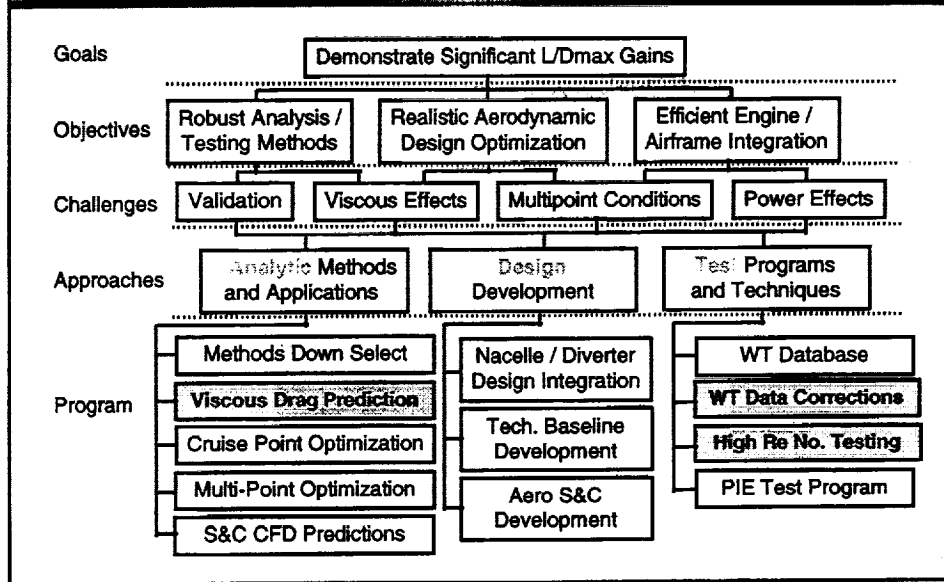
Richard Wahls (LaRC)
Melissa Rivers (LaRC)
Todd Magee (Boeing-LB)
Mike Novean (Boeing-LB)

Aerodynamic Performance Workshop
HSR Annual Airframe Review
Los Angeles, CA
February 9 - 11, 1998

The NASA High Speed Research (HSR) Program is intended to establish a technology base enabling industry development of an economically viable and environmentally acceptable second generation high speed civil transport (HSCT). The HSR program consists of work directed towards several broad technology areas, one of which is aerodynamic performance. The objective of the Configuration Aerodynamics task of the Aerodynamic Performance technology area is the development of aerodynamic drag reduction, stability and control, and propulsion airframe integration technologies required to support the HSCT development process. Towards this goal, computational and empirical based aerodynamic design tools are being developed, evaluated, and validated through ground based experimental testing. In addition, methods for ground to flight scaling are being developed and refined. Successful development of validated design and scaling methodologies will result in improved economy of operation for an HSCT and reduce uncertainty in full-scale flight predictions throughout the development process.

Configuration Aerodynamics Technology Development

Session 2: Viscous Drag Predictions and Testing Methods



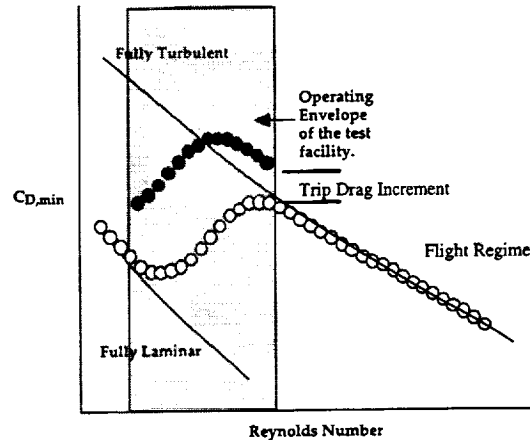
Outline

- Background
- Objectives
- Approach
 - » Facility & Model Description
 - » Test Matrix
- Test Results
 - » Data Quality
 - » Trip Drag
- CFD comparisons
- Concluding Remarks

As outlined above, this presentation begins with a discussion of background information, the primary objectives of this investigation, and the approach taken to meet the objectives. Next, experimental results from a test of a representative HSCT configuration in the Boeing Polysonic Wind Tunnel (PSWT) are presented, followed by comparisons to theoretical results including computational fluid dynamics (CFD). Concluding remarks will close the presentation.

Background

● Reynolds number scaling

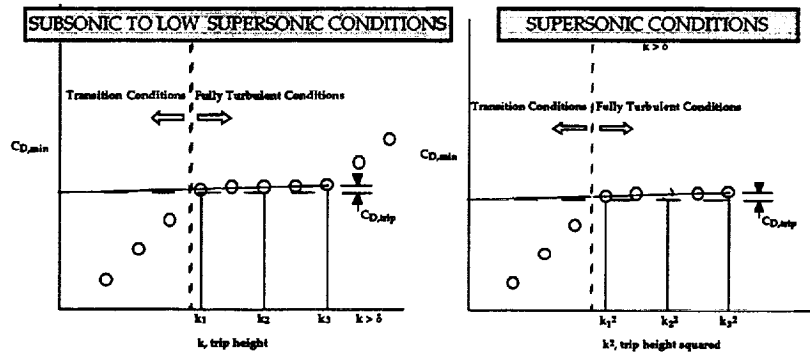


The effect of Reynolds number is fundamental in the ground to flight scaling process, and also impacts the assessment of design improvements of one configuration over another. Ground based experimental testing in conventional wind tunnels occurs at Reynolds numbers significantly below that in flight across the speed regime, thus introducing the complications of boundary layer state variation between ground and flight conditions. Ideally, this complication would be alleviated by ground testing at a sufficiently high Reynolds number to provide fully turbulent flow (open symbols on fully turbulent curve above). Unfortunately, this capability is available in only a few facilities, such as the NTF. To manage this effect, typical testing procedure employs application of roughness elements on wind tunnel model components in order to force boundary layer transition from laminar to turbulent at known locations to more closely simulate the fully turbulent conditions expected in flight. Although the application of roughness elements enables control of the boundary layer state, the consequence is the introduction of another effect not present in flight, namely trip drag due to the roughness elements. Thus, proper ground to flight scaling requires determination of and corrections for trip drag. Given a variable and high Reynolds number test capability sufficient to ensure naturally occurring fully turbulent flow, the chart above indicates how one could determine trip drag.

Background

- Determination of Trip Drag

- » variable/high Reynolds number method
- » variable trip height method



There are several methods for determining trip drag. When a large Reynolds number capability is available in a facility, the technique described previously is preferred. However, a reduced capability test facility is usually the norm. In such a facility, one can test with different sized transition trips on the model, and observe the variation of drag with trip height. Previous studies (Braslow et al for example) indicate the trip height relative to the local boundary layer height impacts how the trip drag is calculated.

In subsonic to low supersonic flow conditions, properly sized and located roughness elements for a given freestream condition can allow a doubling of the trip height with very little effect on the drag. Once the boundary layer is fully turbulent and as long as the trip height, k , is not greater than the boundary-layer thickness, δ , then the values of C_D are not overly affected by the trip. Trip drag can be calculated by extrapolating a linear curve fit (of the C_D data for the $k < \delta$ conditions) back to $k=0$. This will define a C_D that should be equivalent to fully turbulent flow with no trip drag; trip drag for any k value can be calculated by subtracting the C_D value for $k=0$ from the value of C_D for a given k . Also, note that when $k > \delta$, the C_D values for those k values increase rapidly. Thus, for conditions that require the size of the trip, k , to be greater than the boundary layer, a similar method can be employed, however, there exists some disagreement within the HSR community as to whether one should use k^2 instead of k to get an accurate extrapolated curve to $k = k^2 = 0$ and thus, C_D conditions for a fully turbulent boundary layer with no trip drag.

Objectives

- **Primary**
 - » Determine the best method for quantifying trip drag on a HSCT configuration at supersonic Mach
 - » Determine the Reynolds number for fully turbulent flow
 - » Gain HSCT testing experience in an industry blowdown facility capable of slightly higher Reynolds number than available at NASA
- **Secondary**
 - » extension of HSR experimental database to higher Re at supersonic Mach
 - » advance transition detection method based on TSP
- **Issues not addressed**
 - » best trip method, i.e. grit vs dots
 - » best transition detection method

The primary objective of this investigation was an assessment of several trip drag evaluation methods at supersonic speeds on a representative HSCT configuration. Two methods are considered herein; the first method employs variable trip heights at constant flow conditions, and the second method relies on a variable test Reynolds number capability with constant trip heights. Additional primary objectives were an attempt to determine the Reynolds number for fully turbulent flow, and to gain HSCT testing experience in an industry blowdown facility.

Secondary objectives were the extension of the HSR experimental data base to higher Reynolds numbers. Prior to testing in the PSWT, the maximum Re/mac in the data base was approximately 7 to 8 million; the cruise flight Re/mac is on the order of 150 to 200 million. Additionally, a relatively new transition detection technique employing temperature sensitive paint (TSP) was used.

Due to time constraints, desired comparisons of trip type (grit vs. dots), shape, and location and comparisons of different transition detection methods was not possible.

Approach

- Test free & fixed transition from low to high Re in highest Re supersonic facility available (large Re range)
 - » fully turbulent, free transition data for improved trip drag assessment at low Re
 - » free transition from low Re to highest Re attainable
 - » fixed transition at low Re (variable trip heights, *types*, *patterns*)
 - » transition detection method to assess boundary layer state
- Execute a complementary CFD study
 - » provide theoretical fully turbulent data to enhance understanding of experimental data
 - » evaluate predictive capability for Re effects at supersonic Mach

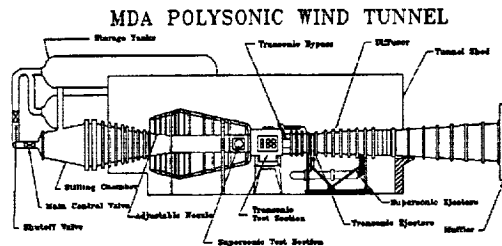
In order to understand forced transition issues, it is valuable to acquire test data with naturally occurring, fully turbulent flow. The importance lies in the ability to anchor data on fully turbulent skin friction drag predictions which can then be extrapolated to flight conditions without the uncertainty of trip drag. On the other side, fully turbulent trip free data provides a reference for low Re data with trip drag corrections.

The approach taken was to test a representative HSCT configuration with both free and fixed transition from low Re to the highest Re available in the US at supersonic conditions. It was planned to evaluate several trip types, patterns, and locations, and several transition detection approaches. As mentioned previously, time constraints did not allow variation of all desired parameters.

A complementary theoretical study, including CFD with the Navier-Stokes flow solver known as CFL3D, was performed to enhance understanding of the experimental data. Additionally, the experimental data provides reference for evaluating the predictive capability of the state-of-the-art flow solver.

Facility Description

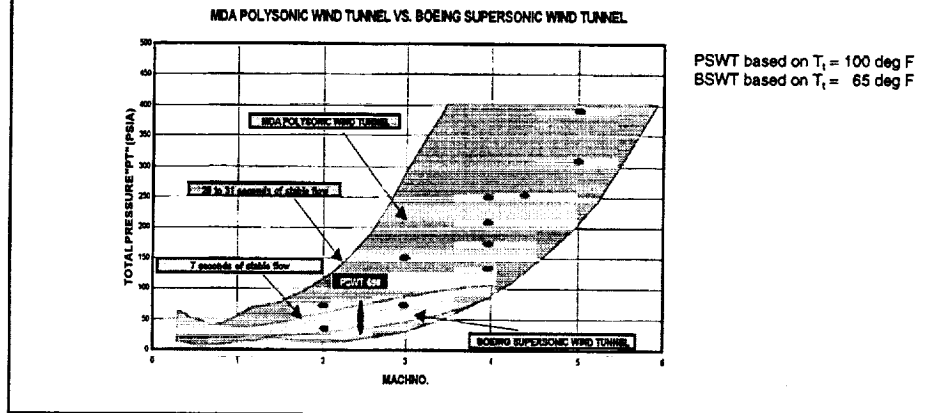
- Boeing Polysonic Wind Tunnel has highest Re capability at supersonic Mach in the US
 - » calibrated at $M = 2.48$ (close to design cruise Mach for HSCT)
 - » 4 FT test section (same as LaRC UPWT & BSWT)
 - » blowdown facility (ejector system used for start/end loads)



The facility in the US with the highest supersonic Re capability is the Boeing (formerly MDA-E) Polysonic Wind Tunnel (PSWT) located in St. Louis, MO. The PSWT is an intermittent pressure-to-atmosphere blowdown tunnel with two 4 by 4 by 6 ft long test sections; one test section is for supersonic testing, and the other for transonic testing. The 4 ft supersonic test section used in this investigation allows existing models sized for the LaRC UPWT to be tested. Start-up & ending loads are larger than experienced at the UPWT due to the fact that the PSWT is a blowdown facility; downstream ejectors are used primarily to reduce these model loads. At present, the PSWT is not calibrated for Mach = 2.40 (HSCT nominal cruise), but is calibrated at Mach = 2.48. For the purposes of this investigation, this difference is not significant.

Facility Description: why this one?

- high Re capability with a large range
 - » overlap with LaRC UPWT on low end
 - » with right hardware, potential to extend HSR high Re data beyond that obtained to date (significantly beyond BSWT)

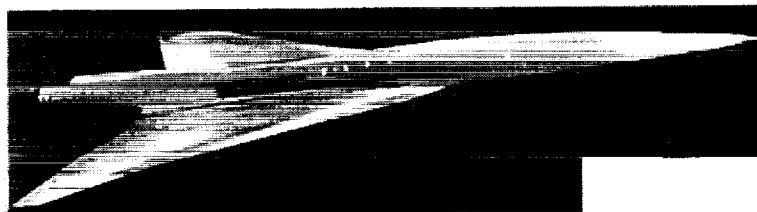


The operating envelop of the PSWT is shown in the chart above; the operating envelope of the Boeing Supersonic Wind Tunnel (BSWT) in Seattle, WA is also shown for reference. Like the PSWT, the BSWT has a 4 by 4 ft supersonic test section and a transonic insert. Unlike the PSWT ejector system, the BSWT employs a snubber system to reduce model start-up and end loads. From the chart, it is clear that the PSWT has a much larger operating envelop due to the significantly higher pressure capability, and can provide significantly longer run times. Dependent on the model and model support strength, however, the full operating envelop may not be available. This was the case in the present investigation, and will continue to be the case for HSCT testing; the limiting condition for the current investigation was set based on sting divergence characteristics, closely followed by start-up and end loads on the balance. Regardless, the range of Reynolds number (both maximum and minimum) exceeds that of the BSWT when operated at the same total temperature; high pressure provides the high Reynolds number advantage, while the ejector system allows a lower minimum Reynolds number condition which overlaps with the LaRC UPWT.

Note that the points shown on the chart at Mach numbers other than 2.48 are representative of conditions used during tests for other programs in the PSWT.

Model/Sting/Balance Description

- 1.675% M2.4-7A Baseline Arrow Wing
 - » Solid wing/body with no surface pressure taps or flaps
 - » Nacelles: available for this model, but not in test plan
- Sting supported using LaRC sting #26
 - » (aka: 2000 lb Normal Force Sting)
- LaRC 756 Balance (6 comp.... 2000 lb NF, 150 lb AF)
 - » expandable front end used
 - » nonexpandable adapter now available



The model chosen for testing in the PSWT was a 1.675 percent scale model of the Boeing-Long Beach baseline arrow wing configuration designated M2.4-7A. Model components include a wing, a body truncated slightly aft of the wing trailing edge, and four diverter mounted flow through nacelles; only the wing-body configuration was tested in this investigation. Neither the wing nor the body was instrumented for surface pressure measurements; the result is a stiffer, stronger wing less susceptible to static aeroelastic deformation under load as compared to an instrumented wing. The model, shown in the chart, was mounted on a six-component strain gage balance, designated LaRC 756, which in turn was supported by a straight sting, designated LaRC sting no. 26; cavity pressures were measured and corrections applied.

The wing planform incorporates a leading-edge break at 70% semi-span and a trailing-edge break at 30% semi-span; the planform in these regions has been smoothly faired. The leading-edge sweep is 71 deg inboard and 61.5 deg outboard. The aspect ratio is 1.84, and at model scale the reference area, mean aerodynamic chord, and wing span are 2.511 ft, 18.886 in., and 2.149 ft, respectively. The body length is 4.395 ft.

PSWT 698 Test Matrix

- Time: 1 shift for 2 weeks ending Sept. 2, 1997
 - » 28 F/M blows (90 runs, 5 days), 19 TSP blows (3 days)
 - » wing trip changes time consuming (significant off-shift work)
- Nominal Conditions:
 - » Mach = 2.48
 - » Re = 5 to 15 million/ft (highest attained 14.21 million per ft)
 - » q = 1000 to 3000 psf
 - » Alpha -3° to +3°, Beta = 0°
- Configurations (trips are the only variable):
 - » 5 wing trip heights (0.0079 to 0.0149 in.) and OFF
 - 0.6 in. streamwise, with 0.2 in. on center
 - » 1 nose trip height (0.0109 in.) and off
 - 1.0 in. from nose, with 0.1 in. on center

The wind tunnel investigation, designated PSWT 698, was conducted at 1 eight hour shift per day for 10 days ending September 2, 1997. This time included model build-up, installation, force testing, TSP testing, and model removal. Over 5 days, 28 force/moment blows consisting of 90 runs were obtained. During this period, wing trip changes were very time intensive, and in fact a significant amount of off-shift work was involved to facilitate timely model changes. Following the force/moment testing, 19 blows dedicated to the TSP transition detection method over 3 days were executed; a large portion of these runs were dedicated to method development.

Nominal test conditions were Mach = 2.48, Re = 5 to 15 million per foot (corresponding to dynamic pressures from 1000 to 3000 psf at $T_t \sim 100$ deg F), and an angle of attack range from -3 to 3 deg. The highest Reynolds number attained was 14.21 million per foot; Re/ft would have been 18.3 million had T_t been 40 deg F rather 136 deg F.

The only configuration variable was the transition trip. Trip dots were used rather than grit as dots have been the most prevalent in HSR testing. On the wing, 5 trip heights ranging from 0.0079 to 0.0149 inches plus the trip off condition were used. Trip heights were quantified based on measurement of every 4th dot to a resolution of ± 0.00025 in.; standard deviations ranged from 0.0004 to 0.0007 in. The trip location was 0.6 in. streamwise from the leading edge, with a dot spacing of 0.2 in. on center. On the forebody, a ring of dots 1.0 in. from the nose with 0.1 in. on center spacing was used in addition to the trip off case. The trip-free configuration and a configuration with the nose trip on and a 0.0109 in. wing trip were the most heavily tested.

Data Quality

- **Uncertainties are Comprised of Systematic (Bias) and Random (Precision) Experimental Errors**
 - » Mark Kammeyer (Boeing St. Louis) has provided a very detailed bias error analysis on the PSWT698 data
 - » Precision errors determined through short, medium, and long term repeatability analysis
- **Precision Errors (Repeatability) are Most Important when Assessing Trip Drag**
 - » ΔC_{Dtrip} removes the influence of many bias errors
 - » Absolute magnitude of force coefficients will be influenced by bias errors

Data quality for this investigation was assessed in two ways: 1) a theoretical uncertainty analysis focusing on systematic or bias errors, and 2) a repeatability assessment based on data acquired throughout the test.

The bias error estimates were provided by Mark Kammeyer (Boeing-St.Louis) using an uncertainty methodology which adheres to AIAA Standard S-071-1995 (Assessment of Wind Tunnel Data Uncertainty) and Coleman & Steele (Experimentation and Uncertainty Analysis for Engineers, 1989). Bias estimates were made at the 95 percent confidence level and were generally based on the working standards by which each instrument was calibrated, the calibration performance, and other factors such as check load results. This analysis highlighted the set point Mach number as a dominant source of uncertainty (based on the variation in centerline Mach number measured in facility calibrations) in the dynamic pressure, and correspondingly in the force/moment coefficients.

Repeatability assessments were made over short and near term periods of time, and are taken as an estimate of data precision. As used in this investigation, short term refers to repeat polars within a blow, and near term refers to repeated blows spanning the duration of the test. Good repeatability is important in an incremental study such as this; bias errors are more likely to impact absolute levels than increments.

Data Quality: Bias Uncertainty

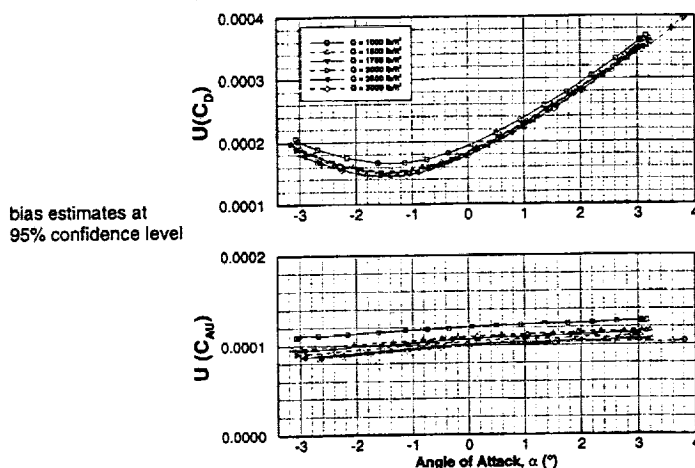
- Summary of Bias Errors for PSWT698 Run 15 - point 1, Mach=2.48, Q=1000psf

Quantity	Bias Error, $\pm B$
Dynamic Pressure, Q	9.785 psf
Reynolds Number, Re	$.0433 \times 10^6$ /ft
Static Pressure, P	0.03269 psia
Angle of Attack, α	0.1189 degrees
Axial Force Coefficient, C_A	1.095×10^{-4}
Normal Force Coefficient, C_N	5.203×10^{-4}
Lift Coefficient, C_L	5.135×10^{-4}
Drag Coefficient, C_D	2.021 counts

This chart provides a summary of estimated bias uncertainties for a typical test point; this particular test point is at a relatively low dynamic pressure of 1000 psf and an angle of attack of approximately -3 deg. The set point Mach number uncertainty drives the uncertainty in the dynamic pressure, which in turn directly affects the force and moment coefficients. A second important factor affecting the coefficients is the accuracy of the force balance. The angle-of-attack measurement bias estimate is very large, and its effect can be seen directly by comparing the drag and axial force coefficient uncertainties in the following chart.

Data Quality: Bias Uncertainty

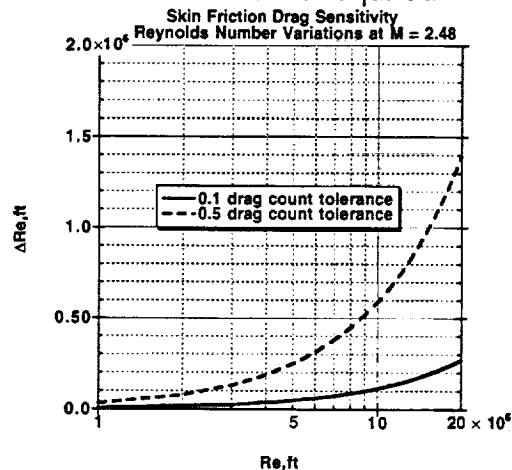
- Angle-of-attack is a driver (affects bias & repeatability)
- Primary factor in bias uncertainty is set point Mach



This chart shows the estimated bias uncertainty for the uncorrected axial force coefficient and the drag coefficient as functions of angle of attack and dynamic pressure. The effect of dynamic pressure is minimal; increasing dynamic pressure slightly decreases coefficient uncertainties. The effect of angle of attack is minimal for the uncorrected axial force coefficient. The uncertainty of the drag coefficient, however, is highly dependent on the angle of attack. Here the drag coefficient uncertainty is observed to almost double from an angle of attack of -1 deg (near $C_{D,\min}$) to +2 deg (cruise C_D). Recall that the dominant factor driving the uncertainty levels is the set point Mach number uncertainty, which should be systematic in nature and is expected to have little impact on data repeatability.

Data Quality: Effect of Re Set Point Variability

- if 0.1 drag count is important Re set point tolerance of ~0.1million/ft is required

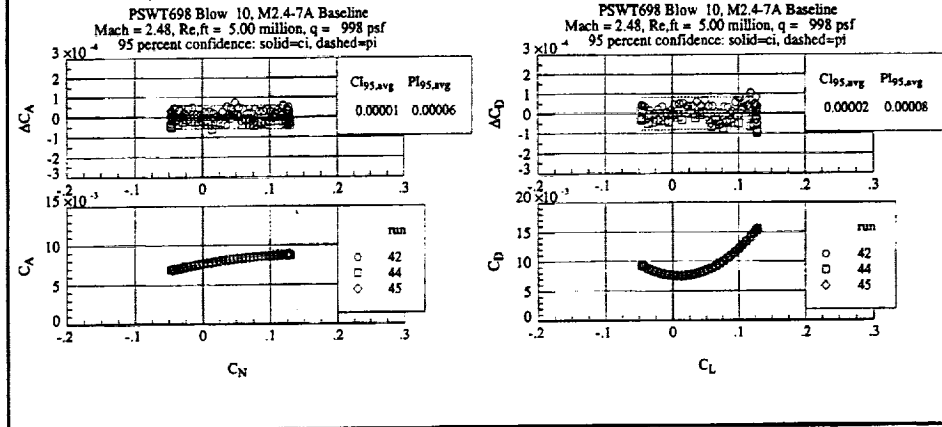


Data on a chart shown previously indicated a relatively low uncertainty in the determination of Reynolds number (approximately 0.04 million per foot at $q = 1000$ psf). However, just because the Reynolds number is determined with a relatively high degree of certainty does not imply that it is set or maintained consistently from run to run or blow to blow. The chart above shows the impact of Re set point inconsistency for the M2.4-7A at Mach = 2.48 as a function of Re, based on equivalent flat plate skin friction theory. If 0.1 counts of drag are important, the Re must be maintained within approximately 0.1 million per foot for the conditions of this investigation.

Due to total temperature variations during the test, the Re set point varied beyond the 0.1 million per foot tolerance at times. Due to the corresponding effect on drag, some data was corrected to appropriate nominal Reynolds numbers to facilitate analysis. As in the chart above, these adjustments were based on equivalent flat plate skin friction theory.

Data Repeatability: Short Term - low q

- 3 polars within 1 blow: adjusted to nominal $Re/ft = 5e6$
- C_A slightly more repeatable, particularly at cruise
- representative of short term repeatability throughout test

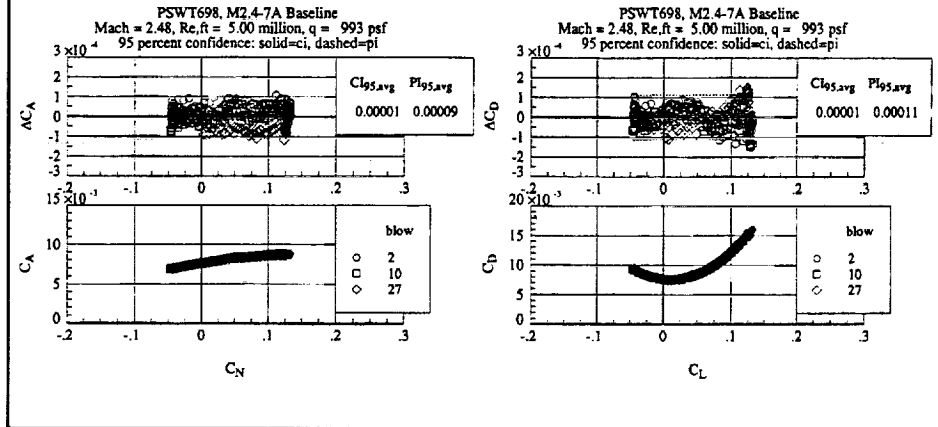


Data repeatability was assessed throughout the investigation over both short and near term periods of time, as defined previously. The methods used are described in detail by Wahls, et al in NASA TP-3522 (A Longitudinal Aerodynamic Data Repeatability Study for a Commercial Transport Model Test in the National Transonic Facility). To summarize, a data mean is determined for a set of repeat polars by a 4th order least squares curve fit; residuals and accompanying curve fit statistics are computed relative to the mean curve. Due to variation in Reynolds number between runs and blows, equivalent flat plate skin friction theory was used to adjust data to nominal conditions.

The chart above shows a sample of short term repeatability for this investigation. In general, C_A and C_D repeatability are quite good in the short term, and C_A is slightly better than C_D , particularly near the cruise C_L (0.10).

Data Repeatability: Near Term - low q

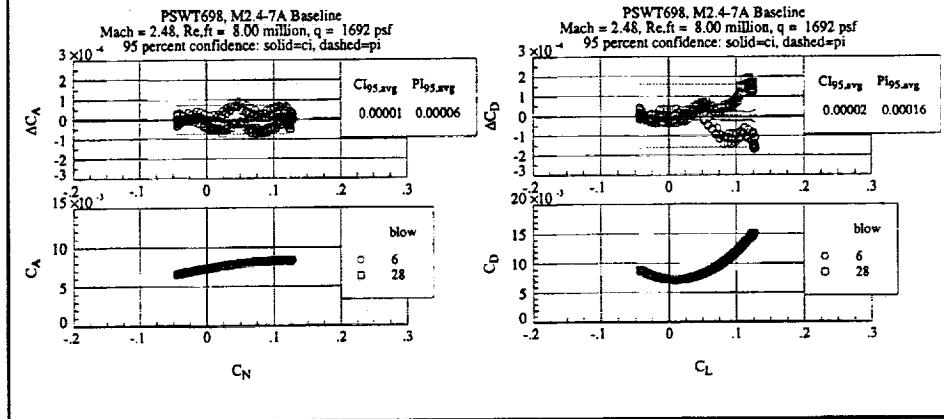
- 3 blows with 3 runs each: adjusted to nominal $Re/ft = 5e6$
- C_A slightly more repeatable, particularly at cruise
- more spread blow to blow than run to run within a blow



The chart above shows a sample of near term repeatability from this investigation. In this case the analysis is based on 3 blows of 3 polars each and spanning the duration of the force and moment phase of the test. The prediction intervals, representative of the bounds about the estimated data mean that will contain any single future point with a probability of 95 percent, are larger than in the short term, presumably due mostly to the effect of angle of attack uncertainty. Two other configuration/flow condition combinations were suitable for near term analysis; each of these cases contained only two rather than three repeated blows as in the case above. One case provides results very similar to those shown above; the other case, however, highlights the impact of angle-of-attack system uncertainties.

Data Repeatability: Near Term - AoA Impact

- 2 blows with 3 runs each: adjusted to nominal $Re/ft = 8e6$
- C_A significantly more repeatable, particularly at cruise
- nonrepeatable, biased angle of attack measurement



The chart above shows the near term repeatability analysis highlighting the potential impact of angle-of-attack measurement system uncertainties. In this case, two blows containing 3 polars each are analyzed. Note that the second blow (28) immediately follows the last blow used in the previous chart. Here, the axial force coefficient repeatability is comparable to that seen previously. However, the drag coefficient is extremely degraded at the cruise condition. This type of data tends to indicate inconsistent angle measurements.

Data Quality: Repeatability Summary

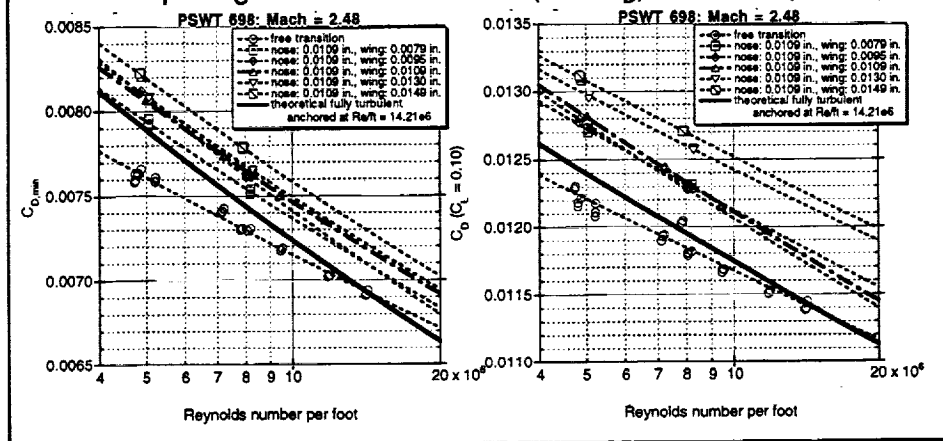
- Short term repeatability is good
 - » $\Delta C_D / \Delta C_A = \pm 0.80 / \pm 0.55$ counts (95% Prediction interval)
 - » $\Delta C_D / \Delta C_A = \pm 0.15 / \pm 0.10$ counts (95% Confidence interval)
- Near term repeatability is good to marginal
 - » $\Delta C_D / \Delta C_A = \pm 1.60 / \pm 0.95$ counts (95% Prediction interval)
 - » $\Delta C_D / \Delta C_A = \pm 0.20 / \pm 0.15$ counts (95% Confidence interval)
- Long term repeatability not considered due to problems with first entry data (PSWT689)

The chart above summarizes the repeatability analysis. Numbers provided represent the worse case observed throughout the analysis. In general, the short term repeatability is good. The near term repeatability is marginal to good, and is slightly degraded with respect to the short term as one might expect. One set of near term repeated blows highlighted a nonrepeatable, biased angle of attack measurement.

Long term repeatability (test to test) was not considered due to known problems with data from the previous entry (PSWT689).

Trip Drag Assessment: Variable Re Method

- Drag data near minimum drag and cruise
- Primary trip height (wing) = 0.0109 inches
- Trip drag - lam. run: ~1.9 cts (min C_D), ~4.0 cts (cruise)

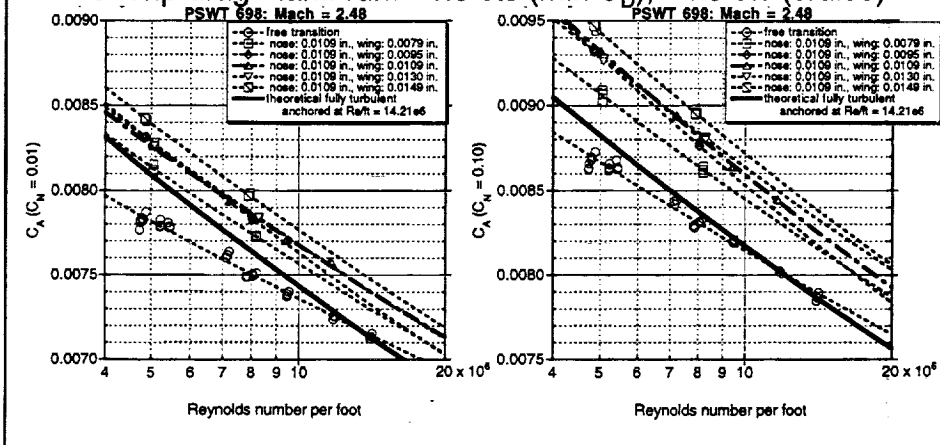


The primary objective of this investigation was an assessment of several trip drag evaluation methods at supersonic speeds on a representative HSCT configuration. The first method relies on a variable test Reynolds number capability with constant trip heights. Drag data are presented above for conditions near minimum drag and cruise lift as function of Re/ft for configurations with free and fixed transition; the fixed transition configurations have a forebody trip ring ($k=0.0109$ in.) around the nose and 5 different trip heights on the wing. The free transition configuration was run from a Re/ft of nominally $5e6$ to $14.21e6$. The primary fixed transition configuration, with $k=0.0109$ in. on the wing, was run at 5 Re/ft conditions up to approximately $11e6$. Other trip heights were run at nominally Re/ft of $5e6$ and $8e6$ only.

The variable Re method relies on the highest Re/ft condition with free transition to be fully turbulent, thus allowing extrapolation to lower Re/ft using equivalent flat plate theory. The theoretical curve is shown on the chart above. Using the theory as a base, the trip drag for a given trip height can be determined as the delta C_D to the theoretically fully turbulent extrapolation, plus the effect of laminar flow forward of the trip. As will be shown on a subsequent chart, the effect of the laminar run is approximately 0.0001. For $k=0.0109$ in., the variable Re method provides trip drag values of approximately 2.9 and 5.0 drag counts at minimum drag and cruise lift, respectively, and shows no significant dependence on Re from $5e6$ to $8e6$.

Trip Drag Assessment: Variable Re Method

- Axial force data near minimum drag and cruise
- Primary trip height (wing) = 0.0109 inches
- Trip drag - lam. run: ~1.9 cts (min C_D), ~4.5 cts (cruise)

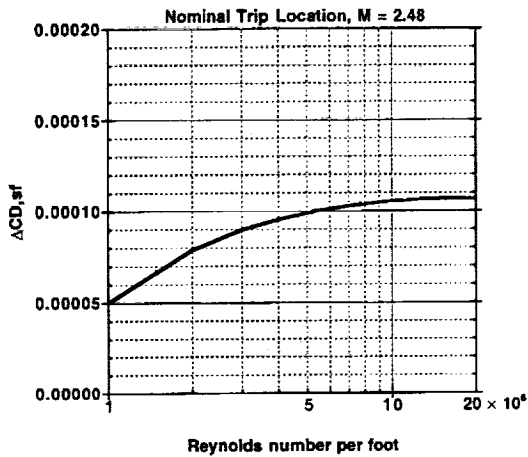


Due to concerns about the quality of drag data at cruise due angle-of-attack uncertainties, the variable Re method was also applied to the axial force coefficient. The trip drag assessment yields similar results to those based on drag; use of the axial force rather than drag provides an increase in trip drag of 0.5 counts at cruise.

Note in the chart above that the free transition data never follows the trend of the fully turbulent theoretical curve. Assuming the theoretical curve is a true representation of fully turbulent behavior, this result brings into question the underlying assumption that the $Re/ft = 14.21e6$ data is fully turbulent. This assumption was not verified herein through transition detection techniques. If fully turbulent flow does not occur until Re/ft is greater than $14.21e6$, the effect would be a reduction of trip drag values as quoted herein.

Effect of Laminar Run

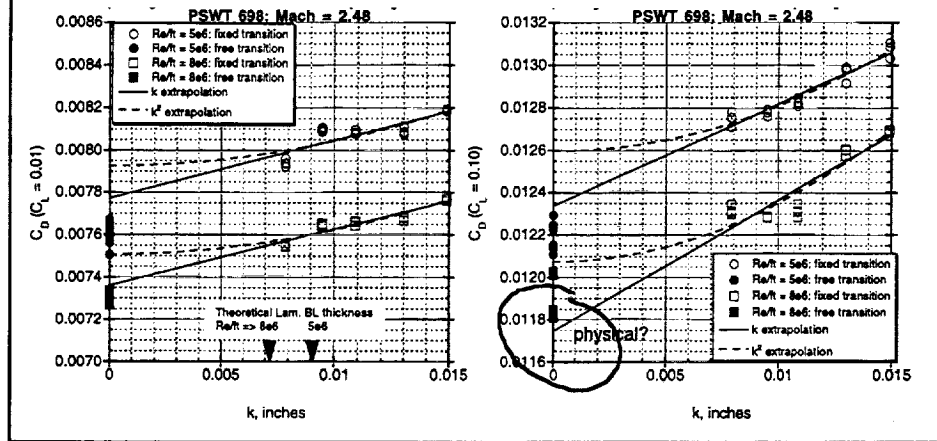
- add ΔC_D to tripped configurations to simulate fully turbulent conditions (~ 1.0 cts. for $Re/ft = 5, 8e6$)



This chart provides the estimated drag increment necessary to correct data for the laminar run forward of the trip dots to fully turbulent flow. This chart is based on equivalent flat plate theory, and is specifically valid only for the current configuration and trip location for Mach = 2.48. Over the range of Re/ft in this investigation, the laminar run correction is approximately 1 drag count (0.0001).

Trip Drag Assessment: Variable Trip Height Method

- Drag data near minimum drag and cruise
- Trip drag: $k^2 < k$ and min. drag < cruise

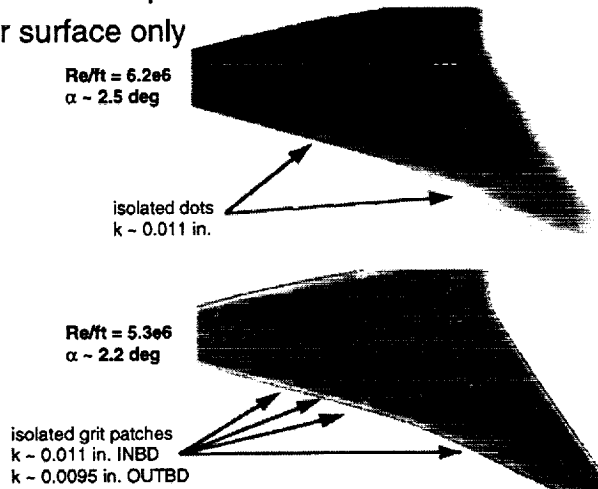


If a high Re facility capable of fully turbulent, free transition flow is not available, one must rely on the variable trip height method. Due to limited availability of high Re facilities, this method is the norm. In this method, drag data are extrapolated to values of zero trip height; the drag corresponding to zero trip height becomes the reference for computing the trip drag. For supersonic flow where trip heights greater than the local boundary layer thickness are the norm, the open question within the HSR community is whether or not extrapolation by k or k^2 is most appropriate.

Shown above are drag data near minimum drag and cruise lift for Re/ft of $5e6$ and $8e6$. Tripped data are extrapolated by both k and k^2 to values of $k=0$; free transition data are shown for reference. One would expect the free transition data to fall below the extrapolated fully turbulent data; in one case above, k extrapolation for $Re/ft=8e6$ at cruise lift, this result was not observed. Within data uncertainty, however, this result is not considered significant. The data does clearly show that the k method always provides higher values of trip drag than the k^2 method. Note that all trip heights are used in the extrapolation, although transition detection was not used to validate the trip effectiveness at most conditions.

TSP Image with Isolated Dots/Grit

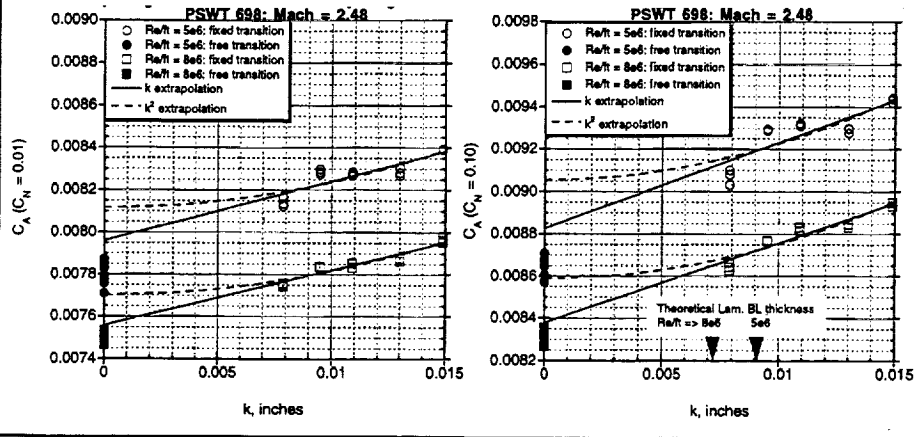
- indications of trip effectiveness
- upper surface only



The images above are limited indications of trip effectiveness using temperature sensitive paint. Images were taken on the upper surface of the wing only, and at angles of attack slightly higher than that for cruise lift. The two cases shown indicate the effectiveness of trip heights of approximately 0.0095 and 0.0110 inches towards the low end of the pertinent Re/ft range of this investigation. It can be assumed that as Re/ft increases, the trips remain effective, and higher trip heights are also effective. If one assumes the effect of angle to be minimal (not necessarily the case), only the effectiveness of the lowest trip height ($k=0.0079$ in.) remains completely open to question.

Trip Drag Assessment: Variable Trip Height Method

- Axial force data near minimum drag and cruise
- Trip drag: $k^2 < k$ and min. drag < cruise



Due to concerns about the quality of drag data at cruise due to angle-of-attack uncertainties, the variable trip height method, as with the variable Re method, was also applied to the axial force coefficient. Near minimum drag conditions, where angle uncertainties are of less consequence, axial-force-based results are similar to drag-based results. At cruise, however, the axial-force-based results yield consistently lower trip drag values.

Trip Drag Results: Summary

- Trip drag (in counts) for $k = 0.0109$ in.
- variable Re method includes laminar run adjustment

		Re/ft = 5e6			Re/ft = 8e6		
		k	k ²	var Re	k	k ²	var Re
$\Delta C_{D,trip}$	CL						
	0.01	3.0	1.4	2.9	2.9	1.4	2.9
	0.10	5.3	2.5	5.1	6.8	3.3	4.9
CN							
$\Delta C_{A,trip}$	0.01	3.1	1.4	2.7	2.9	1.4	3.2
	0.10	4.4	2.0	5.9	4.1	1.9	5.4

- var Re and k method essentially same near min. drag, more variability near cruise but still generally closer to k
- k² method always lower trip drag than k method
- negligible Re effect on trip drag from 5 to 8 million/foot

The chart above summarizes the trip drag results with $k = 0.0109$ in. for both methods, and both extrapolations for the variable trip height method. Included are results based on axial force and drag at near minimum drag and cruise lift conditions at Re/ft = 5e6 and 8e6.

The variable Re method and the k extrapolation of trip height are essentially the same near minimum drag; more variability exists at cruise lift, but the variable Re method generally remains closer to the k than k² extrapolation. The k² method yields consistently lower trip drag values than the k method; the difference is roughly 1.5 counts near minimum drag, and roughly 2 to 3.5 counts near cruise. All methods indicated higher trip drag at cruise lift than near minimum drag, and the Re effect on trip drag from 5e6 to 8e6/ft is negligible.

Finally, due to angle of attack uncertainty, the axial-force-based results are considered more reliable. For the purposes of correction of $k=0.0109$ in. experimental data to fully turbulent conditions, trip drag is taken as 2.9 and 5.0 counts at near minimum drag and cruise lift conditions, respectively.

CFD Comparisons: Overview

- Support experimental program
- Single block C-O topology grid (~2.7e6 pts., $y^+ \sim 1$)
- CFL3D
- Convergence Criteria
 - » < 0.5 ct CD variation over 100 iterations
 - » > 3 orders of magnitude residual reduction
- Matrix: Mach = 2.48 only
 - » Re/ft = 5.26 to 14.21 million at $\alpha = -1, 2$ deg
 - » Re/ft = 5.26 at $\alpha = -1, 0, 1, 2, 3$ deg
 - » S-A turb model used after initial turb model comparisons



A complementary theoretical study, including CFD with the Navier-Stokes flow solver known as CFL3D, was performed to enhance understanding of the experimental data. Additionally, the experimental data provides a reference for evaluating the predictive capability of the state-of-the-art flow solver.

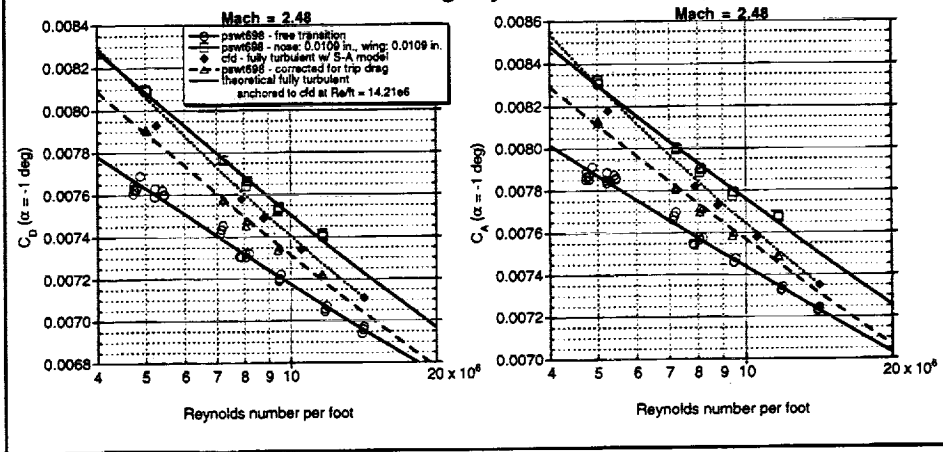
The single block C-O topology grid used in this study had approximately 2.7e6 grid points, and had sufficient grid resolution near the surface to yield y^+ values of approximately 1. Solutions were considered converged when the drag coefficient varied by less than 0.5 counts over 100 iterations, and the residuals reduced by at least 3 orders of magnitude.

The CFD matrix was designed to enhance understanding of the experimental results. First a turbulence model study was performed at $Re/ft = 5.26e6$ at angles-of-attack of -1 and 2 deg. The Spalart-Allmaras model was chosen for further use. Solutions for a complete pitch polar were obtained at $Re/ft = 5.26e6$, and a Re sweep up to 14.21e6 per foot at near minimum drag ($\alpha = -1$ deg) and cruise lift ($\alpha = 2$ deg) were also obtained.

A more detailed discussion of the CFD results is presented in a separate paper by Rivers and Wahls in this workshop.

CFD vs EFD near $C_{D,min}$

- CFD predictions consistently high, but within 1 count of trip drag corrected pswt698 data
- CFD variation w/ Re slightly less than flat plate theory

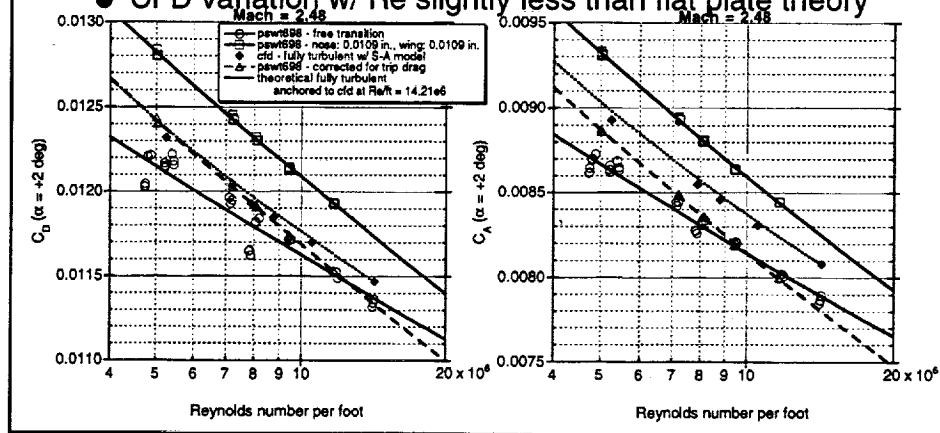


The chart above shows comparisons of theory and experimental data near minimum drag conditions. Experimental data includes the free transition and $k=0.0109$ in. fixed transition configurations, and the trip drag corrected result. The fully turbulent CFD predictions fall between the free and fixed transition experimental data, and are high but within 1 count of the trip drag corrected experimental data.

The theoretical equivalent flat plate skin friction drag variation is anchored to the $Re/ft=14.21e6$ CFD solution. The CFD solution variation with Re is slightly less that of the equivalent flat plate theory, and is very close to the trip drag corrected experimental data.

CFD vs EFD near cruise

- CFD predictions within 1 count of trip drag corrected pswt698 C_D data; C_A predictions high and diverging with increasing Re (2.5 counts at Re/ft ~ 11e6)
- CFD variation w/ Re slightly less than flat plate theory



The chart above shows comparisons of theory and experimental data near cruise lift conditions. Experimental data includes the free transition and $k=0.0109$ in. fixed transition configurations, and the trip drag corrected result. The fully turbulent CFD predictions fall between the free and fixed transition experimental data. Drag predictions are within 1 count of the trip drag corrected experimental data, but have slightly less variation with Re. Axial force predictions are high relative to the trip drag corrected experimental data, and are diverging; the difference is 1 count at low Re/ft and approximately 2.5 counts at Re/ft ~ 11e6.

The theoretical equivalent flat plate skin friction drag variation is anchored to the $Re/ft=14.21e6$ CFD solution. The CFD solution variation with Re is slightly less than that of the equivalent flat plate theory.

Concluding Remarks

- for this data set, trip drag based on k extrapolation proved more consistent with the variable Re approach than did k^2 extrapolation
 - » negligible Re effect (from 5 to 8e6/ft) on trip drag
 - » trip drag approximately 2.9 counts at minimum drag
 - » trip drag approximately 5.0 counts at cruise
- PSWT is a productive facility with extensive Re capability at supersonic conditions that warrants further use, but ...
 - » pitch system accuracy must be improved before further performance (drag) testing ... studies underway at PSWT
 - » short term repeatability generally very good
 - » near term repeatability degraded with increasing alpha due to pitch system variability

The following comments summarize the key points of the investigation.

1) Two methods for determination of trip drag were applied. The variable Re method is assumed to provide the most reliable estimate and is used as a basis for evaluating two variations of the variable trip height method. For this data set, the k extrapolation approach proved more consistent with the variable Re method than did the k^2 extrapolation approach. Trip drag variation between 5 and 8 million per foot was negligible, and was approximately 2.9 and 5.0 drag counts at minimum drag and cruise conditions, respectively.

2) The Boeing PSWT is a very attractive facility for high or elevated Re testing at supersonic Mach numbers. Although the facility offers this higher Re capability and executed an efficient, productive test, significant uncertainty in the pitch measurement system must be reduced before the highest quality drag data required in performance testing can be acquired. Short term repeatability was generally very good, but near term repeatability degraded with increasing angle of attack, highlighting the uncertainty with the pitch system.

Concluding Remarks

- HSR high Re database extended to 22.4e6/mac at supersonic Mach
 - » fully turbulent flow not verified at this Re
 - » cooler T_t (less than 100 deg F) would provide higher Re
 - T_t of 40 to 50 deg F would have provided Re/mac ~28.3e6 (18e6/ft)
- CFL3D with S-A turb. model predicted experimental data and trends reasonably well
 - » C_D and C_A predictions generally within 1 ct of trip drag corrected test data
 - » CFD predictions have slightly less variation w/ Re than equivalent flat plate theory, and mixed results as compared to trip drag corrected test data

3) Free transition data was acquired extending the HSR high Re database to 22.4e6 per MAC at supersonic conditions. Improved model/sting/balance design and/or selection in addition to the use of test total temperatures less than 100 deg F would provide further extension to higher Re. The maximum Re/ft was obtained with total pressure of 80.2 psi, dynamic pressure of 3000 psf, and total temperature of 136 deg F; if the total temperature were reduced to 40 to 50 deg F, the corresponding Re/ft would increase from 14.2e6 to roughly 18e6 (28.4e6/MAC).

4) The CFD predictions using CFL3D with the Spalart-Allmaras turbulence model predicted experimental results reasonably well, including trends with Reynolds number. Drag and axial force predictions were generally within 1 ct of the trip drag corrected test data. The CFD predicted variations with Re were slightly less than for equivalent flat plate theory; the trends compared to the trip drag corrected test data were mixed.

This page is intentionally left blank.



High Speed Aerodynamics, Long Beach

Experimental Bias and Precision Errors: Requirements, Analysis, and Recommendations

Michael G. B. Novean

Todd E. Magee

Configuration Aerodynamics

The Boeing Company, Long Beach

HSR Airframe Technical Review

Los Angeles, California

February 9-13, 1998



This page is intentionally left blank.

Experimental Bias and Precision Errors: Requirements, Analysis, and Recommendations

Michael G. Novean and Todd E. Magee
The Boeing Company
Long Beach, California 90807-5309

Tight error bars on experimental data are required in order to meet HSCT performance requirements. This paper aims to deal with the need for these requirements and their impact upon desired testing accuracy. The definition of some terminology sets the stage for a brief review of how some of the accuracy requirements were generated. Error analyses or estimates from many of the wind tunnels used in HSR testing are presented. The sensitivity of performance coefficients to selected instrumentation accuracies is discussed. Uncertainties due to data corrections are acknowledged as another source of error. Future improvements to both facilities and test processes are suggested.

Motivation, Objectives, and Approach

This slide presents the motivation behind discussing the errors in experimental data. Taking a broad view, it is quite easy to see why there is a need for high quality aerodynamics data. In order to make accurate decisions in sizing the aircraft, accurate inputs are required. Second, from an industry point of view, "guarantees" on the performance of an HSR-type aircraft will have to be made. The aircraft needs to perform like engineers claim that it will.

Now that the need for high quality aerodynamics data has been established, this paper aims to examine the reasoning behind some of the quality requirements that we have tried to impose upon the wind-tunnel data and the impact of these requirements upon the test process. Basically, HSR is trying to put very small error bars around the data.

The approach to the discussion is simple. First, the presentation will open with a discussion behind the sizing of some of the performance data requirements (such as a half count precision at supersonic Mach numbers). Next, the current state of errors in the data will be presented. Finally, some possible improvements will be suggested.

Before beginning the discussion of the requirements from the aerodynamic data, there will be a brief discussion of some of the terminology used in the paper to make sure everyone is on the same page. This begins with the word error. An error in this context does not mean a "blunder" or "mistake" like it is taken to mean in common conversation. An error is simply the inevitable uncertainty that attends all measurements. We can and do attempt to reduce the errors in the data but can never eliminate them.

Motivation, Objectives, and Approach



High Speed Aerodynamics, Long Beach

- **Motivation:** Provide high quality aerodynamic data for decision making
- **Objective:** Examine the data quality requirements and how they impact wind-tunnel testing
- **Approach:**
 - Discuss from where data requirements come
 - Discuss current state of errors in the data
 - Recommend possible improvements to hardware/processes

Terminology

The first two terms discussed are the two groups of errors that exist.

Bias errors, or systematic errors, are the difference between the "true value" and the mean of the population of measured values. As the number of measurements approaches infinity, the bias error approaches the "true bias error". Systematic error is the "mean that would result from an infinite number of measurements of the same measurand carried out under repeatability conditions minus the value of the measurand"¹.

Precision errors, or random errors, are the difference between a measured value and the mean of the population of measured values. Random error is the "result of a measurement minus the mean that would result from an infinite number of measurements of the same measurand carried out under repeatability conditions"¹.

The two figures below show examples of bias and precision errors. Assume that the true value for X is 5.0. The figure on the left shows the case of no precision error but a bias error, β , of 1.0. Another example of bias error would be the marksman who aims at a target and places all of his shots in a very tight circle that is four inches to the right of the bull's-eye. His precision error would be very small but his bias error is rather large. The figure on the right shows the case of no bias error but precision errors. The population has a mean value that matches the true value, but individual samples have random error in them. The random error in sample 1 is 0.25, in sample 2 it is zero, and in sample 3 it is 0.1.

The equation² in the middle of the page points out that bias errors are constant and will affect all samples while the precision error (being random) will change from sample to sample.

Terminology

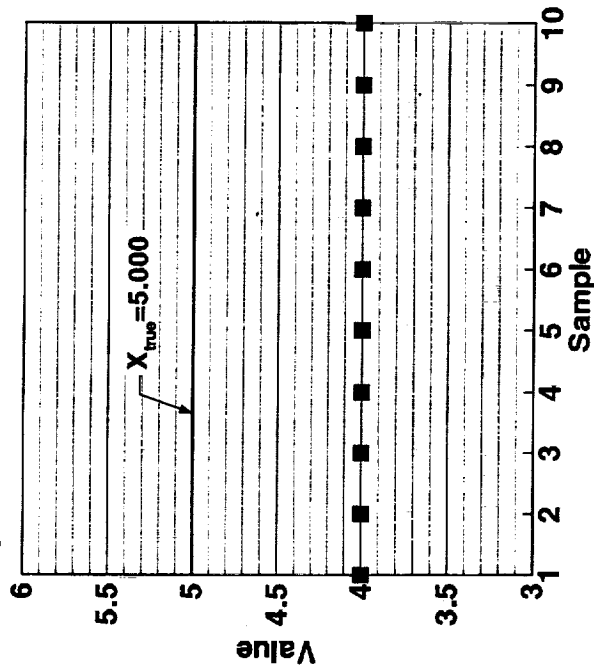


High Speed Aerodynamics, Long Beach

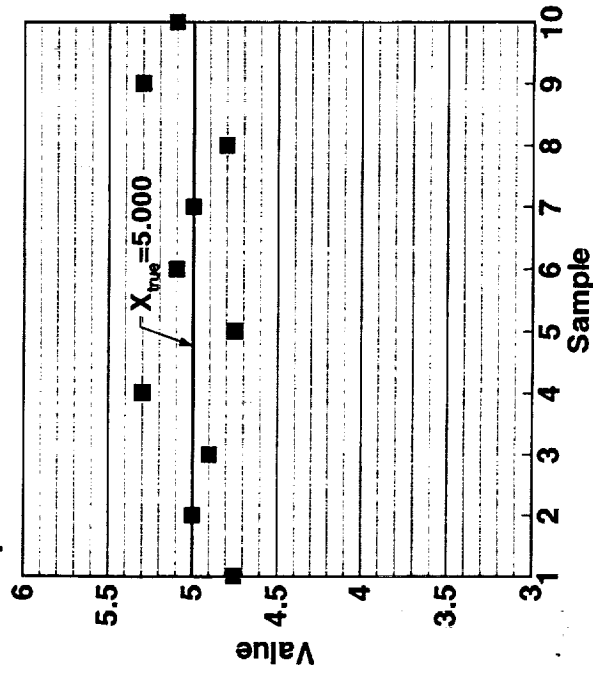
- Bias error (systematic error) - difference between the “true value” and the mean of the population of measured values
- Precision error (random error) - difference between a measured value and the mean of the population of measured values

$$X_{\text{true}} = X_i + \delta_i = X_i + \beta + \varepsilon_i$$

Example of Bias Error and no Precision Error



Example of Precision Error and no Bias Error



Terminology

Both the confidence interval and prediction interval are computed using statistical analysis of the data. This analysis requires the assumption that the scatter in the data is random and that the random scatter can be represented by a Gaussian distribution. The mathematics behind these analysis tools will be discussed in further detail later, the current discussion will just present the definition. Confidence Interval is a measure of the accuracy (assuming zero bias errors) of the experimentally determined mean. One is stating at a certain confidence level (typically 95%), that the true mean value is bounded by the experimental mean plus or minus the confidence interval. The prediction interval is the bounds around the mean within which the next measurement is expected to fall.

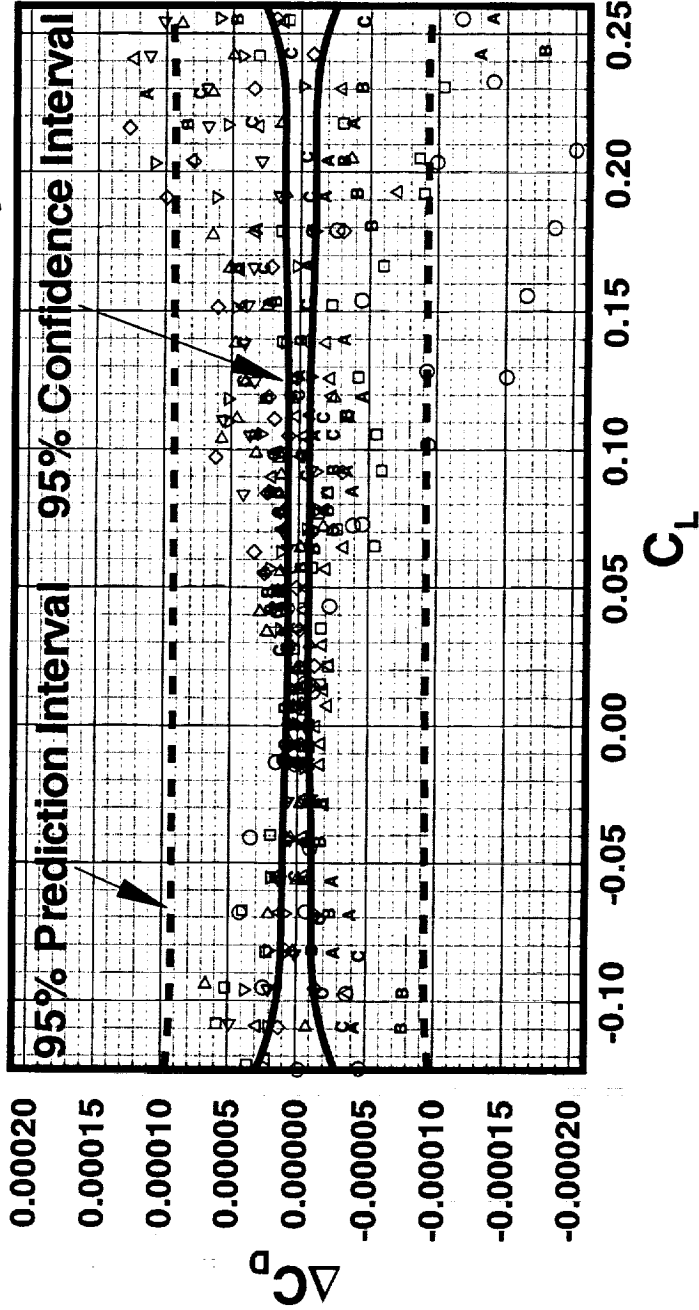
For example, assume 6 TCA drag polars are run in the tunnel. At $\alpha = 3.5$ degrees, the drag is 140 counts and the 95% CI and PI are computed to be 0.2 counts and 0.7 counts, respectively. The CI helps state that the true experimental mean is somewhere between 139.8 counts and 140.2 counts. Based upon the PI value, it is also possible to state at 95% odds that the drag of the next data point taken at $\alpha = 3.5^\circ$ will fall between 139.3 and 140.7 counts.

Terminology



High Speed Aerodynamics, Long Beach

- Confidence Interval - Interval about the estimated mean within which the “true mean value” will lie
- Prediction Interval - Interval about the estimated mean in which the next observation would be likely to lie



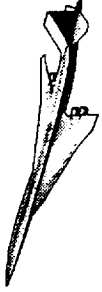
Terminology

A jitter program is a relatively simple code for determining for the calculation of total uncertainty in a value. It is simply a computer code which calculates the partial derivatives of a value by applying small perturbations to a nominal value (that is where the jitter comes from). Then, total uncertainty is estimated by taking the root sum square of individual uncertainty sensitivities. For measurements that share a calibration, a covariance term is present as well (the middle term of the equation).

The concept of statistical control is rather well explained by Doebelin³:

"The concept of the state of statistical control is not a particularly simple one but we try to explain its essence briefly. First we note that it is meaningless to speak of the accuracy of an instrument as an isolated device. We must always consider the instrument plus its environment and method of use, that is, the instrument plus its inputs. This aggregate constitutes the measurement process. Every instrument has an infinite number of inputs; that is, the causes that can conceivably affect the output, if only very slightly, are limitless. Such effects as atmospheric pressure, temperature, and humidity are among the more obvious. But if we are willing to "split hairs", we can uncover a multitude of other physical causes that could affect the instrument with varying degrees of severity. In defining a calibration procedure for a specific instrument, we must specify that certain inputs must be held "constant" within certain limits. These inputs, it is hoped, are the ones that contribute the largest components to the overall error of the instrument. The remaining number of infinite number of inputs is left uncontrolled, and it is hoped that each of these individually contributes only a very small effect and that in the aggregate their effect on the instrument output will be of a random nature. If this is indeed the case, the process is said to be in statistical control."

Terminology



High Speed Aerodynamics, Long Beach

- Jitter program - Code for estimation of total uncertainty (method of getting partial derivatives)

total uncertainty is U_r

$$U_r^2 = \sum_{i=1}^N \left(\left[\frac{\partial r}{\partial x_i} B_{x_i} \right]^2 + \sum_{j=1}^N \frac{\partial r}{\partial x_i} B_{x_i} \frac{\partial r}{\partial x_j} B_{x_j} (1 - \delta_{ij}) \right) + \sum_{i=1}^N \left(\left[\frac{\partial r}{\partial x_i} P_{x_i} \right]^2 \right)$$

- The concept of statistical control - Hold significant inputs “constant” within certain limits

Development of Wind-Tunnel Accuracy Requirements

At the first HSR test team workshop in May 1997, Eric Adamson of BCAG presented an excellent paper explaining the development of wind-tunnel accuracy requirements⁴. BCAG examined the accuracy requirements for HSCT performance testing at the 1g condition using four different criteria:

- consistency with prior subsonic programs
- consistency with AGARD advisory report number 184
- program management's need to accurate A/P performance
- high speed aerodynamics' need to detect incremental design improvements

All four of these approaches yielded similar recommendations on data.

Development of Wind-Tunnel Accuracy Requirements



High Speed Aerodynamics, Long Beach

- BCAG examined HSCAT data requirements in 1990
- Four different approaches were examined
 - Consistency with prior subsonic airplane programs
 - Consistency with AGARD Advisory Report No. 184
 - Program Management's need for accurate airplane performance
 - High Speed Aero.'s need to detect incremental design improvements
- All four approaches yielded similar recommendations

(The above material was presented by E. Adamson (BCAG) at the First HSR Testing Workshop, NASA Ames, May 1997.)

Wind-Tunnel Accuracy Recommendations

The recommendations from the BCAG accuracy requirement study were as follows:

- a total uncertainty to within ± 1 count at 80% confidence in the supersonic Mach range and ± 3 counts in the transonic Mach range
- the ability to detect increments between configurations greater than ± 0.5 counts with 80% confidence at supersonic Mach numbers and ± 1.5 counts at transonic Mach numbers.

Using the assumption that bias errors and precision errors can each consume half of the confidence interval, then the first bullet above can be modified to state a repeatability level of ± 0.5 counts at 80% confidence is desired.

From this buildup, precision (repeatability) requirements were therefore ± 0.5 counts at supersonic Mach numbers and ± 1.5 counts at transonic Mach numbers.

Wind-Tunnel Accuracy Recommendations



High Speed Aerodynamics, Long Beach

- “Require total uncertainty (*bias + repeatability*) to within ± 0.0001 count(s) at 80% confidence (4 to 1 odds) across the supersonic Mach range and ± 0.0003 across the transonic Mach range.”
- “Require the ability to detect increments between configurations greater than ± 0.5 counts with an 80% confidence across the supersonic Mach range and ± 1.5 counts across the transonic Mach range.”

585

(The above material was presented by E. Adamson (BCAG) at the First HSR Testing Workshop, NASA Ames, May 1997.)

Supersonic Repeatability of ± 0.5 counts or better
Transonic Repeatability of ± 1.5 counts or better



Methods of Error Analysis

The figure below shows the methods utilized to estimate the precision and bias errors. For incremental testing, knowledge of precision errors is more important. For example, consider testing of a derivative low-speed transport concept. If the original concept is already in production, Boeing should already have flight test data and therefore an ability to extrapolate from wind-tunnel data to flight. The effect of bias errors (as well as Reynolds number scaling and a variety of other factors) are essentially negated. Consequently, the researcher can concentrate more on reducing the precision errors and achieving confidence in the observed increment between two configurations.

The bias errors for PSWT were obtained in a memorandum from Mark Kammeyer⁵ which shows the bias errors of all measured force and moment coefficients. At the current time, BLB has not analyzed error data for the UPWT and 16' TT although similar type information is available. It is unknown (by BLB) what error analysis data exists for BSWT.

The magnitude of the precision errors is estimated through statistical analysis of multiple repeat runs. The main steps of the process are presented below and the intricacies of the confidence interval and prediction interval are discussed in the following two slides.

Methods of Error Analysis



High Speed Aerodynamics, Long Beach

- **Bias error**
 - PSWT : use jitter program to propagate uncertainties in measurement instruments
 - Other tunnels : unknown (by BLB)
- **Precision error (repeatability analysis)**
 - Acquire multiple repeat runs (same configuration, same test conditions) during test(s) that meet mid-term (reproducibility) or long-term repeatability criteria
 - Combine all runs into a common data set
 - Use statistical tools to estimate Prediction and Confidence Intervals
 - caveat: data must exhibit random behavior

The Procedure for Repeatability Analysis

Precision errors are commonly estimated using a repeatability analysis. This is accomplished by running repeat runs on a given configuration. There are three types of repeat runs. Short-term repeatability occurs over a span of hours and involves back-to-back (or near back-to-back) runs of the same configuration. The tunnel may or may not go off-condition between the repeats. Medium-term repeatability (also called reproducibility) typically occurs over a span of days or weeks. Medium-term repeatability involves the changing of the model to additional configuration(s) before it is restored to its original configuration for the repeat runs. Long-term repeatability typically occurs over the span of months or years and involves the testing of the same model and configuration but in different tunnel entries. The procedure for repeatability analysis is the same for all three types of repeatability, however.

First, all of the data points repeat runs are merged into a common data set. There may be M runs which are all dumped into a common data set consisting of N points. A polynomial is then fit through the entire set of data points. The order of the polynomial is determined by examination of the standard error versus polynomial order curve. Typically, the lowest order polynomial where the standard error curve flattens out is selected. The standard error is defined as

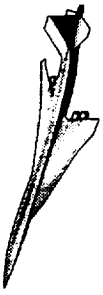
$$SE = \left[\frac{\sum_1^N (Y_i - \hat{Y}_i)^2}{N - K - 1} \right]^{1/2}$$

A second guideline is that the polynomial order, K , is less than or equal to the square root of the number of data points minus 1. That is,

$$K \leq \sqrt{N} - 1$$

This K^{th} order polynomial then represents the mean of the data.

The Procedure for Repeatability Analysis

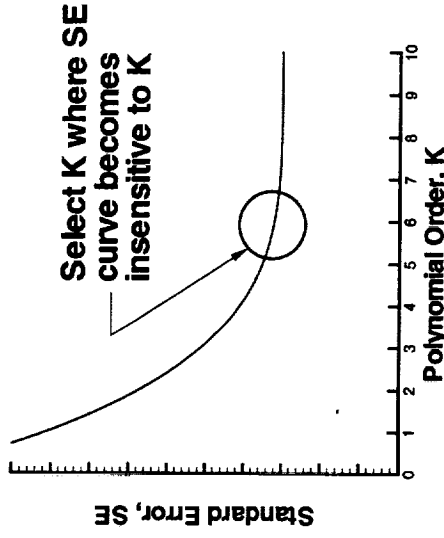


High Speed Aerodynamics, Long Beach

- Use polynomial regression to fit entire set of (X_i, Y_i) data points

$$-\hat{Y}(X) = C_0 + C_1X + C_2X^2 + C_3X^3 + \dots + C_kX^k$$

- Order of fit (K) is determined by the following



and
$$K \leq \sqrt{N} - 1$$

- where N = Total number of data points
- The fit represents the mean of the data

The Procedure for Repeatability Analysis

Next we perform statistical analysis on the data. The residuals for each data point based on the mean line are computed. Residual plots are made to insure that the data assumes a random distribution about the mean fit through the data. The confidence and prediction intervals are then calculated for each x value. The methods are relatively straight-forward and a detailed discussion would be beyond the scope of this paper. References 2 and 6 cover much of the statistical numerics behind these methods.

The Procedure for Repeatability Analysis



High Speed Aerodynamics, Long Beach

- Compute the residuals for each data point based on the mean line
- Compute the confidence and prediction intervals for the data set

$$\Delta Y = Y_i - \hat{Y}_i$$

$$CI(X_0) = \pm t_{(\tilde{\alpha}/2, \nu)} \times SE \times Q(X_0)$$

$$PI(X_0) = \pm t_{(\tilde{\alpha}/2, \nu)} \times SE \times \sqrt{1 + Q(X_0)^2}$$

where

$$t_{(\tilde{\alpha}/2, \nu)}$$

Student t-distribution for a given level of confidence

$$A(t/\nu) = 1 - I_{\frac{\nu}{\nu+t^2}} \left(\frac{\nu}{2}, \frac{1}{2} \right)$$

Student t probability function

$$I_x(a, b) = \frac{X^a(1-x)^b}{aB(a, b)} \left[1 + \sum_{n=0}^{\infty} \frac{B(a+1, n+1)}{B(a+b, n+1)} X^{n+1} \right]$$

Incomplete Beta Function

$$B(a, b) = \int_0^1 t^{a-1}(1-t)^{b-1} dt$$

Beta Function



Bias Error Differences Result in Poor Tunnel-to-Tunnel Repeatability

Due to differing bias errors at different facilities, one should not expect the aerodynamic data numbers to agree between facilities.

Bias Error Differences Result in Poor Tunnel-to-Tunnel Repeatability

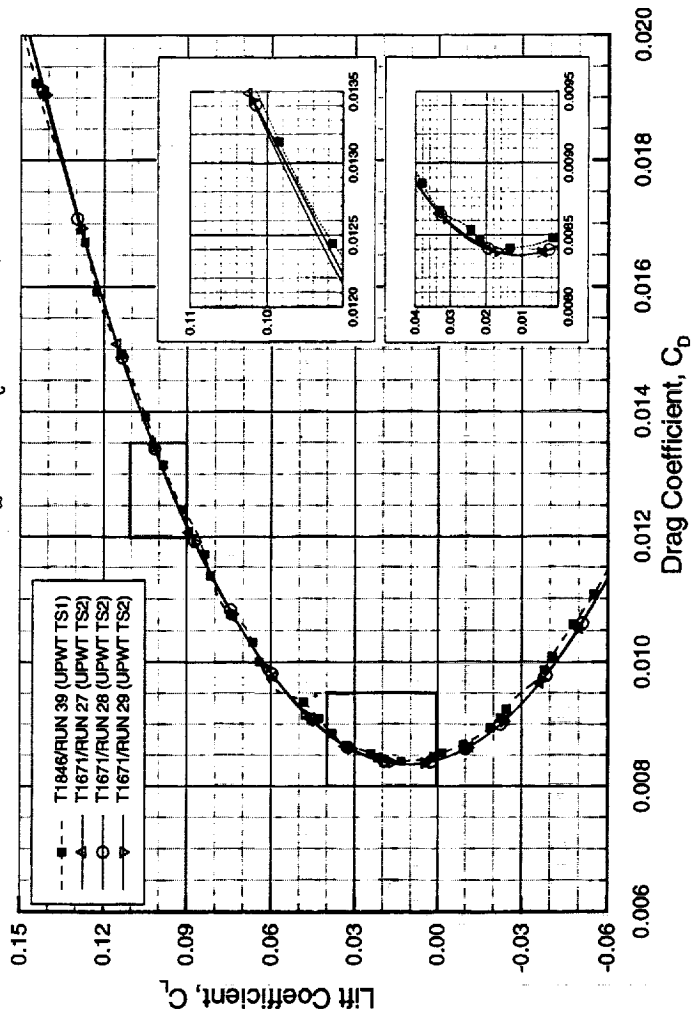


High Speed Aerodynamics, Long Beach

Model 2a

Comparison of Experimental TCA W/B Drag Polars at UPWT TS1 and TS2

Tests 1671 and 1846, $M_\infty=2.4$, $Re_c=6.36 \times 10^6$, Model 2a



Tunnel Precision Error Determined Through Test-to-Test Repeatability

The precision error of the tunnel can be determined through long-term test-to-test repeatability. Typically on HSR tests, a previously tested model will be re-tested to obtain long-term repeatability numbers. This long-term repeatability gives insights to the precision of the data from the facility and also helps serve as a “sanity check” for the current test.

The use of a long-term model can help researchers quickly identify a problem during a new test. If the model fails to repeat well with data from a previous test, the researcher is tipped off that something may be awry. Perhaps the data reduction constants have been inadvertently changed, the model has been damaged between tests, or the nature of the flow in the facility has changed between the tests. The primary use of a long-term repeatability model in testing has to detect if something is amiss. For the test shown in the figure, M2.4-7A at PSWT, the values of confidence and prediction intervals would lead the researcher to believe that things are working well.

Test-to-test repeatability also gives more genuine numbers for confidence and prediction intervals. Here many of the independent variables that we try to hold constant (and equal to certain nominal values) for statistical control probably have changed. For example, the trip dots may have been two thousandths too high in the first test; slightly high but still within the test requirements document’s specified tolerances. This would bias the drag into being slightly higher. Between the long-term repeatability tests, the trip dots were altered and therefore had to be reapplied. Likewise, when the model is placed into the tunnel again a new sting bending calibration was performed. These long-term repeatability numbers allow for variation of more of the inputs than in short-term repeatability and medium-term (reproducibility) studies. Constant errors in the system inputs which would remain as unseen biases from the “true” value, now should become evident as precision errors. Because of this the long-term mean value, confidence and prediction intervals should be more veritable.

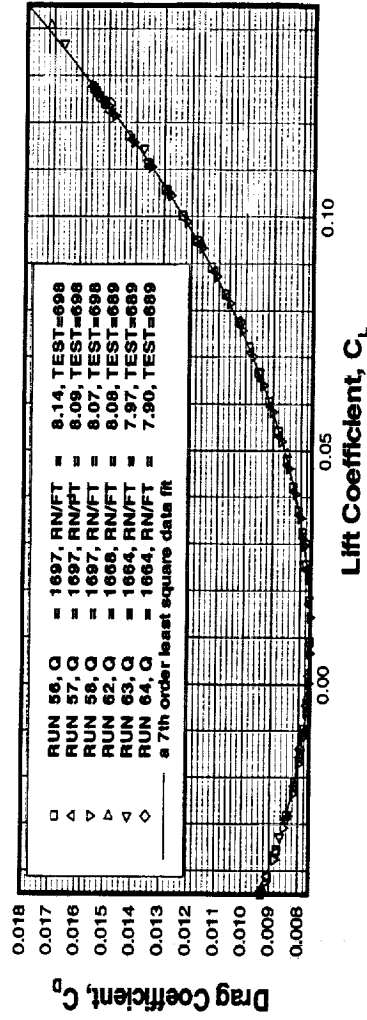
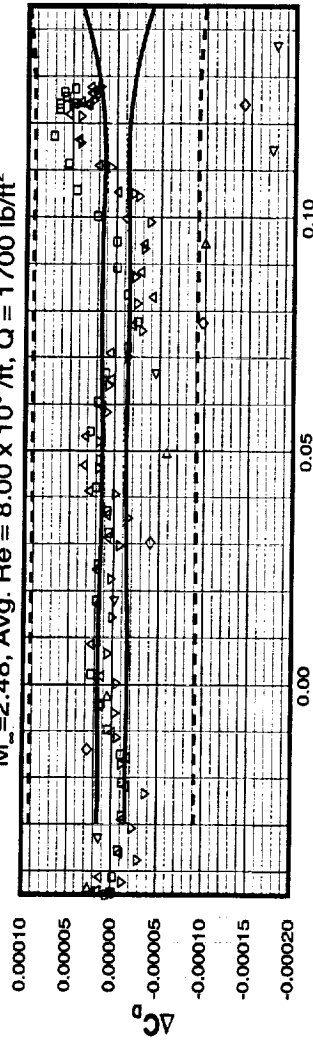
Tunnel Precision Error Determined Through Test-to-Test Repeatability



High Speed Aerodynamics, Long Beach

Example: PSWT

Test-to-Test Repeatability
PSWT689 and 698, 1.675% M2.4-7A Arrow Wing Model
 $M_\infty = 2.48$, Avg. $Re = 8.00 \times 10^6$ /ft, $Q = 1700$ lb/ft²



$CI < \pm 0.2$ cts
 $PI < \pm 1.0$ cts



Lack of Statistical Control Increases Repeatability Values

The contrived example in the figure shows that statistical control is required on the inputs to insure sensible repeatability values. This example shows testing of the TCA performance Model 2b in the NASA Langley UPWT test section #2. The first four runs are made with a trip dot height of $k=0.012$. The last four runs are made with a trip dot height of $k=0.014$. The effect is that the residuals fall into two distinct bands-- neither passing through the mean fit-- because the input conditions of the first set of runs were not effectively duplicated. This failure to maintain control on the inputs leads to the shift in the data.

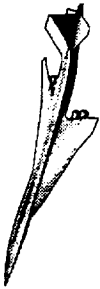
The conclusions from this figure are:

- 1) Effort must be set forth to maintain statistical control on the inputs to testing.
- 2) The accuracy of the measurand for the system inputs must be sufficient to maintain statistical control; no measuring trip dots with a ruler.

In a sense, conclusion 2 is a corollary of conclusion 1.

Please note that for the contrived example, a repeatability analysis should not be performed because the data does not exhibit random behavior.

Lack of Statistical Control Increases Magnitude of Error

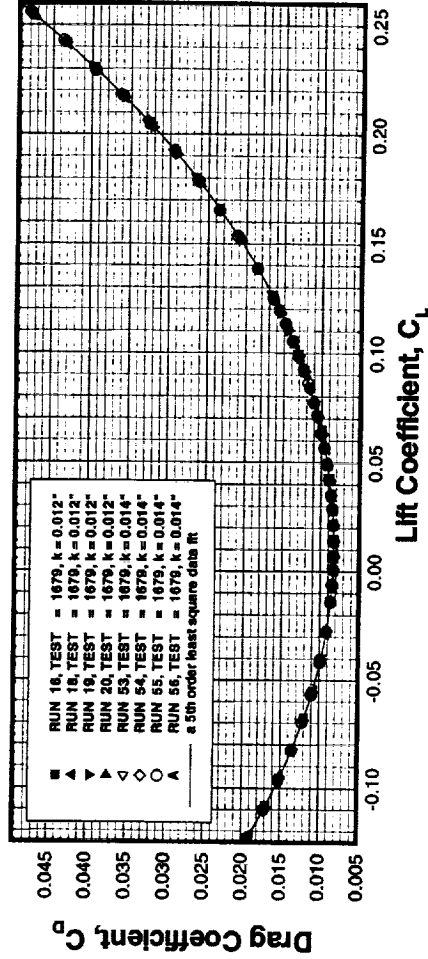
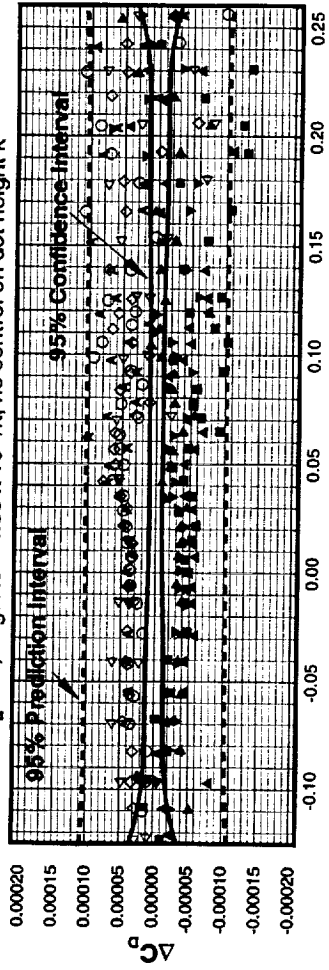


High Speed Aerodynamics, Long Beach

- Example: nominal trip dot height of $k=0.012$ " not maintained

Repeatability Analysis UPWT #2 1.675% Baseline TCA Model 2b

$M_\infty=2.4$, Avg. $Re = 4.00 \times 10^6$ /ft, no control on dot height k



Note: Data does not exhibit random behavior; technically cannot perform repeatability analysis



Data Quality Assessed Through Medium-Term Repeatability

Typically, the within test data quality is gathered by examining the medium-term repeatability (reproducibility). The figure presents the data from the three Mach 2.4 tunnels where HSR conducts testing. The reproducibility numbers for all three tests were of the same order. Prediction intervals are typically around 1 count in magnitude and the confidence interval is less than a quarter count.

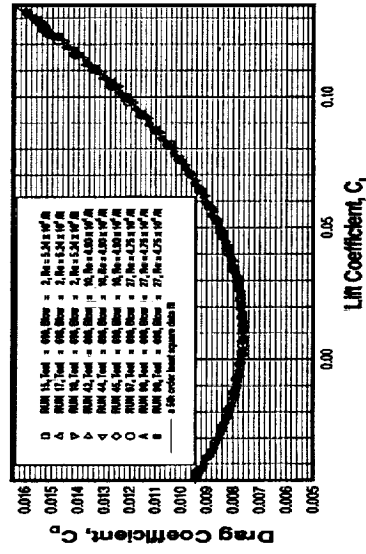
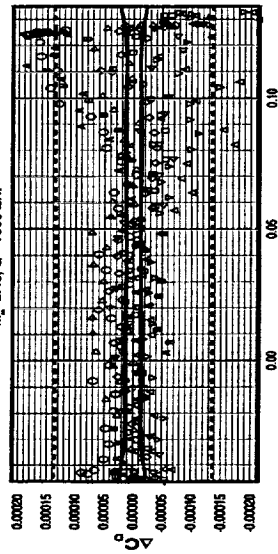
Data "Quality" Assessed Through Medium-Term Repeatability



High Speed Aerodynamics, Long Beach

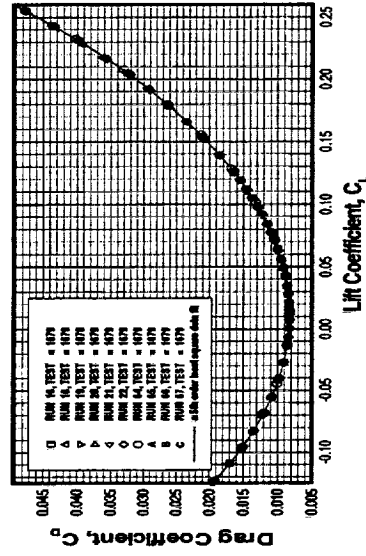
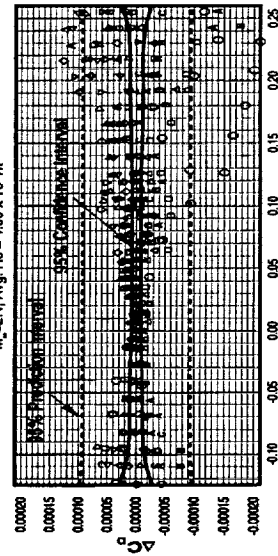
PSWT

Medium Term Repeatability PSWT
1.675% M2 4-7A Arrow Wing Model
 $M = 2.48, Q = 1000 \text{ lb/ft}^2$



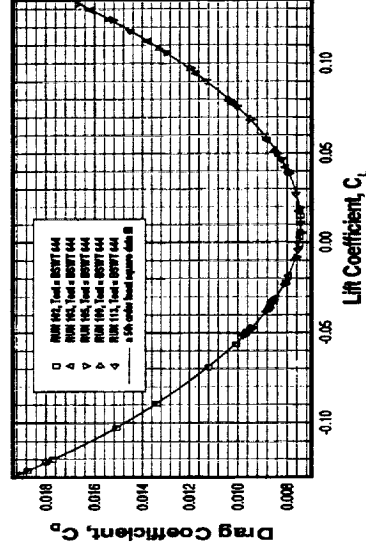
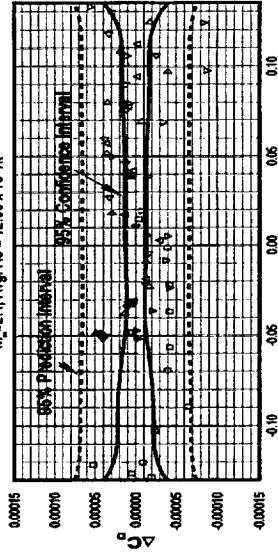
UPWT

Medium Term Repeatability UPWT #2
1.675% Baseline TCA Model 2b
 $M = 2.4, \text{Avg. } Re = 4.00 \times 10^7$



BSWT

Medium Term Repeatability BSWT 644
1.675% Baseline TCA Model 2b
 $M = 2.4, \text{Avg. } Re = 12.00 \times 10^7$



Prediction and Confidence Intervals are similar at all 3 tunnels
~1.0 counts ~0.2 counts



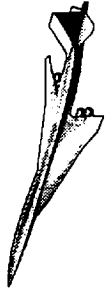
Uncertainty in Angle-of-Attack

Uncertainty in the angle-of-attack measurement can lead to large variations in the drag coefficient. Variations of up to half a count or more can be caused by just a 0.01° uncertainty in angle-of-attack. There are several different methods for the measurement of angle-of-attack. Typically in HSR, the angle at the pitch sector is measured and then a correction for sting bending under aerodynamic loads is applied. Other methods include accelerometer based systems which are mounted on board the model or optical based systems such as the Optotrak in use at Boeing. The on-board systems can have problems with vibrations contaminating the signal while the Optotrak system requires the placement of optical markers onto the model.

At the current time, the sting bending method is very likely inadequate to obtain the desired level of uncertainty in the HSR test data. Looking at the drag polar repeatability plot from Test 1671, one can see that the variation in drag during Test 1671 increases greatly at the ends of the polar. From the residual plot, the differences from the mean curve near minimum drag are very small and they are still less than ± 0.5 counts at $C_L=0.1$, but at the maximum lift conditions ($C_L \approx 0.25$ for $\alpha=10^\circ$) the scatter band is larger than ± 1 count (actually it is worse than shown in the figure as a couple of points fell out of the scale). Looking at the residual plot in general, one can see how the drag data falls in a tight band near zero-lift (which is near zero α) and spreads out as the absolute value of the lift coefficient increases. This increase in scatter is likely due to the relatively large uncertainties in α and the use of the less accurate normal force gage which is making a larger and larger contribution to the drag coefficient.

Common procedures and working standards from tunnel-to-tunnel are required for accurate angle-of-attack measurements. At PSWT, much of the error in the angle-of-attack measurement is due to the sting bending correction. Their current working standard for angle-of-attack during the sting bending calibration is such that at -3° , the sting bending term contribution to the error is double the contribution due to measurement of alpha at the pitch sector. It seems that more attention needs to be paid to the sting bending corrections. Although performing them well is tedious (and cuts into the available test time), it is clearly required.

Uncertainty in Angle-of-Attack

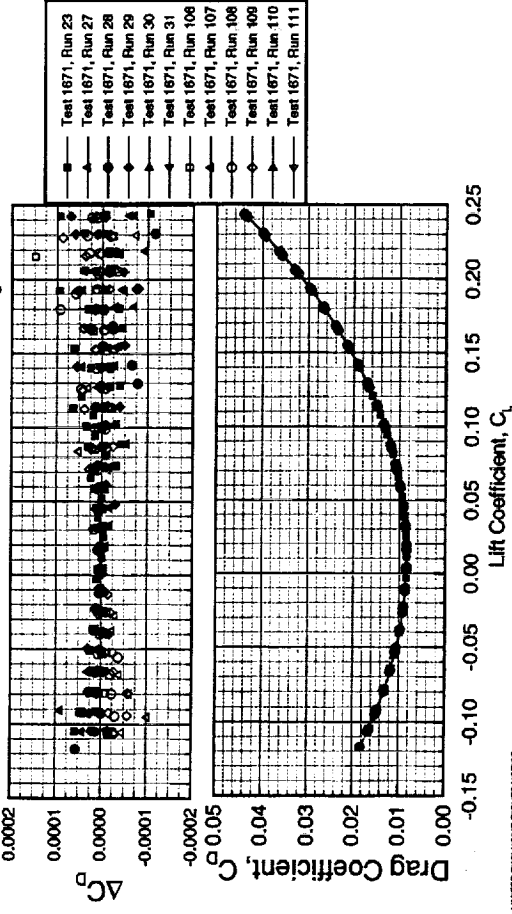


High Speed Aerodynamics, Long Beach

- 0.01° uncertainty in angle-of-attack yields 0.25 cts of uncertainty in drag coefficient (T1671 Model 2a)
- There are several ways to measure α
 - Sector angle plus sting bending
 - On-board accelerometers
 - Optical systems
- Sting bending method is inadequate to obtain desired level of uncertainty
 - Poor α and less accurate NF leads to large variations in C_D at extreme pitch angles
- Common procedures and measurement working standards are required for accurate α measurements

Medium-Term Drag Polar Repeatability 1.675% TCA Model 2a, W/B Configuration

Langley UPWT Test 1671, $M_\infty=2.4$, $Re_c=6.36 \times 10^6$



LIMITED EXCLUSIVE RIGHTS NOTICE
These data are subject to limited exclusive rights under Government Contract NAS1-02020

example of α affecting CD



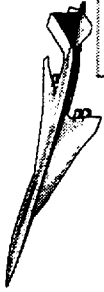
Force and Moment Balances

The table below shows the load ranges and percent uncertainty (in percent full range) in balance components. The balances at the 16' TT and UPWT are typically sized by the aerodynamic loads. The balances at the blowdown facilities are sized for startup loads. The aerodynamic loads do not become an issue until dynamic pressures of 3000 psf are reached (unit Re of 12-14 million per foot). This means that the relative uncertainty in measurements at lower Reynolds numbers is higher because the balance is only lightly loaded. As mentioned above in the angle-of-attack discussion, as the pitch angle increases, the uncertainty in drag increases due to an increase of the normal force contribution to the drag.

As mentioned by the 16' TT staff, the uncertainties in the UT-52 balance are very likely higher in the tunnel due to temperature gradients which are not present at the calibration facility.

Force and Moment Balances

High Speed Aerodynamics, Long Beach



Facility	UPWT	PSWT/BSWT	16' TT
Balance	UT-65	LaRC 756	UT-52
Normal Force Range	800 lbs	2000 lbs	1200 lbs
Normal Force Uncertainty	0.1% Full Scale	0.06% Full Scale	0.07% Full Scale
Axial Force Range	60 lbs	150 lbs	120 lbs
Axial Force Uncertainty	0.1% Full Scale	0.21% Full Scale	0.13% Full Scale
Pitching Mom. Range	2000 in-lbs	3000 in-lbs	2400 in-lbs
Pitching Mom. Uncertainty	0.1% Full Scale	0.11% Full Scale	0.06% Full Scale

- Balances at blowdown facilities are sized for startup loads. Aerodynamic loads become an issue at $q=3000$ psf
- As α increases, uncertainty in drag increases due to NF input
- UT-52 uncertainty likely higher than calibration values due to temperature gradients



Cavity Pressure Corrections

The cavity pressure correction is an axial force correction to account for the base area of the model fuselage where the body accepts the sting and balance. These corrections are on the order of 10 or more counts so mistakes in applying the correction will lead to bias errors which are not insignificant. For example, the area used for the TCA Model 20 correction was selected in order to remain consistent with a prior Ref. H model test. This method was different than what would be used in a performance model test. These differences were on the order of 5 counts for the truncated aft body and 10 counts for the extended aft body. The performance corrections were applied to the Model 20 data for comparisons for the CFD and test data performed by the CA group. When observing increments between different models, an accurate and consistent method of correcting for cavity pressure is required.

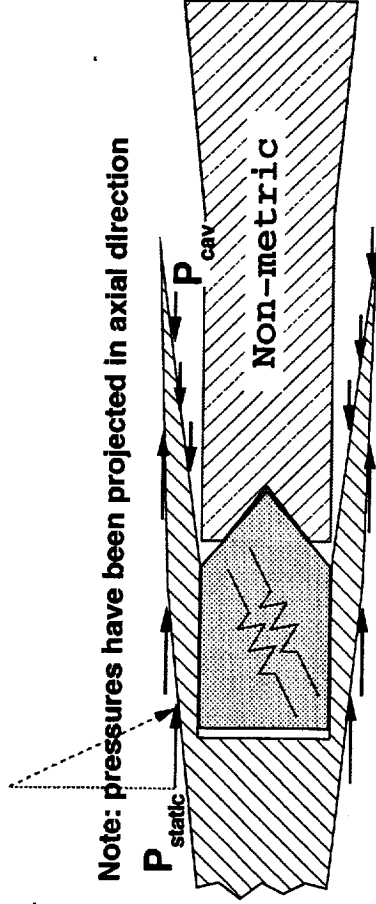
Cavity Pressure Correction



High Speed Aerodynamics, Long Beach

- Attempt to approximate the disturbance that occurs due to the entrance of the sting into a model

$$\bullet \Delta CA_{cav} = \frac{(P_{cav} - P_{static}) * A_{cavity}}{q * S}$$



- Error in Cavity Area:
 - For TCA 2a at Mach 2.4, $\Delta CA_{cav} = O(10 \text{ counts})$
 - For flared TCA 20 at Mach 2.4, $\Delta CA_{cav} = O(15 \text{ counts})$ S&C area, $\Delta CA_{cav} = O(25 \text{ counts})$ with performance area
- Error in P_{cav} : check in UPWT 1701
- Error in P_{static} : using free stream static not local static
- Need to consistently apply a uniform correction method

Flow Angularity Corrections

An incorrect flow angularity correction can lead to errors in angle-of-attack. At least three repeat runs inverted and upright should be made in order to improve the confidence interval and hopefully lead to a good flow angularity correction.

Flow Angularity Correction



High Speed Aerodynamics, Long Beach

- **Flow Angularity:**
 - Incorrect flow angularity correction leads to incorrect angle-of-attack values
 - Recommend a minimum of 3 each upright and inverted runs to reduce confidence interval and get good angularity numbers

Buoyancy Corrections

Wind tunnels which have an axial pressure gradient in the test section may require a buoyancy correction on the data. A variation in the axial pressure usually occurs in facilities which do not have a uniform Mach number in the test section. This is not uncommon in supersonic facilities where the nozzle contours may be slightly incorrectly shaped. The correction for this buoyancy force is given by

$$\Delta F_{DB} = V_m \frac{dP}{dx}$$

In most facilities where there is a known centerline Mach number variation (such as the blowdown tunnels), a buoyancy correction has not been applied. This may be because the variation of pressure over the model length is small so that the buoyancy force is statistically insignificant. However, at PSWT, the 1.675% M2.4-7A model was roughly twice the size of the previous largest model tested in the facility. So the model volume is also much greater than what has been previously tested. A quick investigation should probably be conducted to determine if a buoyancy correction is required.

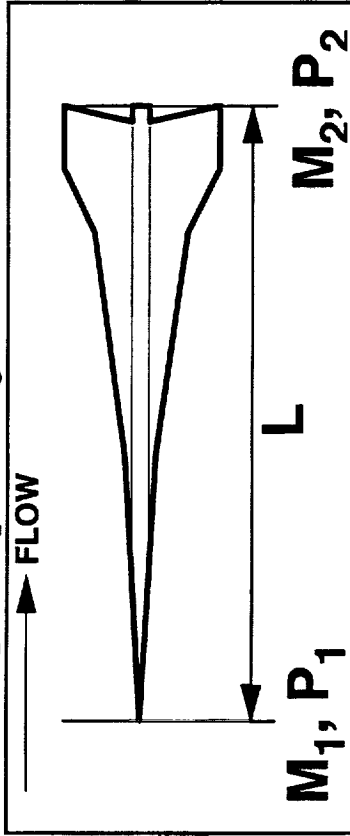
Buoyancy Correction (or lack thereof)



High Speed Aerodynamics, Long Beach

- Axial pressure gradients in wind tunnel test sections result in a buoyancy effect which influences drag

- $\Delta F_{DB} = V_m \frac{dP}{dX}$ V_m = model volume (inch³)
 dp/dx = pressure gradient in direction of flow, lb/inch³



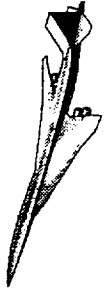
- Pressure gradient is determined from test section centerline Mach number calibration data and model geometry
- As planform/model size increases, drag correction becomes significant
- Most facilities HSR tests do not correct for buoyancy

Nacelle Corrections

The nacelle base pressure correction contains the same potential for error as the body cavity pressure correction. Inaccurate pressure measurements or inaccurate cavity areas will lead to errors in the data. During test 1671, this was a very real possibility. The original nozzle sidewalls were too fat (approximately 0.010" instead of 0.004" called out in the print) and had to be repaired. Any additional rearward facing areas need to be repaired or accounted for or else the data will have errors.

The second correction with the potential for uncertainty is the nacelle core drag correction. This is currently estimated using a flat-plate skin-friction correction which is applied to the wetted area of the nacelle cores. Little work has been done to check the validity of this correction. Use of both CFD and experiment-based nacelle core drag corrections should be considered to validate the current nacelle core methodology.

Nacelle Corrections



High Speed Aerodynamics, Long Beach

- **Nacelle Base Pressure**
 - like body cavity correction, $CD_{NB} = \text{pressure differential} * \text{base area}$
 - original Model 2a sidewalls were 0.010" instead of 0.004" and had to be machined down
 - Any rearward facing areas need to be accounted. For axi-nacelles, 0.004" sidewalls are quite thin.
- **Nacelle Internal Core Drag**
 - current method: flat plate C_f over wetted area
 - works only for straight ducts
 - little validation
 - need to consider CFD and experiment to check validity of current method

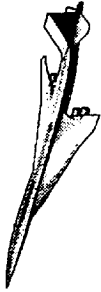
Trip Drag Corrections

There are several potential sources of error for the trip drag correction. Trip drag is commonly estimated using the variable dot height method. Among the sources of error that can lead to an inaccurate trip drag estimation are:

- errors in the estimation of drag coefficient
- errors in the measurement of dot height (the trip dot height gages have a resolution of thousandths or ten thousandths). The dots are typically 0.0012" in height. So the measurement device can be only accurate to as many significant digits as the measurand! The digital trip dot gage will drift with time leading to errors and there is typically a bias between the measurement values of two individuals.
- different tripping efficiencies due to varying dot heights lead to varying laminar runs. No correction for the laminar run behind the dots is made to the data.
- For testing at various Reynolds numbers, the dynamic pressure is typically changed. An increase in dynamic pressure leads to an increase in aeroelastic deformation of the model. So comparisons at different Reynolds numbers are actually being made on slightly different planforms.
- The nature of the best fit through the data (k , k^2 , or other) is unknown and the extrapolation to zero dot height goes over a rather large distance.

All of these inputs lead to a rather inaccurate estimation of the trip drag which can cause bias errors in the data.

Trip Drag Corrections



High Speed Aerodynamics, Long Beach

- There are several sources of error
 - uncertainties in measurement of C_D
 - measurement of dot height (to 0.0005" or 0.0001")
 - model deformation variation with Re
 - no accounting for varying laminar run lengths
 - order of fit unknown
 - large extrapolation to zero dot height
- Result: Bias error in data

Facility/Hardware Recommendations

In an attempt to reduce the uncertainty in HSR experimental tests, the following recommendations are suggested. Some are improvements to facility hardware in order to reduce precision errors, allow for better corrections, or to remove biases.

Onboard angle-of-attack measurement needs to be thoroughly investigated. As was shown for the PSWT 698 bias memo, sting bending is the largest contributor to the uncertainty in angle-of-attack. For all testing at a non-zero angle-of-attack, the sting bending correction will contribute to the uncertainty. For testing at higher angles (especially at the higher Reynolds number facilities), the uncertainty on this correction becomes significant. Sector angle plus sting bending is the angle-of-attack method utilized at virtually all test facilities (UPWT, PSWT, BSWT, and 16' TT). So, an instrumentation breakthrough here would be valuable throughout the program. If sting bending is going to continue to be used, the working standard used for sting bending calibration must be 0.01° or better. Much of the error seen in alpha at PSWT is not due to the measurement hardware but instead due to an inaccurate working standard. Improvement of the working standard should be relatively cheap and quick to accomplish.

It is proposed that the temperature sensitivity of the UT52A balance is investigated. The balance is subjected to a pair of thermal gradients while it is being tested in the 16' TT. The effect of these temperature variations is not understood. A trip dot height gage like the one used in the 16' transonic tunnel should be used at all facilities. This is an off-the-shelf dial indicator gage which is accurate to 0.0001" and has been fitted with a custom built knurled knob to make handling the gage easier.

Last, specialized balances should be used for high Reynolds number testing of the symmetric model. As proposed now, one of the blowdown facilities will be used to test the symmetric model through a wide range of Reynolds numbers. Since the Reynolds number scales linearly with the dynamic pressure, a balance sized for the aerodynamic loads of the highest dynamic pressure will have large uncertainties at the lowest dynamic pressure.

Facility/Hardware Recommendations



High Speed Aerodynamics, Long Beach

- The following hardware and facility upgrades are suggested:
 - Use of an on-board angle-of-attack measurement device if possible
 - Experimental investigation of balance sensitivities to temperature gradients to determine “temperature corrections” for balance
 - A trip dot height gage like the one at the 16’ TT should be used when measuring trip dots
 - The working standard used in angle-of-attack measurements during sting bending calibrations should be $\leq 0.01^\circ$
 - Use specialized balances for high Re testing of symmetric model (one for low q and one for high q)

Best Process Recommendations

The following recommendations refer to the experimental processes being used now. Some are repetition of existing processes while others are suggesting for future improvements.

A process suggestion is the pre-heating of the 16' transonic tunnel during testing there. This process is sometimes used to heat the balance so that it is approaching something of a thermal equilibrium. This (relatively expensive) balance heating process can be bypassed with the use of heat lamps near the model and balance. However, the stagnation temperature of the tunnel tends to rise during testing (at the transonic Mach numbers of interest) which in turn leads to a variation of the test Reynolds number. In test 496, it appeared that larger variations in the stagnation temperature led to variations in the repeat runs. It may be prudent to pre-heat the tunnel before taking measurements or else the process may not be in statistical control.

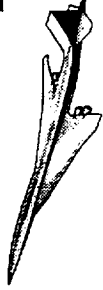
At least three repeat runs should be conducted in the upright and inverted configuration when generating data for the flow angularity correction. This is currently already being done.

The variation of laminar run length must be accounted for when making a trip drag estimate.

A longer time should be allotted for the fabrication of wind-tunnel models and a Quality Analysis (QA) should be conducted on the models to assess the model fidelity.

Standardized data correction and a standardized uncertainty analysis should be conducted for all facilities where HSR plans to test. The facilities should be held to the same level of expectations in their test data. Use of standardized corrections and uncertainty analysis will make test-to-test comparisons simpler and more meaningful. This will also help to ascertain if statistical control is indeed maintained in all tests.

Best Process Recommendations



High Speed Aerodynamics, Long Beach

- The following process improvements are suggested:
 - Aerodynamic heating of the balance for 16' testing; heat lamp was not effective for temperature gradient of test gas.
 - At least 3 repeat runs should be conducted to reduce uncertainty in flow angularity
 - The same person should measure trip dot heights for the whole test to reduce the bias errors in the measurement
 - Account for varying laminar run lengths in trip drag studies
 - Polynomial regression analyses should be conducted for the whole set of repeat runs when assessing repeatability
 - QA should be done on models before testing to determine fidelity
 - Longer time to build models
 - Standardize uncertainty analysis and data corrections for all facilities where we plan to test

Acknowledgments

The authors would like to recognize the valuable inputs and contributions of several individuals. Without their immense knowledge of the subject matter and friendly assistance, this paper would not have been possible. Among these individuals are Mark Kammeyer (Boeing), Eric Adamson (Boeing), Richard Wahls (LaRC), and Mike Hensch (Lockheed at LaRC).

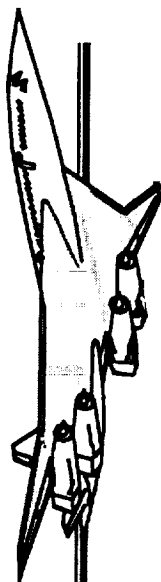
References

- 1.) Taylor, B.N. and Kuyatt, C.E., *Guidelines for Evaluating and Expressing the Uncertainty of NIST Measurement Results*, NIST Technical Note 1297, September 1994.
- 2.) Wahls, R.A., Adcock, J.B., Witkowski, D.P., and Wright, F.L., "A Longitudinal Aerodynamic Data Repeatability Study for a Commercial Transport Model Test in the National Transonic Facility," NASA TP 3522 , August 1995.
- 3.) Doebelin, E., *Measurement Systems: Application and Design*, McGraw-Hill, 1990.
- 4.) Adamson, E., "Development of an Experimental Accuracy Requirements for HSCT High Speed Performance Tests," First HSR Testing Workshop, NASA Ames, May 8, 1997.
- 5.) Kammeyer, M. "PSWT 698 Data Uncertainty Analysis," Memorandum 254.97.058, September 4, 1997.
- 6.) Taylor, J. R., "An Introduction to Error Analysis The Study of Uncertainties in Physical Measurements," University Science Books, 1982.
- 7.) Meyn, L.A., "A New Method for Integrating Uncertainty Analysis into Data Reduction Software," AIAA 98-0632, January 1998.

This page is intentionally left blank.

HSR

High Speed Research



**Configuration Aerodynamics ITD Team
Year End Technical Review**

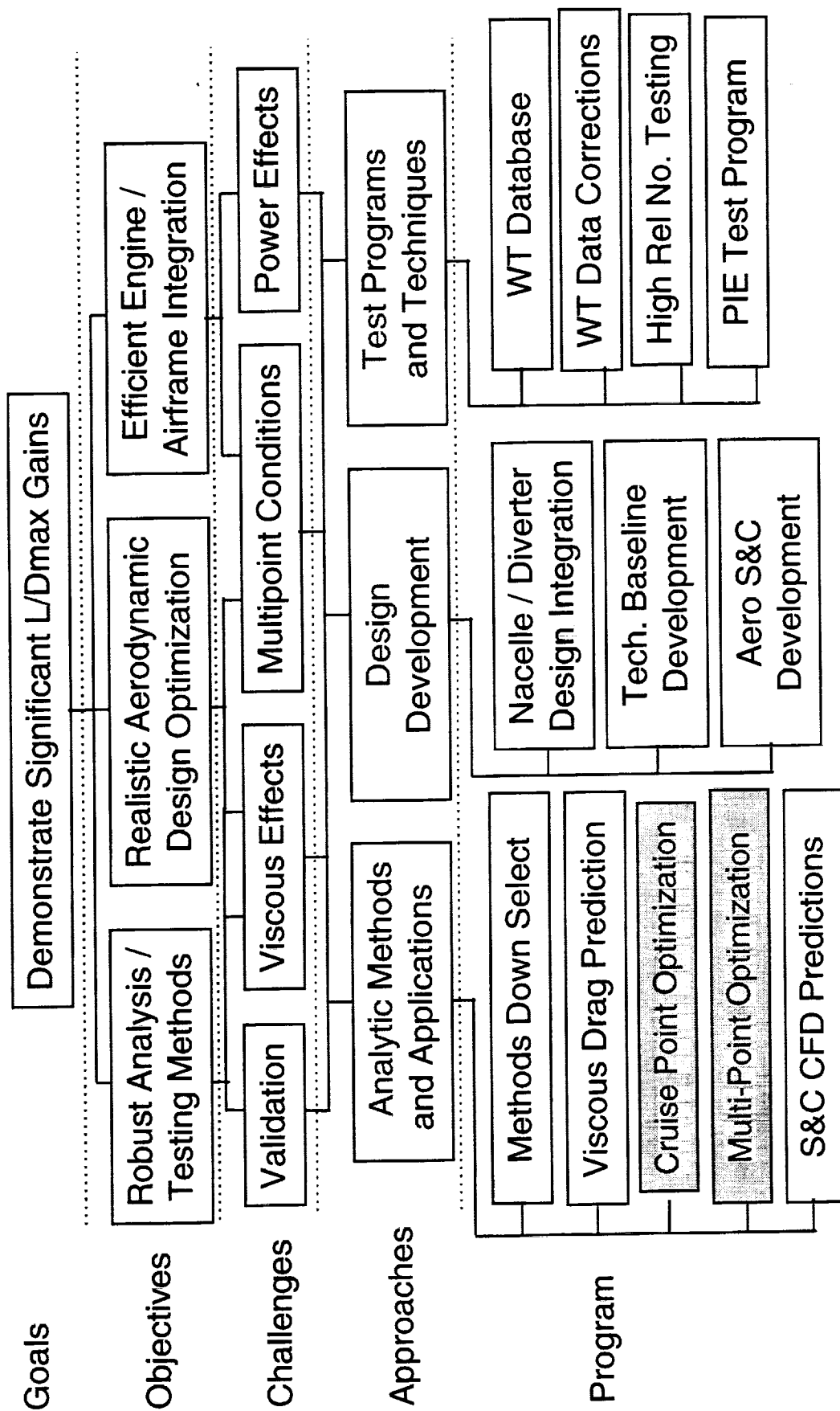
February 9 - 11, 1998

Session 3: Aerodynamic Design Optimization Capability

Session Chairman: Dan Bencze

Configuration Aerodynamics Technology Development

Session 3: Aerodynamic Design Optimization Capability



Configuration Aerodynamics Technology Development

Session 3: Aerodynamic Design Optimization Capability

Objectives:

- Develop, Apply, Validate Non-Linear Design Optimization Methods
- Cruise-Point & Multi-Point Methods
- Inviscid & Viscous Methods

Issues:

- Accurate Modelling of the Complex Geometries
- Lack of Uniqueness Among the Designs
- Need for Viscous Effects
- Multi-Point Design Scenarios

Configuration Aerodynamics 1997 Year-End Review

Session 3: Aerodynamic Design Optimization Capability

8:00 - 8:10	Overview of WBS 4.3.1.2	Dan Bencze, ARC
8:10 - 8:40	BCAG Design Optimization Activities	Rusty Conner, BCA
8:40 - 9:10	Status of SYN107MB Design Optimization Code	James Reuther, ARC
9:10 - 9:45	The AEROSHOP (AERodynamic SHape Optimization) Toolkit	Eric Unger, BLB
9:45 - 9:55	BREAK	
9:55 - 10:25	Optimization Status: Axi vs. 2DB Inlet Nacelles and Transonic Flaps	Ray Hicks, ARC
10:25 - 10:50	Aerodynamic Gradients Using Three Methods	Geojoe Kuruvila, BLB
10:50 - 11:35	CFD-Based Flap Optimization for the TCA in Transonic Flight Conditions	Robert Narducci, BLB
11:35 - 12:00	Viscous Design of TCA Configuration	Steven Krist, LaRC
12:00 - 1:00	LUNCH	
1:00 - 1:25	Progress Towards a Multipoint Optimization Procedure	Robert Narducci, BLB
1:25 - 2:15	Panel Discussion	Presenters



WBS 4.3.1.2
Aerodynamic Design Optimization Capability

BCAG Design Optimization Activities

R. S. Conner

February 10, 1998
Los Angeles, CA



HSCT High Speed Aerodynamics - BCAG

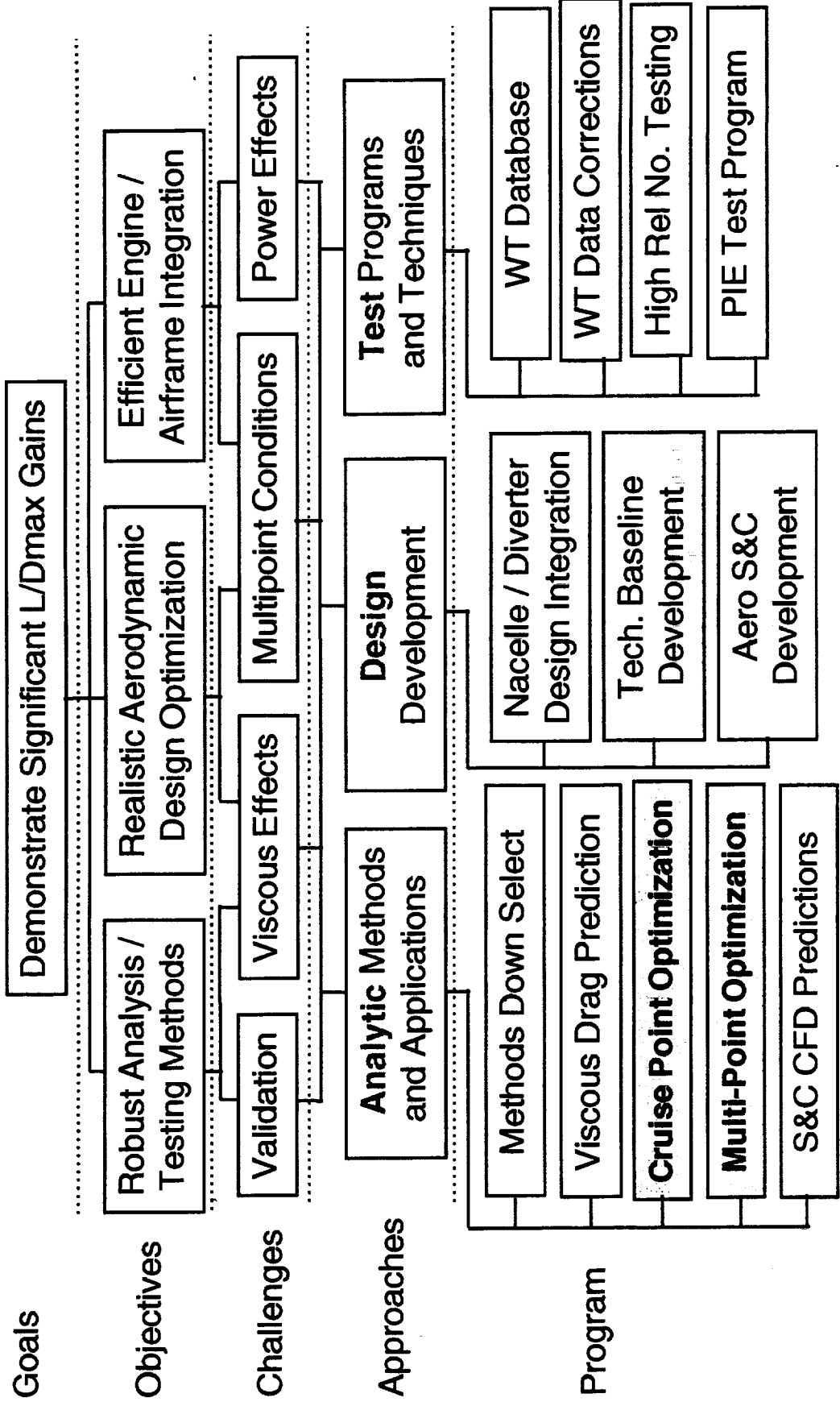


Configuration Aerodynamics Technology Development

Aerodynamic Design Optimization Capability, WBS 4.3.1.2, falls under the Analytic Methods and Applications approach of the Configuration Aerodynamics Technology Development program-on-a-page. More specifically, the two programs addressed are Cruise Point Optimization and Multi-Point Optimization.

Configuration Aerodynamics Technology Development

Session 3: Aerodynamic Design Optimization Capability





The Outline Is Familiar

This presentation follows the standard format. It is, however, not just a final report on '97 work. Since the meeting is occurring months into '98, a review of progress in '98 will also be presented. Beyond this outline, an effort will be made to propose issues that are relevant to this and next year's work, and that could benefit from discussion by the community at this meeting and beyond.



The Outline Is Familiar

- Introduction
- Goals
- Objectives
- Progress
 - '97
 - '98
- Plans
- Issues



HSCT High Speed Aerodynamics - BCAG



Optimization Is a Team Sport

The optimization task requires the efforts of many people. A list of principle contributors is shown here, along with indications of their specific area(s). Two names are new to the optimization task. Chris Vegter and Anutosh Moitra joined the effort this year.

Two areas of work covered later in the presentation are inlet flow quality optimization and the addition of longitudinal trim to cruise point optimization. Gordon Blom performed the inlet flow quality optimization and prepared the material presented here on that work. The work on trim and trimmed cruise optimization was performed by Chris Vegter, with Bill Huffman providing the new routines and Robyn Wittenberg providing the training and guidance.



Optimization Is a Team Sport

- Gordon Blom - N-S optimization
- Rusty Conner - Optimization focal & TRANAIR optimization
- Bill Huffman - Optimization technology
- Chris Vegter - TRANAIR optimization
- Robyn Wittenberg - TRANAIR optimization

- Eric Adamson - Configuration design (TI)
- Chet Nelson - Configuration design (TI) - Lead

- Steve Chaney - N-S verification
- Anutosh Moitra - N-S verification

- Kevin Meija - Wind tunnel verification

- Bob Patton - Lead

- Bob Kulfan - CA ITD member & Boeing ATF



HSCT High Speed Aerodynamics - BCAG

February '98 HSR Airframe Technical Review

The Goal Is Multi-Point Optimization

The goal of this activity is the development and evaluation of multi-point optimization. The current task is limited to the high speed flight regime, subsonic cruise to supersonic cruise, and is based on the use of contemporary nonlinear aerodynamic tools. It is important to understand that the goal is more than a tool, the goal is a process. Tool building is part of the effort, but the result of the process building is the goal.

Since multi-point optimization trades the aerodynamic efficiencies of multiple, disparate flight conditions, it appears that now is the time to begin optimizing to trimmed drag. The magnitude of trim drag at the conditions of interest for multi-point optimization is a significant fraction of the drag improvements due to nonlinear optimization itself. Multi-point optimization will require significant resources. The result of this major expenditure of resources will be far more meaningful if the exercise is based on trimmed drags.

Longitudinal trim dictates that the empenage be added to the optimization model. Only complete configurations are acceptable. With the advent of the PTC configuration and through discussions with TI it also appears that for the foreseeable future complete configurations will include a canard.

The one significant non-aerodynamic contributor to longitudinal trim is engine thrust forces. This will also be included.

Another part of the overall goal of multi-point optimization is to include viscous effects wherever beneficial and/or necessary.

The final, and perhaps most significant aspect of the goal of multi-point optimization is an understanding of who real customer is and how they will use the capability. The real customer will be the configuration designers working on the actual preliminary design of the actual airplane development program, somewhere in the future, sometime after HSR. More detail on how the process will be used on the airplane program and the implications of that use will be given later.



The Goal Is Multi-Point Optimization

- A high speed, nonlinear optimization process
- Trimmed => full configuration => tri-surface
- With thrust forces
- Viscous, at least in part
- Aimed at the eventual customer -> airplane program PD



The Objectives Support the Goal

The specific objectives which support the goal of multi-point optimization are outlined here. The first several indicate the specific extensions to the existing optimization capability that are needed. Beyond the existing cruise point capability, the process must add the ability to optimize flight conditions characterized by efficient deflection of the leading and trailing edge flaps. The two obvious such conditions are subsonic cruise and a representative transonic acceleration point. As noted above, the other capability required for multi-point is longitudinal trim with thrust forces.

In order for the multi-point process to be of use in preliminary design, there must be an ability to provide aerodynamic sensitivities to active constraints. Currently, it is only through the constraints that the aerodynamic optimization process accounts for the needs of the other technical disciplines. The constraints are the result of the multidisciplinary optimization that produced the baseline configuration. The results of discipline-specific optimization, aerodynamic cruise point or multi-point for example, are fed back into the next round of multidisciplinary optimization in terms of aerodynamic sensitivities to the active constraints. This ability is an objective this year.

The next extension of the existing optimization capability that is an objective this year is the inclusion of viscous effects in optimization. This is desirable for two reasons. First, it appears likely that additional benefit can be found at the cruise point if viscous effects are present in the optimization. Second, it also appears that viscous effects are required at the subsonic cruise condition in order to accurately predict the effects of trailing edge flap deflections.

The last extension of the current capability is an inlet flow quality optimization process. Inlet flow quality evaluations of the baseline have shown that the baseline flow does not meet Propulsion's guidelines. Similar evaluations have shown that, in general, cruise point optimization does not improve inlet flow quality.

February '98 HSR Airframe Technical Review



HSCT High Speed Aerodynamics - BCAG



The last two major objectives deal with the creation and evaluation of a new baseline process that applies the nonlinear tools to the configuration design problem, and the multi-point process which will be evaluated against the new baseline. The need for a new baseline process and a working proposal will be described later. The multi-point process will also be discussed.

February '98 HSR Airframe Technical Review



HSCT High Speed Aerodynamics - BCAG



This page is intentionally blank.



The Objectives Support the Goal

- **Extend optimization capability to include:**
 - **Multi-point**
 - **Subsonic**
 - **Transonic**
 - **Longitudinal trim**
 - **w/ thrust forces**
- **Constraint sensitivities**
- **Viscous effects**
- **Inlet flow quality**
- **Establish & benchmark a baseline nonlinear process**
- **Develop & evaluate a nonlinear multi-point process**



HSCT High Speed Aerodynamics - BCAG

February '98 HSR Airframe Technical Review



Broad Progress Was Made in '97

A variety of tasks were accomplished in '97, some more successfully than others. The specific tasks and the three categories they can be grouped into are shown here. First, there were several extensions of optimization capability, next were follow-up activities to the second cycle TCA optimization, and finally, there were efforts to support the two milestones due in '97.

Full configuration (, for '97,) longitudinal trim with thrust effects was developed. To facilitate debugging and checkout prior to incorporation into the general optimization routine, a stand-alone routine was developed which added the empennage to the existing wing/body/nacelle/diverter capability, and supported the trim variables. This was then used to perform constrained optimization of the trim problem. The specifics of this work are described in the next figure.

After the successful development of the basic trim capability, the trim routine was incorporated into the cruise point routine to form the trimmed cruise point capability. This was implemented and testing was started in '97.

Preparation for the inclusion of viscous effects in optimization started with an evaluation of the existing viscous analysis capability. This turned out to be straight forward except for the nacelle/diverter region, which proved to be in need of additional development. The complexity of features and strength of interactions in this region revealed the weaknesses in the existing coupled boundary layer capability. Efforts then turned to addressing two major issues. One is properly obtaining and passing to the boundary layer the local isobar sweep so that the appropriate shock relationship can be used. A temporary workaround was developed while work on a more general solution was started. The second issue is the lack of an accurate calibration of the Drela integral boundary layer for supersonic freestreams and the relatively strong nacelle/diverter shocks. This was addressed by developing a simple problem to serve as a reference calibration solution. This work was started in '97.



HSCT High Speed Aerodynamics - BCAG



The other major extension of the optimization capability pursued in '97 is the ability to optimize the leading and trailing edge flap deflections at subsonic cruise conditions. The ability to do this problem parametrically with analysis was previously demonstrated by Dynacs. The challenge was to accomplish this within optimization, where the deflections are represented by surface transpirations. This proved problematic and has led to an effort to find and address the apparent weakness(es) in the system. The issue does not appear to be one of theoretical ability, but rather one of implementation and process.

The final optimization extension was the initiation of a viscous inlet flow quality optimization. This was accomplished using OVERFLOW together with existing open literature techniques for optimization and geometric movement. This work is described in greater detail after the figure on trimmed optimization.

Two tasks associated with the second cycle TCA optimization were supported in '97 also. The first was participating in the analytic cross checks of the TCA and the three optimized TCA's. Viscous and inviscid solutions were obtained for the cruise Mach number and several angle of attack for both the wing/body and the full wing/body/nacelle/diverter configurations. This task, an addition to the statement of work, required a significant effort on the part of several people but has provided an invaluable benchmarking of the various analysis tool as well as providing a measure of the analytic uncertainty between sites.

The second task was the actual testing of the optimized TCA chosen for experimental validation, now referred to as the nonlinear cruise point validation model or NCV. Two views of the wind tunnel model are shown later in this presentation. The wind tunnel test results were mixed in the attempt to verify the predicted performance improvement. The test did appear to reveal an issue with testing nonlinearly optimized HSCT configurations at relatively low Reynolds number. Results and issues are discussed in greater detail in another presentation, "Nonlinear Cruise-pt. Validation (NCV) Model Wind Tunnel Test Summary & Posttest Analysis", by Kevin Mejia. The NCV model will be retested at the higher Reynolds numbers available at the Boeing Supersonic Wind Tunnel (BSWT) in February '98.

The two milestones that were supported in '97 are shown here also. The first, Cruise Point Design required some additional effort to support the official close-out of the cruise point design task. This is not the end of work on point design, but rather an official recognition of having obtained a specific level of progress.



HSCT High Speed Aerodynamics - BCAG

February '98 HSR Airframe Technical Review



This page is intentionally blank.

February '98 HSR Airframe Technical Review



HSCT High Speed Aerodynamics - BCAG



The second milestone, Multi-Point Formulation, required far more work to support and produced a great deal of useful discussion and coordination. The discussion and coordination has and will continue but the efforts in support of this milestone have provided a useful and important foundation.

February '98 HSR Airframe Technical Review



HSCT High Speed Aerodynamics - BCAG



This page is intentionally blank.



Broad Progress Was Made in '97

- **W/B/N/D/E longitudinal trim w/ thrust forces**
- **Trimmed cruise point design**
- **Viscous analysis**
- **Subsonic flap deflection optimization**
- **Viscous NCV inlet flow quality tune-up optimization**

- **Optimized TCA cross checks exercise**
- **NCV wind tunnel test**

- **Milestone 3-4 : Multi-Point Formulation**
- **Milestone 3-3 : Cruise Point Design**



HSCT High Speed Aerodynamics - BCAG

February '98 HSR Airframe Technical Review



Trim Optimization Was Implemented

The additional details implemented for longitudinal trim are illustrated here. This capability was set up as a new optimization routine just to work the issues of longitudinal trim. The TCA was successfully trimmed to optimal inviscid analytical aerodynamic efficiency using this capability.

The first new variable, C.G., reflects the current program position that the C.G. location will be specified by Aerodynamics for optimal high speed efficiency. The desired location will be provided by the fuel management system. Variable C.G. was requested by TI to support the anticipated future use of the optimization process during airplane program preliminary design.

The next new variable shown here is the all-flying horizontal tail. The current, initial implementation is a simple solid body rotation. Future versions will explore the rest of the basic wing-type variables - twist, camber, thickness, and shear.

The next item is a reasonably complete initial implementation of thrust forces and variable nozzle vector. Thrust forces are divided into two basic forces. Ram drag, currently based on a prescribed inlet Mach number is applied at the center of and normal to the inlet face. Future implementations will determine this Mach number from the flow solution. The other force is the gross thrust, which is applied at the center of the nozzle exit plane. The gross thrust vector is treated as a variable and is allowed to rotate up and down in nacelle coordinates. This is currently implemented as a virtual variable nozzle with no changes to the nozzle geometry. Future implementations will incorporate the corresponding changes to nozzle geometry. Each nacelle is treated separately, although this initial implementation assumes that the nozzle vector is the same for both nacelles. This restriction will be relaxed in future implementations.

There are two other interesting points of this trim implementation. First, the value of the gross thrust is set within the routine to provide unaccelerated longitudinal flight. With the addition of a currently prescribed viscous drag term, the routine sets flight path thrust equal to flight path drag. This means that some of the gross thrust is contributing to lift. This is all accounted for by the routine, and is performed at prescribed total lift and pitching



HSCT High Speed Aerodynamics - BCAG



moment. The use of variable thrust vector leads to the second interesting point. The objective function must now be minimum thrust rather than drag. Otherwise, the optimization will attempt to provide unrealistic lift from the thrust vector.

The fourth and last image on this figure shows the addition of an all-flying canard which will be added in '98. Initially, the canard will be treated like the horizontal tail and will also share in the additional variability planned for future implementations.

Finally, the results of trimming the TCA with this capability are tabulated at the bottom of the figure. The meaningful things to observe are that the nozzle vectors have several degrees of lift, as they should. Their difference is a simple fallout of the installed geometry. The horizontal tail is flying at an angle of attack very near that of the whole configuration. And, the C.G. has moved aft from the reference location of fifty percent MAC.

February '98 HSR Airframe Technical Review



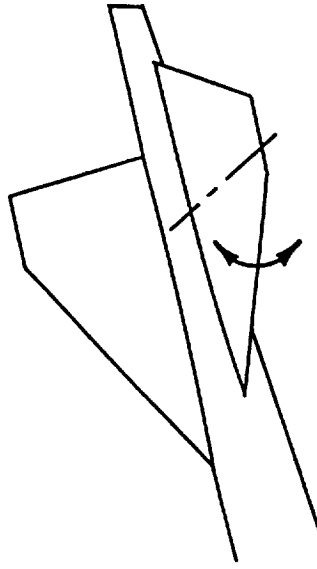
HSCT High Speed Aerodynamics - BCAG



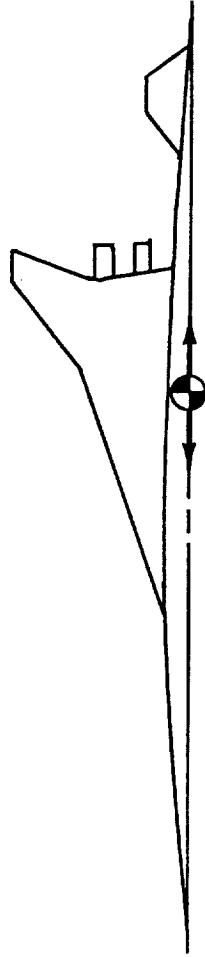
This page is intentionally blank.



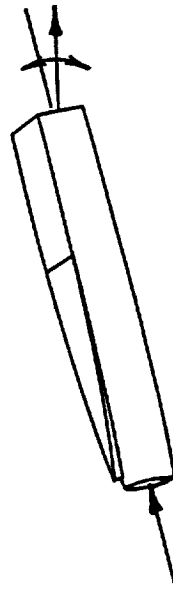
Trim Optimization Was Implemented



All-flying horizontal



Variable C.G.



Thrust forces & vectoring



All-flying canard ('98)

Trim results:

Inbrd thrust = -4.1 deg Tail incidence = 3.6 deg
 TCA CL=.086 Outbrd thrust = -5.5 deg C.G. = 55.3% MAC
 Mach=2.4 (Angles w.r.t. freestream)



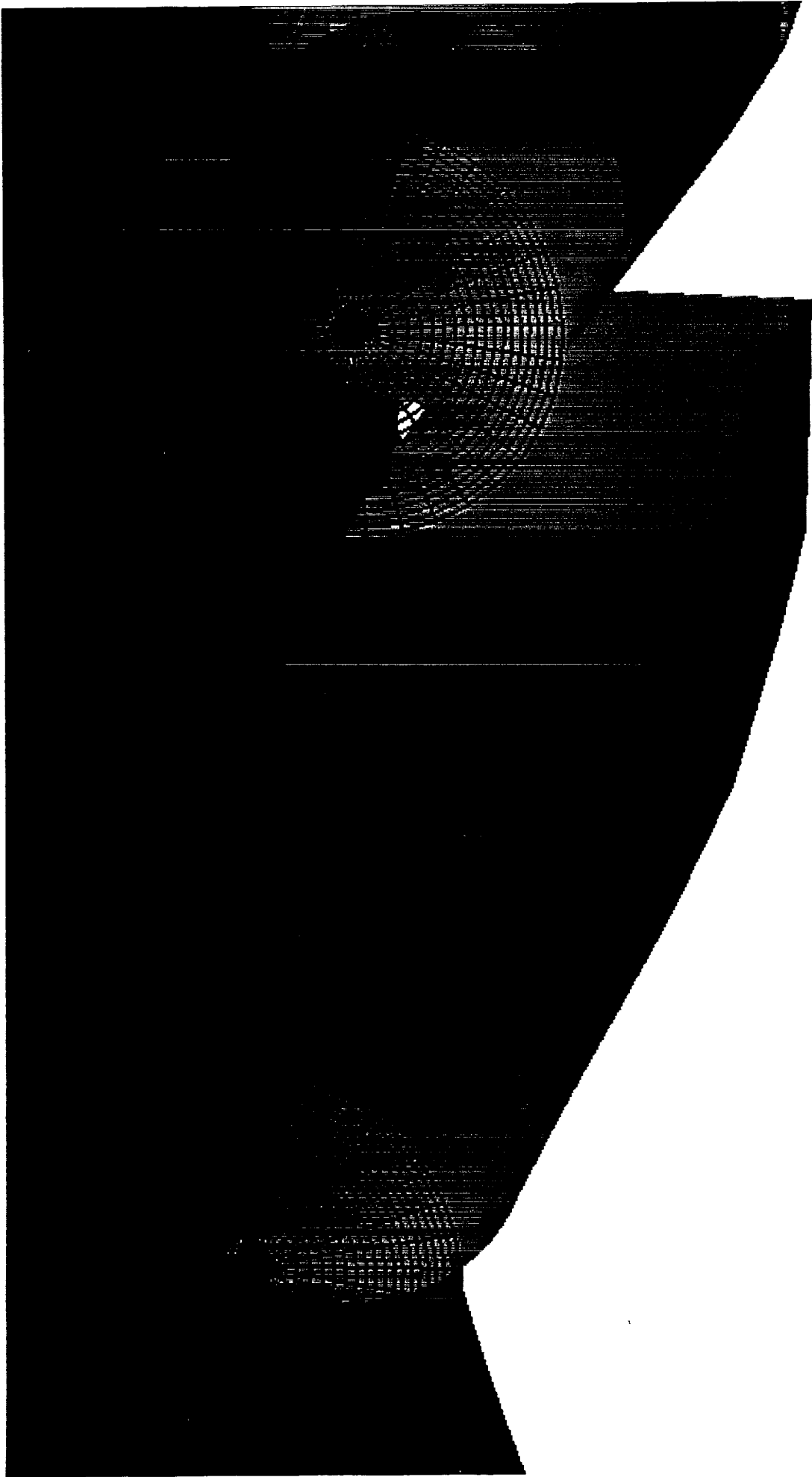
Viscous Numerical Optimization To Improve Inlet Approach Flow

This figure shows the evaluation grids used for the inlet flow quality optimization and their locations. They represent the capture streamtubes at the apex of the inlet spikes. These were added to the OVERFLOW model of the TCA for this optimization.



VISCOUS NUMERICAL OPTIMIZATION TO IMPROVE INLET APPROACH FLOW

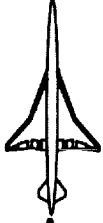
INLET APPROACH FLOWFIELD EVALUATION GRIDS FOR NCV





HSCT High Speed Aerodynamics - BCAG

February '98 HSR Airframe Technical Review

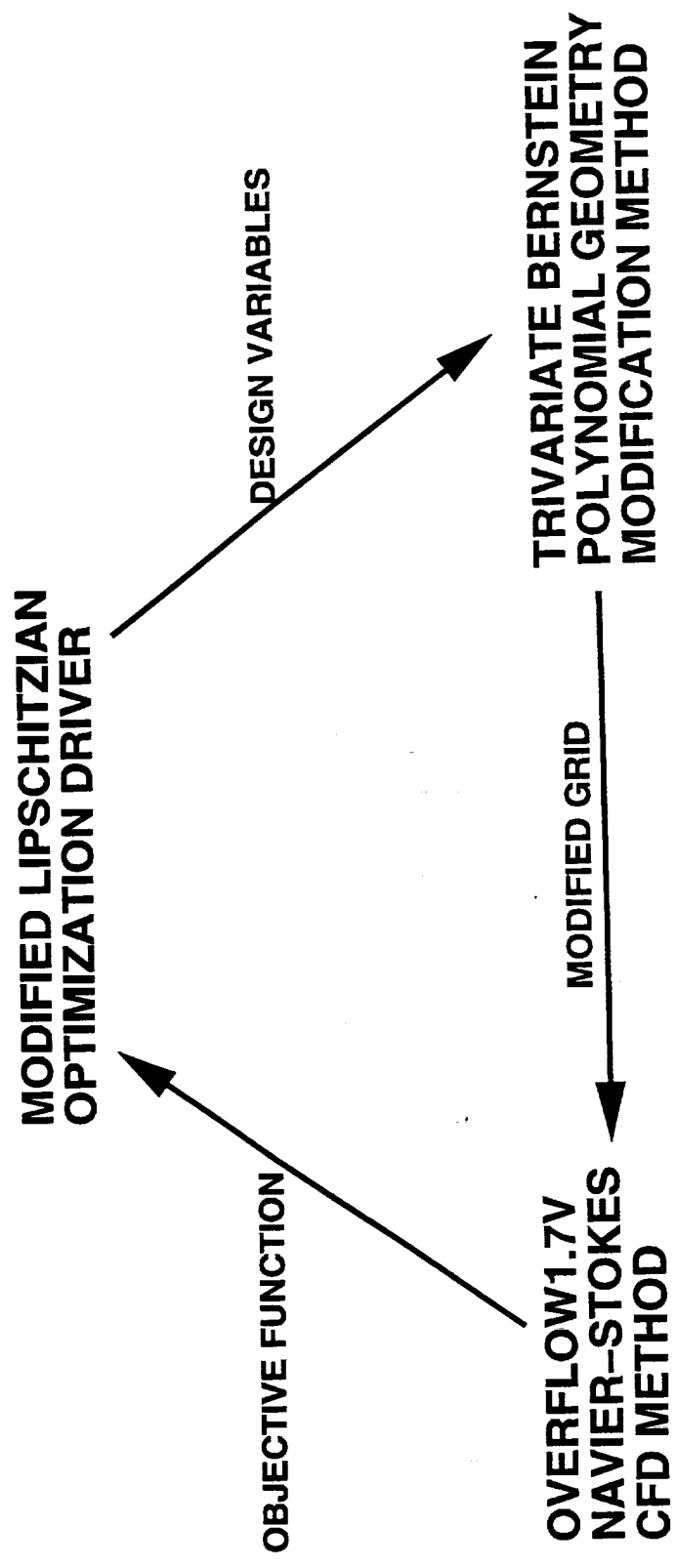


Navier-Stokes Numerical Optimization

This figure illustrates the optimization system used for the inlet flow quality case. OVERFLOW in the viscous mode is used for the flow solver. Subsequent solutions are based on restarts of existing solutions. The optimization driver is a modified Lipschitzian approach, a global optimization technique. The geometric variations in the wing lower surface forward of the inlets use trivariate Bernstein polynomials. These design variables are characterized by very smooth manipulation of a well defined, local region. This will be illustrated later in the presentation.



NAVIER-STOKES NUMERICAL OPTIMIZATION





HSCT High Speed Aerodynamics - BCAG

February '98 HSR Airframe Technical Review



NCV Results (Nacelles-Off)

The NCV wing/body wind tunnel model installed in the UPWT at NASA Langley is shown in this figure. Some of the characteristic geometric features are visible in this view. Test results for this extremely high quality wind tunnel model were mixed. Only about half of the predicted improvement for the wing/body was measured during the test. As indicated before, these results are not conclusive and more information is available in the presentation by Kevin Mejia.

NCV Results (Nacelles-off)

== High Speed Aerodynamics





NCV Results (Nacelles-On)

A close up of the flow-through nacelle/diverter installation of the NCV model is shown in this figure. As with the previous figure, both the model quality and some design features are apparent in this view. The wind tunnel results verified the predicted improvement for the nacelle/diverter increment to within the accuracy of the experiment. Again, more information is provided in the Mejia presentation.

NCV Results (Nacelles-on)

— *High Speed Aerodynamics*



NCV lower surface with nacelles installed



HSCT High Speed Aerodynamics - BCAG

February '98 HSR Airframe Technical Review



Making Progress In '98

The development and evaluation of multi-point optimization is a multi-year task. Efforts in '98 are an uninterrupted continuation of the activities of '97. The four areas of work where significant progress has been made in '98 are shown here.

The initial, trimmed cruise point optimization is well underway. The process building (debugging and experimentation,) associated with blending the two separate routines was completed and an optimization was started. At the time of this presentation, the optimization has completed three of the anticipated six cycles. Six is the number of cycles used for the untrimmed optimization process that produced the NCV configuration. This initial trimmed cruise point optimization is as comparable to the NCV as is possible given the addition of the new variables required for trim. Intermediate results at the end of the second cycle are shown in the next two figures.

The viscous inlet flow quality optimization started in '97 was completed just prior to this meeting. The driver converged on the sufficiently small region of design space within which the global optimum resides. Significant improvements to the inlet flow quality were produced with relatively small changes to the base NCV geometry. More details on this optimization and its results are presented later in this presentation.

Building on the foundation created for the multi-point formulation milestone, additional planning and coordinating has been done. The result is a detailed description of sequenced tasks necessary to develop a true but minimum multi-point capability for this class of vehicles. The idea of a new baseline process based on the application of the nonlinear CFD tools was a particularly interesting outcome of this effort. This idea is presented below after the additional material on inlet flow optimization.

The final progress to be noted is use of the pre-existing multi-point capability within the TRANAIR system. TRANAIR multi-point has been in use in the AST contract for some time. Although there are some enhancements to the system necessary for the class of multi-point optimizations planned for HSR, the basic mechanics are in place and operating now. This year, this effort began to make use of the system, but not for multi-point optimization. The trimmed cruise point optimization is an enhancement of the optimization problem solved in the

February '98 HSR Airframe Technical Review



HSCT High Speed Aerodynamics - BCAG

design of the optimized TCA, now referred to as the NCV. Variables were added to a problem which had been previously sized just to fit within the NAS vn eight hour queue limit. In order to fit the trimmed cruise optimization onto vn, the problem had to be further divided. The multi-point system provides this feature, by definition. TRANAIR multi-point is being used to separate the sensitivity calculations from the optimization proper. Although not a direct use of the capability, this has provided an opportunity to become familiar with the more complex file handling and the system behavior. The transition to actual multi-point use will be faster as a result.

February '98 HSR Airframe Technical Review



HSCT High Speed Aerodynamics - BCAG

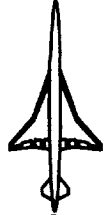


This page is intentionally blank.



Making Progress In '98

- **Initial, trimmed, cruise point optimization**
- **Viscous inlet flow quality tune-up optimization**
- **Coordinated '98 optimization plan**
- **TRANAIR multi-point system**

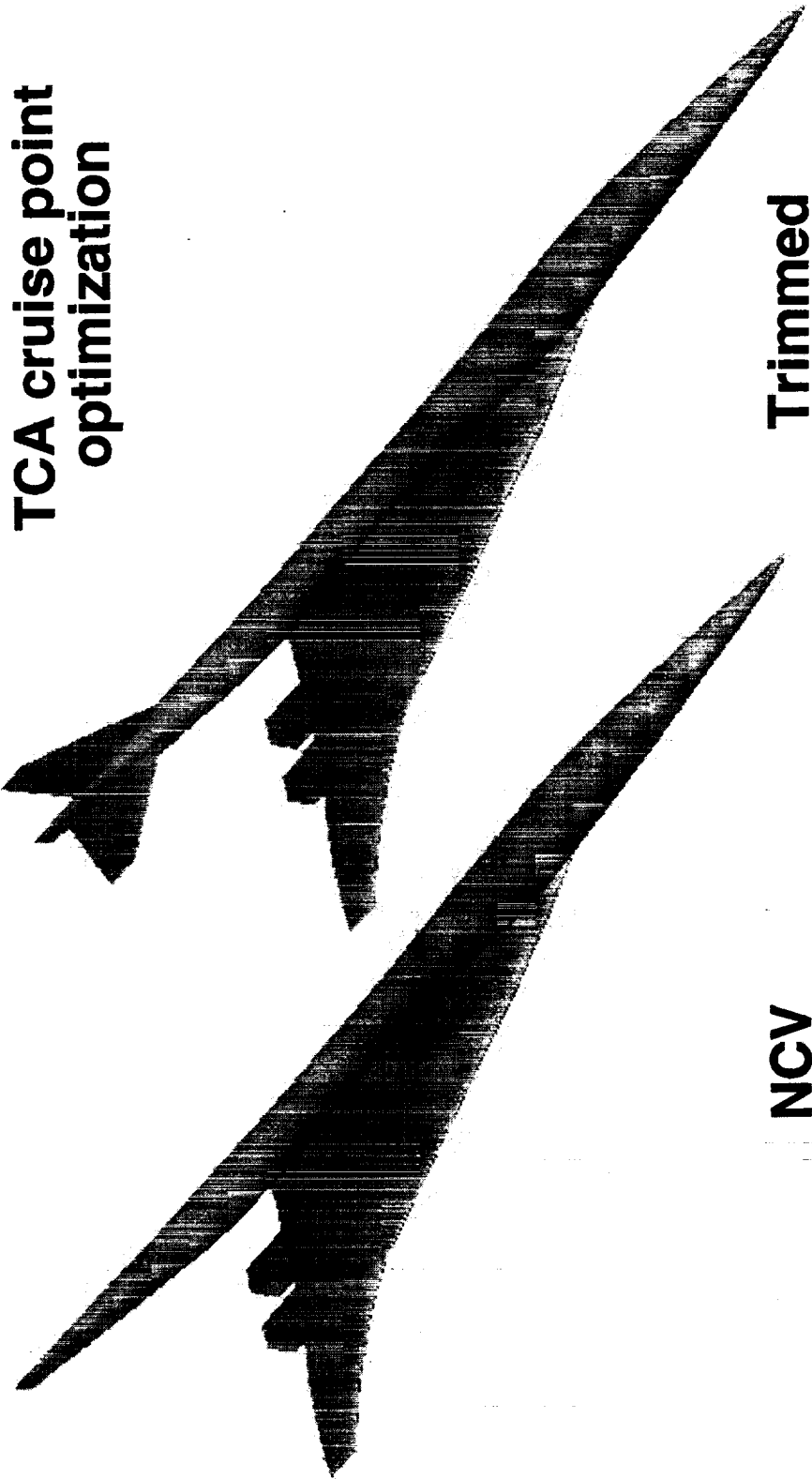


Evaluating the Effects of Trim

This figure illustrates the obvious outward difference due to including trim, the empennage, and provides some idea of the similarity of the two designs at this intermediate state. These geometries are the result of two cycles of optimization, where six are required. Detailed comparisons of intermediate states are qualitative at best. The inherent non-deterministic nature of the optimizer's behavior means that intermediate results are strictly unrepeatable between configurations. Differences in sensitivities will drive comparable cycles to incomparable states. However, qualitative comparison can still be useful. These images do indicate that similar wing features and body cross sections are occurring in the trimmed case when compared to the untrimmed optimization.



Evaluating the Effects of Trim



~Comparable intermediate states



HSCT High Speed Aerodynamics - BCAG

February '98 HSR Airframe Technical Review

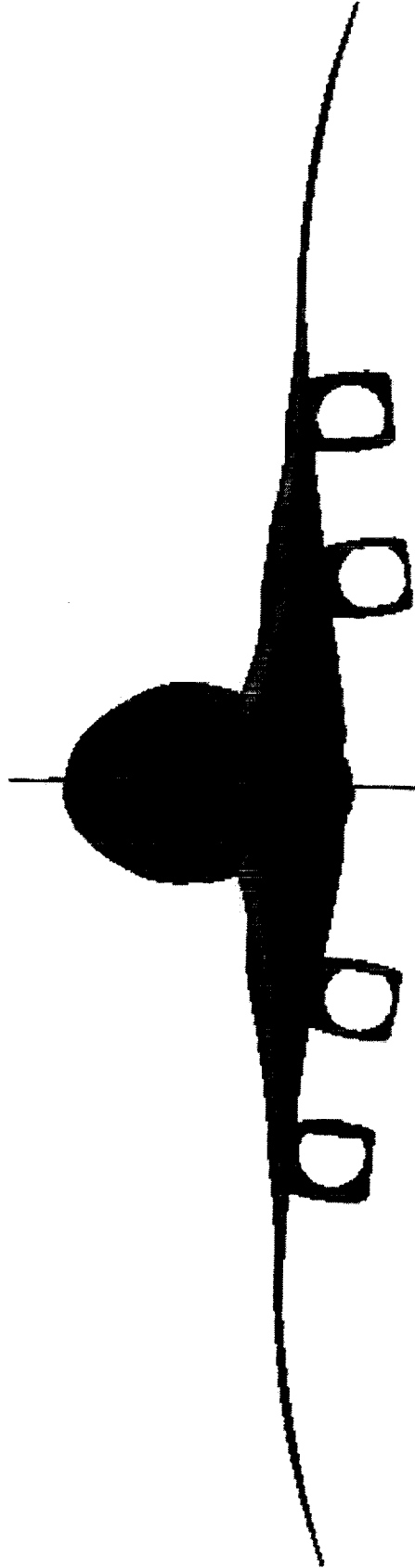


Trim Effects Appear To Be Subtle

This figure compares the same two intermediate geometries in front view at the design attitude, approximately four degrees angle of attack. While some differences are apparent, the designs appear to have more in common than not. The corresponding values of the trim variables are tabulated at the bottom of the figure. Comparing these to the trim-only optimization result shown previously also shows more in common than different. The gross thrust vector angles and the tail incidence are of similar magnitude and the C.G. has moved to a similar location. It remains to be seen if these similarities hold till the conclusion of the trimmed cruise optimization.



Trim Effects Appear To Be Subtle



~Comparable NCV

Trimmed

Intermediate Results

Mach = 2.4
CL = 0.086

Trim Variables

Inbrd thrust	-4.3 deg
Outbrd thrust	-5.2 deg
Tail incidence	3.5 deg
C.G.	54.4 % MAC

(Angles w.r.t. freestream)



HSCT High Speed Aerodynamics - BCAG



Navier-Stokes Numerical Optimization

This figure shows the effect of the inlet flow quality optimization on the local Mach number distributions on the evaluation grids. Inlet #3 is the inboard and #4 is the outboard streamtube. This converged optimization achieved the Propulsion goal of a delta Mach across each inlet of one percent of freestream. Delta Mach is the most important of the three flow quality metrics.



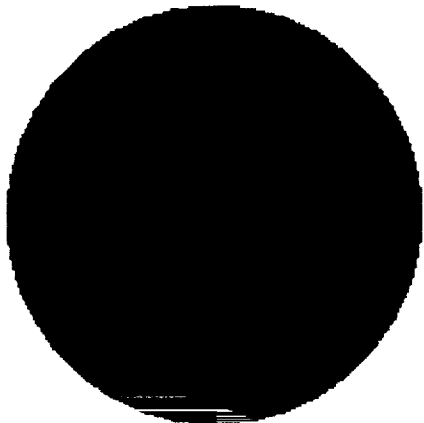
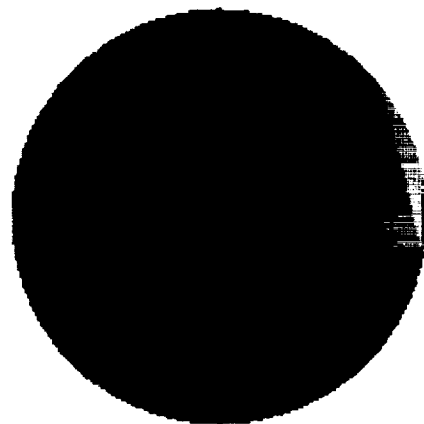
HSCT High Speed Aerodynamics

NAVIER-STOKES NUMERICAL OPTIMIZATION

NCV WBND MACH=2.4 ALPHA=3.00 RN=6.4 MILLION

WING LOWER SURFACE RECONTOURING USING OVERFLOW/LIPSCHITZIAN OPTIMIZATION

#3 INLET APPROACH LOCAL MACH



BEFORE REDESIGN
MAX-MIN = .028

AFTER REDESIGN
MAX-MIN = .024

#4 INLET APPROACH LOCAL MACH



BEFORE REDESIGN
MAX-MIN = .031

AFTER REDESIGN
MAX-MIN = .023



Navier-Stokes Numerical Optimization

This figure illustrates the corresponding upflow distributions. This measure of inlet flow quality was also improved by the optimization.



NAVIER-STOKES NUMERICAL OPTIMIZATION

NCV WBND MACH=2.4 ALPHA=3.00 RN=6.4 MILLION

WING LOWER SURFACE RECONTOURING USING OVERFLOW/LIPSCHITZIAN OPTIMIZATION

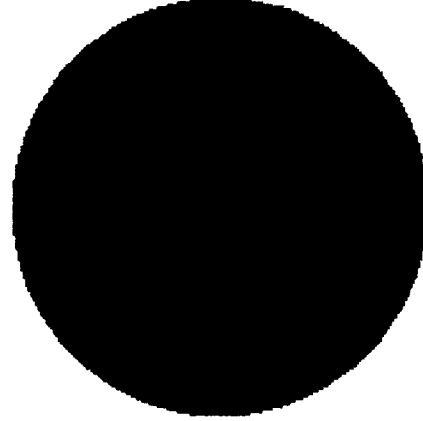
UPFLOW ANGLES IN DEGREES

#3 INLET APPROACH LOCAL UPFLOW

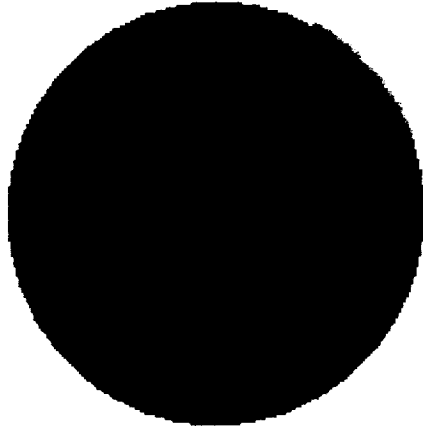


BEFORE REDESIGN
MAX-MIN = .98

#4 INLET APPROACH LOCAL UPFLOW



BEFORE REDESIGN
MAX-MIN = .41



AFTER REDESIGN
MAX-MIN = .38



HSCT High Speed Aerodynamics - BCAG



Navier-Stokes Numerical Optimization

This figure illustrates the corresponding crossflow distributions. This measure of inlet flow quality was not improved by the optimization. This result is not unexpected given the extent and nature of the wing surface design variables, described in a subsequent figure.





NAVIER-STOKES NUMERICAL OPTIMIZATION

NCV WBND MACH=2.4 ALPHA=3.00 RN=6.4 MILLION

WING LOWER SURFACE RECONTOURING USING
OVERFLOW/LIPSCHITZIAN OPTIMIZATION

CROSSFLOW ANGLES IN DEGREES

#3 INLET APPROACH LOCAL CROSSFLOW #4 INLET APPROACH LOCAL CROSSFLOW



BEFORE REDESIGN
MAX-MIN = .94

AFTER REDESIGN
MAX-MIN = .95

BEFORE REDESIGN
MAX-MIN = .80

AFTER REDESIGN
MAX-MIN = .79



HSCT High Speed Aerodynamics - BCAG

February '98 HSR Airframe Technical Review



Navier-Stokes Numerical Optimization Applied To Inlet Approach Flow Quality

A summary of the inlet flow quality optimization is show here. Of particular interest is the lack of change in either lift or drag shown at the bottom of the figure. This result is not unexpected given the small changes in geometry shown on the next figure. This result is useful, also, since it indicates that meaningful inlet flow quality optimization can be applied after the configuration optimization without loss of drag reduction. This is why inlet flow quality is referred to as a tune-up optimization.



HSCT High Speed Aerodynamics

NAVIER-STOKES NUMERICAL OPTIMIZATION APPLIED TO INLET APPROACH FLOW QUALITY

NCV WBND MACH = 2.4 ALPHA = 3.00

VARIATION, MAX - MIN	BEFORE OPTIMIZATION		AFTER OPTIMIZATION 154 OVERFLOW SOLUTIONS	
	#3 INLET	#4 INLET	#3 INLET	#4 INLET
MACH NUMBER	.028	.031	.023	.023
UPFLOW ANGLE RADIANS	.017	.007	.013	.007
CROSSFLOW ANGLE RADIANS	.016	.014	.017	.014
TOTAL VARIATION	.061	.052	.053	.044



OBJECTIVE FUNCTION

CL .05394
CD .01148

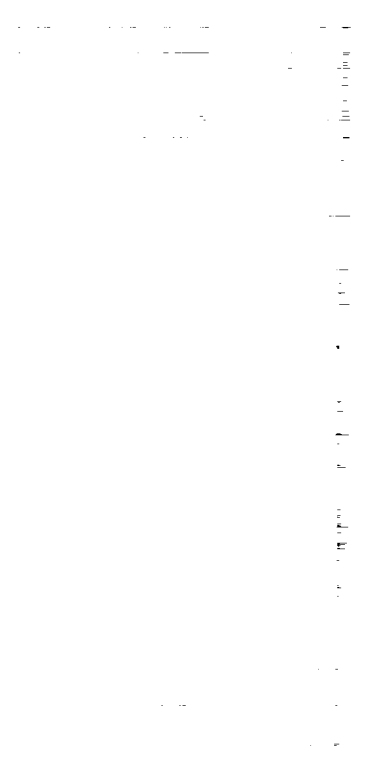


HSCT High Speed Aerodynamics - BCAG



Wing Lower Surface Geometry Change

This figure illustrates the extremely small changes to the wing geometry produced by the inlet flow quality optimization. The magnitudes are less than 0.3 inches, full scale. The extent is relatively small and the variations are very smooth. Qualitatively, the inboard change is a shallow bump and the outboard change is a depression of comparable depth in the previously drag-optimized wing lower surface.

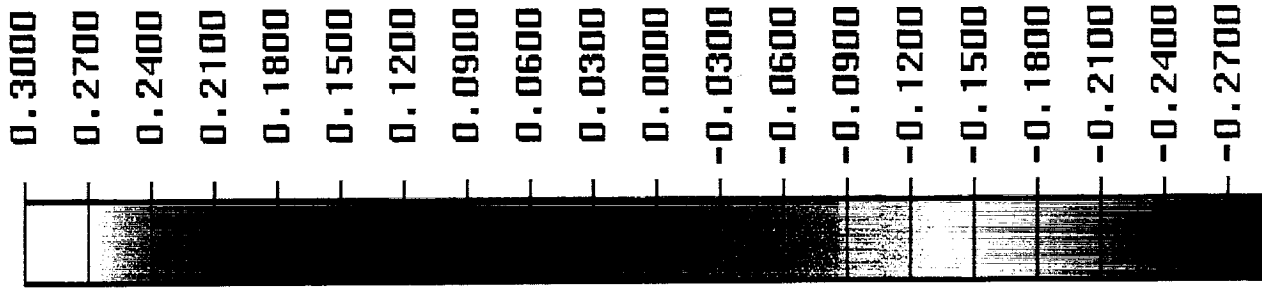




HSCT High Speed Aerodynamics

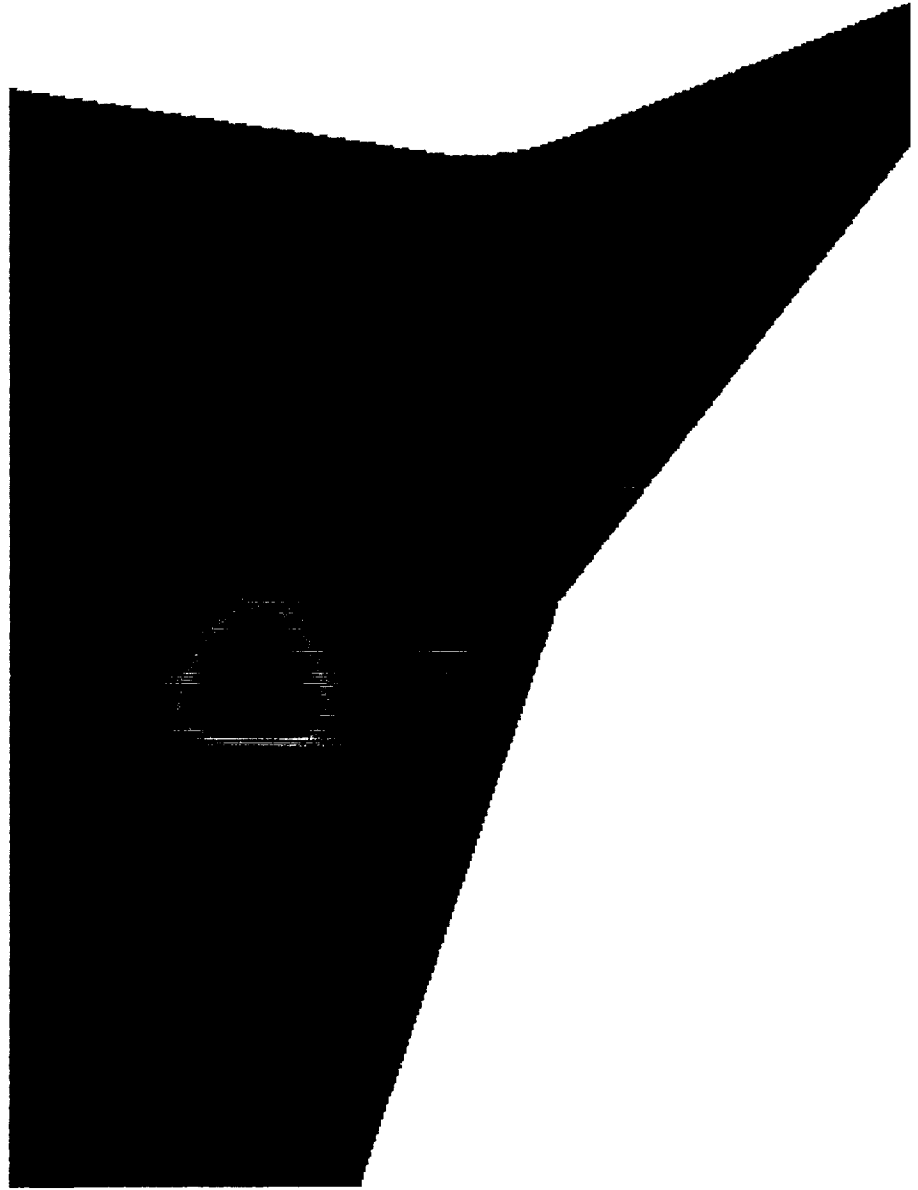
WING LOWER SURFACE GEOMETRY CHANGE

DELTA-Z, INCHES



INLET APPROACH FLOW PROPERTIES REDESIGN

HSCT NCV MACH = 2.4 ALPHA = 3.00 VISCOUS





February '98 HSR Airframe Technical Review

HSCT High Speed Aerodynamics - BCAG



Wing Lower Surface Pressure Change

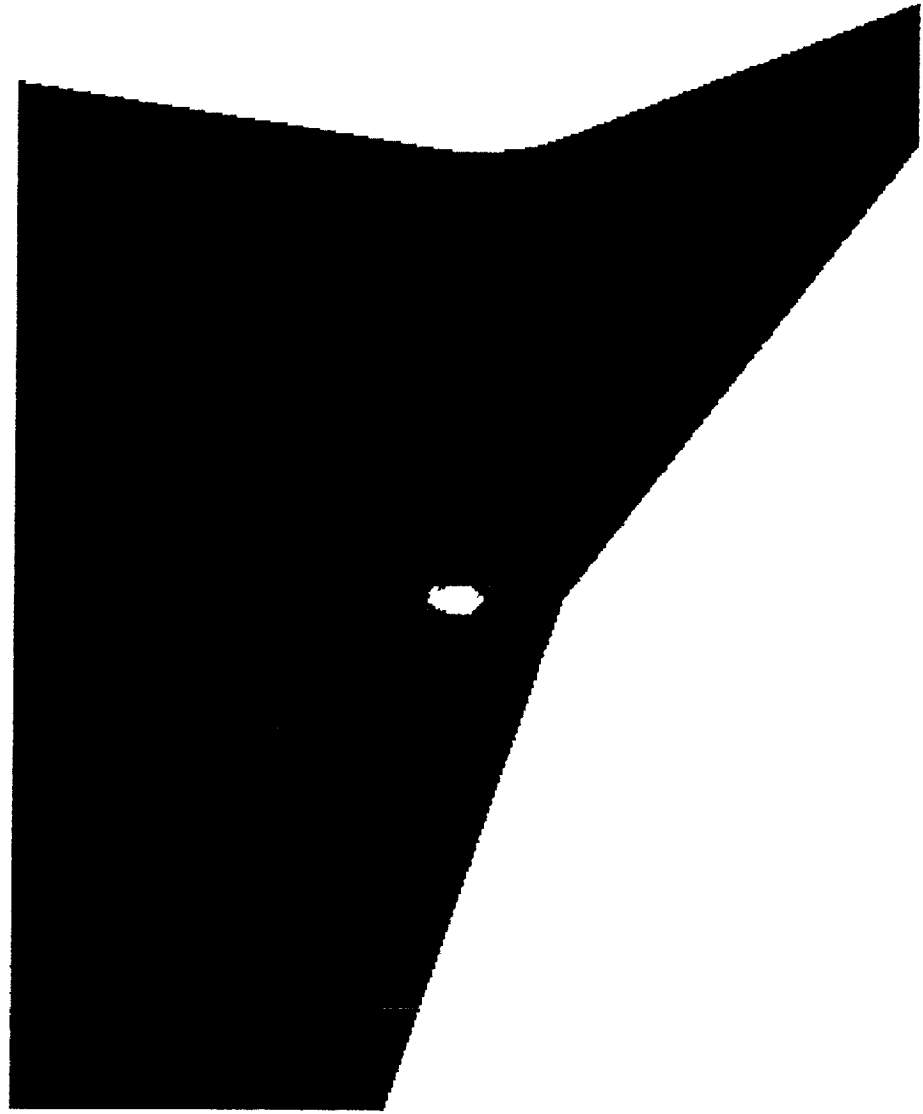
This figure illustrates mild changes in local pressure coefficient that resulted from the inlet flow quality optimization.



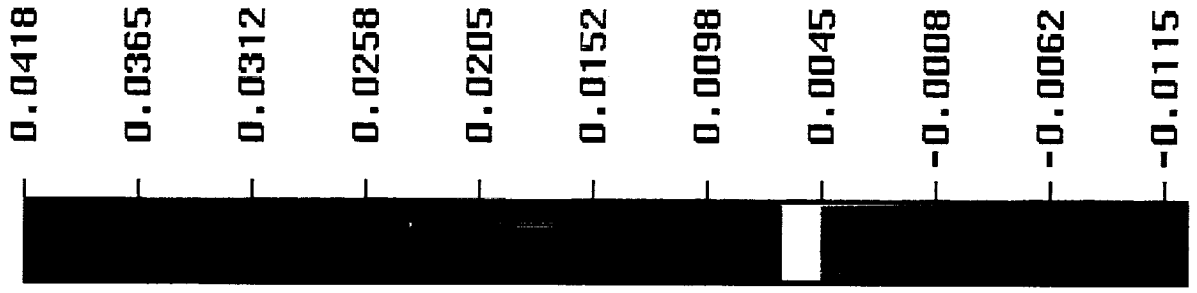
WING LOWER SURFACE PRESSURE CHANGE

INLET APPROACH FLOW PROPERTIES REDESIGN

HSCT NCV MACH = 2.4 ALPHA = 3.00 VISCOUS



DELTA-Cp





HSCT High Speed Aerodynamics - BCAG



A Baseline Nonlinear Process Is Needed

In order to evaluate the possible benefits of a true, full, nonlinear multi-point optimization process, an appropriate baseline process is required. Since it has already been shown that the point design application of nonlinear aerodynamic tools produces benefits relative to the linear optimization process, it seems clear that the linear optimization process is not the appropriate baseline for the evaluation of the nonlinear multi-point optimization process. Further, given that nonlinear point design has yet to be incorporated into the configuration design process, it seems equally clear that this hypothesized baseline nonlinear optimization process is currently undefined. These observations are discussed in more detail in the following figures.



A Baseline Nonlinear Process Is Needed

- **Baseline required for evaluation of full multi-point process**
- **Linear process not appropriate**
- **Baseline nonlinear process currently undefined**



The Linear Design Process Is Tool-Defined

Both to understand why the linear optimization process is not an appropriate baseline, and in order to begin developing an appropriate nonlinear baseline process, an appreciation of the current linear optimization process is useful. This figure illustrates the major steps and flow of the current linear design process. Before describing this process in more detail, some observations may be useful.

This process is the cumulative result of many years of many people's experience applying this linear tool to the configuration optimization of this class of vehicles. It dates back to the original SST program. The process that has resulted from this effort is firmly based on the strengths, weaknesses, and capabilities of the linear tool. So, first, the linear design process has been defined by the tool - the process is tool-defined.

Second, the other principle ingredient in the development of the linear optimization process is the years of effort and experience the collective design community has accumulated in the pursuit of aerodynamic design using this tool. That experience has shaped the process to fit within the constraints of airplane program preliminary design. So, the current linear optimization process is also experience-defined.

Therefore, if one changes either the tool, or the experience base, or both, then the process will change accordingly. The baseline process will be redefined in response to these kinds of changes.

Turning back to the figure, the current linear design process can be thought to start with a multidisciplinary optimization process which produces the constraints for the problem. Manual multi-point optimization between the cruise and transonic conditions is a part of this MDO process. Out of this process falls the wing thickness form. This wing thickness is then used to optimize the body area distribution. The tool limits this step to volume effects only. The body area is determined in the absence of camber and lift. Experience has shown that the process can approximate a multi-point optimization by biasing the Mach number used away from the cruise condition, toward the transonic regime. For the current Mach number 2.4 design, the body is area ruled at a Mach number of 2.1. So, because of the tool and the experience base, the body area rule is performed at the "wrong" lift and the "wrong" Mach number.



HSCT High Speed Aerodynamics - BCAG



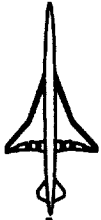
In an independent, parallel step, the wing and body camber are designed. Because of the tool used, the configuration camber is designed only as a camber surface, without volume effects. Again, experience has shown that appropriately better off-design performance can be obtained in this process by designing to a lower lift coefficient than the actual design point. So, again, because of the tool and the experience base, the camber is designed independent of the volume and at yet another "wrong" lift.

The design of the nacelle/diverter lines and locations is another multidisciplinary optimization. From this step comes additional constraints for discipline-specific optimizations, like aerodynamic point design. After the nacelles and diverters are defined, efficient flap deflections are predicted using yet another linear design tool. The final step is to take the results of analyses and obtain the final, trimmed drag coefficients for the conditions of interest. The current conditions for the TCA are, at the appropriate lift coefficient, Mach numbers 2.4, 1.1 and 0.9, cruise, transonic acceleration, and subsonic cruise, respectively.

February '98 HSR Airframe Technical Review



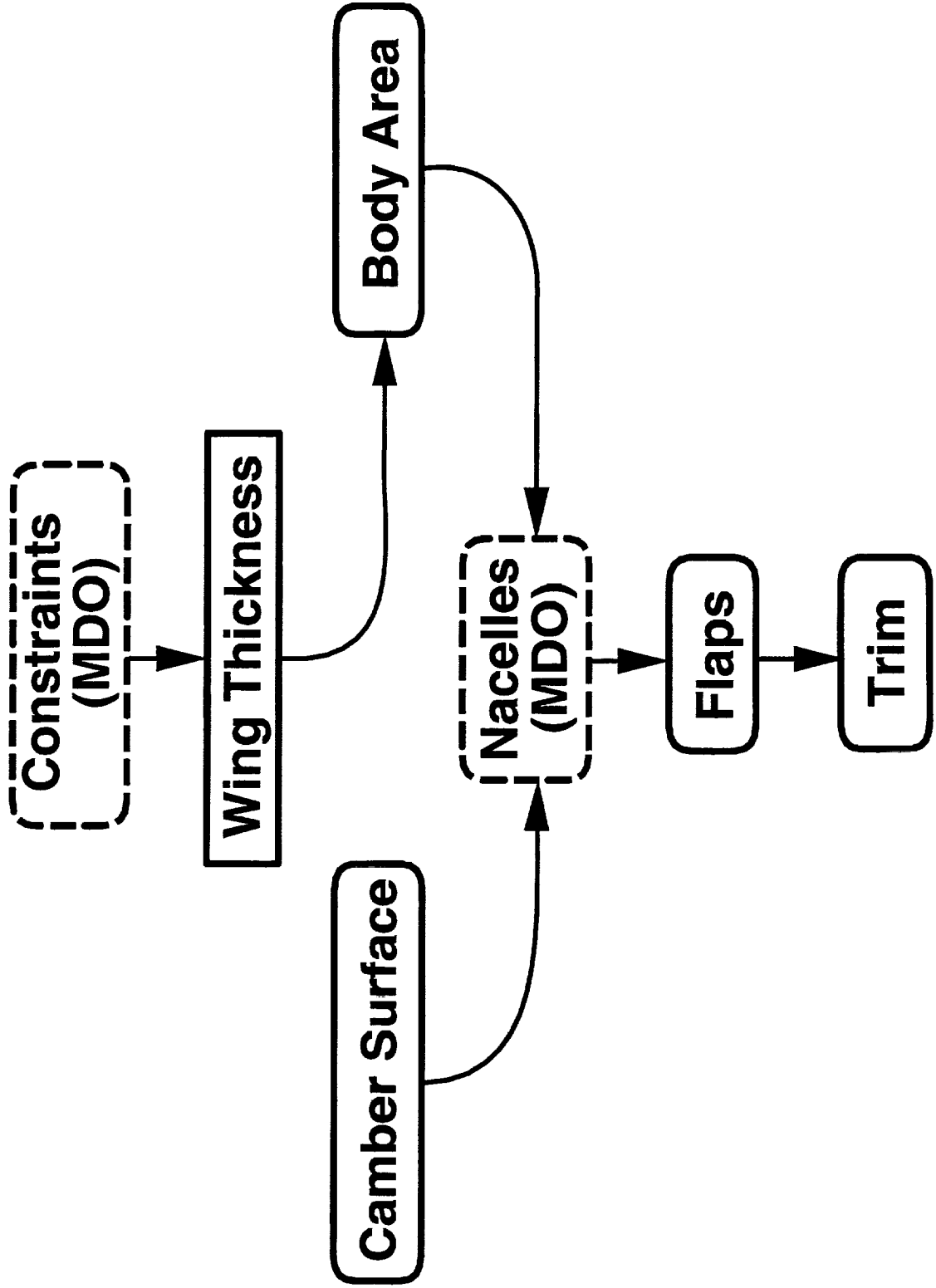
HSCT High Speed Aerodynamics - BCAG



This page is intentionally blank.



The Linear Design Process Is Tool-Defined





HSCT High Speed Aerodynamics - BCAG

February '98 HSR Airframe Technical Review



The Baseline Nonlinear Design Process Will Also Be Tool-Defined

It should be apparent from the discussion of the linear optimization process that not only is the new baseline nonlinear optimization process undefined, but to a real extent, it will not be defined any time soon. All that can be done at this time is to establish a starting point and begin the task of developing the process from that beginning. Discussions on this issue during the development of this year's detailed plan and while preparing for this meeting have provided some guidelines and educated guesses being used now.

The new process will be a nonlinear counterpart to the current linear optimization process. Clearly, it will not be just a copy of the linear process using nonlinear tools. It will instead be largely defined by the strengths and capabilities of the nonlinear tool, which to a certain extent have yet to be explored. It will be further refined by the experience that has and will continue to be gained as this work proceeds into the years ahead.

What is proposed on the following figure is the current working proposal of this group. It will no doubt change with time and as additional understanding and/or experience is gained. Some of the guiding principles are listed here. The proposed process is viewed as a minimum requirement. It can be made more complex, but given the limited resources, the goal is to determine and then limit the exercise to the minimum. As indicated earlier in this presentation, it appears that this is the appropriate time to incorporate longitudinal trim into optimization. It also appears that this should be a common trait between multi-point and the baseline process. And finally, the process should be easily defined as sequence of discrete steps. The goal is a robust, reliable, portable process to support the multiple uses that will be required during the trade studies of preliminary design.

The specific metric for the evaluation of a given design, or in this case, a design by a given process is based on a result of having asked and answered this question many times in the past several years. Experience has shown the total system efficiency, generally measured in terms of takeoff gross weight, is given by the weighted sum of the drag values at the three evaluation conditions noted in the last figure. The weighting factors are configuration specific and are given to CA by TI.



The Baseline Nonlinear Design Process Will Also Be Tool-Defined

- **Nonlinear counterpoint to current linear process**
 - **Current working proposal**
 - **Initial, minimum problem**
 - **Trimmed at all conditions**
 - **A sequence of discrete steps**
 - **Total efficiency = weighted sum of objective function at evaluation conditions**
- **Minimum requirement for evaluation of full multi-point process**



The Proposed Baseline Nonlinear Process Is a Hybrid

The current working proposal for a baseline nonlinear optimization process is actually a hybrid approach. It is, as this presentation has attempted to explain, an educated guess at how the actual preliminary design group will attempt to bring the power of nonlinear tools to bear on the multidisciplinary trade studies central to preliminary design.

The process has the four sequential steps shown in this figure. Not shown is the previously noted position that all conditions and steps will be trimmed. There is also a step 0 that is not shown here. A starting configuration will be created with some version of the current linear optimization process. This appears to be the most efficient way to start the process. So, step 1 is the same supersonic cruise point optimization that the community has been doing for years now. This step will establish the basic wing geometry and will provide a better starting point for the body area ruling to be accomplished in step 2. Step 2 addresses the issue of transonic acceleration, and is a body area tune-up and the transonic flap setting optimization. The proposal is to use a two condition multi-point optimization of the body area variables. Flaps will be active at the transonic acceleration condition so that prescribed lift can be used. Again, the body design and the transonic flap deflections will be established in step 2. Step 3 just determines the optimum flap deflections for the subsonic cruise condition. Finally, step 4 provides the drag of the trimmed analyses of the three conditions for evaluation in the weighted sum.

One of the strengths of this proposed baseline process is that it provides all the pieces needed for the full multi-point process, including a simple multi-point optimization to warm up on.



The Proposed Baseline Nonlinear Process Is a Hybrid

- 1. Supersonic cruise point optimization**
- 2. Transonic acceleration**
 - **Body area tune-up**
 - **Supersonic multi-point, 2 conditions**
 - **Body area @ supersonic cruise**
 - **Body area (& flaps) @ transonic acceleration**
- 3. Subsonic cruise**
 - **Flaps only**
- 4. Trimmed analysis of final geometry at the three conditions**



HSCT High Speed Aerodynamics - BCAG



The Multi-Point Process Is Well Defined

The true, full, nonlinear multi-point optimization process is outlined in this figure. As with the baseline process, this is proposed to be the minimum yet sufficient problem to evaluate the potential benefit of multi-point optimization.

As shown, the problem uses the same three flight conditions as the baseline process. The full variable set currently used for cruise point design will be active for all three conditions. In addition, flap deflections will be used at the transonic and subsonic conditions. The optimization will be trimmed at all conditions. Then, just as with the baseline process, trimmed analyses of the final geometries will be performed to provide inputs to the same weighted sum formula. This is then compared to the baseline value, providing the initial evaluation of the benefit of multi-point optimization.



The Multi-Point Process Is Well Defined

- Three conditions - all trimmed, simultaneous

1. Supersonic cruise
2. Transonic acceleration
3. Subsonic cruise

(Trimmed analysis of the resulting three conditions)

- Same weighted sum of the three trimmed analyses
- Value of multi-point = difference of total efficiencies



The '98 Plan Is Well Defined

The plan for the remainder of '98 is outlined here. Not surprising, it is a continuation of the same activities. The foundational capabilities in viscous and trimmed optimization will be pursued. Once trimmed optimization capability is in hand, efforts will be directed at accomplishing the new, proposed baseline optimization, both in terms of building the process and obtaining the baseline value. This implies solving the current difficulties with flap optimization. Viscous effects will be used to the extent their value is demonstrated, and the schedule permits.

With the very recent completion of the viscous inlet flow quality tune-up optimization and its impressive success, this technique will likely be applied to another similar problem, rather than continue on inlet flow quality. The highly viscous flow around the nacelle/diverter region is a likely candidate.

A post-optimization, active constraint sensitivities capability will be developed and a complete optimization will be performed to attempt to validate one of the more interesting results produced by this capability. TI will be used heavily to help chose the sensitivity to validate.

Finally, if a miracle occurs and this all turns out to be a lot easier than it appears at this point, the capability to begin the full multi-point optimization will be applied to the problem. This is not predicted for '98. Efforts to date indicate that the plan is ambitious, and few if any miracles have occurred this far.



The '98 Plan Is Well Defined

- Viscous optimization
- Trimmed optimization
- Baseline nonlinear optimization
 - Process
 - Result
- Inlet flow quality tune-up optimization
- Sensitivities to constraints
- (Multi-point optimization)



There Are Outstanding Issues

There are several issues which appear to offer opportunities to improve the coordination within the optimization community and within the larger HSR community. These are listed here for a brief discussion.

The collective we should be able to gain more benefit of other's work on optimization if the same configuration is used. It appears that the TCA will serve this need, except for a canard and the correspondingly resized horizontal tail. A common variation on the TCA with a current PTC tri-surface definition would address this issue.

The experience with TCA cruise point optimization seems to indicate that to the resolution of the current tools, there are multiple solutions to the constrained problem. Knowing whether the differences are additive, mutually exclusive, or some combination would be useful if not beneficial.

Between the addition of new components and the accompanying degrees of freedom, and the questions raised as a result of the TCA cruise point optimizations, there appears to be a need for enhancements to the constraint set. To the extent that a new, common configuration would be useful, a new, common constraint set would also be useful.

Since the community has chosen not to incorporate aeroelastic effects directly into optimization, there is no direct experimental validation data for longitudinal trim results. This appears to be an acceptable technical position at this time, but it does mean that a coordinated analytic effort is required if this is to become a capability of the community rather than another source of uncertainty.

Some measure of the analytic uncertainty of the community was provided by the optimized TCA cross check calculations. Is this acceptable or should some of the evermore precious resources be directed at reducing the uncertainty?

Finally, and of least significance, it would improve the efficiency of communication of multi-point issues if there were some official definition of the names of the conditions of interest. This is common practice in fighter design.



There Are Outstanding Issues

- A common configuration for remaining optimizations
- Local minima
- Constraint set refinement
- Validation of rigid trim results
- Cross check uncertainties
- Flight condition nomenclature confusion

February '98 HSR Airframe Technical Review



HSCT High Speed Aerodynamics - BCAG



This page is intentionally blank.

**SYN107-MB AERODYNAMIC SHAPE OPTIMIZATION
METHOD: RECENT IMPROVEMENTS AND CURRENT
STATUS**

<i>James Reuther</i>	RIACS/NASA Ames
<i>Mark Rimlinger</i>	Sterling Software/NASA Ames
<i>David Saunders</i>	Sterling Software/NASA Ames
<i>Raymond Hicks</i>	MCAT/NASA Ames

February, 1998

SYN107-MB AERODYNAMIC SHAPE OPTIMIZATION METHOD: RECENT IMPROVEMENTS AND CURRENT STATUS

James Reuther, RIACS/High Speed Research Branch, NASA Ames
Mark Rimlinger & David Saunders, Sterling Software/High Speed Aerodynamics Branch, NASA Ames
Raymond Hicks, MCAT/High Speed Research Branch, NASA Ames

February 1998

This presentation provides an overview of the improvements and developments that have been incorporated into the aerodynamic optimization capability at NASA Ames Research Center. The main Aerodynamic Shape Optimization (ASO) tool, SYN107-MB, will be discussed with attention to enhancements over the past year. Dr. James Reuther continues to work at RIACS and is devoting much of his time to developing and supporting ASO research needed for the HSR Program. Mark Rimlinger is finishing his Ph.D. from Carnegie Mellon University while concurrently being employed by Sterling Software. He performs most of the multiblock grid generation for the High Speed Aerodynamics Branch at Ames, and has implemented several multiblock grid utilities including the UV procedure which determines (u,v) maps for the surface grids and the MSPLINE tool which changes mesh density in any two of the three index directions. David Saunders, also employed by Sterling Software, is working on the development version of the AEROSURF geometry paneling subsystem following several years of supporting the single-block design code, SYN87-SB. Ray Hicks (recently retired from NASA but continuing to support the HSR Program as an MCAT employee) is well known as a proponent and user of CFD-based design-by-optimization tools. He has most recently been performing the initial applications of SYN107-MB to a comparison of axisymmetric and bifurcated nacelles on the TCA-6 configuration, and making systematic gradient comparisons.

In addition to the work of these four authors, significant contributions to the continuing development of SYN107-MB have been made by Juan Alonso and Antony Jameson of Princeton University (now both at Stanford University), and by John Vassberg of The Boeing Company.

Outline

- **Preliminary Navier-Stokes Design Capability (SYN107-MB)**
- **AEROSURF Geometry Interface**
- **Improvements in Multiblock Mesh Motion**
- **Improvements in Parallel Performance and Communication**
- **Gradient Checks for Transonic Flows**
- **Gradient Checks for Supersonic Flows**
- **Navier-Stokes-Based Constrained Design Example**
- **Future Developments**

Preliminary Navier-Stokes Design Capability (SYN107-MB)

The primary enhancement to the aerodynamic shape optimization capability has been the replacement of the Euler solver with its Navier-Stokes counterpart. (Inviscid solutions remain an option, of course.) Initially, this has been done without the addition of a viscous adjoint solver. Thus only a limited Navier-Stokes design capability is possible. However, for problems of engineering interest, where the objective is to get somewhere near the minimum for an acceptable cost, the Euler adjoint solver certainly helps.

The multiblock N-S flow solver FLO107-MB developed by Intelligent Aerodynamics International replaces the Euler solver FLO87-MB. It is a general multiblock flow solver that allows arbitrary topologies though point-to-point matched meshes. A double halo is used to retain a complete stencil for both the convective and dissipative fluxes across the block boundaries.

One of the great advantages of FLO107-MB is that it is implemented to take advantage of current parallel computing technologies. It is constructed such that it may use any number of processors up to the number of blocks within the mesh to be used. A preprocessor is run to divide the blocks among the available processors in such a way as to load-balance the problem as well as possible. The communications between blocks that are outside a given processor are treated using the MPI standard routines that are now supported on most systems. Ports to the IBM SP2, SGI Origin2000, CRAY J90 and C90, and HP architectures have all been readily accomplished.

Preliminary Navier-Stokes Design Capability (SYN107-MB)

- **Flow Solver (FLO107-MB)**
 - **RANS Equations**
 - **Multiblock Meshes**
 - * Point-to-point matched grids
 - * Cell-centered scheme
 - * Double halo around all blocks
 - **Parallel Decomposition**
 - * **MPI** message passing for portability
 - * Domain decomposition along **block boundaries**
 - * Design on **parallel computers or workstation networks (IBM SP2, SGI Origin2000, CRAY J90 & C90, HP architectures)**

Preliminary Navier-Stokes Design Capability (SYN107-MB), *continued*

The multiblock flow solution algorithm is an extension of the existing single-block Euler and Navier-Stokes algorithms pioneered by A. Jameson and L. Martinelli. As such it retains many features of its heritage. The time stepping is done by a multistage Runge-Kutta-like algorithm, where in the case of multiblock meshes the residuals are updated along the double fringe at each stage. The spatial discretization is a standard cell-centered finite volume scheme. Two dissipation schemes are available: the original blended 1st- and 3rd-order difference scalar dissipation scheme and the newer CUSP dissipation scheme. Convergence is accelerated with both implicit residual smoothing and full multigridding. Each coarser level within the multigridding retains the same double halo construction so that the speed-up realizable via the multigridding should not be hindered by the block boundaries.

The Baldwin-Lomax turbulence model has been implemented, with the Spalart-Allmaras model and Menter's two-equation SST model currently under development.

- **Solution Algorithm**
 - * **Runge-Kutta** explicit time-stepping
 - * **Cell-centered** finite volume spacial discretization
 - * **1st and 3rd order** blended **scalar** dissipation
 - * **CUSP** dissipation
 - * **Residual smoothing**
 - * **Multigridding**
- **Turbulence Models**
 - * **Baldwin-Lomax**
 - * **Spalart-Allmaras** (under development)
 - * **Menter's SST 2-equation** model (under development)

Euler Adjoint Solver (ADJ87-MB)

The adjoint solver in SYN107-MB is unchanged from that of SYN87-MB except that a few bugs have been corrected and support for additional cost functions has been included. ADJ87-MB is based on the Euler equations and hence does not account for changes in the cost function due to viscous effects. The lack of a viscous adjoint solver corresponding to the viscous flow solver has various important implications. First and foremost is the fact that the use of an Euler adjoint is mathematically inconsistent with a cost function evaluated via a set of viscous governing equations. Therefore, it is impossible to obtain gradients from this approach that match those obtained using finite differencing. However, for problems of engineering interest, the objective is not necessarily to find the true optimum at all cost, but to get within a reasonable vicinity of the minimum for a cost that is acceptable.

It is interesting to note that other design approaches also tolerate a similar inconsistency for reasons of engineering interest. Quasi-inverse design methods such as those used by Campbell assume a relationship between the pressure distribution and the local surface curvature. This relationship effectively provides an inconsistent gradient in order to obtain improved designs. These approaches, which may be applicable for a small sub-class of problems, are likely to fail in situations where the heuristic assumptions used to obtain gradient information cease to be valid.

With these ideas in mind, it is important to consider both the advantages and the limitations of the present design technique. If the aerodynamic figure of merit to be minimized has a direct dependence on viscosity such as through the friction drag, the approach is rendered invalid since the inviscid adjoint system lacks direct sensitivity to viscosity. However, for problems in which viscosity plays an indirect role the proposed design technique is bound to produce useful results. Some important aerodynamic shape optimization problems fall into this latter category. Take for example the problem of pressure drag minimization for commercial transport aircraft. Without breakthroughs in either laminar flow control or turbulent skin friction reduction technologies, most of the aerodynamic performance improvements attainable for a given configuration can be achieved through pressure drag minimization (both induced drag and wave drag). In addition, since the pressure gradient normal to a viscous boundary layer for aircraft at cruise conditions is negligible, the pursuit of inviscid methods for aerodynamic shape optimization has yielded moderate success.

However, inviscid design methods must be used cautiously even for inverse pressure distribution or pressure drag minimization problems, since the viscous effects will indirectly alter these quantities. The most noticeable effect is due to the boundary layer displacement thickness. The magnitude and importance of the effective changes in wing shape caused by the presence of the boundary layer depend on the flow field in question, and generally become more pronounced under transonic conditions. The position and strength of shock waves as well as the level of pressure recovery at the trailing edge can be strongly impacted by the existence of a boundary layer. In transonic flow, it is thus highly desirable to take viscous effects into account when designing the aerodynamic shape of a wing to minimize pressure drag. Also, when the effect of the boundary layer on the outer flow couples very strongly, as is the case at transonic buffet or at maximum lift coefficient conditions, the ability to perform meaningful design without a viscous adjoint can be questioned.

The **basic algorithm** to solve the Euler-based adjoint equations follows the strategy employed to solve the N-S equations in SYN107-MB. The N-S multiblock mesh is used by both solvers, with the same parallel decomposition and similar solution algorithms. The **cost functions** permitted, either alone or in combination, are C_D at fixed α , C_D at fixed C_L , L/D at fixed α , target C_{ps} , and C_M constraints.

- **Adjoint Solver (ADJ87-MB)**
 - Adjoint Based on Euler Equations
 - Multiblock Implementation - Same as FLO107-MB
 - Parallel Decomposition - Same as FLO107-MB
 - Solution Algorithm - Same as FLO107-MB
- **Cost Functions**
 - CD at Fixed Alpha & CD at Fixed CL
 - L/D at Fixed Alpha
 - Target Pressure Distribution
 - CM Constraint

Mesh Motion (WARP-MB)

The multiblock approach to mesh deformation, even in the presence of Navier-Stokes meshes, is similar to that of SYN87-MB (see last year's "Development and Validation of a Multiblock Adjoint-Based Design Method") but it has recently been enhanced to overcome possible limitations of on the size of the perturbations, as will be discussed below.

Design Variable and Constraint Treatment

In order to accommodate geometry changes and impose geometric constraints on an arbitrary aerodynamic configuration, a general methodology has been developed. Available choices for the design variables span a wide spectrum, ranging from employing the locations of the actual mesh points to relying on the analytic control points used in a CAD definition of the geometry.

In the case of using the actual mesh points, no underlying geometry database exists. Constraints, if present, must be imposed directly on the locations of these mesh points. This approach will surely prove problematic in general. Consider, for example the difficulties involved in the imposition of a wing fuel volume constraint. In addition, the treatment of surface intersections (such as the wing-body) raises difficulties for this approach since the path for the motion of the mesh points lying directly on these intersections is ill-defined. However, an advantage of using the mesh points as design variables is that, when combined with an analytic mesh mapping transformation, the calculation of the gradient can be performed without explicitly computing the variations in the mesh metrics. Unfortunately, obtaining such a general mapping transformation increases in difficulty with added geometric complexity.

The alternative of using an underlying geometry database, which may be modified either by the direct application of design variables or by changes in the coefficients of its possibly analytic definition, also has its advantages. First, since the raw unintersected geometries are available, constraints and design changes affecting intersections are easily treated. This can be done without regard to the actual mesh that is used for the flow and adjoint calculations. However, these strengths are counterbalanced by the fact that additional computational work is required to calculate the mesh metric variations.

In the current research, we have used an **underlying geometry database** where a set of simple geometric entities (wings, nacelles, fuselage, etc.) are input to the design algorithm in addition to the multiblock mesh used for the calculations. **Design variables** which are defined as a set of analytic shape functions are applied directly to these geometric entities. Linear and nonlinear geometric constraints are then evaluated on these primary entities. At any particular point in the design process, changes to the mesh surfaces are obtained by first intersecting all of the geometric entities to perform these functions will be described below. The location of each surface configuration. The **AEROSURF** subsystem used to perform these functions will be described below. The location of each surface mesh point on this parametric patch representation of the geometry is determined for the initial configuration in a pre-processing step (the **UV procedure**). Thus, a (u,v) map from the patched geometry to the computational surface mesh points is also a part of the necessary input. The perturbed surface mesh point locations are determined by **evaluating the parametric geometry patches** at these predetermined locations. Once the surface mesh points have been updated, the volume mesh may be perturbed (see following section on mesh motion) and either the solution or the gradient can be calculated. The important feature of this approach is that a set of simple geometric entities lies at the core of the entire design process. This technique retains the typical way in which aerodynamic vehicles are defined, and provides strict control over how surface intersections are treated. Furthermore, since the chosen design variables act directly on the geometric entities, at the end of the design process these entities may be output for future analysis.

- **Mesh Motion (WARP-MB)**
 - **Faces, Edges and Corners** of all Blocks Automatically Moved
 - Independent (Parallel) Internal Block Perturbations (**WARP3D**)
- **Design Variable and Constraint Treatment**
 - Arbitrary Number of Basic Geometry Entities (Wings, Nacelles, Fuselage, etc.)
 - **Design Variables** are Applied Directly to **Geometry Entities**
 - Geometric Constraints are Calculated
 - Perturbed Geometry Entities are **Automatically Intersected**, and Interpolated as **Parametric Surface Patches (AEROSURF)**
 - Perturbed Surface Mesh is Obtained via **Parametric Interpolations** within **Perturbed Patches**
- **Optimization Algorithm (NPSOL)**
 - **SQP** Method
 - **Linear** Constraints Always Enforced
 - **Nonlinear** Constraints Enforced at Design Convergence

Optimization Algorithm (NPSOL)

In order to impose geometric constraints, the multiblock approach was coupled to the constrained nonlinear optimization package of Gill, Murray, Saunders and Wright. NPSOL implements a sequential quadratic programming (SQP) method that requires relatively few function and gradient evaluations. Search directions for both primal and dual variables (the design variables and Lagrange multipliers for the nonlinear constraints) are computed by solving a quadratic program (QP). The QP Hessian is a quasi-Newton approximation to the Lagrangian, and the QP constraints are linearizations of the original constraints (including all linear constraints, which are satisfied throughout). The step length is chosen to reduce an augmented Lagrangian merit function involving the primal and dual variables. SQP methods and other optimization strategies are discussed in *Practical Optimization* by Gill, Murray, and Wright. A complete treatment of the NPSOL algorithm and its merit function are given in the *NPSOL User Guide* and a related reference by Gill, Murray, Saunders, and Wright: "Some theoretical properties of an augmented Lagrangian merit function", in *Advances in Optimization and Parallel Computing*, P. M. Pardalos (ed.).

AEROSURF Geometry Interface

The AEROSURF geometry engine serves the role of taking a set of simple, unintersected geometry entities (wings, nacelles, fuselage, etc.), intersecting them, and paneling the results to form a parametric patched representation of the geometry. The design process is then keyed to the fact that this patched representation is always constructed in an identical fashion for each shape perturbation as the design proceeds. Thus the parametric surface patch representation is the primary interface between the overall design algorithm and the CFD analysis utility. On the design side are the optimization algorithm, the method of applying design variables, and the method of calculating constraints. All this work is performed not on a complex CFD mesh but directly on a set of simple geometry entities. On the CFD analysis side we have the mesh morphing method, the flow solver, and the adjoint solver.

The following flow chart depicts the central role of the geometry representation.

AEROSURF Geometry Interface

- **Basic Approach**
 - **Geometric Surface Representation Serves as Interface between Design Algorithm and CFD Analysis**
 - Design Algorithm Includes
 - * Optimization algorithm (NPSOL)
 - * Application of design variables to **simple geometric entities** (wings, nacelles, fuselage, etc.)
 - * Calculation of **geometric constraints**
 - CFD Analysis
 - * Mesh deformation
 - * Flow solution
 - * Adjoint solution

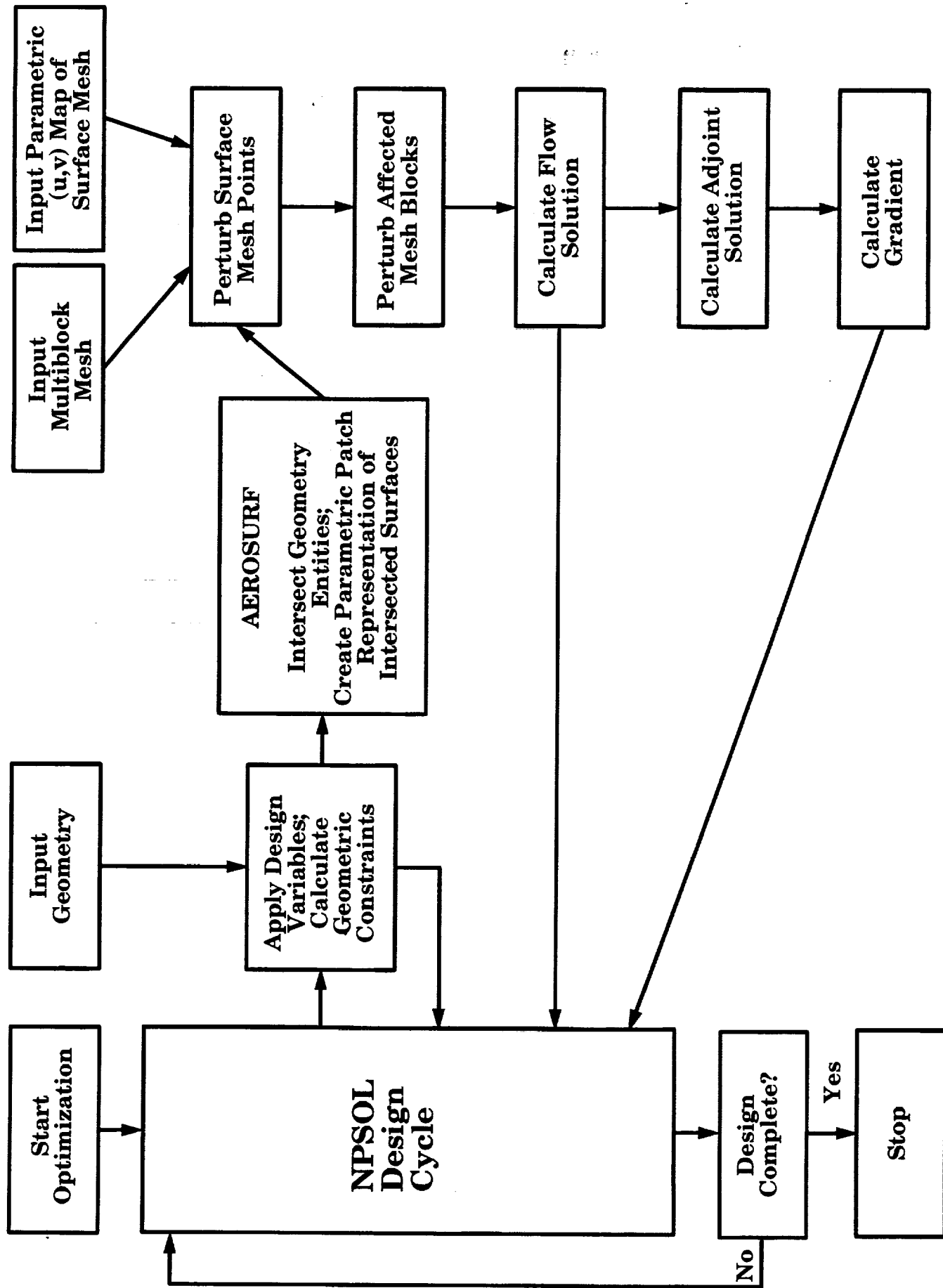
SYN107-MB Flow Chart

As indicated above, the new AEROSURF geometry engine serves as the interface between the shape optimization algorithm and the CFD-based calculation of the cost function and its gradient with respect to the design variables. The shape changes are applied to the underlying geometry entities, not the computational surface grid. Every change in one or more of the design variables (as part of a gradient calculation or during a search along a calculated step in the design space) leads via **AEROSURF** to reintersecting the geometry components, and repaneling of the intersected surfaces as parametric patches from which the computational surface grid is recalculated by bidirectional parametric interpolation at the (u,v) points representing the initial surface mesh.

Not shown on the chart is the pre-processing step performed by the **UV procedure**, which determines this (u,v) map for the initial multiblock grid. In fact, AEROSURF also operates in stand-alone form to provide UV with the patched surface corresponding to the initial CFD grid. For each surface grid point on a given multiblock face coincident with the geometry, UV uses QNMDIF (Gill, et al.) to perform a 2-variable distance minimization within each of the surface (sub)patches specified as being associated with that multiblock face. The result with the shortest distance, over all processed (sub)patches, between the target point and the (x,y,z) evaluated at the optimized (u,v) is chosen for the (u,v) map and is normally below the small tolerance used. Any discrepancies between the patched surface from AEROSURF and the surface grid (probably from GRIDGEN) can lead to difficulties in the UV process. Most of the recent enhancements to UV have been prompted by the need to reduce the number of "trouble" points encountered, particularly for Navier-Stokes applications, such as on the fuselage near the wing root. Extreme cell-skewing in the fuselage surface patch at the root leading edge has also caused difficulties for UV, but the skewing has been eliminated in the development version of AEROSURF via some redistribution in uv space. If necessary, UV can process subpatches as small as one cell. Thus, just a few trouble points typically remain to be (u,v) -mapped interactively by "hand", and the UV process can be considered a solved problem. UV also has an option to deal directly with (trimmed) NURBS surfaces (still missing from AEROSURF). Nevertheless, the difficulties encountered with mapping troublesome points on regular (quadrilateral) patches have prompted consideration of 3-point methods. The minimum-distance calculation for a point and a triangle has a direct solution via linear least squares techniques, while triangulated surfaces have their advantages and disadvantages. Time will tell; for now, there are more pressing issues.

Further details of the enhanced AEROSURF and WARP-MB procedures follow below.

SYN107-MB Flow Chart



Current AEROSURF Capability

The AEROSURF geometry package currently in SYN107-MB is the first generalization of the original wing/body module, WBSURF. It handles multiple wing-type components and also nacelle surfaces. A wing-type surface can be a canard, tailplane, or body-mounted pylon. A nacelle surface is defined by one or more airfoil-type cuts in cylindrical coordinates referred to the specified centerline. Wing-type intersections with the fuselage and/or nacelles are treated, but under-wing pylons or diverters (requiring wing/wing-type intersections) were not treated initially—more on this below. (Presently, for HSCT applications, the multiblock grid can certainly include nacelles and diverters, but an interim scheme is employed to ensure that their surface grids follow any wing surface perturbations: the vertical motion of each nacelle/diverter grid point is determined from the motion of its projection onto the wing, which may result in some distortion of the nacelle shapes.)

The present implementation does address an issue initially overlooked: that of forcing 4 patch edges at every corner. The simplest illustration of this is the fuselage nose patch: unless a patch boundary is forced forward from the wing root leading edge, the parametric scheme for perturbing the surface grid points can produce spurious results, because the body grid point initially at the leading edge is not guaranteed to stay there unless it has a v value of 0 or 1 corresponding to the otherwise-unnecessary patch boundary. In other words, significant topological surface features must not appear at the interiors of patch edges. Consideration of the panel between a wing trailing edge and an aft-mounted pylon indicates, moreover, that the artificial patch boundaries (aft of the trailing edge and forward of the pylon leading edge in this case) are best introduced in a final patch-splitting step after all the initial paneling. This way, paneling above the wing, for instance, does not have to anticipate the split that will be necessary to force an axial edge through the pylon root leading edge. Such a split has to be carried all the way forward to the nose.

Capability of AEROSURF Development Version

The first enhancements of the original AEROSURF package provided for variable patch densities (as opposed to those implied by the input geometry sections), for large dihedral or anhedral on any wing surface (via "roll" angles associated with the normal sections— 90° in the case of TCA-6 diverters, for instance, or maybe less for winglets), and for capturing specified cranks in the leading or trailing edges of wing-type surfaces.

The extension needed for proper handling of HSCT-type nacelle/diverters has proved much more arduous than anticipated, partly because of indefinite point counts on the wing/diverter intersection curves, and because of the need to work in parametric space—i.e., many patch edge distributions were needed as (u,v) coordinates, not (x,y,z) s. The problem of "off-the-trailing-edge" wing/diverter intersections was treated via temporary extension of the wing surface to ensure a full intersection, followed by forcing of wing trailing edge points in the intersection curves. The point counts along opposing sides of adjacent diverters are also forced to match. Likewise, the portion of the wing/body intersection opposite the inboard diverter has to be updated to match the on-wing point count of that diverter intersection. The approach taken was to include diverter centerlines among the specified wing cranks, thus capturing those features in the initial plain wing paneling, which is then repaneled around the diverters.

The wing/body intersection protection first implemented in SYN87-SB (single-block design code) has also been incorporated in AEROSURF (i.e., modifying body sections as necessary using the wing geometry and a small safety margin). At the time of writing, the main loose ends are how to close the diverters on the aft nacelle surfaces, and updating the patch-splitting scheme (above).

- **Current AEROSURF Capability**
 - Arbitrary Geometry Inputs (**Wings, Nacelles, Fuselage**)
 - Wings Include Tails, Canards, Pylons, Winglets
 - Geometry Inputs Point are Definitions (**Body & Airfoil Cuts**)
 - **Intersection Capability Includes Wing/Fuselage and Wing/Nacelle**
 - Automatic Surface Meshing as Parametric Patches
- **Capability of AEROSURF Development Version**
 - **Wing/Wing Intersections** (e.g. Wing/Diverter)
 - Corresponding Paneling of Wing Around Pylons/Diverter
 - Wing-Below-Body Intersection Protection
 - Loose End: Closing of Diverter on Aft Nacelles
- **Long Term Goal (AEROSURF II)**
 - **NURBS Surfaces as Input Geometry Entities**
 - **NURBS Control Points as Design Variables**
 - **NURBS Entities are Trimmed to Form Parametric Representation of Intersected Surfaces**

Long Term Goal (AEROSURF II)

While the UV mapping preprocessor has the option to work with trimmed NURBS surfaces, this ideal for interfacing with CAD systems remains on the wishlist for AEROSURF and the rest of SYN107-MB's geometry manipulations (shape perturbations and geometric constraints). The present technology for gridding surfaces defined by smooth, discretized sections is thoroughly refined and extremely efficient, as it must be for repaneling of arbitrary configurations hundreds of times in a typical design run. NURBS-based analogues of all the utilities currently in use are likely to be either less efficient or still in need of implementation, or both.

A reasonable first step in this direction would be to work with the sections in the form of NURBS curves rather than surfaces. This is not inconsistent with fabrication considerations for the "simple" (i.e., unintersected) geometry entities currently treated with AEROSURF. The tools for manipulating airfoil-type cuts at NURBS curves have already been implemented at Ames. In fact, the OAW-3 Oblique All-Wing transport design designed at Ames was provided to CAD/CAM in NURBS curve form for model construction. A key simplifying step involved ensuring that all sections of the surface employed the same knot string, thus facilitating lofting between defining sections via standard interpolations applied to their control points.

Whichever steps are taken to improve the CAD/CFD and CFD/CAM interfaces, they are destined to take second priority to more pressing requirements of the HSR Program.

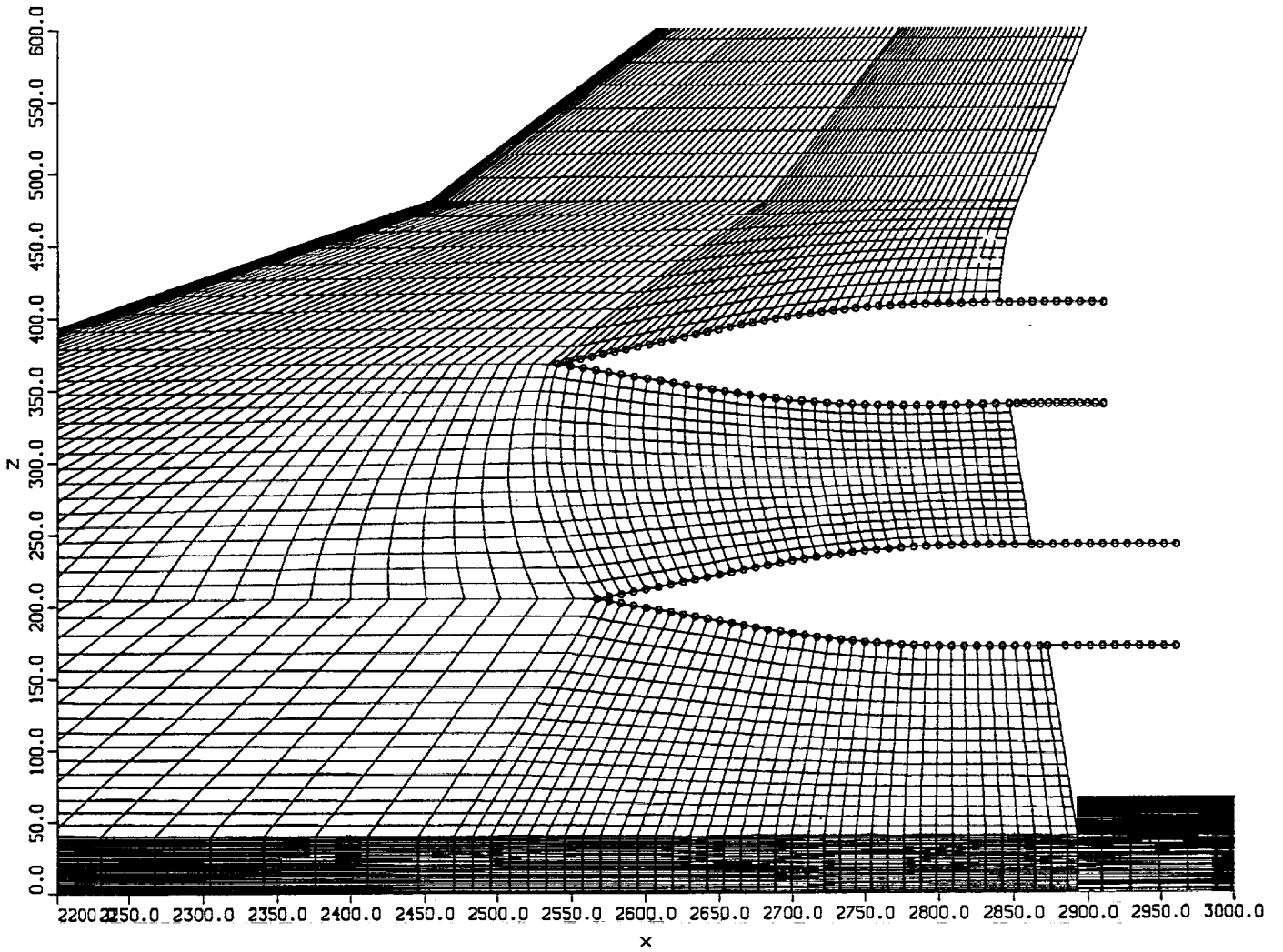
AEROSURF Example

The accompanying illustration shows details of the patched surfaces generated by the development version of AEROSURF around the TCA-6 diverters. All surface interpolations are parametric. The off-the-trailing edge portions of the diverters are deliberately of different lengths in order to check the point-count matching of the on-wing portions between the diverters. AEROSURF handles one or more such diverters, or conventional pylons forward of the trailing edge.

It should be made clear that, since the parametric patches are not the computational block faces seen by the flow and adjoint solvers, there is no need for smooth variation across patch boundaries. Regular paneling with adequate fidelity and high efficiency are the only crucial requirements.

AEROSURF Example

Parametric Surface Patches Around TCA-6 Diverters



Multiblock Mesh Motion Improvements

The multiblock mesh perturbation scheme has recently been improved to accommodate larger surface deflections. The original scheme made the assumption that all perturbations could be confined to a single layer or halo of blocks surrounding the configuration. This proved to be inadequate for the design study where the TCA-6 baseline was being optimized with both the axisymmetric and bifurcated nacelles. The short height of the diverters meant the first layer of mesh blocks under the wing were unusually shallow. This was exacerbated by the large deflections called for in the wing shape to capture the benefit of the nacelle/diverters.

Before presenting the fix to the problem, a brief discussion of the **original** multiblock mesh perturbation strategy will be helpful.

In order to perturb the multiblock mesh, two capabilities are required. First, the block corners, edges and faces must be moved in a manner that follows the desired geometric changes and simultaneously retains mesh continuity throughout the domain. The second requirement is to move all the points interior to each block such that the spacing distributions and smoothness of the original mesh are retained. This latter requirement is accomplished by the WARP3D algorithm. Since our current flow solver and design algorithm assume a point-to-point match between blocks, each block may be independently perturbed by WARP3D, provided that perturbed surfaces are treated continuously across block boundaries. The methodology used to achieve the first requirement of maintaining continuity in the blocking structure is given as follows:

1. All faces that are directly affected by the design variables (active faces) are explicitly perturbed.
2. All edges that touch an active face, either in the same block or in an adjacent block, are implicitly perturbed by a simple arc-length-based algorithm.
3. All inactive faces that either include an implicitly perturbed edge or abut to an active face are implicitly perturbed by a quasi-3D form of WARP3D.
4. WARP3D is used on each block with one or more explicitly or implicitly perturbed faces to determine the adjusted interior points.

Note that much of the mesh, especially away from the surfaces, will not require mesh perturbations and thus may remain fixed through the entire design process. Close to the surfaces, many blocks will either contain an active face or touch a block which contains an active face, either by an edge or by a corner. As the design variations affect the active faces, the above scheme ensures that the entire mesh will remain attached along block boundaries. Added complexity is needed to accomplish step (2) since the connectivity of the various edges and corners must be indicated somehow. This task is accomplished with pointers to and from a set of master edges and master corners. During the design calculation, perturbations to any edges or corners are fed to these master edges and master corners which in turn communicate these changes to all connected edges and corners.

To **improve the methodology**, it was necessary for perturbations occurring on "active" faces that are coincident with the geometry surfaces to be cascaded out onto faces that are not coincident with the geometry. This cascading into the domain also had to be done in a manner which continued to ensure the integrity of the multiblock boundaries. The approach settled on is outlined as follows.

Again, "active" corners, edges, and faces are updated directly from surface changes. Then weighted deflections to these active faces are added to "design" faces. These design faces are faces in the multiblock mesh that are not coincident with the geometry surface but are deemed to be close enough to the geometry that they must be perturbed as well. The design faces may be influenced by one or

Multiblock Mesh Motion Improvements

- **Initial Scheme**
 - ("Active") Block Faces, Edges, & Corners Coincident with Geometry Surface are Updated
 - ("Implicit") Faces & Edges Touching but not Coincident with Surfaces are Perturbed via Arc-Based Method
 - Interiors of All Blocks with Either Active or Implicit Components are Perturbed with WARP3D
 - Blocks in the Domain Not Touching the Geometry Remain Fixed

more active faces, via a weighted combination. The edges and corners of each new design face are then averaged with any neighboring design face to ensure consistency. The averaged edges and corners are then used to update the interiors of the design faces. The entire process is then completed as before by computing all "implicit" edges and faces (those touching active or design faces) and updating them via arc-length-based techniques. Finally, WARP3D updates all block interiors as before.

The current improved implementation has the **limitation** that the user must specify the design faces and their influencing sources (active faces). However, research is under way to develop a topology-based strategy to determine the design faces and their sources automatically.

Illustrations of the original and improved mesh perturbation schemes appear below. They should be compared with the first of the three graphics (that of the unperturbed multiblock grid) as well as with each other.

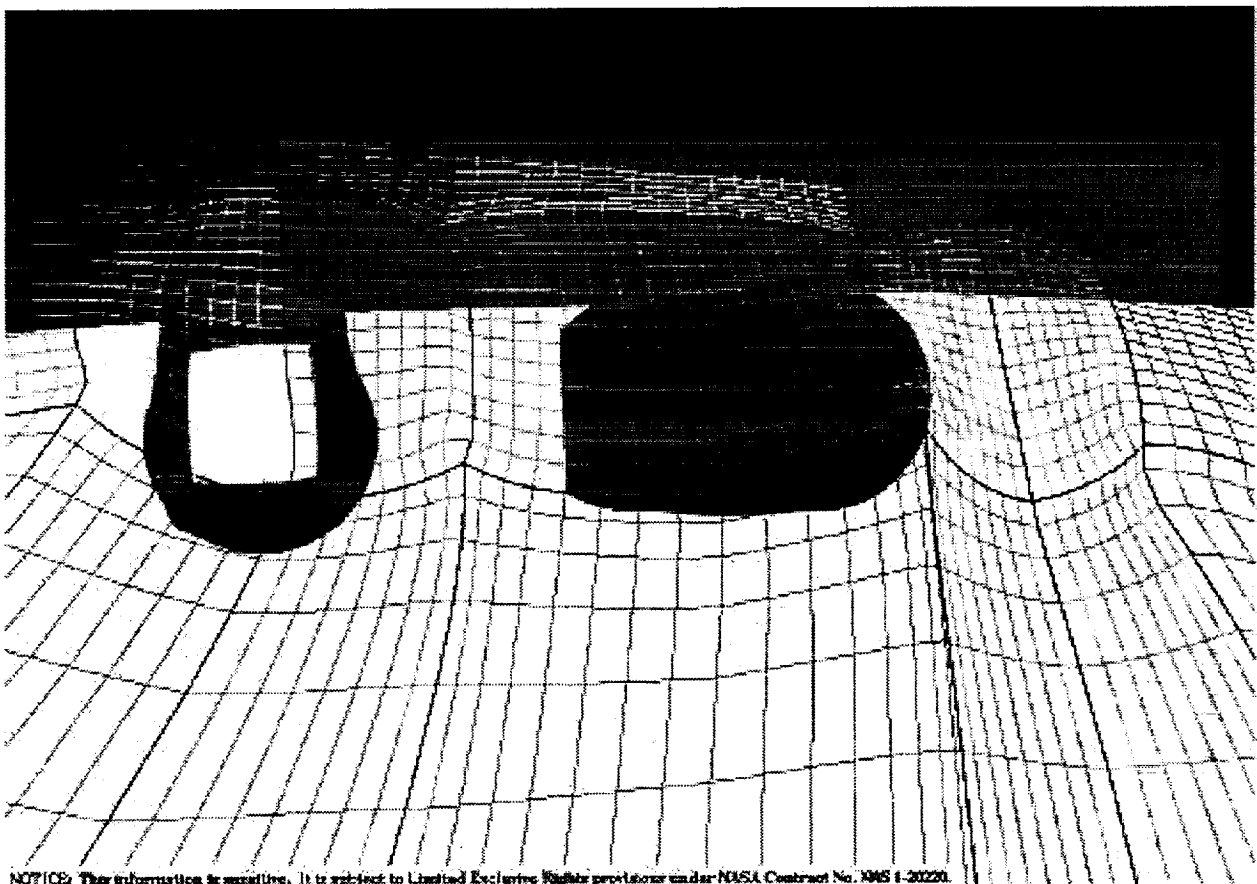
- **Generalized Scheme**
 - (“Active”) Block Faces, Edges, & Corners Coincident with Geometry Surface are Updated
 - (“Design”) Faces Not Touching the Geometry Surface are Updated with Weighted Contributions from Active Faces
 - Edges and Corners of Design Faces are Averaged with Contributions from other Design Faces if Necessary
 - Design Faces are Modified to Reflect Averaged Corners & Edges via Arc-based Method
 - Faces & Edges Touching but not Coincident with Either an Active Face or a Design Face are Perturbed via Arc-Based Method
 - Interiors of All Blocks with Active, Design, or Implicit Components are Updated via WARP3D
- **Mesh Motion Limitations and Future Enhancements**
 - Current Generalized Method Requires User Specification of Design Faces
 - Topology-Based Method is Needed to Determine Design Faces & Weights

TCA-6 Baseline Multiblock Mesh (Unperturbed)

This view shows the initial multiblock mesh for TCA-6 at a certain ~streamwise index forward of the nacelles, superimposed on the shaded nacelle/diverters and part of the lower wing surface, which is also shaded. Some 3-D effects explain part of the apparent warping in the mesh plane. The mesh is also rather coarse and has since been doubled in density in the vertical and axial directions. Note the shallow depth of the top blocks adjacent to the lower wing, forced by the diverter heights. This proved to be the downfall of the original mesh perturbation scheme.

A sample result from the original WARP-MB is shown in the second color graphic.

TCA-6 Baseline Multiblock Mesh



NOTICE: This information is unclassified. It is subject to Limited Exclusive Rights provisions under NASA Contract No. NAS 1-20220.

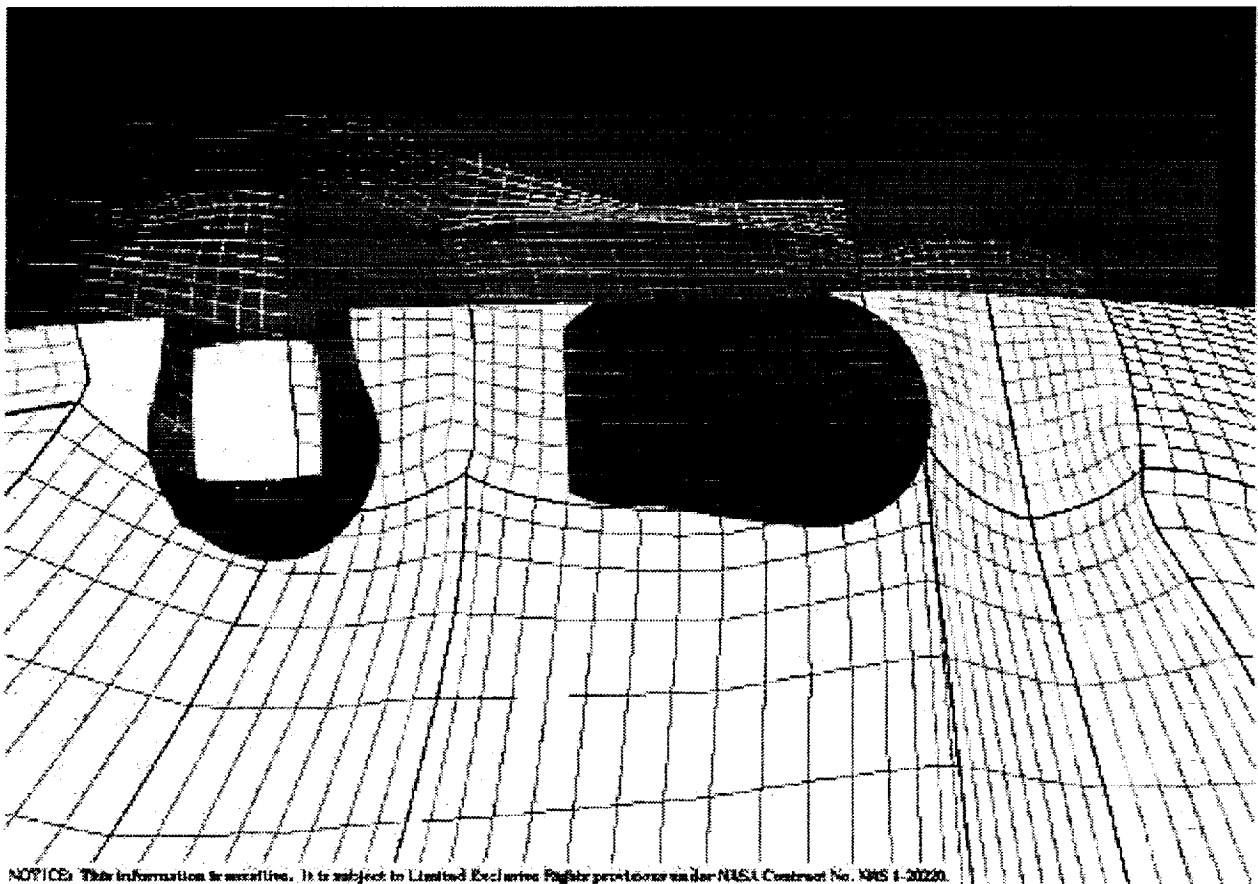
TCA-6 Baseline Multiblock Mesh

Sample Perturbation by the Original WARP-MB (Interim Design with Axisymmetric Nacelles, by Ray Hicks)

This illustration shows one of Ray Hicks's interim results during wing optimization in the presence of the axisymmetric nacelles. It is a less extreme result than others encountered by Ray, some of which violated the original assumption that the first layer of blocks at the surface could absorb all perturbations. Notice that a fairly large bump on the lower wing surface has squeezed the top center block (yellow) while leaving the blocks below that undisturbed. Similarly, the block next to the wing above (forward of) the inboard nacelle has absorbed all of the shape change in that part of the wing by expanding.

The equivalent result for this case from the improved WARP-MB is shown in the third color view.

**Ray's Axisymmetric Design
Old WARP-MB**



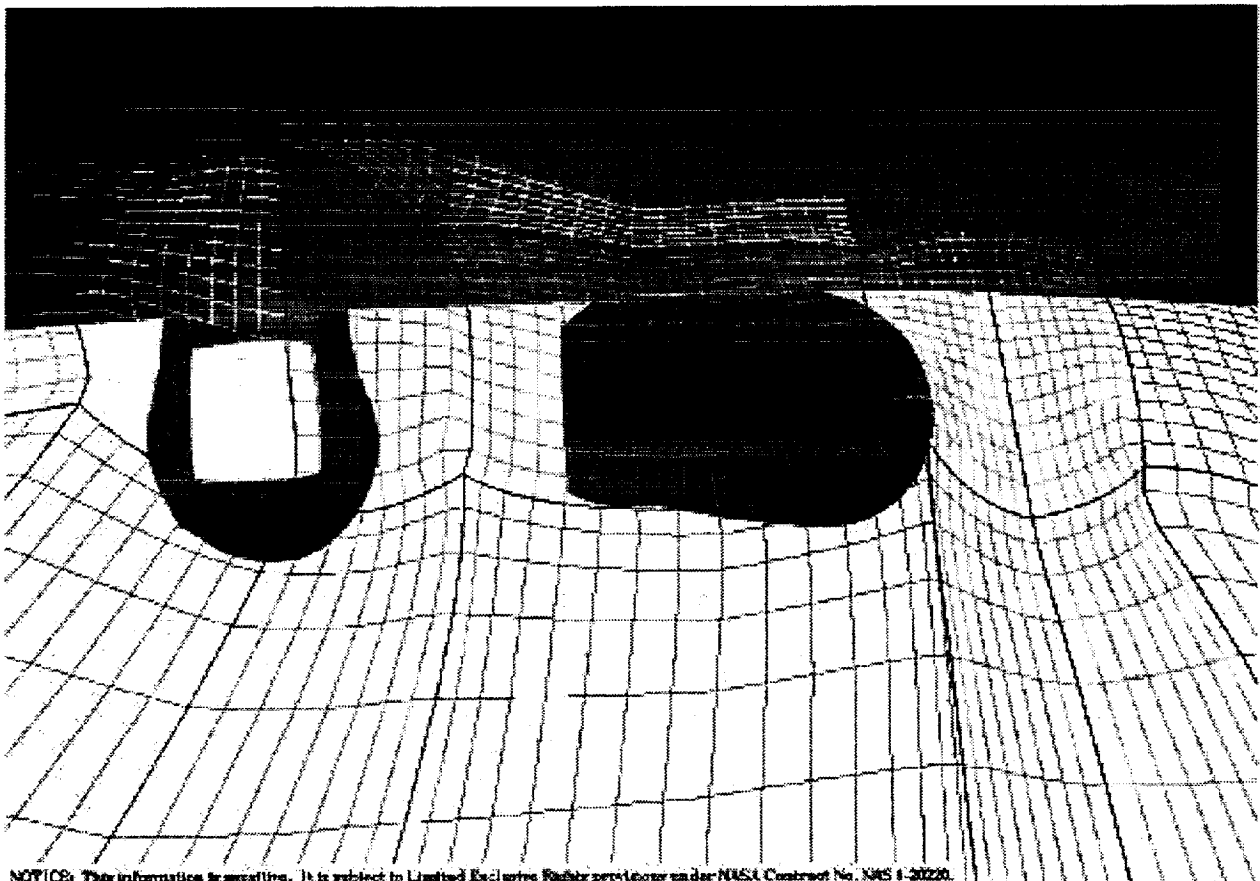
NOTICE: This information is unclassified. It is subject to Limited Exclusive Rights provisions under NASA Contract No. NAS 1-50220.

**Ray's Axisymmetric Design
Old WARP-MB**

Comparable Perturbation by the Improved WARP-MB (Interim Design with Axisymmetric Nacelles, by Ray Hicks)

This illustration shows how the improved mesh perturbation scheme has extended the deflection beyond the first layer of blocks, keeping the depth of the initial layer roughly constant in spite of the significant surface shape change. Evidently, the user-specified "design" faces here were limited to the outer faces of the inner layer of blocks, although another layer could have been specified if necessary.

**Ray's Axisymmetric Design
New WARP-MB**



NOTICE: This information is sensitive. It is subject to Limited Exclusive Rights provisions under NNSA Contract No. NNSA 4-30220.

**Ray's Axisymmetric Design
New WARP-MB**

Improvements to the Parallel Performance and Communication

This discussion outlines the basic (baseline or original) parallel communication scheme then describes recent enhancements. It should be noted that these parallel performance enhancements were achieved by the exhaustive efforts of Juan Alonso and John Vassberg.

The **basic strategy** for parallelizing the multiblock flow and adjoint solvers consists of using domain decomposition, SPMD (Single Program Multiple Data) processing, and the MPI standard library for message passing in portable form. Well-suited to distributed-memory systems such as the IBM SP2, this approach on shared-memory systems is subject to the vagaries of different MPI implementations. MPI appears to be particularly inefficient on the CRAY J90 and C90, for instance, but has not been problematic on the new SGI Origin2000 systems.

Note: The optimization package itself is not parallelized. Its cost is insignificant for hundreds of variables and constraints compared with the cost of a single objective function evaluation..

The baseline parallel scheme is exactly consistent with the serial (single-processor) multiblock solution: the results produced by both programs are identical, including the convergence history of the method. Updates to the solution vector in all processors occur at every stage of the Runge-Kutta time-stepping scheme and in every level of a multigrid W-cycle. In addition, the baseline computations are performed with 64-bit arithmetic. Therefore, flow residuals in the calculation can normally be converged approximately 13 orders-of-magnitude before roundoff effects stall the convergence process. (Grid quality, or lack of it, can affect convergence.)

The multiblock strategy allows the independent update of the internal cells of every block in the mesh by using a halo or ghost cell approach. The information in this halo of cells surrounding each block is transferred from the corresponding physical cells in the interior of the neighboring blocks.

The original scheme utilized a **three-pass communication model** which allows for the computation of solutions on arbitrarily oriented multiblock meshes. Under this model, updated halo information is transferred across the six faces of each block during each phase of the three-pass communication. The first pass transfers face information, the second pass provides edge data, and the final pass is required to update the solution across the block corners. With this three-pass approach, each block is guaranteed to have the proper information in its complete halo (including edges and corners) regardless of the topology of the mesh. This is a particularly challenging situation when more than four blocks meet at a given edge. The double halo is used to compute the 3rd-order artificial dissipation terms while preserving a fully conservative scheme. Although the current discretization of the viscous fluxes requires only a single level halo, future variations which require the presence of a double halo can be accommodated with this procedure.

In addition to the above, the blocks of the baseline solution are distributed to the individual processors in such a manner that the total numbers of grid cells per processor are as similar as possible. While finding the optimum distribution is recognized to be an NP-Complete problem, a simple algorithm is employed which routinely yields a load balancing close to the optimum. The essence of this algorithm is to take the largest of the remaining blocks (yet to be distributed) and assign it to the processor with the smallest current load. Repeating this procedure until all blocks have been distributed, an effective load balance algorithm is obtained.

Improvements to Parallel Performance & Communication

- **Basic Strategy**
 - **SPMD** (Single Program Multiple Data) Strategy
 - **MPI** (Message Passing Interface) Library for Message Passing
 - **Design Algorithm has Five Distinct Modules**
 - * Flow Solver
 - * Adjoint Solver
 - * Geometry Modification and Constraint Calculation
 - * Mesh Perturbation Algorithm
 - * Optimization Algorithm
 - **Block Boundaries in the Multiblock Domain provide Natural Parallelization for the First Four Modules**
 - For the **Flow & Adjoint Solvers, MPI is Used to Update Halo** Quantities at Every Stage of the Time-Stepping
 - For the **Application of Design Variables and Mesh Perturbations** No Message Passing is Needed

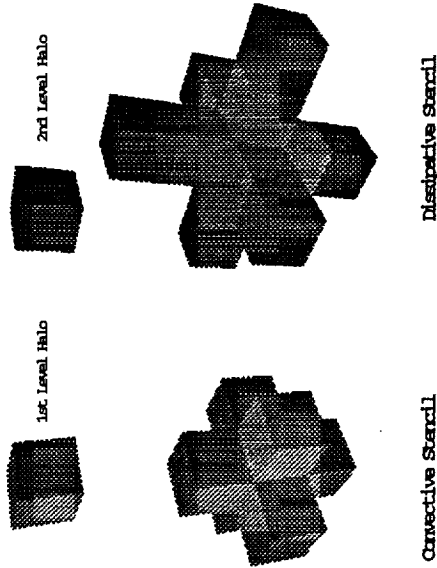
Improvements to the Parallel Performance and Communication, *continued*

The test case used to benchmark the effectiveness of the enhancements described below involves a 72-block grid about a wing-fuselage-nacelle geometry. The total number of cells is 734,976 of which roughly 300,000 are halo cells (a very high proportion). This case was chosen specifically because it accentuates the penalty of communication. Yet, on a high-speed, low-latency network such as those on the IBM SP2 or the SGI Origin2000, the corresponding flow solutions scale reasonably well with the number of processors. The use of the original three-pass communication model was necessary for handling a completely general block structure. Drawbacks of this approach are that redundant communications are performed and that the second and third passes must wait until the previous passes have completed before they are started.

The source of redundant data passing can be seen by following the flow of information from one block to a neighboring block coincident with an edge or a corner of the originating block. For example, across an edge, information from one block to another (located above and to the right) can flow in one of two ways. Firstly, the data could flow from the originating block to its right-hand neighbor, then this information could be transferred from this neighbor to the block directly above it. Alternatively, the data could first move upward, then to the right. Because of the complexity involved in determining which path the data should flow along and which it should not, the baseline three-pass model transfers the information in both directions. Similarly, for communications across corners, this redundancy is three-fold.

- **Needed Communication**

- Multiblock Decomposition/Multigrid Acceleration
- CFD Stencil



- Multistage Time Stepping
 - * Convective Fluxes at All Stages and All Levels
 - * 1st Order Dissipation on Odd Stages at All Levels
 - * 3rd Order Dissipation Only on Fine Mesh at Odd Stages

Improvements to the Parallel Performance and Communication, *continued*

Hence, an obvious source of improvement is to remove redundant data transfers from the communications model. This is accomplished by adopting a **single-pass scheme** which reproduces exactly the end state of the original three-pass model. In order to ensure identical results, the original three-pass model is used to initialize the communication lists of the one-pass method. This is accomplished in the following manner: after the blocks of the grid system have been assigned to an appropriate processor through the load balancing procedure, the solution vector is "colored" with information that describes its starting location prior to any communication. This encoding includes information such as block and processor numbers and local cell indices. With this state set, the solution vector is processed with the original three-pass communication model. Upon completion of this data transfer, every halo cell in the distributed system has been reset with information which points back to its origin, i.e. block number, processor number and "distant" cell index. At this stage, new communication lists are constructed and returned to the source processor which stores them for future use by the one-pass model.

For the benchmark test case, the one-pass model reduces the total message length by about 11% on the fine mesh. However, because there is no forced synchronization between passes as in the three-pass model, the overhead reduction approaches 25%.

In the baseline code, communication always transferred the actual values of the solution vector. In order to preserve 64-bit accuracy, all of these values were transferred as 64-bit floating-point numbers. In the present one-pass model, an additional choice of communication model has been implemented. We refer to this communication model as the **delta update** procedure.

Inclusion of a delta form in the present work is motivated by the fact that these delta increments can be transferred as 32-bit numbers while maintaining 64-bit accuracy in the converged solution. Maintaining this level of precision during the course of convergence requires an occasional reset of the halo values with a 64-bit communication, although the large majority of the communication is now performed using only 32-bit numbers. For this occasional reset, we have maintained the capability to transfer actual full precision values of the solution vector.

For all practical purposes, the communication overhead of the new delta form is half that of the baseline (full precision) transfers.

As mentioned above, the original load-balancing algorithm was guided solely by the number of cells being distributed to the complete set of processors. This form of load balancing has proved to be quite acceptable for platforms with state-of-the-art communication capabilities such as the IBM SP2. However, for a cluster of workstations linked together with a lower performance network, this technique can be further refined.

A **new load-balancing algorithm** has been developed which includes the penalties associated with out-of-processor communication. In this setting, the load is defined as the time it takes each processor to complete all of its tasks—numerical processing as well as sending and receiving the necessary messages. The predicted times of each of these tasks are derived using experimentally obtained MFLOPS (Millions of Floating Point Operations per Second) ratings, and the MPI latency and bandwidth values associated with the particular distributed platform.

- **Load Balancing and Communication**
 - CPU Time
 - * Balance the Number of Computational Cells on Each Processor
 - Bandwidth
 - * Place Adjacent Blocks on Same Processor
 - Latency
 - * Gather All communication Between Any Two Processors Into a Single Pass regardless of the number of blocks in each processor

Improvements to the Parallel Performance and Communication, *continued*

The new load-balancing algorithm is very similar to that of the original method, but the "size" of each block is now initialized assuming that the information of all halo cells will be transferred to another processor. The algorithm then proceeds by taking the largest of the remaining blocks (yet to be distributed) and temporarily assigning it to every processor. When assigned to each processor, a temporary update of the load of that processor is made by adding the size of the current block to that processor's previous load. This assignment is rewarded by a decrease in the equivalent size if neighboring blocks are already assigned to that processor and thus no communication is necessary. After all temporary assignments have been done, the processor whose load is the smallest after the assignment is selected and the block is permanently assigned to that processor. The previous steps are repeated until all blocks have been distributed.

In the baseline method, we stated that a double-layer halo surrounds each block and it is utilized to facilitate calculation of the 3rd-order artificial dissipation fluxes. However, upon close inspection of the 5-stage Runge-Kutta scheme and multigrid processes, we note that the dissipative fluxes are not recomputed as often as the solution updates occur. In particular, these dissipative terms are typically reset during only the *odd* Runge-Kutta stages on the *finest* mesh and never computed in any of the coarser levels of the multigrid scheme.

Immediately, we can **omit transferring the outer-layer halo data** during the even (of 5) Runge-Kutta stages in the **fine** mesh. This reduces the fine-mesh communication by 20%.

For a 4-level multigrid W-cycle in the baseline code, more than 45% of the total data transferred during the cycle resides in the coarser-level meshes. (A W-cycle with 4 multigrid levels traverses the 2nd-level grid exactly twice when communication is involved; 4 times in the 3rd and 4th levels. The number of halo cells of a coarse-mesh is at least 1/4th that of the next finer mesh. Hence, the baseline communication in the coarse grids is at least 81% as intense as it is in the finest mesh. Further study of a grid with only one interior cell in the 4th-level mesh shows that the baseline communication in the coarser grids can approach 183% that of the finest mesh.) By updating only the data of the **inner halo** during the **coarse-level communication**, an additional improvement is realized.

The above two improvements combine to reduce the total amount of data transferred per multigrid cycle. Relative to the baseline communication, this reduction in overhead is between 33.3% and 54.7%, depending on the granularity of the mesh involved.

- **Original Scheme**
 - **Three Pass Halos (Block Faces, Edges and Corners)**
 - **Double Precision Messages**
 - **Double Layer Halos on Every Stage of Every Multigrid Level**
 - **Load Balancing Based Only on Mesh Cell Count**
- **Improvements**
 - **One Pass Halo (Combined Face, Edge and Corner Processor to Processor Communication)**
 - **Single Precision Messages for Incremental Changes in Flow Variables (Preserves Full Double Precision Accuracy)**
 - **Double Layer Halos Only at the Odd Stages of the Finest Mesh (Single Layer Otherwise)**
 - **Load Balancing Based on Mesh Cell Count, Block Proximity and Number of Messages**

Communication Improvement Summary

For the 72-block mesh under discussion, the relative improvements in communication overhead with respect to the original scheme can be summarized as follows:

- 20% reduction in overhead with one-pass (benchmark)
- 50% reduction in overhead with delta form (in general)
- 50% reduction in overhead with new load balancer (benchmark, Ethernet)
- 33%-55% reduction in overhead with single-halo transfers (in general)
- Communication reduced by a minimum of 75% when combined

The following figures show the scalability of the design code with changes to the parallel implementation for the 72-block grid case. Note that this calculation is dominated by communication and inherently has poor scalability. Furthermore, since the blocks are odd, fixed sizes, the basic strategy of using the multiblock boundaries to decompose the problem puts an inherent upper limit on the scalability as the number of processors rises. In other words, even with perfect communications, the method cannot attain linear speed-ups.

Communication Improvement Summary

- 20% reduction in overhead with one-pass (benchmark)
- 50% reduction in overhead with delta form (in general)
- 50% reduction in overhead with new load balancer (benchmark, Ethernet)
- 33%-55% reduction in overhead with single-halo transfers (in general)
- Communication reduced by a minimum of 75% when combined

Improvements to the Parallel Performance and Communication, *continued*

The first figure shows the case for the calculation run on the IBM SP2 using different numbers of processors. The curves show the effects of the distinct aspects of the improved communication strategies.

IBM SP2 Results in US Mode

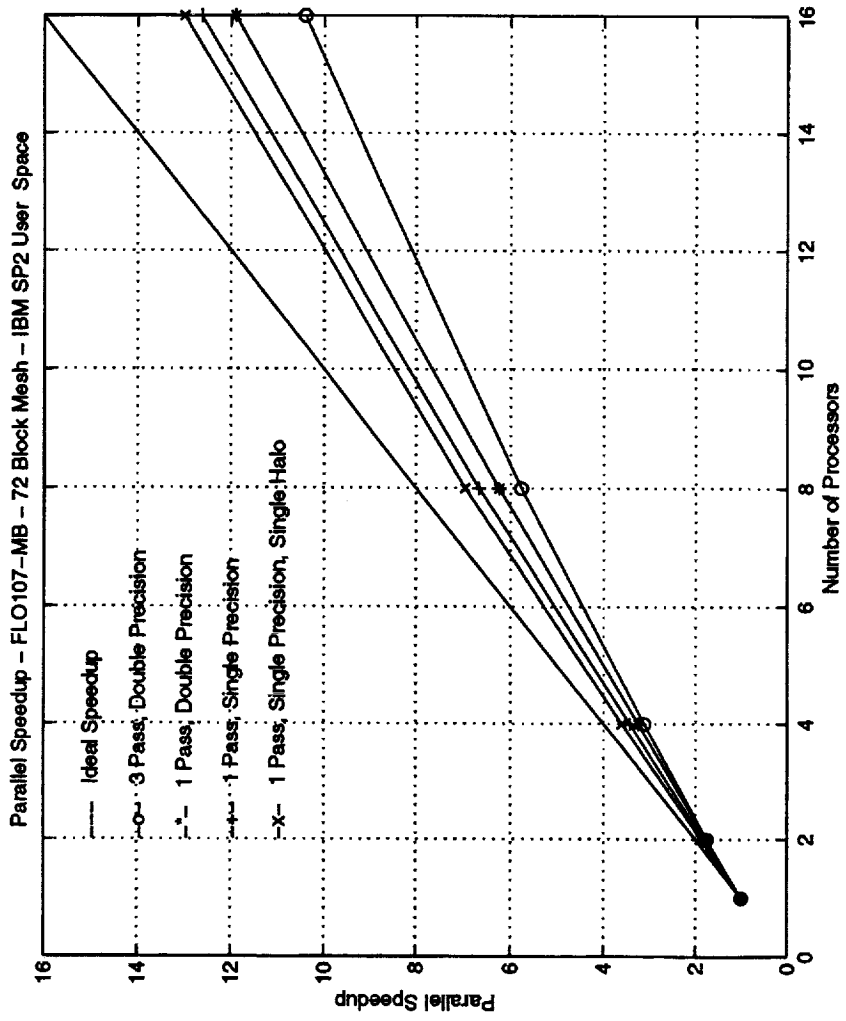


Figure 1:

Improvements to the Parallel Performance and Communication, *continued*

The second figure shows the same calculation on a cluster of HP workstations using switched-100BaseT Ethernet communications hardware. Again, performance improvements are seen but the overall levels of the performance for all calculations fall short of those seen on the SP2 because of the degradation in network performance.

HP Cluster Switched 100BaseT

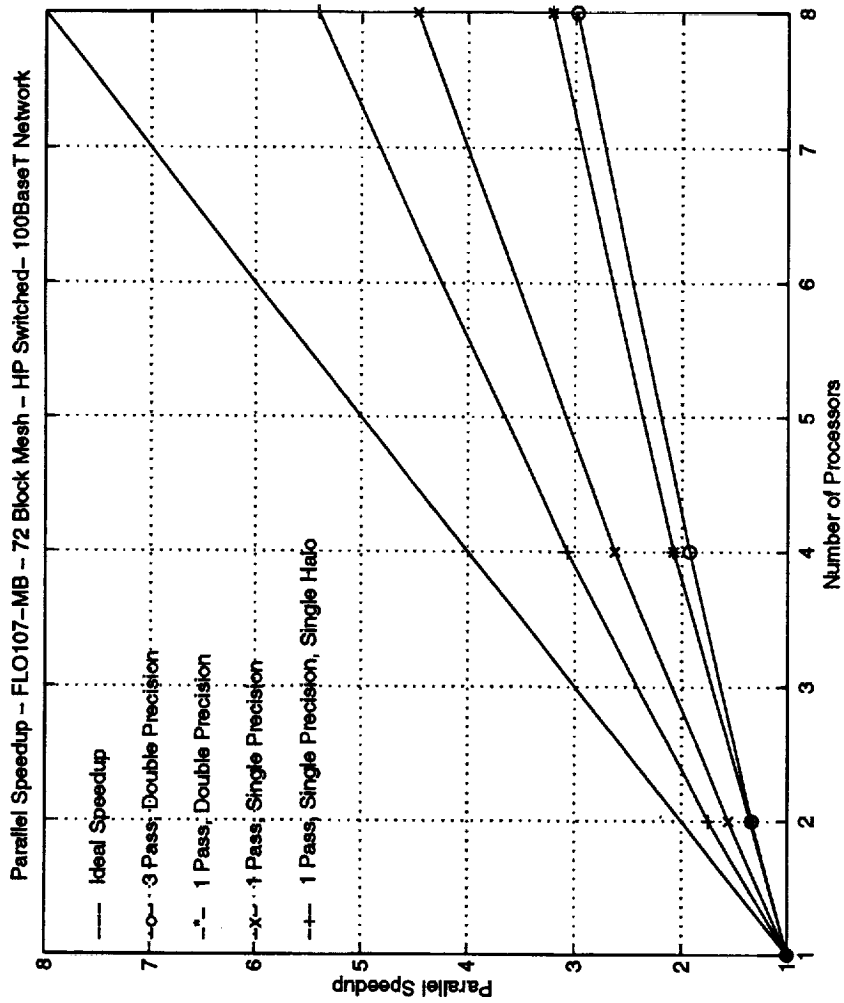


Figure 2:

Improvements to the Parallel Performance and Communication, *continued*

This third figure shows the parallel speed-ups for a more realistic problem and up to 32 IBM SP2 processors. The mesh has 4.2 million points including halos, and represents a full business jet configuration. The 240-block mesh is a very fine Euler mesh used for accurate drag predictions. The scalability curve seen in the figure demonstrates the true power of parallel computing.

Fine Mesh Scalability

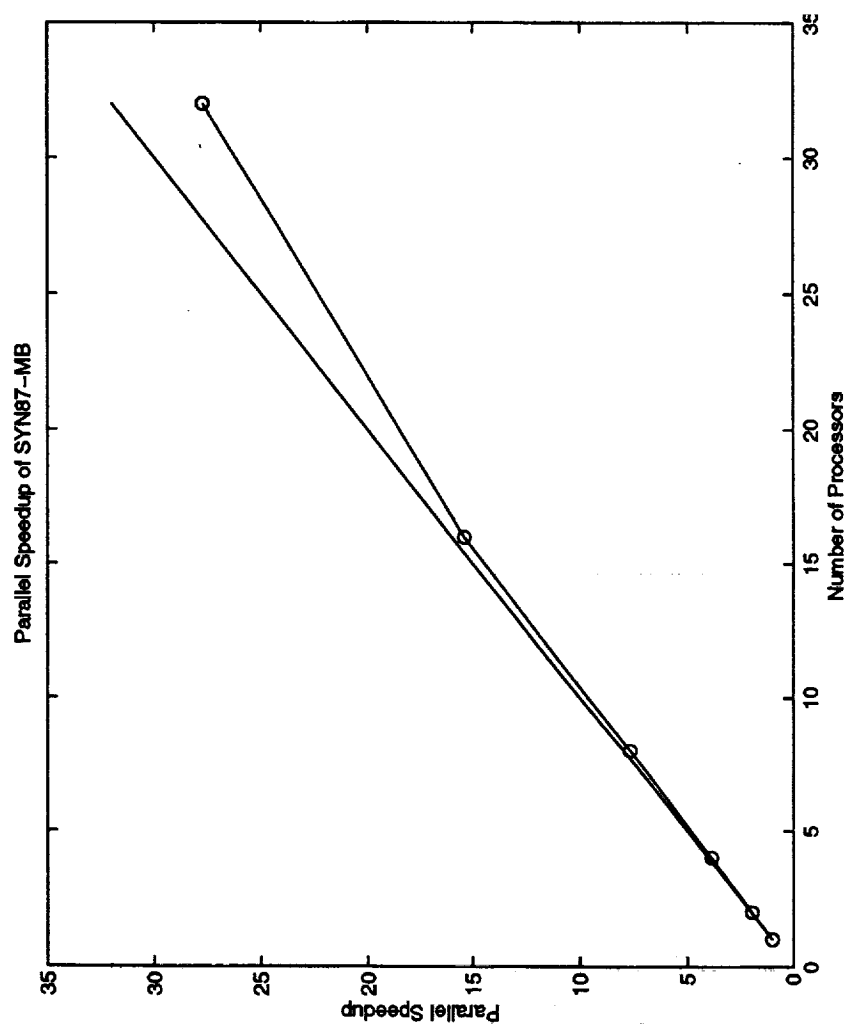


Figure 3:

Gradient Checks for Transonic Flows

The most critical element in determining the validity of adjoint-based sensitivities is the establishment of their accuracy level. Two main alternatives for the development of the adjoint equations exist: the continuous and the discrete approaches. The discrete approach, if rigorously implemented, will produce gradients that exactly match those obtained by using accurate finite differences. Thus, comparing such gradients serves as a consistency check for the method. In the case of the continuous approach that we use throughout this work, gradient comparisons have a different interpretation. The adjoint equations derived in the discrete approach may be thought of as one of the possible discretizations of the continuous adjoint equations. Therefore, unless this particular discretization of the continuous adjoint equations is used, the gradients produced using the continuous approach will differ from those obtained by finite differencing in proportion to the truncation error of the approximation. For example, if the schemes used to discretize the flow and adjoint equations are both second order accurate, the differences between the discrete and continuous adjoint solutions should also be of second order. Consequently, the differences between the two formulations should vanish in the limit of zero mesh spacing. This conclusion, which has been demonstrated in the recent work of Anderson and Venkatakrishnan, can be helpful in determining the proper mesh resolution required for accuracy in the adjoint solution; if a properly implemented continuous adjoint formulation fails to provide sensitivity information that closely matches the result of finite differencing, the probable cause is that the cost function being evaluated is poorly resolved on the mesh in question.

Finite difference gradients are subject to two classes of error: numerical cancellation error (error caused by inaccuracies in cost function due to the lack of solver convergence and machine precision) and gradient discretization (truncation) error (error due to the discrete finite difference approximation used to estimate the gradient). In order to address these issues, two studies (one for transonic flow, one for supersonic flow, both inviscid) are presented to establish the level of convergence and discrete step size necessary to produce accurate gradients, and to compare them with the gradients obtained by using the current adjoint implementation.

For the first gradient study, an inverse transonic wing design test problem is defined. Although only the pressures on the surface of the wing are driven towards a target, the design is carried out in the presence of a fuselage and nacelle. The same gradient calculation is carried out on a sequence of coarse, medium, and fine meshes containing 157,676 cells, 734,976 cells, and 4,280,320 cells respectively. These cell counts include all halo cells. The medium and coarse meshes are obtained by recursively taking alternate points in the original fine mesh in each coordinate direction. The medium mesh is used to study the effect of flow solver convergence and step size, while all three meshes are used to determine the mesh sensitivity of the gradients.

Gradient Checks for Transonic Flows

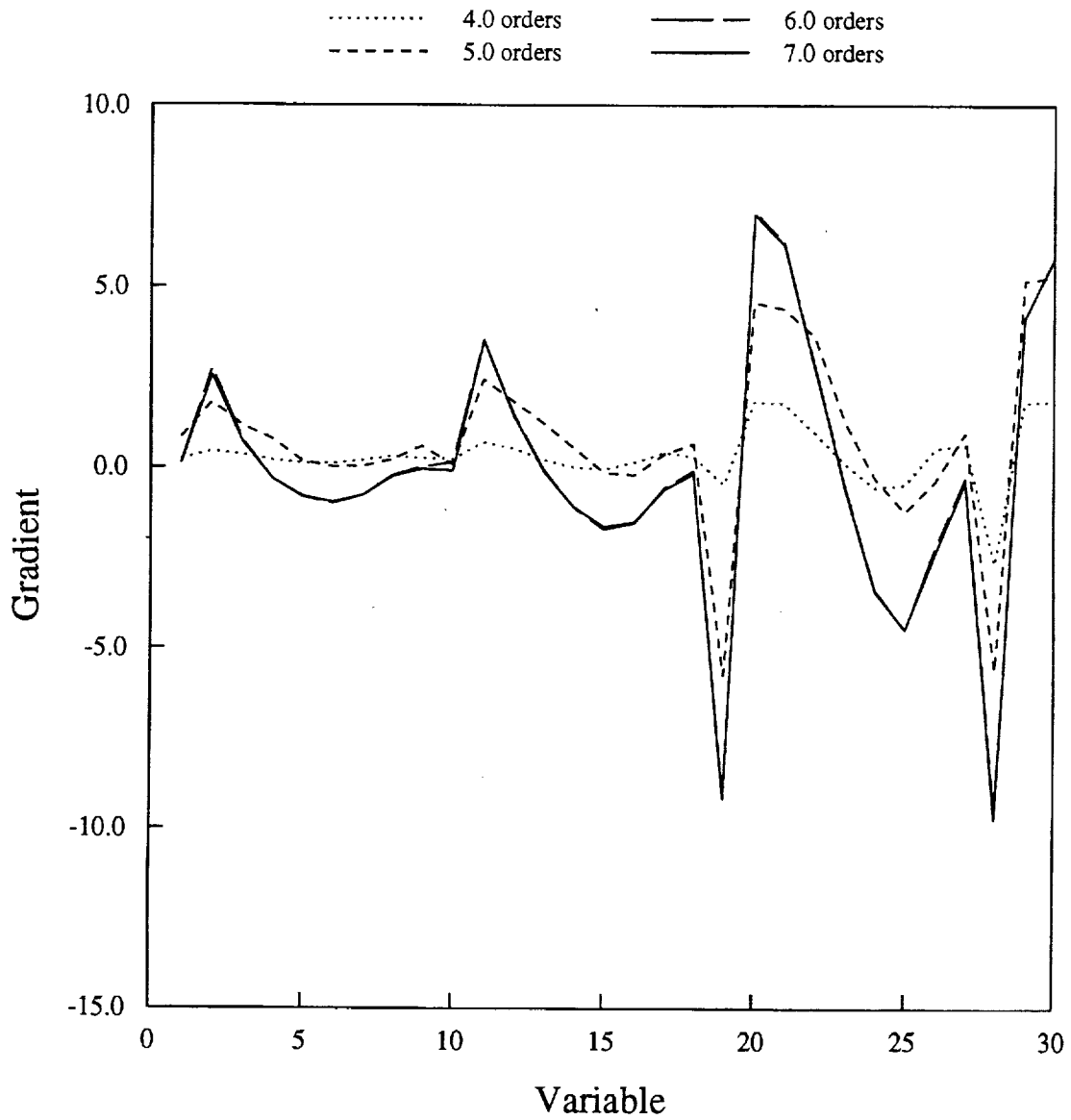
- **Finite Difference Gradient Accuracy vs. Flow Solver Convergence (Cancellation Error)**
- **Finite Difference Gradient Accuracy vs. Step Size (Truncation Error)**
- **Adjoint Gradient Accuracy vs. Flow Solver Convergence**
- **Adjoint Gradient Accuracy vs. Adjoint Solver Convergence**
- **Adjoint vs. Finite Difference Gradient Comparison**
- **Mesh Sensitivity Study**

Gradient Checks for Transonic Flows, *continued*

The first two gradient figures show the values of gradient components obtained using one-sided differencing for different values of flow solver convergence and step size. Only the first 30 out of a total of 108 Hicks-Henne design variables are compared because of the prohibitive computational cost of calculating all gradient components using finite differences. It can be seen from the first figure that, for a step size of 0.0001, a flow solver convergence level of at least 6 orders of reduction in average residual is necessary to achieve accurate gradients. For a flow solver convergence of 7 orders, the second figure indicates that the discretization error is acceptably small for step sizes of 0.001 or smaller. From the results in these figures, one can be certain that if a convergence level of 7 orders of magnitude and step sizes of 0.0001 are used for the calculation of finite difference gradients, the sensitivities will be accurate and provide a good reference for comparison with sensitivities obtained using the continuous adjoint method.

Gradient Accuracy for Finite Difference Method

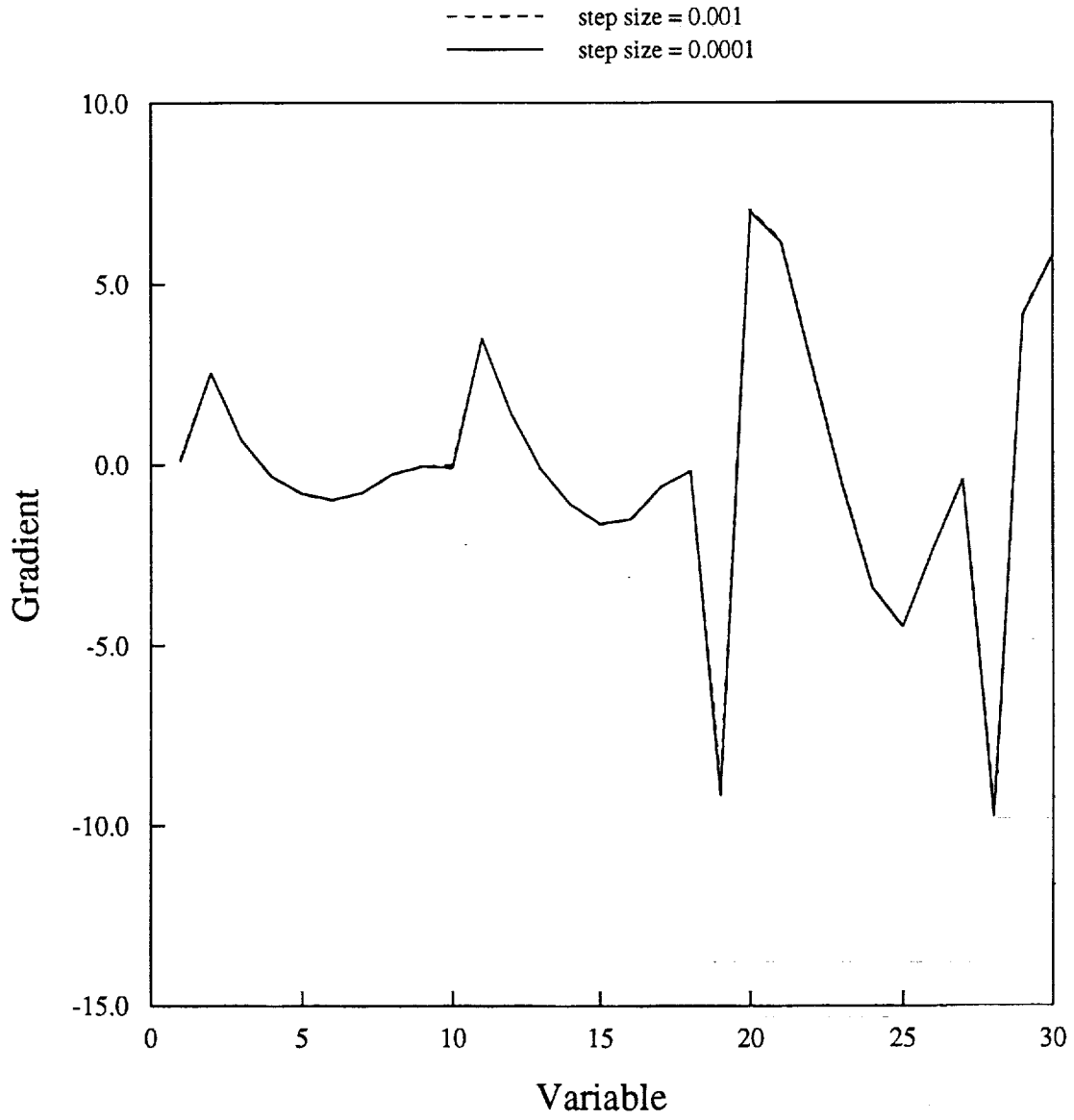
Accuracy for Different Levels of Flow Solver Convergence: Step size = 0.0001.



This page is intentionally left blank.

Gradient Accuracy for Finite Difference Method

Accuracy for Different Stepsizes: Flow convergence 7 orders.

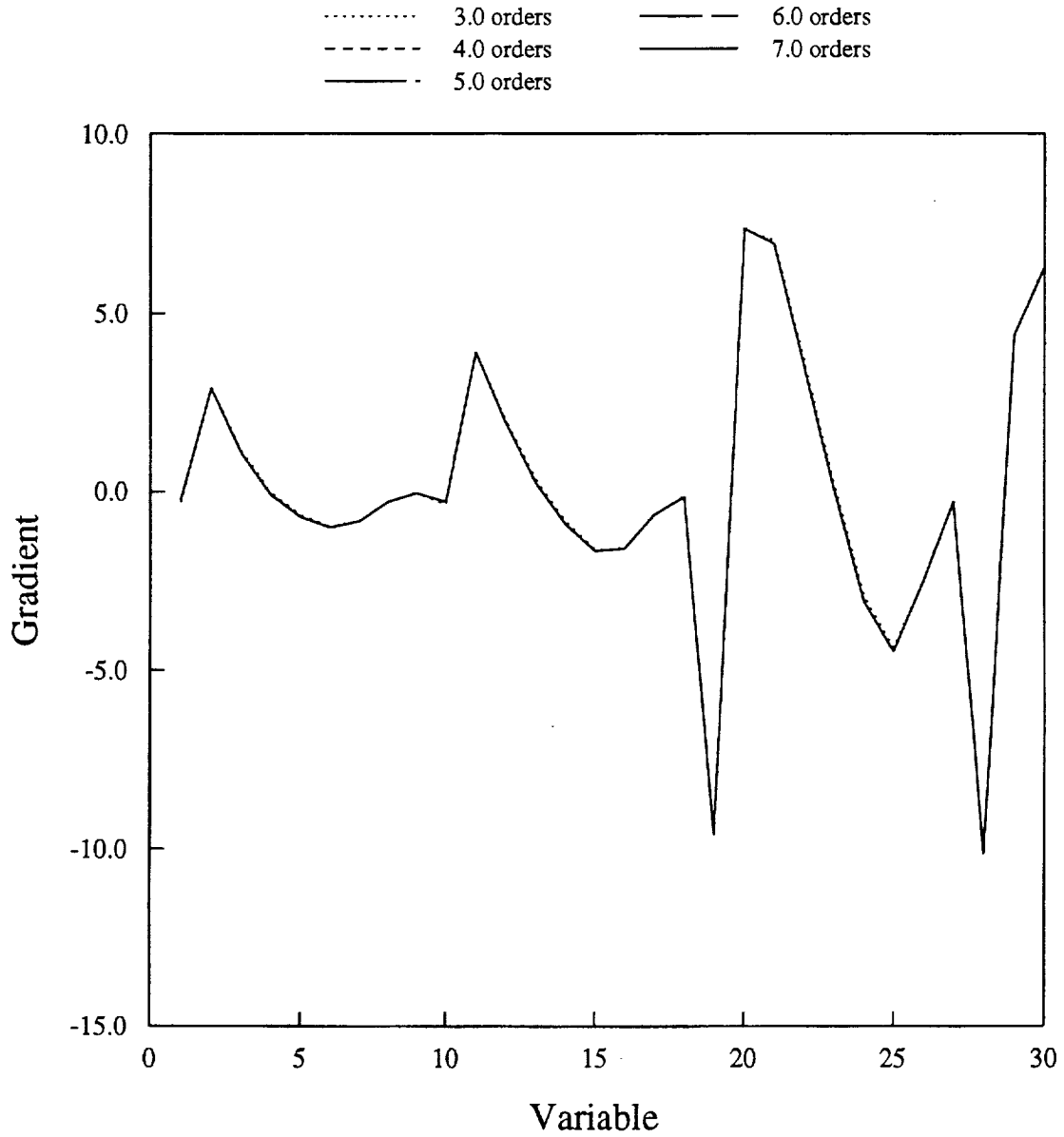


Gradient Checks for Transonic Flows, *continued*

Adjoint-based gradients must also be resolved properly to ensure realistic comparisons. In contrast with using the finite difference method, gradients obtained via the adjoint method do not contain a gradient discretization error since they are independent of step size. Instead, they have sources of numerical cancellation error resulting from inadequate convergence of the flow and/or adjoint solvers. Thus, by examining the levels of convergence in both systems it is possible to obtain adjoint sensitivities which are accurate given the choice of discretization for the overall adjoint system and the choice of mesh resolution. The **third figure** of this study shows the dependence of the continuous adjoint gradients on the flow solver convergence, while the **fourth** shows their dependence on the level of convergence of the adjoint solver. From these two figures we can conclude that accurate gradient information can be obtained using the continuous adjoint formulation provided that the flow and adjoint solvers are converged by at least 4 and 2 orders of magnitude respectively. It is thus apparent that the level of convergence required to obtain accurate gradient information with the continuous adjoint formulation is drastically lower than that necessary in the finite difference method. This relaxation of the convergence requirement makes the use of an adjoint formulation even more attractive. The 1996 thesis by James Reuther, *Aerodynamic Shape Optimization Using Control Theory*, provides an explanation of the mechanisms by which accurate gradient information can be obtained with moderate convergence in both the flow and adjoint systems.

Gradient Accuracy for Adjoint Method

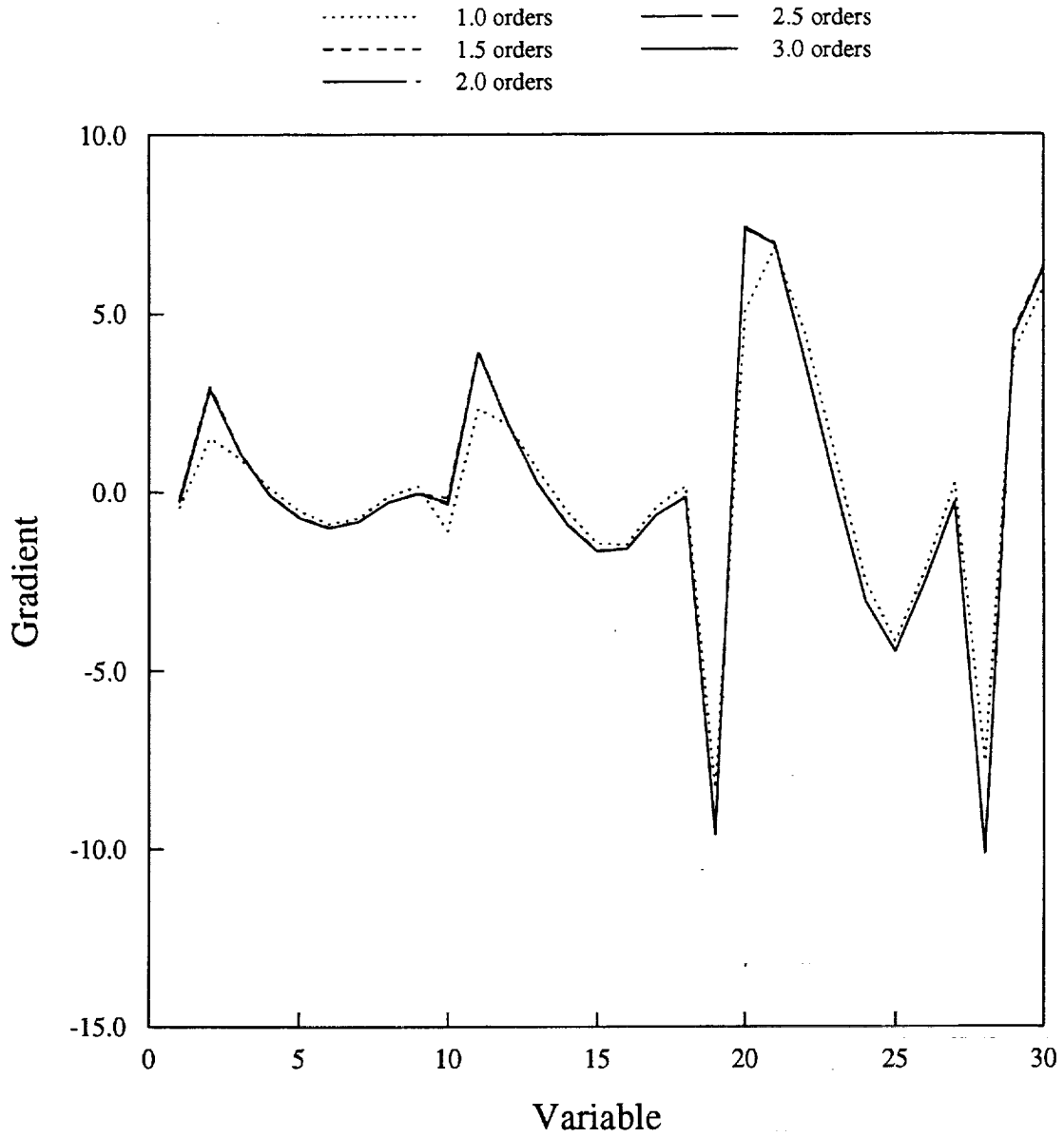
Accuracy for Different Levels of Flow Solver Convergence: Adjoint convergence 2.5 orders.



This page is intentionally left blank.

Gradient Accuracy for Adjoint Method

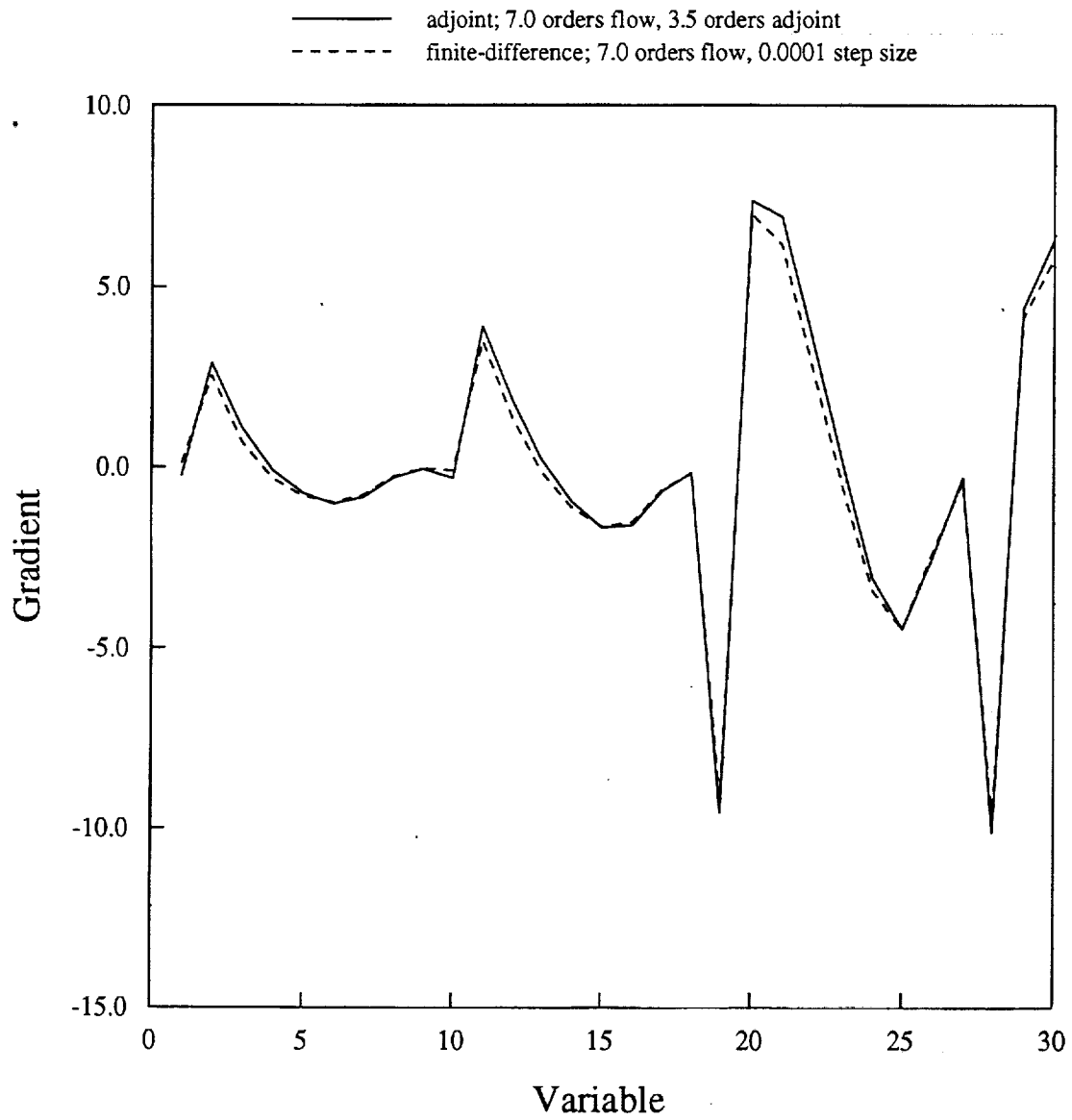
Accuracy for Different Levels of Adjoint Solver Convergence: Flow convergence 7.0 orders.



Gradient Checks for Transonic Flows, *continued*

The next three figures compare the effects of mesh density on adjoint and finite difference sensitivities. First, for the medium mesh case used above, the flow solver was converged 7 orders of magnitude in both approaches. The co-state system was converged 3 orders and a constant step size of 0.0001 was chosen for the calculation of the finite difference gradients. Since these choices of convergence tolerances and step sizes should eliminate all sources of numerical cancellation and gradient discretization errors from the comparisons, the explanation of the small discrepancies evident in the medium mesh figure must be a consequence of the difference in discretization between the adjoint system used in this work and the discretization that would have been obtained via a discrete adjoint implementation. It should now be possible to show that the differences between the adjoint and finite difference sensitivities will diminish as the mesh is refined.

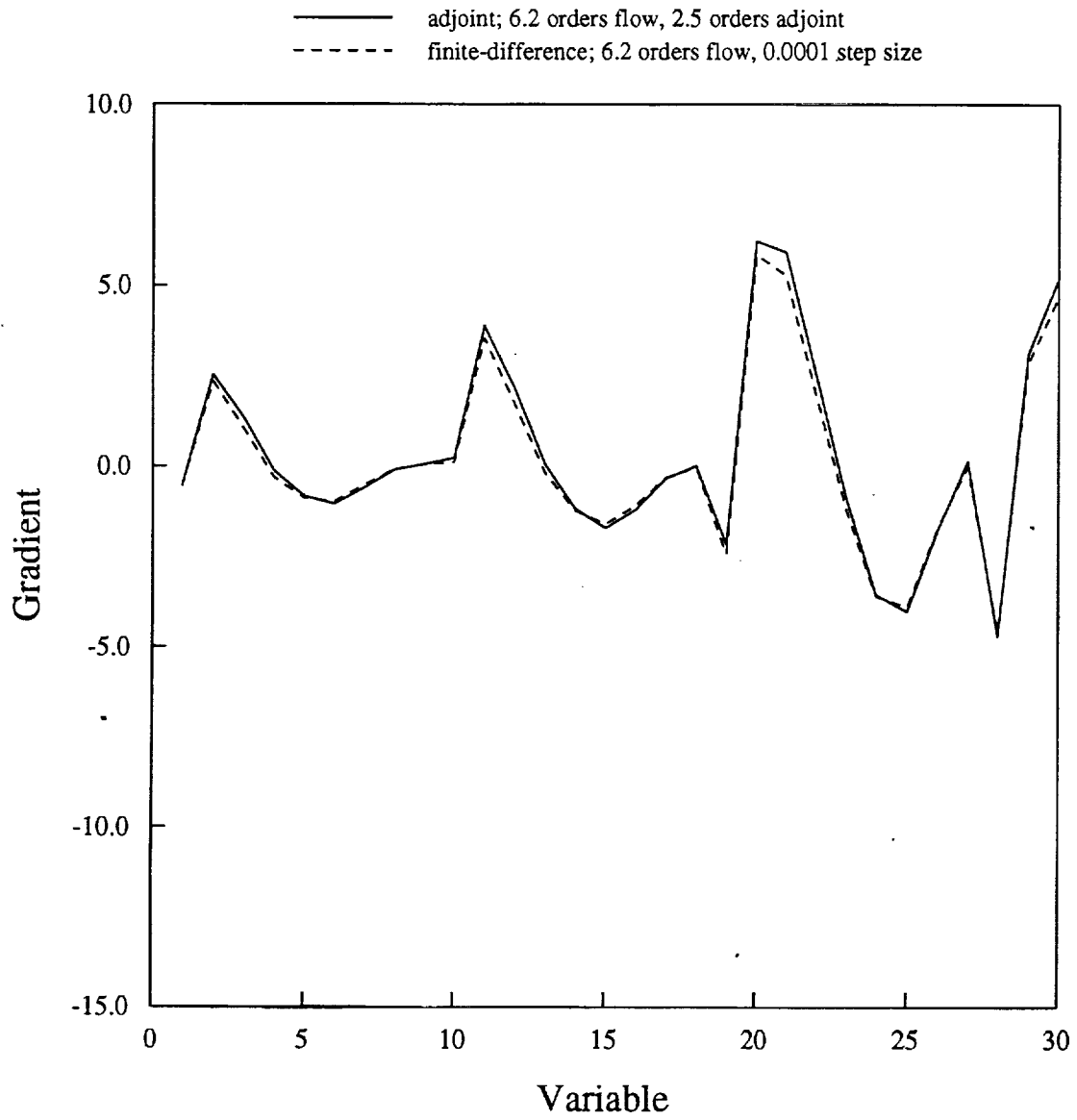
Gradient Accuracy Comparisons Adjoint vs Finite-Difference Medium Mesh



Gradient Checks for Transonic Flows, *continued*

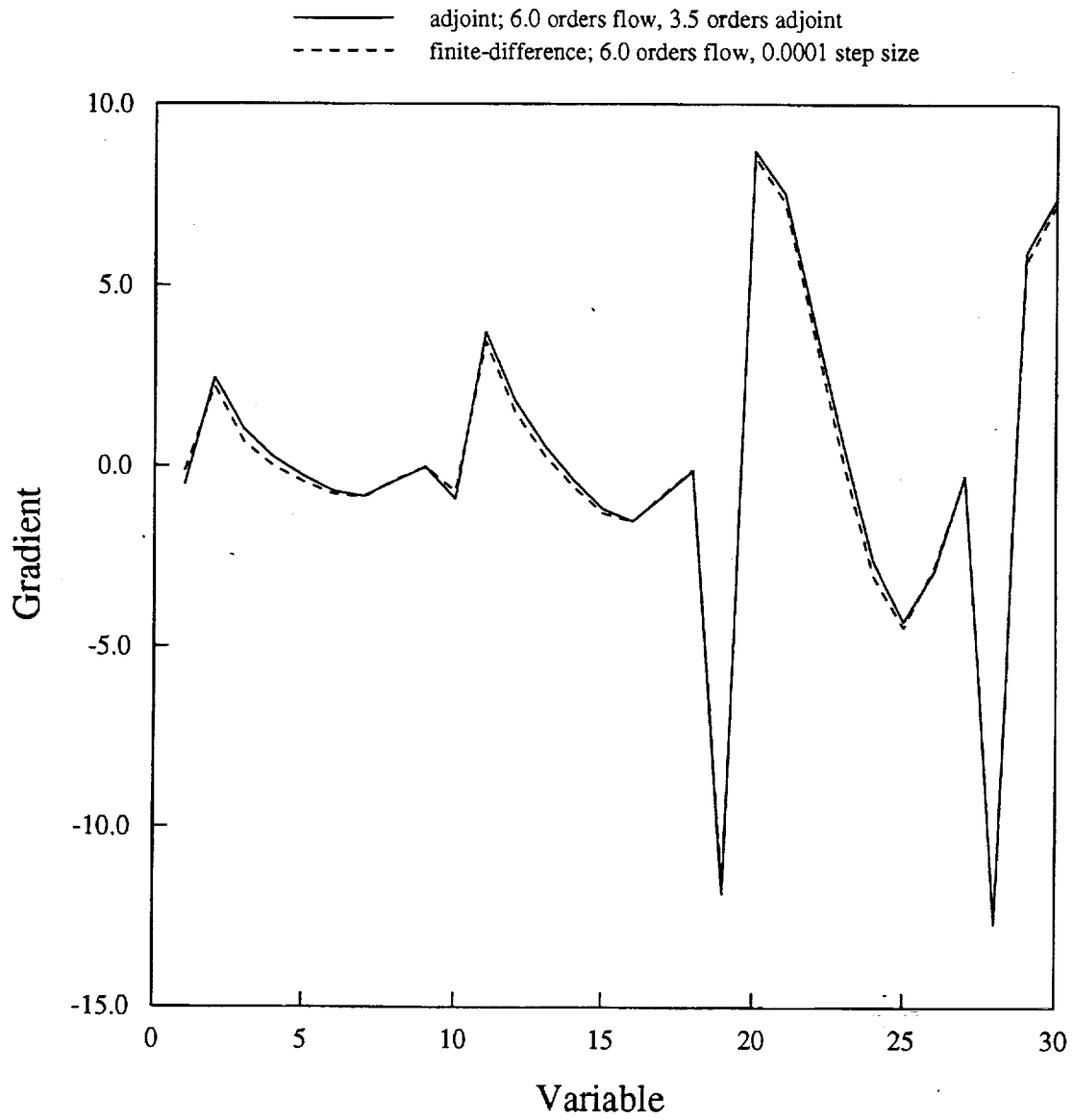
The following **coarse mesh** and **fine mesh** figures show comparisons of the same gradients for both the coarse and the fine meshes with convergence tolerances adequately adjusted to provide low numerical errors on each mesh. It is apparent from these comparisons that, while the general character of the gradients remains the same in all three meshes, there is a tendency for the relative magnitudes of the individual gradient components to increase as the mesh is refined. This suggests that the cost function of the design problem may not be properly resolved on any of the meshes explored here. However, the figures do show that the discrepancy between the adjoint and finite difference gradients decreases as the mesh is refined. The L^2 norm of the difference between the most accurate finite difference gradients and the sensitivities obtained using the adjoint formulation on each of the three meshes is computed to be 0.010883, 0.009506, and 0.002684 for the coarse, medium, and fine meshes. The reduction in the norm of the error as the mesh is refined supports the assertion that the continuous adjoint method is consistent with other techniques of obtaining sensitivities in the limit of infinite mesh density.

Gradient Accuracy Comparisons Adjoint vs Finite-Difference Coarse Mesh



This page is intentionally left blank.

Gradient Accuracy Comparisons Adjoint vs Finite-Difference Fine Mesh



Gradient Checks For Supersonic Flows

A similar gradient study is now presented for the TCA-6 baseline with axisymmetric nacelles at Mach 2.4, $\alpha = 3.75^\circ$, but restricted to one mesh containing 180 blocks and 1.5 million cells including halos. The objective function is $10(D/L)$, and the design variables are nine SIN2 functions uniformly distributed from 10% chord to 90% chord at 10% intervals along a lower wing surface section between the nacelles (the region of maximum geometric change during optimization because of the high pressures emanating from the nacelles and diverters). The SIN2 functions had width exponents of 6.0, giving a fairly narrow range of influence for each design variable.

Gradient Checks for Supersonic Flows

- **Finite Difference Gradient Accuracy vs. Flow Solver Convergence (Cancellation Error)**
- **Finite Difference Gradient Accuracy vs. Step Size (Truncation Error)**
- **Adjoint Gradient Accuracy vs. Flow Solver Convergence**
- **Adjoint Gradient Accuracy vs. Adjoint Solver Convergence**
- **Adjoint vs. Finite Difference Gradient Comparison**

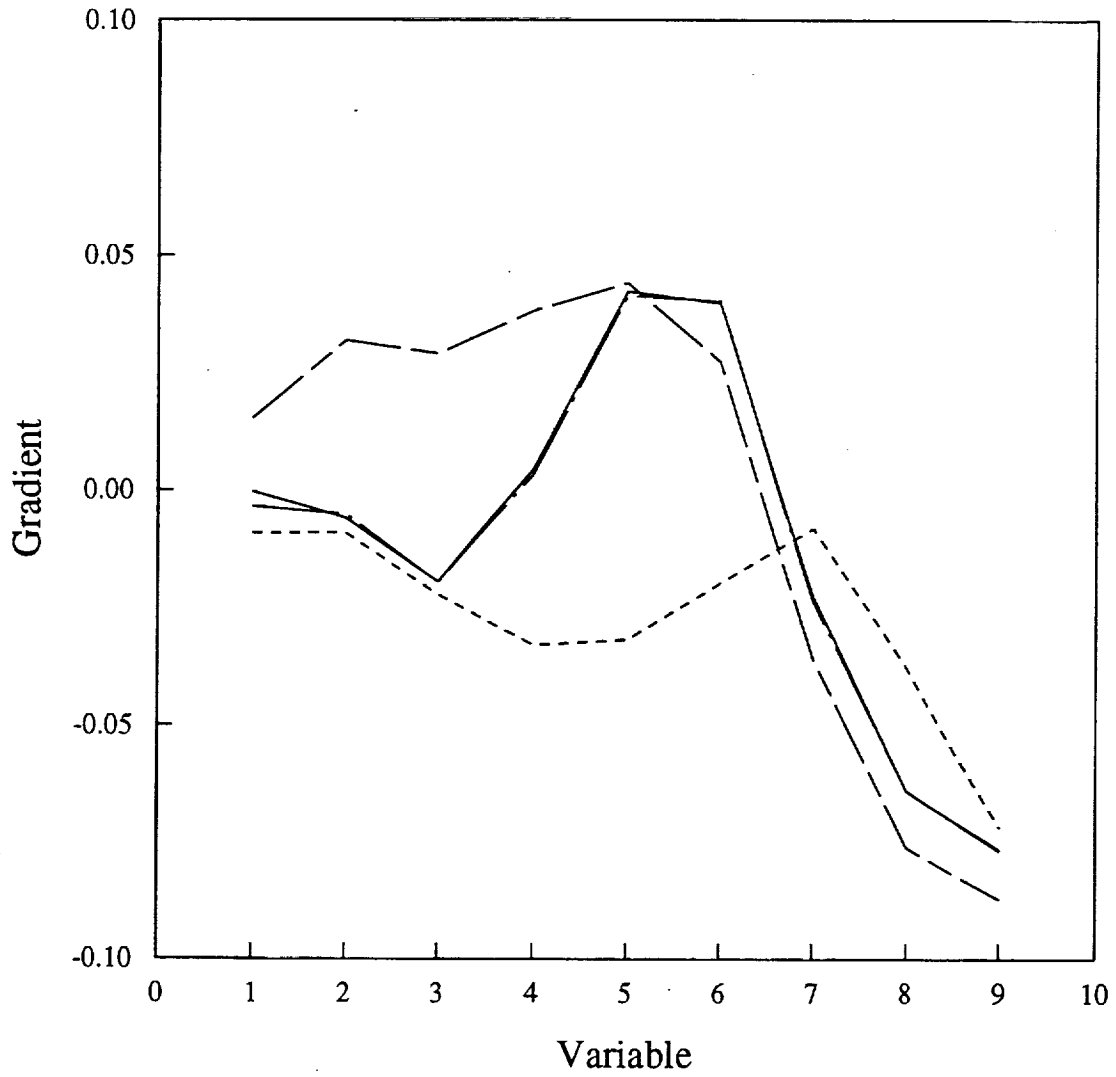
Gradient Checks for Supersonic Flows, *continued*

The **first two figures** compare the effects of flow solver convergence and step size on the finite difference gradients. As above, 6 orders of convergence are a bare minimum for finite differencing (6.5 being preferable), combined with step sizes of 0.0001.

Gradient Accuracy for Finite Difference Method

Accuracy for Different Levels of Flow Solver Convergence: Stepsize 0.0001.

..... 3.0 orders ——— 6.0 orders
- - - - 4.0 orders ——— 6.5 orders
— — — 5.0 orders

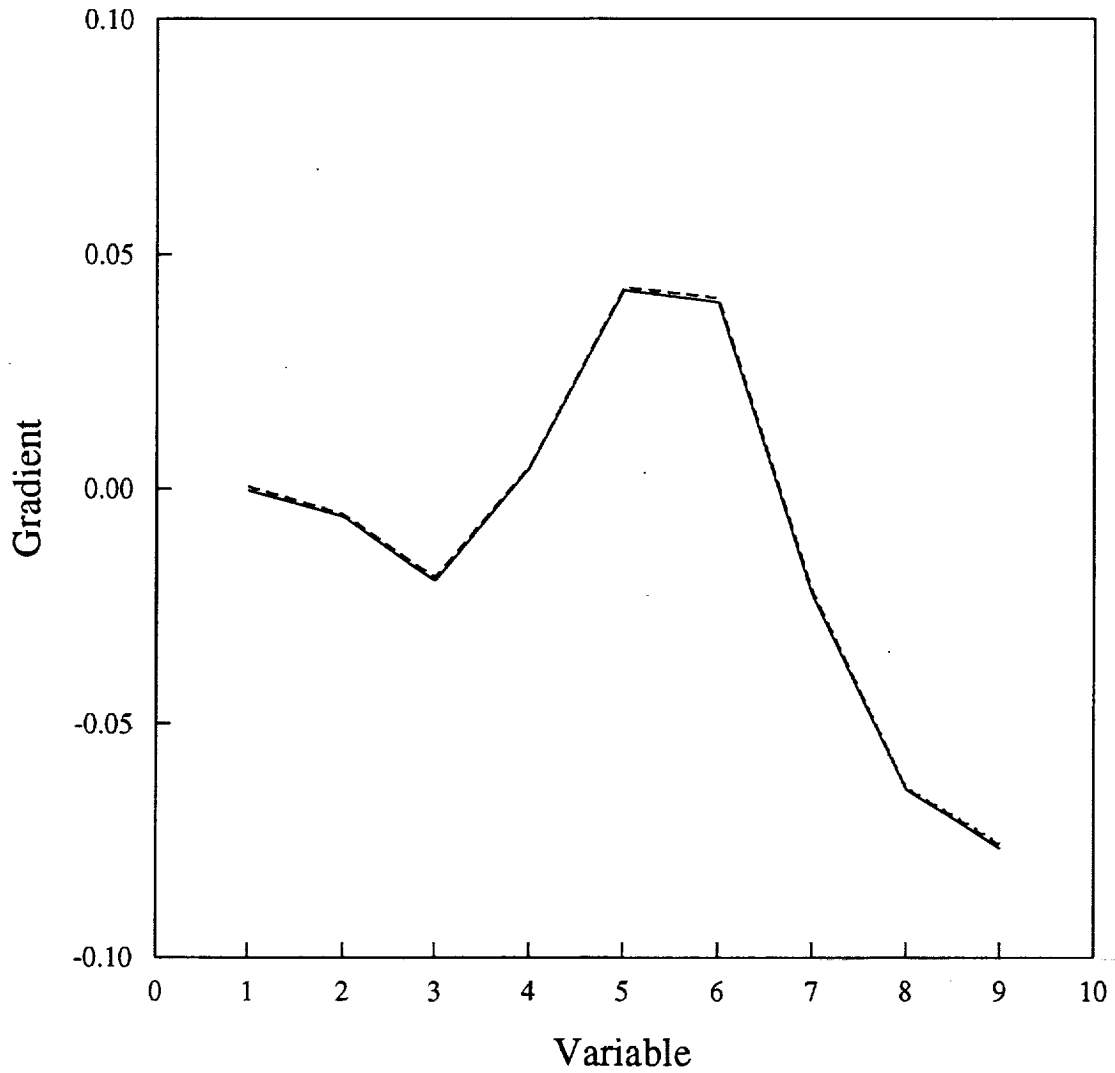


This page is intentionally left blank.

Gradient Accuracy for Finite Difference Method

Accuracy for Different Stepsizes: Flow convergence 6.5 orders.

..... stepsize = 0.001
----- stepsize = 0.0005
———— stepsize = 0.0001

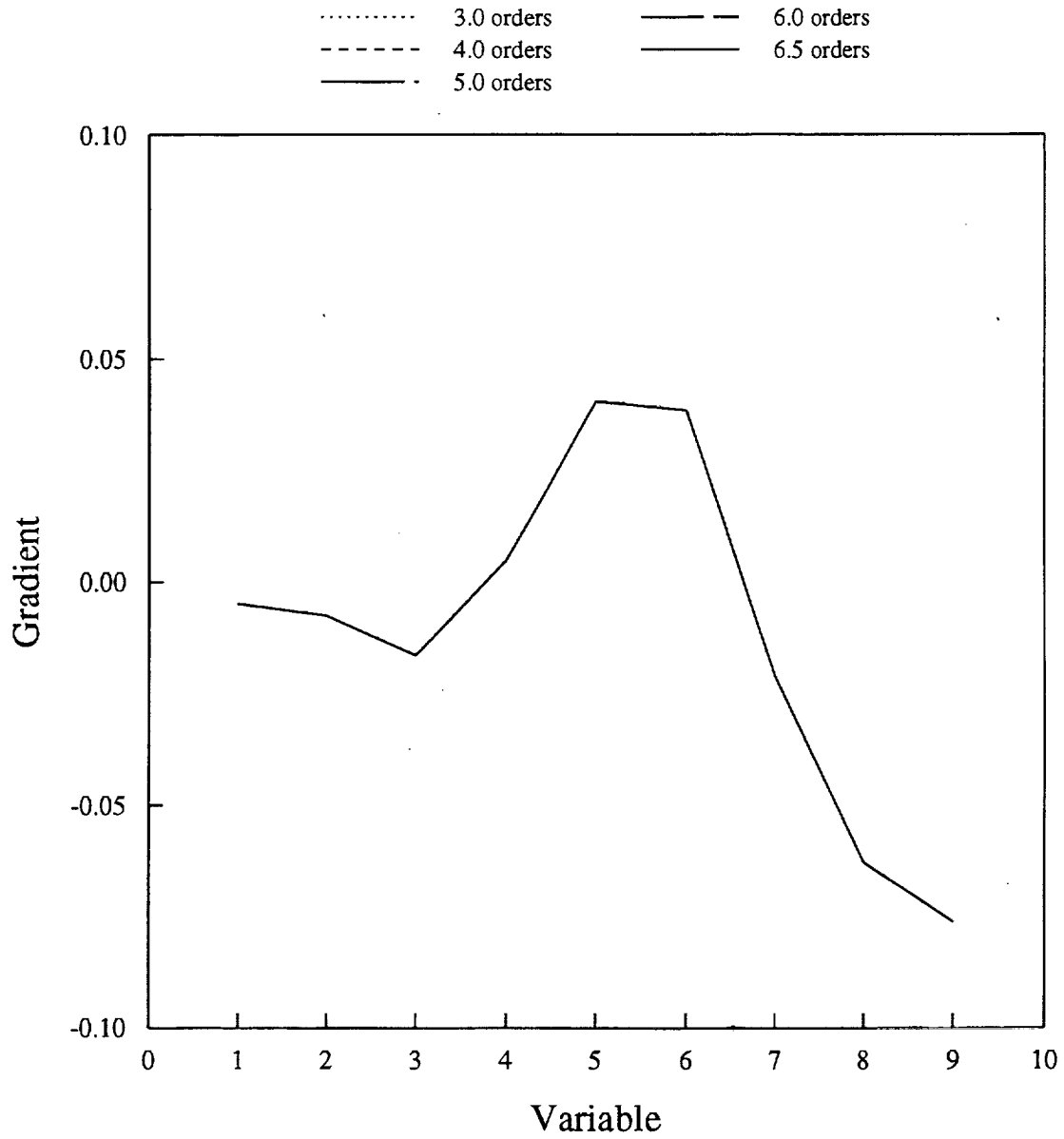


Gradient Checks for Supersonic Flows, *continued*

The **second two figures** show the effects of flow solver convergence and adjoint solver convergence on the adjoint-based gradients. Much as for the transonic case, converging the flow solver more than 3 orders (for 3 orders of adjoint convergence) appears unnecessary. The comparison of adjoint solver convergence effects shows more of a difference between 2 and 3 orders than for the transonic case, at least for some of the variables, but 3 orders should suffice. It should be noted that these adjoint convergence comparisons were performed with bifurcated nacelles on the TCA geometry rather than the axisymmetric nacelles. This explains the difference in character of these gradients from the other supersonic gradients shown. Use of the wrong nacelles was unintended, and time constraints prevented repeating the comparisons with the axisymmetric nacelles.

Gradient Accuracy for Adjoint Method

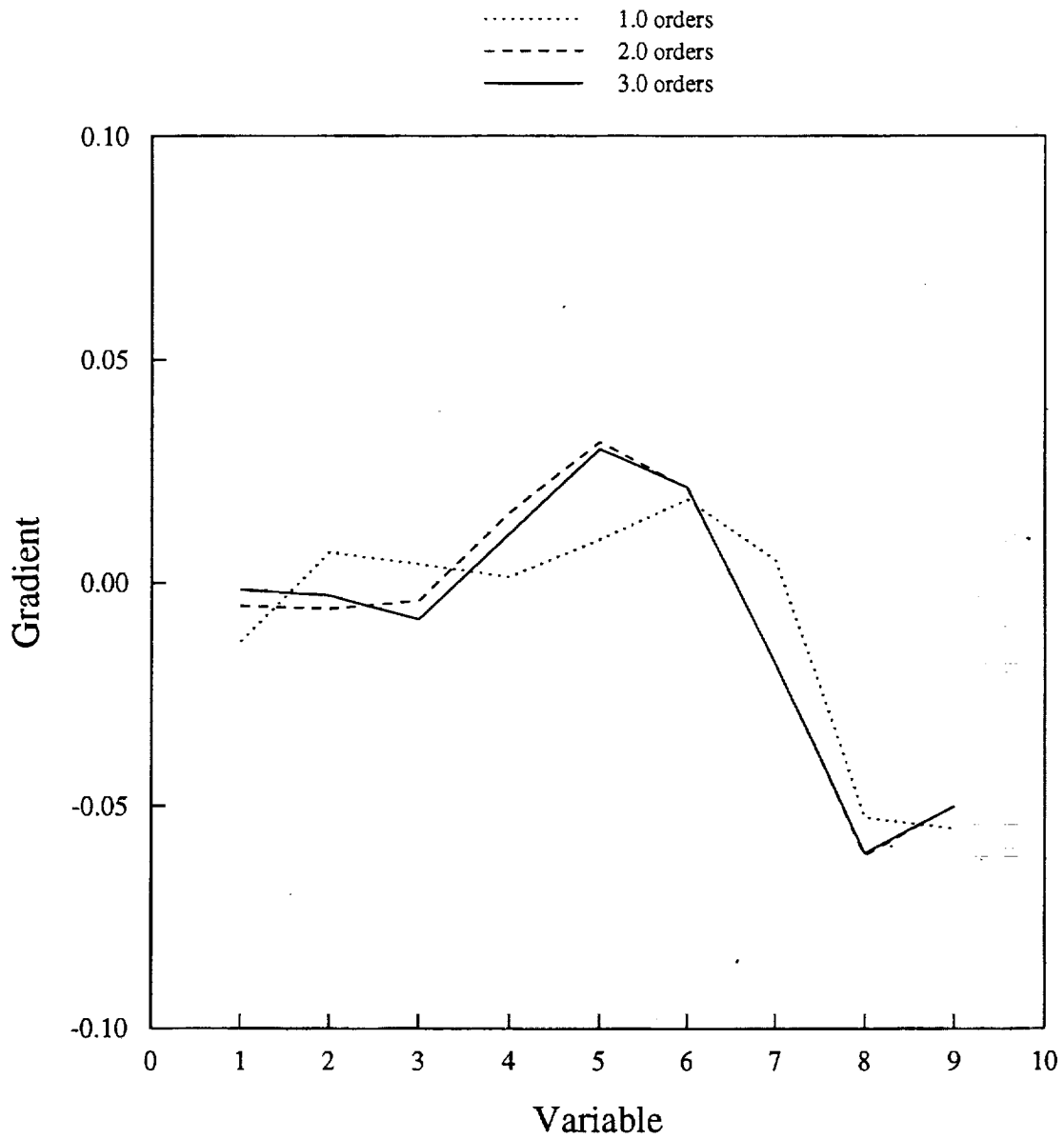
Accuracy for Different Levels of Flow Solver Convergence: Adjoint convergence 3 orders.



This page is intentionally left blank.

Gradient Accuracy for Adjoint Method

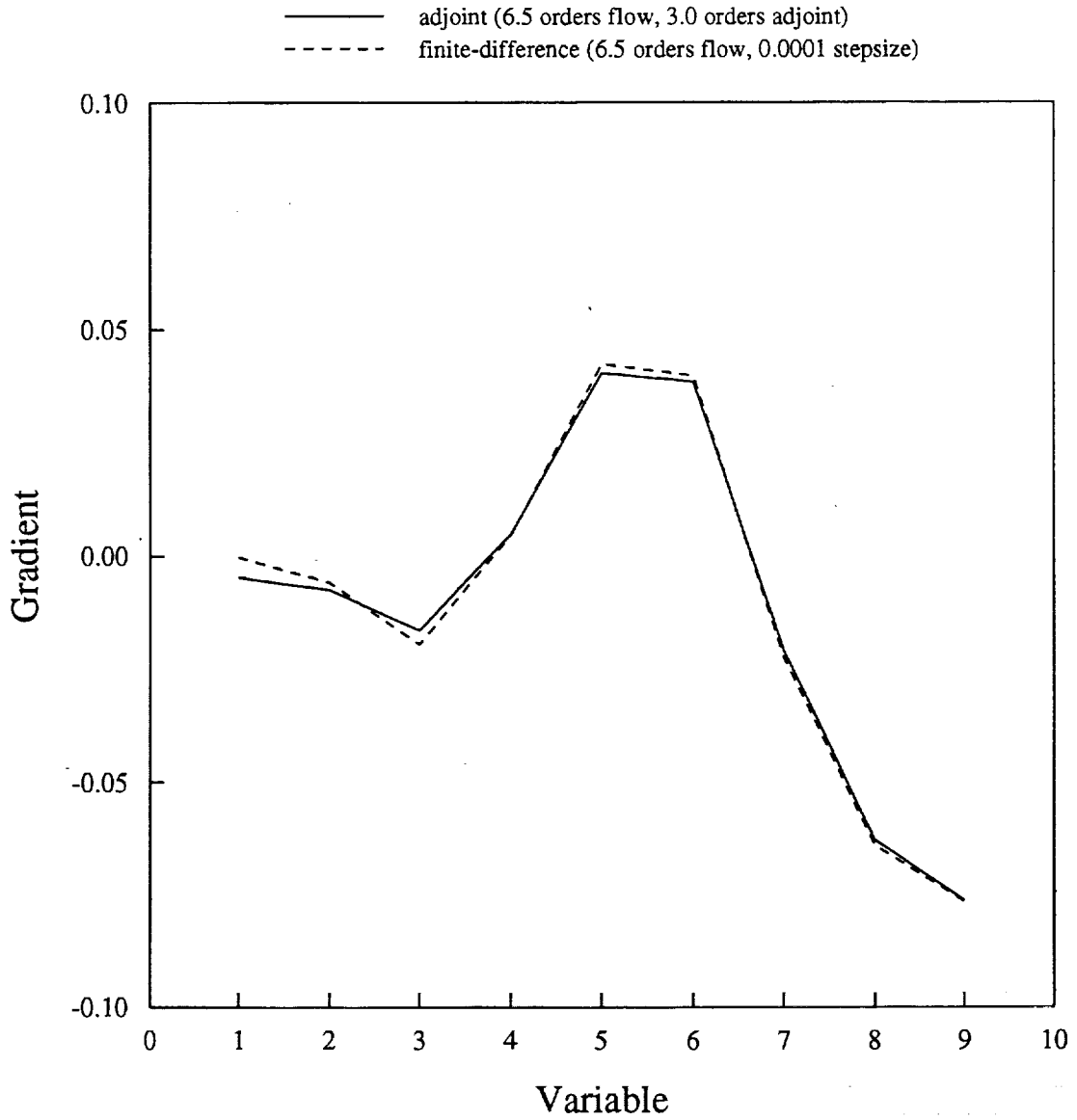
Accuracy for Different Levels of Adjoint Solver Convergence: Flow convergence 6.5 orders.



Gradient Checks for Supersonic Flows, *continued*

The **fifth figure** shows that the adjoint-based gradients agree very well with the best finite-difference gradients, with the discrepancies somewhat greater where the gradient magnitudes are small as might be expected.

Gradient Accuracy Comparisons Adjoint vs Finite-Difference Best Gradients from Each Method



Navier-Stokes-Based Constrained Design Example

As an illustration of the new Navier-Stokes-based optimization capability, a viscous redesign of the wing of a complete business jet configuration is presented. The mesh has a general C-O topology and a flow-through nacelle, with 240 blocks and 5.8 million computational cells. While a complete configuration is being modeled, only the wing is treated as a viscous solid surface. The other components are handled with inviscid boundary conditions. The Navier-Stokes calculation uses an all-turbulent boundary layer with a Baldwin-Lomax turbulence model. The wall normal spacing of the first cell was such that at the cruise condition a $y^+ = 1$ would be attained at the half span trailing edge assuming a flat plate turbulent boundary layer. At the cruise condition (Mach = 0.80 and an altitude of 40,000 ft) the Reynolds number is 1.45 million/ft. The design point is chosen to be Mach = 0.82 with a $C_L = 0.35$.

Navier-Stokes-Based Constrained Design Example

- **Mesh**
 - Wing-Body-Nacelle-Pylon-Empennage Geometry
 - 240 blocks
 - 5.8 Million Mesh Cells
- **Wing Redesign in the Presence of Body, Nacelles, Pylon, Vertical Tail and Horizontal Tail**
 - Improve Aerodynamic Performance at Design Point
- **Starting Conditions**
 - Generic Business Jet Configuration
 - Design Point 2: $M = 0.82$, $CL = 0.35$

Navier-Stokes-Based Constrained Design Example, *continued*

The design algorithm, with a no-slip boundary condition on the wing and the viscous terms turned on, is run in drag minimization mode at fixed lift. A single Navier-Stokes analysis uses 300 multigrid cycles to converge 4.7 orders of magnitude and consumes 2.0 hours of wall clock time on 32 processors of an IBM SP2.

The design variables consisted of 18 Hicks-Henne Sine functions at six wing defining sections for a total of 108 variables. Spar thickness constraints were enforced at each defining station at $x/c = 0.2$ and $x/c = 0.8$. Maximum thickness was forced to be preserved at $x/c = 0.4$ for all six defining sections. Each section was also constrained to have the thickness preserved at $x/c = 0.95$ to ensure an adequate included angle at the trailing edge. A total of 55 linear geometric constraints were imposed on the configuration.

- **Cost Function**
 - Minimize Configuration Drag Keeping Mach Number and Lift Fixed
- **Design Variables**
 - 108 Hicks-Henne Functions at 5 Wing Defining Stations
 - 55 Geometric Wing Constraints (Wing Spars, and Trailing Edge Closures)
- **Results**
 - 21.5% Drag Reduction in 5 Design Cycles
 - Inviscid Adjoint

Navier-Stokes-Based Constrained Design Example, *continued*

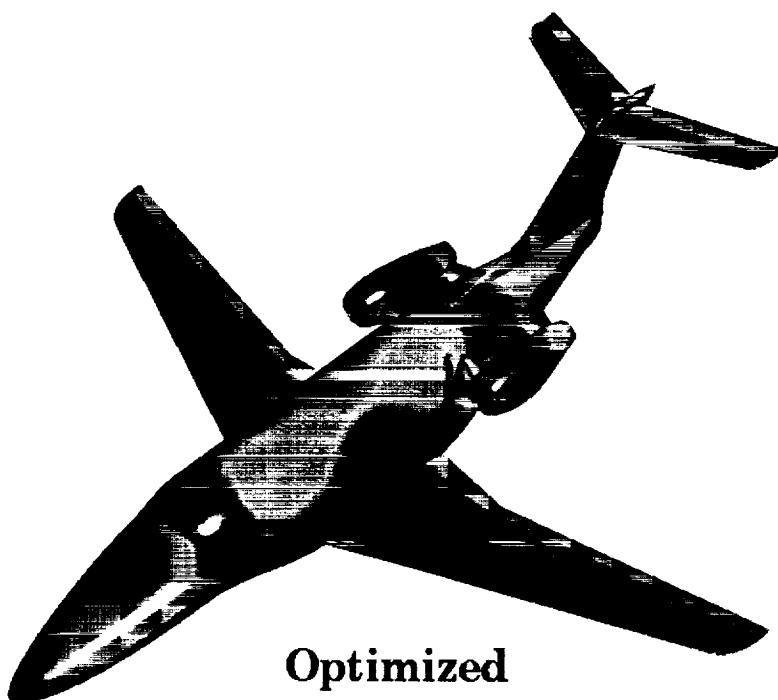
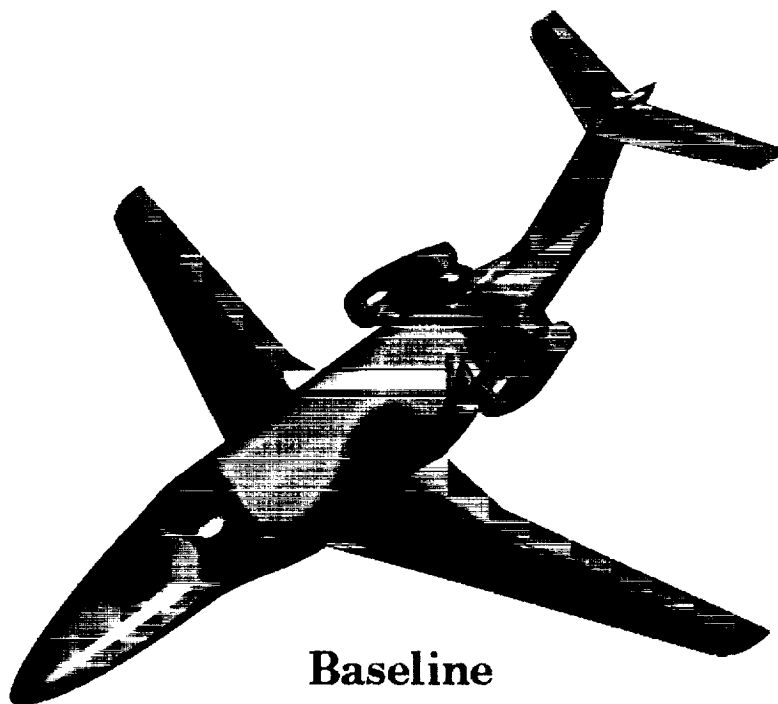
The figure shows an iso-Cp colored representation of the initial design and the final design after 5 NPSOL design iterations. Note that the strong shock present on the upper wing surface in the initial configuration has been eliminated. The character of the changes to the pressure distribution follow those that occurred for a related Euler-based design, but the Navier-Stokes design tends to have a more benign behavior in the pressure distributions. The overall pressure drag for the complete configuration was reduced by 21.5%.

Recall that an inviscid adjoint solver was instrumental in this substantial improvement. Also, only 5 NPSOL steps were taken where considerably more could have improved the design slightly. More importantly, since this was only a single-point design, the result may suffer unacceptable off-design behavior. In earlier work we have treated the case of inviscid design at multiple design points while here we addressed the case of viscous design at a single design point. Eventually, both the multipoint and viscous design capabilities must be used concurrently.

Transonic Business Jet Configuration

Iso-Cp Contours, Navier-Stokes

$M = 0.82$, $C_L = 0.35$



Navier-Stokes-Based Constrained Design Example, *continued*

The corresponding improvement for the Euler-based design analyzed with the Navier-Stokes equations has a 20.5% improvement as contrasted with the 21.5% for the Navier-Stokes-based design. The tables below compare the costs of Euler and Navier-Stokes analyses and of the two comparable design runs.

The Navier-Stokes result must be taken with caution since the sensitivity of the pressure distributions to the presence of the boundary layer can vary widely depending on the configuration. Furthermore, had we used a true viscous adjoint it may have been possible to lower the pressure drag for the configuration even further. Clearly, much further testing of the design approaches developed here is needed. These calculations must be taken as the preliminary steps towards Navier-Stokes-based aircraft design.

Overall Computational Statistics

Analysis	# of Cells	# of Processors	# of Multigrid Cycles	Wall Time
Euler	4.1 Million	32	150	0.7 Hours
Navier-Stokes	5.8 Million	32	300	2.0 Hours

Table 1: Results Using IBM SP2

Design	# of Design Cycle	# of Processors	Reduction in Drag	Wall Time
Euler	6	32	20.5 %	13.5 Hours
Navier-Stokes	5	32	21.5 %	28.0 Hours

Table 2: Results Using IBM SP2

Navier-Stokes-Based Constrained Design Example, *continued*

The present calculation took 28 hours for 5 design cycles on 32 processors of an IBM SP2. The table shows a breakdown of the approximate costs in time.

Breakdown of Computational Cost for Navier-Stokes Design

Design	Time per Analysis	# per Design Iteration	# of Design Steps	Approximate Time
Flow Analysis	1.0-1.5 Hours	3	5	21.0 Hours
Adjoint Analysis	0.5-1.0 Hours	1	5	5.0 Hours
Mesh Perturbations and Gradient calculations	0.3	1	5	1.5 Hours
				28.0 Hours

Table 3: Results Using IBM SP2

This page is intentionally left blank.



High Speed Aerodynamics, Long Beach

The AEROSHOP Toolkit (AERodynamic SHape Optimization)

Eric R. Unger
Robert P. Narducci
James O.Hager
Peter M. Hartwich
Raul Mendoza
Geojoe Kuruvila

Configuration Aerodynamics
The Boeing Company, Long Beach CA

HSR Airframe Technical Review
Los Angeles, CA
February 9-13, 1998



This page is intentionally left blank.

The AEROSHOP Toolkit (AEROdynamic Shape Optimization)

Eric R. Unger, Robert P. Narducci, James O. Hager,
Peter M. Hartwich, Raul Mendoza, Geojoe Kuruvila

The Boeing Company
Long Beach, California 90807-5309

This paper is an overview of the capabilities and structure of BLB's new AEROSHOP design toolkit. The development of this code has taken place over the past year leveraging key components of previous work in Configuration Aerodynamics (CA) at Boeing Long Beach (BLB), and new tools developed in the High-Lift element. AEROSHOP is a versatile tool that will be used for all of BLB's CA optimization work. Also presented here is a sample cross-section of some of the recent optimization experiences using AEROSHOP on various problems from transonic flap optimization to integrated wing/body/nacelle/diverter/empennage design. The code is continuously being enhanced to extend its capabilities to configurations with canards, evaluating design sensitivities in a production mode using alternative methods, and fully exploiting parallel processing.

Outline

The following is an outline of the presentation.

Outline



High Speed Aerodynamics, Long Beach

- Introduction and background
- AEROSHOP capabilities
- AEROSHOP structure and components
- Example optimization cases
- Conclusions and future work

What is AEROSHOP?

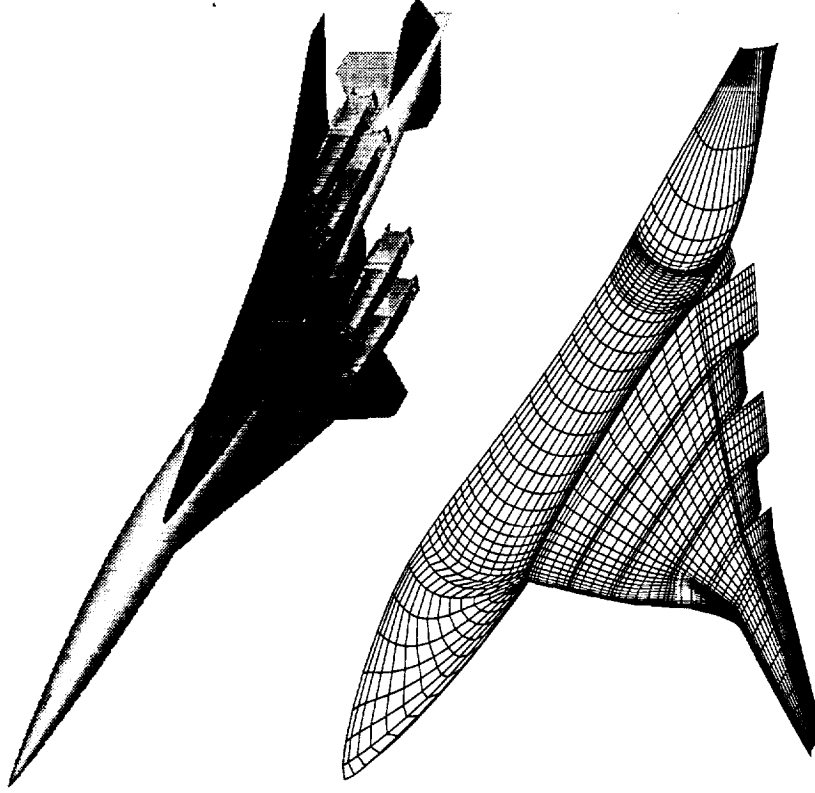
The AEROdynamic SHape OPTimization (AEROSHOP) system is a toolkit to optimize the shape of an aircraft. The system is very general, using UNIX shell scripts to link off-the-shelf analysis software needed to improve the design. This software can be as simple or as detailed as the user wishes. To the AEROSHOP environment, the complexity of a given code is irrelevant (although implementing it in an automatic mode may not be).

AEROSHOP has been developed at Boeing Long Beach (BLB) to improve versatility and to position Boeing to do future work more effectively. This system has become BLB's default optimization utility.

What is AEROSHOP?



High Speed Aerodynamics, Long Beach



- Optimization toolkit
- Platform for general optimization problems
- Modular environment using UNIX shell scripts to integrate stand-alone codes



Why AEROSHOP?

At the end of BLB's Cycle 2 optimization exercise, it became clear that the previous optimization code, MDO3D, had reached the limits in its flexibility and capability. Two new types of problems were on the horizon: transonic flap optimization and integrated wing/body/nacelle/diverter optimization. These two problems had very different optimization system requirements, which spelled the need for a modular code that could handle diverse configurations. Furthermore, computer systems are in continuous flux and parallel processing systems appear to be the computational platforms in the future. A need exists for an optimization system to address this new reality. AEROSHOP addressed these issues in a format that is also easy to maintain and has subsequently grown into a powerful design optimization system.

Why AEROSHOP?



High Speed Aerodynamics, Long Beach

- MDO3D reaching its limits in flexibility and capability
- Need for modularity
 - Alternate analysis codes (or new versions of existing codes) now and in the future
 - Wide range of geometric complexity
 - Ease of maintenance
 - Multiple computer platforms
 - Reduced memory requirements

AEROSHOP History

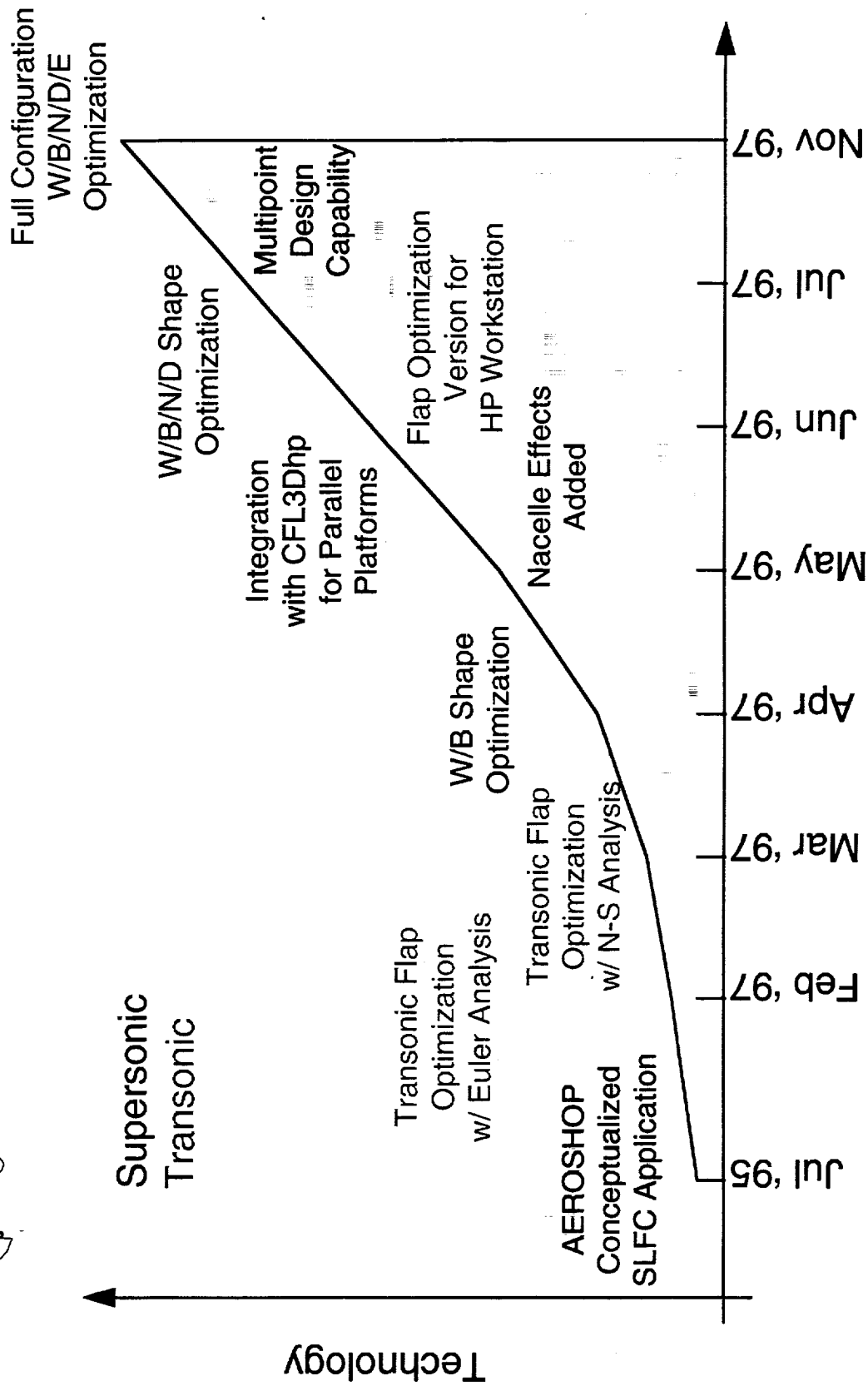
AEROSHOP was originally developed under the HSR Supersonic Laminar Flow Control (SLFC) program as a tool to minimize the amount of suction applied to a wing to maintain laminar flow. However, this code was very modular and formed an excellent backbone to a much more general and capable aerodynamic optimization system.

The first aerodynamic shape development work on AEROSHOP occurred in Feb. 1997, when CFL3D, QGRID, and a high-lift developed flap deflection code were incorporated into the system. This new code was the platform for the very successful transonic flap optimization study. Soon after that, the system was further generalized to handle wing/body shape optimization, with nacelle effects modules completed and integrated into the system by May 1997. Next, parallel processing became a focus with the incorporation of CFL3Dhp and a flap optimization version of the code for the HP workstation. In June, modules were completed that would allow for the automatic grid generation about an integrated wing/body/nacelle/diverter configuration. These routines were immediately incorporated into the AEROSHOP system and optimization testing began that same month. The next major development milestone in the AEROSHOP system was the implementation of a multipoint design problem, capable of having an objective function that considers both a supersonic and transonic Mach number. The most recent developments to AEROSHOP include an ability to handle wing/body/nacelle/diverter/empennage configurations, adjoint-based sensitivity calculations, and more complete parallel implementations.

AEROSHOP History



High Speed Aerodynamics, Long Beach



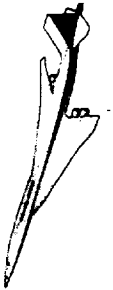
Technology



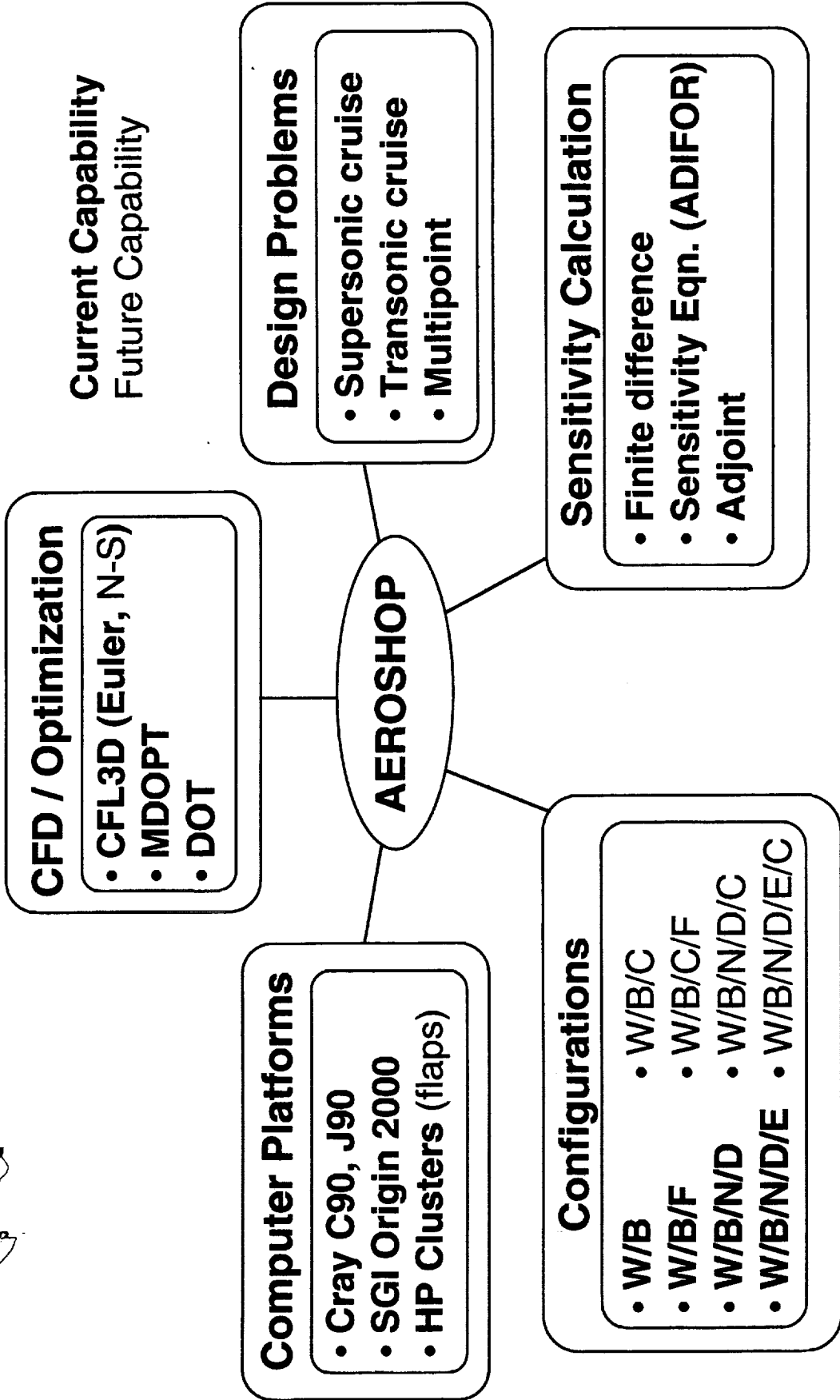
AEROSHOP Capabilities

Shown below are some of the capabilities of the AEROSHOP system and a list of the platforms it can run on. Some of these platforms, SGI Origin 2000, and the HP workstation cluster are exclusively parallel systems. Some development work is still needed to handle configurations with canard. It is likely that gridding these types of configurations will require (or at least work better with) overset grids. At this time we are still evaluating the suitability of overset grids in AEROSHOP. Also not completed is an implementation of adjoint-based sensitivities on configurations requiring multiblock patched grids. Finally, note that while CFL3D is both an Euler and Navier-Stokes solver, the general grid clustering modules that would be necessary to consider N-S optimization have not been implemented.

AEROSHOP Capabilities



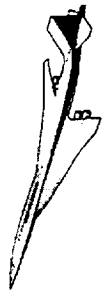
High Speed Aerodynamics, Long Beach



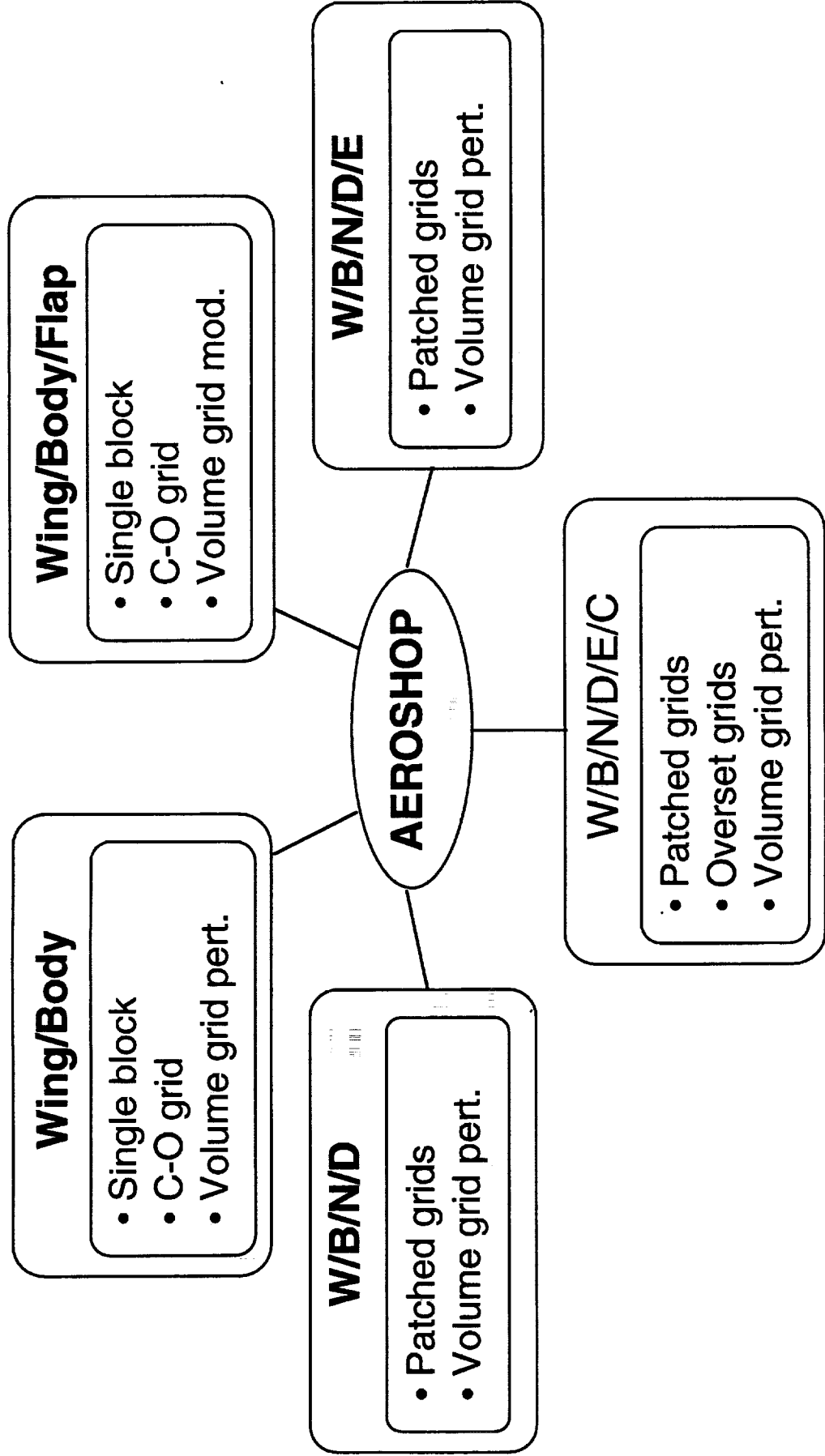
Configuration Capabilities

Shown below are the various configurations that AEROSHOP can optimize. Both the wing/body and wing/body/flap cases use a single-block C-O type grid for analysis. Configurations with nacelles and diverters require a patched multiblock grid. In the near future, AEROSHOP will be able to handle configurations with canards which will likely require the use of overset grids. Note that all volume grid generation uses perturbation methods.

Configuration Capabilities



High Speed Aerodynamics, Long Beach



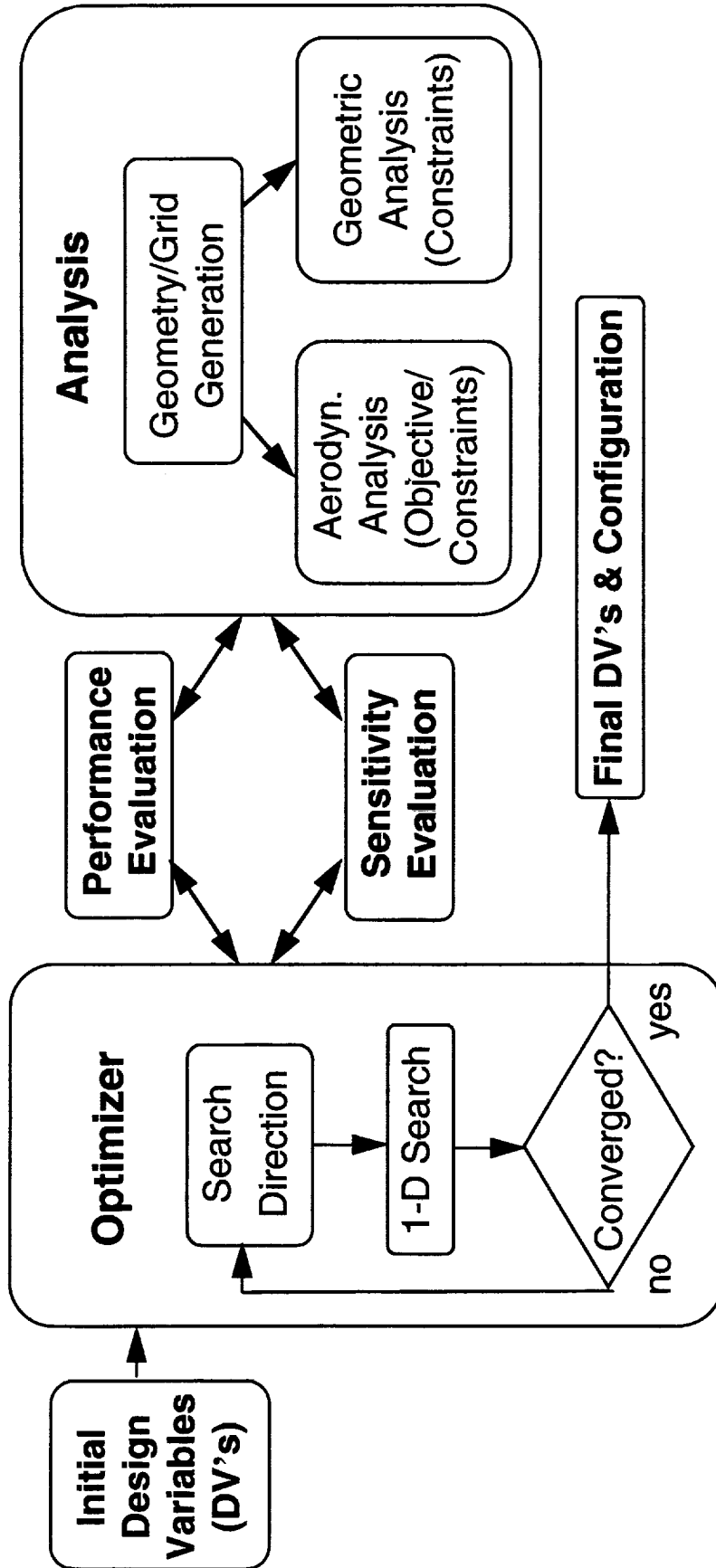
AEROSHOP Structure

Shown below is a very top-level diagram of the AEROSHOP system. AEROSHOP is essentially made up of an optimizer module which is given an initial set of design variables. The optimizer requires either performance evaluations of the current configuration (as defined by the design variables) or a sensitivity of the current configuration to the design variables. This information is needed so that the optimizer can select the correct search direction and find a minimum drag design. When a performance analysis is needed, the performance module calls the routines necessary to generate the geometry and the grids which are then passed to the aerodynamic analysis and geometric analysis modules. Both the aerodynamic and geometric analysis modules return the values of the objective function and constraints. If a sensitivity calculation is called for, the process can be more complex. At the simplest level, a finite-difference calculation is used, and this module asks for multiple analysis results (as with the performance evaluation). If an adjoint or ADIFOR-based sensitivities are desired, the sensitivity module must call very complex codes.

AEROSHOP Structure



High Speed Aerodynamics, Long Beach



W/B/N/D Geometry/Grid Generation

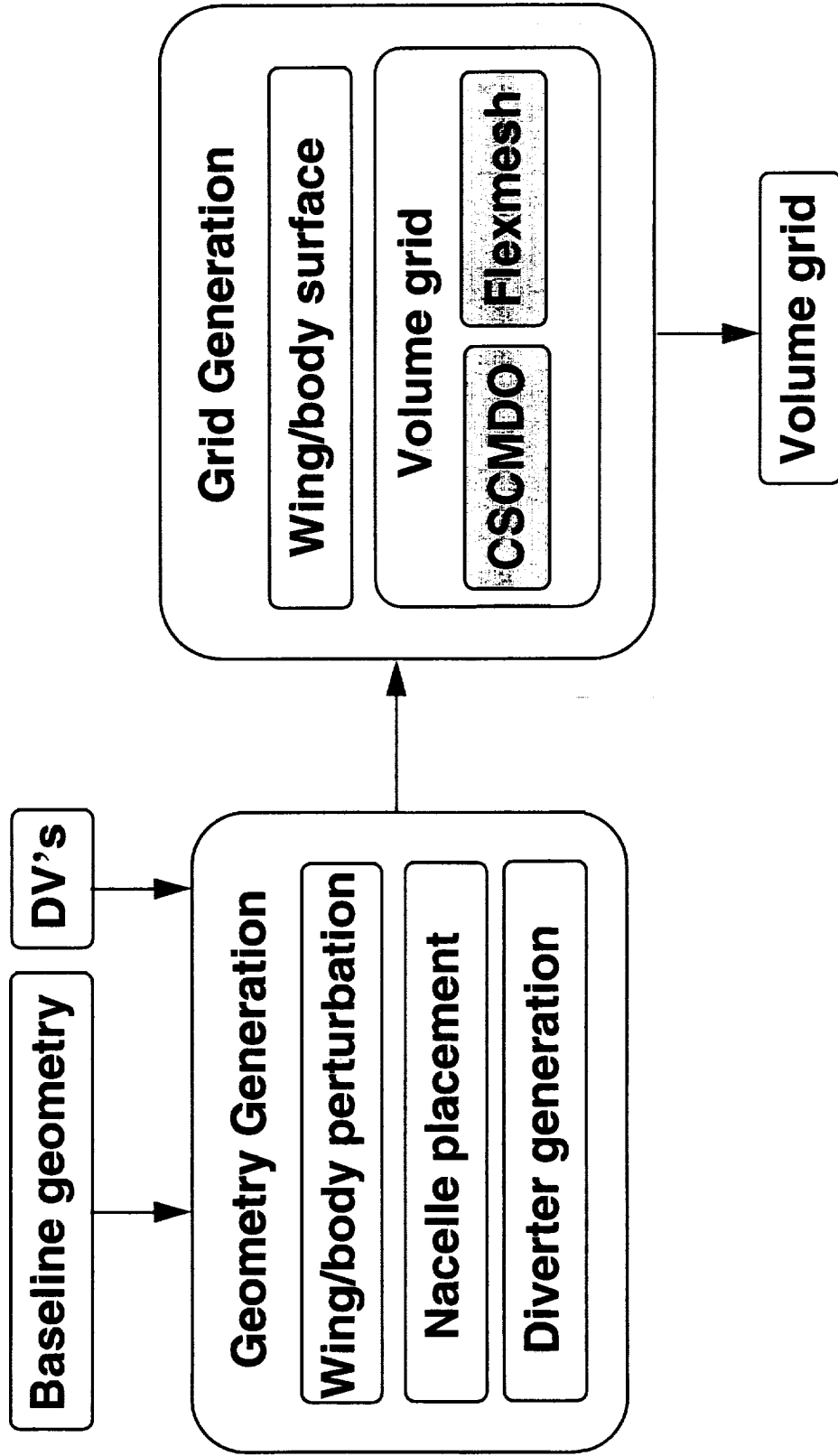
A top-level diagram of the geometry and grid generation in AEROSHOP is shown below. Presented in its basic form, the geometry generation module takes a baseline geometry and input design variables and then perturbs the wing/body surface. Next, the nacelles are rolled and pitched to follow the lower surface of the wing (assuming a W/B/N/D configuration is being optimized). The final geometry step is the generation of a new diverter between the new wing and the translated and rotated nacelles.

The grid generation module uses the current defining geometry and creates a CFD surface grid on the wing/body using the QGRID code. This surface grid is then passed to either CSCMDO or FlexMesh to create multiblock wing/body surface and to perturb the multiblock volume grid. Again, if only a wing/body configuration is being optimized, the volume is single block, and the nacelle/diverter work is unnecessary.

W/B/N/D Geometry/Grid Generation



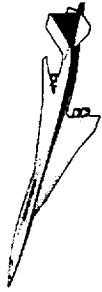
High Speed Aerodynamics, Long Beach



Wing/Body Surface Grid Generation

Wing/body surface grid generation is handled by the QGRID code. This code places a C-O topology surface grid on a wing/body geometry. In its present implementation in AEROSHOP, QGRID is only responsible to generate surface grids, however, the code can also create a volume grid from scratch. One of the challenges of using the QGRID code on the TCA configuration was the position of the wing. The wing protrudes below the fuselage at about the mid-chord position. In order to create a grid, QGRID needs a distinct wing/body intersection line on the fuselage. Since this is not possible with the TCA configuration, extensive modifications were made to the code. In its AEROSHOP application, QGRID automatically splices part of the wing into the fuselage in order to function properly. An illustration of this splice is shown in the figure below.

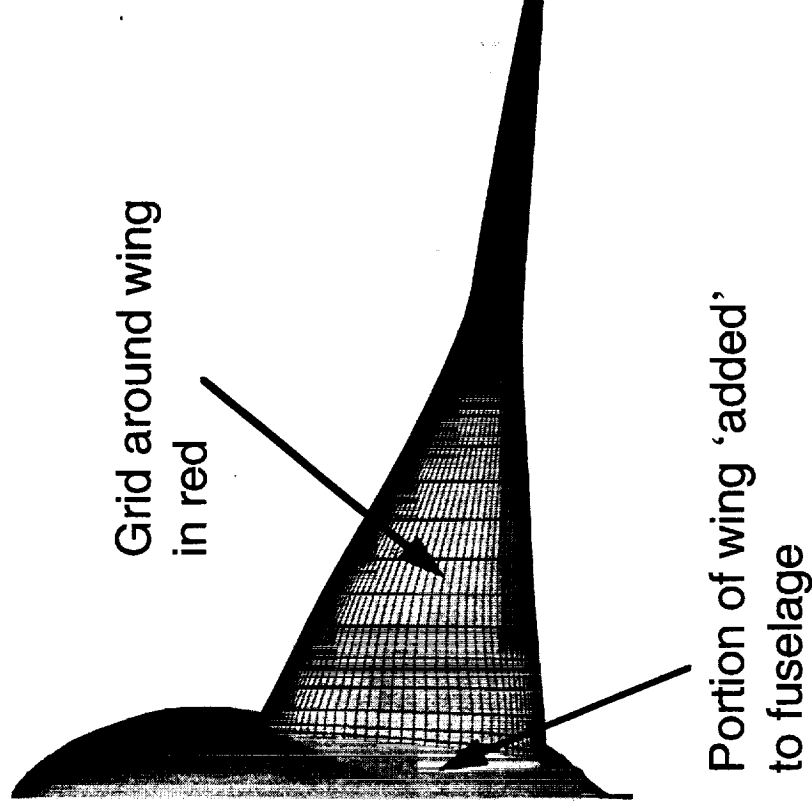
Wing/Body Surface Grid Generation



High Speed Aerodynamics, Long Beach

QGRID

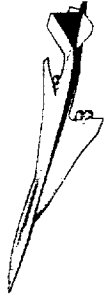
- Generates surface grid for W/B configurations
- Basic W/B grid of C-O topology
- Modified to handle more general TCA-type configuration
- Serves as background to W/B/N/D grid generation



W/B/N/D Volume Grid Generation

CSCMDO is the primary tool that AEROSHOP uses to create W/B/N/D (and W/B) volume grids. The code takes the input wing/body surface grid and the nacelle and diverter surface grids and generates the necessary multiblock wing/body surface and volume grids. CSCMDO is driven by an extensive input deck which is very labor intensive to create and update. Positive aspects of CSCMDO are that it is absolutely general in its applications (and has been recently been extended to W/B/N/D/E grids) and that it produces output grids of high quality (see below).

Wing/Body/Nacelle/Diverter Grid Generation

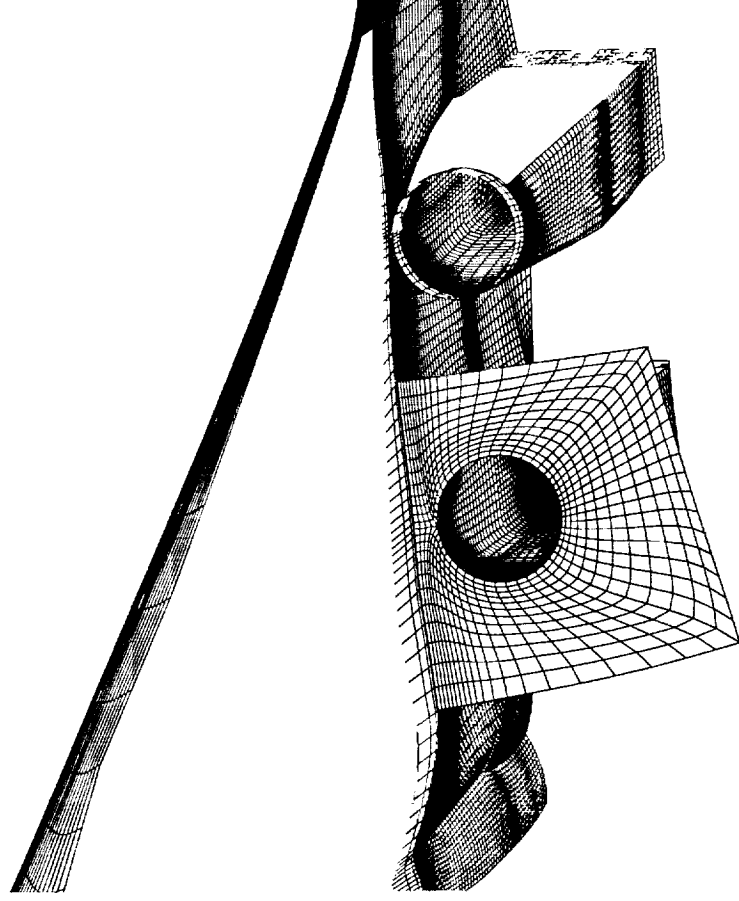


High Speed Aerodynamics, Long Beach

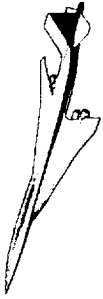
Primary system uses

CSCMDO

- Development of input deck is very labor intensive and needs frequent updates
- System is very general and has been extended to W/B/N/D/E configurations
- Output grids are of high quality using 1 min of C90 CPU time

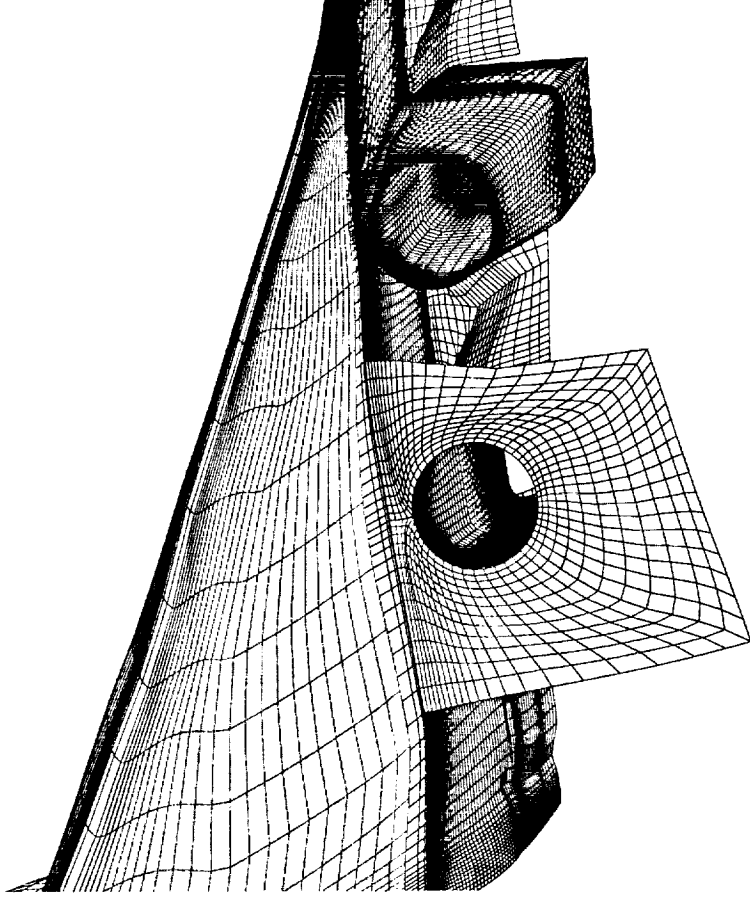


Wing/Body/Nacelle/Diverter Grid Generation



High Speed Aerodynamics, Long Beach

- Secondary system is based on Flexmesh**
- No input deck required
 - System is useful for quick transition to different problem types
 - Output grids can be skewed, with overall system less stable than CSCMDO-based one
 - Surface grid generation necessary



Sensitivity Calculation



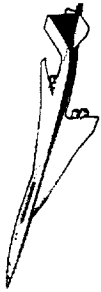
High Speed Aerodynamics, Long Beach

- Finite-difference derivatives
 - Easy to implement
 - Fairly accurate (with proper step size)
 - All previous work based on this approach
- Sensitivity Equation (ADIFOR)
 - Accurate derivative with no step size issues
 - Substantial system requirements
 - Parallel processing needed to improve efficiency
- Adjoint
 - Accurate derivative with no step size issues
 - Very efficient
 - Future of much of BLB optimization work

Parallel Finite-Difference Process

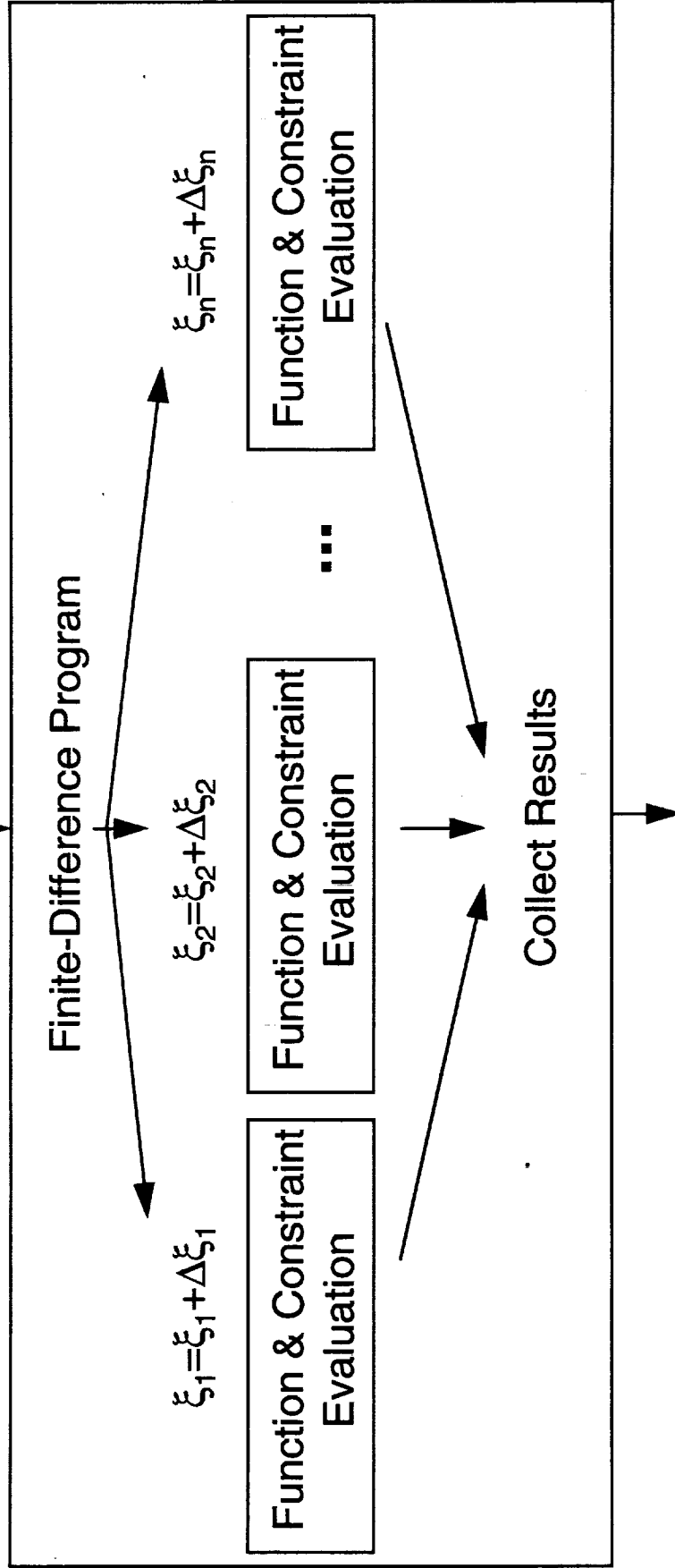
Shown below is a diagram of a coarse-grain implementation of finite-difference based sensitivity calculations. In this type of parallel application, each computer processor performs an entire analysis for each perturbed design variable. If the number of design variables and the number of processors used are equal, then an entire sensitivity calculation can take place in the wall-clock time of a single analysis.

Parallel Finite-Difference Process



High Speed Aerodynamics, Long Beach

Called from sensitivity routine



Return to sensitivity routine



Flow Solver and Optimization

The solution for the aerodynamic forces in AEROSHOP is currently being handled by the CFL3D code (although any code could be substituted). This well known and well validated code solves either the Euler or thin-layer Navier-Stokes equations. CFL3D can efficiently solve on multiblock patched and overset grids. A parallel version, CFL3Dhp, has recently been developed that uses fine-grained parallelization to further increase throughput on certain computer platforms.

There are two different optimization modules in AEROSHOP at present. The most widely used is MDOPT, which is a version of the NPSOL optimizer. This code is a fully constrained optimization procedure using a Lagrangian approach and it appears to work well on large and complex problems. A second optimizer is DOT. This tool is similar to MDOPT in its overall capabilities; however, it relies on a usable/feasible optimization method.

Flow Solver and Optimization



High Speed Aerodynamics, Long Beach

- CFL3D aerodynamic analysis
 - Euler and Navier-Stokes
 - Multiblock, patched, and overset grids
 - Efficient solutions
 - Parallel capability (coarse grained - CFL3Dhp)
- MDOPT optimization
 - Modification to NPSOL
 - Fully constrained design with linear and nonlinear constraints
 - Lagrangian method
- DOT optimization
 - Fully constrained design
 - Usable/feasible method

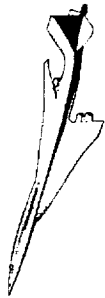
Transonic Flap Optimization

The HSCT, designed primarily for supersonic cruise, must rely on flaps for subsonic, transonic, and low supersonic flights. Obtaining flap deflection angles for minimum drag at off-design Mach numbers can have a significant impact on aircraft sizing.

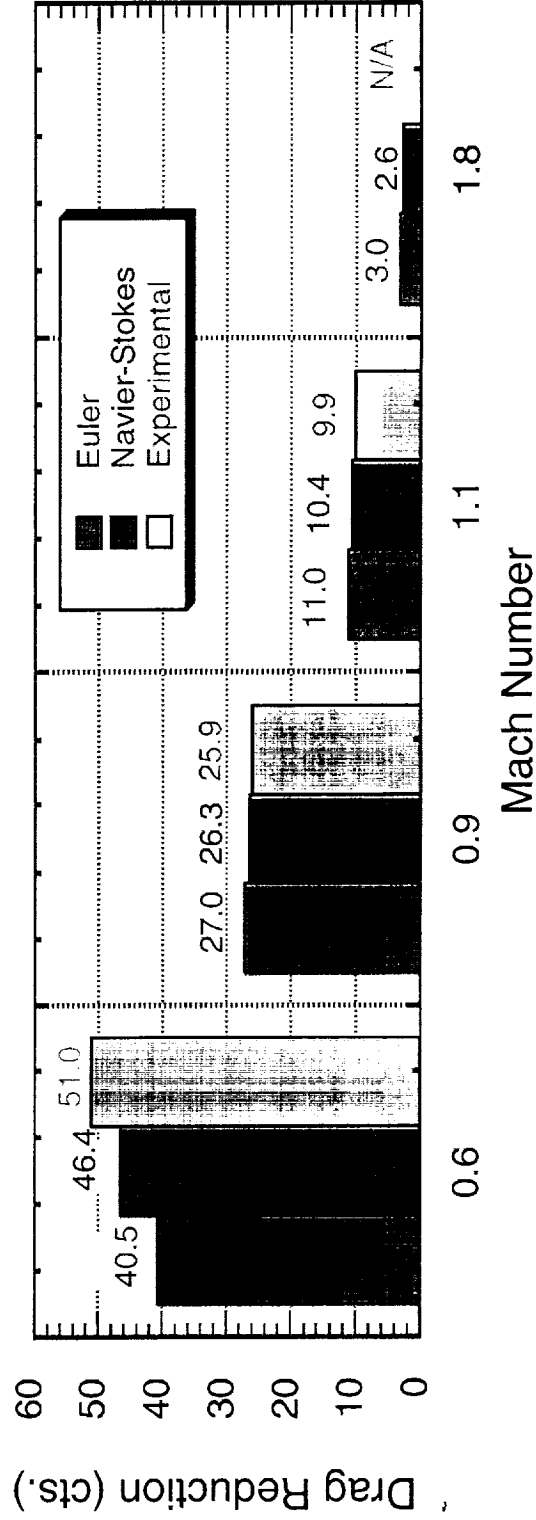
In this work, AEROSHOP was applied to obtain optimum flap deflections at a series of off-design conditions. The technology, based on Euler analyses was applied to the TCA configuration. Drag improvements were verified with a detailed N-S analysis of baseline and optimized flap configurations. Finally, improvements were experimentally validated through extensive wind-tunnel testing.

Transonic Flap Optimization

High Speed Aerodynamics, Long Beach



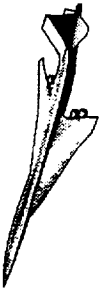
- Euler optimization
- Navier-Stokes analysis and verification
- Experimental validation



Integrated W/B/N/D Optimization

A system to automatically generate wing/body/nacelle/diverter grids was developed and incorporated into AEROSHOP recently. Three major cases have been looked at to date with the optimization and analysis tools having been run hundreds of times. On reasonable geometries, the system has proven to be quite stable and has yielded significant design improvements over the BLB Cycle 2 configuration. Each of these three cases used all of the TCA constraints that were required to create the BLB Cycle 2 configuration. The first of these cases, was an initial test run with 35 design variables on the wing. The second case, used 75 design variables on the wing and the fuselage (most were on the wing). The final case used 65 design variables on the wing alone and added a local wing dihedral constraint and a much tighter C_L limit.

Integrated Wing/Body/Nacelle/Diverter Optimization



High Speed Aerodynamics, Long Beach

- Robust grid generation system
- Several cases to date ($M=2.4$):
 - All TCA constraints utilized for all cases
 - Approximately 8 CPU hours/cycle for 65 design variables using finite-difference based sensitivities
 - About 20 MW of memory required to run.

Convergence Histories for Integrated W/B/N/D Optimization

Shown below are convergence histories for a sample optimization case. The upper plot shows the convergence of the objective function (D/L) while the lower one shows the changes in the three spar constraints. After the ninth iteration, a change was made in the design variables. At the final iteration, that cruise drag reduction was 2.1 counts.

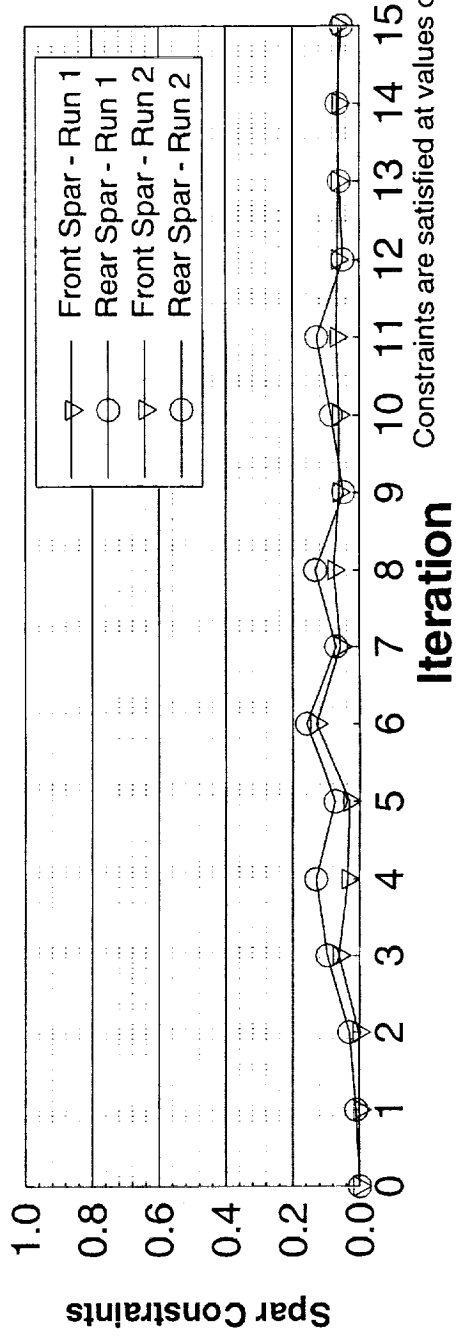
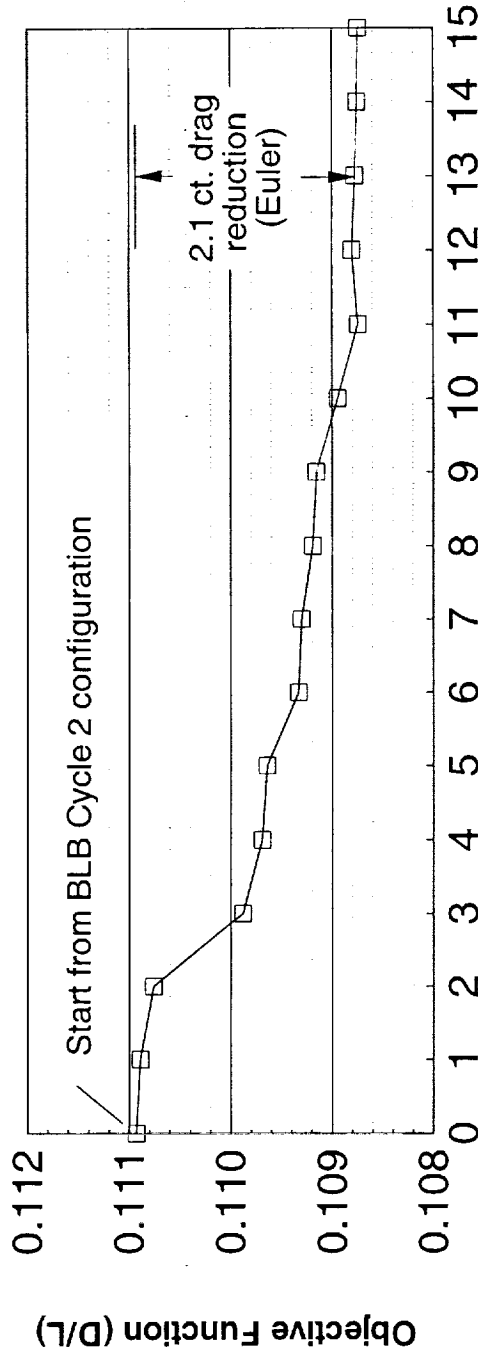
While not the only constraints used for optimization, the spar constraints are the most active and have a large impact on the optimization. Note that at the final cycles, the spar constraints are very nearly satisfied. If this constraint plot is compared to the objective function plot an interesting correlation can be seen. In many instances, large reductions in the objective function result in somewhat large constraint violations. In most instances, these violations are quickly satisfied in the next iteration.

Convergence History for Integrated TCA Wing/Body/Nacelle/Diverter Optimization



HSCT Aerodynamics, Long Beach

AEROSHOP w/ CFL3D Euler; $M_\infty=2.4$



Drag Polars for the TCA Baseline and Optimized W/B/N/D Configurations

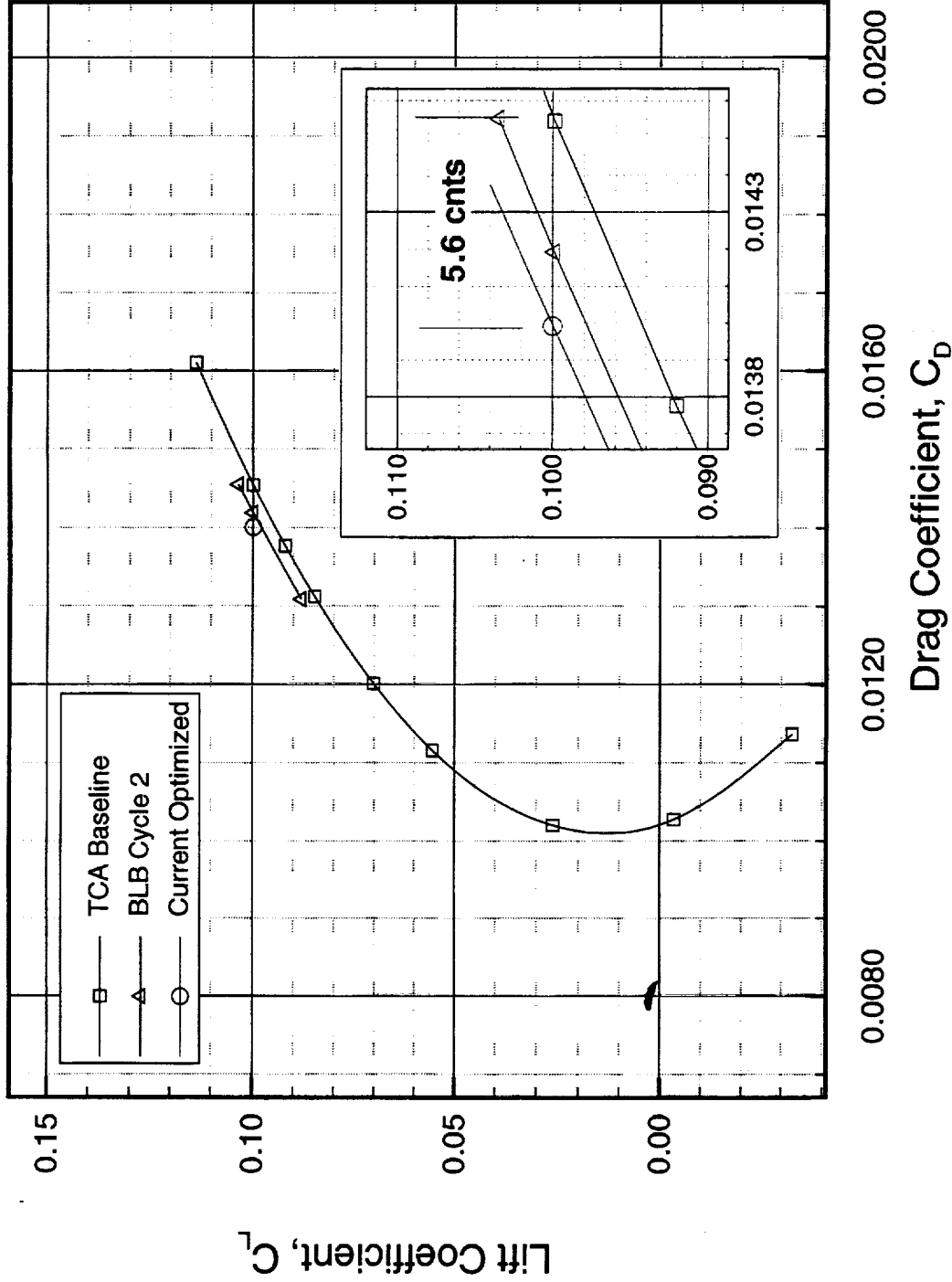
Drag polars for the TCA baseline and optimized wing/body/nacelle/diverter configurations are shown. At the current optimization level, the Euler drag reduction at cruise is 5.6 counts. This reduction is 2.1 counts over the previous BLB Cycle 2 design showing the effectiveness of AEROSHOP's integrated W/B/N/D optimization.

Drag Polars for the TCA Baseline and Optimized W/B/N/D Configurations



HSCT Aerodynamics, Long Beach

CFL3D Euler, $M_\infty=2.4$, $C_{DV}=72.5$ cts. (Full Fuse; $Re_c=6.36 \times 10^6$)



Configuration Comparisons for TCA W/B/N/D Optimization

Shown below are isometric views of the TCA Baseline configuration along with the current optimization case. The new configuration shows some wing contouring in the nacelle region but is still fairly smooth.

Configuration Comparisons for TCA W/B/N/D Optimization

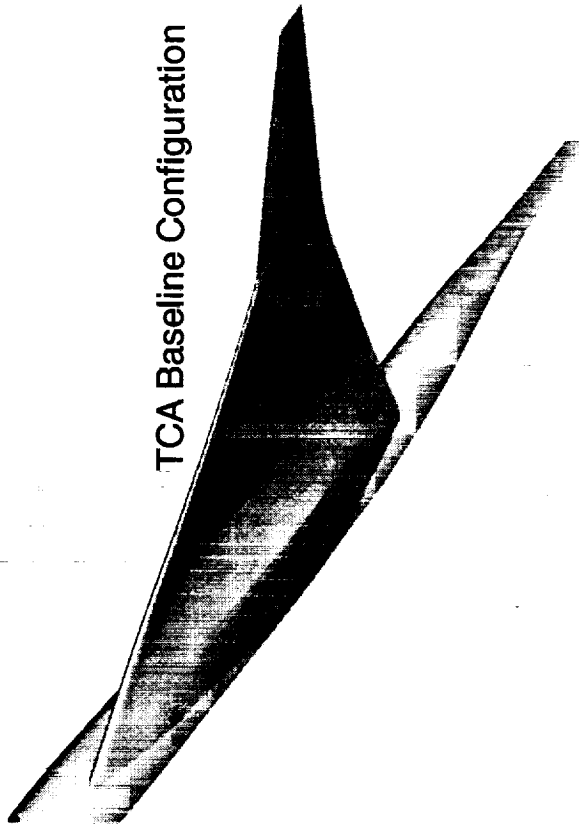


HSCT Aerodynamics, Long Beach
AEROSHOP w/ CFL3D Euler, $M=2.4$

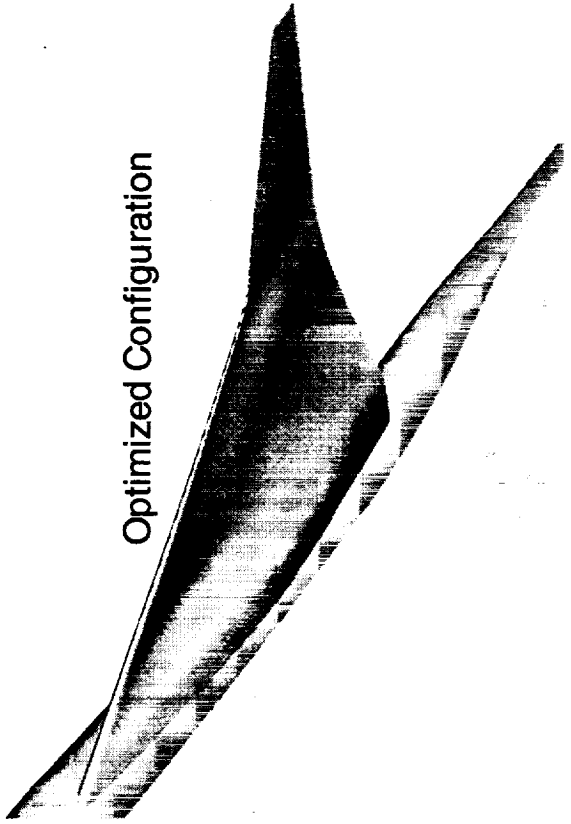


TCA Baseline Configuration

Optimized Configuration



TCA Baseline Configuration



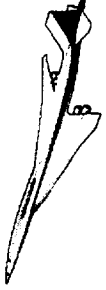
Optimized Configuration



TCA Wing Dihedral/Anhedral Optimization

During the optimization of the TCA configuration, BCAG consistently produced a configuration which exhibited a "tip-droop", a combination of inboard dihedral and outboard anhedral. At that time, only BCAG could optimize with actual nacelles and diverters present. Both BLB and ARC used approximate nacelle effects and did not get the tip-droop as BCAG did. A stand-alone Navier-Stokes analysis applied to the TCA wing/body/nacelle/diverter configuration confirmed a drag reduction with such a shape, so the question was if the integrated nacelles and diverters were responsible for producing the tip-droop. To understand this, several small optimization test cases were set up for the BLB Cycle 2 configuration. The first of these used two dihedral design variables and an angle-of-attack on a wing/body configuration (no nacelles or nacelle effects). The goal of the optimization was to increase L/D as much as possible while maintaining lift. The results of the test indicated that no improvement was possible (using those three design variables). The second case was also unable to achieve any improvement using active nacelle effects. The third case however achieved some improvement in L/D when the actual integrated nacelles were included in the optimization. The final case achieved the largest improvement using actual integrated nacelles along with nine local dihedral design variables (along with angle-of-attack). These cases clearly demonstrated that integrated nacelles are crucial to capturing this effect during optimization.

TCA Wing Dihedral/Anhedral Optimization



High Speed Aerodynamics, Long Beach

- Cases used to test the impact of integrated nacelles on optimization of local wing dihedral/anhedral
 - Benefits of wing tip-droop verified in N-S analysis when manually applied to configurations
 - Tip-droop not present in designs (ARC & BLB Cycle 2) where only nacelle effects were used
 - Repeatability of results from BCAG
- Four cases looked at ($M=2.4$):
 - W/B
 - W/B with nacelle effects
 - W/B/N/D with 2 dihedral/anhedral DVs
 - W/B/N/D with 9 dihedral/anhedral DVs

TCA Cycle 2 Wing Dihedral/Anhedral Study

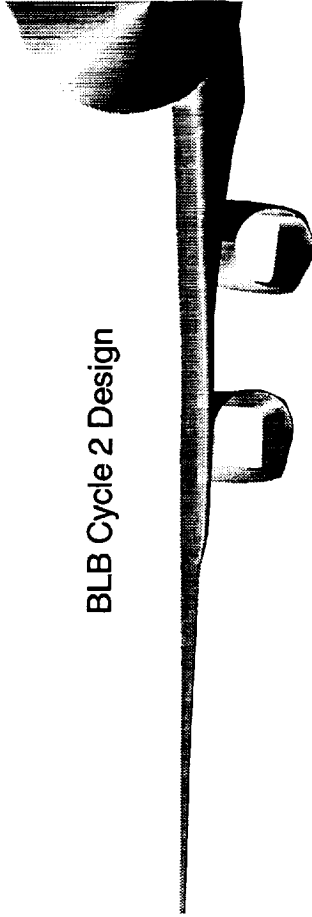
This chart shows front shaded images of the BLB Cycle 2 configuration and the two optimized designs that used the integrated nacelles and diverters. In both of these cases, the tip-droop is quite prevalent. For the second optimized design, where 9 dihedral variables were used, the outer wing panel exhibits distinct curvature while the change to the inner wing panel is smaller.

TCA Cycle 2 Wing Dihedral/Anhedral Optimization

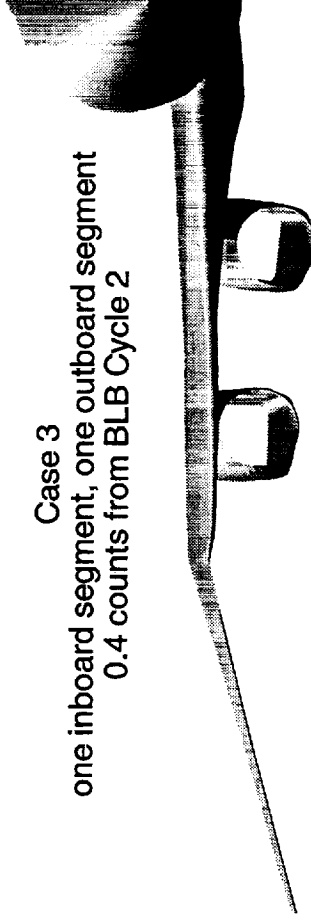
High Speed Aerodynamics, Long Beach

Front View of Shaded Geometries

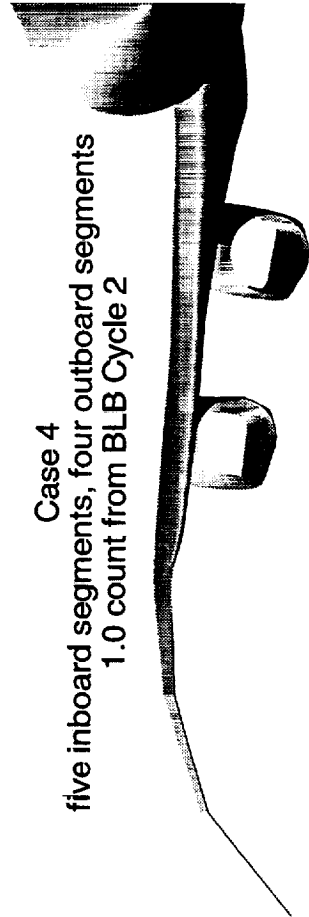
AEROSHOP with CFL3D Euler, Integrated W/B/N/D Optimization, $M_\infty = 2.4$



BLB Cycle 2 Design



Case 3
one inboard segment, one outboard segment
0.4 counts from BLB Cycle 2



Case 4
five inboard segments, four outboard segments
1.0 count from BLB Cycle 2

Integrated W/B/N/D/E Optimization

Two design cases are being run to evaluate the integrated wing/body/nacelle/diverter/empennage design capability and to investigate the effect of the pitching moment constraint on the design. The BLB TCA Cycle 2 geometry is being optimized using 55 design variables, about two thirds of which are on the wing.

Integrated W/B/N/D/E Optimization



High Speed Aerodynamics, Long Beach

- Case used to test and evaluate integrated W/B/N/D/E optimization capability
- Evaluate effect of C_M constraint on design
- 55 design variables
 - Wing: twist, camber, local dihedral, and plunge
 - Fuselage: camber, area, shape, and incidence
 - Empennage incidence
 - Angle-of-attack
- All TCA constraints were utilized along with C_M on selected cases

Effect of Tail Incidence at Constant C_L

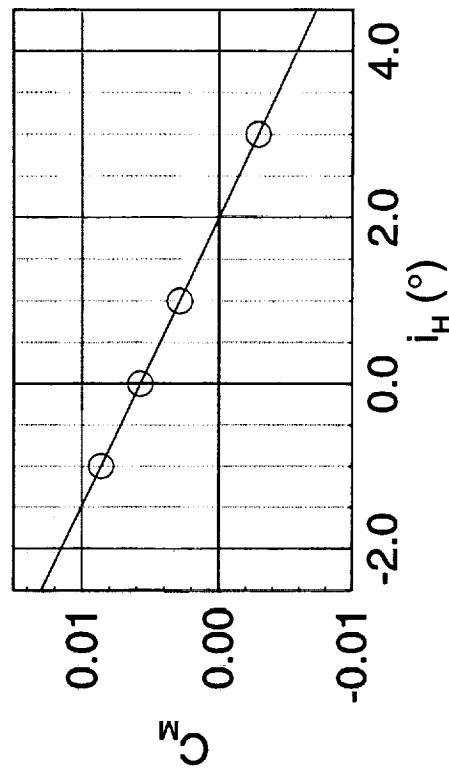
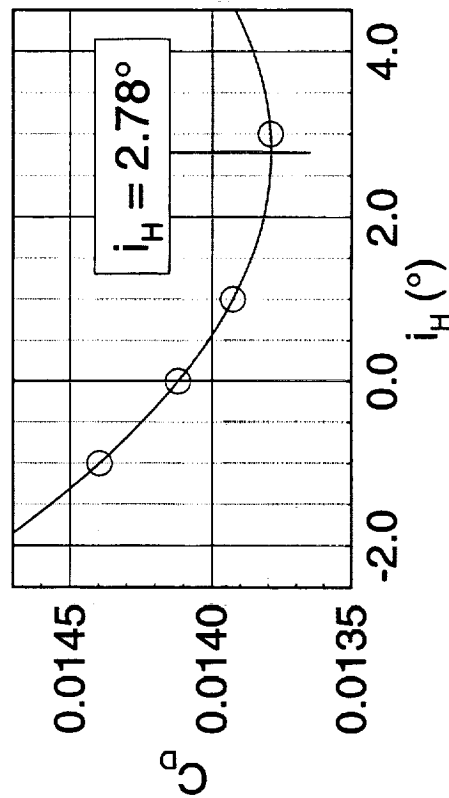
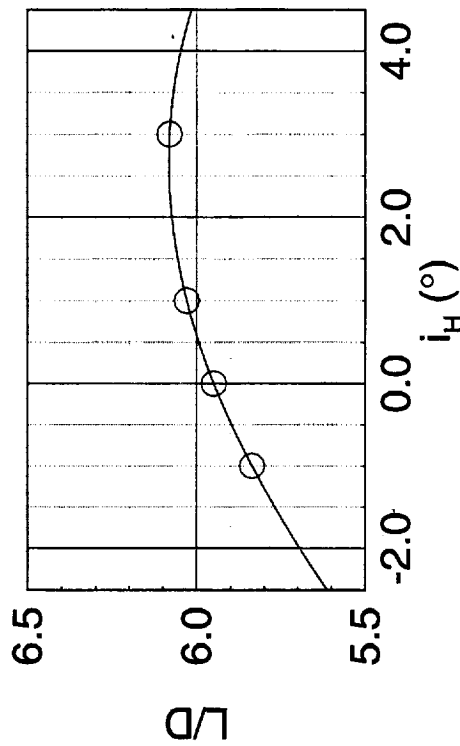
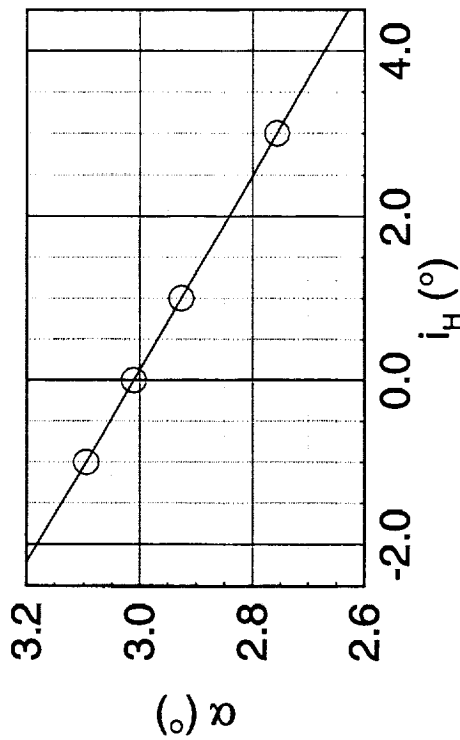
One of the motivations for optimization with the empennage is demonstrated below. If the horizontal tail on the BLB Cycle 2 configuration is deflected to produce lift, the overall impact on the configuration at the cruise configuration is a drag reduction of over three counts. Of course, this result ignores having to trim the aircraft. The hope with optimization is that this benefit can be further exploited with an unconstrained (in pitching moment) design and to see if some of this benefit can be realized in a constrained design.



Effect of Tail Incidence at Constant C_L

High Speed Aerodynamics, Long Beach

BLB TCA Cycle 2, W/B/N/D/E, CFL3D Euler,
 $M_\infty=2.4$, $C_L=0.084$, $Re_c=6.36 \times 10^6$ ($C_{Dv}=80.78$ cts)



Forces on the BLB Cycle 2 W/B/N/D/E Configuration

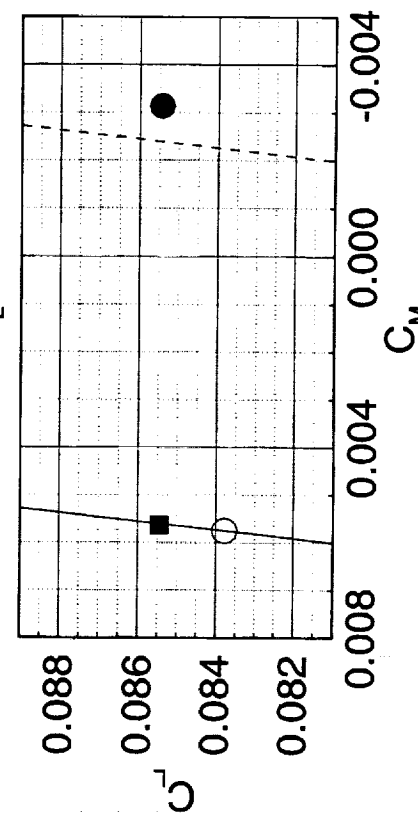
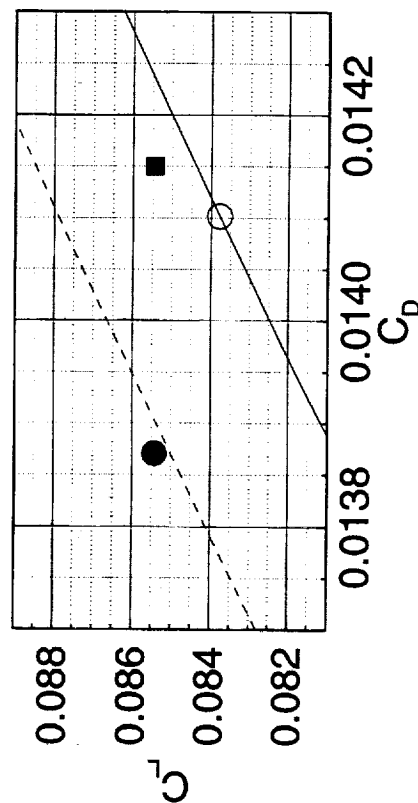
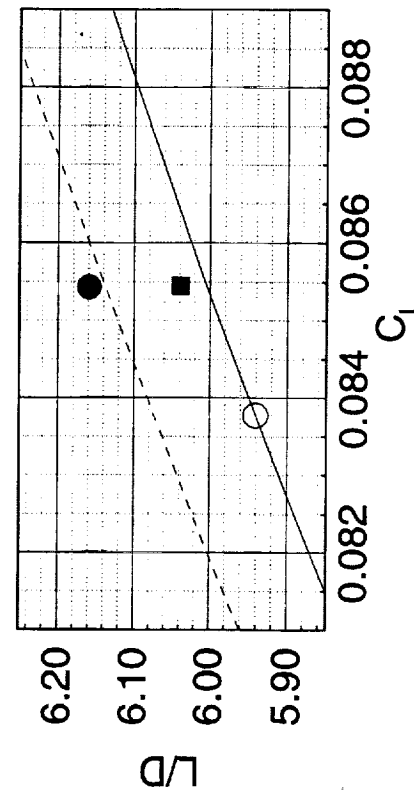
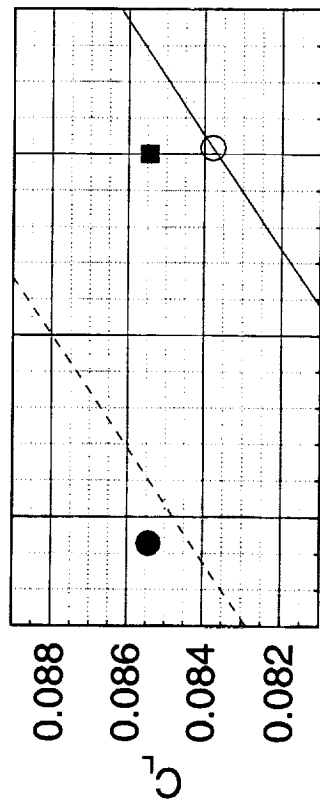
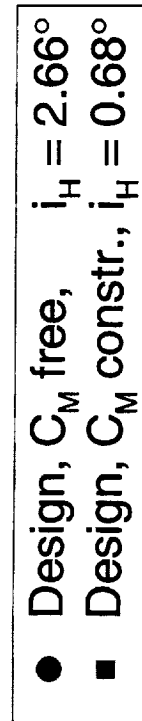
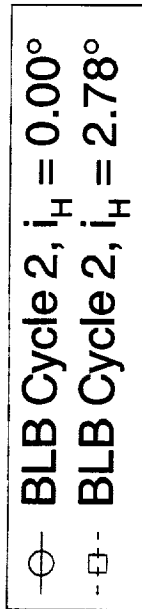
The performance of the optimized and BLB TCA Cycle 2 configuration with different tail settings are shown. While it is possible to reduce the drag of the BLB TCA Cycle 2 configuration by deflecting the horizontal tail nose-up (LE up), optimization (C_M free) was able to achieve approximately 0.6 counts of additional drag reduction. Optimization with a fixed pitching moment was able to achieve approximately 0.75 counts of drag reduction over the BLB Cycle 2 configuration.

Forces on the BLB TCA Cycle 2 W/B/N/D/E Configuration



High Speed Aerodynamics, Long Beach

CFL3D Euler, $M_\infty=2.4$, $Re_c=6.36 \times 10^6$ ($C_{Dv}=80.78$ cts)



TCA Design with Moveable Tail

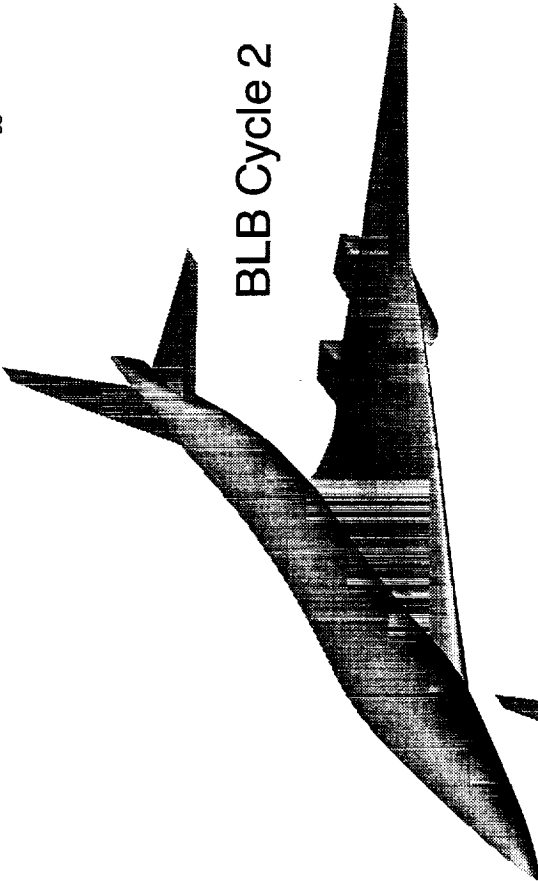
This chart shows shaded images of the BLB Cycle 2 configuration and the two optimized designs that used the integrated nacelles/diverters and empennage. The case with the pitching moment free shows larger amounts of wing camber modification.



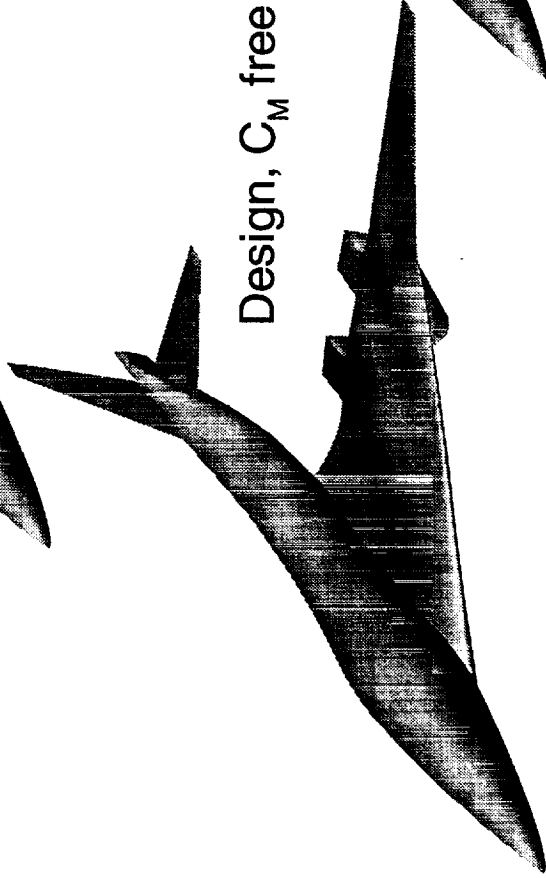
TCA Design with Moveable Tail

High Speed Aerodynamics, Long Beach

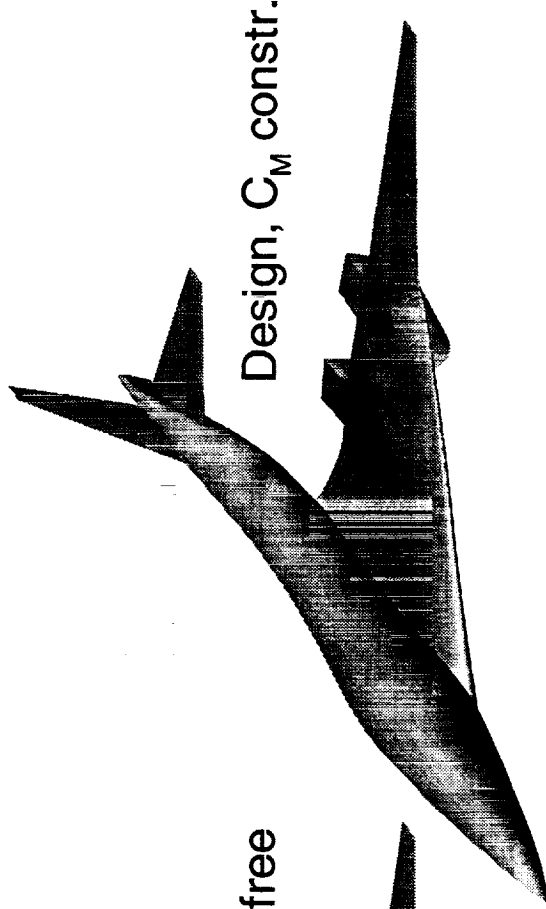
W/B/N/D/E, AEROSHOP, CFL3D Euler, $M_\infty=2.4$, $Re_c=6.36 \times 10^6$



BLB Cycle 2



Design, C_M free



Design, C_M constr.

Multipoint Optimization

In one approach to multipoint design, the shape of the HSCT is optimized with considerations of aerodynamic performance at the supersonic and transonic cruise conditions weighed according to its impact on TOGW. This approach allows for wing and fuselage shape to change according to supersonic and transonic requirements. An advantage of multipoint design is that it does not allow single-point design features that have large adverse effects at other design conditions. Likewise, beneficiary features at the transonic condition that have little impact on the supersonic cruise point performance may be introduced into the design.

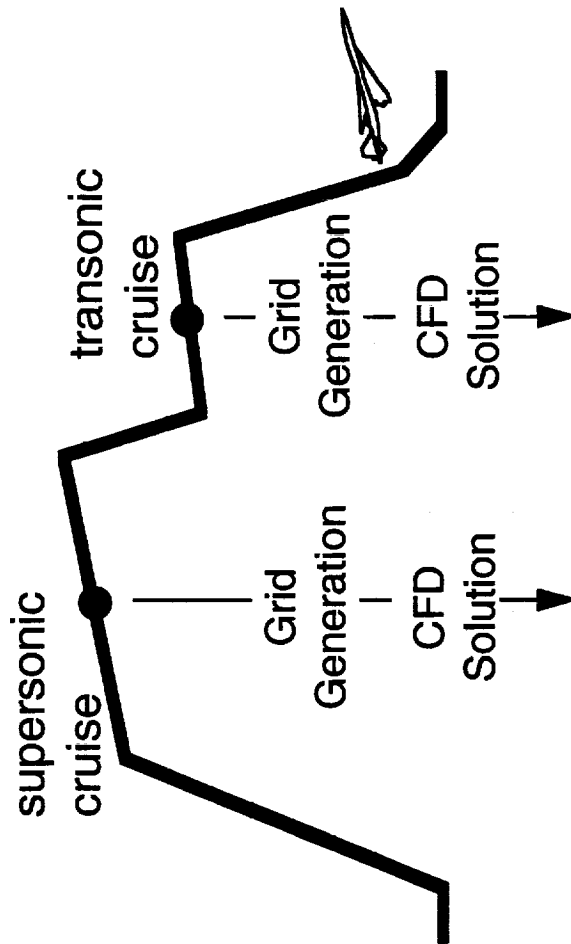
Multipoint Design

High Speed Aerodynamics, Long Beach

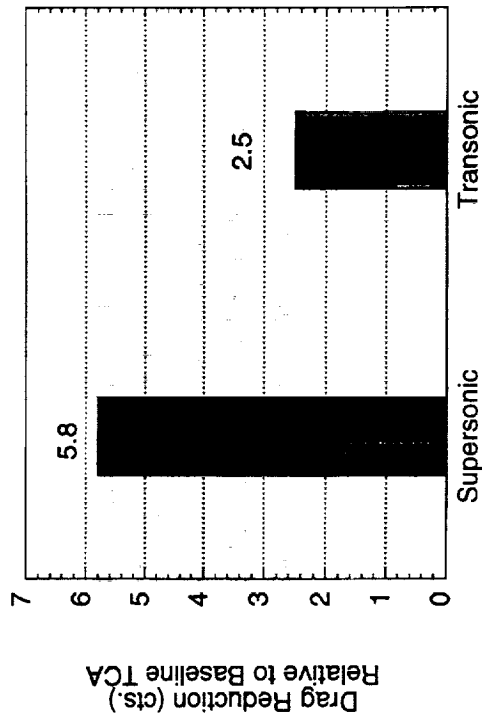


- One approach to multipoint design is to simultaneously optimize supersonic and transonic flight performance

Weighting factors, W_s and W_t , are associated with TOGW



$$F = W_s \Delta C_{Ds} + W_t \Delta C_{Dt}$$



Conclusions

AEROSHOP is a versatile platform to handle multiple optimization tasks now and in the future. To date, the system has been demonstrated on multiple problems including transonic flap optimization, integrated W/B/N/D optimization, integrated W/B/N/D/E optimization, and multipoint optimization. The code represents considerable corporate experience in configuration analysis and design and it incorporates several new technologies such as parallel processing and adjoint sensitivities.

Conclusions



High Speed Aerodynamics, Long Beach

- AEROSHOP is a good platform for optimization
 - Modular
 - Leveraged from previous experience and codes
- Demonstrated on multiple problems
 - Transonic flap optimization (experimentally validated)
 - Integrated W/B/N/D optimization at $M=2.4$
 - Integrated W/B/N/D/E optimization at $M=2.4$
 - Multipoint design optimization

Future Challenges

AEROSHOP is a tool continuously under development. As new technologies become available, they will be incorporated into the system if they have potential payoffs. In the near term, full implementations of several key features are necessary. These features include, adjoint sensitivities on multiblock problems, more complete integration of ADIFOR-based sensitivities, canard integration and optimization, flap optimization with nacelles and diverters, full configuration optimization, and a better implementation of parallel processing.

Future Challenges



High Speed Aerodynamics, Long Beach

- Canard integration and optimization
- Flap optimization with nacelles and diverters
- Full configuration multipoint optimization
- Full implementation of parallel processing
- Transition alternate sensitivity approaches to production mode

This page is intentionally left blank.

TCA6 Configuration Optimization

HSR Airframe Technical Review

Los Angeles, California February 9-13, 1998

Raymond Hicks

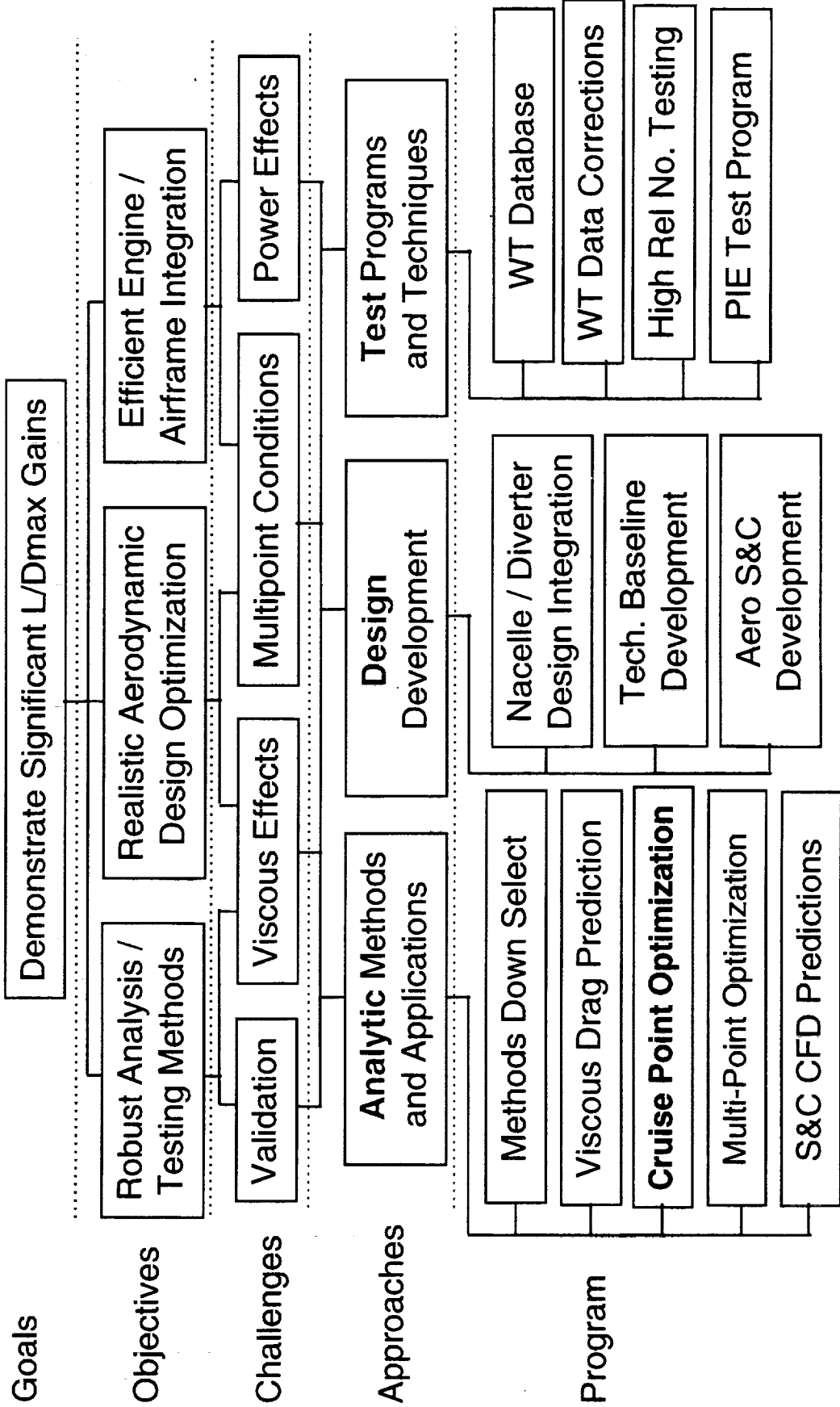
Mark Rimlinger

James Reuther

This page is intentionally left blank.

Configuration Aerodynamics Technology Development

Session 3: Aerodynamic Design Optimization Capability



TCA6 Optimization Studies

This report describes the status of two optimization studies in configuration design using the TCA6 baseline and the Ames optimized geometry (970103). The first study discussed will be flap/slat optimization using SYN87 with a single block grid with finite difference and adjoint gradients at Mach 0.90 and an angle of attack of 4.0 degrees. The second study presented is a preliminary comparison of the improvement in the lift/drag ratio obtainable with axisymmetric and bifurcated inlets on the TCA6 baseline configuration. The flap/slat optimization study was conducted in three phases. Four arbitrarily chosen high lift devices were examined during phase 1. Flap and slat deflections were accomplished by vertical shear and both inboard and outboard flaps and slats of constant percent chord were explored. The inboard and outboard ends of the high lift devices were aligned with the free stream direction and gaps were not modeled. Flap and slat ends and edges blended smoothly into the wing. The second phase of the study involved the use of approximate geometry of the outboard flap and slat of the TCA6 wind tunnel model. The slat used during this phase had a constant chord of 26% of the local wing chords while the flap had a constant chord of 22% of the local wing chords. Both high lift devices had the same span as the wind tunnel model. Deflections were again accomplished by using vertical shear. The third phase used an improved grid with better cell aspect ratios in critical areas of the computational space and rotation instead of shear was used for deflections. The outboard slat for this phase had the same linearly varying chord lengths as the wind tunnel model. All flap/slat studies were conducted using SYN87SB.

Preliminary results from an optimization study conducted to determine whether axisymmetric or bifurcated inlets give better improvement in the lift-drag ratio for the TCA6 Baseline configuration will also be presented. This study used the multi-block Euler/Navier-Stokes design code SYN107MB in Euler mode. The results presented here cannot be considered definitive since a major limitation in the design code was found early in the optimization process which prevented further progress. At the time of this writing in late January the code had not been fixed so the results shown will be approximately one month old. However, the data comparisons for the two inlet types presented is considered to be valid and is probably an indication of the final outcome of the study.

TCA6 Configuration Optimization

- Inboard and outboard flap/slat with shear deflections - $M = 0.90$
- Approximate outboard wind tunnel model flap/slat with shear deflections - $M = 0.90$
- Improved modeling of wind tunnel flap/slat with rotation and better grid - $M = 0.90$
- Experiment - CFD correlation with and without flap/slat deflections - $M = 0.90$
- TCA6 baseline with axisymmetric and bifurcted inlets - $M = 2.40$

Inboard and Outboard Flap/Slat Optimization

High lift devices were located on the inboard and outboard wing panels for this phase of the study. All devices had streamwise ends, no gaps and sheared deflections. The majority of the optimization runs were conducted at Mach 0.90 and $\alpha = 4.0$ degrees using the Euler design code SYN87SB. Inboard and outboard flap and slat chords varied in unison from 10% chord to 30% chord in 5% chord increments during the optimization study. The inboard leading and trailing edge devices had spans of 240 inches while the outboard elements had spans of 282 inches. The design variables were the flap and slat deflections and the objective function was $10(D/L)$. All results presented are for a flow solver convergence of 5 orders of magnitude. A study of solver convergence ranging from 3 to 6 orders showed that 5 orders was adequate for this investigation. The single block grid had 614,705 points and was subdivided into several subblocks by the automatic grid generator to facilitate configuration modeling. Most of the optimization runs consisted of 12 major iterations with a limited study using 18 iterations to determine the reliability of the results. The high lift elements used during this phase of the study were not intended to model the TCA6 flaps and slats.

Inboard & Outboard Flap/Slat Optimization

$M = 0.90$

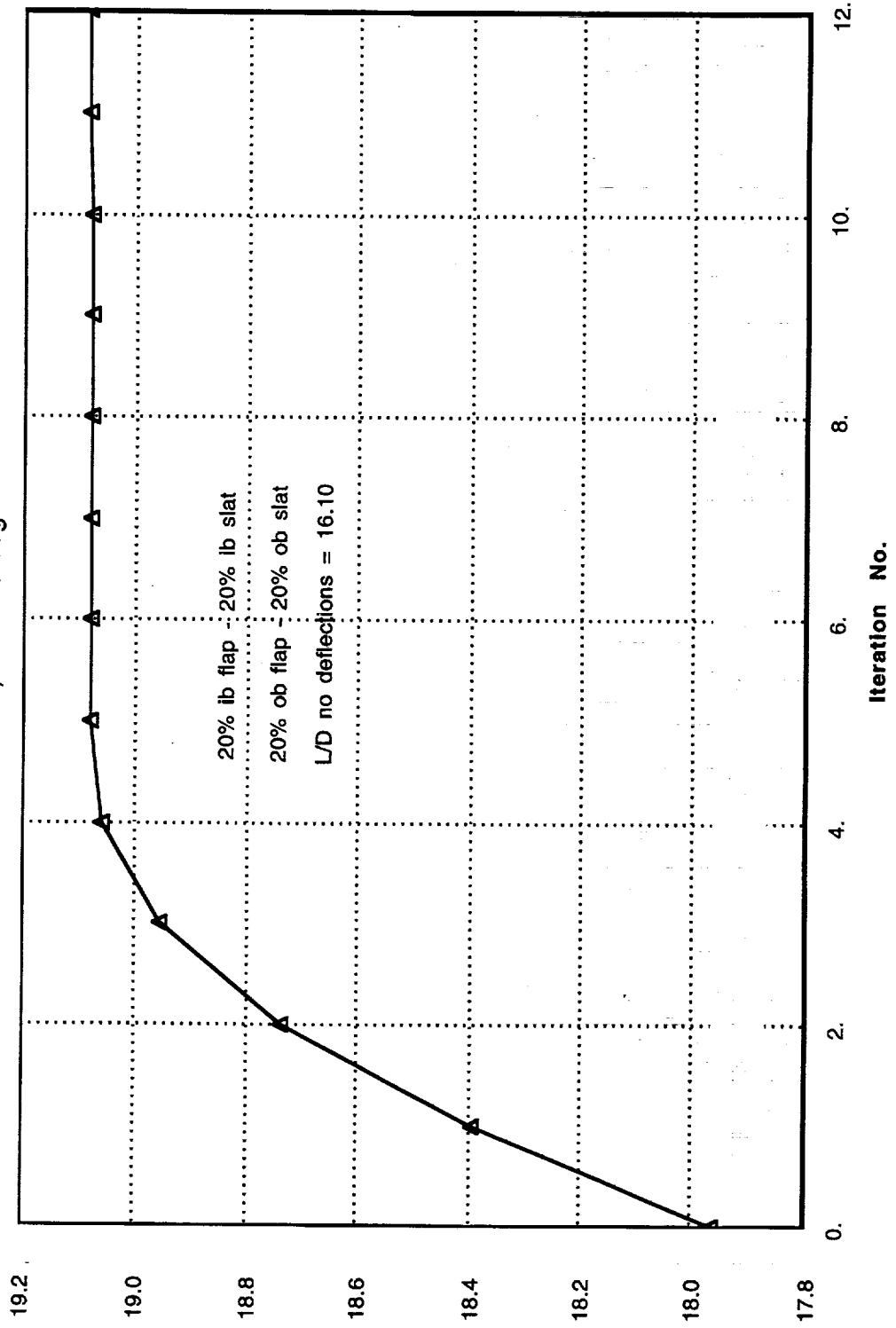
- SYN87MB adjoint mode - shear deflections - streamwise flap/slat ends
- TCA6 baseline & Ames optimized (970103) configurations
- Inboard flap/slat 203 to 443 inches
- Outboard flap/slat 505 inches to tip
- Flap/slat chord range 10% to 30% wing chord
- Flow solver converged 5 orders
- 12 optimization iterations
- 193 x 49 x 65 grid

TCA6 Baseline - L/D

Lift-drag ratio variation with optimization iteration for the 20% chord flaps and slats is shown here. The aerodynamic coefficient variations for the other flap/slat combinations will not be shown due to space limitations and because the trends are similar to those shown. Initial flap and slat deflections of 1.0 and 4.0 degrees were required for the outboard high lift elements to achieve convergence of the flow solution with this version of the code, hence the values shown for the lift-drag ratio for the 0th iteration is not the lift-drag ratio for the configuration with undeflected high lift devices. This value is shown in the text on the figure. Note that the final lift-drag ratio of 19.09 is achieved at the 6th iteration. The rapid convergence of the objective function will seem surprising when the variation of the lift and drag coefficients and the flap and slat deflections are observed in the following figures. The 20% chord flap and slat combination gave the greatest improvement in the lift-drag ratio of all combinations investigated. The improvement shown here is nearly 3 units in the lift-drag ratio and was not exceeded by any of the more precise flap/slat modelings discussed later.

Flap - Slat Optimization TCA Baseline

M = 0.90, $\alpha = 4.0$ deg.



L/D

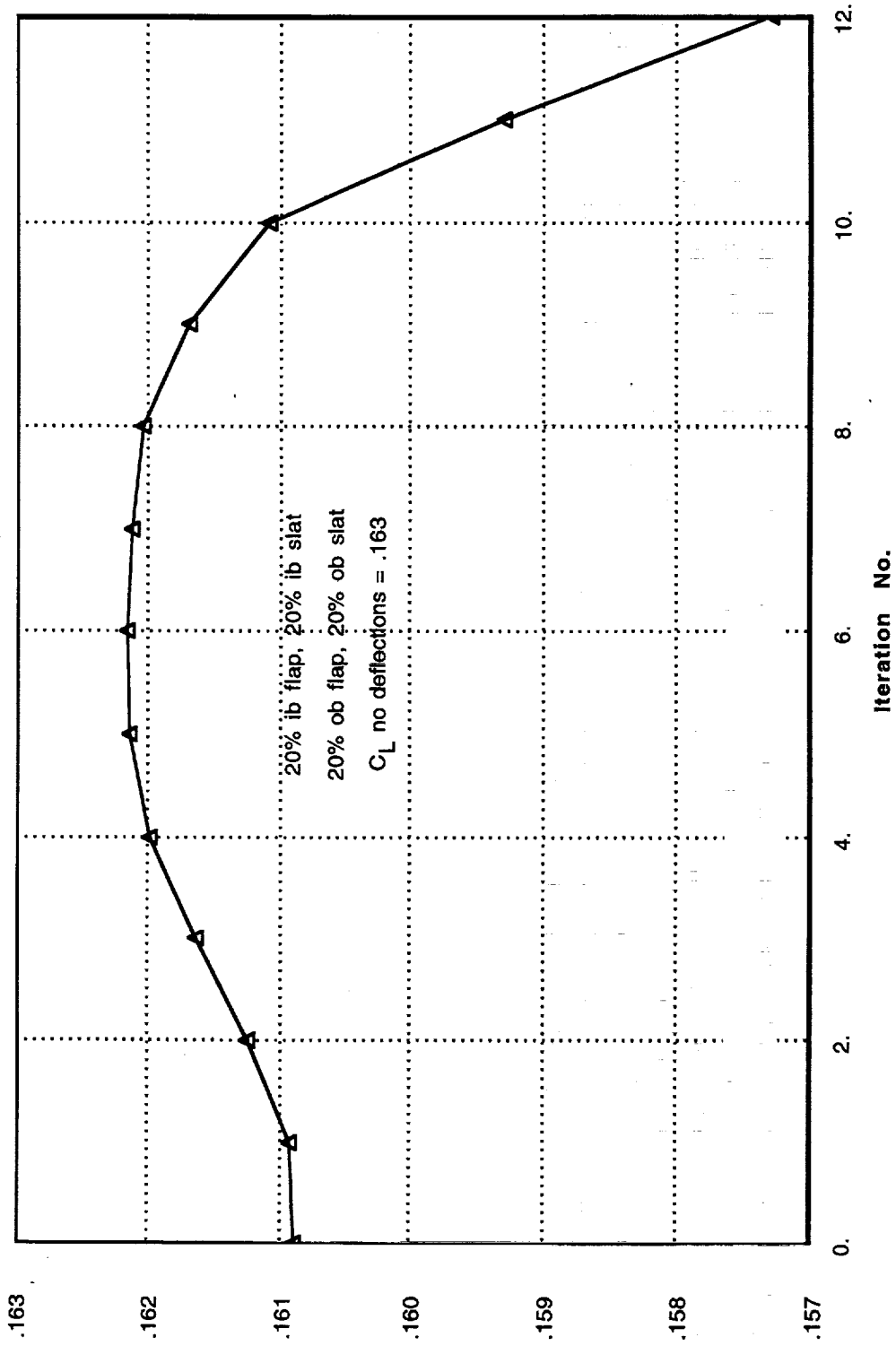
845

TCA6 Baseline - C_L

The lift coefficient history shown here does not correlate well with the rapid convergence of the lift-drag ratio shown in the preceding figure. The trend shown here correlates with the trailing edge flap deflection to be shown later. It is interesting that the lift coefficient does not appear to have reached a constant value even after 12 iterations while the objective function become constant after 6 iterations. The final lift coefficient is nearly 0.006 below the level without high lift device deflections indicating that the optimization code is, at least to some extent, attempting to take the trivial path of changing the local angle of attack by reflexing the inboard flap with a corresponding move along the drag polar without a real drag polar shift or rotation which is the desired result. It might be prudent to run these design problems at constant lift coefficient rather than constant angle of attack despite the fact that the former is a less efficient mode of optimization.

Flap - Slat Optimization TCA Baseline

M = 0.90, $\alpha = 4.0$ deg.

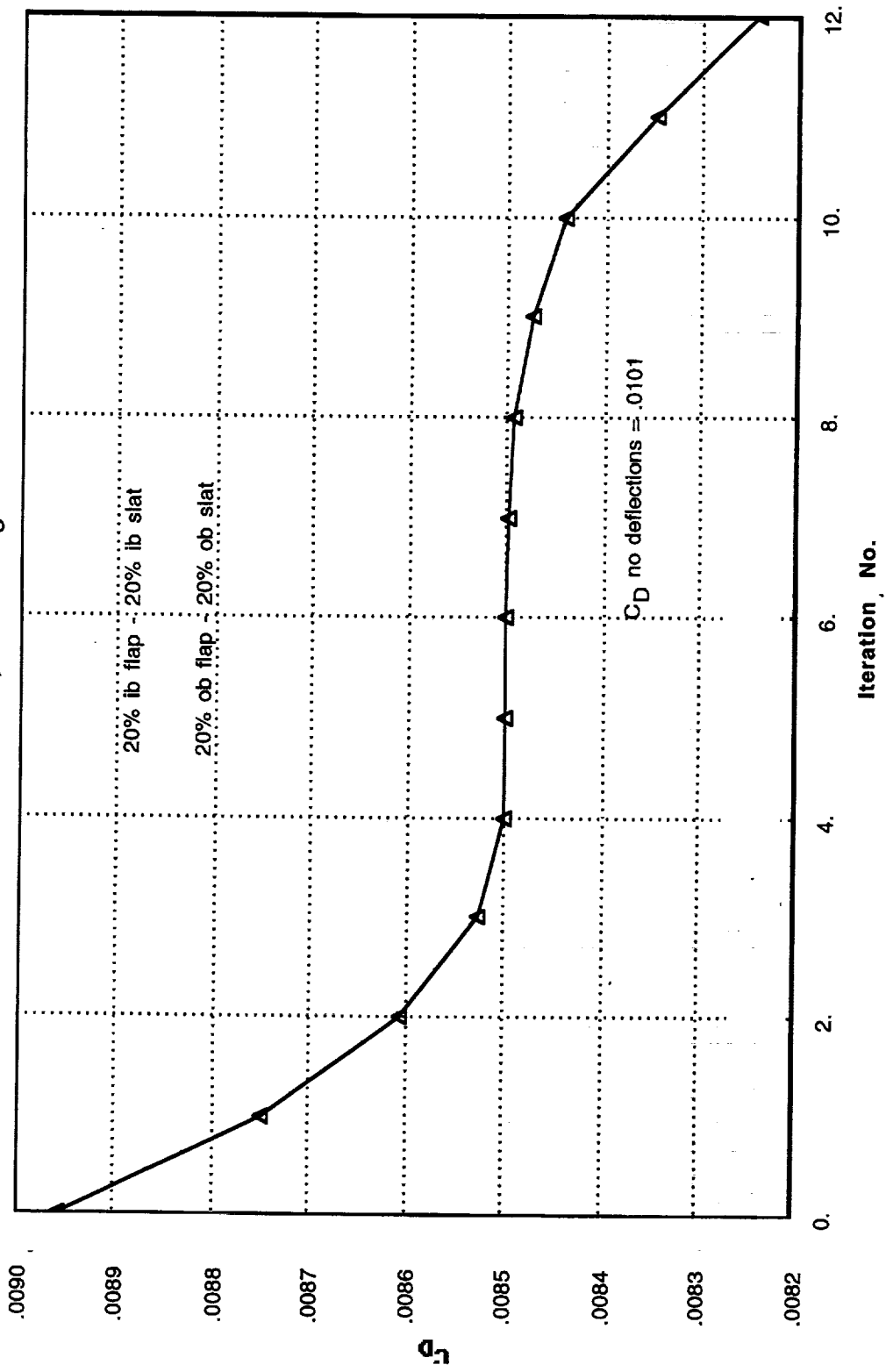


TCA6 Baseline - C_D

The drag coefficient curve shows the same lack of convergence shown in the last figure for the lift coefficient. The final drag reduction of approximately 19 counts for a lift coefficient of approximately 0.16 is the same as the drag reduction found during wind tunnel testing of outboard high lift devices with leading and trailing edge deflections of 3.0 and 8.0 or 6.0 and 8.0 degrees respectively. The outboard flap and slat on the wind tunnel model had different chord lengths than those used here. A comparison of the optimum CFD deflections and aerodynamic coefficients with experimentally determined optimum values will be discussed later in this presentation for a more precise computational model of the TCA outboard flap and slat.

Flap - Slat Optimization TCA Baseline

$M = 0.90, \alpha = 4.0 \text{ deg.}$

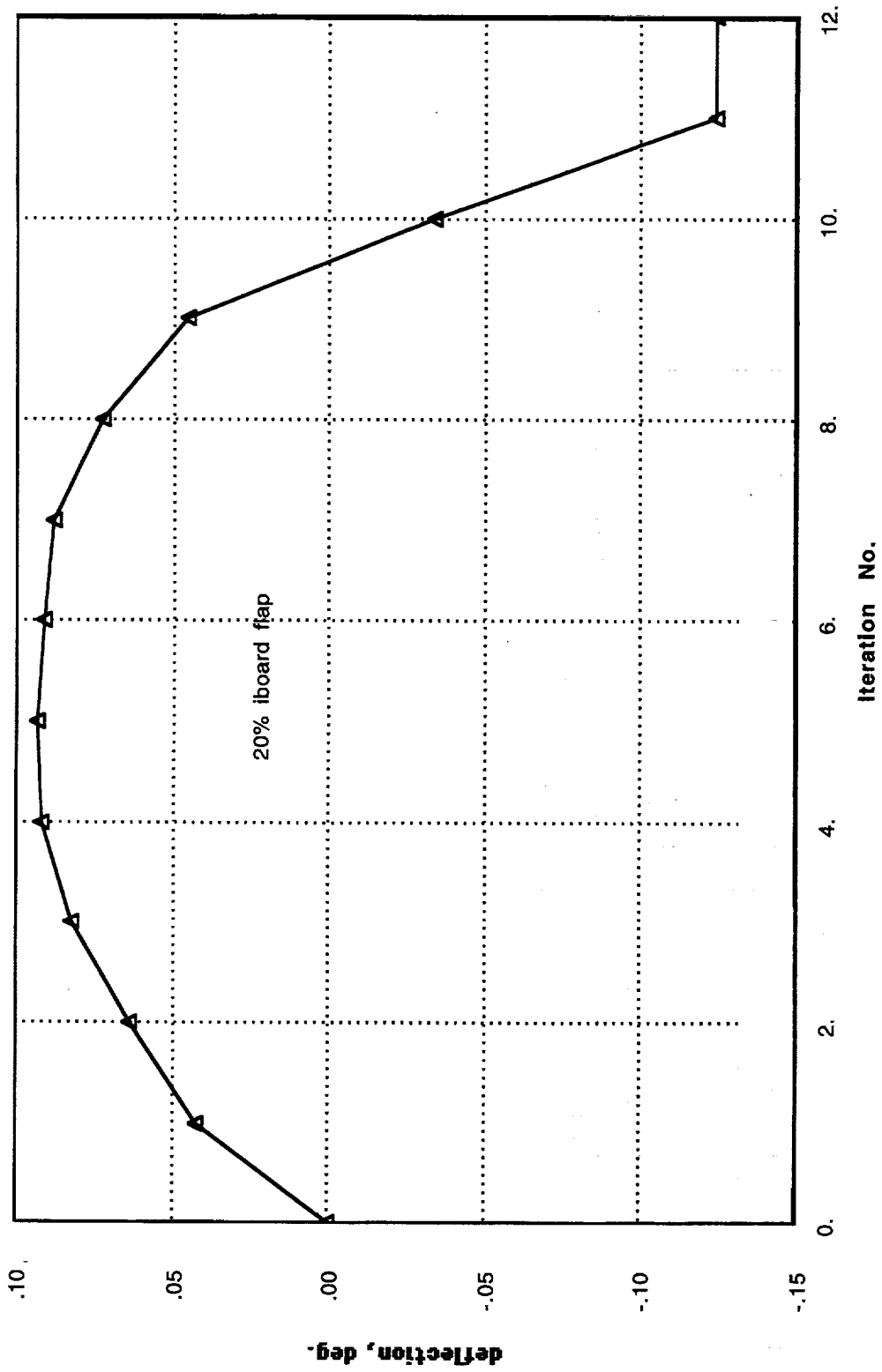


TCA6 Baseline - 20% Inboard Flap

The final inboard flap deflection shows a small reflex which is consistent with the decrease in lift coefficient discussed earlier. This might not have occurred if the optimization study was conducted at constant lift coefficient. However, the final value is only 0.125 degrees less than the initial deflection. A negative deflection means trailing edge up as per convention. The small change in deflection of this flap during the optimization process indicates that it might be more efficient to fly without an inboard trailing edge flap and save the weight and complexity associated with the high lift device. However, the geometric and flow approximations inherent in this design code may render these results somewhat unreliable. Note that there appears to be an attempt to reach a constant deflection at the 11th iteration.

Flap - Slat Optimization TCA Baseline

M = 0.90, $\alpha = 4.0$ deg.

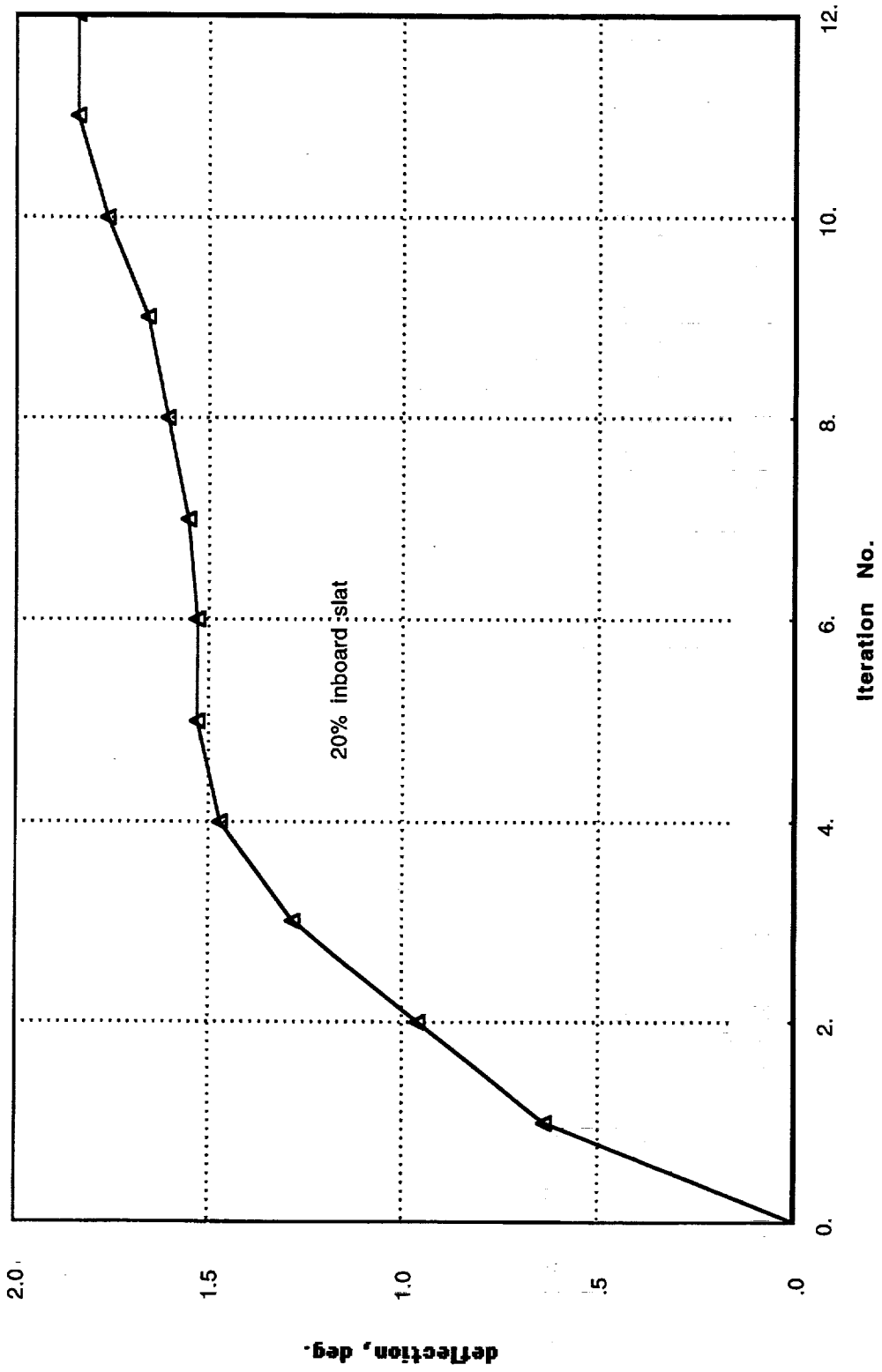


TCA6 Baseline - 20% inboard Slat

The optimization code makes a larger change in the deflection of the inboard slat as shown here than it did with the inboard flap as shown in the last figure; the final value being approximately 1.90 degrees. Note that the inboard slat appears to reach a converged value at the 11th iteration which is similar to the result for the inboard flap shown in the last figure. The inboard slat deflection trend with iteration number is monotonic whereas the trend for the inboard flap was not monotonic. The small final deflection shown here may be due to the blunt subsonic leading edge and indicates that if these results are meaningful the airplane may not need an inboard slat, at least for transonic flight.

Flap - Slat Optimization TCA Baseline

$M = 0.90, \alpha = 4.0 \text{ deg.}$

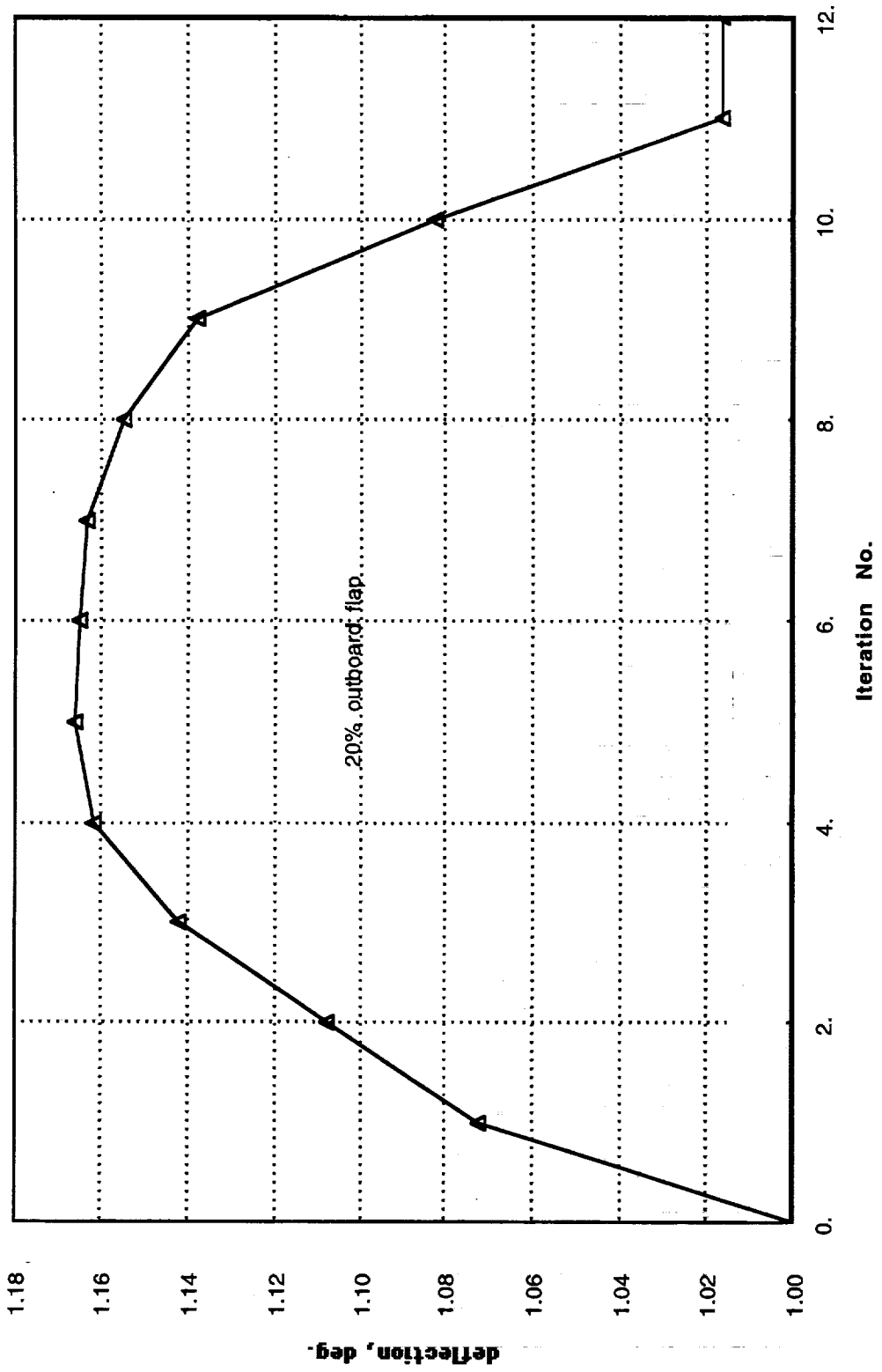


TCA6 Baseline - 20% Outboard Flap

Note the similarity in the shape of the deflection curve for the outboard flap shown here and the inboard flap shown previously. Both flaps reach a constant value at the 11th iteration and go through initial deflection increases before reaching their final values. The initial deflection of 1.0 degree required to achieve convergence of the flow solver appears to vary near optimum. The final value of flap deflection was approximately 0.02 degrees greater than the starting deflection. It is interesting that the optimum flap deflection values found by this design code are very different from the wind tunnel optima, to be discussed later, showing that the two design spaces are very different.

Flap - Slat Optimization TCA Baseline

M = 0.90, $\alpha = 4.0$ deg.

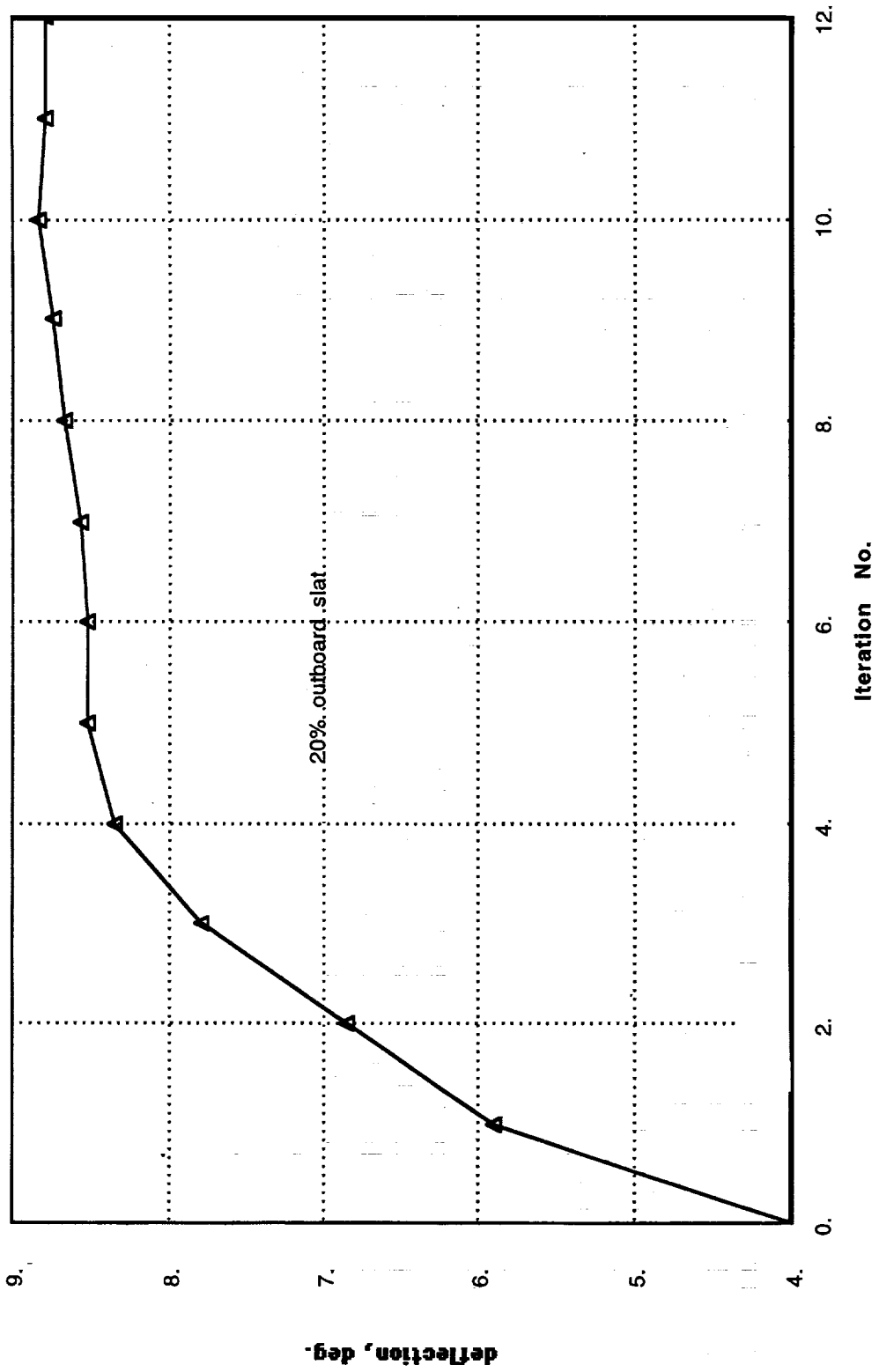


TCA6 Baseline - 20% Outboard Slat

The deflection history for the outboard slat shows monotonic behavior and a final deflection of approximately 8.9 degrees which is not greatly different from the 8.0 degree optimum deflection found during wind tunnel testing. An experiment-CFD correlation will be given later to address the validity of the CFD results. It is interesting that the outboard slat is the high lift device which the optimization code makes most use of during the design process. This is probably related to the sharp supersonic leading edge and its corresponding pressure peak at this angle of attack. The optimization code recognizes the drag associated with this peak and acts to reduce it even in inviscid flow. The initial deflection of 4.0 degrees shown in the figure in combination with the initial deflection of 1.0 degree for the outboard trailing edge flap was required to achieve flow solver convergence as discussed above. Note that the outboard slat appears to reach a final value earlier than the other three high lift devices.

Flap - Slat Optimization TCA Baseline

M = 0.90, $\alpha = 4.0$ deg.

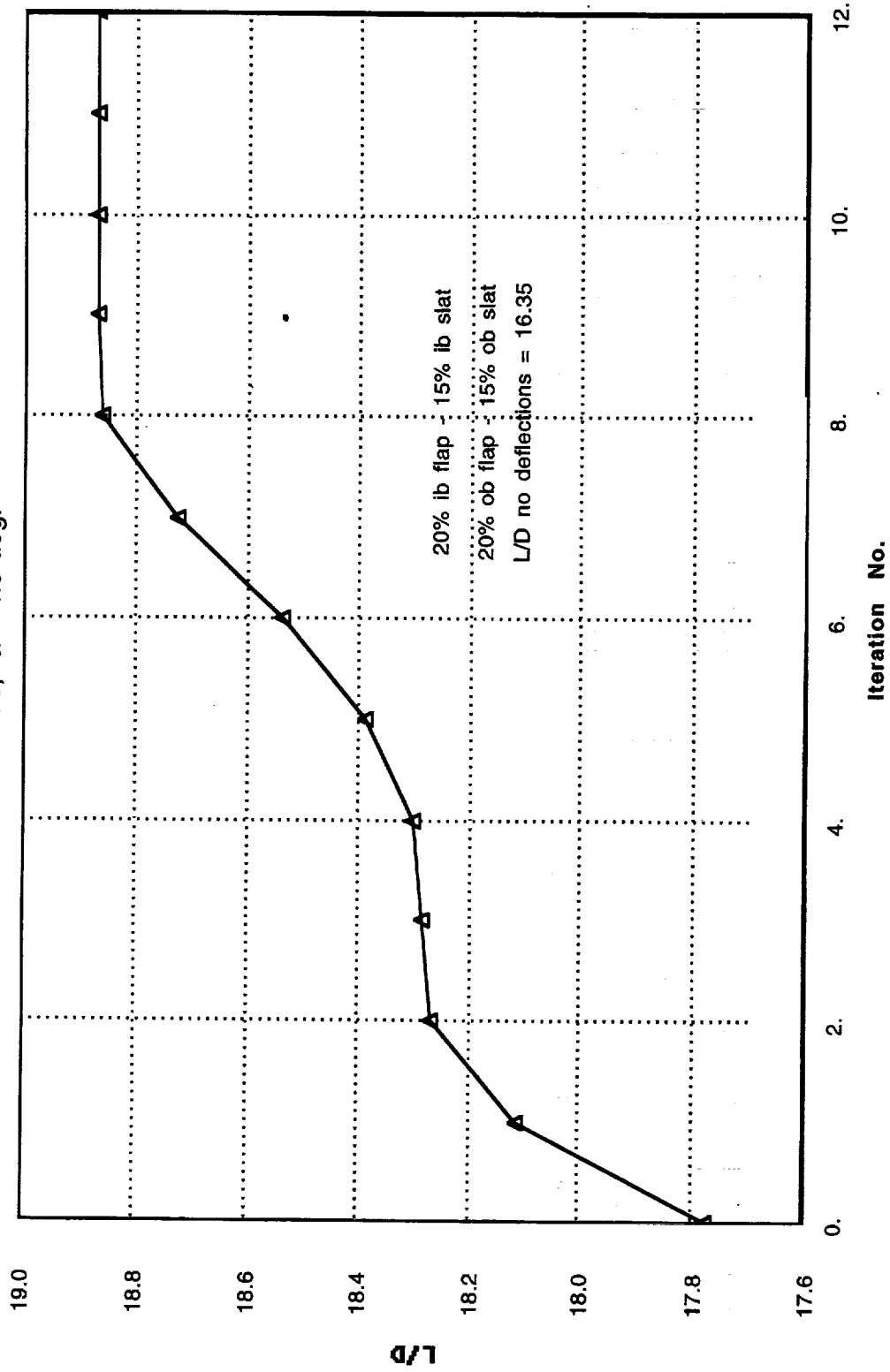


Ames Optimized Configuration (970103) - L/D

More optimization iterations were required to attain a converged value of the lift-drag ratio for the Ames optimized TCA configuration than for the baseline (compare this figure with that for the baseline shown earlier). The baseline configuration reached a final value after 6 iterations whereas the 970103 needed 8 iterations. The improvement in the lift-drag ratio for the optimized configuration is slightly smaller than that for the baseline configuration (approximately 2.5 vs 3.0 units in lift-drag ratio). The initial value of lift-drag ratio is 16.35 for Ames optimized configuration with undeflected high lift devices compared with 16.10 for the baseline. The lift-drag ratio value for the 0th iteration includes initial outboard flap and slat deflections of 1.0 and 4.0 degrees respectively to obtain convergence of the flow solver. The flap/slat combination in percent chord giving the best improvement in the lift-drag ratio was 20% inboard and outboard flaps and 15% inboard and outboard slats. It is interesting that the optimized configuration achieves the best improvement in the lift-drag ratio from smaller leading edge slats than the baseline. Some of the difference in improvement in the baseline and optimized configurations may be related to the more negative camber of the optimized wing. The camber reduction for the 970103 configuration is due to the presence of nacelle and diverter pressures during wing design. If this flap-slat optimization study had been conducted with nacelle and diverter pressures included the final results might have been different. The main reason for omitting such effects was compatibility with the wind tunnel data available at the time of this study.

Flap - Slat Optimization - Ames Optimized (970103)

M = 0.90, $\alpha = 4.0$ deg.

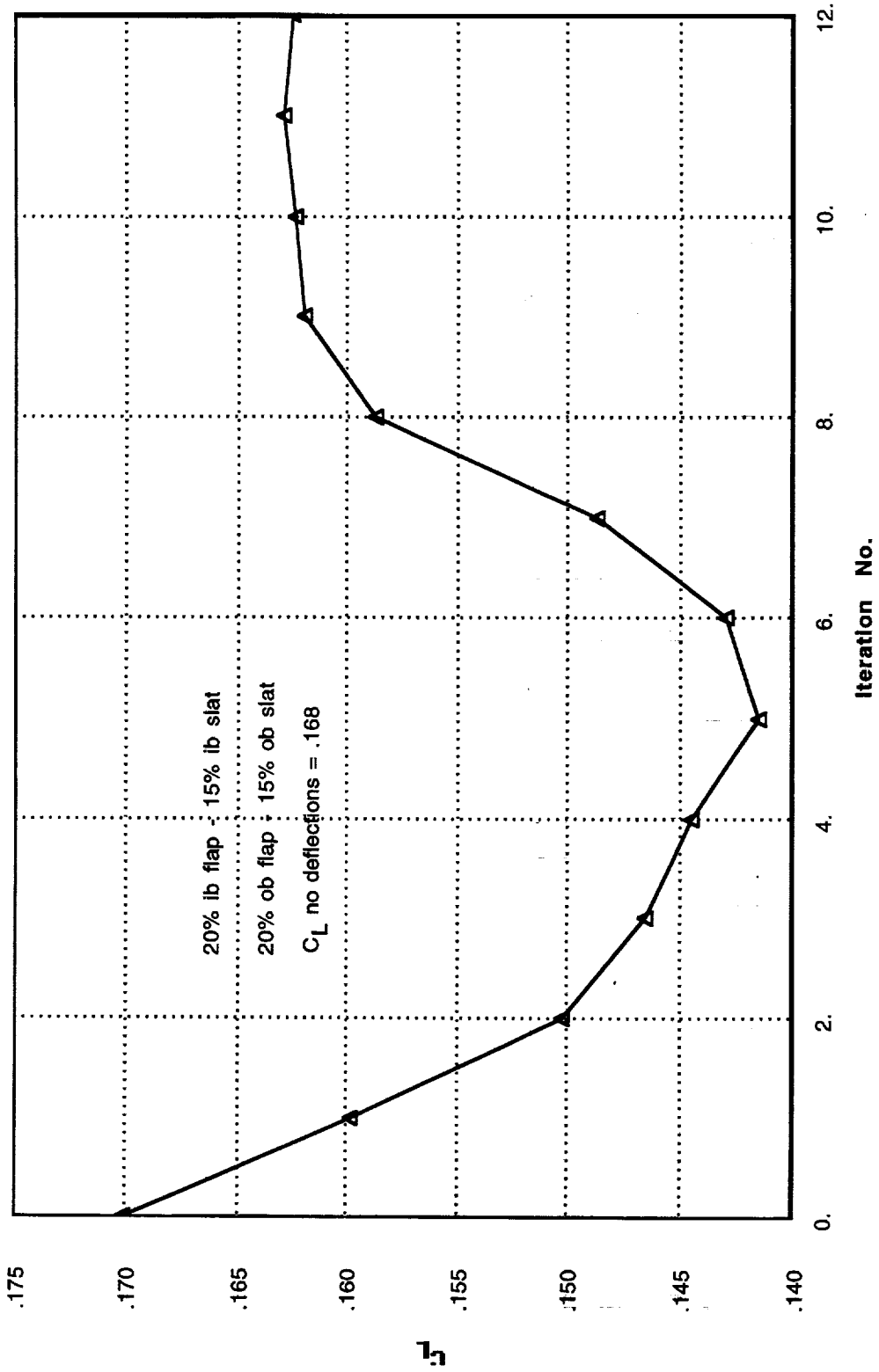


Ames Optimized Configuration (970103) - C_L

The lift coefficient history for the Ames optimized configuration shows the opposite reversal in direction as that shown previously for the baseline and the magnitude of the change during the design process is greater for the optimized configuration. Another difference between the two configurations is that the lift coefficient appears to reach a converged value before the 12th iteration whereas the lift coefficient for the baseline was still changing at the 12th iteration. Again, the differences in trends and final results for the optimized and baseline configurations may be related to the lack of nacelle/diverter pressures during this design process. The coefficient values for the configuration with undeflected high lift devices are included as text in the figures.

Flap - Slat Optimization - Ames Optimized (970103)

M = 0.90, $\alpha = 4.0$ deg.

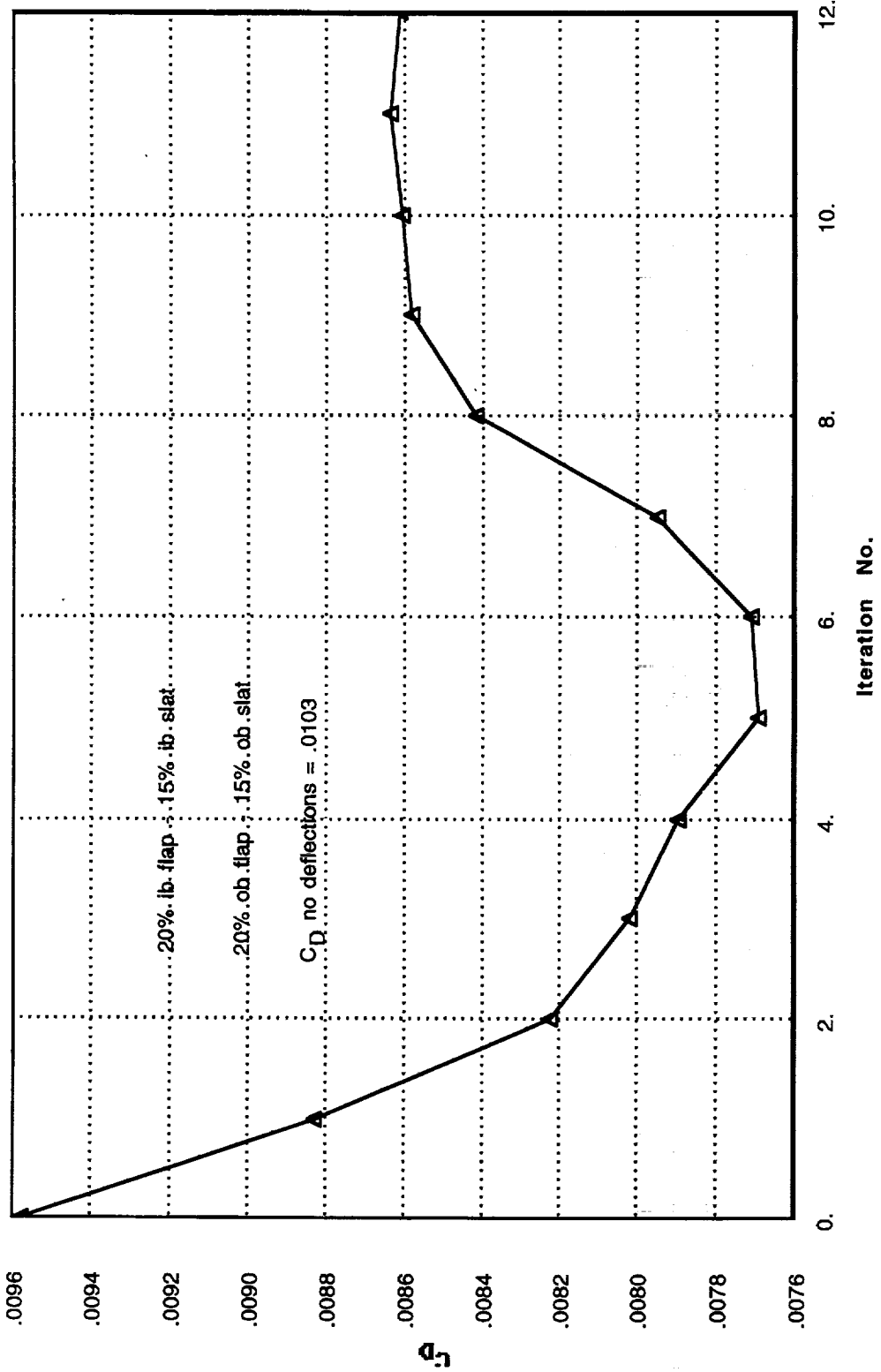


Ames Optimized Configuration (970103) - C_D

The drag coefficient variation during the design process for the optimized configuration is not monotonic as was observed for the baseline configuration. Note that at the 5th optimization iteration the drag reduction was nearly 28 counts while the final reduction is approximately 17 counts. The 28 count reduction is accompanied by a large loss in lift making the improvement in the lift-drag ratio smaller than for the final design iteration. The final drag reduction for the optimized configuration is 2.0 counts less than for the baseline configuration. Recall that all optimization runs for this configuration begin with initial outboard flap and slat deflections of 1.0 and 4.0 degrees to achieve convergence of the flow solver for this grid and flap/slat modeling.

Flap - Slat Optimization - Ames Optimized (970103)

M = 0.90, $\alpha = 4.0$ deg.



20% lb. flap, 15% lb. slat.

20% ob. flap, 15% ob. slat.

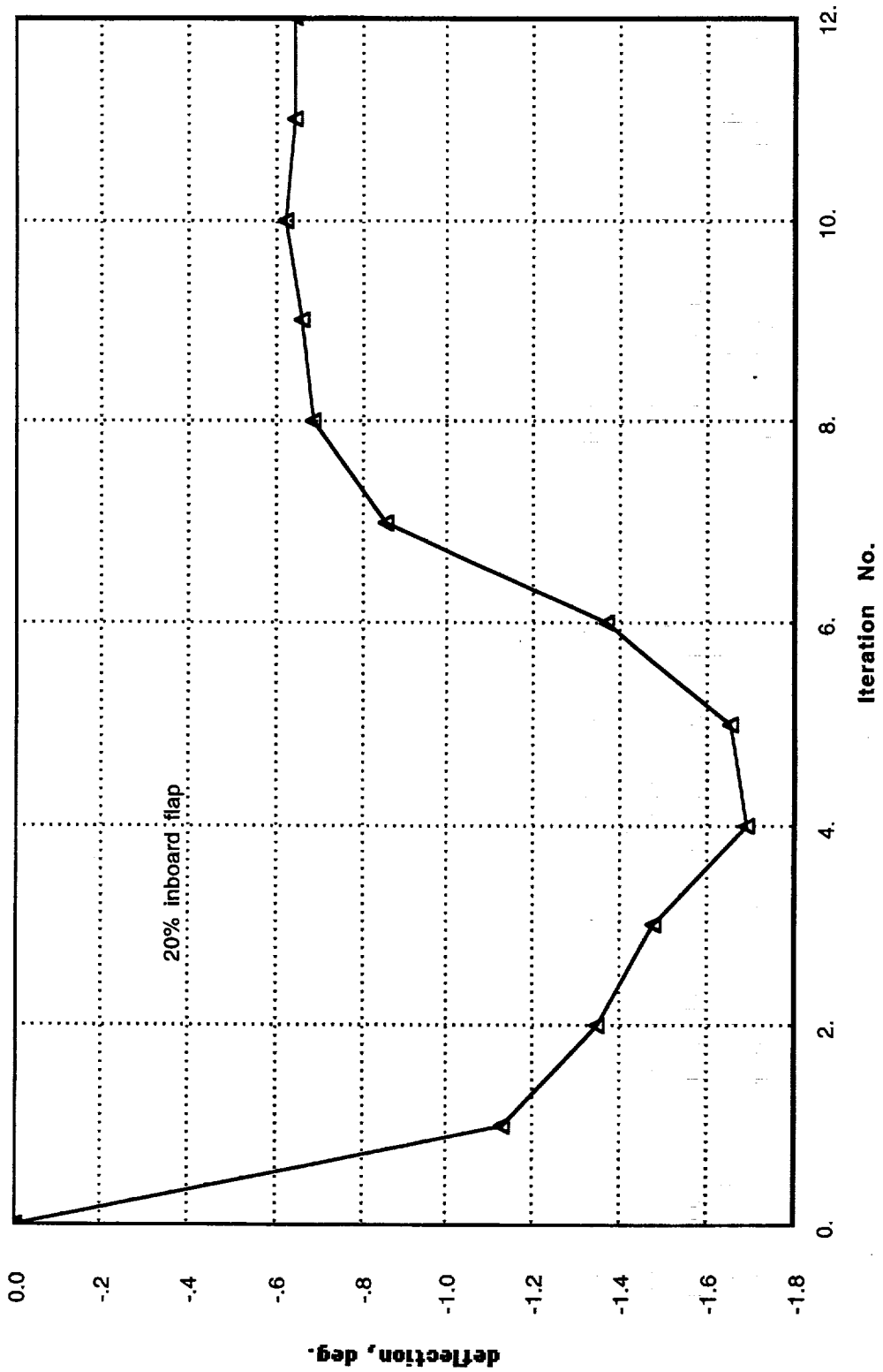
C_D no deflections = .0103

Ames Optimized Configuration (970103) - 20% inboard flap

The inboard flap undergoes a reversal in deflection during the optimization process and shows intermediate and final deflections of greater magnitude than observed previously for the baseline configuration. However, negative final deflections were found for both configurations but the intermediate deflections for the baseline were positive rather than negative as observed for the optimized configuration. The final negative deflection for the inboard flap is consistent with the reduction in lift coefficient noted earlier.

Flap - Slat Optimization - Ames optimized (970103)

M = 0.90, $\alpha = 4.0$ deg.

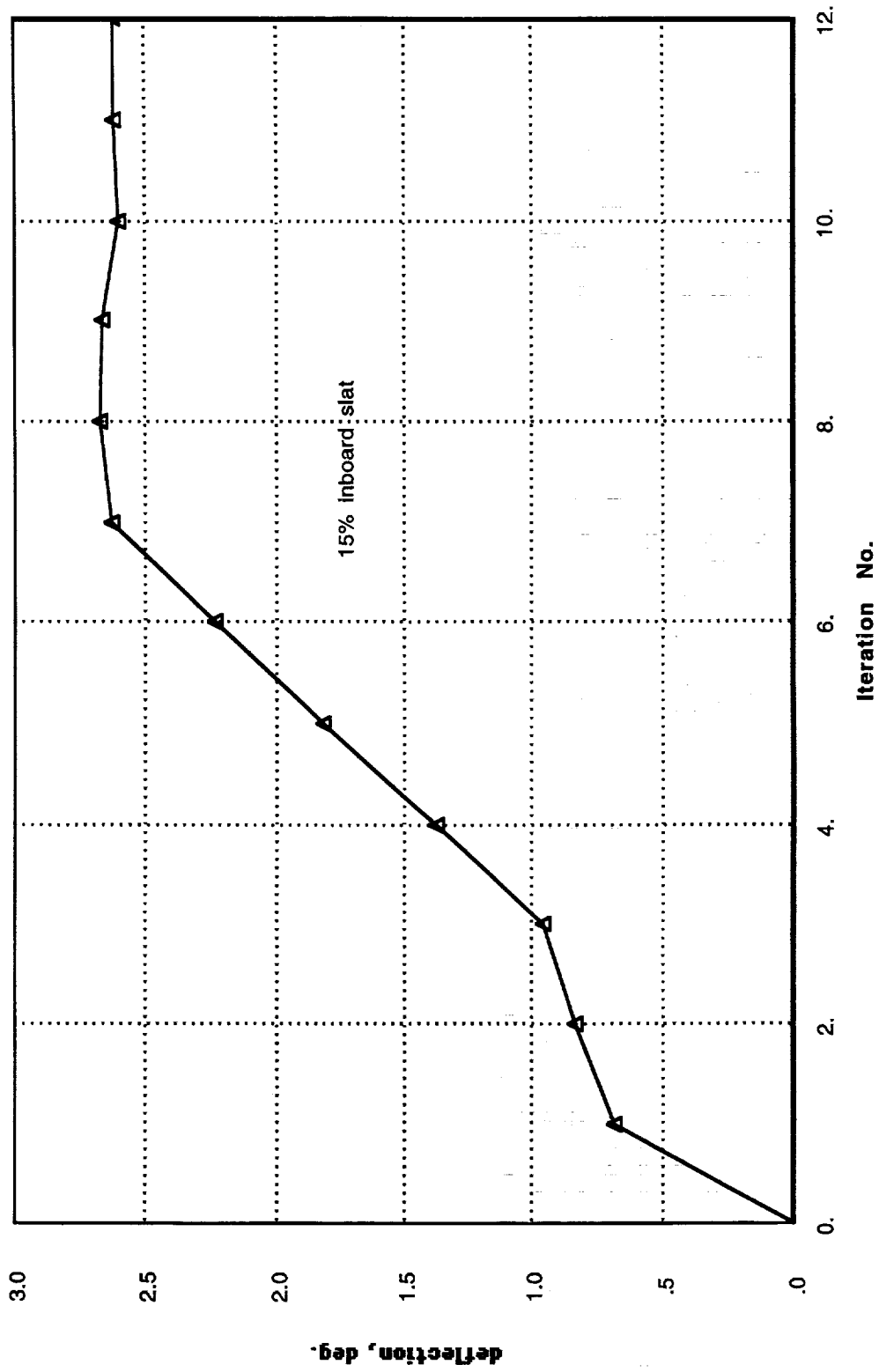


Ames Optimized Configuration (970103) - 15% inboard slat

Unlike the inboard flap the inboard slat shows monotonic behavior with a final deflection about 1.0 degree larger than that observed for the baseline configuration. The larger final deflections observed for the inboard high lift devices on the optimized configuration compared with the baseline may be related to the smaller inboard wing camber for the optimized configuration relative to the baseline. The reduced camber for the optimized configuration results from the addition of thickness to the lower surface of the wing during design to capture high pressures on a forward facing slope with a corresponding drag reduction.

Flap - Slat Optimization - Ames Optimized (970103)

M = 0.90, $\alpha = 4.0$ deg.

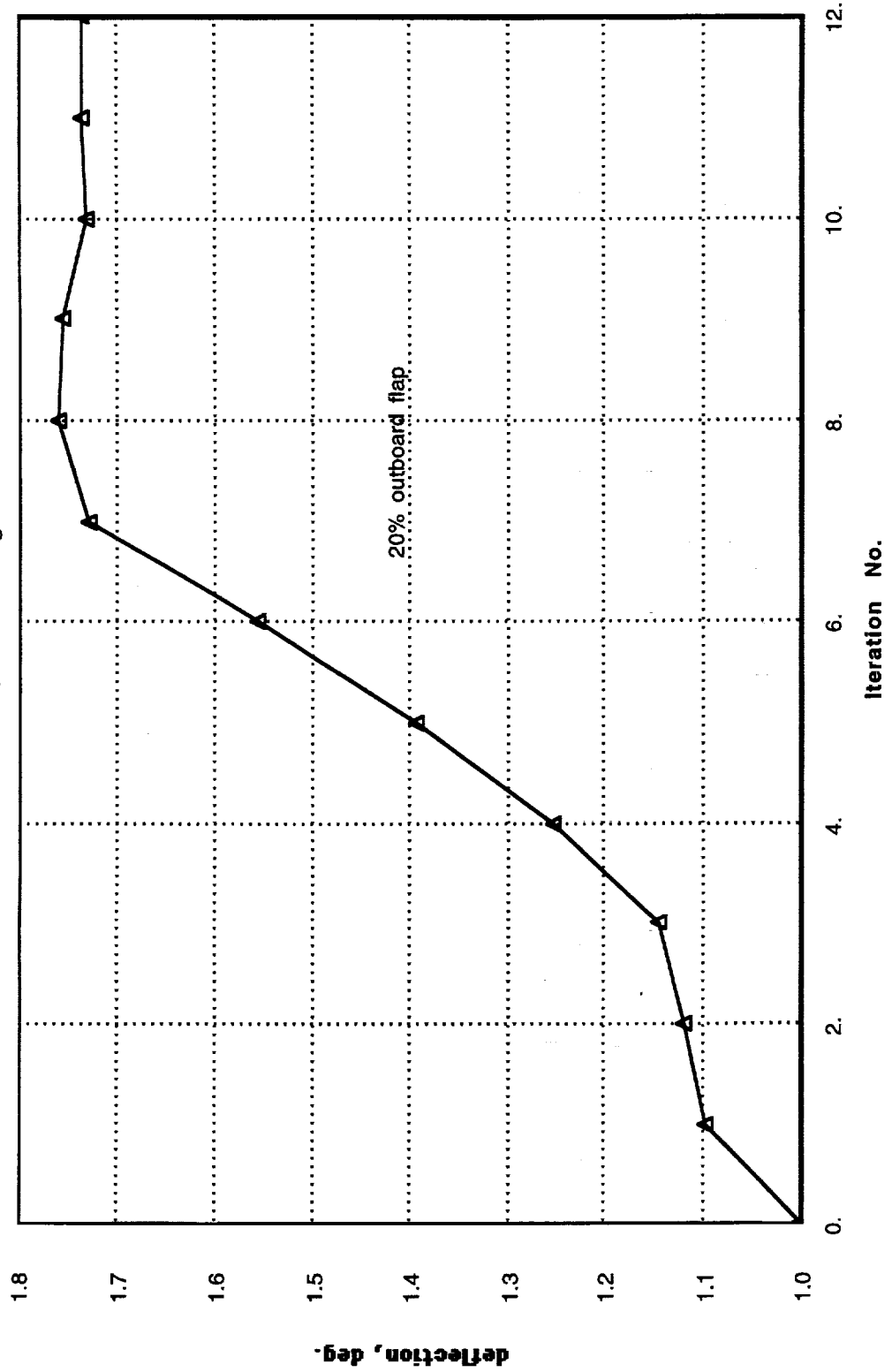


Ames Optimized Configuration (970103) - 20% outboard flap

Again a different trend during design is observed for the outboard flap on the optimized configuration compared with that for the baseline with a final deflection nearly 1.0 degree larger. The final deflection appears to represent a more converged value than that observed for the baseline. The larger outboard flap deflection for the optimized configuration compared with the baseline is not so easily explained by the nacelle/diverter effects discussed above since the nacelle influence is greatly diminished on the outboard wing panel. However, the outboard trailing edge device may be partially within the Mach cone emanating from the outboard nacelle/diverter. Note that the lift coefficient reduction found with this design seems to be driven more by the inboard than outboard flap deflection.

Flap - Slat Optimization - Ames Optimized (970103)

M = 0.90, $\alpha = 4.0$ deg.

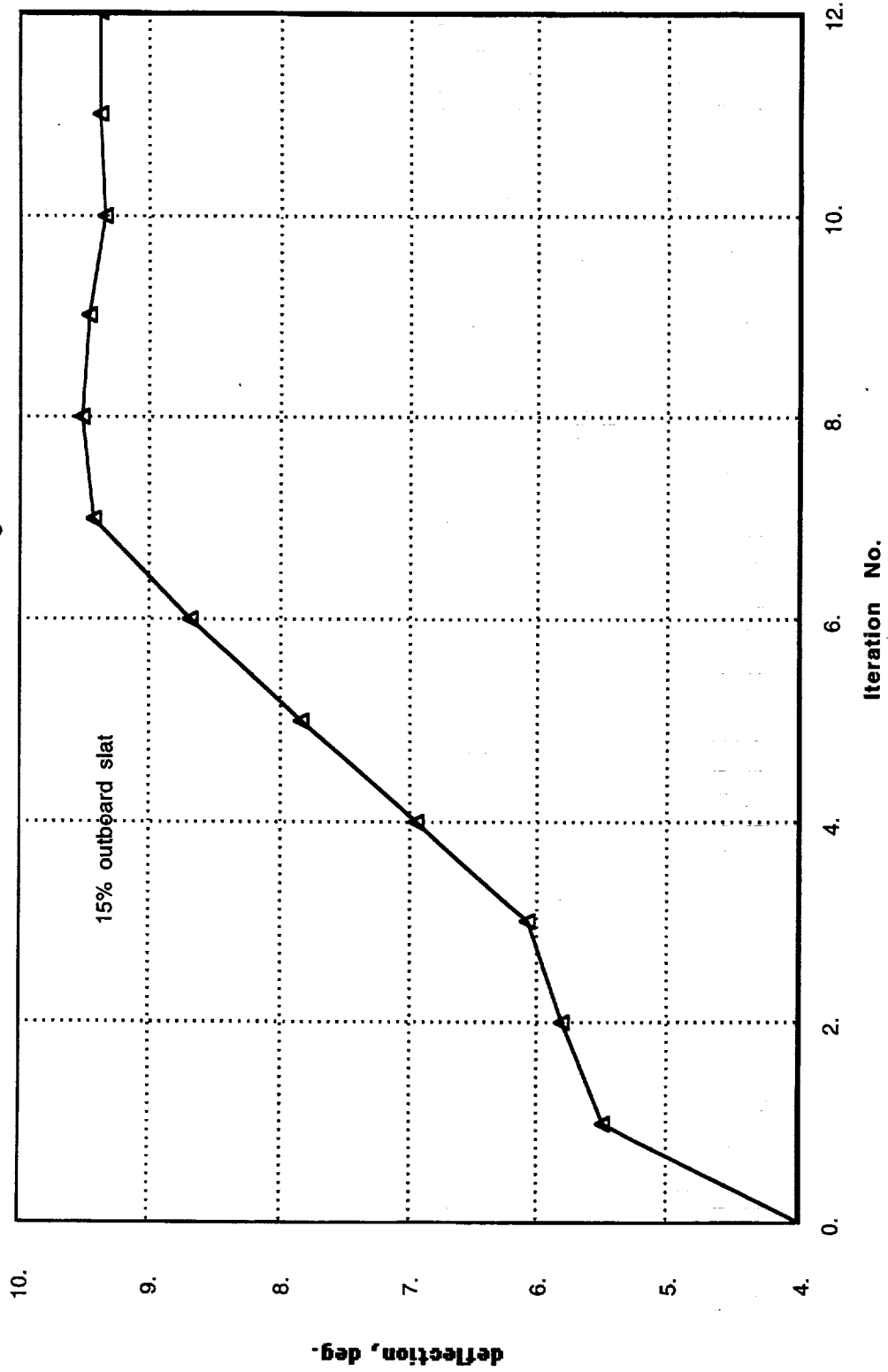


Ames Optimized Configuration (970103) - 15% outboard slat

The deflection histories and final deflections for the outboard slats on the baseline and optimized configurations are similar as seen by comparing this figure with that shown previously for the baseline but the final deflection is again larger for the optimized configuration. The larger deflections for the optimized configuration compared with the baseline are at least partially due to the decambering of the optimized wing caused by the high nacelle/diverter pressures on the lower surface of the wing. Again the final deflection of the outboard slat appears to be fairly well converged. The use of flaps and slats of the same span and percent chords for the inboard and outboard high lift devices may have limited the gains achievable during this study but limited time and CPU resources prevented a more thorough investigation.

Flap - Slat Optimization - Ames Optimized (970103)

M = 0.90, $\alpha = 4.0$ deg.



TCA Baseline Flap/Slat Optimization Summary

This table summarizes the results obtained from the brief study of the use of several flap/slat combinations using both inboard and outboard devices to improve the transonic cruise performance of the TCA6 baseline wing/body configuration. The final lift coefficient for all combinations except the 20/10 combination showed a decrease in lift coefficient of approximately 0.006 indicating that it might have been better to run this optimization study at constant lift coefficient rather than constant angle of attack. The largest drag reduction of 19 counts was achieved by three flap/slat combinations. This drag reduction is comparable to the largest drag reduction achieved during wind tunnel testing of the TCA6 wing/body model with outboard flap and slat for a lift coefficient of 0.16. A larger improvement might be achievable with CFD optimization at a different angle of attack since it is well known that the optimum deflections are a strong function of angle of attack. Note that the optimum deflections for both inboard high lift devices and for the outboard flap are fairly similar for all flap/slat combinations. The greatest optimum deflection differences are observed for the outboard slat.

TCA Baseline Wing-Body
 Flap/Slat Optimization Summary
 $M = 0.90$ $\alpha = 4.0$ deg.

Config	L/D	CL	CD	Ibflap	Ibslat	Obflap	Obslat
baseline	16.10	.163	.0101	0.00	0.00	0.00	0.00
30 - 20	19.08	.156	.0082	-0.19	1.70	0.80	8.60
30 - 10	18.85	.157	.0084	-0.25	2.20	0.93	11.30
20 - 20	19.09	.157	.0082	-0.13	1.80	1.02	8.80
20 - 10	18.80	.163	.0086	-0.04	2.20	1.41	11.60
25 - 15	19.03	.157	.0083	-0.19	1.75	0.95	9.40
25 - 10	18.81	.154	.0082	-0.45	2.40	1.09	11.90

Ames 970103 Flap/Slat Optimization Summary

The final lift-drag ratios shown here for the Ames optimized configuration indicate that the largest gain in lift-drag ratio is less than that for the baseline shown in the last table and that the variation in lift-drag ratio improvement for the various flap/slat combinations is small. A larger improvement in the lift-drag ratio might have been achieved for the 970103 configuration if the nacelles and diverters had been included in the computational model since the wing was designed with those effects present. The highest lift-drag ratio improvement is only 0.10 better than the smallest gain. The best and worst gains for the baseline differed by 0.29. Lift coefficient reductions were found for all flap/slat combinations again showing that it might have been better to conduct this optimization study at constant lift coefficient despite lower computational efficiency for that mode. The highest drag reduction was 18 counts for the optimized configuration compared with 19 counts for the baseline. The optimum deflections for the inboard flap are similar for all flap/slat combinations while the inboard slat shows some variation. The optimum deflections for the outboard slat shows the largest variation with the 20/10 combination giving a deflection of 10.70 degrees. The optimum deflections for the outboard flap differ by only 0.59 degrees from the smallest to the largest.

Ames Optimized Wing-Body (970103)
 Flap/Slat Optimization Summary
 $M = 0.90, \alpha = 4.0 \text{ deg.}$

Config	L/D	CL	CD	Ibflap	Ibslat	Obflap	Obslat
970103	16.35	.168	.0103	0.00	0.00	0.00	0.00
30 - 20	18.77	.160	.0085	-0.60	2.30	1.15	8.00
20 - 20	18.80	.161	.0085	-0.62	2.25	1.53	7.90
20 - 10	18.78	.163	.0086	-0.65	3.00	1.70	10.70
25 - 15	18.86	.161	.0085	-0.62	2.74	1.38	9.30
20 - 15	18.87	.163	.0086	-0.63	2.60	1.74	9.40

TCA Baseline with Approximate Wind Tunnel Model Geometry

This phase of the flap/slat optimization study used the TCA6 baseline wing/body configuration with an approximation to the wind tunnel model outboard flap and slat geometry. The wind tunnel model outboard slat had a linear variation of chord length from 23% of the local wing chord at the inboard end to 30% chord at the tip. The version of SYN87SB in use at the time of this phase of the study required constant chord leading and trailing edge high lift devices hence a weighted average of the wind tunnel model slat was used with a constant chord of 26% of the local wing chords. The trailing edge flap had chord lengths of 22% of the local wing chords, the same as the wind tunnel model outboard flap. Flap and slat deflections were achieved by use of vertical shear of the flap ordinates and the flap and slat edges blended smoothly into the wing without gaps. The Flap and slat ends were aligned with the free stream direction. The study was conducted at Mach 0.90 and $\alpha = 4.0$ degrees. The grid used during this phase was identical to that used during the previous phase so initial flap and slat deflections of 1.0 and 4.0 degrees respectively were required to achieve flow solver convergence with multi-grid.

**Flap/Slat Optimization
Approximate Wind Tunnel Model Geometry**

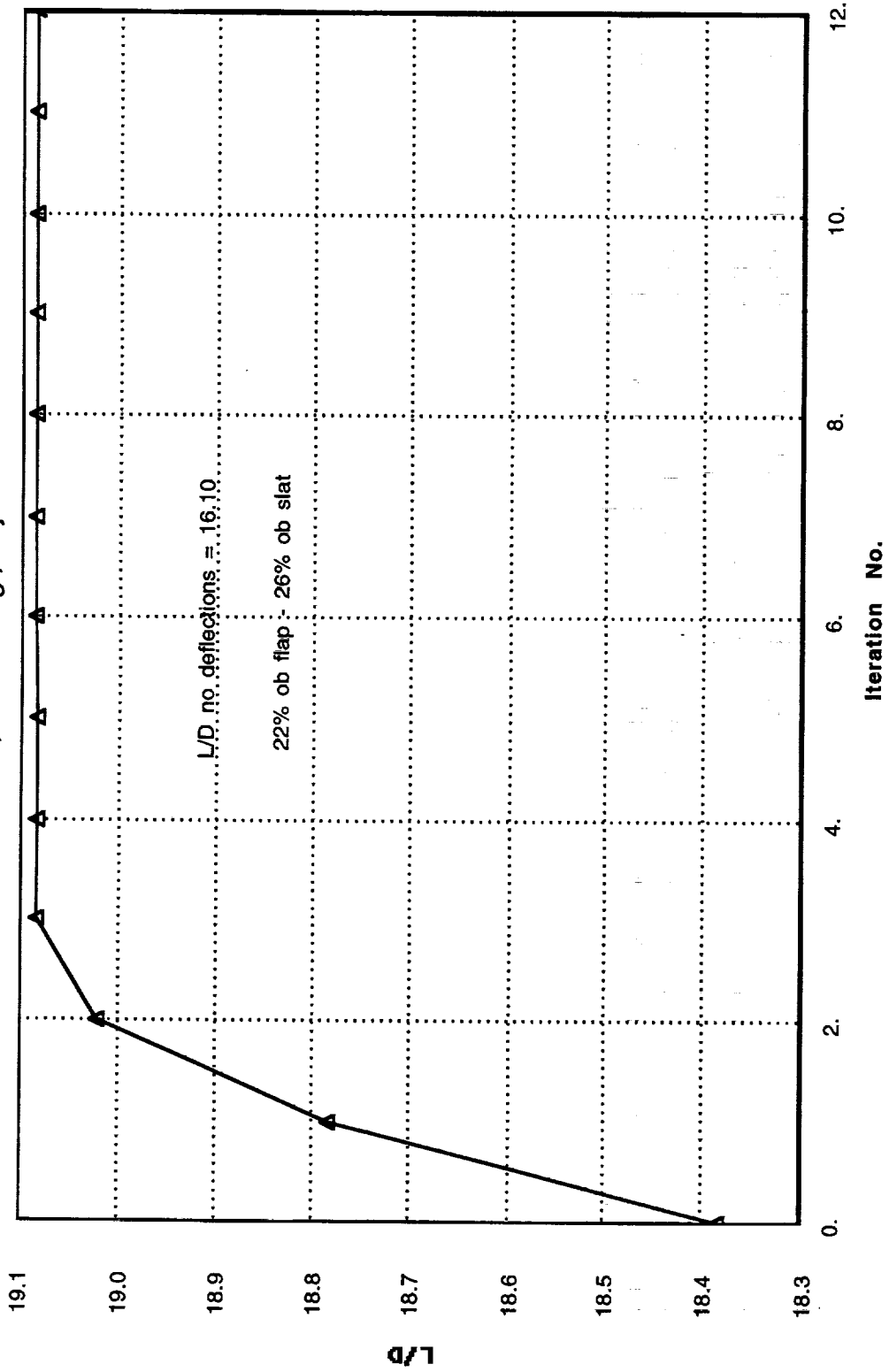
- $M = 0.90$, $\alpha = 4.0$ deg.
- Wind tunnel slat 23% chord inboard end - 30% chord outboard end
- Wind tunnel flap 22% chord
- CFD slat 26% chord
- CFD flap 22% chord
- CFD flap/slat deflections using shear

Approximate Wind Tunnel Model Geometry - L/D

The lift-drag ratio curve shows more rapid convergence to the final optimized value than the two cases shown previously where four high lift devices were used. Note that the final value of 19.09 is the same as that achieved when both inboard and outboard high lift devices were used for optimization. It is interesting that elimination of the inboard flap and slat did not change the improvement in the lift-drag ratio at $\alpha = 4.0$ degrees. If this result is reliable some simplification in aircraft construction might be possible by eliminating the inboard high lift devices. The results shown here were obtained using adjoint gradients in SYN87SB. Finite difference gradients were also explored but little difference in the final improvement in the objective function was observed so those results will not be shown due to time limitations.

Flap - Slat Optimization - TCA Baseline

M = 0.90, $\alpha = 4.0$ deg., Adjoint

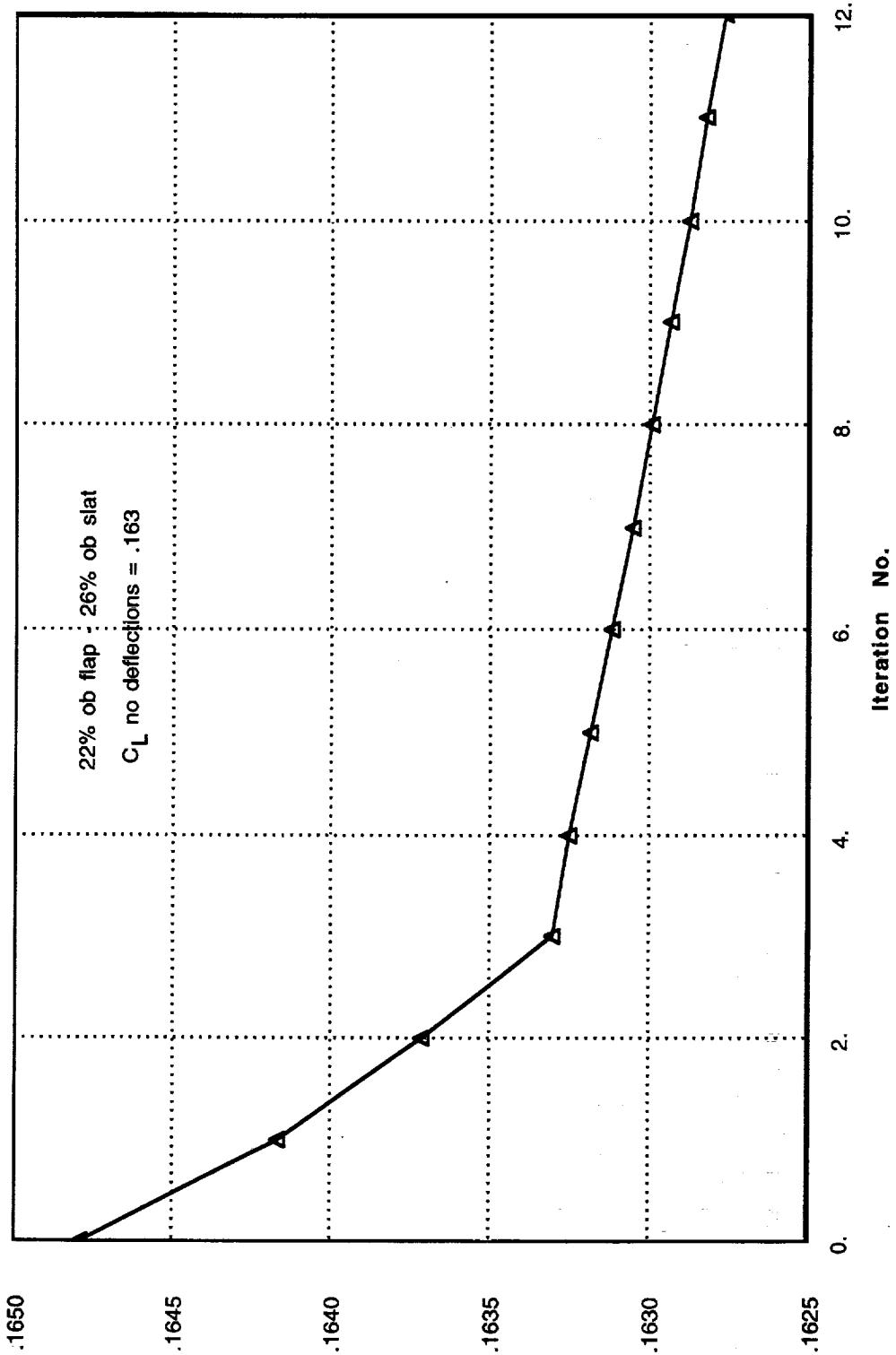


Approximate Wind Tunnel Model Geometry - C_L

The lift coefficient shows a small monotonic decrease during optimization and does not appear to reach a converged value despite the rapid convergence of the lift-drag ratio shown in the preceding figure. The objective function was $10(D/L)$, the same as used in the last phase of the study. The decrease in the lift coefficient shown here is considerably smaller than that shown for the two optimization cases shown previously and may be related to the elimination of the inboard flap as a design variable for this phase of the study since negative deflections for that element were found in both previous cases where an inboard trailing edge flap was used.

Flap - Slat Optimization - TCA Baseline

M = 0.90, $\alpha = 4.0$ deg., Adjoint

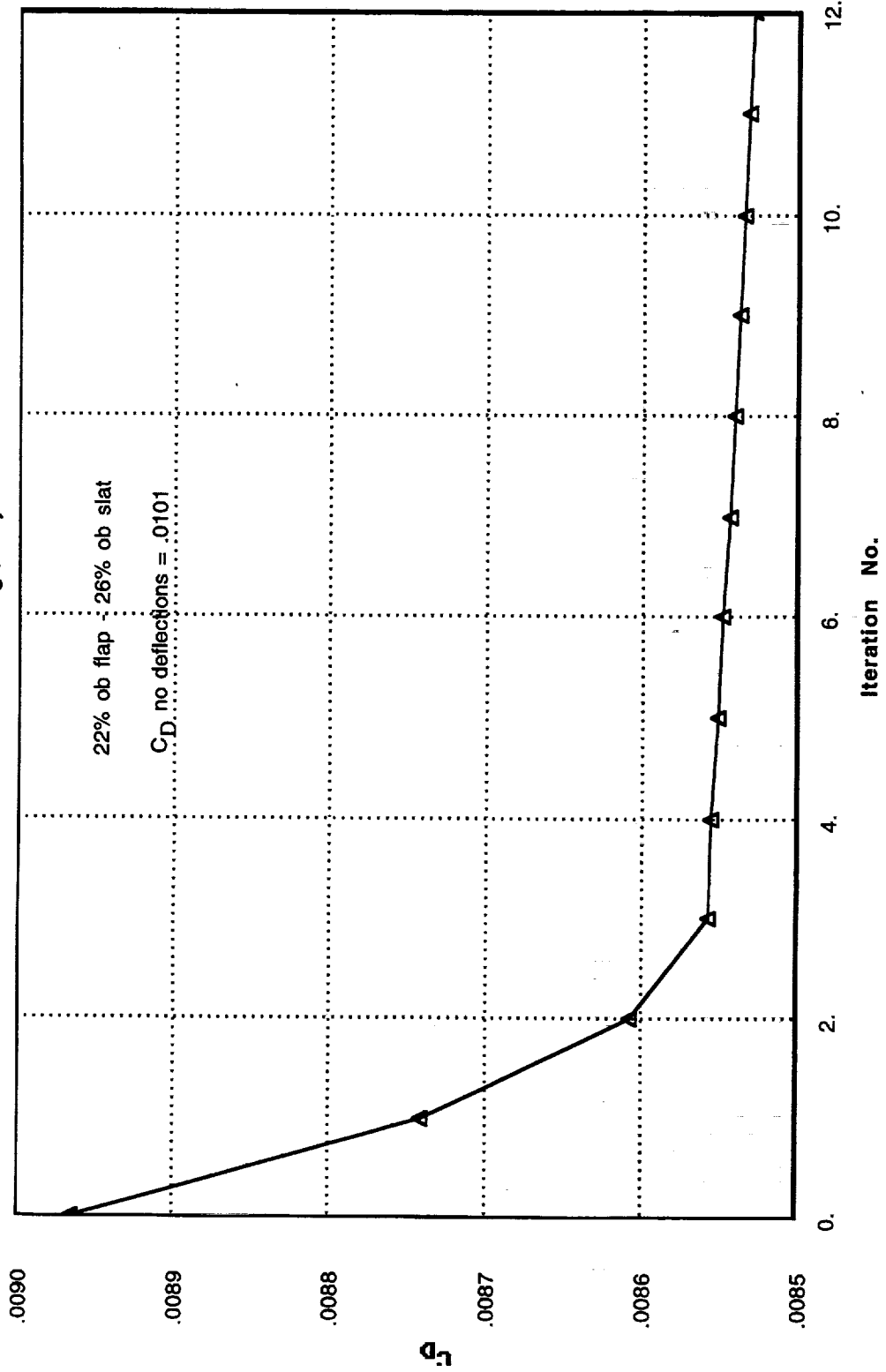


Approximate Wind Tunnel Model Geometry - C_D

The drag coefficient also shows a monotonic decrease with iteration number and appears to approach a stable value approximately 16 counts less than that of the TCA baseline with undeflected outboard flap and slat. Note that this drag decrease is smaller than the 19 count decrease achieved with both inboard and outboard flaps and slats shown previously. The smaller decrease in lift coefficient in combination with the smaller drag reduction relative to that found with four high lift devices explains the equivalent improvement in the lift-drag ratio from two or four elements for the TCA baseline. Both optimization studies achieved nearly 3 units of improvement in the lift-drag ratio.

Flap - Slat Optimization - TCA Baseline

M = 0.90, $\alpha = 4.0$ deg., Adjoint

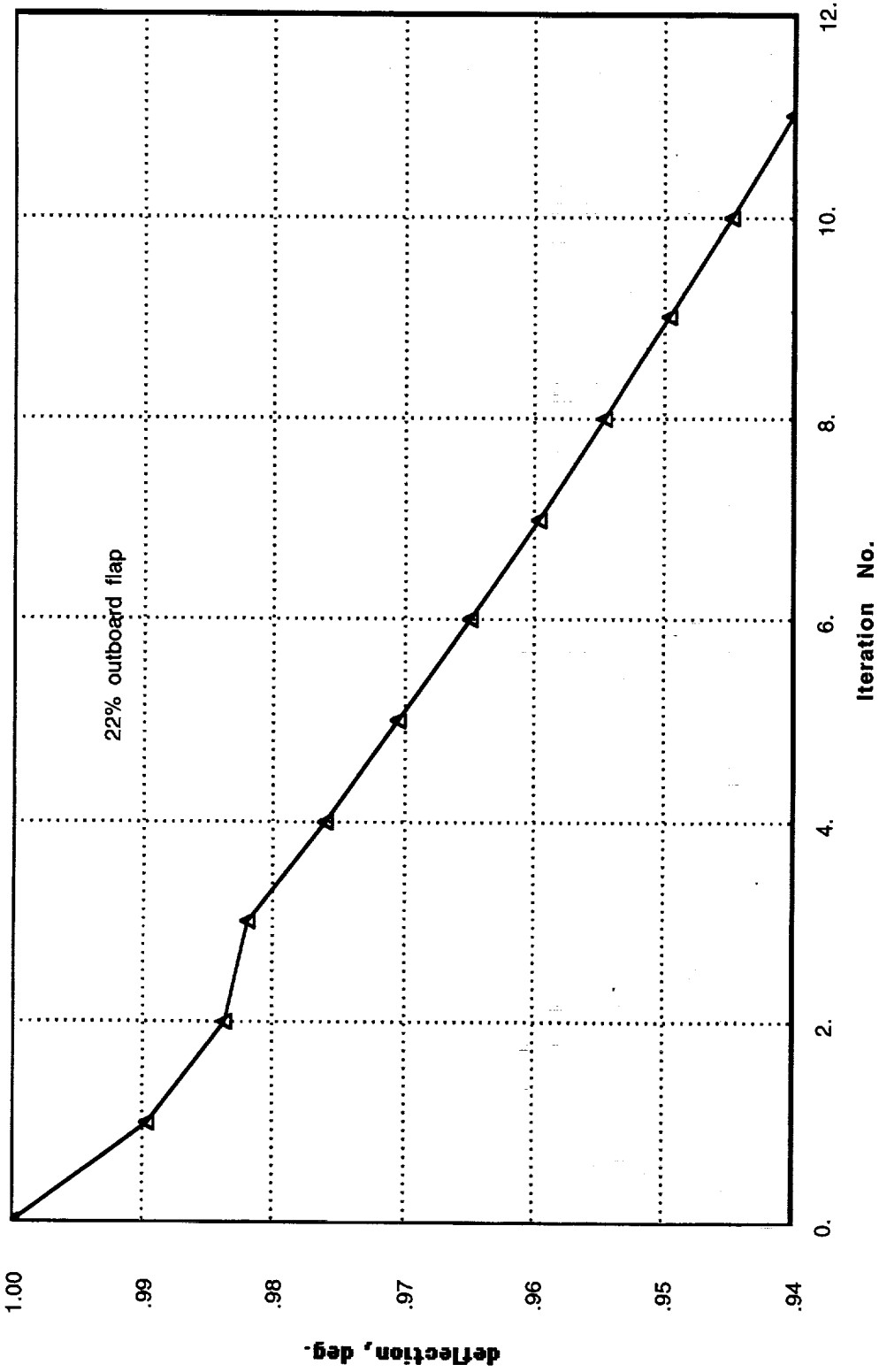


Approximate Wind Tunnel Model Geometry - Outboard Flap

The outboard flap shows a small monotonic decrease from the initial deflection of 1.0 degree reaching a value only 0.06 degrees below the starting deflection. This result is similar to the results shown previously for four high lift devices. Both results indicate that the initial deflection of 1.0 degree is nearly optimum for the outboard flaps in both cases. Again it is interesting to observe the rapid convergence of the objective function and the lack of convergence for the flap deflection although the change in deflection is small. Note that the flap deflection is plotted to a much finer scale than the lift drag ratio.

Flap - Slat Optimization - TCA Baseline

M = 0.90, $\alpha = 4.0$ deg., Adjoint

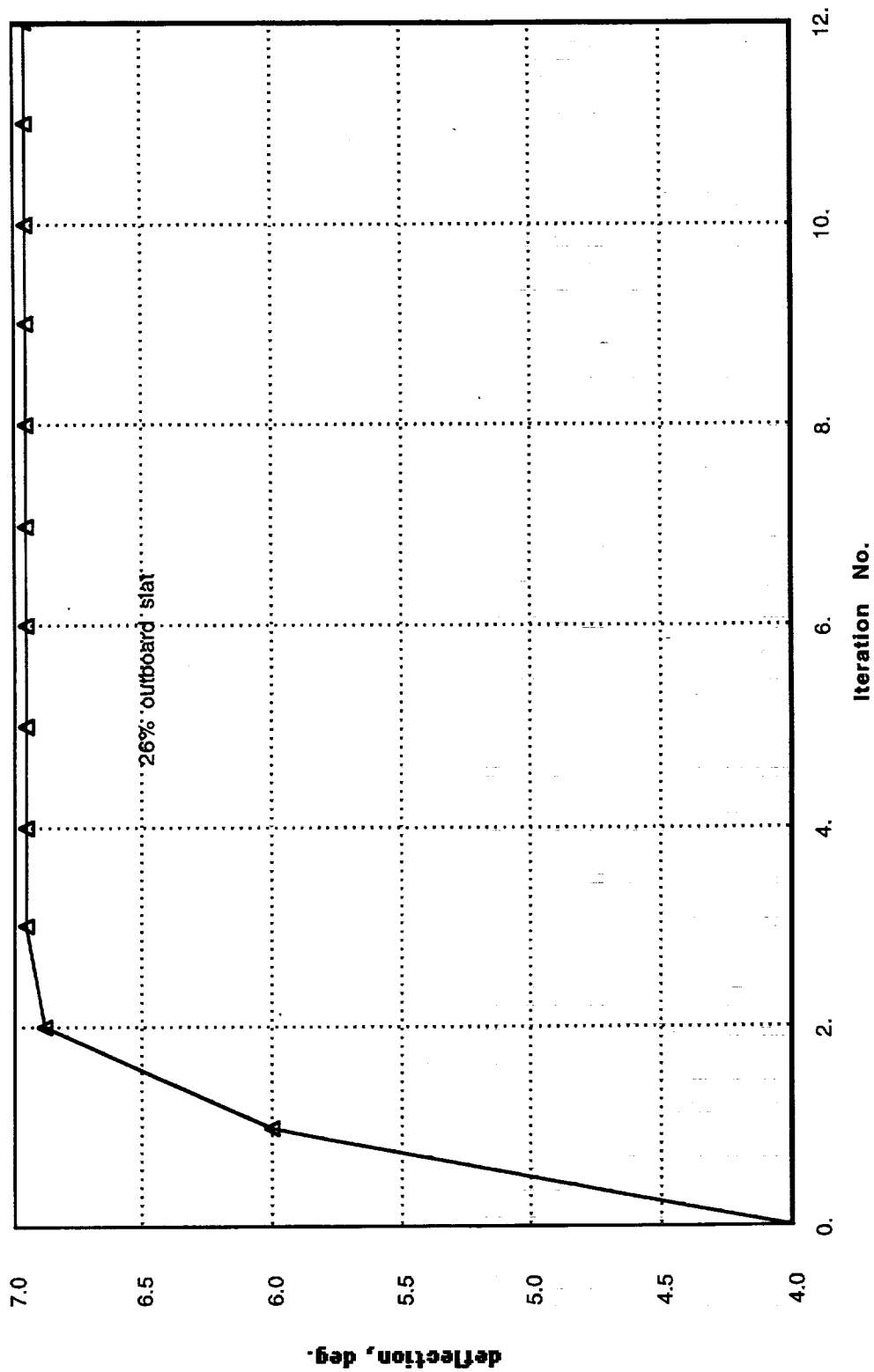


Approximate Wind Tunnel Model Geometry - Outboard Slat

The leading edge slat variation with optimization iteration appears very similar in shape to the lift-drag ratio curve with both reaching constant values at the third iteration. The plotting scale for the slat deflection is much coarser than that used for the flap deflection. If the flap deflection were plotted to the scale used here it would appear to be nearly constant. The final outboard slat deflection found for this approximate wind tunnel model geometry is considerably less than that found for the outboard slat included in the best set of four high lift devices (approximately 7.0 degrees compared with 8.8 degrees). Also note that this outboard slat reaches a constant value in three optimization iterations compared with eleven iterations for the outboard slat used in combination with three other high lift devices discussed previously.

Flap - Slat Optimization - TCA Baseline

M = 0.90, $\alpha = 4.0$ deg., Adjoint



.TCA Baseline with Improved Wind Tunnel Model Geometry

The third phase of the flap/slat optimization study using SYN87SB was conducted using an improved grid with better cell aspect ratios in critical areas of the flow and improved flap/slat modeling. Flap and slat deflections were achieved by rotation rather than shear and leading edge slats with variable percent chord length was possible. The flap and slat ends were still aligned with the free stream and the ends and gaps were not properly modeled. The flap ends and edges were blended into the adjacent wing over one cell width. Fully converged flow solutions could now be obtained when pressure peaks were present along the leading edge of the outboard wing panel with undeflected flaps and slats and multigridding. A brief experiment-CFD correlation was conducted to determine if the new code refinements improved the prediction of aerodynamic coefficients for the TCA baseline configuration at $M = 0.90$ with and without flap and slat deflections.

**TCA Baseline Outboard Flap/Slat Optimization
With Improved Geometry Modeling
M = 0.90**

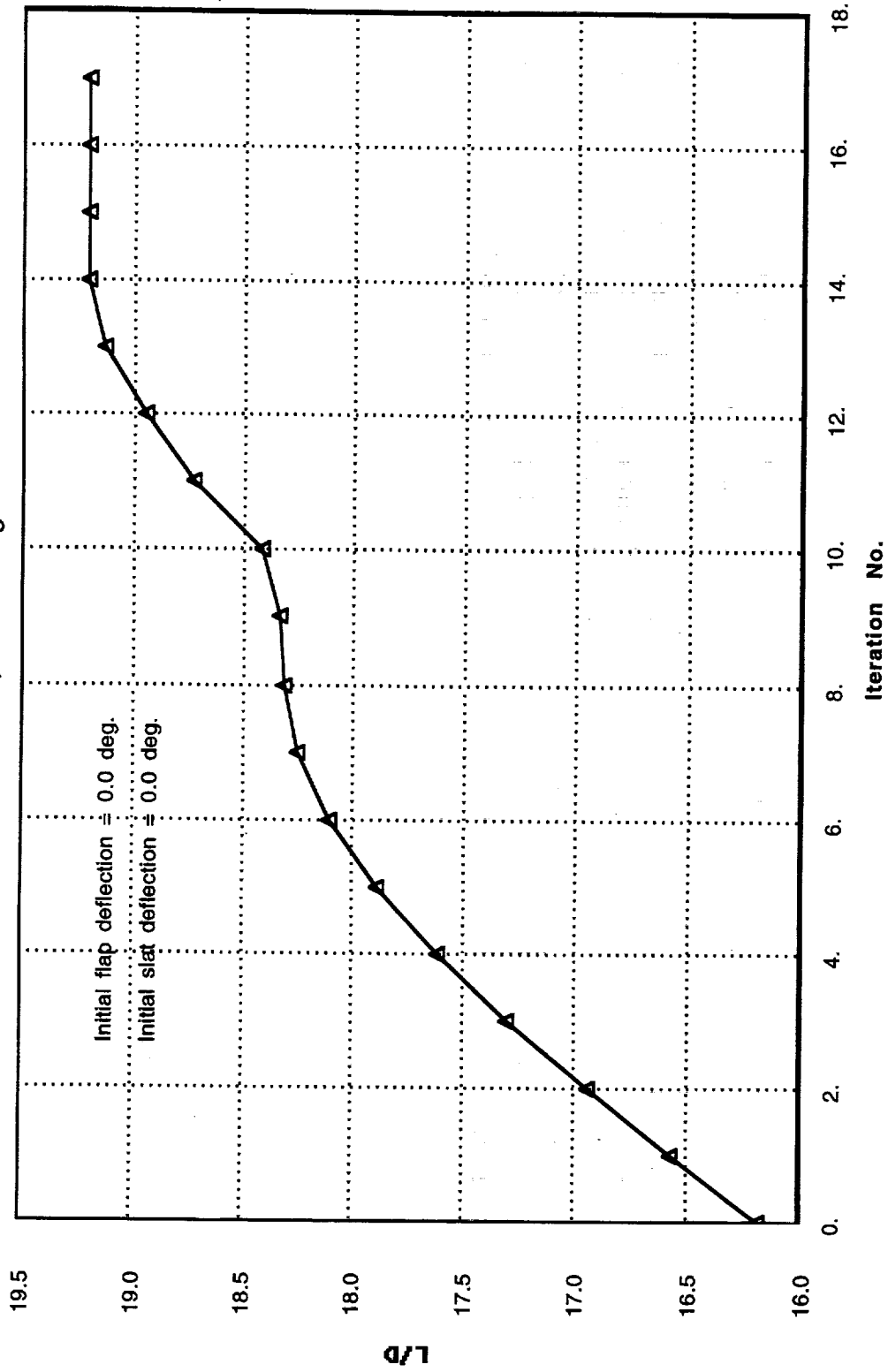
- Improved grid - better cell aspect ratios
- Slat with variable chord
- Flap/slat deflections using rotations instead of shear
- Better flow solver convergence for flow with leading edge pressure “peaks”
- Experiment-CFD correlation

Improved Wind Tunnel Model Geometry - L/D

The lift-drag ratio history obtained from use of SYN87SB with the improved grid and high lift device modeling is shown here. The optimization code was permitted to run 18 iterations instead of 12 as used previously because the flap and slat deflection was set to zero for the start of the optimization run placing the initial geometry farther from a valley in the design space. This means that the zeroth optimization iteration gives the lift-drag ratio for the baseline configuration with undeflected flap and slat. The lift-drag ratio for the TCA6 baseline configuration with undeflected flap and slat increased from 16.10 for the previous grid to 16.17 for the improved grid. The final lift-drag ratio after 17 iterations is 19.20. This compares with a final value of 19.09 for the original grid so the improvement in the lift-drag ratio is still approximately 3 units showing that the improved grid, deflections by rotation and more accurate slat modeling did not change the magnitude of the performance improvement from optimization. Note that 12 iterations would not have been enough to achieve a converged objective function when starting with zero deflections. The optimization code terminated after 17 iterations because no further improvement could be obtained.

Flap - Slat Optimization - TCA Baseline w/outboard flap/slat

M = 0.90, $\alpha = 4.0$ deg.



Initial flap deflection = 0.0 deg.

Initial slat deflection = 0.0 deg.

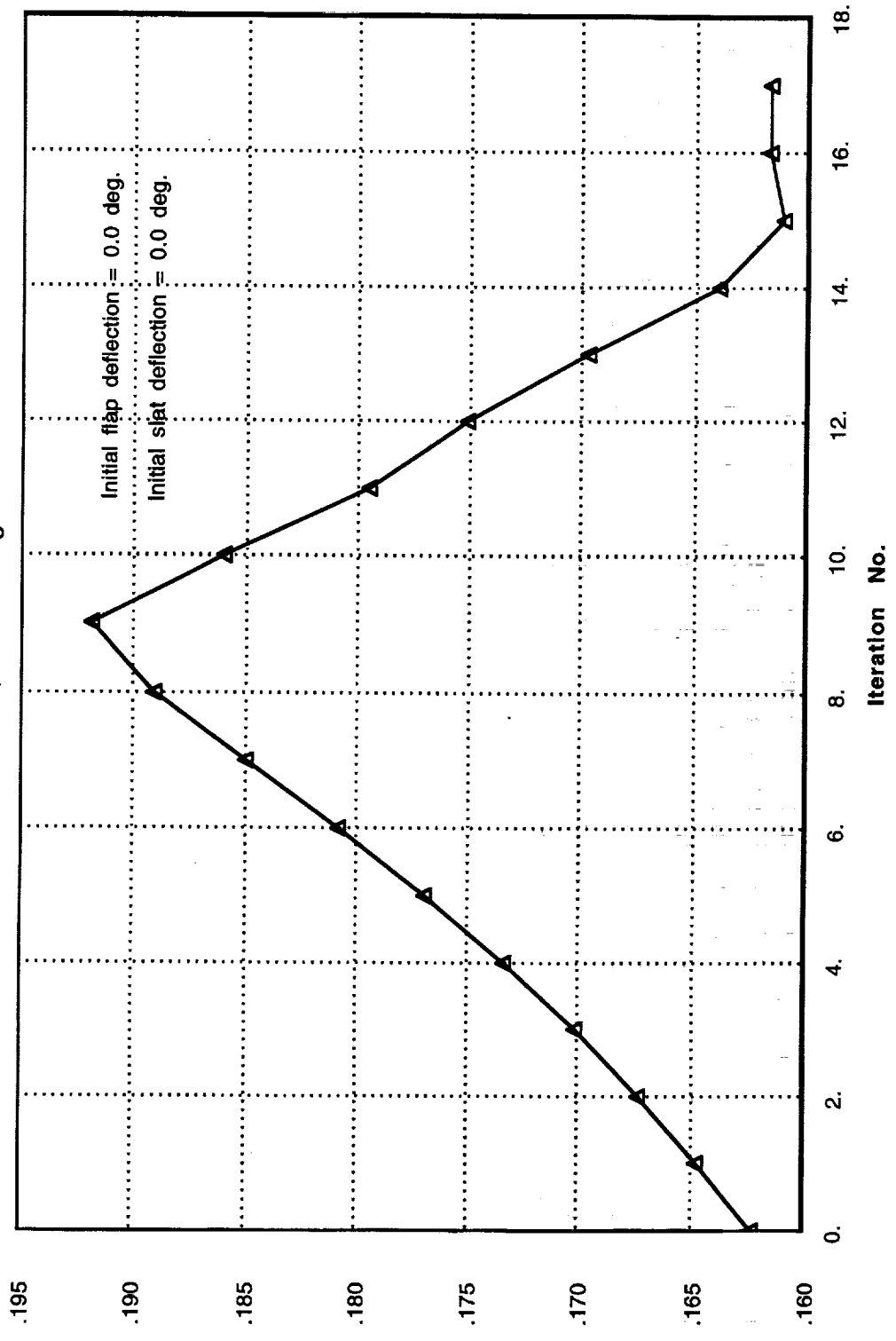
L/D

Improved Wind Tunnel Model Geometry - C_L

The lift coefficient variation with optimization iteration shows a fairly large increase followed by a decrease before converging to a value nearly equal to the initial coefficient. This trend is very different from that shown previously for the original grid with the less accurate modeling of the wind tunnel model flap and slat where the lift coefficient showed a small monotonic decrease over the 12 optimization iterations. Most of the difference in lift coefficient trend is due to starting optimization with zero deflections rather than to the grid and geometry modeling changes in the code. Note that the last three values of the lift coefficient are fairly constant compared with those for the less accurate geometry modeling shown previously. The large excursion in lift coefficient correlates with flap deflection changes to be shown later. These large parameter variations during the optimization cycle may be related to small errors in the gradients of the objective function with respect to deflection.

Flap - Slat Optimization - TCA Baseline w/outboard flap/slat

M = 0.90, $\alpha = 4.0$ deg.

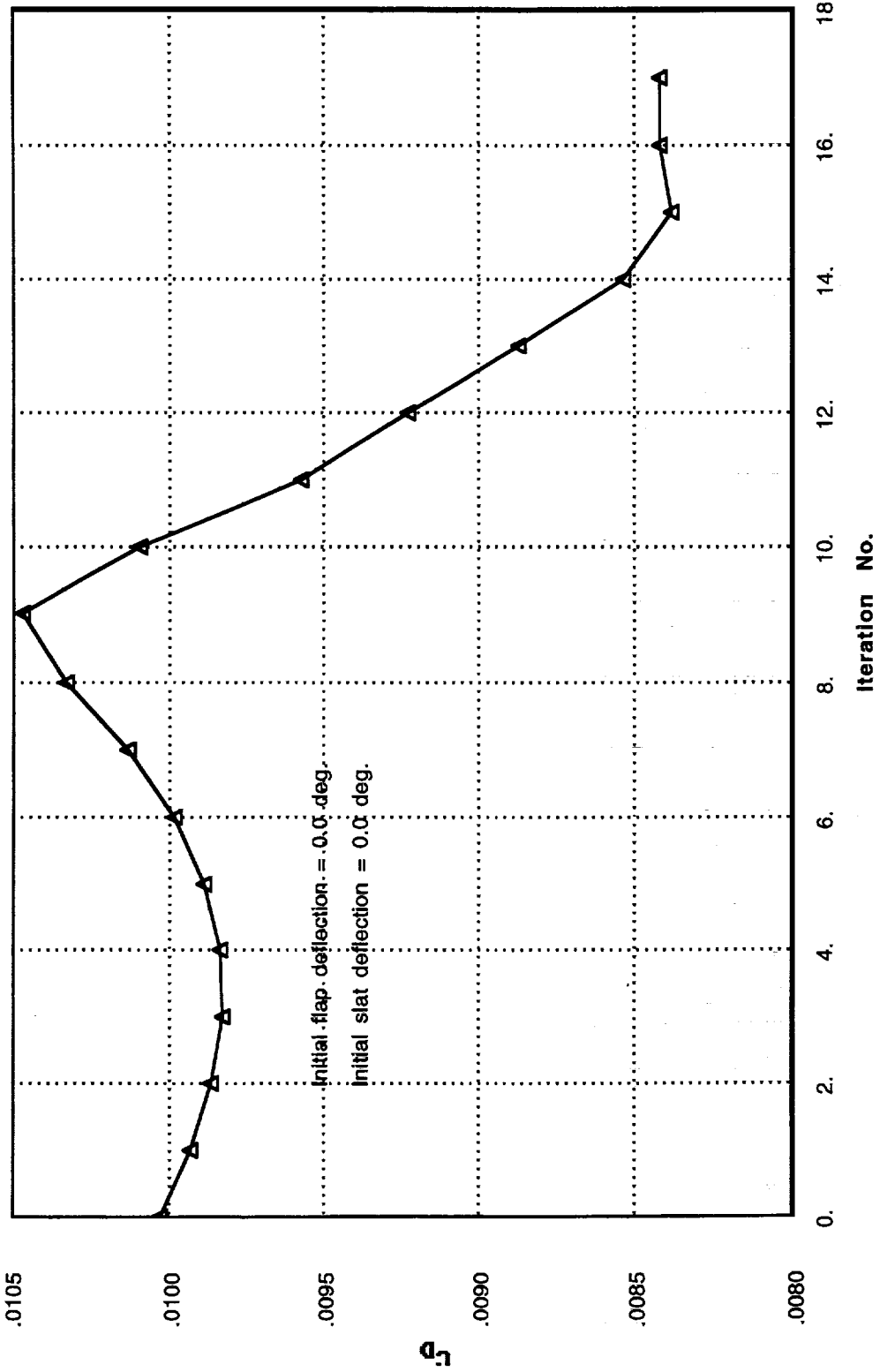


Improved Wind Tunnel Model Geometry - C_D

The drag coefficient variation with optimization iteration also shows nonmonotonic behavior with a converged value of approximately 84 counts. The 16 count improvement is nearly identical to that obtained with the original grid and less accurate slat geometry and deflection modeling and is 3 counts less than that obtained with four high lift devices. The greatest difference between this and the previous optimization run is the fact that more optimization iterations are needed to obtain a converged solution when the design variables are initialized to a value farther from the known optimum. If the designer has *a-priori* knowledge of the approximate location of a minima in the design space the design variables should be set accordingly unless the code is being tested to determine the effect of different initial values of the design variables on the final optimum.

Flap - Slat Optimization - TCA Baseline w/outboard flap/slat

M = 0.90, $\alpha = 4.0$ deg.

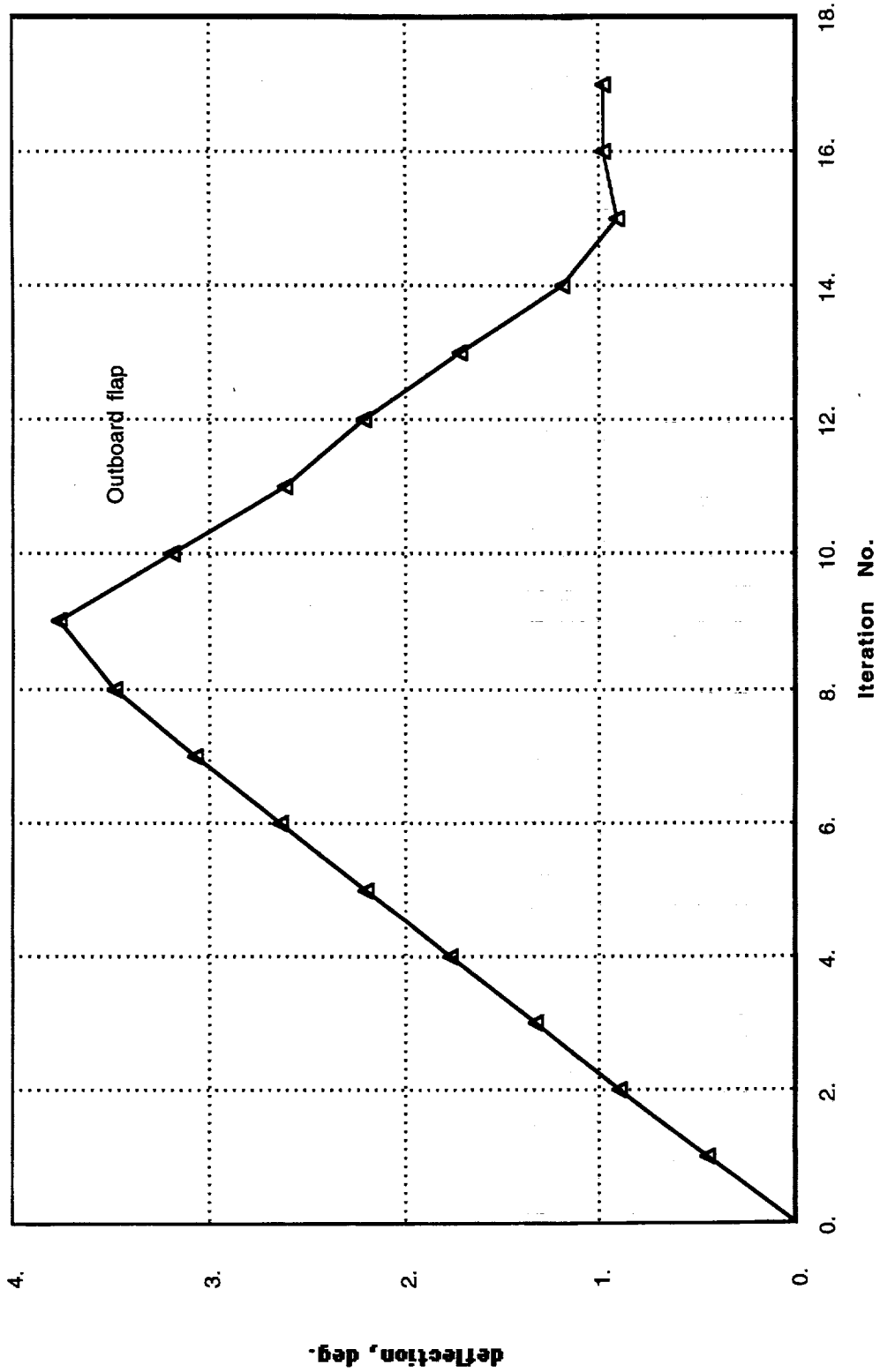


Improved Wind Tunnel Model Geometry - Outboard Flap

The outboard flap deflection shows a variation with optimization iteration very similar to that shown for the lift coefficient; a not very surprising result since lift coefficient should follow trailing edge deflection. Note that after the fairly large excursion of nearly 4 degrees the flap finally approaches a deflection very near the initial deflection of 1.0 degrees used with the old grid to achieve convergence of the flow solver. The final deflection here is also very close to the final deflection observed previously for both the four design variable case and the two design variable case with less accurate geometry modeling and the original grid.

Flap - Slat Optimization - TCA Baseline w/outboard flap/slat

M = 0.90, $\alpha = 4.0$ deg.

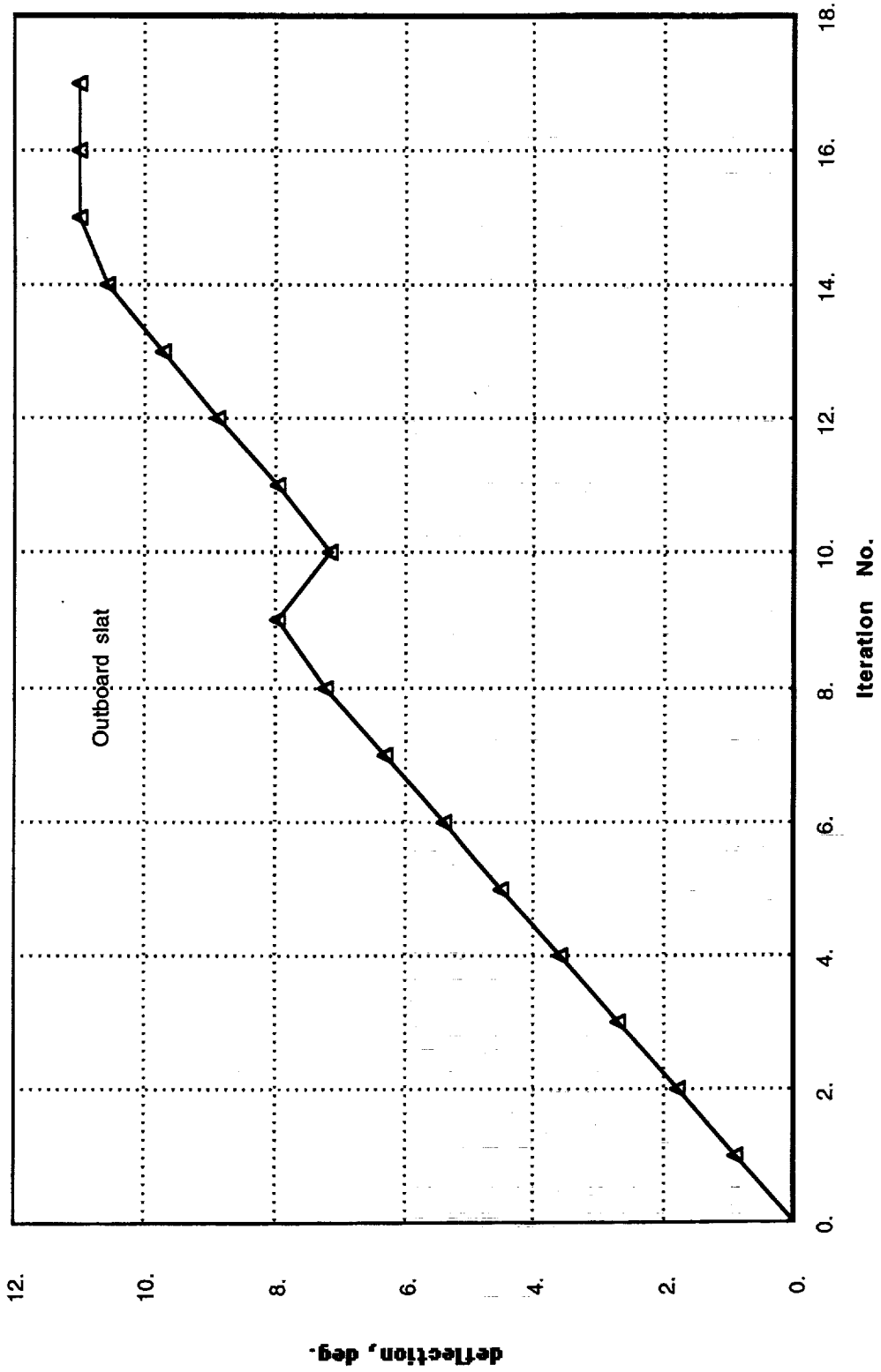


Improved Wind Tunnel Model Geometry - Outboard Slat

The outboard slat shows a final deflection for the improved grid and geometry modeling approximately 4 degrees greater than that found with the original geometry modeling and grid. This is quite surprising given the similar improvement in the objective function and drag reduction. This seems to indicate that the design space is fairly flat in the region of the optimum or has many local minima of approximately equal objective function value but with quite different values for the design variables. It also may imply that the design space has a very different shape with the new grid and geometry modeling. The local decrease in deflection at the 9th iteration correlates with the reversal in the lift coefficient curve shown previously but the relation between the two is not obvious.

Flap - Slat Optimization - TCA Baseline w/outboard flap/slat

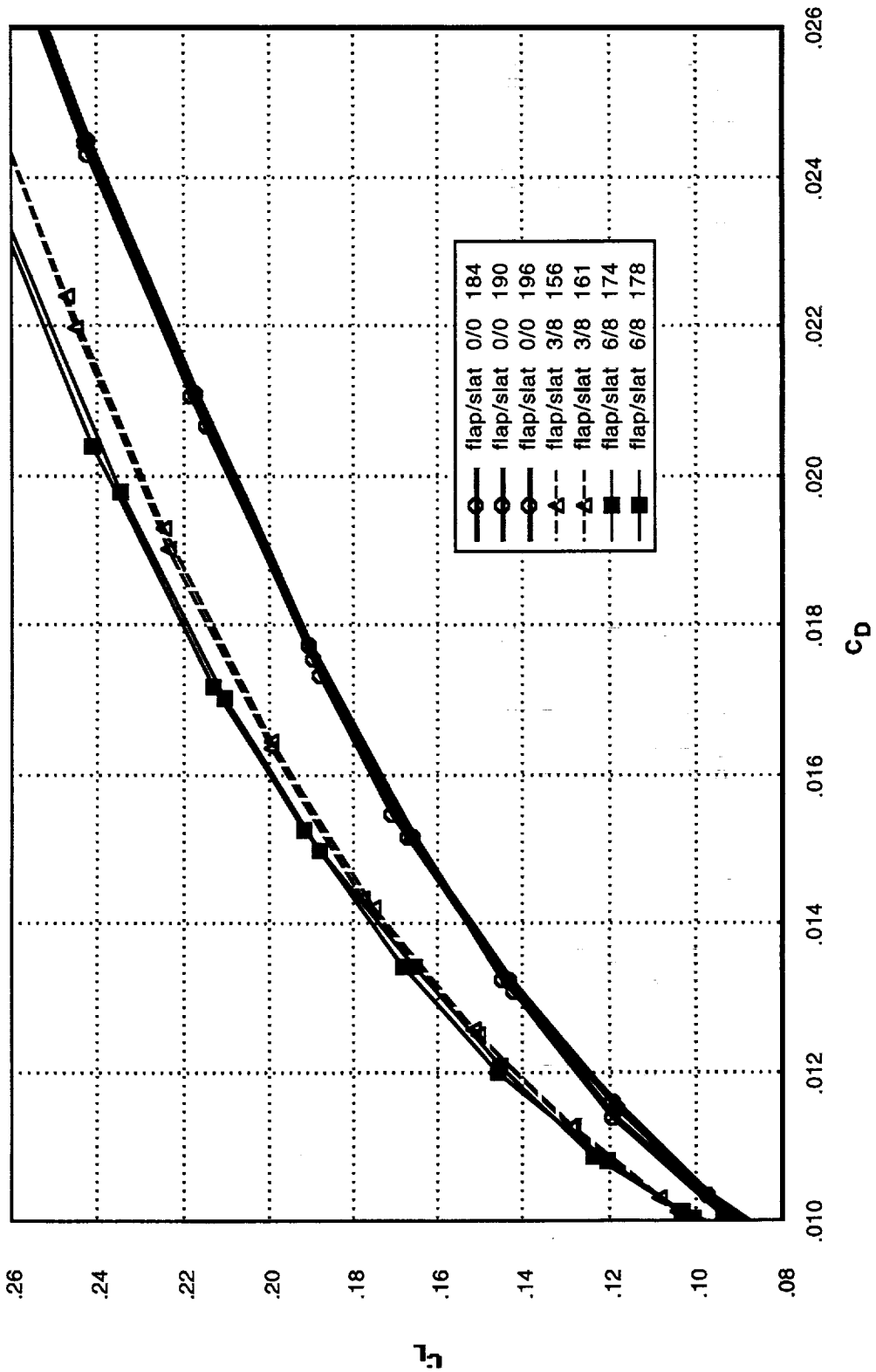
M = 0.90, $\alpha = 4.0$ deg.



TCA Baseline Wind Tunnel Drag Polars

A brief experiment-CFD correlation study was conducted to determine the accuracy of the SYN87SB drag polars and lift curves for the TCA baseline with and without flap and slat deflections and to assess the reliability of the optimization results shown previously. The wind tunnel drag polars shown here were obtained during testing of the baseline wing/body model in the Langley 16 Ft. transonic wind tunnel. This phase of the wind tunnel test was conducted to determine optimum outboard flap and slat deflections for Mach 0.90 and lift coefficients near 0.20 for the wing/body configuration. The wind tunnel data corresponds to the flight conditions and flap/slat geometry used during the third phase of the CFD optimization study discussed above. The drag data shown in this figure are for flap and slat deflections of 0/0, 3/6 and 6/8 degrees respectively. This data shows drag reductions ranging from approximately 19 counts at a lift coefficient of 0.16 (where the optimization runs were performed) to 27 counts for the 6/8 flap/slat combination at a lift coefficient of 0.20. Note that the repeatability is good for this range of lift coefficients. The wind tunnel run numbers are shown at the end of each line in the legend.

TCA Baseline - Test 484 - Langley 16 ft.
M = 0.90, Flap - Slat Study - wing/body

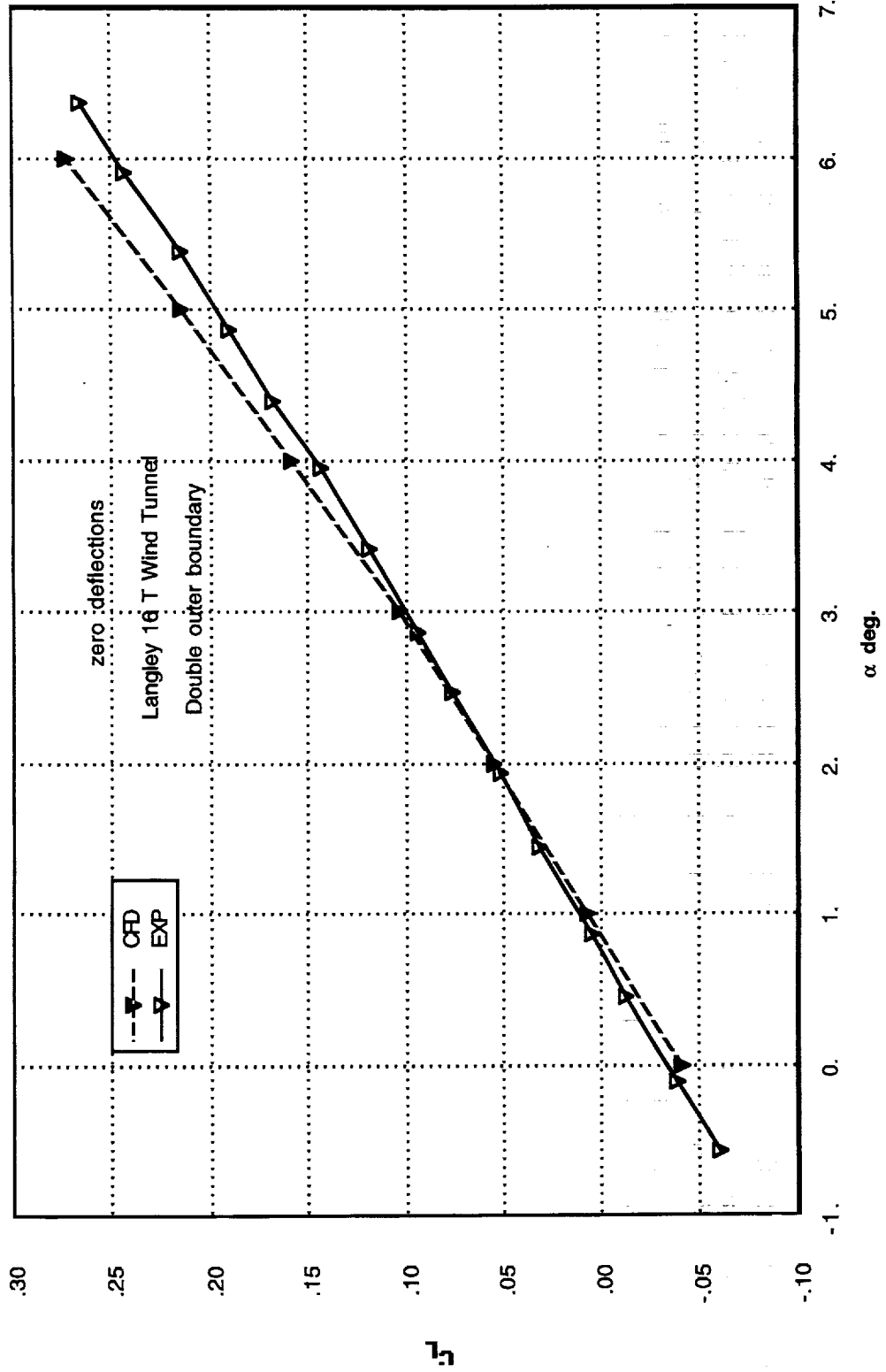


Experiment - CFD Correlation No Deflections - Lift curve

The computational lift curve has a larger slope and more nonlinearity than the experimental data for the flow conditions shown in this figure. The CFD data shown were obtained with the improved grid used for the third phase of the optimization study and with a larger outer boundary than that used for the previous calculations. Previous phases of this investigation have shown that the improved grid and larger outer boundaries have only small effects on the aerodynamic coefficients. Some of the increase in lift-curve slope is due to the inviscid flow of the CFD solutions but other inaccuracies must be present to explain the relatively poor correlation shown here. Of course it is always possible to blame the lack of agreement on the free-air boundary conditions and problems with the wind tunnel data such as angle of attack but analysis of these effects are beyond the scope of this work.

TCA Baseline Wing/Body Experiment-CFD Correlation

SYN87-SB, M = 0.90, Improved Grid

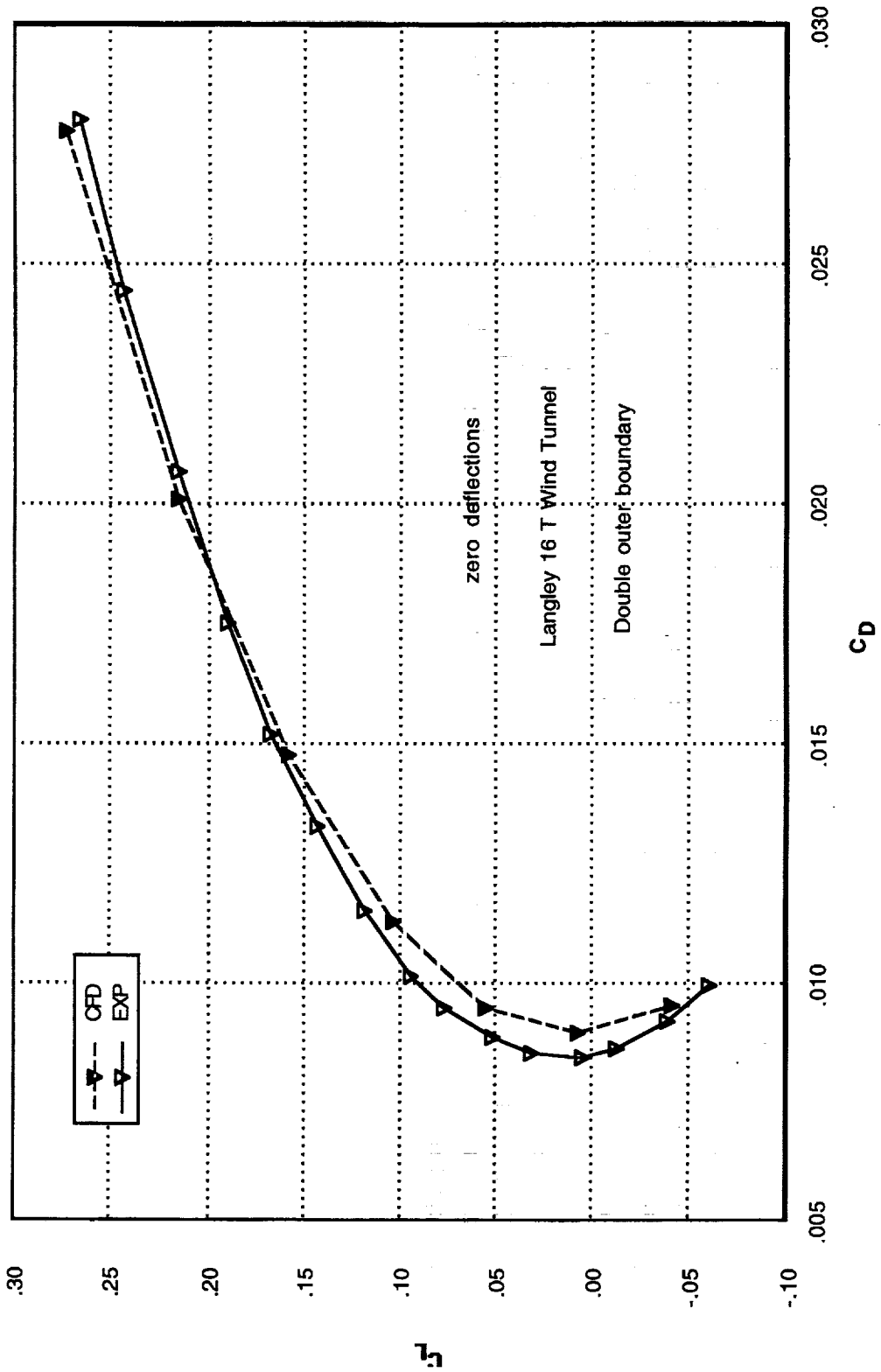


Experiment - CFD Correlation No Deflections - Drag Polars

The computational drag polar shows greater pressure drag at low lift and lower induced drag than the experimental data for the TCA baseline configuration with undeflected flap and slat. A skin friction drag coefficient of 85 counts has been added to the computational drag. The rotation of the computational polar with respect to the wind tunnel data is partly due to neglecting viscosity in the computations but other wind tunnel effects not properly modeled by CFD also effect this correlation.

TCA Baseline Wing/Body Experiment-CFD Correlation

SYN87-SB, M = 0.90, Improved Grid

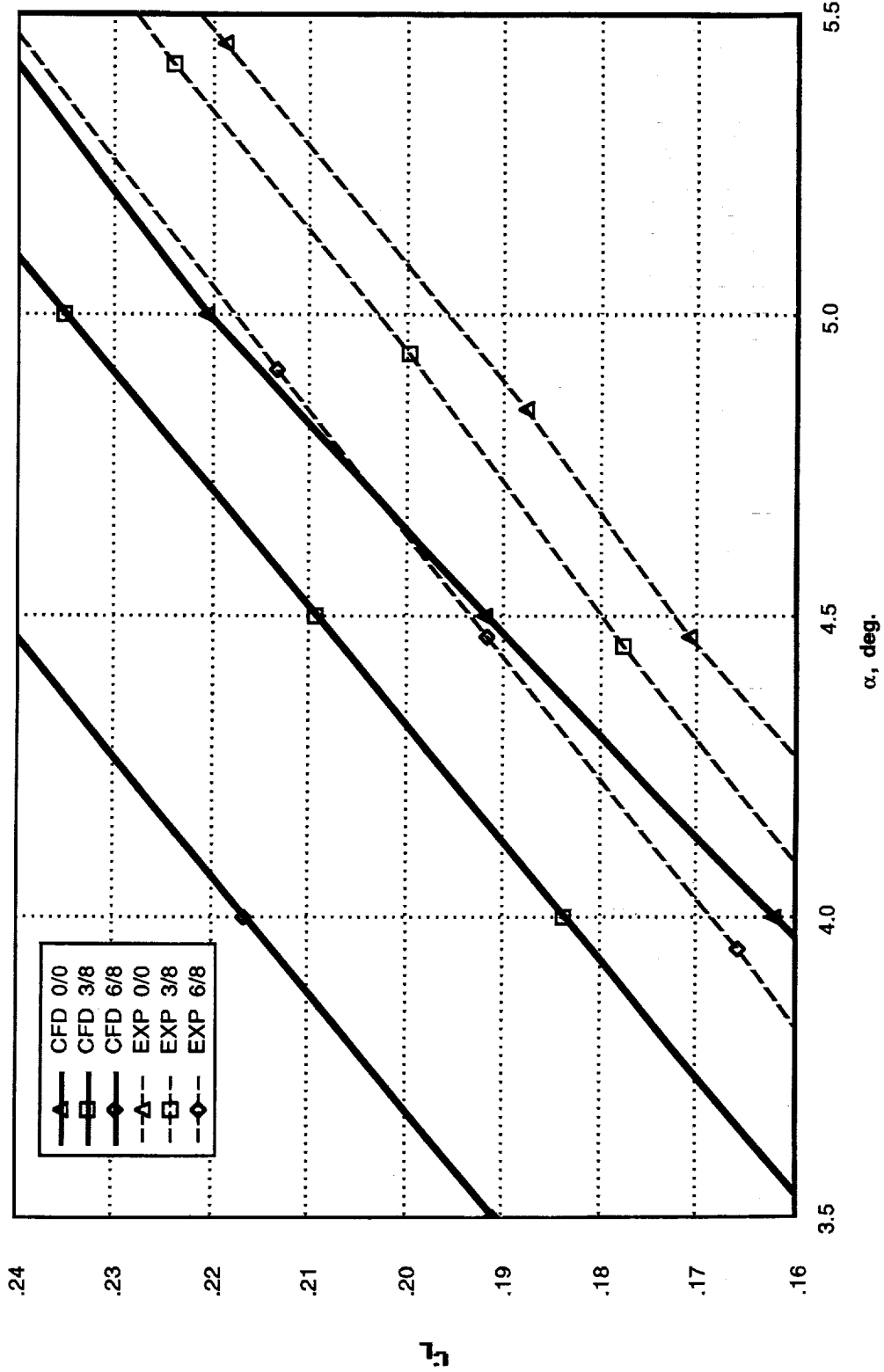


Experiment - CFD Correlation - Lift Curves - Expanded Scale

The two most obvious inaccuracies with the computational data shown here is the poor lift curve slope correlation with the experimental data for the case with undeflected flap and slat and the overprediction of the camber effect due to flap deflection. The experimental and computational lift curve slopes agree fairly well for the two cases with deflected high lift devices. The lack of CFD-experimental lift curve slope correlation for undeflected high lift devices is difficult to explain since the computational modeling of the wind tunnel model geometry is most accurate for that case. The computational lift curve shifts due to flap deflection for the 3/8 and 6/8 degree flap/slat deflections are approximately twice the experimental shifts due primarily to a lack of viscosity in the flow equations. This casts some doubt on the reliability of SYN87SB or any other code solving inviscid flow equations for flap/slat optimization.

TCA Baseline Wing/Body Experiment-CFD Correlation

SYN87-SB - M = 0.90

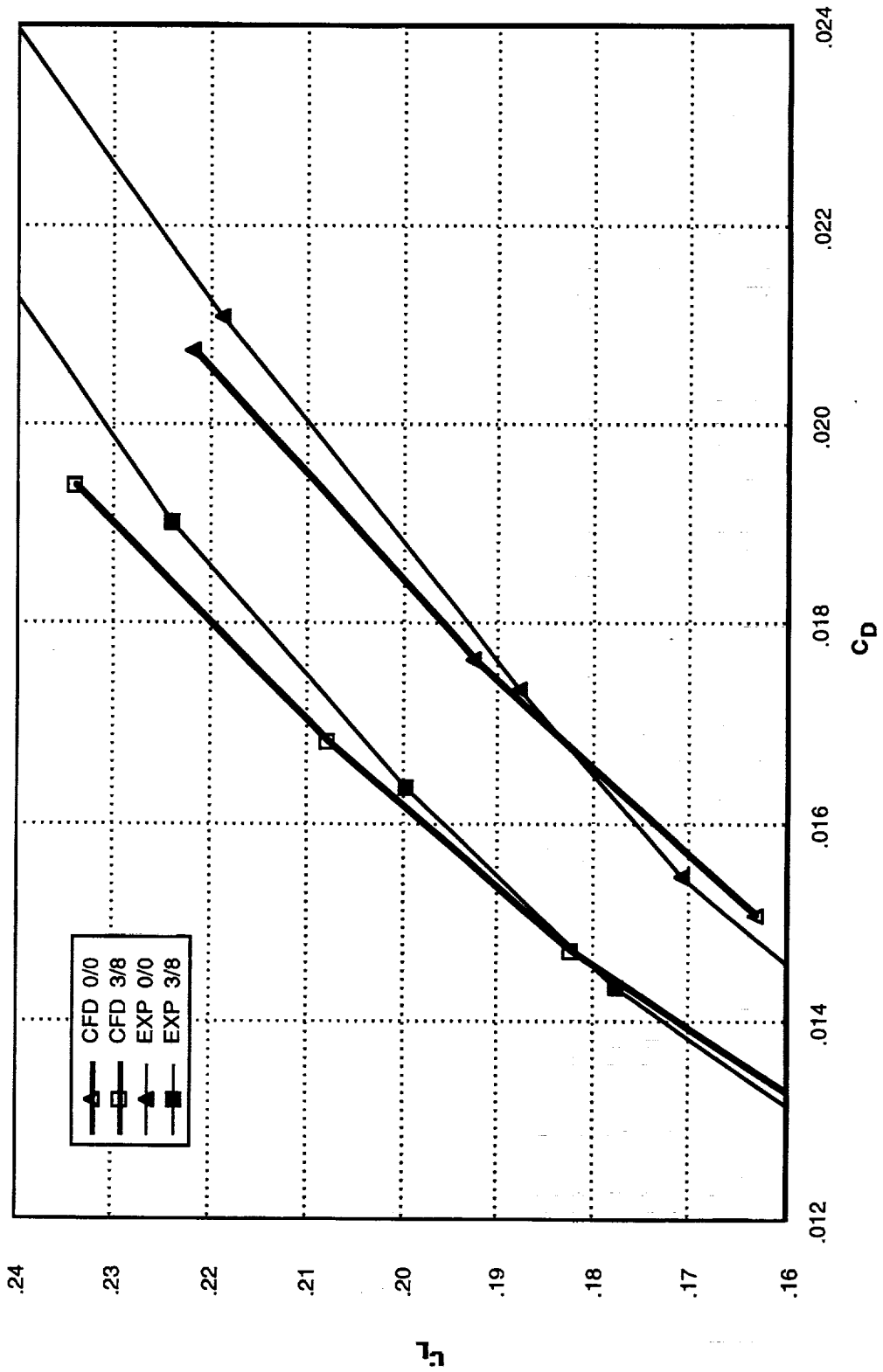


Experiment - CFD Correlation - Drag Polars - 0/0, 3/8

The CFD drag polars for no deflections and the 3.0 degree flap and 8.0 degree slat are rotated with respect to the experimental polars showing that the computations overpredict the viscous drag and underpredict the induced drag as discussed above. Despite the rotated computational polars the drag reduction due to deflection of the high lift devices agrees well with experiment for these deflections; a result that may be fortuitous. The computational drag coefficient includes a skin friction coefficient of 85 counts.

TCA Baseline Wing/Body Experiment-CFD Correlation

SYN87-SB, M = 0.90

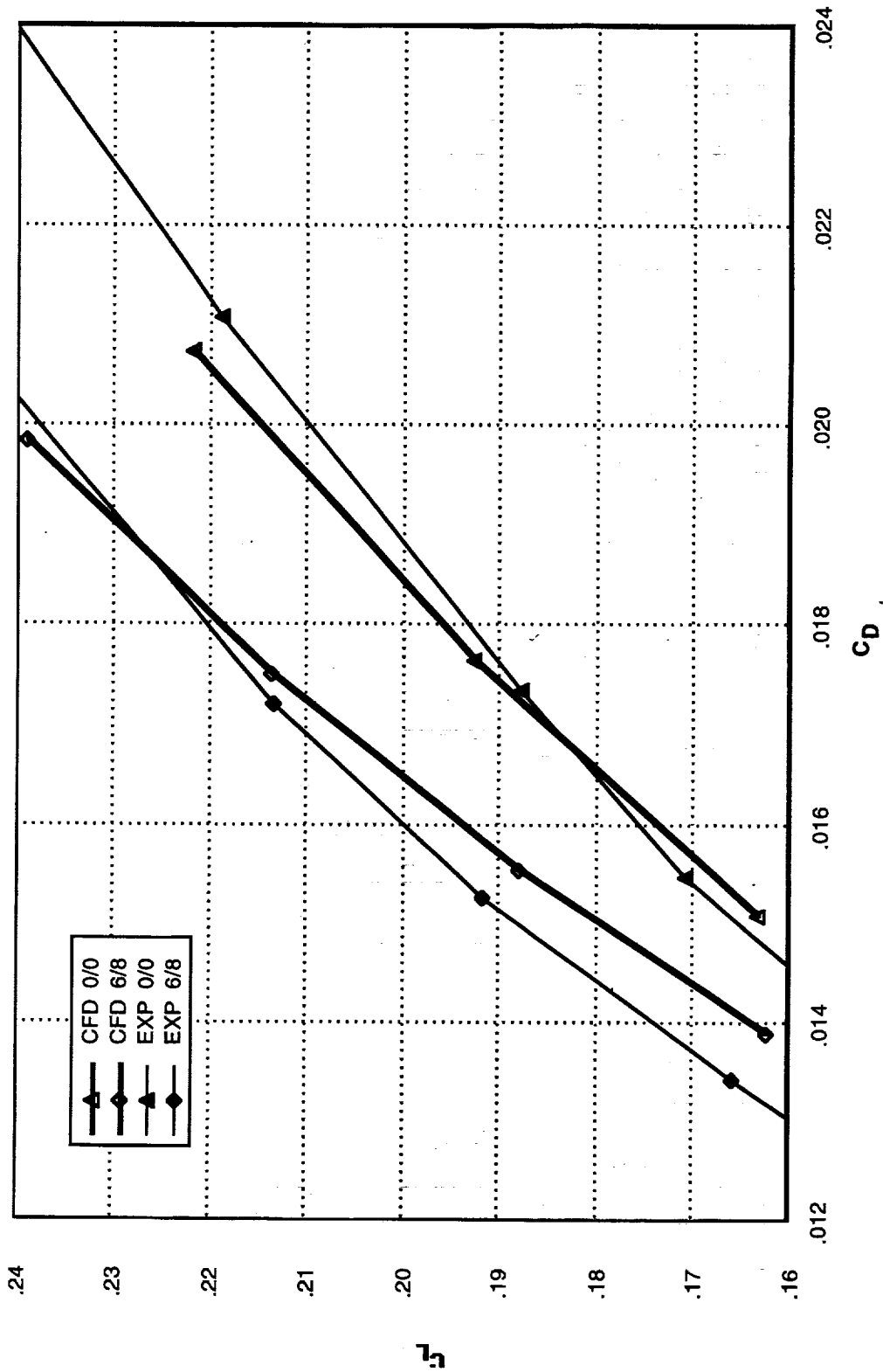


Experiment - CFD Correlation - Drag Polars - 0/0, 6/8

Computational and experimental drag polars for the baseline configuration with undeflected flap and slat and with flap and slat deflections of 6.0 and 8.0 degrees respectively are compared in this figure. The large rotation of the computational polar for deflected high lift devices gives an incorrect drag reduction due to deflections at all lift coefficient shown in the figure. The computational drag increment appears to increase more rapidly with lift coefficient than the corresponding experimental increment. The computational polar for the 6/8 flap/slat deflections shows considerably less induced drag than the experimental polars; a discrepancy that can probably be attributed to the lack of viscous terms in the flow equations.

TCA Baseline Wing/Body Experiment-CFD Correlation

SYN87-SB, M = 0.90



Concluding Remarks - Flap/Slat Optimization

This brief flap/slat optimization study at Mach 0.90 and an angle of attack of 4.0 degrees using an inviscid Euler equation solver has shown that in a somewhat ideal world a 3 unit improvement in the lift-drag ratio for the TCA baseline is possible by use of either inboard and outboard or just outboard high lift devices. In fact, the study has shown that with the geometry modeling and flow limitations used here, the inboard flap and slat are not needed. The largest improvement in the lift-drag ratio for the Ames optimized configuration was 2.50 units. The smaller improvement in the lift-drag ratio for the optimized configuration may be due to omitting the nacelles and diverters from the computational model.

A comparison of CFD with experimental data showed that the computational data generated by SYN87SB overpredicts the lift curve slope for the baseline configuration without flap and slat deflections and overpredicts the camber effect resulting from flap deflections. The optimum computational flap and slat deflections were found to be different from the wind tunnel optimum. However, the optimization results reported here are for an angle of attack of 4.0 degrees and it is well known that optimum deflections are a function of angle of attack so optimization performed at different angles of attack might find optimum deflections that agree more closely with the wind tunnel results.

Concluding Remarks

- SYN87-SB overpredicts lift curve slope for zero flap/slat deflections
- SYN87-SB drag reduction does not correlate with experiment for 6/8 flap/slat
- SYN87-SB drag reduction correlates with experiment for 3/8 flap/slat
- SYN87-SB optimum flap/slat deflections are different from experiment
- Best L/D improvement due to flap/slat optimization - 3 units
- Geometric approximations limit accuracy
- Inviscid flow limits accuracy
- Study should be repeated with SYN107-MB in NS mode

TCA6 Wing Optimization with Axisymmetric and Bifurcated Inlets

An optimization study was initiated to determine if a wing designed in the presence of axisymmetric nacelles would have better performance than a wing designed in the presence of bifurcated nacelles. The design results shown here have not met that goal because a serious grid warping limit was found with SYN107-MB which limited the magnitude of the wing shape perturbations necessary to achieve drag reductions. The largest drag reduction for the bifurcated nacelles was limited to approximately 1.5 counts. Hence, the results presented here must be considered preliminary but they may be indicative of the relative merits of axisymmetric and bifurcated nacelles. The TCA6 baseline geometry without empennage was used for this wing design study. The multi-block Euler/Navier-Stokes equation solver SYN107-MB was used at a Mach number of 2.40 and an angle of attack of 3.75 degrees giving a lift coefficient of approximately 0.10. When the grid warping limit is corrected the study will be completed. The optimization results shown here were obtained with 198 sine shape functions uniformly distributed over the upper and lower wing surfaces with 9 functions distributed from 10% to 90% chord in increments of 10% chord along each of 11 rows. The region of influence of the shape functions ranged from 101 inches from the centerline to the tip with linear lofting between rows.

**TCA6 Wing Optimization
Axisymmetric and Bifurcated Inlets**

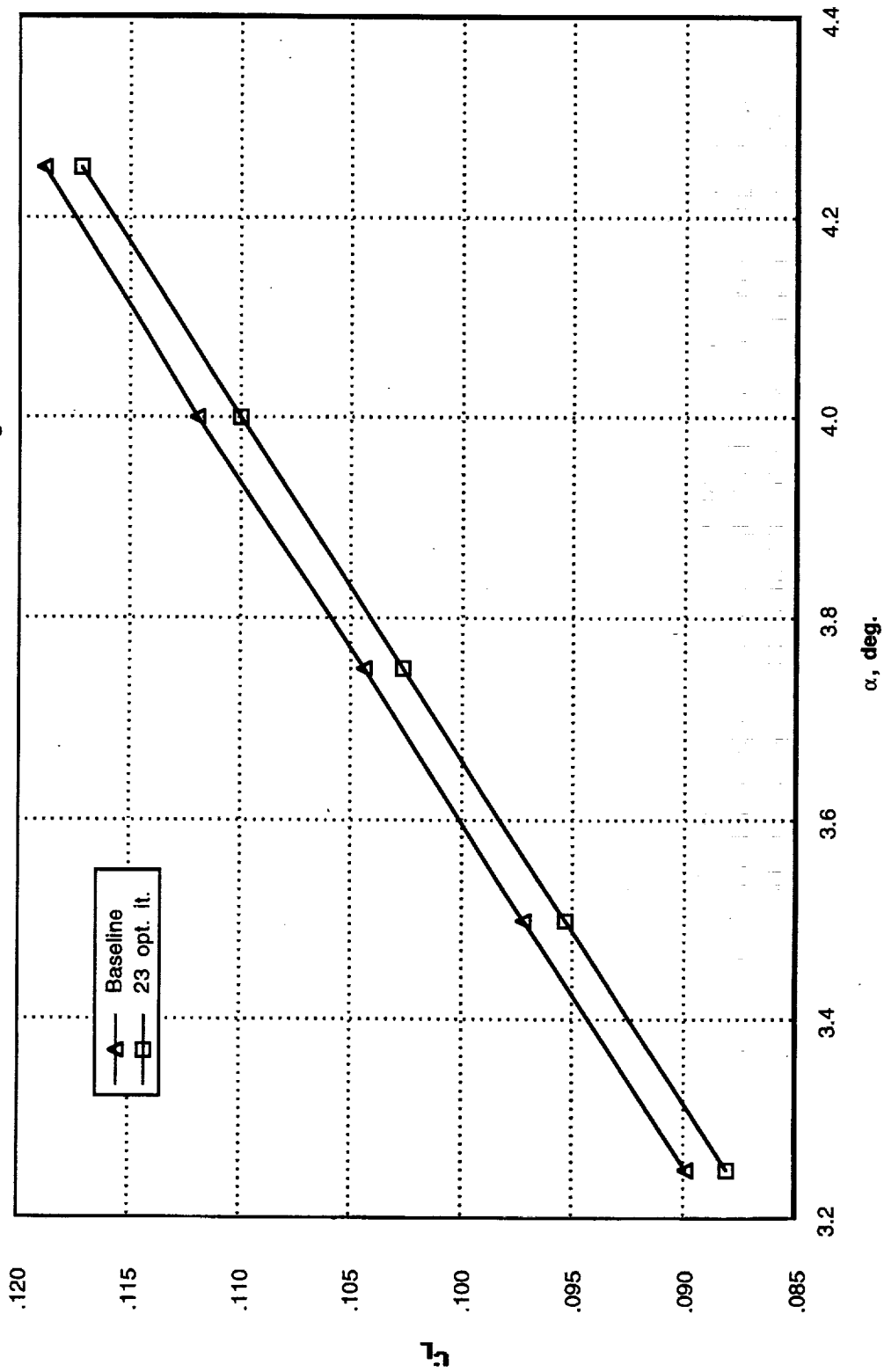
- SYN107-MB - Adjoint mode
- Sine shape functions
- 198 design variables - $x/c = .10, .20, \dots, .90$
- Linear lofting between perturbed wing stations - loft range 6 stations
- Wing design region 101 inches from centerline to tip
- Upper and lower wing surfaces designed
- Design conditions - $M = 2.40$, $\alpha = 3.75$ deg.

Lift Curves - Bifurcated Inlets

Lift curves for the TCA6 baseline configuration and an intermediate optimized configuration are shown here. Twenty three optimization iterations were performed before the grid warping limit was reached. Grid warping is applied to the grid blocks adjacent to the wing surface and causes negative cell volumes when the grid from the inner blocks intrudes into the next layer of blocks causing flow solver divergence. Grid warping is used to generate a new grid for each geometry perturbation generated by the optimization process. The lift curve after 23 iterations shows that the wing has been decambered by the addition of thickness to the lower surface between and upstream of the nacelles to capture the high pressures emanating from the nacelles and diverters on a forward facing slope with a corresponding decrease in drag. This decambering has been observed previously during development of the Ames optimized configuration (970103) designed by SYN87-SB using pseudo-nacelles.

TCA6 Optimization - Bifurcated Inlets

SYN107-MB, $M = 2.40$, $\alpha = 3.75$ deg.

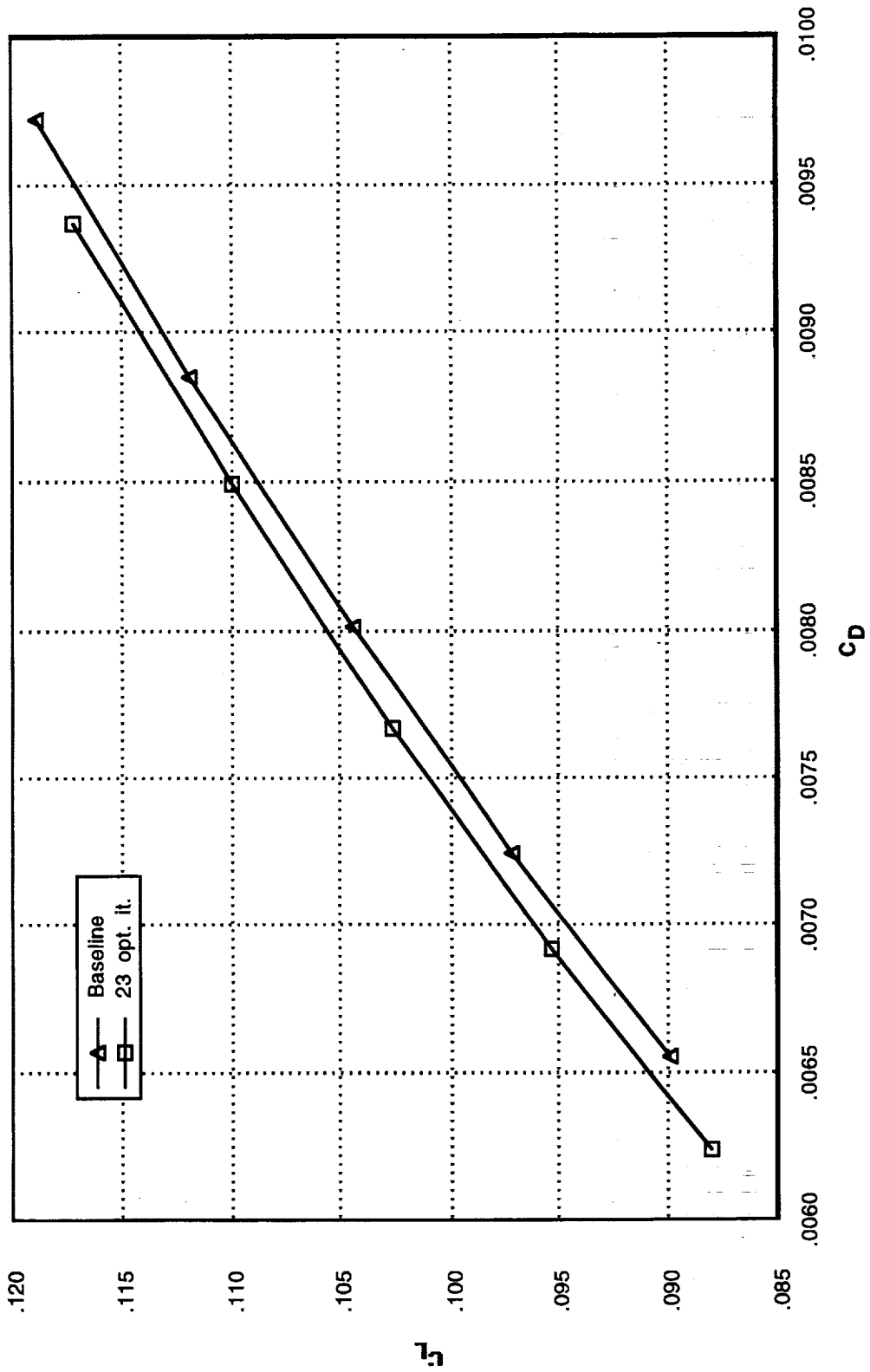


Drag Polars - Bifurcated Inlets

Drag polars for the intermediate optimized and baseline configurations show that the wing shape changes discussed above result in a fairly constant shift in the polar over the range of lift coefficients presented in the figure. More optimization iterations are needed to determine if a polar rotation will develop later in the design process.

TCA6 Optimization - Bifurcated Inlets

SYN107-MB, $M = 2.40$, $\alpha = 3.75$ deg.

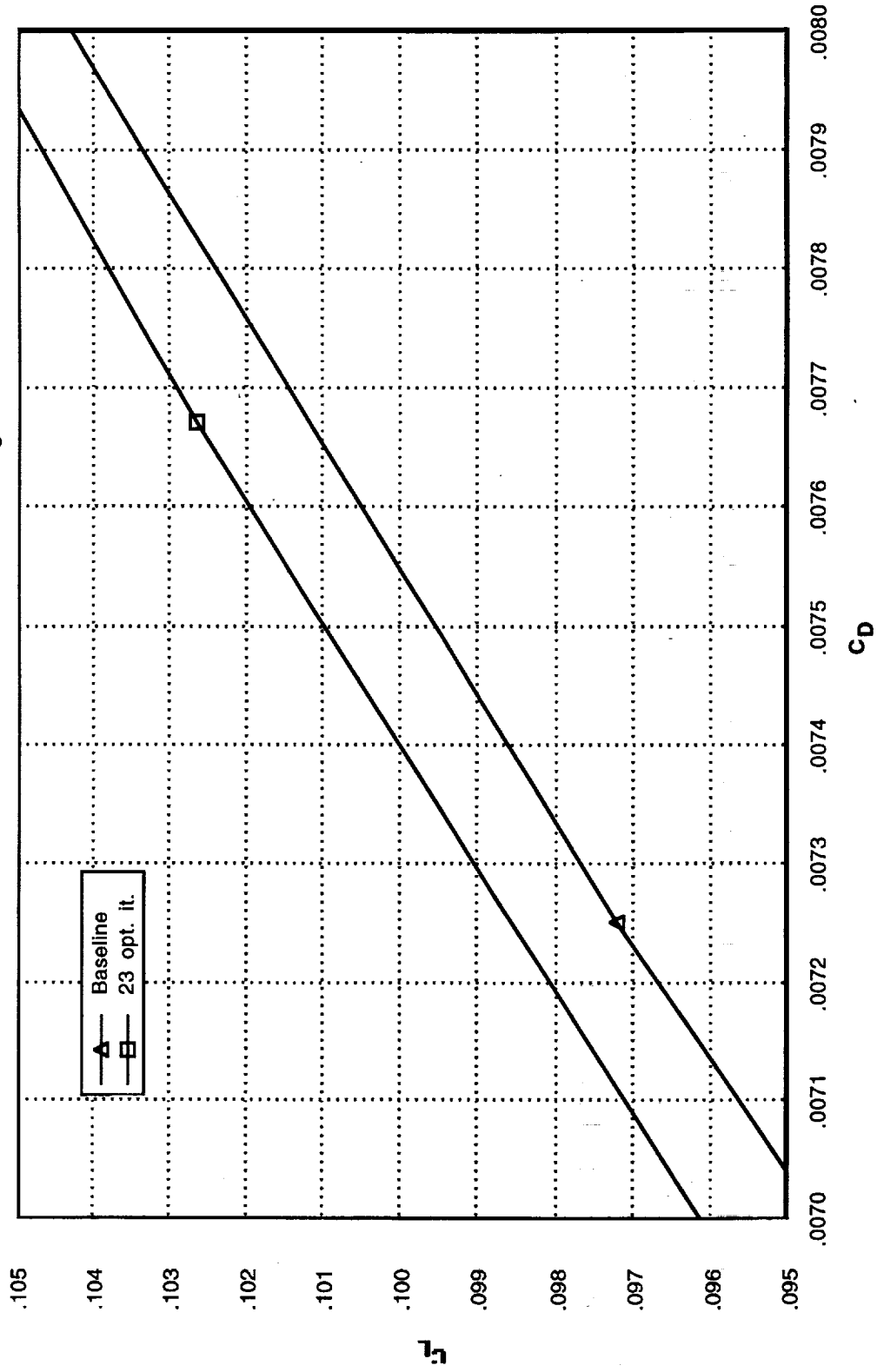


Drag Polars with Expanded Scale - Bifurcated Inlets

The drag polars shown in the previous figure have been plotted to an expanded scale so the drag reduction can be determined more precisely. Note that after 23 optimization iterations a drag reduction of approximately 1.5 counts has been achieved. The drag improvement has been achieved primarily by creating a "bump" on the lower surface of the wing between and upstream of the nacelles to generate a thrust component resulting from capturing the high pressures emanating from the nacelles and diverters on a forward facing slope.

TCA6 Optimization - Bifurcated Inlets

SYN107-MB, $M = 2.40$, $\alpha = 3.75$ deg.

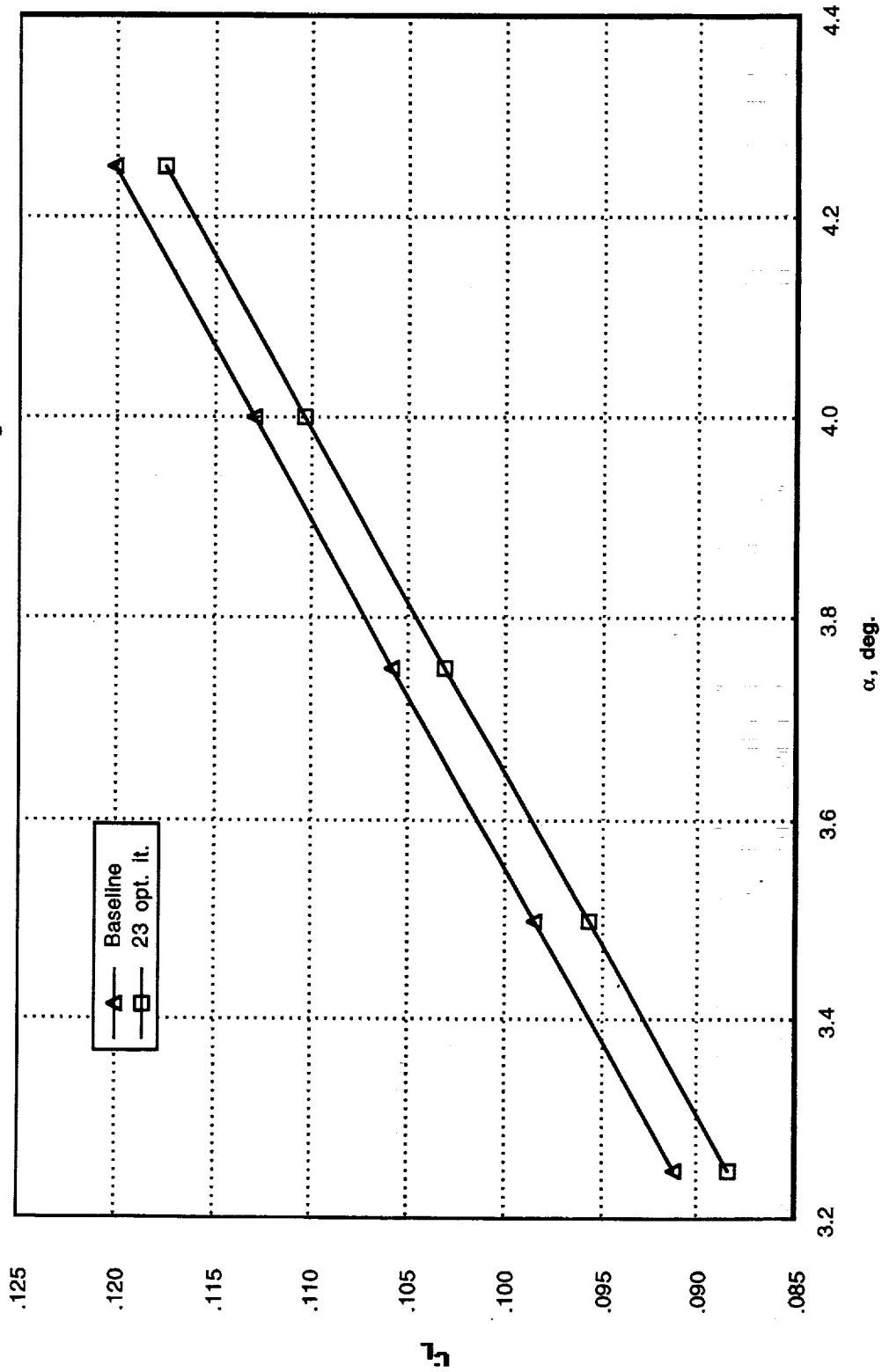


Lift Curves - Axisymmetric Inlets

The lift curves for the TCA baseline and an intermediate optimized configuration with axisymmetric inlets shows greater decambering of the wing than was observed for the bifurcated inlets. More decambering occurred because the pressures emanating from the nacelles and diverters are stronger for the axisymmetric inlets than for the bifurcated inlets resulting in the development of a larger "bump" between and upstream of the nacelles with a correspondingly greater lift reduction and a larger thrust component. The greater drag reduction will become more apparent when the drag polars are considered next.

TCA6 Optimization - Axisymmetric Inlets

SYN107-MB, $M = 2.40$, $\alpha = 3.75$ deg.

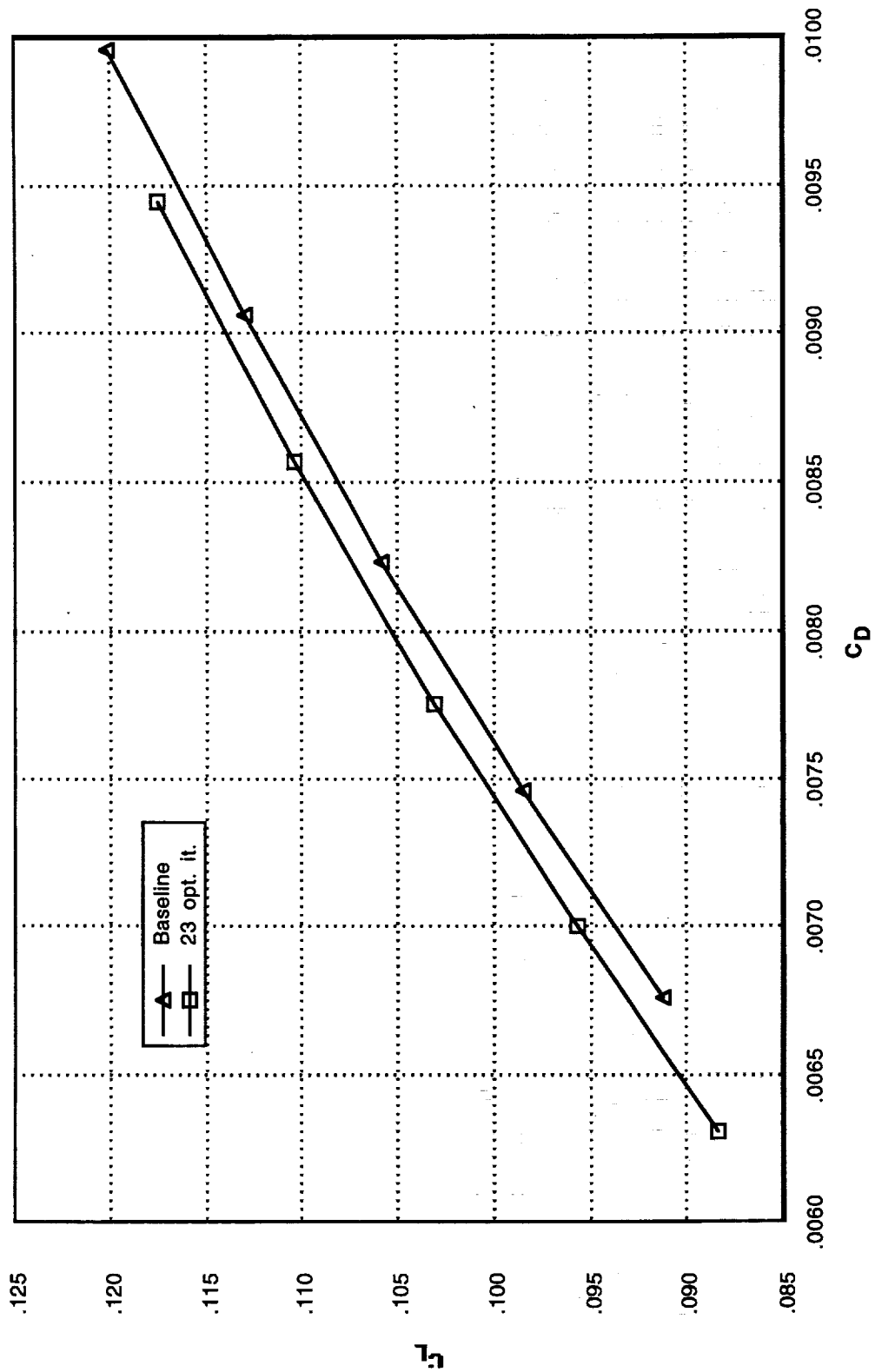


Drag Polars - Axisymmetric Inlets

The drag polars for the baseline and intermediate optimized configurations with axisymmetric inlets show a fairly constant drag reduction for the optimized configuration after 23 iterations indicating that the lower drag is primarily a reduction in pressure drag with little change in the induced drag.

TCA6 Optimization - Axisymmetric Inlets

SYN107-MB, $M = 2.40$, $\alpha = 3.75$ deg.

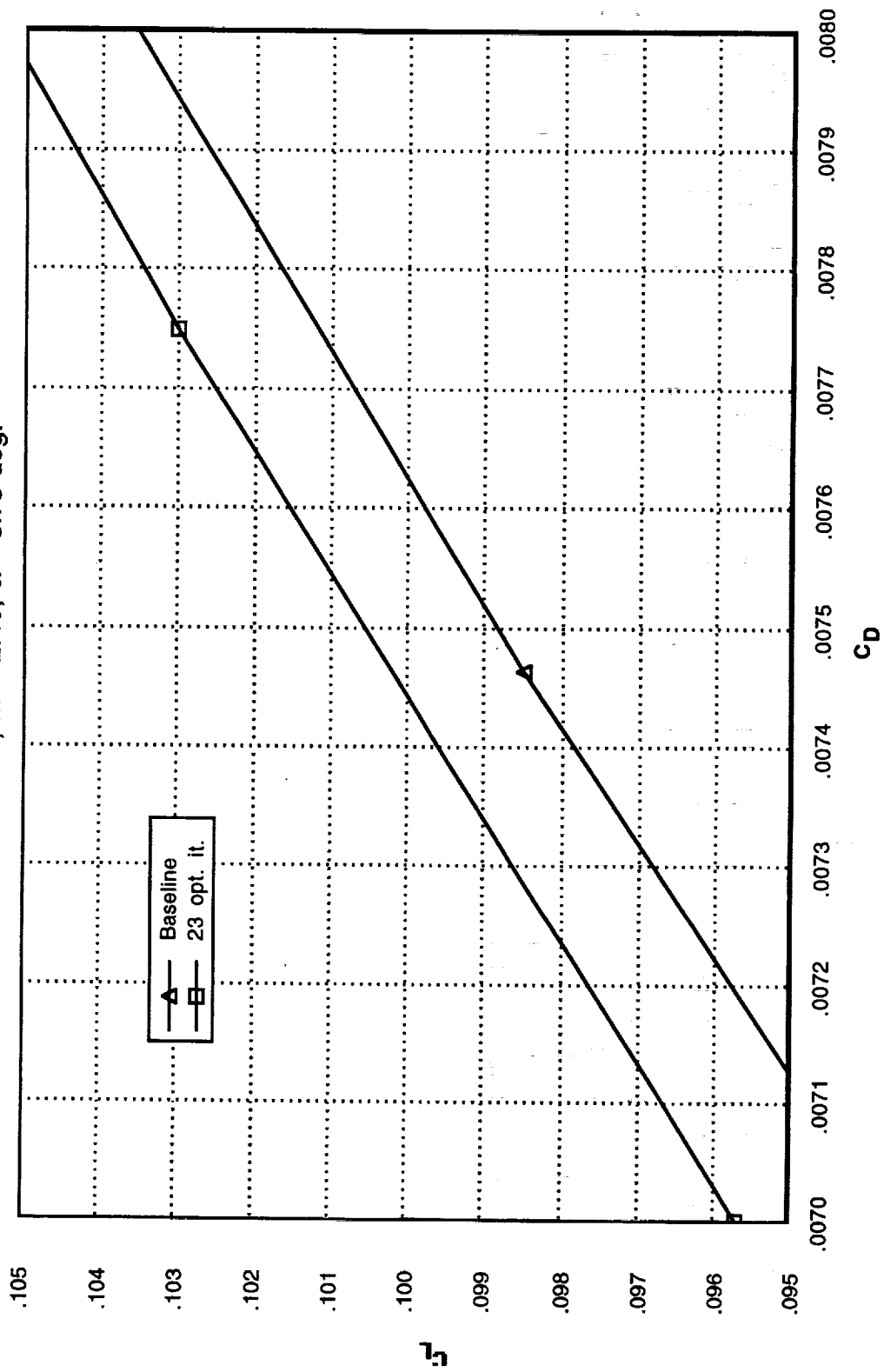


Drag Polars with Expanded Scale - Axisymmetric Inlets

The drag reduction for the intermediate optimized configuration with axisymmetric inlets is approximately 1.8 counts after 23 optimization iterations. This compares with a drag reduction of 1.5 counts for the optimized configuration with bifurcated inlets after the same number of iterations. Note that the drag coefficient at a lift coefficient of 0.10 for the optimized configuration with axisymmetric inlets is 74.5 counts compared with 74 counts for the optimized configuration with bifurcated inlets. This gives a slightly higher lift-drag ratio for the configuration with bifurcated inlets at this lift coefficient and stage of optimization. While it is risky to draw conclusions from this brief optimization study it appears that the higher initial drag for the configuration with axisymmetric inlets may be offset by a larger drag reduction. This may allow the choice of inlet type to be based on non-aerodynamic factors.

TCA6 Optimization - Axisymmetric Inlets

SYN107-MB, $M = 2.40$, $\alpha = 3.75$ deg.

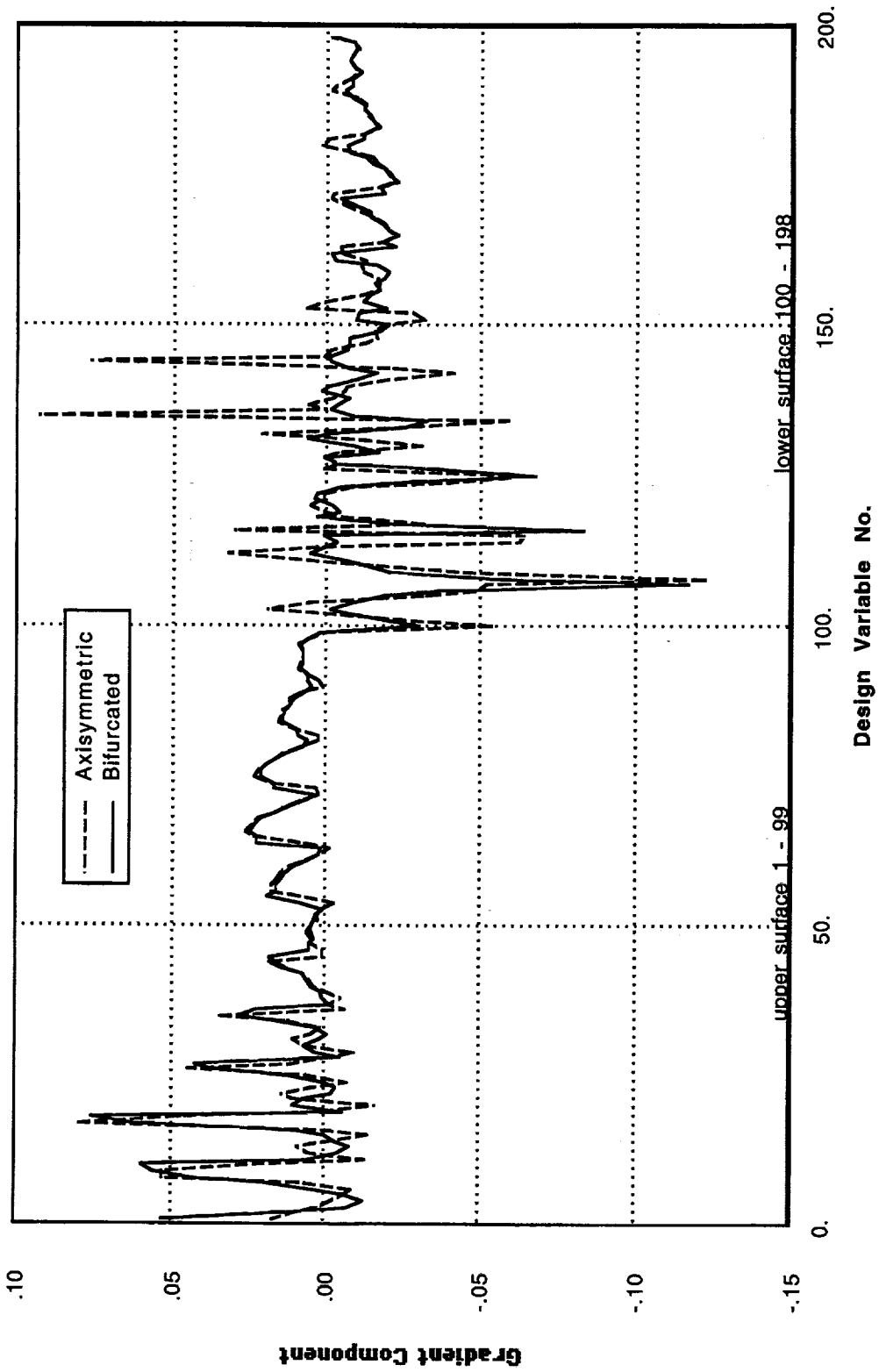


Gradient Comparison - Axisymmetric and Bifurcated Inlets

The gradient components for the intermediate optimized configurations with axisymmetric and bifurcated inlets calculated by SYN107-MB using adjoint mode and SIN2 shape functions are compared after 23 iterations. Design variables 1 through 99 are located on the upper surface of the wing while 100 through 198 are on the lower surface. Design variable 1 through 9 are located at the 6th wing defining station and 91 through 99 are located at the tip. The shape function rows were located every third wing station except near the tip with linear lofting 3 stations in each direction giving a total of 11 shape function rows. The wing had 38 defining stations from centerline to tip. Note that the gradient components for the two inlet types correlate well on the upper surface but large differences are observed over the inboard region of the lower surface. The differences noted near the nacelles on the lower surface are due to the pressure differences associated with the two inlet types.

TCA6 Gradient Comparison - SYN107-MB - Adjoint - SIN2

M = 2.40, $\alpha = 3.75$ deg., 23 Optimization Iterations



REPORT DOCUMENTATION PAGE			Form Approved OMB No. 0704-0188	
Public reporting burden for this collection of information is estimated to average 1 hour per response, including the time for reviewing instructions, searching existing data sources, gathering and maintaining the data needed, and completing and reviewing the collection of information. Send comments regarding this burden estimate or any other aspect of this collection of information, including suggestions for reducing this burden, to Washington Headquarters Services, Directorate for Information Operations and Reports, 1215 Jefferson Davis Highway, Suite 1204, Arlington, VA 22202-4302, and to the Office of Management and Budget, Paperwork Reduction Project (0704-0188), Washington, DC 20503.				
1. AGENCY USE ONLY (Leave blank)	2. REPORT DATE December 1999	3. REPORT TYPE AND DATES COVERED Conference Publication		
4. TITLE AND SUBTITLE 1998 NASA High-Speed Research Program Aerodynamic Performance Workshop <i>Volume I—Configuration Aerodynamics</i>			5. FUNDING NUMBERS WU 537-07	
6. AUTHOR(S) S. Naomi McMillin, Editor				
7. PERFORMING ORGANIZATION NAME(S) AND ADDRESS(ES) NASA Langley Research Center Hampton, VA 23681-2199			8. PERFORMING ORGANIZATION REPORT NUMBER L-17758A	
9. SPONSORING/MONITORING AGENCY NAME(S) AND ADDRESS(ES) National Aeronautics and Space Administration Washington, DC 20546-0001			10. SPONSORING/MONITORING AGENCY REPORT NUMBER NASA/CP-1999-209692/ VOL1/PT1	
11. SUPPLEMENTARY NOTES				
12a. DISTRIBUTION/AVAILABILITY STATEMENT Unclassified—Unlimited Subject Category 02 Availability: NASA CASI (301) 621-0390			12b. DISTRIBUTION CODE Distribution: Nonstandard	
13. ABSTRACT (Maximum 200 words) NASA's High-Speed Research Program sponsored the 1998 Aerodynamic Performance Technical Review on February 9–13, in Los Angeles, California. The review was designed to bring together NASA and industry High-Speed Civil Transport (HSCT) Aerodynamic Performance technology development participants in areas of: Configuration Aerodynamics (transonic and supersonic cruise drag prediction and minimization), High-Lift, and Flight Controls. The review objectives were to: (1) report the progress and status of HSCT aerodynamic performance technology development; (2) disseminate this technology within the appropriate technical communities; and (3) promote synergy among the scientists and engineers working HSCT aerodynamics. In particular, single- and multi-point optimized HSCT configurations, HSCT high-lift system performance predictions, and HSCT simulation results were presented along with executive summaries for all the Aerodynamic Performance technology areas. The HSR Aerodynamic Performance Technical Review was held simultaneously with the annual review of the following airframe technology areas: Materials and Structures, Environmental Impact, Flight Deck, and Technology Integration. Thus, a fourth objective of the Review was to promote synergy between the Aerodynamic Performance technology area and the other technology areas of the HSR Program.				
14. SUBJECT TERMS High-Speed Research; High-Speed Civil Transport			15. NUMBER OF PAGES 941	
			16. PRICE CODE A99	
17. SECURITY CLASSIFICATION OF REPORT Unclassified	18. SECURITY CLASSIFICATION OF THIS PAGE Unclassified	19. SECURITY CLASSIFICATION OF ABSTRACT Unclassified	20. LIMITATION OF ABSTRACT UL	



